Karlsruhe Institute of Technology

Accurate calibration of the Raman system for the Karlsruhe Tritium Neutrino Experiment

Zur Erlangung des akademischen Grades eines
DOKTORS DER NATURWISSENSCHAFTEN
von der Fakultät für Physik
des Karlsruher Instituts für Technologie
genehmigte
DISSERTATION
von

Diplom-Physiker
Magnus Richard Hermann Schlösser
aus Siegburg (NRW)

Referent: Prof. Dr. G. Drexlin
Institut für Experimentelle Kernphysik, KIT

Korreferent: Prof. Dr. H. H. Telle
Department of Physics, Swansea University (Wales)

Tag der mündlichen Prüfung: 26. April 2013

Contents

Contents iv

List of Figures viii

List of Tables x

Zusammenfassung 1

Abstract 3

1 Introduction 5
- 1.1 Discovery of the neutrino . . . 6
- 1.2 Neutrino oscillations . . . 7
- 1.3 Role of massive neutrinos . . . 13
  - 1.3.1 Particle Physics . . . 13
  - 1.3.2 Cosmology . . . 16
- 1.4 Measurement of the neutrino mass . . . 18
  - 1.4.1 Indirect methods . . . 18
  - 1.4.2 Direct methods . . . 22

2 The KATRIN Experiment 29
- 2.1 Tritium β-decay experiments . . . 29
  - 2.1.1 Tritium β-decay and the neutrino mass . . . 29
  - 2.1.2 The MAC-E-Filter measurement principle . . . 31
  - 2.1.3 Results of previous neutrino mass experiments at Mainz and Troitsk 33
- 2.2 The Karlsruhe Tritium Neutrino Experiment (KATRIN) . . . 34
  - 2.2.1 Projected sensitivity on neutrino mass . . . 34
  - 2.2.2 Experimental overview . . . 35
- 2.3 Properties of the WGTS . . . 38
  - 2.3.1 Column density . . . 39
  - 2.3.2 Isotopologue composition . . . 40
- 2.4 Accuracy requirements for the monitoring of the source gas composition . 41

3 Theory of quantitative Raman spectroscopy **47**
3.1 Introduction to Raman Spectroscopy 48
3.1.1 Rotational and vibrational states in diatomic molecules 49
3.1.2 Basic principles of the Raman effect 51
3.1.3 Description of Raman intensities 55
3.2 Raman spectroscopy on hydrogen isotopologues 58
3.3 Calibration for quantitative analysis 62
3.3.1 Possible methods 63
3.3.2 Calibration strategy for the KATRIN LARA system 64

4 Experimental setup **67**
4.1 Raman system hardware 67
4.1.1 Overview of the scheme of Raman measurements 67
4.1.2 Raman systems at the TLK 68
4.1.3 Components of the Raman systems 71
4.2 Spectrum acquisition, processing and analysis 77
4.2.1 Data acquisition 77
4.2.2 Data processing 79
4.3 Analysis of actual system performance 86

5 Calibration based on theoretical intensities and spectral sensitivity **91**
5.1 Motivation and overview 91
5.2 Calculation of theoretical intensities 92
5.3 Verification of theoretical intensities via depolarization measurements . . 97
5.3.1 Definition of the depolarization ratio 98
5.3.2 Model of depolarization ratios as observed in the experiment . . . 99
5.3.2.1 Influence of light collection geometry 99
5.3.2.2 Influence of polarization aberrations 100
5.3.2.3 Comparison to a previous correction model 106
5.3.3 Routine for correcting observed depolarization ratios 107
5.3.4 Measurement of depolarization ratios of all six hydrogen isotopologues 110
5.3.4.1 Experimental setup 110
5.3.4.2 Measurements procedure and analysis 113
5.3.4.3 Validation of the correction routine 118
5.3.4.4 Results and discussion 120

5.3.4.5 Summary and conclusion 123
5.4 Measurement of the system's spectral sensitivity 125
5.4.1 Requirements for the determination of the spectral sensitivity . . . 125
5.4.2 Possible calibration sources for the measurement of the spectral sensitivity 126
5.4.3 NIST-traceable luminescence standard SRM 2242 128
5.4.3.1 Systematic investigations 131
5.4.4 Resulting spectral sensitivity and discussion 136
5.5 Discussion of the calibration results 138
5.6 Conclusions 139

6 Calibration based on accurate gas samples 141
6.1 Motivation and overview 141
6.2 Calibration method 143
6.3 Experimental setup of the Hydrogen Deuterium Equilibration loop 145
6.4 Measurements 147
6.4.1 Preparations and pre-measurements 147
6.4.2 Calibration measurements 147
6.5 Discussion of the measurement results 148
6.5.1 Calibration results and uncertainties 148
6.5.2 Remarks on the use of the permeator 154
6.5.3 Possible improvements for further reduction of systematic uncertainties 154
6.5.4 Upgrade for the use with tritium 155
6.6 Conclusions 156

7 Comparison of calibration methods 159
7.1 Discussion of calibration results 159
7.2 Implications for the KATRIN experiment 161

8 Summary and outlook 165

A Statistical terms 171

B Complete derivation of integration formula for depolarization measurements 173
B.1 Bounds of integration 175
B.2 Final integration formula 178

C Jones calculations for polarization aberrations in the Raman collection system 181

D Measurements of polarization aberrations in Raman cell windows 185

D.1 Polarization aberrations induced by the half wave plate 185

D.2 Measurement of stress-induced birefringence in Raman cell windows . . . 186

D.2.1 Qualitative measurement with a polarization sensitive microscope 187

D.2.2 Quantitative measurement at a single point 190

E Error estimation in depolarization ratio measurements 191

F Relation between experimental error of Raman intensities and depolarization ratios 195

G Full tabulation of measured depolarization ratios 197

H Demonstration of bootstrapping on HYDE data 201

I Publications 205

Bibliography 239

Danksagung 260

List of Figures

1.1 Example for neutrino oscillation in two-flavor scheme 9
1.2 Neutrino mass scenarios 15
1.3 Cosmological matter density and neutrino masses 17
1.4 Simulation of the density distribution of baryons with and without hot dark matter 19
1.5 Double β-decay 21
1.6 Single β-decay 24
1.7 Results of tritium β-decay experiments from over 20 years 25
1.8 Principle of cryogenic microcalorimeters 26

2.1 The electron energy spectrum of tritium β-decay 31
2.2 Principle of the MAC-E-Filter 32
2.3 Setup of the KATRIN experiment 35
2.4 Conceptual design of the Windowless Gaseous Tritium Source and Inner Loop 37
2.5 View into the experimental hall of the Tritium Laboratory Karlsruhe (TLK) 39
2.6 Schematic view of the WGTS cryostat and beam tube cross-section 40
2.7 Final state distributions 43
2.8 Dependence of the systematic shift of $m(\nu_e)^2$ on the LARA calibration error 44

3.1 Illustration of a Raman scattering process 47
3.2 Sketch of measurement setup for observing of the Raman effect 49
3.3 Model for rotation of diatomic molecules 50
3.4 Potential curves of the (an-)harmonic oscillator 51
3.5 Energy level diagrams for photon scattering 53
3.6 Schematic view of a typical Raman spectrum of a diatomic molecule . . . 54
3.7 Definition of Raman scattering angles and polarization states 56
3.8 Polarization ellipsoid of a diatomic molecule 57

3.9 Typical Raman spectra of a gas mixture containing all six hydrogen 59
3.10 Analysis principle for the calibration of the LARA systems of KATRIN . . 65

4.1 Sequence of hardware step in a Raman measurement 68
4.2 Sketch and picture of MonLARA system 69
4.3 Sketch and picture of HighResLARA system 70
4.4 Cross-sectional view from top and photo of the Raman cell 73
4.5 The Appendix as interface between glove-box and the LARA system . . . 74
4.6 Transmittance curve of Semrock Razor RazorEdge® filter (LP03-532RU-25) 75
4.7 Signal-to-noise ratio (SNR) of a H_2 Raman line, as a function of binning segments 78
4.8 Flow-chart for integrated, processing chain, indicating the action of each individual step 80
4.9 Sketch of Rolling Circle Filter (RCF) action. 83
4.10 Background removal study for a Raman spectrum of N_2, over-laid with shaped background light 84
4.11 Raman spectra of DT with fitted peaks 85
4.12 Demonstration of *ShapeFit deluxe* for a typical Raman spectrum of H_2, HD, D_2 87
4.13 Performance tests for a H_2 : HD : D_2 gas mixture 88

5.1 Graphical overview of the chapter content 93
5.2 Theoretical Raman signal intensity for each $Q_1(J'')$ line of the six hydrogen isotopologues 96
5.3 Depolarization of initially linearly polarized light after a scattering interaction 97
5.4 Sketch of on-axis $(z = 0)$ and off-axis $(z \neq 0)$ light transmission 100
5.5 Visualization of polarization aberrations from stress-induced birefringence in a laser window 101
5.6 Influence of polarization aberrations in the laser excitation and the light observation paths on the effective depolarization ratio 105
5.7 Calculated shift $\Delta\rho$ of the observed depolarization ratio from the SP0SA value induced by optical components in the light collection path 106
5.8 Difference between the (numerical) model and the one of Teboul 106
5.9 Detailed view of $Q_1(J'' = 0)$ line of H_2 108
5.10 Two-step routine for extraction of depolarization values ρ_{SP0SA} from data sets which comprise polarization aberrations 109
5.11 Dependence of normalized Raman signal on the half-wave plate angle . . 111
5.12 Optical components in the light collection path affecting the collection solid angle 112

5.13 Dependence of the Raman signal on the collection angle 113
5.14 Overview Raman spectrum of an equilibrated mixture of T_2, HT, and H_2 . 116
5.15 High resolution spectra of the Q_1-branch of all six hydrogen isotopologues 117
5.16 Polarization cleanness of various Raman cells, as determined in Step 1 of the correction procedure 119
5.17 Statistical plot of deviations between measured and theoretical depolarization ratios 122
5.18 The NIST luminescence standard SRM 2242 129
5.19 Replication of the Raman scattering region by the SRM 2242 luminescence standard 130
5.20 Different incident positions of the laser beam on SRM 2242 132
5.21 Influence of the laser polarization on the measured spectra 134
5.22 Difference in the spectral shape for measurements with and without Raman window 135
5.23 Spectra of a white light LED measured with two different LARA systems . 137
5.24 Spectral sensitivity of the detection system of the MonLARA system . . . 138

6.1 Graphical overview of the chapter content 142
6.2 Setup of the HYDE loop 146
6.3 Raman spectrum of H_2, HD, D_2 obtained in a calibration measurement . . 149
6.4 Fitting of the HYDE data at a catalyst temperature of $25\,^{\circ}\mathrm{C}$ 150
6.5 Influence of the catalyst temperature on the fit results of the relative response function $R_{x,\mathrm{rel}}$ 152
6.6 Fit results of the equilibrium constant $K(T)$ 153
6.7 Time trend of catalyst temperature and relative intensity ratio of H_2/D_2 influenced by permeator operation 155

7.1 Spectrum of a circulating tritium sample with high purity 162

A.1 Bow-and-arrow analogy for accuracy, precision and trueness 172

B.1 Sketch for angles and distances to a circular aperture 174
B.2 Sketch of collection geometry 175
B.3 Sketch for clarification of the φ-dependence 176
B.4 Sketch of inverse collection geometry 180

D.1 Setup to measure the laser beam cleanness quantitatively 186
D.2 Measurement curve of the polarization cleanness vs. the half-wave plate tilt angle 187

D.3 Setup of the polarization-sensitive measurements by using a microscope and two Polaroid sheet polarizers 188
D.4 Visualization of polarization aberrations in windows of the Raman cell . . 189

E.1 Two-step procedure to extract depolarization values ρ_{SP0SA} from data sets with unclean beam polarization 193

H.1 Bootstrapping example with HYDE data 203

List of Tables

1.1 Leptons and their anti-partners in the Standard Model 7

1.2 Best fit values of the three neutrino oscillation parameters 13

3.1 Selection rules and notation convention in Raman spectra 54

3.2 Nuclear spin statistics and influence on relative intensities 57

4.1 Overview of selected components of the LARA systems used for measurements within this thesis 71

4.2 Signal to noise ratios and precision of the selected Raman measurement . 88

5.1 Parameter overview for the investigated polarization scenarios 104

5.2 Apertures and distances of the Raman collection geometry of the LARA systems in Swansea and at the TLK 114

5.3 Different cells and their gas fillings used in Raman depolarization measurements and for the determination of excitation beam polarization cleanness 115

5.4 Demonstration of the capability of the depolarization ratio correction procedure 119

5.5 Selected set of results of depolarization ratios for all six hydrogen isotopologues 121

5.6 Comparison of corrected depolarization ratios of H_2 with experimental and theoretical data from literature 123

5.7 Raman response functions obtained via theoretical Raman signal amplitudes and the related uncertainties 139

6.1 Overview of the results of the relative response functions for different catalyst temperatures 151

7.1 Comparison of response functions obtained from both calibration approaches 160

7.2 Systematic uncertainty in a KATRIN-like measurement 163

C.1 Physical significance of the Pauli coefficients a_k 182

E.1 Geometrical input parameters and their effect on the depolarization ratios 192

G.1 Overview on the fillings of the various laser Raman cells 197
G.2 Overview on obtained depolarization ratios 198

Zusammenfassung

Neutrinos sind mit Abstand die leichtesten Fermionen des Standardmodells der Teilchenphysik und gleichzeitig noch diejenigen, die am häufigsten im Universum vorkommen. Ursprünglich wurden sie für masselos gehalten, jedoch konnte durch spätere Neutrinooszillationsexperimente gezeigt werden, dass sie eine sehr kleine Masse besitzen müssen. Die absolute Massenskala der Neutrinos ist sowohl in der Teilchenphysik als auch in der Kosmologie von entscheidender Wichtigkeit.

Unter den verschiedenen Methoden zur Messung der Massenskala hat sich die modelunabhängige Hochpräzisionsspektroskopie von Elektronen des Tritiumbetazerfalls als sensitivste erwiesen. Auf diesem Prinzip beruht das Neutrinomassenexperiment der nächsten Generation, das Karlsruhe Tritium Neutrino Experiment (KATRIN). Dabei ist angestrebt die Sensitivität der Vorgängerexperimente in Mainz und Troitsk, die um die Jahrtausendwende durchgeführt wurden, von $2\,\mathrm{eV/c^2}$ auf $200\,\mathrm{meV/c^2}$ $(90\%\ \mathrm{C.L.})$ zu verbessern.

Dieses Ziel kann nur erreicht werden, wenn die systematischen Unsicherheiten des Experiments minimiert werden. Ein Schlüsselparameter ist dabei die isotopische Zusammensetzung des Tritiumgases, das die fensterlose Betaelektronenquelle darstellt. Diese Zusammensetzung muss kontinuierlich im Gasstrom überwacht werden, wozu sich Ramanspektroskopie als Methode der Wahl herausgestellt hatte. Um die zuvor genannten Sensitivitätsanforderungen des KATRIN-Experiments zu erfüllen, muss die tatsächliche Gaszusammensetzung innerhalb von Messzeiten in der Größenordnung von einer Minute erfasst werden. Hierbei soll eine Richtigkeit von 10% sowie eine Präzision von 0.1% erreicht werden. Die Tritiumquellenüberwachung mittels Ramanspektroskopie muss diese Bedingungen für die gesamte Bandbreite der Isotopologe des Wasserstoffs ($\mathrm{H_2}$, HD, $\mathrm{D_2}$, HT, DT, and $\mathrm{T_2}$) erfüllen. Dies kann durch eine genaue Kalibrierungsprozedur erreicht werden, die einen zentralen Aspekt dieser Dissertation darstellt.

Im Rahmen dieser Arbeit wurden verschiedene, unabhängige Kalibrierungsmethoden untersucht. Zwei davon stellten sich als am vielversprechendsten heraus, da sie komplementär die besten Ergebnisse lieferten. Zum einen ist dies eine Technik, bei der mittels der Herstellung von genau definierten Gasproben eine hohe Genauigkeit erreichbar ist, aber die nur eingeschränkt auf tritiierte Spezien angewendet werden kann. Zum anderen wird ein Ansatz verfolgt, bei dem mittels theoretischer Ramansignale (= theoretische Ramanintensitäten aus der Quantenmechanik zusammen mit der spektralen Sensitivität des Ramansystems) alle sechs Isotopologe abgedeckt werden können. Beide Methode zeigten ihre individuelle Stärken und Schwächen, allerdings konnte mittels eines Kreuzkalibrierungsvergleichs gezeigt werden, dass sie in der Kombination sehr erfolgreich sind.

Im ersten Fall wurde ein speziell angefertigter Mischkreislauf für $\mathrm{H_2}$, HD und $\mathrm{D_2}$ verwendet. Dabei wurden die statistischen und systematischen Unsicherheiten der Kalibrierungsmethode ausführlich untersucht.

Für die zweite Methode wurden *ab initio* Übergangsmatrixelemente aus der Literatur herangezogen. Diese beschreiben die molekulare Polarisierbarkeit der Moleküle. Die theoretischen Vorhersagen dieser Werte konnten durch genaue Depolarisationsmessungen experimentell bestätigt werden. Zu diesem Zweck wurde ein Zwei-Stufenkorrektur-

verfahren entwickelt, wodurch alle im Messaufbau auftretenden Aberrationen berücksichtigt werden konnten. Außerdem musste die spektrale Sensitivität des Ramansystems bestimmt werden. Dazu wurde ein NIST-kalibrierter Lumineszenzstandard mit sehr geringer Ungenauigkeit in der Kalibrierung verwendet, der außerdem eine beinahe perfekte Nachahmung der Ramanstreuungsgeometrie ermöglichte.

Vergleichsstudien der beiden oben genannten Methoden wurden für die nicht radioaktiven Wasserstoffisotopologe (H_2, HD, D_2) durchgeführt. Die Ergebnisse zeigten eine Übereinstimmung der relativen Kalibrierfaktoren von besser als 2% auf. Dies liegt innerhalb der geschätzten (dominierenden) Unsicherheit der zweiten Kalibriermethode von ca. 3%. Diese Ergebnisse deuten darauf hin, dass die Anforderung an die Richtigkeit von 10% für die Spezies mit höchster Wichtigkeit für KATRIN (T_2, DT, D_2 and HT) in jedem Fall übertroffen werden können.

Die im Rahmen dieser Arbeit entwickelten Kalibrierungsmethoden bieten ein großes Potential, um in weiteren Anwendungen mit ähnlichen Anforderungen wie bei KATRIN eingesetzt zu werden. Darin eingeschlossen sind Kernfusionskraftwerke, in denen Tritium sowie Deuterium als Fusionsbrennstoffe eingesetzt werden, die Anwendung als Echtzeitmessung von Spurengasen oder die Regelung von Verbrennungsprozessen.

Zusammenfassend ist zu sagen, dass die Ergebnisse der Forschungsarbeit, die dieser Dissertation zugrunde liegen, in entscheidender Weise dazu beigetragen haben, dass das eingesetzte Ramansystem in der Lage ist, die Präzisions- und Richtigkeitsanforderung von KATRIN zu übertreffen. Dadurch wird das Verständnis der Parameter und Eigenschaften der gasförmigen Tritiumquelle in Echtzeit maßgeblich verbessert. Dies stellt eine wesentliche Voraussetzung für die angestrebte hochpräzise Neutrinomassenanalyse dar. Dadurch wird geholfen eine der faszinierendsten offenen Fragen der Astroteilchenphysik nach der ureigenen Natur der Neutrinos zu beantworten.

Abstract

Neutrinos are by far the lightest fermions in the Standard Model of particle physics and also the most numerous fermionic particles in the Universe. Originally, they were believed to be massless. However, later neutrino oscillation experiments indicated that neutrinos actually carry (some very small) mass, making them the lightest fermions in the Standard Model of particle physics. Their absolute mass scale is highly relevant both in particle physics and cosmology.

Several methods for measuring the neutrino mass scale exist of which high-precision electron spectroscopy of the tritium β-decay is the most sensitive, model-independent method today. Within the context of said method, the Karlsruhe Tritium Neutrino experiment, KATRIN, is the next-generation direct neutrino mass experiment. It is targeted at improving the current experimental sensitivity realized in the Mainz and Troitsk experiments of the late 1990s, from $2\,\mathrm{eV/c^2}$ down to $200\,\mathrm{meV/c^2}$ (90% C.L.).

This can only be achieved if systematic uncertainties are minimized; a key parameter is the isotopic composition of the tritium gas in the windowless source. This composition needs to be monitored inline and in near-time, and Raman spectroscopy was selected as the method of choice, being non-destructive and non-contact. For the KATRIN experiment to achieve the aforementioned sensitivity, the actual source gas composition needs to be determined on short sampling time scales of the order of one minute with a trueness of better than 10%, and a precision of 0.1%. This implies that the Raman source monitoring measurements need to mimic or better these boundary conditions; and it is essential that they are met for the full range of hydrogen isotopologues (H_2, HD, D_2, HT, DT, and T_2) encountered in the source. Consequently, accurate calibration procedures are paramount, and it is this aspect which is central to this thesis.

Within the framework of this thesis, several (independent) calibration methods have been studied. Two were identified as being the most promising methods, yielding excellent, complementary results: (i) a gas sampling technique, which encompasses high accuracy, but which is difficult to apply to tritiated species; and (ii) an approach via theoretical Raman signals (theoretical intensities from quantum theory plus spectral sensitivity of the Raman system), which covers all six isotopologues. Both methods exhibited their individual merits and difficulties; however, in cross-calibration test they proved to be very successful.

For the first approach, a custom-made mixing device for H_2, HD, D_2 was employed and the statistical and systematic uncertainties of the calibration method were thoroughly investigated.

For the latter method, *ab initio* transition matrix elements adapted from the literature were incorporated. These are associated with the molecular polarizability, and the theoretical predictions have been verified by accurate Raman depolarization measurements. For this a (two-step) correction model has been developed, which was applied successfully and which was capable to account for all aberrations related to the experimental setup. In addition, the spectral sensitivity of the Raman system needed to be determined. For this a NIST-traceable luminescence standard (with very small calibration uncertainty) was adapted to almost perfectly replicate the Raman light excitation geometry.

Comparative studies of the two above methodologies were carried out for the non-radioactive hydrogen isotopologues (H_2, HD, D_2); the results yielded an agreement of better than 2% for the relative Raman response functions. This is less than the estimated (dominant) uncertainty of the theoretical Raman signal approach of about 3%. These results suggest that the trueness requirement of 10% for the species with high relevance for KATRIN (T_2, DT, D_2 and HT) will, in all likelihood, be exceeded.

The calibration approaches developed within the framework of this thesis offer great potential to be applicable to other applications with conditions and requirements similar to KATRIN. This includes nuclear fusion power plants where tritium and deuterium are used as fusion fuel; or the real-time monitoring and control of environmental gases and combustion processes.

In summary, the results obtained in the research work underlying this thesis have contributed in a significant way to implement a Raman analysis system, which exceeds the precision and trueness requirements for KATRIN. This means that the properties of the gaseous source of KATRIN experiment are well-understood which is an essential prerequiste in the envisaged high-precision analysis of the neutrino mass data. This therefore will help to unravel one of the most fascinating open issues of astroparticle physics - the intrinsic nature of neutrinos.

Chapter 1

Introduction

The work in hand is focused thematically on the accurate calibration of a Raman system at the Karlsruhe Tritium Neutrino Experiment (KATRIN), which is targeted to measure the neutrino mass by means of high precision electron spectroscopy of the β-decay of tritium with a sensitivity of $200\,\mathrm{meV/c^2}$. This ambitious goal can only be reached if the systematic uncertainties of key experimental parameters are well-controlled and minimized. One major parameter in this regard is the isotopic composition of the tritium gas, which needs to be accurately monitored. This task is performed by the aforementioned Raman system.

This introductory chapter puts KATRIN into the context of recent neutrino physics research which is interlinked to the underlying question of the origin of neutrino masses. Furthermore, it will motivate the intention of this thesis with the regard to KATRIN. Therefore, in this introduction three fundamental questions will be answered

1. *What are the intrinsic neutrino properties such as their absolute mass and CP properties?*
2. *What is the role of neutrinos in shaping large-scale structures in the Universe?*
3. *How is this thesis related to KATRIN and to its sensitivity on the neutrino mass?*

In the following section the neutrino and its properties are introduced in a historical approach. As an outset, a preliminary answer to the first question should be given.

Neutrinos are neutral, weakly interacting elementary fermions which are described today as fundamental particles in the Standard Model of particle physics. Interestingly, they are by far the most abundant and the lightest fermionic particles in the Universe.

In everyday life neutrinos do not appear to play a key role in our existence, since the baryonic matter from which we are made of consists mainly of nucleons and electrons.

However, without neutrinos which react by the weak interaction only, life would not be possible since the Sun would not be able to produce long-term fusion energies [Kay12]. This is exemplified at the start of the famous pp chain, where two protons p are fused to a deuterium nucleus d, a positron e^+, and a neutrino ν:

$$\begin{array}{lccccccccc} & p & + & p & \rightarrow & d & + & e^+ & + & \nu \\ \text{Spin}: & \frac{1}{2} & & \frac{1}{2} & & 1 & & \frac{1}{2} & & \frac{1}{2} \end{array} . \tag{1.1}$$

The intrinsic spin of the particles is indicated [Kay12], underlining that the neutrino allows for conservation of angular momentum. As this process is governed by the interaction scale of weak interactions and requires the emission of a neutrino, it ensures a solar lifetime of $\sim 10^{10}$ years.

1.1 Discovery of the neutrino

Initially, early studies of the β-decay hinted at the existence of a new particle. The assumed decay of a mother nucleus[1] $M(A, Z)$ into a daughter nucleus $D(A, Z+1)$ was

$$M(A, Z) \rightarrow D(A, Z+1) + e^- \,. \tag{1.2}$$

From conservation of momentum and energy in this two-body decay, a discrete energy spectrum of the emitted β-electrons is expected. However, the energy spectrum was found to be continuous (see Fig. 1.6). The first suggestion of the existence of the neutrino was given by Wolfgang Pauli in 1930 (His famous letters and publications are collated in [Pau85].). By this postulation it was possible to understand the energy spectrum, since the two-body decay (Eq. 1.2) is turned into a three-body decay

$$M(A, Z) \rightarrow D(A, Z+1) + e^- + \bar{\nu}_e \,. \tag{1.3}$$

Furthermore, the neutrino as fermionic particle (spin $\frac{1}{2}$) conserves angular momentum in the same way as discussed in Eq. 1.1. Some years later, Enrico Fermi derived a theory for the shape of the β-electron spectrum [Ferm34]. At this time he already estimated that the mass of the then undetected neutrino must be much smaller than that of the electron or even zero.

The small cross-section of the neutrino prevented its discovery for more than 25 years after its postulation. Finally, the direct discovery of the neutrino took place at a nuclear fission reactor which was the strongest source for (anti-)neutrinos available. C. L. Reines, F. Cowan and co-workers used the now famous inverse β-decay reaction for the detection of the neutrino [Cow56]

$$\bar{\nu}_e + p^+ \rightarrow e^+ + n \,. \tag{1.4}$$

The signature of this reaction was a delayed coincidence between $511\,\mathrm{keV}$ photons from positron annihilation, and MeV scale gammas from the deexcitation of an intermediate Cd^* nucleus subsequent to neutron capture [Zub11].

In 1962, the second neutrino type which is related to the muon, ν_μ, was discovered by a group around L.M. Ledermann, M. Schwartz, and J. Steinberger [Dan62]. In this case, the neutrinos were produced by pion decay at a proton accelerator at Brookhaven National Laboratory.

The third neutrino, the ν_τ, was finally discovered by the DONUT collaboration at the Tevatron in 2000 [DON01].

It is of major impact for the understanding of the flavor part of the Standard Model to ask if there are further neutrino flavors besides the three yet-discovered species. In this

[1] Z and A are atomic number (number of protons) and mass number (number of nucleons), respectively.

Table 1.1: Leptons and their anti-partners in the Standard Model. All listed particles are elementary fermions with spin $s = 1/2$. Anti-particles have opposite charge and lepton number.

Generation 1	2	3	Electric charge	Lepton number	Interaction
ν_e	ν_μ	ν_τ	0	+1	weak
e^-	ν^-	τ^-	-1	+1	weak, electromagnetic
$\bar{\nu}_e$	$\bar{\nu}_\mu$	$\bar{\nu}_\tau$	0	-1	weak
e^+	ν^+	τ^+	+1	-1	weak, electromagnetic

regard, the number of light (active) neutrinos N_ν (with $m(\nu) < m_{Z^0}/2 \approx 45\,\mathrm{GeV/c^2}$) can be determined from the total decay width of the Z^0 resonance at an e^+e^- collider. Precision measurements at LEP resulted in [ALE06]

$$N_\nu = 2.9841 \pm 0.0083\ . \tag{1.5}$$

Tab. 1.1 gives an overview of the six leptons and their anti-partners in the Standard Model (SM) of particle physics. For each charged lepton, there exists an uncharged lepton of the same flavor.

Neutrinos in the Standard Model should be massless particles which is a consequence of the experimental discovery of parity violation and the corresponding V-A theory of weak interactions [Sch95].

Neutrinos are the only elementary fermions which are neutral. Therefore, it may be the case that they are their own anti-particles. Tab. 1.1 implies that this is only possible if the lepton number L, which is conserved in the SM, would be violated. Neutrinos with this properties are called Majorana[2] neutrinos [Rod11].

1.2 Neutrino oscillations

In this subsection, observations of flavor-changing oscillations of neutrinos are introduced which can be considered as proof that neutrinos have a non-vanishing rest mass.

The Sun is a strong source for electron neutrinos, ν_e, as they are generated in the pp chain fusion process starting with the reaction shown in Eq. 1.1. In addition, neutrinos at high energies are produced by other reactions with different fluxes as compared to the pp - neutrinos (see *e.g.* [Bah05]).

The first theoretical predictions of solar neutrino fluxes were performed by J. Bahcall [Bah64] and date back to 1964. At the same time (back to back in the same journal) R. Davis proposed the first solar neutrino experiment [Dav64]. The experiment was realized in the Homestake mine in South Dakota using a tank of 615 tons of liquid $\mathrm{C_2Cl_4}$ as target material. The detection of neutrinos was based on the radiochemical reaction $\nu_e + {}^{37}\mathrm{Cl} \rightleftharpoons {}^{37}\mathrm{Ar} + \mathrm{e}^-$. After exposure to solar neutrinos, the argon was then extracted and counted in an elaborate process [Dav68]. From 1970-1994 around 800 neutrinos were

[2]The "standard" neutrinos are dubbed Dirac neutrinos.

collected [Cle98]. Although the statistics of each extraction cycle was rather low, it became evident rather soon that there was a genuine deficit of ν_e's relative to the prediction. For a long time, this mismatch, the "solar neutrino problem", was attributed to uncertainties in the solar model, in nuclear cross-sections, or in the experiment itself [Raf12]. The solar neutrino deficit was later confirmed by other experiments using different techniques such as Gallex [GAL99], GNO [GNO05], SAGE [SAG02], and Super-Kamiokande [Sup98a].

Another explanation for the deficit was suggested by V. Gribov and B. Pontecorvo in 1969 [Gri69]. They suggested the possibility of a neutrino oscillations similar to the oscillation of neutral kaons [Poh04].

In the present understanding of solar neutrino phenomena (as well as of other sources) the concept of neutrino flavor oscillations such as $\nu_\mu \to \nu_e$ is paramount. This is due to the fact that flavor oscillations, in the simplest 2-flavor case, require two mass eigenstates, which have different mass.

A non-vanishing mass implies that a weak (flavor) eigenstate ν_α ($\alpha = e, \mu, \tau$) needs not necessarily be identical to a mass eigenstate ν_i ($i = 1, 2, 3$).

This idea was mainly pushed forward by Pontecorvo [Pon68] and Maki, Nakagawa and Sakata [Mak62]. In case of 3-flavor mixing, a unitary transformation relates the eigenbases of mass and flavor states

$$|\nu_\alpha\rangle = \sum_i U_{\alpha i} |\nu_i\rangle \,, \tag{1.6}$$

$$|\nu_i\rangle = \sum_\alpha U^*_{\alpha i} |\nu_\alpha\rangle \,. \tag{1.7}$$

The 3×3 matrix U is often called the Pontecorvo-Maki-Nakagawa-Sakata (PMNS) matrix[3] which can be parameterized in the following from [PDG12]:

$$U = \begin{pmatrix} c_{12}c_{13} & s_{12}c_{13} & s_{13}e^{-i\delta} \\ -s_{12}c_{23} - c_{12}s_{23}s_{13}e^{i\delta} & c_{12}c_{23} - s_{12}s_{23}s_{13}e^{i\delta} & s_{23}c_{13} \\ s_{12}s_{23} - c_{12}c_{23}s_{13}e^{i\delta} & -c_{12}s_{23} - s_{12}c_{23}s_{13}e^{i\delta} & c_{23}c_{13} \end{pmatrix} \begin{pmatrix} e^{i\alpha_{21}/2} & 0 & 0 \\ 0 & e^{i\alpha_{31}/2} & 0 \\ 0 & 0 & 1 \end{pmatrix} \tag{1.8}$$

where $s_{ij} = \sin\theta_{ij}$, $c_{ij} = \cos\theta_{ij}$, and θ_{ij} is a mixing angle. These values describe the composition of the three different mass eigenstates in a certain flavor eigenstate or vice versa. Depending on whether the massive neutrinos are Dirac or Majorana particles they have 1 or 3 phases related to CP violation [PDG12]. The Dirac phase is denoted by δ, and the two Majorana phases are given by α_{21} and α_{31}.

In the following the concept of neutrino oscillations is discussed in more detail for the generic two flavor case, that means that only ν_e and ν_μ are considered. Therefore U is reduced to the 2×2 case

$$\begin{pmatrix} \nu_e \\ \nu_\mu \end{pmatrix} = \begin{pmatrix} \cos\theta & \sin\theta \\ -\sin\theta & \cos\theta \end{pmatrix} \begin{pmatrix} \nu_1 \\ \nu_2 \end{pmatrix} \,. \tag{1.9}$$

[3] Note that this matrix is similar to the unitarian Cabbibo-Kobayashi-Maskawa (CKM) matrix in the quark sector [Kob73].

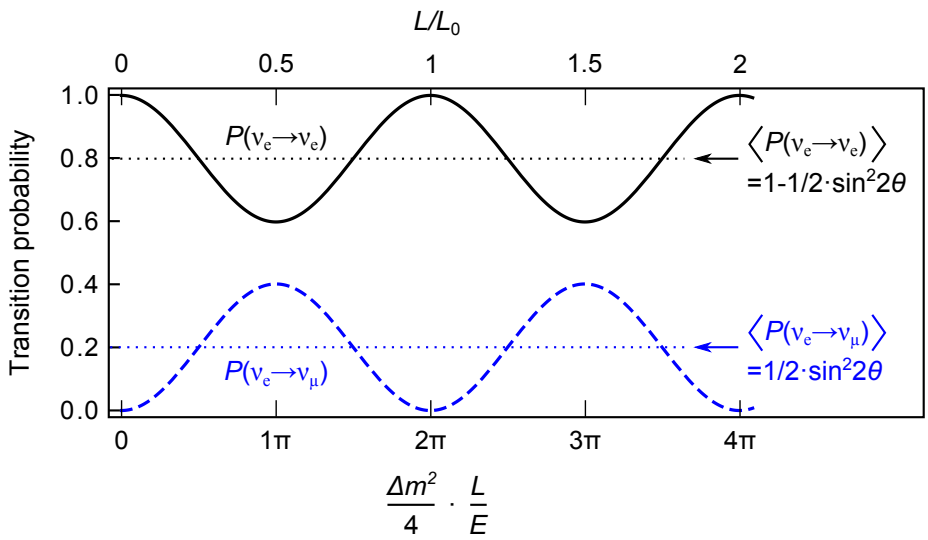

Figure 1.1: Example for neutrino oscillation in two-flavor scheme. Transition probability as a function of L/L_0 and $\Delta m^2/4 \cdot L/E$. *Upper curve:* Probability for ν_e disappearance $P(\nu_e \to \nu_e)$. *Lower curve:* Probability for ν_μ appearance $P(\nu_e \to \nu_\mu)$. In the given example the mixing angle is $\theta \approx 20°$ which leads to $\frac{1}{2}\sin^2 2\theta = 0.2$. The figure is inspired by [Sch97].

When the time and space evolution of the eigenstates in Eqs. 1.6 and 1.7 is considered, the following transition probability for the ν_μ appearance can be obtained [Zub11]

$$P(\nu_e \to \nu_\mu) = \sin^2(2\theta) \cdot \sin^2\left(\frac{\Delta m^2}{4}\frac{L}{E}\right) \quad \text{with } \Delta \mathrm{m}^2 = \mathrm{m}_2^2 - \mathrm{m}_1^2 \,. \tag{1.10}$$

The disappearance probability of ν_e is then given by $P(\nu_e \to \nu_e) = 1 - P(\nu_e \to \nu_\mu)$. Both transition probabilities are visualized in Fig. 1.1. The two sine terms in Eq. 1.10 fully describe the quantum-mechanical nature of flavor oscillations. The one containing the mixing angle θ defines the oscillation amplitude and the one containing energy E and mass squared difference Δm^2 determines the oscillation frequency. The characteristic oscillation length is thus given as

$$L_0 = \frac{4\pi E}{\Delta m^2} \,. \tag{1.11}$$

From aforementioned considerations one can distinguish three kinematical ranges [Gei03]:

$\mathbf{L/E \ll 1/\Delta m^2}$ This is either the case, if E is large or if L is small. Then, the sine function is approximately linear and the effect from oscillation is small even if the mixing is rather large.

$\mathbf{L/E \sim 1/\Delta m^2}$ In this scenario the sinusoidal oscillation pattern can be observed.

$\mathbf{L/E \gg 1/\Delta m^2}$ This case is given, if E is small or if L is large. Thus, the sinusoidal pattern becomes unmeasurable since the oscillation has become too fast. In this case only an average oscillation effect $\sim \frac{1}{2}\sin^2 2\theta$ can be observed.

In order to measure all three mixing angles (θ_{12}, θ_{23}, θ_{13}) in the PMNS matrix (see Eq. 1.8) as well as Δm^2_{31} and Δm^2_{21}, one needs to perform selected experiments at different neutrino energy regimes and baselines. The employed sources of neutrinos are the Sun (solar neutrinos), the atmosphere, nuclear reactors and particle accelerators. Each of them is briefly introduced together with the most important experimental findings.

Solar neutrinos

Radio-chemical experiments for the investigations of solar neutrinos have already been introduced above (Homestake, Gallex, GNO or SAGE). The first real-time neutrino detectors were Kamiokande [Kam96] and its successor Super-Kamiokande [Sup98a] in the Kamioka mine in Japan. The Super-Kamiokande (SK) detector is a large cylindrical tank with $50,000\,\mathrm{t}$ of pure water as target material. The neutrinos can scatter off electrons in the water, and as charged particles they produce a Cerenkov light cone from which the direction and the energy can be reconstructed. With a threshold of $5\,\mathrm{MeV}$, this technique is mainly sensitive to so-called $^8\mathrm{B}$ neutrinos from the sun. In contrast to the radio-chemical reactions, however, this technique allows to measure all neutrino flavors in real-time by neutrino-electron scattering [Gei03]

$$\nu_x + e^- \rightarrow \nu_x + e^- \; (x = e, \mu, \tau) \; . \tag{1.12}$$

The real-time measuring ability allowed to search for day/night effects and to observe seasonal fluctuations in the neutrino rate.

A different detection principle was used by the Sudbury Neutrino Observatory (SNO) experiment which was performed in a nickel mine in Sudbury, Canada [SNO01]. The spherical detector was filled by $1000\,\mathrm{t}$ of heavy water ($\mathrm{D_2O}$). In addition to the elastic scattering (ES) reaction (Eq. 1.12), neutrinos could induce charged current (CC) and neutral current (NC) reactions of deuterium (D)[Gei03]:

$$CC : \nu_e + D \rightarrow p^+ + p^+ + e^- \; , \tag{1.13}$$

$$NC : \nu_x + D \rightarrow n + p^+ + \nu_x \; . \tag{1.14}$$

Due to the low energies of solar neutrinos, CC reactions are only possible for electron neutrinos, while NC reactions are sensitive to all flavors. Thus, the NC/CC ratio is significantly affected if neutrinos do mix. The analysis showed that the total solar neutrino flux ($\nu_e + \nu_\mu + \nu_\tau$) is in accordance with the Standard Solar Model, but only $\sim 1/3$ of the Sun's neutrinos arrive on Earth as ν_e [Zub11]. The solar problem was solved.

In 2008, the SNO collaboration published solar oscillation data including measurements from other sources in a global analysis [SNO08]. Solar neutrino experiments are sensitive to the Δm^2_{21} mass difference and θ_{12} mixing angle, which therefore sometimes are indexed by "solar", with the following values:

$$\theta_{12} = 34.4^{+1.3}_{-1.2} \; (90\%\,\mathrm{C.L.}) \; , \tag{1.15}$$

$$\Delta m^2_{21} = \Delta m^2_{\mathrm{sol}} = 7.59^{+0.19}_{-0.21} \cdot 10^{-5}\,\mathrm{eV}^2/\mathrm{c}^4 \; (90\%\,\mathrm{C.L.}) \; . \tag{1.16}$$

Atmospheric neutrinos

In 1912, Victor Hess [Hes12] first noticed that the Earth's atmosphere is continuously being bombarded by primary cosmic rays (predominantely protons). Their energies reach from values below 10^8 eV up to more than 10^{20} eV [Sig12]. These primary particles interact with molecules in the upper atmosphere whereby neutrinos are generated (*e.g.* from pion or kaon decay) in secondary processes [Gei03]. In these processes ν_e and ν_μ and their corresponding anti-neutrinos states are produced in a predictable ratio. The atmospheric neutrino energies can extend up to very high energies beyond the TeV scale. Typically, the neutrino energy is an order of magnitude lower than the energy of the corresponding primary particle [Zub11].

Neutrinos are almost uniformly produced everywhere in the atmosphere and thus arrive at an underground detector from all directions. Since the neutrinos have traveled different distances L $(10-10^4\,\mathrm{km})$ before their detection, the measured ratio of ν_e/ν_μ should depend on the measured zenith angle if neutrinos oscillate indeed.

The first evidence for oscillations of neutrinos from the atmosphere (and thereby the first clear evidence for massive neutrinos) was given by the Super-Kamiokande collaboration in 1998 [Sup98b]. This effect was confirmed later by the Soudan 2 experiment in Minnesota [Sou03] and the MACRO experiment at LNGS[4] [MAC01].

Finally, Super-Kamiokande released data for neutrino energies between $100\,\mathrm{MeV}$ and $10\,\mathrm{TeV}$. The energies are several orders higher compared to the solar neutrino scale and the oscillation length is different, thus another parameter region in Δm^2 can be probed. The obtained oscillation parameters, now for oscillation of the $\nu_\mu \to \nu_\tau$, were [Sup05]

$$\sin^2 2\theta_{23} > 0.92\ (90\%\,\mathrm{C.L.})\ , \tag{1.17}$$

$$1.5\cdot 10^{-3} < \Delta m^2_{31} = \Delta m^2_{\mathrm{atm}} < 3.4\cdot 10^{-3}\,\mathrm{eV}^2/\mathrm{c}^4\ (90\%\,\mathrm{C.L.})\ . \tag{1.18}$$

Accelerators neutrinos

The L/E range of atmospheric-neutrino experiments can also be probed by artificial, and in some cases energy-tuneable neutrino sources. In a typical experimental setup the baseline is usually fixed and the neutrinos can be produced with well-known energies [PDG12]. In particular, the measurements of θ_{23} and $\Delta m^2_{\mathrm{atm}}$ should thus be more accurate as compared to the atmospheric measurements. The processes which produce neutrinos in a high-energy accelerator-based beam are the same as in atmospheric decays [Gei03].

In general, a particle accelerator is required to produce an intense ν_μ beam, and a rather massive neutrino detector in the kiloton scale located several hundred kilometer away. Another, smaller detector with identical properties is positioned close to the point of neutrino production to measure the undistorted spectrum and profile of the neutrino beam [PDG12].

The first long-baseline experiment was K2K (KEK-to-Kamioka) which used the KEK facilities to produce neutrinos from a proton beam to send short ν_μ pulses to the $250\,\mathrm{km}$ remote Super-Kamiokande detector [K2K06]. A follow-on experiment with higher neutrino energies was the MINOS experiment which used the Fermilab Main Injector for producing

[4] LNGS is the Gran Sasso Underground Laboratory in Italy.

neutrinos between $3\,\mathrm{GeV}$ and $12\,\mathrm{GeV}$, and an iron-scintillator calorimeter at the Soudan mine $730\,\mathrm{km}$ away. The resulting $\nu_\mu \to \nu_\tau$ oscillation parameters are [MIN11]

$$\sin^2 2\theta_{23} > 0.90\ (90\%\,\mathrm{C.L.})\ , \tag{1.19}$$

$$\Delta m^2_{31} = \Delta m^2_{\mathrm{atm}} = 2.32^{+0.12}_{-0.08} \cdot 10^{-3}\,\mathrm{eV}^2/\mathrm{c}^4\ (90\%\,\mathrm{C.L.})\ . \tag{1.20}$$

Finally, the on-going T2K is an experiment with a baseline distance of $295\,\mathrm{km}$ between the J-PARC accelerator in Tokai (Japan) and Super-Kamiokande. For an assumed mixing angle θ_{23} of $\sin^2 2\theta_{23} = 1$ and mass difference $\Delta m^2_{23} = 2.4 \cdot 10^{-3}\,\mathrm{eV}^2/\mathrm{c}^4$ the result yields a hint for a non-zero value of the final neutrino mixing parameter θ_{13} [T2K11]

$$\mathrm{normal\,hierarchy}:\ 0.03 < \sin^2 2\theta_{13} < 0.28\ (90\%\,\mathrm{C.L.})\ , \tag{1.21}$$

$$\mathrm{inverted\,hierarchy}:\ 0.04 < \sin^2 2\theta_{13} < 0.34\ (90\%\,\mathrm{C.L.})\ . \tag{1.22}$$

Reactor neutrinos

The first (anti-)neutrinos were detected at nuclear fission reactors since they are the strongest terrestrial neutrino sources [Zub11]. In order to test Δm^2 in the region of $10^{-2} - 10^{-3}\,\mathrm{eV}^2/\mathrm{c}^4$, where the important genuine 3-flavor-mixing parameter θ_{13} can be determined, a baseline of about a $1\,\mathrm{km}$ is needed. By using two or more detectors at different distances (at least one near and one far detector) systematic effects can be significantly reduced. In 2012, three experiments could provide a measurement of θ_{13} independently from the accelerator-based experiments, but with better statistics and reduced systematics (It should be noted in this context that reactor-based and accelerator-based experiments are complementary, due to the different parameters contributing to the oscillation signal). The results released by Double Chooz at France [Dou12], RENO at South Korea [REN12], and Daya Bay at China [Day12] are in very good agreement, with a combined analysis of all results yielding [PDG12]

$$\sin^2\theta_{13} = 0.0251 \pm 0.0034\ (90\%\,\mathrm{C.L.})\ . \tag{1.23}$$

Summary

The observation of neutrino oscillations has been an outstanding scientific finding. The results above were a selection of most important results among many investigations which finally allowed to measure the parameters in the PMNS matrix. The collated results are found in Tab. 1.2. It should be noted that the current data from atmospheric [Sup05] and accelerator [K2K06, MIN11] oscillations do not reveal the sign of $\Delta m^2_{\mathrm{atm}}$. This important fact leaves open the hierarchy of the neutrino masses. The following three scenarios are possible [PDG12]:

Normal hierarchy $m_1 < m_2 < m_3$. This would imply that $\Delta m^2_{\mathrm{atm}} = \Delta m^2_{31} > 0$.

Inverse hierarchy $m_3 < m_1 < m_2$. This is corresponding to $\Delta m^2_{\mathrm{atm}} < 0$.

Quasi-degenerate $m_1 \approx m_2 \approx m_3$. In this case all masses are significantly larger than the mass splittings ($m_i \gg \sqrt{|\Delta m^2_{\mathrm{atm}}|}$).

Table 1.2: Best fit values of the three neutrino oscillation parameters. The values are derived from a global fit of neutrino oscillation data by the PDG [PDG12].

Parameter	Best fit ($\pm 1\sigma$)	Units
$\Delta m^2_{\mathrm{sol}}$	$7.58^{+0.22}_{-0.26}$	$10^{-5}\,\mathrm{eV}^2/\mathrm{c}^4$
$\lvert\Delta m^2_{\mathrm{atm}}\rvert$	$2.35^{+0.12}_{-0.09}$	$10^{-3}\,\mathrm{eV}^2/\mathrm{c}^4$
$\sin^2\theta_{12}$	$0.312^{+0.018}_{-0.015}$	-
$\sin^2\theta_{23}$	$0.42^{+0.08}_{-0.03}$	-
$\sin^2\theta_{13}$	0.0251 ± 0.0034	-

Due to their nature as quantum-mechanical interference phenomenon, neutrino oscillations do not give information on the absolute neutrino mass scale. Nevertheless, assuming that the mass of the lightest neutrinos is much smaller than the one of the heaviest neutrino, one can obtain a lower limit for the heaviest state, which is approximately given by $\sqrt{|\Delta m^2_{\mathrm{atm}}|} = 0.048\,\mathrm{eV/c^2}$.

The observation of neutrino oscillations has answered in part the initial question on neutrino properties with regard to their (strong) mixing effect and confirmed that they do have mass. The existence of massive neutrinos now poses a new question about how the neutrinos obtain their masses.

1.3 Role of massive neutrinos

1.3.1 Particle Physics

In the formalism of the Standard Model of particle physics all particles initially need to be massless to guarantee gauge invariance [Zub11]. The particles receive mass by the concept of spontaneous symmetry breaking through the Higgs mechanism [Hig64, Kib67]. According to this mechanism, fermions obtain their mass through coupling to the vacuum expectation value v of the scalar Higgs field ϕ_0. The Higgs doublet $\phi_0 = \frac{1}{\sqrt{2}}\binom{0}{v}$ is coupled to the left-handed fermion doublet (*e.g.* $\binom{\nu_{eL}}{e_L}$) and the right-handed singlet (*e.g.* e_R). This coupling is called Yukawa coupling, and in the case of electrons the corresponding Lagrange density is given by [Zub11]

$$\mathcal{L}_{\mathrm{Yuk}} = -c_e\left[\bar{e}_R\phi_0^\dagger\begin{pmatrix}\nu_{eL}\\ e_L\end{pmatrix} + (\bar{\nu}_{eL},\bar{e}_L)\phi_0 e_R\right] \tag{1.24}$$

$$= -\underbrace{c_e\frac{v}{\sqrt{2}}}_{m_e}\bar{e}e\,. \tag{1.25}$$

Here c_e is an arbitrary coupling constant and the electron mass term is identified in Eq. 1.25. All fermion particles in the Standard Model gain their mass accordingly. Another consequence of the Higgs mechanism is the existence of a scalar gauge boson, the so-called Higgs-particle. A scalar particle with properties as expected from the Higgs-particle was

recently found at the LHC by the CMS [CMS12] and ALTAS [ATL12] collaborations, and the evidence of its existence is an important finding for the theory of the Standard Model.

However, neutrinos are assumed to be massless in the Standard Model, because there are no right-handed ν_R singlet states for neutrinos[5] due to the principle of maximal parity violation [Sch95]. Therefore, neutrinos cannot couple to the vacuum expectation value like the electron in Eq. 1.25.

From the observation of neutrino oscillations it was followed that neutrinos are evidently massive. For this reason, neutrinos need to acquire mass by a different mechanism than the Standard Model Higgs-mechanism.

Neutrino masses from beyond the Standard Model In the following, possible extensions to the current Standard Model to obtain massive neutrinos are considered.

- A simple extension is to add a right-handed neutrino singlet ν_R to the particle content of the theory. This allows a Yukawa coupling term like in Eq. 1.25 [Zub11]. However, the Yukawa coupling constant c_ν would be about six orders of magnitudes smaller compared to the charged fermions [Moh07]. Therefore this mechanism is deemed to be rather unlikely.

- Another extension is the so-called See-Saw type I mechanism [Moh80] in which a heavy right-handed Majorana neutrino N_R and a light neutrino ν_L are introduced. For each neutrino eigenstate a Dirac-Majorana mass matrix can be considered[6] [Zub11]

$$\mathcal{L}_{\mathrm{DM}} = \frac{1}{2}\left(\bar{\nu}_L, \bar{N}_L^C\right)\begin{pmatrix} 0 & m_D \\ m_D & m_R \end{pmatrix}\begin{pmatrix} \nu_R^C \\ N_R \end{pmatrix} + h.c. \tag{1.26}$$

  The 2×2 mass matrix has no Majorana mass term for ν_L ($m_L = 0$), but a very large term for N_R ($m_R \gg m_D$). The Dirac mass terms m_D are of the order of the charged fermion masses ($\mathrm{MeV} - \mathrm{GeV}$) [Zub11]. From diagonalizing the mass matrix, the following relations for the mass of the light and the heavy neutrino can be obtained

$$m(\nu) \approx \frac{m_D^2}{m_R}\,, \tag{1.27}$$

$$m_N \approx m_R\,. \tag{1.28}$$

  In this mechanism the very small neutrino masses are a natural consequence, if m_N is in the order of the GUT-scale ($\approx 10^{16}\,\mathrm{GeV/c^2}$) [Moh07]. Eq. 1.27 suggests that neutrino masses scale in the same way as the squared masses of the charged fermions [Zub11] (the example is given for the leptons)

$$m(\nu_e) : m(\nu_\mu) : m(\nu_\tau) \sim m_e : m_\mu : m_\tau\,. \tag{1.29}$$

  The result would thus be a hierarchical neutrino mass scenario.

[5] There are also no left-handed $\bar{\nu}_L$ single states for anti-neutrino.
[6] The Hermitian conjugate is abbreviated by $h.c.$.

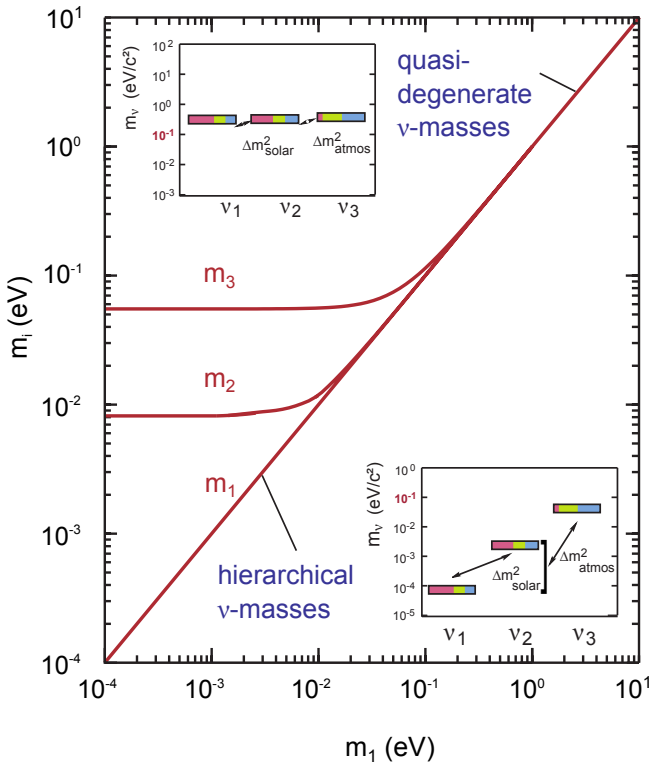

Figure 1.2: Neutrino mass scenarios. The values of the three neutrino mass eigenstates m_1, m_2 and m_3 are plotted as function of the lightest neutrino eigenstate m_1 in a double logarithmic plot. The mass splitting shown is obtained from neutrino oscillation measurements. For very small values of m_1 a hierarchical scenario is obtained, while for larger m_1 the eigenstates are quasi-degenerate. Note that the color coding (red, yellow, blue) of bars representing the mass eigenstates ν_i is according to the mixture of the flavor eigenstates (e, μ, τ). According to [KAT05].

- In the See-Saw type II [Laz81] only a small modification is made for the mass matrix. The Majorana mass term for the left-handed light neutrino is now $m_L > 0$. This leads to an extra term to Eq. 1.27 which couples to the vacuum expectation value of the Higgs field. In case that this factor would dominate, the resulting mass scenario would be quasi-degenerate. [Zub11]

- Other approaches involve Higgs-triplets (*e.g.* [Sch80]), supersymmetry (*e.g.* [Moh06]), extra dimensions (*e.g.* [Ark01]) or further theoretical assumptions [Smi06].

The various theoretical models are able to predict a large variety of different mass scenarios. Neutrino oscillation experiments are able to provide the mass differences, but not the absolute scale which is of major interest in discriminating among the different theoretical models. Fig. 1.2 shows an overview for the various scenarios as a function of the lightest mass eigenstate. The selection of the mass scenario realized in nature and a hint on the appropriate theory behind can thus only be obtained from absolute neutrino mass measurements (*e.g.* like KATRIN).

1.3.2 Cosmology

The current standard model of cosmology firmly rests on the concept of a Big Bang, implying that the Universe evolved from hot dense state to the cold era today [Ber06, PDG12]. An important consequence of this theory is the existence of background fields. In 1964, the so-called cosmic microwave background (CMB) was discovered [Pen65] which can be understood as the "afterglow" of the photons following their decoupling from matter. Today the CMB temperature is at $2.7\,\mathrm{K}$. As an analogue to the CMB, cosmology predicts a relic neutrino background as well, which should have an even lower temperature of $1.95\,\mathrm{K}$ today [Les12]. However, relic neutrinos have not yet been detected directly.

In the early Universe one can assume thermal equilibrium, which means that the particle density n is large enough that the reaction rate of creation and annihilation between the particles ($\Gamma \propto n\sigma$) is higher than the expansion rate of the Universe (H) [Zub11]. As the temperature T drops with the expansion of space, a point where $\Gamma < H$ is reached eventually for a certain particle species, so that this particle species decouples from the equilibrium (freeze out). The decoupling of neutrinos can been seen as instantaneous at a decoupling temperature of roughly $T_{\mathrm{dec}} \approx 1\,\mathrm{MeV}$ [Dol02].

The total matter-energy budget of the Universe is composed of different contributions as shown in Fig. 1.3. One important part is related to so-called dark matter which interacts only via weak and gravitational interactions. The neutrino is one of many candidates for this dark matter, and so far the only one which is known to exist. The relic neutrino density from the Big Bang today is about 339 neutrinos and anti-neutrinos per cm^3 [Les12]. Their energy density is given as the sum of the neutrino mass eigenstates

$$\Omega_\nu = \frac{\sum_i m(\nu_i)}{93.14\,\mathrm{h}^2\,\mathrm{eV/c}^2} \tag{1.30}$$

where h is the dimension-less Hubble parameter: $h = H/[100(\mathrm{km/s})/\mathrm{Mpc}]$.

After the thermal decoupling of relic neutrinos, they behave like a collision-free fluid. The neutrinos are able to free-stream on a scale λ_{FS} with a characteristic, thermal velocity. For the time period where they are relativistic, relic neutrinos are traveling with the speed of light (hence they are called hot dark matter) and thus their free-streaming length can equal the Hubble-radius [Les12].

For the non-relativistic case the free-streaming length becomes [Les12]

$$\lambda_{\mathrm{FS}} = 8\frac{1+z}{\sqrt{\Omega_\Lambda + \Omega_m(1+z)^3}}\left(\frac{1\,\mathrm{eV}}{m(\nu)}\right)h^{-1}\,\mathrm{Mpc}\,. \tag{1.31}$$

where Ω_Λ and Ω_m are the density fractions of the cosmological constant and matter, respectively. The red-shift is given by z. These characteristic free-streaming scales have to be put into context of the characteristic Jeans scales of gravitating matter, where gravitational perturbations grow and the density changes locally. The weakly interacting neutrinos can escape out of areas of higher density and propagate to areas of lower density, thus damping small-scale perturbations. Perturbations which are smaller than the free streaming length (see Eq. 1.31) are completely erased [Zub11]. This effect results in a correlation of the neutrino mass with the growth of large-scale structures, effecting damping out structures of the order of $1\,\mathrm{Gpc}$ for eV-scale neutrinos.

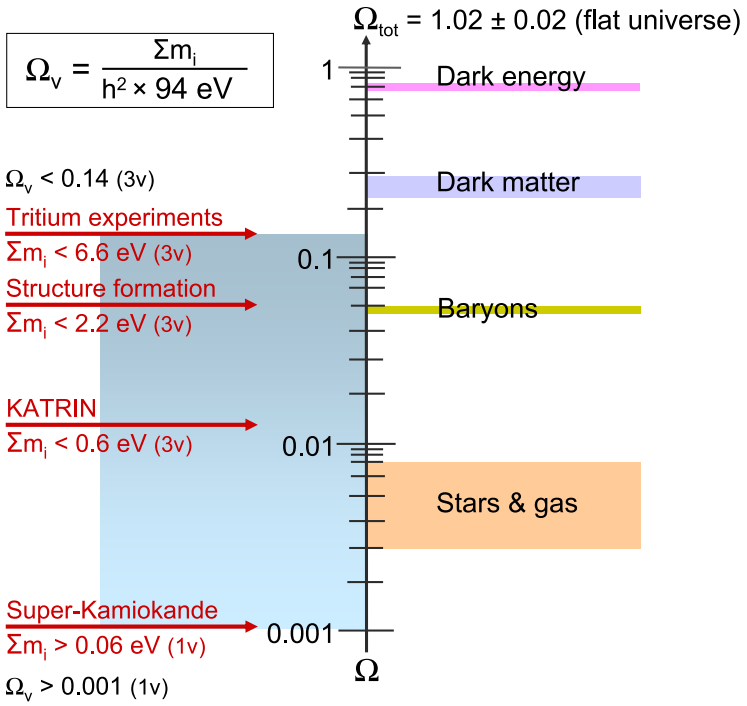

Figure 1.3: Cosmological matter density and neutrino masses. The neutrino mass contribution Ω_ν is compared to the other matter densities (dark energy, cold dark matter and baryons). The allowed neutrino hot dark matter contribution Ω_ν is bound by experimental data. The lower bound results from oscillation data of atmospheric ν's. The upper bound is given by the results from current tritium β-decay experiments and studies of structure formation. KATRIN will investigate the parameter space $\Omega_\nu > 0.01$, where relic neutrinos would play a significant role in the evolution of large scale structures. According to [KAT05].

1.4 Measurement of the neutrino mass

Over the past decades, several different concepts for the measurement of the absolute mass scale of the neutrino have been developed. All methods can be separated into two basic classes, which can be grouped into direct and indirect methods.

- **Direct methods** rely purely on kinematic reconstructions of particles (*e.g.* from a weak decay). The essential part is making use of the relativistic energy-momentum relationship:

$$E^2 = p^2c^2 + m^2c^4 \,. \tag{1.32}$$

  Here E, p and m are total energy, momentum and rest mass, respectively. Eq. 1.32 indicates that direct methods are always sensitive to the square of the neutrino mass, $m^2(\nu)$. Direct methods comprise time-flight-studies of astrophysical neutrinos and investigations of weak decays of nuclei and particles.

- **Indirect methods** do not involve the detailed investigation of the kinematics of the particle via Eq. 1.32. Instead, they are based on models incorporating specific neutrino properties, in particular in those scenarios where their mass influences certain phenomena. By (not) observing these phenomena and by measuring their effects quantitatively one can trace back the underlying neutrino mass. Although these methods, in principle, are very sensitive to neutrino masses, their results are model-dependent, as discussed below [Ott08]. Indirect methods encompass the determination of the effective Majorana neutrino mass from neutrinoless double beta decay, or to obtain mass bounds from cosmological observations.

It should be noted, however, that even direct methods cannot be claimed to be fully model-independent. Although their basic assumption only relies on fundamental physics concepts (like Eq. 1.32), the experiments have to be performed in a non-ideal environment which interacts with the system of interest. Examples are given in the corresponding paragraphs below.

1.4.1 Indirect methods

Cosmology The influence of massive neutrinos on cosmological observables has been discussed in Section 1.3.2. Therefore, the measurement of an ensemble of key cosmological observables can be employed to derive the neutrino mass, or at least an upper limit.

Within the discussion above it was shown that the relic neutrino density Ω_ν is correlated to the sum of the neutrino mass eigenstates (see Eq. 1.30). The combined analysis of data from the observations of the CMB by the WMAP satellite and from other sources results in the bound on the sum of neutrino masses [Kom11]

$$\sum_i m(\nu_i) < 0.58\,\mathrm{eV/c^2}\ (95\%\,\mathrm{C.L.})\,. \tag{1.33}$$

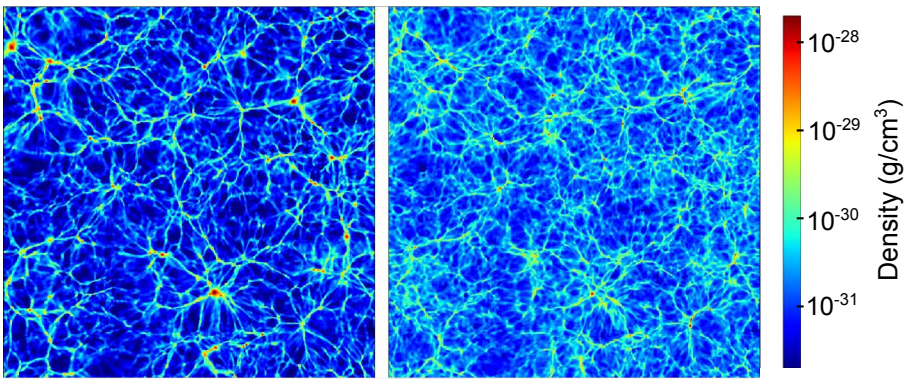

Figure 1.4: Simulation of the density distribution of baryons with and without hot dark matter. Each slice is $200\,h^{-1}\,\mathrm{Mpc}$ wide and shows baryonic mass density. *Left panel*: Simulation result with vanishing neutrino mass. *Right panel*: Simulation with $\Omega_\nu = 0.04$ ($\sum_i m(\nu_i) = 1.9\,\mathrm{eV/c^2}$). According to [Aga11].

Very recently, the Planck satellite mission launched in 2009 [Pla10] published its first results including data of 15.5 months of CMB survey. For CMB data alone the collaboration states an upper limit of the neutrino mass [Pla13]:

$$\sum_i m(\nu_i) < 0.66\,\mathrm{eV/c^2}\ (95\%\,\mathrm{C.L.})\ . \tag{1.34}$$

This limit is either weakened or tightened if other data sources than the Planck CMB data are included, demonstrating that results from cosmological observation are "rather model dependent and vary strongly with the data combination adopted" [Pla13].

Furthermore, the impact of massive neutrinos on larger scales was discussed. Fig. 1.4 shows two different generic scenarios. Massive neutrinos suppress the growth of density perturbations and the density of baryonic filaments becomes more diffuse [Aga11]. Observational data are based primarily on the distribution of galaxies as a measure for the large-scale structures, which can be recorded by scanning telescopes like in the Sloan Digital Sky Survey (SDSS) [Aih11]. Again it should be noted, however, that the derived neutrino mass bounds strongly depend on the employed data set and pre-assumptions as demonstrated by S. Hannestad [Han10]. Therefore, one recent result is given as an example. The latest results from the SDSS-III Baryon Oscillation Spectroscopic Survey (BOSS) including data from galaxy clustering and cosmic microwave background [San12] lead to the following limit of the sum of the neutrino masses

$$\sum_i m(\nu_i) < 0.61\,\mathrm{eV/c^2}\ (95\%\,\mathrm{C.L.})\ . \tag{1.35}$$

Neutrinoless double beta decay The process of double beta decay is a weak interaction process of second order, where simultaneously two neutrons undergo β-decay in a nucleus. It can only occur if single β-decay is energetically forbidden or strongly suppressed due to a change of the nuclear spin [Doi85].

The two-neutrino double beta decay[7], $\beta\beta(2\nu)$, is given as

$$2n \rightarrow 2p^+ + 2e^- + 2\bar{\nu}_e \ . \tag{1.36}$$

This decay is consistent with the Standard Model of particle physics and it is independent of the neutrino nature (Majorana or Dirac).

A far more interesting possibility would be the observation of the neutrinoless double beta decay[8], $\beta\beta(0\nu)$, for which the following relation would be valid

$$2n \rightarrow 2p^+ + 2e^- . \tag{1.37}$$

The search for $\beta\beta(0\nu)$ involves physics beyond the Standard Model of particle physics for the following reasons.

- Eq. 1.37 violates the conservation of lepton number, L. In this case two electrons ($L = +2$) are emitted and no corresponding particles with ($L = -2$).
- In the left panel of Fig. 1.5 the Feynman graph of the $\beta\beta(0\nu)$ is sketched. At one vertex, one of the two neutrons emits a β-electron together with a virtual (anti-) neutrino, which is absorbed by an inverse β-decay by the second neutron. This process is only possible if neutrino and anti-neutrino are their own anti-particles, and if they do not carry a conserved lepton number L. In this case the exchanged virtual particle would be a Majorana neutrino ν_m [Doi85].
- Assuming the neutrino would be of Majorana-type, it then would act as neutrino (helicity[9] $H = -1$) at one vertex, and as anti-neutrino (helicity $H = +1$) at the other vertex. The possibility of a "helicity flip[10]" is only given if the neutrino has a non-zero mass (see V-A theory, *e.g.* in [Sch95]).

The probability of the "helicity flip" scales with the effective Majorana neutrino mass m_{ee}. The decay rate of the $\beta\beta(0\nu)$-process is given by the inverse half-life $T^{0\nu}_{1/2}$ [Ell02]

$$\left(T^{0\nu}_{1/2}\right)^{-1} = G^{0\nu}(E_0, Z) \left|M^{0\nu}\right|^2 m_{ee}^2 \tag{1.38}$$

and thus is proportional to the absolute square of the effective Majorana neutrino mass

$$m_{ee} = \left|\sum U_{ei} m(\nu_i)^2\right| \ . \tag{1.39}$$

The factor $G^{0\nu}(E_0, Z)$ is the exact phase-space integral [Ell02] depending on the energy endpoint E_0 and nuclear charge Z, and $\left|M^{0\nu}\right|^2$ is the total nuclear matrix element consisting of a Gamov-Teller and a Fermi part.

It should be noted, that $U_{ei} m(\nu_i)^2$ and not $|U_{ei} m(\nu_i)|^2$ appears in Eq. 1.39 due to the virtual nature of the exchanged particle. This leads to a dependence of the effective neutrino mass on the Majorana phases (see Eq. 1.8) [Ell02], in contrast to the directly measured

[7] Originally proposed by M. Goeppert-Mayer in 1935 [Goe35].
[8] Originally suggested by H. W Furry in 1939 [Fur39].
[9] The helicity is defined as the projection of the spin $\boldsymbol{s}$ onto the momentum direction $\boldsymbol{p}$: $H = (\boldsymbol{s} \cdot \boldsymbol{p})/(|\boldsymbol{s}| \cdot |\boldsymbol{p}|)$.
[10] This term denotes in principle that a massive neutrino has two helicity components.

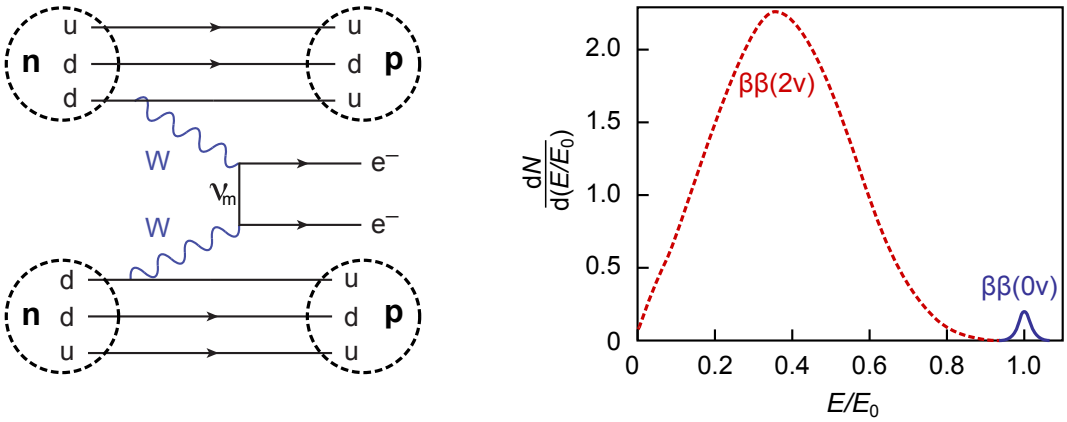

Figure 1.5: Double β-decay. *Left panel:* Feynman diagram of the neutrinoless double β-decay. Two neutrons decay simultaneously into two protons and two electrons by exchanging a virtual Majorana neutrino ν_{m}. *Right panel:*. Illustration of the sum energy spectra of both electrons involved in the double beta decay. The energy axis is scaled to the energy endpoint E_0 ($\approx Q$). The red, dashed line represents the $\beta\beta(2\nu)$-decay spectrum and the blue, solid line represents the $\beta\beta(2\nu)$-decay spectrum (intensity normalized to 10^{-2}). The energy resolution at the endpoint is taken to be about 5%. According to [Ell02].

neutrino mass (see Eq. 1.44), where an incoherent sum enters and the Majorana phases do not influence the signal.

Another rather larger uncertainty is induced by the calculation of the nuclear matrix elements $\left|M^{0\nu}\right|^2$. The complicated nuclear structure of heavy nuclei ($Z > 46$) leads to uncertainties of a factor of $\sim 2-3$ in the matrix elements, which implies a factor of up to ~ 10 in the experimental observable half-life [Ell02].

Experimental determination of neutrino masses from $\beta\beta(0\nu)$ The common strategy to search for $\beta\beta(0\nu)$-decay processes is the following. Since in $\beta\beta(0\nu)$-decays no energy is carried away by neutrinos, the sum of both emitted electrons should add up to E_0. The right panel in Fig. 1.5 shows a continuous $\beta\beta(2\nu)$-spectrum between $0 < E < E_0$ and the $\beta\beta(0\nu)$-peak at $E = E_0$. The scaling between the $\beta\beta(2\nu)$- and $\beta\beta(0\nu)$-spectrum shown here is however not representing a realistic case, as the $\beta\beta(0\nu)$ has been increased by several orders of magnitude with respect to the continuum. The decay rate, $\left(T^{0\nu}_{1/2}\right)^{-1}$, can be obtained from the $\beta\beta(0\nu)$-count rate, the knowledge of the β-source mass, and the experimental detection efficiency. The effective Majorana neutrino mass m_{ee} is then derived from Eq. 1.38.

Two requirements have to be met to obtain a high sensitivity: (i) an ultra-low count rate of $\beta\beta(0\nu)$-decays requires that the background events, *e.g.* from natural radioactivity, need to be suppressed to the lowest possible level, and (ii) the energy resolution needs to be sufficient to provide a good signal-to-background ratio against random background, and in particular against smearing out of $\beta\beta(2\nu)$-events near E_0 [Ell02].

A part of the Heidelberg-Moscow-collaboration, which investigated the ^{76}Ge-decay, claims evidence for an effective Majorana neutrino mass of $m_{ee} = (0.32 \pm 0.03)\,\mathrm{eV/c^2}$ [Kla06].

This result is disputed heavily in the community and challenged by recent results from the EXO-200 experiment using $^{136}\mathrm{Xe}$ as source-target material [EXO12a]. There, an upper bound for an effective neutrino mass is given at $140 - 380\,\mathrm{meV/c^2}$ (depending on the matrix element calculation). Thus it contradicts the previous claim at 68% C.L. [EXO12b], but a direct comparison using $^{76}\mathrm{Ge}$ is highly desirable [GER04].

In order to obtain a sensitivity for the effective Majorana neutrino mass of the order of $50\,\mathrm{meV/c^2}$, a source/detector array approaching the ton-scale needs to be employed [Ell02]. Many experiments are currently aiming at this size. Some examples are CUORE [CUO05], GERDA [GER04], KamLAND-Zen [Kam13], MAJORANA [MAJ12], and SNO+ [SNO12].

1.4.2 Direct methods

The measurement of the neutrino mass by indirect methods always involves a strong dependence on the underlying model (*e.g.* models on cosmological evolution, or the presumed Majorana nature of neutrinos). This drawback calls for direct methods which have virtually no model-dependence.

Time-of-flight studies of supernova neutrinos A very interesting method to derive neutrino masses is given by time-of-flight measurements of neutrinos from bright astrophysical sources, such as core-collapse supernovae. A star which ends in a supernova of this type needs to be rather massive with a minimum of at least eight solar masses [Woo05]. After the fusion processes have ceased, the core of the then supergiant cannot longer resist the gravitational forces of its outer shells. This induces the core-collapse and a neutron star[11] is formed [Jan07]. About 99% of the energy released is emitted in form of neutrinos which are generated thermally *e.g.* by the reaction $\gamma \rightleftharpoons e^+ + e^- \rightleftharpoons \nu_i + \bar{\nu}_i$ [Raf12].

Only once in the history of neutrino astronomy, a neutrino signal could be detected and used subsequently for the measurement of the mass. In February 1987, the SN 1987A supernova exploded in the Large Magellanic Cloud, which is about $50\,\mathrm{kpc}$ away [Raf12] and more than a dozen neutrinos were detected by several neutrino detectors [Kam87, IMB87, Ale87].

In this case, the neutrino mass can be derived from the spread of the arrival time and from the reconstruced neutrino energies E_ν using the relativistic energy-momentum relationship (see Eq. 1.32). The time-of-flight t_F from the neutrino emission at the outer shell of the hot proto-neutron star to the detector for a distance L is given by [Zub11]

$$t_F = \frac{L}{v} = \frac{L}{c}\frac{E_\nu}{p_\nu c} \tag{1.40}$$

$$= \frac{L}{c}\frac{E_\nu}{\sqrt{E_\nu^2 - m_\nu^2 c^4}} \approx \frac{L}{c}\left(1 + \frac{m(\nu)^2 c^4}{2E_\nu^2}\right) . \tag{1.41}$$

[11] In specific cases even a black hole is formed.

Two neutrinos of different energies E_1 and E_2 ($E_2 > E_1$), which are emitted at the supernova with a time difference Δt_0, arrive on Earth with the following delay

$$\Delta t = t_2 - t_1 = \Delta t_0 + \frac{Lm(\nu)^2}{2c}\left(\frac{1}{E_2^2} - \frac{1}{E_1^2}\right) . \tag{1.42}$$

The parameters Δt, L, and $E_{1,2}$ can be obtained from the experiment or from astronomy; only Δt_0 and $m(\nu)$ are unknown. Accordingly, an analysis of the neutrino mass needs to take into account (model-dependent) theoretical considerations on the spread of initial emission times Δt_0 (see *e.g.* [Fis10c]). A Bayesian data analysis of the SN1987A neutrinos has resulted in an upper limited of [Lor02]

$$m(\nu) < 5.7\,\mathrm{eV/c^2}\ (95\%\,\mathrm{C.L.}) . \tag{1.43}$$

Single beta decay At present, the investigation of the kinematics of weak decays from the β-spectrum endpoint is the most sensitive direct method to determine the neutrino mass. The charged decay products can be measured precisely and allow a determination of the neutrino mass, even though the neutrino leaves the experimental system undetected [Wei13].

Usually, the measured observable is the "average electron neutrino mass squared" [Dre13]

$$m(\nu_e)^2 = \sum |U_{ei}^2| m(\nu_i)^2 . \tag{1.44}$$

This sum averages over the neutrino mass eigenstates $m(\nu_i)$ which contribute to the flavor eigenstate of the electron neutrino according to the square of the absolute values of PMNS matrix elements $|U_{ei}^2|$. This sum is incoherent, since no Majorana or other phases of U enter the mass term. This is in contrast to the effective mass m_{ee} in the neutrinoless double β-decay (see Eq. 1.39). In the latter case the CP violating phases can lead to cancellations of the terms of the mass eigenstates.

The decay mode of the single β-decay was introduced by Eq. 1.3. The corresponding Feynman-graph is shown in the left panel of Fig. 1.6.

In this decay, the Q-value is given by the mass difference between mother $M(A, Z)$ and daughter $D(A, Z + 1)$ atom

$$Q = (m(A, Z) - m(A, Z + 1))\, c^2 . \tag{1.45}$$

Obeying the fundamental laws of conservation, energy and (angular) momentum are distributed to the decay products (daughter atom, electron, and anti-neutrino), to inner excitations of the daughter atom (or molecule), and to the rest mass of the neutrino.

The impact of the small neutrino mass only shows up in the endpoint region of the observed electron spectrum as shown in the right panel of Fig. 1.6 [Zub11]. It is only in this very narrow region that neutrinos are non-relativistic, so that Eq. 1.32 can be employed to measure their mass.

The energy spectrum of the β-decay electrons can be derived from Fermi's famous Golden rule [Ferm34]

$$\frac{\mathrm{dN}}{\mathrm{dt}} = \frac{2\pi}{\hbar}\left|M^2\right| \rho . \tag{1.46}$$

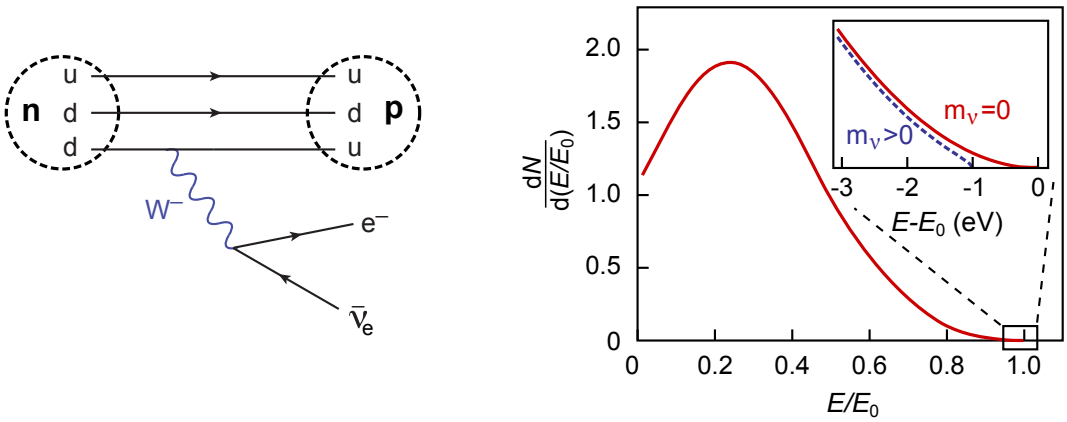

Figure 1.6: Single β-decay. *Left panel:* Feynman diagram of the β-decay of a neutron. A down-quark decays into an up-quark and a lepton pair (e^-, $\bar{\nu}_e$) via the W boson. *Right panel:* Electron spectrum of the β-decay. The energy axis is scaled to the energy endpoint E_0 ($\approx Q$). The inset shows the endpoint region at which the spectrum is sensitive on the neutrino mass. Two cases are given here: (i) a vanishing neutrino mass $m(\nu) = 0$, and (ii) and an arbitrary neutrino mass of $m(\nu) = 1\,\mathrm{eV}$.

M and ρ are the transition matrix element and the density of final states, respectively. The derivation of the spectral shape is given in Section 2.1.1 of the next chapter.

As outlined, only near the endpoint the spectrum is modified by the neutrino mass. The fraction of β-electrons in this range is proportional to Q^{-3} [Gat01], while the phase space factor increases with Q^5. Nevertheless, β-emitters with low Q-values are favored for neutrino mass measurements for technical reasons.

Tritium β-decay experiments From all isotopes, tritium is the most favorable β-emitter for direct neutrino mass measurements [Dre13] due to its unique physical properties.

- The half-life is $t_{1/2} = (12.32 \pm 0.02)$ y [Luc00] and thus rather short. This provides high decay rates per unit amount of radioactive material.
- Furthermore, it has one of the lowest endpoint energies at $E_0 = 18.6\,\mathrm{keV}$ [Nag06] which is of advantage technically.
- The decay of tritium is superallowed so that the nuclear matrix element M_{nucl} is independent of the electron energy and the neutrino mass which facilitates the analysis.
- Also the simple electronic structure and small nuclear charge allows for small systematic uncertainties (*e.g.* calculation of final states).

The main disadvantage is in general related to the fact that larger amounts of tritium are only available in molecular form (T_2). The daughter molecule $^3\mathrm{HeT}^+$ can thus be excited rotationally and vibrationally in the decay. The related systematic uncertainties on the neutrino mass measurement are discussed in Section 2.4.

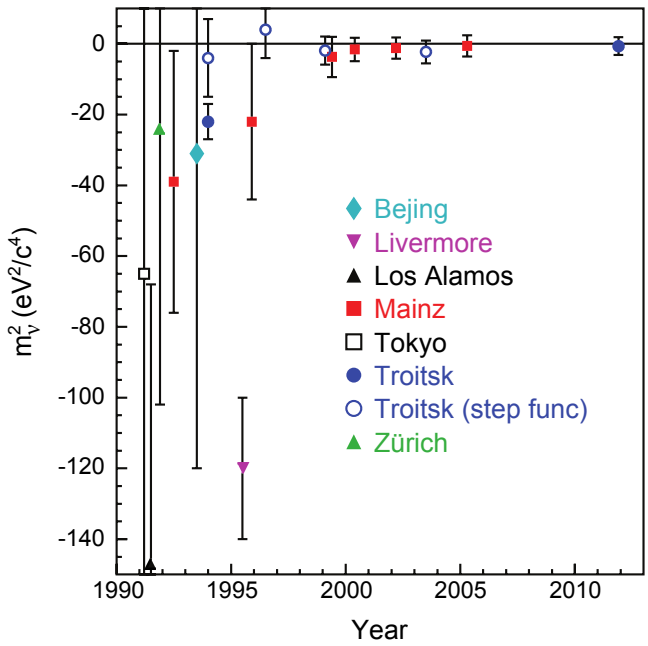

Figure 1.7: Results of tritium β-decay experiments from over 20 years. Initially, the observable $m(\nu_e)^2$ was always in the unphysical region $m(\nu_e)^2 < 0$ due to systematic effects and only later it approached values compatible with statistical scattering around $m(\nu_e)^2 = 0$. Note that only the Mainz and Troitsk used electrostatic spectrometers of the MAC-E-Filter type. The other experiments employed magnetic spectrometers. According to [Dre13].

The first tritium β-decay experiments started already in the late 1940s [Cur49], and since then many experiments have followed. Fig. 1.7 shows the evolution of the results from tritium β-decay experiments over the last two decades. Specifically, the introduction of a new type of spectrometer of the electrostatic retarding type has resulted in the most sensitive measurements of the neutrino mass so far. Those so-called MAC-E-filters combine high luminosity, low background and a high energy resolution [Wei03]. Its working principle and features are discussed in Section 2.1.2. The currently best upper limits on the neutrino mass are held by the Mainz [Pic92] and Troitsk [Lob85] experiments which both employed MAC-E-Filters. The published limits are $m(\nu_e) < 2.3\,\mathrm{eV/c^2}$ [Kra05] and $m(\nu_e) < 2.05\,\mathrm{eV/c^2}$ [Ase11] at (95% C.L.), respectively.

Cryo-bolometer experiments A complementary approach to the investigation of the β-spectrum of tritium involving spectrometers is the use of cryogenic microcalorimeters [Boo96, Gat01]. In this approach, the radioactive β-emitter is embedded in the detectors, so that the total energy of the electron and the daughter atom is converted into phonons and thus into a measurable temperature rise. The measurement principle is given in Fig. 1.8. This technique is, in principle, similar to the one used for specific detectors of double β-decay [CUO05] or (when disregarding the charge readout) cold dark matter [EDE12]. The advantage of this approach is that final state effects are less important since the total energy, except that of the neutrino, is measured, in principle. However, the potential impact of long-lived excitations in the solid-state material of the detector is still under investigation at present.

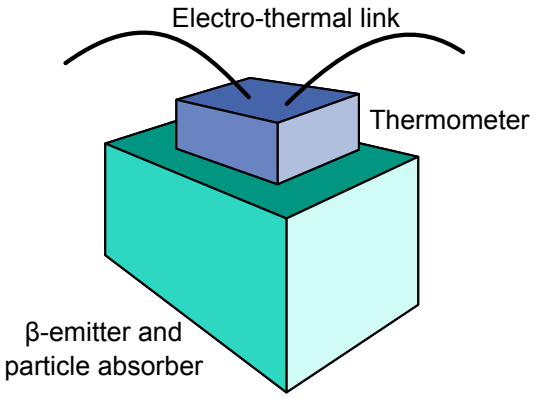

Figure 1.8: Principle of cryogenic microcalorimeters. Here, the β-emitter serves at the same time as energy absorber. The released energy $\Delta W_{\mathrm{therm}}$ induces a temperature rise by $\Delta T = \Delta W_{\mathrm{therm}}/C$, where C is the heat capacity. The temperature increase is read out by a sensitive thermometer (TES). Wires link the thermometer to a thermal bath. According to [Wei03].

One suitable β-emitter for microcalorimeters is $^{187}\mathrm{Re}$ which yields the lowest known Q-value of $Q = 2.67\,\mathrm{keV}$ [Fir99] and (as major drawback) a half-life of $4.3 \cdot 10^{10}\,\mathrm{y}$

$$^{187}\mathrm{Re} \rightarrow {}^{187}\mathrm{Os}^{+} + \mathrm{e}^{-} + \bar{\nu}_{\mathrm{e}}\,. \tag{1.47}$$

The endpoint energy is about 7 times lower than that of tritium, thus the relative fraction of decays in the region of interest for neutrino mass analysis is about 350 times higher [Wei13]. This is however counterbalanced by the much higher β-activity of tritium per unit mass.

One drawback of microcalorimeters is, that the total spectrum has to be measured, which is in contrast to the integrating MAC-E-filter. That may result in pile-up effects due to the time resolution of the detection technique. Thus, only very small detectors in the mg - scale can be operated. In order to obtain the required statistics, the experiments need to be built of multiple arrays comprising thousands of single modules.

Two groups have been working on neutrino mass measurement with $^{187}\mathrm{Re}$. In the MANU experiment at Genoa metallic rhenium was employed. Initially, three rhenium crystals of the order of $1\,\mathrm{mg}$ were installed. In the course of the experiment, the so-called Beta Environmental Fine Structure was observed for the first time, and it was shown that this is an important systematic effect in microcalorimeter measurements with rhenium [Gat99]. In 2001, a neutrino mass limit of $m(\nu_e) < 26\,\mathrm{eV/c^2}$ (95% C.L.) was obtained [Gat01]. Another group at Milano (MIBETA experiment) used arrays of 10 microcalorimeters each made of $250 - 300\,\mu\mathrm{g}$ of $\mathrm{AgReO_4}$ [Arn03]. In 2004, they reported an upper limit of the electron anti-neutrino mass [Sis04]

$$m(\nu_e) < 15\,\mathrm{eV/c^2}\ (90\%\ \mathrm{C.L.})\,. \tag{1.48}$$

In order to push forward the neutrino mass measurements based on cryogenic microcalorimeters into the sub-eV range, the MARE[12] collaboration was formed [Nuc08]. In

[12]MARE = Microcalorimeter Arrays for a Rhenium Experiment

a first phase, the methodology of various microcalorimeter techniques is investigated further. Later, arrays with a total of 50,000 single modules are planned to be deployed within five years. The statistical sensitivity is targeted to be better than $0.25\,\mathrm{eV/c^2}$ after $10\,\mathrm{y}$ of operation. Recently, a start of the experiment with 72 channels (expandable to 288 channels) was announced [MAR12].

Finally, it should be noted that also the electron capture (EC) process of $^{163}\mathrm{Ho}$ may be a suitable process for calorimetric neutrino mass measurements. However, certain fundamental questions, *e.g.* concerning the Q-value of $^{163}\mathrm{Ho}$ and its clean production, need to be answered first [Gal12]. The MARE collaboration is currently investigating this path, also as well as the ECHO collaboration [Ran12], which is based on a new detector technology, the so-called metallic magnetic calorimeters [Bur08]. In case that $^{163}\mathrm{Ho}$ would turn out to be a suitable candidate, then a large scale experiment with about 10^5 detectors would be needed to obtain sub-eV sensitivity.

KATRIN - the next generation neutrino mass experiment Direct neutrino mass measurements are independent of the underlying physics model since they only rely on kinematic variables in weak decays and conservation of energy and momentum. The current best laboratory limits on the neutrino mass are provided by measurement of the β-decay of tritium, where the Mainz and Troitsk experiments obtained upper limits of the order of $2\,\mathrm{eV/c^2}$. A major improvement in sensitivity down to the $200\,\mathrm{meV/c^2}$ range will be achieved by the Karlsruhe Tritium Neutrino experiment (KATRIN) [KAT05]. This sensitivity will allow to investigate the mass regime of quasi-degenerate neutrinos which allows to distinguish between different neutrino mass models (*c.f.* Section 1.3.1 and Fig. 1.2), as well as to fully probe the cosmologically interesting mass range for massive neutrinos [Wei13]. An indication from cosmology that the neutrino masses are indeed in the order of the KATRIN sensitivity was recently published by Burenin [Bur13].

KATRIN comprises a windowless gaseous tritium source of highest luminosity which is combined with a high resolution electrostatic filter (MAC-E-Filter type). This will reduce statistical uncertainties significantly as compared to the predecessor experiments. It should be noted that cryogenic microcalorimeter techniques for neutrino mass measurements, as discussed above, are an interesting alternative, but they are still in the early R&D phase. At the current status, they are not able to cope with the design sensitivity of KATRIN.

Further details of the physics related to KATRIN and its experimental setup will be given in Chapter 2. It will be shown that the statistical uncertainty has to be reduced by higher source luminosity and longer measurement time as compared to Mainz and Troitsk. Furthermore, systematic uncertainties have be reduced for the same amount in order to reach the design sensitivity. It should be emphasized that the majority of the systematic uncertainties are related to parameters of the tritium source [Bab12].

One key aspect in respect thereof is the stability of the gas composition, as the gas in the source does not exclusively consist of $\mathrm{T_2}$, but is mixed with smaller parts from the other hydrogen isotopologues (DT, $\mathrm{D_2}$, HT, HD, and $\mathrm{H_2}$). It is thus of crucial importance that this composition is monitored accurately. Raman spectroscopy is well suitable to perform this challenging task. In order to provide quantitative measurements of the true gas composition, the best achievable calibration is needed. Accordingly, the topic of this thesis is focused on the development of novel calibration strategies, and their validation and

application to the KATRIN Raman system. This principle target will be discussed from Chapter 3 onwards. Chapter 4 introduces the experimental setup of the Raman system and related data processing methods which have been developed in the framework of this thesis. Then the calibration strategies and results by two complementary approaches are outlined and described in detail in Chapters 5 and 6. It is important to underline already at this stage, that two independent approaches were required to arrive at a valid and accurate calibration of the LARA system. The comparison of both methods is given in Chapter 7. Finally, a summary with the resulting implications for KATRIN and an outlook beyond this work is found in Chapter 8.

It should be noted furthermore that the present investigations targeted at solving a major systematic uncertainty of the KATRIN experiment has led to several Raman-related achievements which are of relevance for the broader scientific community. For example, a novel concept for the accurate analysis of measurements of depolarization ratios was developed which can be applied to any depolarization measurement conducted under similar conditions such as spurious polarization aberrations or elongated scattering regions. This method was then successfully applied to the measurement of the depolarization ratio of all six hydrogen isotopologues. This now allows direct comparison to theoretical quantum mechanical calculations. The latter is also of relevance to further advance confidence in the quantum-mechanical calculations of the final-state distributions, which is an essential aspect when measuring neutrino masses in the meV range with KATRIN and other experimental approaches such as Project 8 [Pro12].

Chapter 2

The KATRIN Experiment

This chapter gives an overview of tritium β-decay experiments, introduces the Karlsruhe Tritium Neutrino Experiment (KATRIN) which is targeted to measure the neutrino mass with a sensitivity of $200\,\mathrm{meV/c^2}$, and finally outlines the motivation of this thesis. The chapter is structured as follows: Section 2.1 briefly describes the physics of tritium β-decay and the principle of a MAC-E-Filter. The section ends with a view back on previous neutrino experiments. In Section 2.2 the requirements of the KATRIN experiment are discussed and an overview of its main components is given. Then, a deeper insight into the physical properties of the windowless gaseous tritium source is given in Section 2.3 and the implications for control and monitoring of this most complex KATRIN component are deduced. Finally, Section 2.4 focuses on the requirements for the laser Raman system of KATRIN, which imply that an accurate calibration of this system is required in order to stay within the stringent budget of systematic uncertainties so that KATRIN can reach its design sensitivity.

The main references for this chapter are the Technical Design Report of KATRIN [KAT05] and a recent review paper [Dre13].

2.1 Tritium β-decay experiments

Up to the date of the compilation of this thesis, the most sensitive direct searches for the neutrino mass are based on the tritium β-decay and the investigation of the energy spectrum of β-electrons close to the kinematic endpoint [Dre13].

2.1.1 Tritium β-decay and the neutrino mass

The super-heavy hydrogen isotope tritium (T) is unstable and decays according to the following reaction into a daughter nucleus via the emission of a pair of leptons, an electron, and an electron anti-neutrino:

$$\mathrm{T} \rightarrow {}^{3}\mathrm{He}^{+} + \mathrm{e}^{-} + \bar{\nu}_{\mathrm{e}}\,. \tag{2.1}$$

In 1934, Enrico Fermi published a fundamental theory of β-decay [Ferm34], based on the neutrino hypothesis by Wolfgang Pauli in 1930 (the relevant letters and publications

are summarized in [Pau85]). This theory allows to derive essential features of the decay, and also serves to derive an expression of the β-electron spectrum which is used in the analysis of the neutrino mass.

The calculation of the electron energy spectrum starts with Fermi's famous Golden rule

$$\frac{\mathrm{dN}}{\mathrm{dt}} = \frac{2\pi}{\hbar} \left|M^2\right| \rho \,. \tag{2.2}$$

M is the transition matrix element and ρ describes the density of final states. In principle, Eq. 2.2 needs to be integrated over all possible discrete and continuous final states.

The derivation results[1] in the following expression for the differential decay rate as function of the energy ($\dot{N}(E) = \mathrm{d^2N/(dtdE)}$)

$$\begin{aligned}\dot{N}(E) = C \cdot F(E, Z+1) \cdot (E + m_e c^2) \cdot \sqrt{(E + m_e c^2)^2 - m_e^2 c^4} \\ \cdot (E_0 - E) \cdot \sqrt{(E_0 - E)^2 - m(\nu_e)^2 c^4} \cdot \Theta\left(E_0 - E - m(\nu_e)c^2\right) \,.\end{aligned} \tag{2.3}$$

The kinetic energy and the rest mass of the electron are denoted by E and m_e, respectively. The endpoint energy E_0 of the electrons (=maximum kinetic energy) is given by the reaction energy, Q, and the recoil energy[2] of the $^3\mathrm{He}^+$ nucleus, E_{rec}: $E_0 = Q - E_{\mathrm{rec}}$ assuming $m(\nu_e) = 0$. The Fermi function, $F(E, Z+1)$, takes into account the Coulomb interaction of the emitted β-electron and the daughter nucleus with charge $Z+1$ [Hol92]. The Heaviside step function $\Theta(\dots)$ ensures conservation of energy.

Note that the β-decay of tritium is of the superallowed type which implies that the nuclear matrix element M_{nucl} is energy independent [Ott08]. Accordingly, it can be contracted in the constant C

$$C = \frac{G_F^2 \cdot \cos^2\theta_C}{2\pi^3\hbar^7 c^5} \cdot \left|M_{\mathrm{nucl}}^2\right| \,. \tag{2.4}$$

with Fermi's coupling constant G_F and θ_C denoting the Cabbibo angle.

The formula given in Eq. 2.3 is an approximation only, and therefore will be extended with regard to two important aspects for high-resolution β-spectroscopy. First, as discussed in the introduction chapter, the neutrino mass $m(\nu_e)$ is treated as a superposition of three mass eigenstates $m(\nu_i)$ as stated in Eq. 1.44. As will be shown below, the present experimental resolution does not allow to disentangle these mass states, so that an average mass is measured (*c.f.* Eq. 1.44). Second, all final states of the daughter system (atom or molecule[3]) with individual probabilities P_j and excitation energies V_j have to be accounted for. Thus each final state j has a corresponding specific endpoint $E_j = E_0 - V_j$. Both effects are integrated into Eq. 2.3 by a double summation.

[1] The reader is referred to [Wei03], [Ott08], and [Dre13] for the full derivation.

[2] The variation of the recoil energy in the endpoint region ($E_0 - 30\,\mathrm{eV} \dots \mathrm{E_0}$) amounts to only $\Delta E_{\mathrm{rec}} = 3.5\,\mathrm{meV}$, and therefore can be assumed as constant [Mas07].

[3] In the case of a decaying atom only electronic excitation need to be considered. Molecules also can be excited to vibrations and rotations.

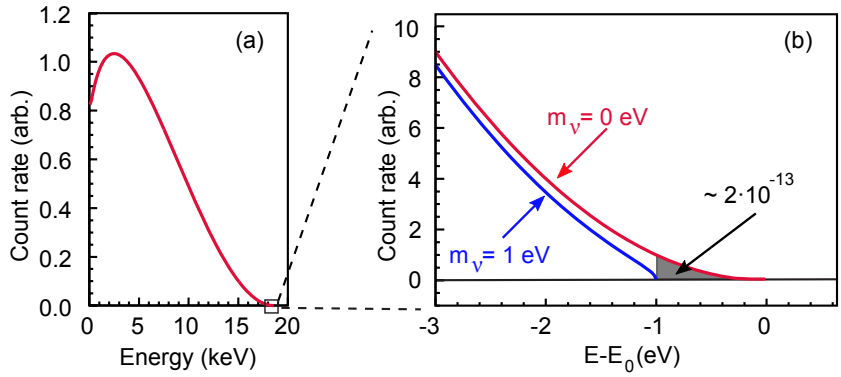

Figure 2.1: The electron energy spectrum of tritium β-decay. (a) Full energy range, (b) energy range around the kinematic endpoint of about $E_0 = 18.6\,\mathrm{keV}$. The spectrum is shown for two exemplary cases: (i) for a vanishing neutrino mass $m(\nu_e) = 0\,\mathrm{eV/c^2}$, and (ii) for a neutrino mass of $m(\nu_e) = 1\,\mathrm{eV/c^2}$. The shaded area represents only a fraction of $2 \cdot 10^{-13}$ of all tritium β-decays.

This finally leads to following expression (slightly modified from [Dre13])

$$\dot{N}(E) = C \cdot F(E, Z+1) \cdot (E + m_e c^2) \cdot \sqrt{(E + m_e c^2)^2 - m_e^2 c^4} \cdot \left(\sum_{i,j} |U_{ei}^2| \cdot P_j \cdot (E_j - E) \cdot \sqrt{(E_j - E)^2 - m(\nu_i)^2 c^4} \cdot \Theta\left(E_j - E - m(\nu_i) c^2\right) \right) . \tag{2.5}$$

Fig. 2.1 shows the overall energy spectrum of electrons from β-decay and a zoom into the endpoint region at about $E_0 = 18.6\,\mathrm{keV}$. The latter reveals the influence of a non-vanishing neutrino mass on the spectral shape. It underlines the generic fact that a finite neutrino mass leads to a shift of the spectral endpoint. Furthermore, the spectrum is distorted in an energy interval of several eV due to the extended momentum range where neutrinos are non-relativistic. The neutrino mass $m(\nu_e)$ can be obtained via fitting Eq. 2.5 to the measured data, while taking into account a variety of instrumental-related effects.

2.1.2 The MAC-E-Filter measurement principle

The spectral shape close to the endpoint in Fig. 2.1 indicates two major issues when measuring the neutrino mass. First, a high energy resolution in the order of $1\,\mathrm{eV}$ is required to observe the mass-dependent transition of the energy-momentum relation of the emitted neutrino over a specific momentum range. Second, the tritium source has to provide a very high β-intensity since the emission probability of an electron in the region-of-interest is tiny. The respective β-decay count rate should be at least a factor of two higher than the rate of background events, calling for an almost background-free detection technique.

A technique which combines both features is based on the so-called MAC-E-Filter principle (Magnetic Adiabatic Collimation with an Electrostatic filter). This spectrometer type is based on the pioneering work of Kruit and Read [Kru83], as well as of Beamson and

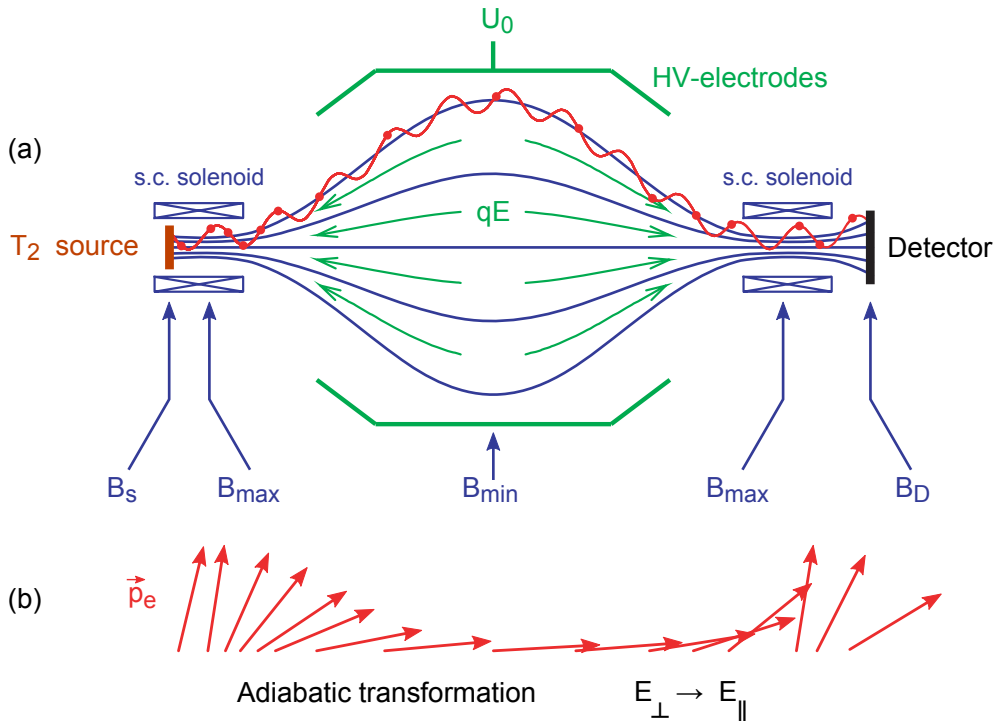

Figure 2.2: Principle of the MAC-E-Filter. A detailed explanation is given in the main text. *(a)* An inhomogeneous magnetic field B is generated by a system of superconducting solenoids (blue). These solenoids magnetically guide β-decay electrons from the tritium source to the electron detector. The decrease of the magnetic field between solenoids (plane of energy analysis) increases the area of the field lines. The electric retardation field is generated in such way that it is parallel to the magnetic field lines. *(b)* The momentum is transformed by a gradient force due to the adiabatic invariance of the magnetic moment of the electron μ in the inhomogeneous B-field. The highest degree of parallelism is obtained in the central region of B_{min}.

co-workers [Bea80]. It was further refined and adapted for neutrino mass measurements in Mainz [Pic92] and Troitsk [Lob85].

The main principle of the MAC-E-Filter is shown in Fig. 2.2. A tritium source and an electron detector are located each in a superconducting solenoid. The solenoids generate a magnetic guiding field for electrons from the β-source to the detector. During propagation, the electrons gyrate around the field lines in a cyclotron motion since their starting momentum is isotropic in general, and thus not parallel to the magnetic field lines. Their kinetic energy can be decomposed into a component $E_{\perp}$ transverse and a component $E_{||}$ longitudinal to the magnetic field lines. The method of magnetic guidance allows for an accepted solid angle of about 2π, in principle.

The magnetic field, B, reaches its minimum value in the middle between both solenoids. At this plane the field strength is several orders of magnitudes lower than at the center of the solenoids. As the transition of the magnetic field to its minimum value and back again is adiabatic, in a non-relativistic approximation the magnetic moment of the electron μ is

constant [Jac98]

$$\mu = \frac{E_\perp}{B} = \text{const} \ . \tag{2.6}$$

The strong decrease of the magnetic field B thus leads to a reduction of the $E_\perp$ component by the same amount, in order to keep μ invariant. The transversal component is thus transformed by the magnet gradient force into the longitudinal direction due to the adiabaticity of this process, with a small transversal component remaining at the mid plane. When discussing the MAC-E-Filter principle, it is important to recall that the magnetic flux $\Phi = \boldsymbol{A} \cdot \boldsymbol{B}$ is conserved. This leads to an increase of the beam cross-sectional area A by the same factor as the magnetic field B drops. The final result is a broad beam of electrons flying nearly parallel to the field lines at the center of the MAC-E-Filter. This is called magnetic adiabatic collimation of the MAC-E-Filter.

The second part is related to the electrostatic filter. The analysis of the kinetic energy of the electrons is performed in the plane of lowest magnetic field and thus in the area where the transformation into longitudinal energy is maximal. Accordingly, an electrostatic barrier created by cylindrical electrodes allows to filter the electrons. The filter can only be passed by electrons with higher kinetic energy than the potential from the retardation voltage U_0. This feature turns the MAC-E filter into a high pass filter. The adiabatic transformation into the longitudinal direction is of course imperfect by its very nature. For an isotropic β-source, the relative sharpness of the MAC-E-Filter is given by the ratio of the (minimal) magnetic field in the plane of energy analysis and the (maximal) field at the so-called pinch magnet which can be placed anywhere between source and detector

$$\frac{\Delta E}{E} = \frac{B_{\text{min}}}{B_{\text{max}}} \ . \tag{2.7}$$

At KATRIN, the plane of highest magnetic field B_{max} (at the pinch magnet) is located at the detector-facing side of the main spectrometer (see *e.g.* [Fra10]) generating a field of $6\,\text{T}$. With a minimum field in the central spectrometer plane of $0.3\,\text{mT}$, a relative sharpness, $\Delta E/E$, of $1:20000$ can be achieved. More details on the filter and its features are available in [Pic92, Bon99, KAT05].

2.1.3 Results of previous neutrino mass experiments at Mainz and Troitsk

Two research groups have independently developed and operated MAC-E-Filters for the measurement of the neutrino mass from tritium β-decay up to now. The experiments were located at Mainz [Pic92] and Troitsk [Lob85] and mainly differed in the employed tritium sources which exhibit different systematic uncertainties.

At Mainz, the experiment included a MAC-E-Filter type spectrometer with a diameter of $1\,\text{m}$ and a quench-condensed molecular tritium film as β-source operated a $T < 3\,\text{K}$ [Bor00]. Several solid state effects like inelastic scattering of β-electrons in the T_2 film [Ase00], the excitation of neighboring molecules [Kol88] and self-charging [Bor03] were identified as main systematic uncertainties. The analysis of the data set (the so-called Mainz phase II [Kra05]) led to a resulting observable of

$$m(\nu_e)^2 = (-0.6 \pm 2.2_{\text{stat}} \pm 2.1_{\text{sys}})\ \text{eV}^2/\text{c}^4 \ . \tag{2.8}$$

This can be translated, using the Feldman-Cousins method [Fel98], into an upper limit for the neutrino mass of

$$m(\nu_e) < 2.3\,\mathrm{eV/c^2}\ (95\%\ \mathrm{C.L.})\ . \tag{2.9}$$

The Troitsk group employed a slightly larger spectrometer with $1.2\,\mathrm{m}$ in diameter and a windowless gaseous tritium source (WGTS) [Bel95]. In 1999, a result was published which included an unexplained spectral anomaly near the endpoint [Lob99]. Taking into account this distortion, an upper limit of $m(\nu_e) < 2.5\,\mathrm{eV/c^2}$ $(95\%\ \mathrm{C.L.})$ was reported.

In 2011, the group at Troitsk reanalysed their data from 1994-2004 with refined methods. Specifically, time-dependent effects in their WGTS and the selection of periods with good data stability and quality were carefully considered. This new analysis has resulted in [Ase11]

$$m(\nu_e)^2 = (-0.67 \pm 1.89_{\mathrm{stat}} \pm 1.68_{\mathrm{sys}})\ \mathrm{eV^2/c^4}\ , \tag{2.10}$$

which corresponds via Feldman-Cousins [Fel98] to a new upper limit of

$$m(\nu_e) < 2.05\,\mathrm{eV/c^2}\ (95\%\ \mathrm{C.L.})\ . \tag{2.11}$$

2.2 The Karlsruhe Tritium Neutrino Experiment (KATRIN)

The Karlsruhe Tritium Neutrino Experiment (KATRIN) is targeted to improve the current experimental sensitivity as obtained from Mainz and Troitsk from $2\,\mathrm{eV/c^2}$ by a factor of ten to $200\,\mathrm{meV/c^2}$ [KAT05]. This major step in sensitivity can only be achieved by substantially increasing the statistics and reducing systematic effects significantly at the same time.

2.2.1 Projected sensitivity on neutrino mass

Detailed investigations reported in [KAT05] have shown that the reference KATRIN setup will feature, after three years of measurements, a statistical uncertainty of the observable $m(\nu_e)^2$ of $\sigma_{\mathrm{stat}} = 18 \cdot 10^{-3}\,\mathrm{eV^2/c^4}$. This value is of the same level as the total systematic uncertainty, which is anticipated to be $\sigma_{\mathrm{sys,tot}} \leqslant 17 \cdot 10^{-3}\,\mathrm{eV^2/c^4}$. Both errors add up quadratically to the total uncertainty

$$\sigma_{\mathrm{tot}} = \sqrt{\sigma_{\mathrm{stat}}^2 + \sigma_{\mathrm{sys,tot}}^2} \approx 25 \cdot 10^{-3}\,\mathrm{eV^2/c^4}\ . \tag{2.12}$$

This would imply that a 5σ significance is given for discovering a neutrino mass of

$$m(\nu_e) = 350\,\mathrm{meV/c^2}\ . \tag{2.13}$$

In case that no neutrino mass signal would be seen in the data, the total uncertainty can be translated into a new upper mass limit of

$$m(\nu_e) \leqslant \sqrt{1.64 \cdot \sigma_{\mathrm{tot}}} \tag{2.14}$$

$$\leqslant 200\,\mathrm{meV/c^2}\ (90\%\,\mathrm{C.L})\ . \tag{2.15}$$

In order to reach this ambitious goal, the next-generation experiment KATRIN needs to be designed along the following requirements [KAT05]:

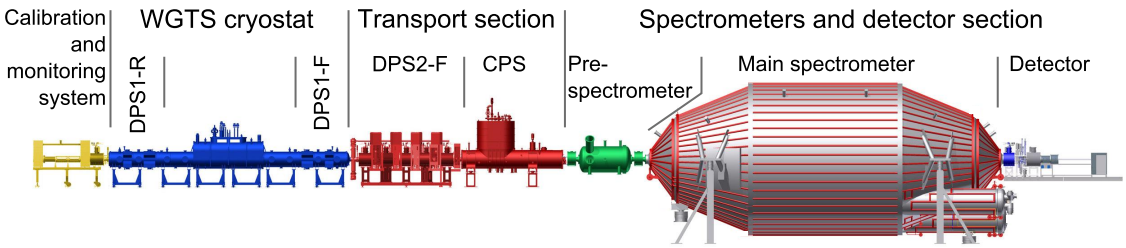

Figure 2.3: Setup of the KATRIN experiment. For the explanation of the main components see text.

- It is aimed to increase the signal rate at the endpoint of the β-spectrum by a factor of 100 compared to the predecessor experiments at Troitsk and Mainz. Further improvement of the statistics is achieved by a 10 times longer measurement time (three "full-beam" years or, equivalently, five calendar years).

- The energy resolution of MAC-E-Filter type spectrometer should be $\Delta E < 1\,\mathrm{eV}$ at $18.6\,\mathrm{keV}$.

- The overall background rate measured at the electron detector should be $< 10^{-2}\,\mathrm{cps}$.

- All sources of systematic uncertainties of $m(\nu_e)^2$ need to be reduced by a factor of 100, so that statistical and systematic uncertainties are of similar size. The total systematic uncertainty budget $\sigma_{\mathrm{sys,tot}} \leqslant 17 \cdot 10^{-3}\,\mathrm{eV}^2/\mathrm{c}^4$ is composed of five main sources of uncertainties (see [KAT05, Dre13]). Accordingly, the individual systematic uncertainties should not surpass the uncertainty budget of

$$\sigma_{\mathrm{sys,ind}} \leqslant 7.5 \cdot 10^{-3}\,\mathrm{eV}^2/\mathrm{c}^4 \,. \tag{2.16}$$

  The two sources of uncertainties from the tritium source which are directly related to this thesis are discussed in detail in Section 2.3.

2.2.2 Experimental overview

The aforementioned requirements were considered and implemented in the design of the KATRIN experiment. A side view on the $70\,\mathrm{m}$ long setup is provided in Fig. 2.3. All relevant main components will be introduced in a compact way below. The reader is referred to the KATRIN design report [KAT05] for further reading; additionally, recent publications or PhD theses which focus on specific sub-systems in more detail are cited at the end of each paragraph. Towards the end of this chapter, the focus is set on the windowless gaseous tritium source since this thesis is closely related to measuring important source properties.

The description is following the road of the electron from its point of origin in the source to its point of detection at the detector surface.

The Windowless Gaseous Tritium Source (WGTS) KATRIN will make use of a high luminosity gaseous molecular tritium source as pioneered by the Troitsk [Bel95] and Los Alamos [Rob91] groups. In Fig. 2.4 its conceptual design is visualized. Molecular tritium ($5 \cdot 10^{19}$ molecules/s) is injected in the middle of a stainless steel tube with a length of $10\,\mathrm{m}$ and a diameter of $90\,\mathrm{mm}$. At both ends of the tube, tritium is pumped out at specific pump ports. This generates a longitudinal tritium density profile as sketched in the top panel of Fig. 2.4. The β-activity of the source is about 10^{11} electrons per second. The superconducting solenoid system surrounding the source tube guides the β-electrons adiabatically to the front and rear ends of source. The nominal magnetic field strength inside of the tube will be at $3.6\,\mathrm{T}$. The WGTS is housed inside of a large and rather complex cryostat which is able to provide a stable temperature of the source tube at $30\,\mathrm{K}$ [Gro09]. The WGTS is connected to the Inner Loop which provides a stable circulation of the gas through the source [Stu10b] and sustains the high tritium purity of the gas.

The key parameters of the WGTS as well as the extensive control and monitoring equipment are the focus of Section 2.3, where also the motivation for this thesis is found.

Further reading: [Stu10b, Bab12].

The transport system The two systems downstream of the WGTS forming the Source and Transport Section (STS) altogether are the Differential Pumping Section (DPS)[4] and the Cryogenic Pumping Section (CPS). Their tasks are to magnetically transport the electrons to the spectrometer section and further reduce the residual tritium which was not pumped out at the WGTS exit. These additional tritium retention systems are required to limit the amount of tritium entering the spectrometer. Decaying tritium within the spectrometer volume would lead to an elevated rate of background events [Mer13, Kos12]. The tritium flow has to be reduced by 14 orders of magnitude by two very different techniques. The DPS actively removes tritium from the beam tube by turbomolecular pumps [Luk12], while the CPS employs a passive cryosorption concept [Gil10].

Further reading: [Kos12].

The spectrometer system KATRIN employs a combination of two spectrometers of the MAC-E-Filter type. A pre-spectrometer ($3.4\,\mathrm{m}$ length and $1.7\,\mathrm{m}$ diameter) is connected to the downstream end of the CPS marking the begin of the tritium-free area of the experiment where tritium levels are on a negligible level. This smaller-sized spectrometer offers the option of prefiltering, in which all electrons with kinetic energies of $E_0 - 300\,\mathrm{eV}$ would be reflected so that only the electrons of highest energies enter the main spectrometer.

The task of the main spectrometer is to analyze the high-energy part of the β-decay electrons which carry information on the neutrino mass with an energy resolution of $\Delta E = 0.93\,\mathrm{eV}$ at $18.6\,\mathrm{keV}$ (see Eq. 2.7). Several auxiliary systems provide highly accurate and stable control over the electrostatic retarding potential (*e.g.* see [Thu09, Val10, Erh12]) as well as on the magnetic fields (*e.g.* see [Rei09, Wan09]) in the spectrometer.

Further reading: [Fra10, Pra11, Mer12].

[4]Note that the DPS1-F/R are part of the WGTS cryostat already, and the stand-alone system is called DPS2-F (see Fig. 2.3).

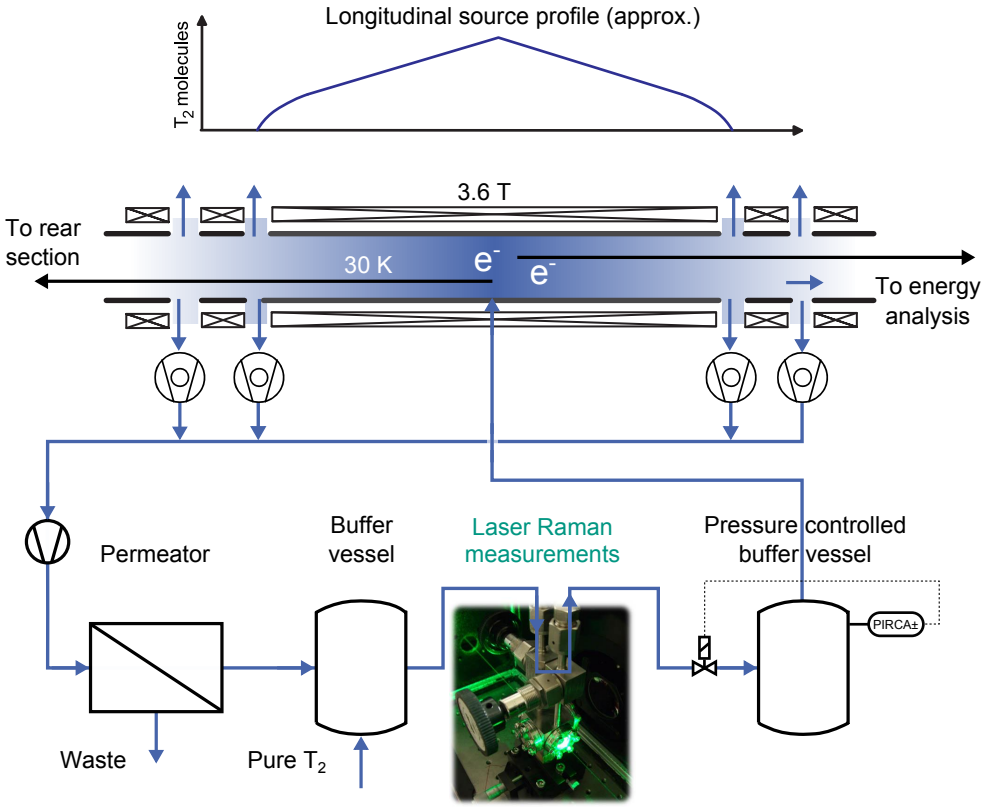

Figure 2.4: Conceptual design of the Windowless Gaseous Tritium Source and Inner Loop. A stable tritium source profile (*top panel*) needs to be obtained during regular KATRIN operation. The density is highest at the injection point in the middle of the source tube and lowest at the pumping ports at the end of the tube. The gas circulation is provided by the Inner Loop [Stu10b]. Its parts are sketched in the bottom half of the figure. Pure tritium is obtained from the TLK infrastructure and filled into a buffer vessel. The composition of the gas is measured at a pressure of $100 - 200\,\mathrm{mbar}$ by a laser Raman system while it streams into the next buffer vessel. This vessel is pressure controlled and by this means it can provide a stable injection pressure which corresponds to a stable tritium flow rate (as long as the conductances of the injection capillary and the WGTS beam tube remain constant). The injected gas is pumped out by turbomolecular pumps and the return flow of the gas is then filtered from impurities by a permeator. This device consists of a PdAg membrane which is only permeable by hydrogen isotopologues (T_2, DT, D_2, HT, HD, and H_2); more details on permeators are given in Section 6.5.2. The impurities are handled by the TLK infrastructure and replaced by batches of "fresh" high-purity tritium.

The Focal Plane Detector The detector at the end of the KATRIN beamline is a silicon-based PIN diode array with a detection efficiency of $> 90\%$ [Van12]. It has been designed to count electrons which were transmitted through the MAC-E-Filters. It is highly segmented into a total of 148 pixels of the same area to obtain a spatial resolution over the entire transmitted flux tube of $191\ \mathrm{Tcm}^2$. This is of major importance for detecting inhomogeneities in the tritium source or spectrometer potentials. The system is at present close to being integrated with the main spectrometer for the extensive spectrometer commissioning phase starting in spring 2013.

Further reading: [Har12].

Calibration and monitoring system Upstream of the WGTS cryostat a calibration and monitoring system is located which has three major purposes: (i) It houses the rear-wall which will define the plasma potential relative to the spectrometer retarding voltage [Bab12]; (ii) It measures the source activity via β-induced X-ray spectroscopy [Roe12, Pri13]; and (iii) it provides an angular resolved electron gun [Val11] for the measurement of the column density of the molecular gas source via inelastic electron-gas scattering. At present the system has completed its conceptual design phase.

Further reading: [Bab12].

Experimental location The KATRIN experiment has to cycle tens of grams of tritium per day through the WGTS. The offical license for handling up to $40\,\mathrm{g}$ of the radioactive gas and the appropriate extensive infrastructure are available only at few places worldwide such as the Tritium Laboratory Karlsruhe (TLK) at the Karlsruhe Institute for Technology (KIT) [Pen00, Doe08]. The TLK has set-up and operated a closed tritium cycle for storing, processing, and purifying of the various gases, and offers a research experience of 20 years. These conditions are unique in the civil tritium research and they make the TLK the perfect host facility for the KATRIN experiment. A view of TLK infrastructure units with their glove box structure is provided in Fig. 2.5.

2.3 Properties of the WGTS

A gaseous molecular tritium source, which was employed in previous direct neutrino mass experiments (see [Rob91] and [Bel95]), is able to provide a high luminosity. This is of key relevance to achieve a high statistical sensitivity in the neutrino mass search. The essential parameters[5] are the column density $\mathcal{N}$ and the isotopic composition (T_2, DT, HT, D_2, HD, H_2). The column density is defined as the number of molecules within the magnetic flux tube volume relative to the cross-sectional area in units of cm^{-1}. The activity $\mathcal{S}$ of the source is given as [Bab12]

$$\mathcal{S} = C_S \cdot \epsilon_\mathrm{T} \cdot \mathcal{N} \,. \tag{2.17}$$

where ϵ_T denotes the tritium purity and the proportionality constant C_S contains the experimental properties (acceptance angle, detector efficiency, ...).

[5]The nomenclature from the paper of Babutzka *et al* [Bab12] is employed here.

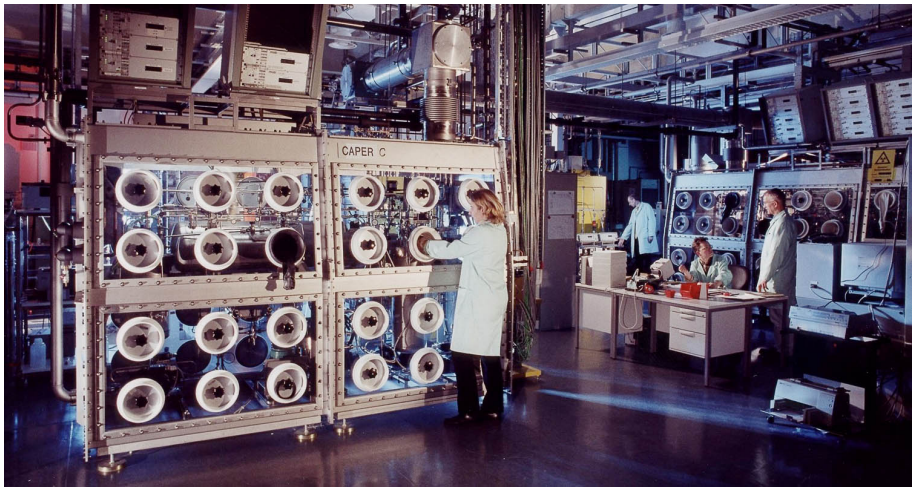

Figure 2.5: View into the experimental hall of the Tritium Laboratory Karlsruhe (TLK). The person in the front works at a glove box which acts as secondary containment for the primary tritium system inside of it. This measure prevents contamination hazard for the workers and the laboratory.

For the determination of the neutrino mass it is important to control the two parameters, ϵ_{T} and $\mathcal{N}$, and to monitor their stability so that even tiny fluctuations can be accounted for in the off-line analysis.

2.3.1 Column density

The gas column of the WGTS is built up and stabilized by the following approach [Bab12] (see Fig. 2.4):

1. The gas is continuously injected into the middle of the source tube with an injection pressure p_{in} of about $10^{-3}\,\mathrm{mbar}$.
2. The gas streams to both ends of the central of the $10\,\mathrm{m}$ long and $90\,\mathrm{mm}$ wide beam tube, and it is pumped out there with constant pumping speed resulting in an outlet pressure p_{out} of about 1/20 of p_{in}.
3. The gas flow inside of the tube is governed by the viscosity of the gas which itself is a function of the temperature. For this reason the beam tube temperature has to be stabilized at a temperature region of about $30\,\mathrm{K}$.

The stability of the column density of the WGTS is one of the major sources of systematic uncertainty at KATRIN [KAT05]. In order to stay within the assigned uncertainty budget for the column density (see Eq. 2.16), it is required to obtain a precision of $\Delta_{\mathrm{prec}}(\mathcal{N})/\mathcal{N} \leqslant 0.1\%$. Simulations have shown that it is necessary to stabilize p_{in} on the 0.1% level, p_{out} to about 3% and source tube temperature to better than $30\,\mathrm{mK}$ ($\triangleq 0.1\%$) [KAT05, Sha04, Hoe12].

The gas circulation is provided by the Inner Loop system sketched in Fig. 2.4 [Stu10b]. This closed loop system has been optimized to achieve a stable column density of $\mathcal{N} = 5 \cdot 10^{17}$

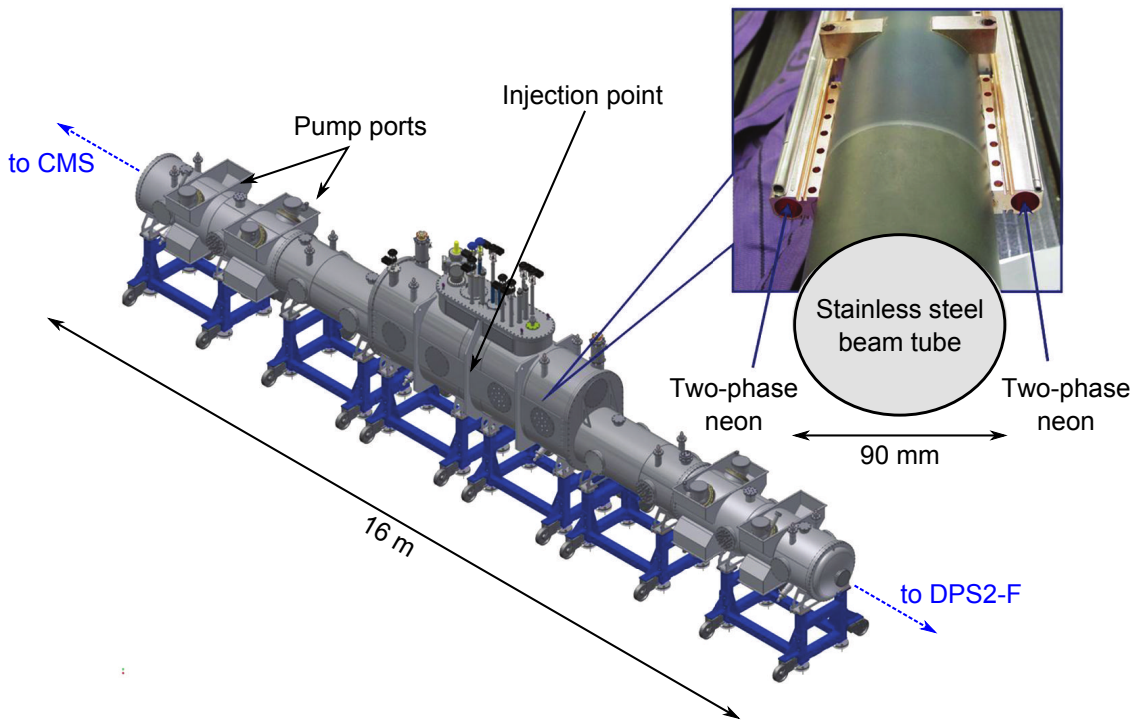

Figure 2.6: Schematic view of the WGTS cryostat and beam tube cross-section. The ports for the turbomolecular pumps are indicated only at one end. The inlet shows the beam tube to which the two phase liquid neon cooling system is attached. Adapted from [Dre13].

molecules per cm^2. The observed stability of the injection pressure p_{in} in a test experiment surpassed the required 0.1% by about an order of magnitude [Pri10a].

The WGTS is housed in a single more than $16\,\mathrm{m}$ long cryostat (see Fig. 2.6) which is able to provide a relative temperature stability of the source tube by a two-phase neon system [Gro09]. The achieved stability at a WGTS mock-up named "Demonstrator" was $\Delta T = 1.5\,\mathrm{mK\,h^{-1}}$ which is better than specified, too [Gro13].

The column density, $\mathcal{N}$, is strongly related to the probability of inelastic scattering of the electrons off the source gas [Liu87]. $\mathcal{N}$ is thus not only related to the β-rate, but also to energy losses, which distort the β-spectrum. For these reasons, the determination of N and the knowledge of the isotopic composition is of primary importance for KATRIN.

2.3.2 Isotopologue composition

The other parameter which needs to be considered for the stability of the activity $\mathcal{S}$ in Eq. 2.17 is the tritium purity.

The tritium purity ϵ_{T} is given as the ratio of the number of tritium atoms to the total sum of atoms in the WGTS. The targeted purity value for the KATRIN measurement period is $\epsilon_{\mathrm{T}} > 0.95$. This corresponds to a composition of about 90% molecular tritium, T_2, as the main gas constituent with a small admixture of DT ($< 10\%$). The other hydrogen isotopologues (HT, D_2, HD, and H_2) will be present as trace amounts only.

The stabilization of the gas composition is realized by connecting the Inner Loop to the tritium infrastructure of TLK as shown in Fig. 2.4. This interface allows extraction of parts of the impurities of the source gas and replacing them by (almost) pure tritium (up to 98% [Dör05]).

The monitoring of the gas composition is performed by a laser Raman system (LARA) which is integrated within the Inner Loop. Raman spectroscopy is an excellent instrument for the determination of the gas composition of the source gas. It is able to monitor all isotopologues simultaneously [Stu10a]. The principles of Raman spectroscopy and the experimental setup will be discussed in following chapters in detail, as they are closely related to the topic of this thesis.

The requirements on the accuracy of this system are discussed in the subsequent section.

2.4 Accuracy requirements for the monitoring of the source gas composition

The accuracy of the monitoring system of the gas composition should be considered under two different aspects, which are precision and trueness.

Trueness is the fundamental quantity which describes the difference between the mean value of a measured observable and the true (reference) value. The precision is related to the square root of the statistical variance of several measured values around their mean value. Thus, trueness is linked to systematic uncertainty, and precision to the statistical uncertainty [JCG08].

A measurement can be called accurate if it is both, true and precise. A more detailed discussion of the two terms is found in Appendix A.

The KATRIN requirements for precision and trueness are discussed in the following.

Precision requirement The number of tritium atoms in the source governs the activity $\mathcal{S}$ of the source (see Eq. 2.17). Therefore, it is relevant to stabilize and monitor the tritium purity, ϵ_{T}, on the same 0.1% precision level like the other parameters related to $\mathcal{N}$. By fulfilling this requirement it is possible to stay within the systematic uncertainty budget, $\sigma_{\mathrm{sys,ind}}$, related to the tritium source.

Trueness requirement Until now, only relative changes of the gas composition were considered, which can be measured if the system's precision is sufficient. Trueness is not relevant at this point.

However, the composition of source gas is not only influencing the activity $\mathcal{S}$. Furthermore, non-negligible processes alter the β-electron energy and thus the shape of the β-spectrum. In general, the shape distortions are specific to each hydrogen isotopologue species involved. The relevant processes are summarized in the following list [KAT05].

- **Nuclear recoil of the daughter molecule**
  The momentum of the outgoing lepton pair is balanced by the daughter molecule ($^3\mathrm{HeT}^+$, $^3\mathrm{HeD}^+$, or $^3\mathrm{HeH}^+$), which results in a specific recoil energy, E_{rec}. An approximation of this recoil energy for electron energies close to the endpoint, E_0, is given by [KAT05]

$$E_{\mathrm{rec}} \approx E \cdot \frac{m_e}{m_{\mathrm{daugther}}} \,. \tag{2.18}$$

  The mass of the daughter molecule of the decay $\mathrm{T}_2 \rightarrow {}^3\mathrm{HeT}^+$ is 1.5 times higher than of the decay $\mathrm{HT} \rightarrow {}^3\mathrm{HeH}^+$. Thus, the recoil energy scales inversely: $E_{\mathrm{rec}}^{\mathrm{T}_2} = 1.72\,\mathrm{eV}$ and $E_{\mathrm{rec}}^{\mathrm{HT}} = 2.58\,\mathrm{eV}$, respectively [Sae00]. As a result, the (unobserved) recoil energies of the different hydrogen isotopologues has to be taken into account on a statistical basis.

- **Doppler broadening**
  The molecules in the source obey a thermal velocity according to the Maxwell-Boltzmann distribution [Hoe12] superimposed by a bulk velocity due to the diffusion of the molecules to both ends of the beam tube. Thus, the kinetic energy of the emitted electrons is affected by the quasi-stochastic movement of the decaying molecules. The non-relativistic approximation for the energy broadening of an electron with $E \approx E_0$ emitted by a molecule flying parallel to the magnetic field lines is given by [KAT05]

$$\Delta E = m_e \cdot |\boldsymbol{v}_{\mathrm{e}}| \cdot |\boldsymbol{v}_{\mathrm{mol}}| \,. \tag{2.19}$$

  In this relation, $\boldsymbol{v}_{\mathrm{e}}$ is the velocity of the emitted electron and $\boldsymbol{v}_{\mathrm{mol}}$ is the mean speed of the molecule at $30\,\mathrm{K}$. The largely different masses of the hydrogen isotopologues imply different values of $\boldsymbol{v}_{\mathrm{mol}}$. Therefore, the broadening for T_2 is about $\Delta E = 148\,\mathrm{meV}$, for HT is $\Delta E = 181\,\mathrm{meV}$. Moreover, the different molecular masses imply a certain demixing effect along the beam axis.

- **Electron scattering with source molecules** The β-electrons which are guided to the spectrometer have a rather larger probability to undergo inelastic [Ase00] and elastic scattering [Liu85] with the molecules in the gas column. In these processes the energy and momentum of the electrons is changed. For example, the energy loss of the β-electrons by elastic scattering is given by [KAT05]

$$\Delta E = 2\frac{m_{\mathrm{e}}}{m_{\mathrm{mol}}} \cdot E \cdot (1 - \cos\theta) \tag{2.20}$$

  which again depends on the molecular mass, m_{mol}. In general, the scattering angle θ is very small since the scattering is mostly forward peaked, which makes the contribution of the term in Eq. 2.20 quite low.

  According to [Liu87], the inelastic scattering cross-section is in first order proportional to the square of the intermolecular distance. This distance is related to the reduced mass of each isotopologue and thus the scattering cross-section will scale accordingly.

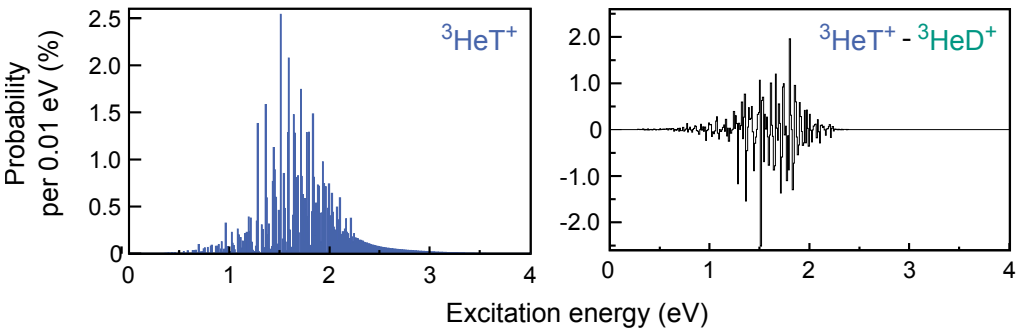

Figure 2.7: Final state distributions. *Left panel:* Final state distribution for the daughter molecule $^3\mathrm{HeT}^+$. *Right panel:* Difference of final state distributions of $^3\mathrm{HeT}^+$ and $^3\mathrm{HeD}^+$. It shows that the final state distributions are slightly different due to the different masses. Note that the nuclear recoil energy is already accounted for in these distributions.

- **Final state distribution** In Eq. 2.5 the final energy states V_j were introduced to which a daughter molecule can be excited after the β-decay. The first electronic excited electronic state of $^3\mathrm{HeT}^+$ appears at about $27\,\mathrm{eV}$ [Sae00]. This rather large energy thus has no effect in the narrow region-of-interest around E_0 for the neutrino mass analysis at KATRIN. However, the nuclear recoil can give rise to a large number of rotational-vibrational states with a mean energy of about $1.89\,\mathrm{eV}$ for $^3\mathrm{HeT}^+$ [Dos06]. The energy states and the probabilities depend on the type of the daughter molecule, as shown in Fig. 2.7.

These systematic effects have been incorporated into the analysis models and simulation packages for KATRIN (*e.g.* see [Hoe12]). However, as input, they crucially require an accurate knowledge of the gas composition as provided by the laser Raman system.

In the KATRIN Design Report an estimate for the systematic uncertainty assigned to the description of the final state distribution is given. The shift on the neutrino mass square corresponding to this theoretical uncertainty is estimated to be $6 \cdot 10^{-3}\,\mathrm{eV}^2/\mathrm{c}^4$ [KAT05].

The isotopic composition weights the contributions of the final states from the different tritium containing isotopologues (T_2, DT and HT). This means that systematic uncertainties in the measurement of the composition will additionally add up to the previously mentioned systematic shift. This additional impact resulting from the trueness of the LARA system was not considered by the Design Report. In general, a high trueness of an analytical system is achieved by an appropriate calibration. In Section 3.3, this topic is discussed in detail. In this context, calibration is understood as one or several methods to determine certain system-dependent factors which link the measured Raman signal to the actual composition. Thus, the calibration uncertainty of the Raman system is related to systematic errors in these factors.

At the beginning of the works related to this thesis, the uncertainty of $m(\nu_e)^2$ related to the calibration trueness was investigated. Dedicated simulations with the KATRIN simulation package, Kassiopeia [Bab11], were performed, in close collaboration with Markus Hötzel and Wolfgang Käfer. These simulations contained a full WGTS model including all aforementioned species-dependent effects [Hoe12, Kae12]. The investigation strategy and the results were published soon after [Sch12a].

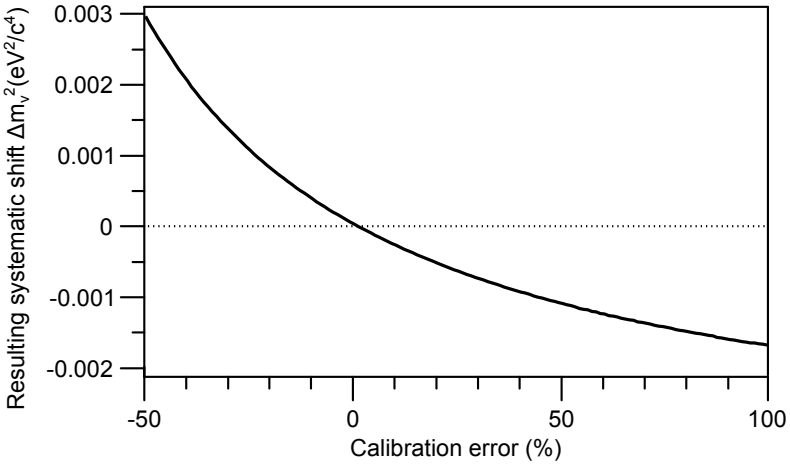

Figure 2.8: Dependence of the systematic shift of $\mathbf{m(\nu_e)^2}$ on the LARA calibration error. In this simplified case, the LARA calibration error ($\sigma_{\mathrm{cal,LARA}}$) is defined as the percentage of misinterpretation of the calibration factor between the main species in the WGTS, $\mathrm{T_2}$ and DT. The relation between observed (measured) and true, relative tritium amount is given by Eq. 2.21.

The dependence of the calibration uncertainty, $\sigma_{\mathrm{cal,LARA}}$, and associated systematic shift, $\Delta m(\nu_e)^2$, is related to the tritium purity, ϵ_{T}. It is obvious, that the calibration of the system becomes irrelevant when the purity parameter approaches $\epsilon_{\mathrm{T}} = 1$. Therefore, the investigations were performed by adopting the reference purity value of $\epsilon_{\mathrm{T}} = 0.95$ ($90\%\,\mathrm{T_2}$, $10\%\,\mathrm{DT}$). In Fig. 2.8 the corresponding systematic shift of $m(\nu_e)^2$ is shown as a function of the LARA calibration error for an assumed vanishing neutrino mass ($m(\nu_e) = 0\,\mathrm{eV/c^2}$). The relation between observed (measured) and true, relative tritium amount is given by

$$n_{\mathrm{obs,T_2,rel}} = \frac{n_{\mathrm{true,T_2}} \cdot (1 + \sigma_{\mathrm{cal,LARA}})}{n_{\mathrm{true,T_2}} \cdot (1 + \sigma_{\mathrm{cal,LARA}}) + n_{\mathrm{true,DT}}} \,. \tag{2.21}$$

It can be deduced that the systematic shift in $\Delta m(\nu_e)^2$ would be $\leqslant 3 \cdot 10^{-3}\,\mathrm{eV^2c^{-4}}$ for realistic calibration errors $\sigma_{\mathrm{cal,LARA}} \ll 50\%$.

In order to keep the combined systematic uncertainty from the description of the final-state distribution and the LARA calibration as low as possible, one aims for a calibration uncertainty of 10% or smaller. In this case, the uncertainty contribution resulting from the trueness of the LARA calibration will not significantly contribute to the total uncertainty [Sch12a]. Independent estimates using a toy model rather than the full source simulation lead to a comparable result [Kae12].

Said considerations only account for the case of neutrino mass measurements by KATRIN in standard operation mode (*i.e.* isotopic purity $\epsilon_{\mathrm{T}} \approx 0.95$ and measurements interval up to $30\,\mathrm{eV}$ below the endpoint energy). However, additional, auxiliary measurements are scheduled in which the knowledge of the gas composition is even more demanding. The energy loss function of the β-electrons inside the gaseous tritium source will be measured with the help of a mono-energetic electron-gun which probes the gas density and the characteristic energy loss of the scattered electrons [Bab12]. Therefore, different source

gas compositions will be prepared to disentangle the isotopic influence on the scattering losses. In this process the scenario changes from having only one primary constituent, T_2, with the rest being only impurities, to a scenario with constituents of similar magnitude. Thus in the latter scenario, the same (relative) calibration uncertainties would imply larger (absolute) shift in the composition.

It is considered that KATRIN may also be utilized for the search of sterile neutrinos from the eV scale [Rii11, For11] up to the keV scale [Veg13], with the latter being a candidate for warm dark matter [Aba06]. In these investigation the measurement interval will no longer be limited to the endpoint region of the spectrum, but be rather expanded to the entire spectrum. In this case much higher rates are present and significantly larger systematic effects with regard to gas dynamics and energy losses are expected. Thus, for these future investigations, the monitoring requirements are assumed to be even higher.

Summary of the accuracy issues of the KATRIN LARA system and objectives of this thesis An introduction to the Raman effect and its application for quantitative spectroscopy will be provided in Chapter 3. The feasibility of using Raman spectroscopy for the monitoring of the source gas composition was proved already in [Lew07, Sch09, Stu10a]. There, it could be demonstrated that the required precision of 0.1% can be achieved during a long-term test with circulating gas samples within a sampling time of $250\,\mathrm{s}$ [Fis11, Stu10b].

Following these early investigations, major optimizations in the experimental LARA setup, the data read-out and the data-processing methods were implemented in the course of this PhD thesis. These steps have enhanced the sensitivity of LARA by more than one order of magnitude as reported in Chapter 4 (experimental setup and routines).

Therefore, it can be claimed that the precision requirement of the KATRIN experiment is well-in-hand. On the other side, the fundamental open issue of calibration and thus of the LARA system's trueness was not touched prior to this thesis.

Therefore, the principle goal of this thesis was to develop different calibration strategies, to apply them and to further optimize them with regard to the LARA system of KATRIN, to validate them with regards to systematic uncertainty (trueness), and to finally evaluate the impact of the calibration to the neutrino mass analysis of KATRIN.

The path to this final goal is given along the chapters of this thesis. At the end of Chapter 3 various calibration possibilities will be discussed with regard to their individual advantages and drawbacks, from which the overall strategy for KATRIN will be identified. It consists of two approaches, which on their own would not be suitable for the calibration of the LARA system for all six hydrogen isotopologues. Only by combining these approaches the requirements can be met successfully. In Chapter 5, the first method is introduced which is able to cover all six hydrogen isotopologues. This approach is sample-free and is based on theoretical Raman intensities and the spectral sensitivity of the Raman system. However, the validity of the available theoretical data needs to be proved. This is done within a second, independent calibration method. Its methodology and results are discussed in Chapter 6. Finally, Chapter 7 is dedicated to the comparison of both calibration methods and to the discussion of their impact on the KATRIN physics analysis.

Chapter 3

Theory of quantitative Raman spectroscopy

Light has the ability to scatter off molecules. In this process the direction of the outgoing photon is changed with regard to the incident one, but the photon's wavelength stays constant. The probability of this elastic interaction is quite low; for example, only about 10^{-5} of the incoming photons are Rayleigh-scattered after being transmitted through $1\,\mathrm{m}$ of air [Sne05]. In 1923, Adolf Smekal predicted the existence of an even rarer possibility of inelastic scattering [Sme23]. This effect was then discovered experimentally by C.V. Raman and K.S. Krishnan in 1928 [Ram28], so that later it was being named after its principal discoverer as the "Raman effect". In Fig. 3.1 the inelastic scattering process of a photon with a diatomic molecule is visualized. It details the energy transfer to the molecule during the process while the photon energy is reduced by the amount of transferred energy.

Today, the Raman effect is used for numerous spectroscopic investigations [Lyo98]. The

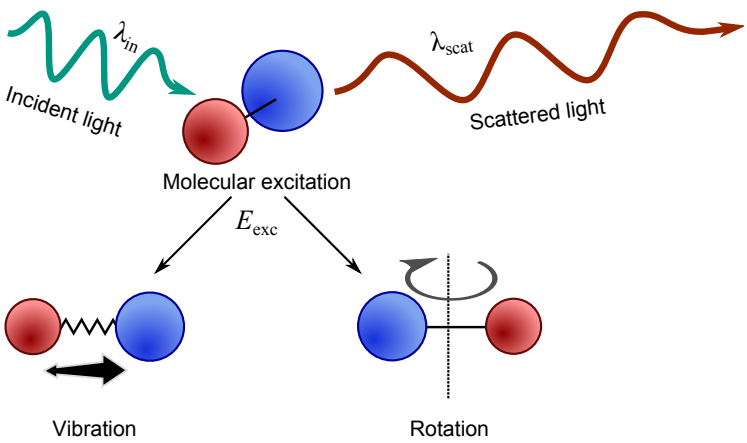

Figure 3.1: Illustration of a Raman scattering process. A photon with a certain energy hc/λ_{in} scatters off a molecule. In the case of inelastic scattering, a quantized amount of energy, E_{exc}, is transferred into rotational and/or vibrational excitation of the molecule. The energy of the scattered photon is reduced accordingly by the energy portion $hc/\lambda_{\mathrm{scat}} = hc/\lambda_{\mathrm{in}} - E_{\mathrm{exc}}$, so that its wavelength is increased ($\lambda_{\mathrm{scat}} > \lambda_{\mathrm{in}}$). Note that the inverse process is also possible; this will be included in the discussion below.

spectral analysis of the Raman-scattered light elucidates the qualitative and quantitative composition of a target sample. A multitude of applications is found in the analysis of gases [Sch03], in material science [Web00], in life-science [Pet03], and in many further fields. Various aspects of quantitative analysis using Raman spectrometry are summarized in the review by Pelletier [Pel03].

The intention of this chapter is to provide a sufficient theoretical science base for the reader to follow the content of this thesis. It starts with an introduction to properties of the excited states in diatomic molecules and to the Raman effect. The focus will then be directed onto Raman intensities and the special features of Raman spectroscopy when all hydrogen isotopologues are included. Subsequently, a summary is given of the research and development (R&D) activities and milestones related to Raman spectroscopy of tritium containing gas samples by external groups and groups at the Tritium Laboratory Karlsruhe (TLK). Finally, the important issue of calibration is discussed and various possible realizations are presented. The chapter concludes with the calibration strategy adapted for the Laser Raman system of KATRIN.

The following introduction into the fundamentals of molecular excitation and the Raman effect is based on the textbooks by Atkins, Long, as well as Haken and Wolf. [Atk06, Lon02, Hak06].

3.1 Introduction to Raman Spectroscopy

A typical setup for Raman spectroscopy is shown schematically in Fig. 3.2, while a detailed discussion of the actual setup is given in the following Chapter 4.

The intensity of the inelastically scattered (Raman) light is generally very small as compared to the elastically scattered (Rayleigh) light. Only one out of $10^7 - 10^8$ photons is participating in Raman scattering [Pet03]. In general, this is a sensitivity limiting drawback. Despite this, Raman has several advantages over other spectroscopic techniques.

For Raman spectroscopy one needs a single laser only, operating at a fixed wavelength to cover a wide spectral range. Other techniques which are based on emission/absorption spectroscopy, such as Laser Induced Fluorescence, require tunable lasers or a combination of lasers making such a system more complex [Tel07].

Raman spectroscopy also overcomes another typical drawback of emission/absorption spectroscopy. These techniques are generally unable to detect (homonuclear) molecules, that do not exhibit a permanent dipole moment like O_2, N_2 and, of course, H_2, D_2 and T_2. This restriction is not given for Raman scattering and thus all six hydrogen isotopologues, the three homonuclear (H_2, D_2, T_2) ones and the three heteronuclear (HD, HT, DT) ones, are detectable by Raman spectroscopy.

In summary, Raman spectroscopy is an excellent choice for the measurement of the isotopic purity of the WGTS source gas for KATRIN. The procedure is non-destructive, non-contact and can be performed in-line of the chemical engineering process while also allowing for near-time process control and data analysis [Sch09].

Within this thesis specific aspects of Raman intensity will be investigated with greater detail. The introduction to the excited states and to the Raman scattering is based on a

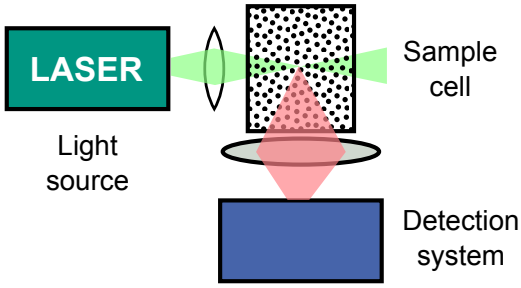

Figure 3.2: Sketch of measurement setup for observing of the Raman effect. The general components of a standard Raman experiment are shown for a 90° observation geometry. This geometry is preferred to reduce the intensity of the primary collected light which may be diffusely reflected into the detection system.

semi-classical model. A pure quantum mechanical approach would describe the processes and energies in a more precise way, but given experimental precision and resolution, this is of no relevance for the results presented here. For further reading, the following textbooks are recommended on which the theory of the sections below is based on: [Atk06, Lon02, Hak06].

3.1.1 Rotational and vibrational states in diatomic molecules

In order to understand the Raman effect in the context of diatomic molecules like the six hydrogen isotopologues (H_2, HD, HT, D_2, DT and T_2), first the possible excited energy states within molecules needs to be introduced.

The possible modes of excitation in molecules are electronic, vibrational, and rotational ones. Only the latter two are in the energy range considered here and thus of relevance for the non-resonant Raman spectroscopy employed in this thesis.

In spectroscopy the energy of states, the transition energy between states, and the photon energy are expressed usually in wavenumbers $\tilde{\nu}$ (in units of cm^{-1}). The relation to frequency ν (in Hz) and wavelength λ (in nm) is the following:

$$\tilde{\nu} = \frac{1}{\lambda} = \frac{\nu}{c} = \frac{E}{hc} \tag{3.1}$$

with h being Planck's constant and c denoting the speed of light.

Rotational states A generic model for the energy configuration of circular motions of a diatomic molecule is the rigid rotator with quantized energy for each rotational quantum number J. The eigenenergy spectrum $\tilde{F}(J)$ in units of cm^{-1} is given as

$$\tilde{F}(J) = BJ(J+1) \tag{3.2}$$

with $B = h(8\pi^2 c)^{-1}\Theta^{-1}$ as the rotational constant being characteristic for the molecule with the mass-dependent moment of inertia Θ.

It can be shown experimentally that this term is only a coarse approximation since the internuclear distance of both atoms in the molecule is centrifugally stretched, especially if

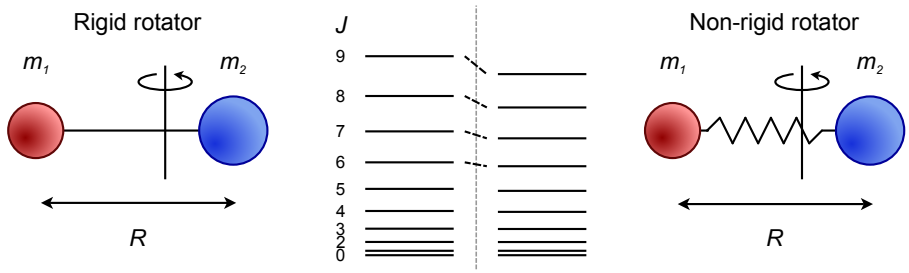

Figure 3.3: Model for rotation of diatomic molecules. *Left:* Model and energy spectrum of a rigid rotator. The distance between both atoms is fixed. *Right:* Model and energy spectrum of a non-rigid rotator. Here, the rigid connection between both atoms is replaced by a flexible one with spring constant k. This allows for centrifugal stretching which shifts the energy levels to lower values.

excited to high J values. Therefore a correction term is introduced by using a stretching constant D. The modified energy spectrum is then given as

$$\tilde{F}(J) = BJ(J+1) - DJ^2(J+1)^2 \,. \tag{3.3}$$

For higher precision, *e.g.* if the lines are resolved with better energy resolution, further correction terms can be added (see [Her63]), but this higher order effect is not relevant here.

Vibrational states The approach of describing vibrational states is similar to the one applied to rotational states of diatomic molecules. First, a generic model is employed to which then correction terms are applied to arrive at the required accuracy.

The starting approximation in this case is a harmonic oscillator with the following energy spectrum

$$\tilde{G}(v) = \omega_e \left(v + \frac{1}{2}\right) \tag{3.4}$$

with v being the vibrational quantum number. The constant $\omega_e = (2\pi c)^{-1}\sqrt{k\mu^{-1}}$ contains the reduced mass μ of the molecule and a spring constant k characterizing the coupling between both atoms. The well-known energy spectrum of the harmonic oscillator is given in the left panel of Fig. 3.4.

Of course, the simple harmonic potential has to be replaced by a more realistic one. The Morse potential in general is a suitable empirical *ansatz*, as shown in the right panel of Fig. 3.4. It can be seen that the equidistant energy spacing of the harmonic oscillator is not longer valid in the anharmonic case. The correction is introduced by adding an anharmonicity constant $x_e\omega_e$ to Eq. 3.4:

$$\tilde{G}(v) = \omega_e \left(v + \frac{1}{2}\right) - x_e\omega_e \left(v + \frac{1}{2}\right)^2 \,. \tag{3.5}$$

Again, higher-order corrections are possible but not relevant in this context.

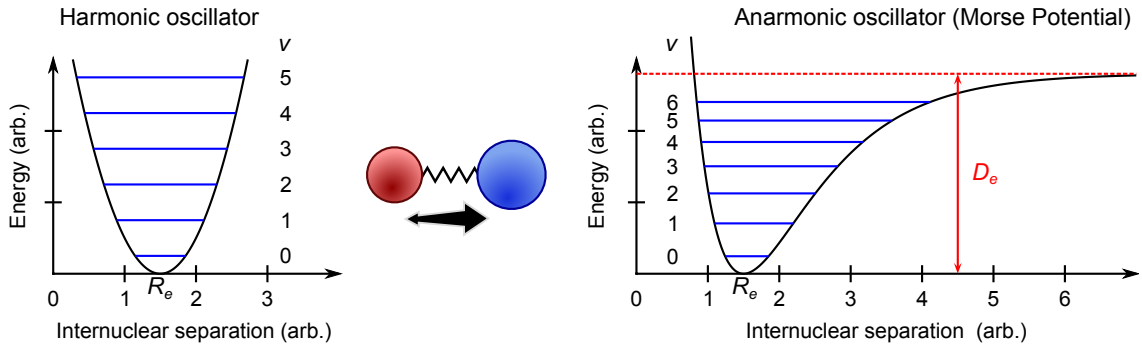

Figure 3.4: Potential curves of the (an-)harmonic oscillator. R_e is the equilibrium position of the internuclear distance and v is the vibrational quantum number. *Left:* The parabolic harmonic potential causes equidistant energy levels. *Right:* The anharmonic potential here is approximated by a Morse potential. The principle of equidistant states is no longer valid for higher v values. The potential converges to a dissociation energy D_e for an internuclear separation of $R \to \infty$. Above this energy no bound states appear.

Vibrational-rotational states Until now rotational and vibrational excitations have been considered to be independent of each other. In Raman spectroscopy beyond pure rotational spectroscopy one generally deals with combinations of both types of excitations.

Accurate vibrational-rotational energy states can be obtained by taking into account the interaction between rotations and vibrations. The anharmonicity of the Morse potential leads to an increase of $\langle R \rangle$, the mean of the internuclear separation, for higher vibrational quantum numbers v. A larger $\langle R \rangle$ in turn leads to a shift of the rotational energy levels. This coupling of vibrational and rotational excitation is expressed by replacing the B and D constants in Eq. 3.3 with a v-dependent term:

$$B \to B_v = B - \frac{\alpha}{2}\left(v + \frac{1}{2}\right) , \tag{3.6}$$

$$D \to D_v = D - \beta\left(v + \frac{1}{2}\right) \tag{3.7}$$

with α and β being molecular specific correction constants.

Finally, the terms for coupled vibrational-rotational excited energy levels, in units of cm^{-1}, are

$$\tilde{T}(v, J) = \tilde{G}(v) + \tilde{F}(v, J) \tag{3.8}$$

$$= \omega_e\left(v + \frac{1}{2}\right) - x_e\omega_e\left(v + \frac{1}{2}\right)^2 + B_v J(J+1) - D_v\left(J(J+1)\right)^2 . \tag{3.9}$$

This formula provides the energy terms relevant to the work described in this thesis in sufficient precision. Further corrections are discussed for example by Herzberg [Her63].

3.1.2 Basic principles of the Raman effect

Light can interact with molecules via absorption or emission if the resonance condition $\Delta E = h\nu$ and certain selection rules are met. In this case ΔE is the energy difference between two energy states within the molecule. The Hamiltonian describing the interaction

between the photon and the molecule is given by the electric dipole moment $\boldsymbol{p}$ and the $\boldsymbol{\mathcal{E}}$-vector of the photon field [Lee79]

$$H = -\boldsymbol{p} \cdot \boldsymbol{\mathcal{E}} \ . \tag{3.10}$$

This is a first order process due to the direct proportionality to the electrical field strength and the fact that only one photon is involved. However, the involved molecule has to have a permanent electric dipole moment.

Aside from first order interactions it is possible that photons scatter off the molecule. In this case, the above-mentioned resonance condition does not need to be met. The classical explanation for this phenomenon is that the $\boldsymbol{\mathcal{E}}$-vector of the field couples to the electrons in the shell of the molecules and thus is able to induce the so-called frequency-dependent linear electric dipole moment [Lon02]

$$\boldsymbol{p}_{\text{ind}} = \boldsymbol{\alpha} \cdot \boldsymbol{\mathcal{E}} \tag{3.11}$$

with $\boldsymbol{\alpha}$ being the polarizability tensor of the molecule. One could consider inserting this induced dipole moment into Eq. 3.10 which then would lead to a quadratic dependence of the interaction on $\boldsymbol{\mathcal{E}}$. This indicates that the processes discussed here are of second order, with two photons being involved in the scattering process: one in-going and one out-going.

The polarizability reflects how strongly the molecular system reacts to an external electric field by inducing a dipole moment. The components $\alpha_{\rho,\sigma}$ of the polarizability tensor $\boldsymbol{\alpha}$ can be expanded into a Taylor series with respect to the normal coordinates of a vibration Q_k, Q_l around the equilibrium[1] indexed by "0" [Lon02]

$$\alpha_{\rho,\sigma} = (\alpha_{\rho,\sigma})_0 + \sum_k \left(\frac{\partial \alpha_{\rho,\sigma}}{\partial Q_k} \right)_0 Q_k + \frac{1}{2} \sum_k \sum_l \left(\frac{\partial^2 \alpha_{\rho,\sigma}}{\partial Q_k \partial Q_l} \right)_0 Q_k Q_l + \dots \ . \tag{3.12}$$

As a simplification, in the following only a specific mode of vibration $k = i$ is chosen and higher orders of Q than the first are neglected. Thus one can rewrite Eq. 3.12 as

$$\boldsymbol{\alpha}_i = \boldsymbol{\alpha}_0 + \boldsymbol{\alpha}_i' Q_i \ . \tag{3.13}$$

This new form is composed of the equilibrium polarizability tensor $\boldsymbol{\alpha}_0$ and one which is the product of $\boldsymbol{\alpha_i}'$ and Q_i.

This $\boldsymbol{\alpha_i}$ (Eq. 3.13) can be inserted into Eq. 3.11; furthermore, a simple harmonic motion around the equilibrium is assumed, thus $Q_i = Q_{i0} \cos(\omega_i t + \delta_i)$. The oscillation frequency of the selected mode is ω_i and δ_i denotes an arbitrary phase factor. The external electric field is assumed to be oscillating at a different frequency ω_{ext}: $\boldsymbol{\mathcal{E}} = \boldsymbol{\mathcal{E}}_0 \cos(\omega_{\text{ext}} t)$.

With this Eq. 3.11 becomes

$$\boldsymbol{p}_{\text{ind}} = \boldsymbol{\alpha}_0 \boldsymbol{\mathcal{E}}_0 \cos(\omega_{\text{ext}} t) + \boldsymbol{\alpha}_i' Q_{i0} \boldsymbol{\mathcal{E}}_0 \cos(\omega_i t + \delta_i) \cos(\omega_{\text{ext}} t) \ . \tag{3.14}$$

One then can use the trigonometric identity $\cos A \cos B = 1/2 \left(\cos(A + B) + \cos(A - B) \right)$ and obtains

$$\boldsymbol{p}_{\text{ind}} = \boldsymbol{\alpha}_{\text{Ray}} \boldsymbol{\mathcal{E}}_0 \cos(\omega_{\text{ext}} t) + \boldsymbol{\alpha}_{\text{Ram,i}} \boldsymbol{\mathcal{E}}_0 \cos((\omega_{\text{ext}} \pm \omega_i) t \pm \delta_i) \tag{3.15}$$

[1] In this semi-classical approach only vibration around the equilibrium is considered.

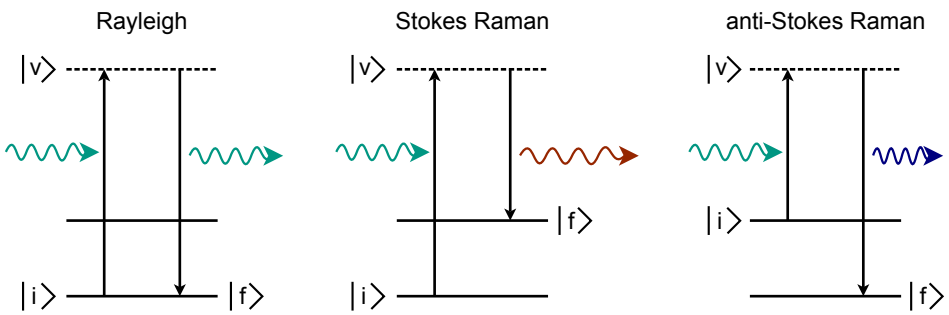

Figure 3.5: Energy level diagrams for photon scattering. The incident photon excites the molecule into a virtual, intermediate quantum state $|v\rangle$ followed by a transition to the final state accompanied by the emission of the scattered photon. *Rayleigh scattering*: The initial and final state are the same $|i\rangle = |f\rangle$, thus no change in wavelength is observed. *Stokes Raman scattering*: the energy of $|i\rangle$ is lower than of $|f\rangle$. The scattered photon is red-shifted $\hbar\omega_{\text{in}} > \hbar\omega_{\text{out}}$. *Anti-Stokes Raman scattering*: the energy of $|i\rangle$ is higher than of $|f\rangle$. The scattered photon is blue-shifted $\hbar\omega_{\text{in}} < \hbar\omega_{\text{out}}$.

with $\boldsymbol{\alpha}_{\text{Ray}} = \boldsymbol{\alpha}_0$ and $\boldsymbol{\alpha}_{\text{Ram,i}} = 1/2\boldsymbol{\alpha}'_i Q_{i0}$.

In Eq. 3.15 the first part of the induced dipole moment oscillates with the frequency of the external field, while the second part reduces or increases the frequency by the oscillation frequency of the selected mode, respectively.

The frequency conserving component (ω_{ext}) accounts for the so-called (elastic) Rayleigh scattering. The component with ($\omega_{\text{ext}} - \omega_i$) gives rise to red-shifted radiation related to (inelastic) Stokes Raman scattering. The other component ($\omega_{\text{ext}} + \omega_i$) is responsible for a blue-shifted radiation related to anti-Stokes Raman scattering. These three different interaction possibilities of light with the molecule are sketched in Fig. 3.5. It illustrates that the change in wavelength always involves a change of the previously introduced energy states within the molecule.

All three processes involve two photons which each carry a spin of $S = 1$. This leads to a selection rule for a Rayleigh / Raman transition of $\Delta J = 0, \pm 2$. The lower state is associated with J'' and the excited state with J' [Tel07]. Tab. 3.1 summarizes the different combinations of vibrational Δv and rotational ΔJ transitions, including the nomenclature for related branches. In the case of a harmonic oscillator the selection rule for vibrational transitions is $\Delta v = 0, \pm 1$. Overtones with $\Delta v = \pm 2, 3, \ldots$ become allowed for the anharmonic case. However, in this thesis only $\Delta v = +1$ transitions are considered.

Fig. 3.6 sketches a schematic view of a typical Raman spectrum of a diatomic molecule. It includes the notation convention introduced in Tab. 3.1.

Up to this point, the Raman effect has been introduced classically. It should be noted that the classical polarizability tensors $\boldsymbol{\alpha}_{\text{Ray}}$ and $\boldsymbol{\alpha}_{\text{Ram}}$ are replaced by their quantum mechanical analogues, the *transition* polarizability tensors. They can quantitatively be related to fundamental molecular properties [Lon02].

Finally, the wavenumber (or wavelength) of the incident light is shifted by an amount of energy corresponding to vibrational-rotational transitions within the molecule in the Raman scattering process; therefore, Raman line positions can be calculated. However,

Table 3.1: Selection rules and notation convention in Raman spectra. In this thesis the usual notation convention of KATRIN LARA group for the branches in the Raman spectra is used as introduced by Richard Lewis [Lew07]. The anti-Stokes Raman branch is only stated for completeness of the notation, but it does not play any role in the scope of this thesis because of the selected experimental configuration. Note that the Raman shift of anti-Stokes is negative.

Type of scattering	Pure rotation	Selection rules Δv	ΔJ	Branch name	Raman shift $\Delta\tilde{\nu}$
anti-Stokes Raman	yes	0	-2	O_0	$\tilde{\nu}_0 - \tilde{\nu}_{\text{rot}}$
Rayleigh	-	0	0	Q_0	-
Stokes Raman	yes	0	$+2$	S_0	$\tilde{\nu}_0 - \tilde{\nu}_{\text{rot}}$
Stokes Raman	no	1	-2	O_1	$\tilde{\nu}_0 - \tilde{\nu}_{\text{vib}} + \tilde{\nu}_{\text{rot}}$
		1	0	Q_1	$\tilde{\nu}_0 - \tilde{\nu}_{\text{vib}}$
		1	$+2$	S_1	$\tilde{\nu}_0 - \tilde{\nu}_{\text{vib}} - \tilde{\nu}_{\text{rot}}$

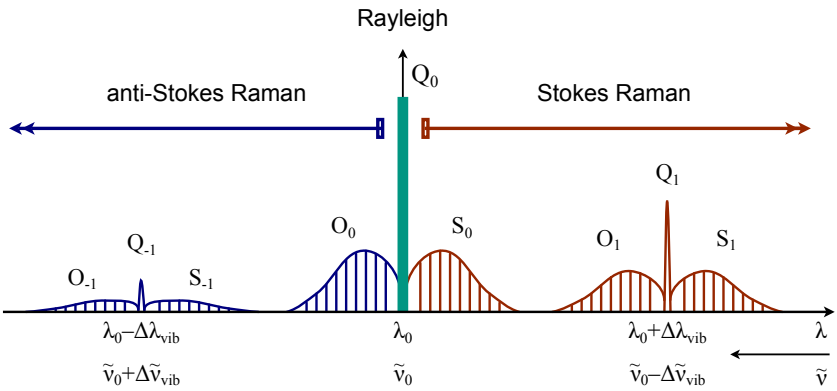

Figure 3.6: Schematic view of a typical Raman spectrum of a diatomic molecule. The Rayleigh line, Q_0, at the frequency of the primary line $\tilde{\nu}_0$ is surrounded by pure rotational Raman lines (S_0, O_0). The selection rules are according to Tab. 3.1. The index of the branches indicates the Δv. The anti-Stokes lines are normally much fainter at room temperature, because the thermally excited states are less populated according to the Boltzmann distribution. Note that the axis is labeled with wavelength λ. For the representation in wavenumbers $\tilde{\nu}$ the diagram has to be read in reversed order. According to [Hak06].

the simple classical description does not allow one to derive absolute Raman scattering intensities. This is the topic of the subsequent section.

3.1.3 Description of Raman intensities

One of the main objectives of this work has been the calibration of the KATRIN LARA system. Accordingly, it is necessary to discuss the Raman intensities of a diatomic molecule in appropriate detail. It should be mentioned at this point that the focus for quantitative analysis is on the Q_1-branches which do not involve a change of rotational wavenumber in the scattering process, thus $J'' = J'$.

The intensity of light which is scattered by diatomic molecules via the Raman effect is given as [Lon02]

$$I(\varphi, \theta)_{p^s,p^i} = k_{\tilde{\nu}} \cdot \tilde{\nu}_s^4 \cdot N_i \cdot \Phi(\varphi, \theta, a, \gamma)_{p^s,p^i} \cdot \mathcal{I} \,. \tag{3.16}$$

The individual factors will be explained below. It should be noted that Eq. 3.16 applies only if one measures scattered power rather than the number of scattered photons [McM06]. In most dispersive/charge-coupled devices (CCDs) the latter case is given, thus the equation has be modified to

$$I(\varphi, \theta)_{p^s,p^i} = k_{\tilde{\nu}} \cdot \tilde{\nu}_0 \cdot \tilde{\nu}_s^3 \cdot N_i \cdot \Phi(\varphi, \theta, a, \gamma)_{p^s,p^i} \cdot \mathcal{I} \,. \tag{3.17}$$

Note that this expression is given for a selected molecule and a certain transition. The terms and constants in said equation are discussed in the following list.

$(\varphi, \theta)_{p^s,p^i}$**:** The angles φ and θ describe the direction of the scattered beam relative to the scattering plane. The parameters p^s and p^i represent the polarization state of the scattered and incident light, respectively. A visualization of the definitions of angles and polarization planes is provided in Fig. 3.7.

$k_{\tilde{\nu}}$**:** The constant is given by

$$k_{\tilde{\nu}} = \frac{\pi^2}{\epsilon_0^2} \approx 1.259 \cdot 10^{23}\,\mathrm{F}^{-2}\mathrm{m}^2 \tag{3.18}$$

with ϵ_0 being the permittivity of vacuum.

$\tilde{\nu}_s$**,** $\tilde{\nu}_0$**:** The wavenumbers are given for scattered light and the excitation line, respectively. The wavenumber of the scattered light is obtained from $\tilde{\nu}_s = \tilde{\nu}_0 - \Delta\tilde{\nu}_i$ with $\Delta\tilde{\nu}_i$ being the Raman shift corresponding to a certain molecular state i.

N_i**:** The population factor N_i expresses the number of molecules in the initial state i

$$N_i = N \frac{g_i \exp\left(-\frac{E_i}{kT}\right)}{Z} \,. \tag{3.19}$$

N represents the total number of irradiated molecules proportional to the partial pressure, kT is the thermal energy, E_i the energy of the initial state consisting of vibrational and rotational parts, and Z describes the molecular partition function

$$Z = \sum_j g_j \exp\left(-\frac{E_j}{kT}\right) \,. \tag{3.20}$$

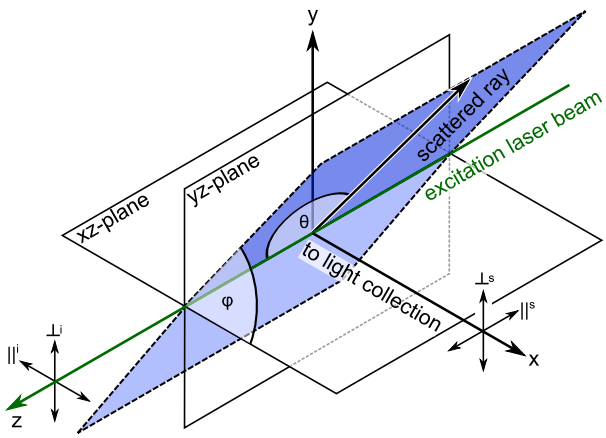

Figure 3.7: Definition of Raman scattering angles and polarization states. The scattering plane is determined by the incident light beam along the z-axis and its azimuth angle φ with respect to the light collection x-axis. The zenith angle θ is defined as the angle between the z-axis and the scattered ray in the scattering plane. In the direction of the x-axis, imaging lenses and polarization optics are found. The $\perp$ and $||$ symbols represent the polarization direction of linear polarized light relative to the xz-plane. The notation of the variables is according to Long [Lon02].

The statistical weight g_i is composed of the individual weights of the vibrational g_v and rotational $g_{J''}$ states: $g_i = g_v \cdot g_{J''}$. In the case of diatomic molecules, the vibrational states are non-degenerated and thus $g_v = 1$.

The statistical weight $g_{J''}$ depends on the nuclear spin degeneracy g_N and the rotational quantum number J'':

$$g_{J''} = g_N \cdot (2J'' + 1) \; . \tag{3.21}$$

In the following the symmetry of the total wave function needs to be considered. For heteronuclear molecules (*e.g.* HD, HT, DT) no parity can be defined resulting in $g_N = 1$, but in the case of homonuclear molecules the nuclear spin statistic has to be taken into account:

$$\Psi_{\text{tot}} = \Psi_{\text{spin,nuc}} \cdot \Psi_{\text{elec}} \cdot \Psi_{\text{space}} \; . \tag{3.22}$$

The wave function of molecules with two fermionic nuclei (H_2, T_2) has to be anti-symmetric under inversion since it has to follow Pauli's principle. According to this the wave function of molecules with bosonic nuclei (D_2) has to be symmetric. The influence of nuclear spin statistics on hydrogen isotopologues is demonstrated in Tab. 3.2. This effect is visualized in Chapter 5 for calculated intensities (Fig. 5.2) and measured intensities (Fig. 5.15).

$\Phi(\varphi, \theta, a, \gamma)_{p^s,p^i}$ The line strength function Φ is given by the isotropic averages of squares of the transition polarizability tensor components [Lon02]. These components depend on the experiment's geometry and light polarization.

The four line strength functions for $\perp$- and $||$-polarized light are given below[2], as

[2]Note that these function play an important role in Chapter 5.

Table 3.2: Nuclear spin statistics and influence on relative intensities. The rotational line intensities of the homonuclear hydrogen isotopologues H_2, D_2 and T_2 are effected by the nuclear spin. This leads to a $3:1$ (H_2, T_2) or $1:2$ (D_2) alternation of g_N for the odd:even values of J''.

Isotopologue	H_2, T_2	D_2
Total nuclear spin I	$\frac{1}{2}$	1
Nuclear spin degeneracy $2I+1$	2	3
Quantum statistics	Fermi-Dirac	Bose-Einstein
Nuclear spin statistical weight g_N		
J'' odd / J'' even	3 / 1	3 / 6
Relative intensities of Raman lines		
J'' odd / J'' even	3 / 1	1 / 2

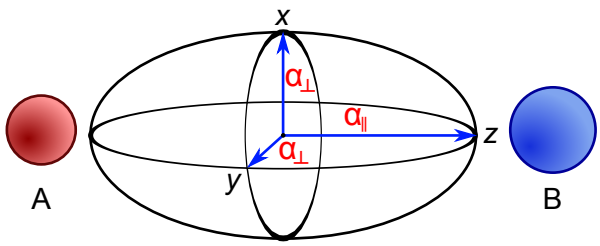

Figure 3.8: Polarization ellipsoid of a diatomic molecule. The values of the polarizability along the principal axes is given by $\alpha_{||}$ (and $\alpha_{\perp}$) for the parallel (and perpendicular) direction relative to the molecular axis. The average polarizability is defined as $a = 1/3 \cdot (\alpha_{||} + 2\alpha_{\perp})$ and the polarizability anisotropy is given by $\gamma = \alpha_{||} - \alpha_{\perp}$.

functions of the angles φ and θ [Lon02]

$$\Phi(\varphi,\theta,a,\gamma)_{\perp^s,\perp^i} = a^2\cos(\varphi)^2 + b^{(2)}\frac{\gamma^2}{45}\left(4-\sin(\varphi)^2\right) \ , \tag{3.23}$$

$$\Phi(\varphi,\theta,a,\gamma)_{\perp^s,||^i} = a^2\sin(\varphi)^2 + b^{(2)}\frac{\gamma^2}{45}\left(3+\sin(\varphi)^2\right) \ , \tag{3.24}$$

$$\Phi(\varphi,\theta,a,\gamma)_{||^s,||^i} = a^2\cos(\theta)^2\cos(\varphi)^2 + b^{(2)}\frac{\gamma^2}{45}\left(3+\cos(\theta)^2\cos(\varphi)^2\right) \ , \tag{3.25}$$

$$\Phi(\varphi,\theta,a,\gamma)_{||^s,\perp^i} = a^2\cos(\theta)^2\sin(\varphi)^2 + b^{(2)}\frac{\gamma^2}{45}\left(3+\cos(\theta)^2\sin(\varphi)^2\right) \ . \tag{3.26}$$

The tensor invariants, which are given by the average polarizability, a, and the polarizability anisotropy, γ, in the line strength function are specific for each isotopologue and molecular transition. The geometrical meaning in the polarizability ellipsoid is visualized in Fig. 3.8.

The factor $b^{(2)}$ in the above equations is the Placzek-Teller factor; for rotational states, J'', in a Q_v-branch it is given as [Lon02]

$$b^{(2)}_{J''} = \frac{J''(J''+1)}{(2J''-1)(2J''+3)} \ . \tag{3.27}$$

In some experimental cases the initial linear polarization is not pure, but contains a polarization contaminant deviating from perpendicular polarization direction. For example, this could happen if the cleanness of the polarization is deteriorated by stress-induced birefringence. In a mathematical description, such an admixture can be described by introducing a parameter $\xi = \cos^2 \beta$. In this context, β is the angular deviation from the vertical polarization direction. A value $\xi = 1$ corresponds to perfect vertical (linear) polarization. A value $\xi = 0.5$ then represents a beam whose components of polarization, $\perp^i$ and $||^i$, would be of equal magnitude, and a value $\xi = 0$ corresponds to perfect horizontal (linear) polarization.

As an example, Eq. 3.23 would be modified in the following way

$$\Phi_{\text{effective}}(\varphi, \theta, a, \gamma) = \xi \cdot \Phi(\varphi, \theta, a, \gamma)_{\perp^s, \perp^i} + (1 - \xi) \cdot \Phi(\varphi, \theta, a, \gamma)_{\perp^s, ||^i} \,. \tag{3.28}$$

$\mathcal{I}$**:** It denotes the irradiance of the incident excitation light. Note that this term has no impact on the calculation of relative intensities since it is canceling out.

The expression of the intensity above was given in terms of wavenumber or Raman shift. Sometimes it is recommended to provide it in terms of wavelength, *e.g.* if the spectral calibration curve is provided in these units.

The Raman intensity for a certain isotopologue x is then given as

$$I_{\text{Raman,x}}(\lambda_s, N_x) = C \cdot \lambda_0^{-1} \cdot \lambda_s^{-3} \cdot N_x \cdot \Phi_x \cdot \mathcal{I} \,. \tag{3.29}$$

In this notation, Φ_x represents the line strength function under a defined polarization configuration with the a and γ utilized for the respective isotopologue x, after integration over the solid angle of observation. C absorbs all constant coefficients which would appear in the equation.

This equation represents a simplification since all isotopologues x are treated as if they would contribute with a single Raman line only. However, the equation will be used as a starting point in Section 5.2 to then be extended to respective requirements.

3.2 Raman spectroscopy on hydrogen isotopologues

In this section three items will be discussed with regard to the application of Raman spectroscopy on hydrogen isotopologues. First, the very requirements for Raman systems are defined which allow to measure all six hydrogen isotopologues simultaneously. Second, *ab initio* calculations providing the tensor invariants a and γ are introduced. And finally, earlier Raman experiments on all hydrogen isotopologues involving tritium are summarized.

Pre-requisites of the experimental systems From the theoretical point of view, Raman spectroscopy on hydrogen isotopologues can be deemed to be a rather simple application, as the diatomic molecules consist of two light nuclei and two electrons only.

The isotopic effect for the three atoms, H, D and T, is very pronounced due to their mass ratio $1 : 2 : 3$. This provides a very good separation of the spectral lines which is related

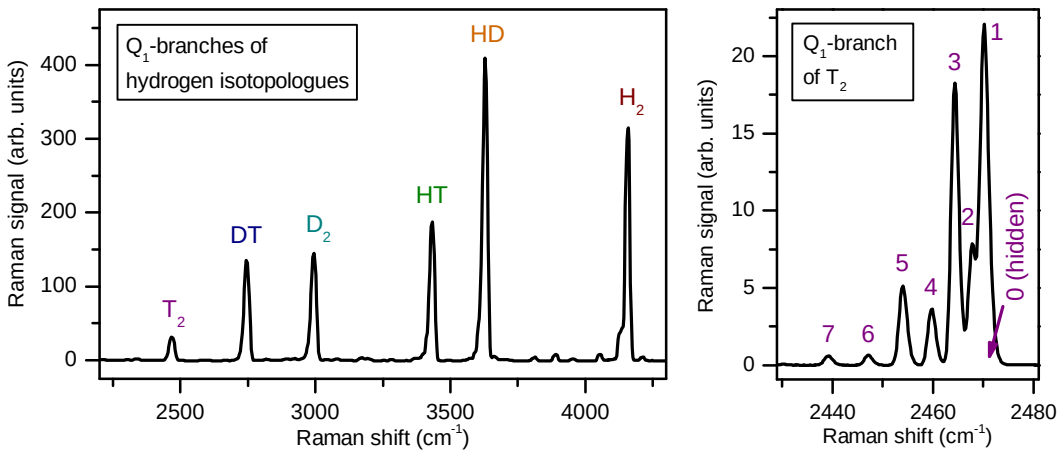

Figure 3.9: Typical Raman spectra of a gas mixture containing all six hydrogen. *Left:* Overview spectrum with medium spectral resolution. All assigned peaks are the Q_1-branches of the corresponding molecule. The minor, unassigned lines are the S_1- and O_1-lines of the six hydrogen isotopologues. Note that individual Q_1-lines are not resolved. *Right:* High resolution spectrum of the Q_1-branch of T_2. The numbers indicate the rotational quantum number J'' of the individual Q_1-lines. The $J'' = 0$ line is convoluted with the $J'' = 1$ line. The intensity distribution of the resolved Q_1-lines is mainly given by the Boltzmann distribution modulated by the g_N factor according to the nuclear spin statistic introduced in Tab. 3.2.

to the reduced mass of the isotopologues. The Q_1-branches are chosen for extraction of intensities and thus for analysis. In Fig. 3.9 a spectrum of all six species is shown. When using a laser with emission wavelength of $532\,\mathrm{nm}$ the Raman system has to cover a certain spectral region. The Q_1-branches in this spectrum range from T_2 at a Raman shift of $2464\,\mathrm{cm}^{-1}$, which corresponds to a wavelength of $612\,\mathrm{nm}$, to H_2 at a Raman shift of $4162\,\mathrm{cm}^{-1}$, which corresponds to a wavelength of $683\,\mathrm{nm}$. It should be noted that the Raman system should also cover the S_0-branches (see Fig. 4.13 in next chapter). Then the spectral region needs to be extended to about the excitation line of the laser, here $0\,\mathrm{cm}^{-1}$ and $532\,\mathrm{nm}$, respectively.

The temperature of the gas to be analyzed is normally around room temperature ($T = 300\,\mathrm{K}$, $kT \approx 200\,\mathrm{cm}^{-1}$). The vibrational energies of the hydrogen isotopologues can be inserted into Eq. 3.19 to obtain the initial population of the vibrational excitation. It is found that $N_{v=1}/N_{v=0} \approx 10^{-6}$ and thus one can assume that the isotopologues are in the vibrational ground state [Sch09]. The excitation energies of the rotational transitions are of the order of the thermal energy kT, therefore a few excited states are usually populated at room temperature. In the right panel of Fig. 3.9 the Q_1-branch of T_2 is shown in high resolution with individual rotational lines being resolved (recall that $\Delta v = +1,\ \Delta J = 0$). The lines exhibit a thermal distribution with overlaying modulation of the statistical weight (see Tab. 3.2). The fact that the Q_1-branch has a substructure and is not represented by only a single line can also be noticed in the asymmetry of the branches in the medium resolution acquisition (left panel of Fig. 3.9). Accordingly, the individual shapes of the peaks need to be taken into account in the data analysis (see Section 4.2.2).

In the previous work of the author three reasons were given as to why the Q_1-branches have advantages over the S_0-branches with regard to quantitative analysis [Sch09]. Here,

only a short summary is presented:

1. The Q_1-branches as recorded with medium resolution by and large integrate the intensity of the underlying lines. In general, this implies a higher peak intensity and virtual temperature-independence.
2. S_0-branches are much closer to the excitation line at $532\,\mathrm{nm}$. The first rotation lines of $\mathrm{T_2}$ and DT would be suppressed by a laser line cut-off filter installed in the detection system (see Section 4.1.3).
3. The spectral region of the S_0-lines of all hydrogen isotopologues coincides with parasitic peaks which have their origin in Raman scattering within the fused silica ($\mathrm{SiO_2}$) of the laser windows of the sample cell [Wal82].

Theoretical values for the polarizability The Raman intensity was introduced above as being calculable from different factors and constants. It was discussed that all necessary constituents are available with sufficient accuracy, with the exception of the tensor invariants a and γ of the polarizability tensor for each line and molecule.

This latter point has been studied intensively by theoreticians for over 50 years. Here, a brief summary is provided.

The molecular system of hydrogen is often seen as a model case for comparative studies of theory and experiment. The quantum mechanical system consists of two electrons and two nuclei only. Despite the presumed simplicity, enormous efforts were necessary to arrive at accurate quantitative values from *ab initio* calculations. The beginnings of the early calculations go back to the 1930s [Mro32]. These basic attempts were significantly improved about 20 years later by making use of the novel variation-perturbation method by Ishiguro *et al* [Ish52] enabling the calculation of energies and molecular polarization. In the following decades many research groups actively worked on theoretical approaches to various physical quantities of molecular hydrogen. Important contributors amongst others were Kolos and Wolniewicz [Kol63, Kol64, Kol68] and Rychlewski [Ryc82]. A comprehensive overview of all relevant contributions up to the late 1980s was given by Schwartz and LeRoy [Sch87]. Each contribution led to further refinement of the results by adding more correction terms in order to improve the model or by using more elaborate potential functions.

In 1984, Hunt *et al* published *ab initio* calculations of the polarizabilities for all six hydrogen isotopologues [Hun84]. These values were only calculated for the static case meaning that the wavelength of an oscillating field is infinite. This can therefore only reflect a simplification of real experiments. In 1986, the potential curve for $\mathrm{H_2}$ was refined by Kolos *et al* [Kol86]; those data were then used as a basis for the calculations by Schwartz and LeRoy [Sch87]. Specifically, the efforts by LeRoy's group addressed the calculation of the off-diagonal matrix elements related to the average polarizability, a, and polarizability anisotropy, γ, encountered in Raman spectroscopy, for all vibrational-rotational states of diatomic hydrogen isotopologues.

Schwartz and LeRoy state that the values for the tritium containing molecules were obtained via a scaling method beyond the non-adiabatic corrections calculated for $\mathrm{H_2}$, HD, and $\mathrm{D_2}$ [Sch87]. Therefore, the results are to be viewed with some caution. The results

were presented for the static case ($\lambda = \infty$) and for one specific wavelength of the argon ion laser ($\lambda = 488\,\mathrm{nm}$).

In order to obtain adequate a and γ values for the case of the green Nd:YAG (frequency-doubled) of $\lambda = 532\,\mathrm{nm}$, Robert J. LeRoy was contacted and he was able to provide the whole tabulation of polarizabilities for all relevant lines from recalculation [LeR11].

Finally, a serious deficit of all aforementioned theoretical calculations should be mentioned: None of the authors provides any accuracy statements or confidence band in the context of their theoretical derived values. However, the knowledge of the trueness of these values is essential if they should be employed for calibration.

A certain part of the work reported in this thesis is therefore dedicated to methods to determine a specific degree of confidence for these theoretical values (see Chapter 5).

Previous Raman studies on all hydrogen isotopologues including tritium Raman spectroscopy is employed for the analysis of the tritium content of the WGTS source gas in KATRIN and it has been developed by the KATRIN Laser Raman group at the TLK in collaboration with the group in Swansea over the course of the past few years (starting with the PhD thesis of Richard Lewis [Lew07]).

However, Raman spectroscopy was used for investigation and monitoring purposes of hydrogen isotopologues mixtures by other groups, too. The special interest there did stem from potential applications for tritium analytics in the process cycle of nuclear fusion reactors in which $\mathrm{T_2}$, DT, and $\mathrm{D_2}$ play a distinct role as fusion fuel.

Already in 1978 Edwards *et al* obtained various spectroscopic constants from measuring rotational and vibrational-rotational Raman spectra of $\mathrm{T_2}$ [Edw78]. Almost one decade later Veirs and Rosenblatt provided the Raman line positions of all six hydrogen isotopologues with an accuracy of $\pm 1\,\mathrm{cm}^{-1}$ [Vei87]. In 1992, Engelmann performed the first Raman measurement with tritium at the KIT[3] [Eng92]. She focused on high resolution spectroscopy of S_0 and Q_1-branches and investigated the exchange reaction of tritium with methane. At the same time, a group around O'Hira designed a Raman system for remote, real-time analysis of isotopologue compositions at the Tritium System Test Assembly at Los Alamos [Ohi92]. They later reported further improvement like lower detection limits at their Raman systems at the Tritium Process Laboratory in Japan [Ohi96, Ohi00].

First Raman experiments at the TLK were performed by Taylor *et al* [Tay01]. They used an actively stabilized external resonator to effectively enhance the Raman signal by a factor of > 40. This multi-pass setup however was never employed with tritium containing gas samples.

For the following years research and development of Raman spectroscopy at the TLK was not further pursued until Richard Lewis installed the first Raman system for KATRIN at the TLK [Lew07]. It could be demonstrated that the LARA system integrated into a mock-up of the Inner Loop, TILO, should be able to fulfill the KATRIN requirements [Lew08] within rather long acquisition times of the order of $t = 1000\,\mathrm{s}$. However, the measurements were conducted with non-radioactive isotopologues only. In the following the author of this thesis carried out first Raman measurements with tritiated species

[3] At this time it was named as national research center KfK (Kernforschungszentrum Karlsruhe)

and performed a series of systematic investigations to improve the understanding of the system and its sensitivity [Sch09]. Further investigations on the laser stability by Sebastian Fischer followed [Fis10a]. An important result was provided by a long-term experiment in which high purity tritium gas was circulated. The investigation was conducted at LOOPINO, another Inner Loop mock-up installed by Michael Sturm, under KATRIN-like conditions with the LARA system giving proof-of-principle that the precision and stability requirements can be met successfully [Fis11, Stu10b]. The various improvements from the initial status at this time to the present status up to the finishing of the thesis in hand, are documented and discussed in Section 4.3.

Due to the rather unexpected observed damage to the optical coating of the sample cell windows, Kerstin Schönung set up a test experiment to investigate the influence of tritium gas on optics [Sch11d]. These investigations are currently continued by Vera Schäfer [Sch13f] and Sebastian Fischer [Fis13].

Embedded into these activities, the investigation of calibration strategies for Raman spectroscopy as highly accurate quantitative analysis tools was then the task of this PhD thesis. The respective co-workers (like bachelor, diploma and PhD students) and the collaborative achievements are indicated at the relevant positions in the following chapters.

3.3 Calibration for quantitative analysis

In this section the focus shifts from the theoretical description of molecular excitations and Raman intensities to the quantitative application of Raman spectroscopy. This objective necessitates a proper calibration which starts with Raman signals to arrive at the actual true composition of the sample.

From a spectrum as shown in Fig. 3.9 the total Raman signal of each isotopologue x can be extracted, which is taken in general as the area under a certain Q_1-branch peak. This Raman signal amplitude, S_x, is then related to the number of molecules in the sample, N_x. A system-dependent response function, R_x, provides the proportionality between the Raman signal and the number of particles,

$$S_x = R_x \cdot N_x \; . \tag{3.30}$$

Often, relative Raman signal amplitudes, $S_{x,\mathrm{rel}}$, are used for quantitative analysis rather than the absolute S_x values[4]. They can be obtained by normalizing the individual signal amplitudes to the sum of the signal amplitudes of all isotopologues in the sample. Accordingly, Eq. 3.30 can be modified to

$$S_{x,\mathrm{rel}} = \frac{S_x}{\sum\limits_{j=1}^{n} S_j} = \frac{R_x \cdot N_x}{\sum\limits_{j=1}^{n} R_j \cdot N_j} \; . \tag{3.31}$$

The objective of the calibration is to determine accurate values for R_x for any constituent in the sampled gas. In the case of hydrogen isotopologues: $x = \mathrm{T}_2, \ldots, \mathrm{H}_2$, the response

[4]Relative Raman signal amplitudes are in general not prone to fluctuation in the irradiance of the excitation beam.

functions can be normalized to any base, depending on the calibration method. For easier comparison of the R_x, as determined by different calibration approaches, it is recommended to normalize the absolute response functions to the mean of all response functions determined by one calibration method to arrive at the relative response functions, $R_{x,\mathrm{rel}}$,

$$R_{x,\mathrm{rel}} = \frac{R_x}{R_{\mathrm{mean}}} = n \cdot \frac{R_x}{\sum\limits_{j=1}^{n} R_j} \,. \tag{3.32}$$

3.3.1 Possible methods

Three possible approaches to obtain an accurate calibration of the KATRIN Raman system have been contemplated:

(i) the use of one or more reference methods for cross-calibration;

(ii) the measurement of spectra of well-known calibration samples;

(iii) the use of literature or theoretical values for the Raman cross-sections in combination with a measurement of the system's spectral sensitivity.

When dealing with radioactive tritium-containing gas mixtures, one is faced with a range of challenges with respect to these calibration possibilities in addition.

First, hardly any reference method is available for the compositional measurement of tritium mixtures, which would provide sufficient trueness (see *e.g.* [Dem12, Nis06]). The Tritium Laboratory Karlsruhe (TLK), as a laboratory with renowned expertise in tritium analytics, has currently no system available to provide the required trueness.

Second, the production and usage of accurate samples is a commonly employed technique in analytical chemistry. Specifically, such samples are very accurate in solid or liquid form, especially if they are produced by gravimetric preparation. The production of gaseous samples is less straightforward. Nevertheless, accurate and homogeneous gas mixtures can in general be provided. However, this is substantially more complicated, as described in the ISO standard 6142 [ISO01]. When dealing with tritium gas mixtures additional difficulties are encountered:

(a) radio-chemical reactions (such as self-equilibration or gas-wall interactions) due to the intrinsic β-activity of tritium [Sou86],

(b) limited T_2 purity (a maximum purity of up to 98% can be obtained at the Tritium Laboratory Karlsruhe [Dör05].),

(c) the necessity to efficiently remove the Raman inactive tritium β-decay product $^3\mathrm{He}$ from stored tritium before mixing (about 0.5% of the tritium sample at hand will decay every month), and

(d) the technical efforts for the installation of a tritium compatible system which are restricted by the safety regulations.

Third, experimentally verified literature values for the Raman scattering cross-sections for the radioactive hydrogen isotopologues T_2, DT and HT are not available. However, the *ab initio* calculations mentioned further above allow one to predict so-called "theoretical intensities" for all six hydrogen isotopologues (see *e.g.* Schwartz and LeRoy [Sch87]). However, the trueness of these values is not discussed within said publication. Thus, the question arises as to the level of confidence of these theoretical values.

3.3.2 Calibration strategy for the KATRIN LARA system

In the previous paragraph it was discussed that each of the possible calibration approaches has certain drawbacks, constraining its applicability for the given calibration task for the Raman systems of KATRIN.

A good calibration can therefore only be obtained by a combination of two of the discussed approaches. The calibration issue is solved by taking advantage of approaches (ii) and (iii) as visualized in Fig. 3.10.

Accordingly, it is intended to use theory values and the (measured) spectral sensitivity of the system to arrive at the aforementioned relative response functions, $R_{x,\mathrm{rel}}$. The use of theory values requires a consistency check of the employed model which includes means to obtain a handle on the confidence in those values. Additionally, the spectral sensitivity has to be determined reliably. In doing so, the total systematic uncertainty should be substantially smaller than the required upper limit of 10%, in particular also with regard to future increase in neutrino mass sensitivity of KATRIN.

Subsequently, the $R_{x,\mathrm{rel}}$ values are verified by a calibration with accurately prepared gas samples consisting of the non-radioactive isotopologues H_2, HD and D_2. The restriction to the sub-set of non-tritiated species is necessary since a tritium-certified mixing system has not been available at the time of these measurements. The employed method and the apparatus should fulfill certain requirements to obtain highly accurate gas samples.

Once a successful agreement of the relative response functions for the three non-radioactive isotopologues has been obtained by both approaches, this fact should then provide sufficient confidence in deducing the relative response functions of the tritiated isotopologues without direct experimental verification.

In a future step, which is beyond the scope of this thesis, the gas sampling method may be extended to cover all isotopologues to allow for a complete comparison.

In this context, it should be recalled, that for the use within the KATRIN experiment, the calibration techniques should be able to provide the required trueness of the response functions of the order of 10% (a better accuracy is desirable).

In Chapter 5 the first calibration method based on theoretical intensities and spectral sensitivity is introduced and discussed in detail. Chapter 6 then deals with the calibration based on accurate gas samples. Finally, the results from both methods are compared and the implications for KATRIN are discussed in Chapter 7.

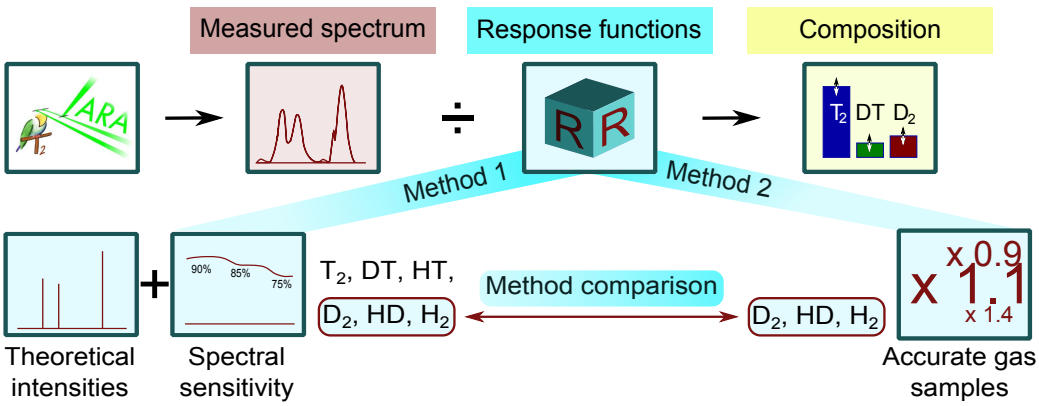

Figure 3.10: Analysis principle for the calibration of the LARA systems of KATRIN. In order to arrive at the sample composition N_x from a given Raman signal S_x, a calibration is needed to obtain the response functions R_x as linking elements. The first calibration approach makes use of theoretical intensities and the measurements of the system's spectral sensitivity and thus is able to cover all six hydrogen isotopologues. The second independent approach is (in the current implementation) only able to cover the non-radioactive isotopologues. The validity of both calibration approaches can be assumed if they lead to the identical response functions within the assumed systematic uncertainties of the individual approaches.

Chapter 4

Experimental setup

This chapter contains all necessary information to understand how Raman light is produced experimentally, how a spectrum is generated and how finally accurate intensities are extracted from such spectra. Therefore, the chapter is divided in two parts. First, the Raman systems employed for acquiring spectra in this thesis are described. Second, the spectral analysis methods are highlighted which are used to pre-process the spectra before Raman intensities are derived from it.

4.1 Raman system hardware

Detailed descriptions of the single components and a deeper introduction in the KATRIN requirements for these systems are given in the previous diploma thesis by the author [Sch09]. Therefore, this section will be rather concise. In the first subsection, the general scheme of the components involved in Raman measurements is presented. Then in the second subsection, the two Raman systems which have been employed for various tasks throughout this thesis are introduced and their very differences are discussed.

4.1.1 Overview of the scheme of Raman measurements

The quantitative analysis of unknown hydrogen gas samples involves hardware equipment which is needed to perform spectroscopy. In Fig. 4.1 the sequence of the individual hardware components involved in the acquisition of a spectrum is shown and it is summed up in the following enumeration [Sch09]:

1. A laser provides a (nearly) monochromatic light beam.
2. In the Raman cell laser light scatters off the gas molecules of the sample within a defined volume.
3. The scattered light is collected by a combination of optical lenses and imaged onto a fiber bundle.
4. The collected light is transported by the fiber bundle into the filter unit.

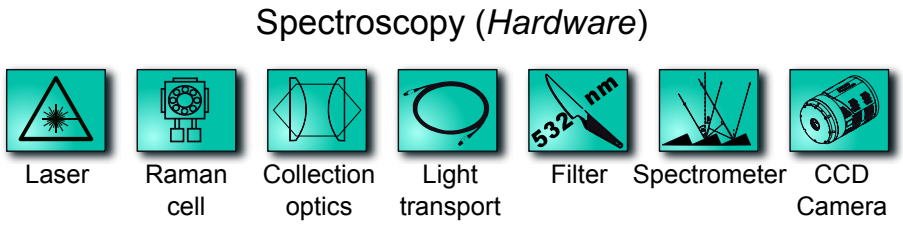

Figure 4.1: Sequence of hardware steps in a Raman measurement. For a full explanation see main text.

5. The edge filter is used for suppression of light from (elastic) Rayleigh-scattering and from diffusely reflected excitation-source light by more than six orders of magnitude.

6. In the spectrometer a grating is used for wavelength dependent diffraction.

7. The spectrum is finally detected by a CCD array detector producing a raw, two-dimensional spectrum.

Subsequent software procedures and methods for processing of raw data are discussed below at Section 4.2.

4.1.2 Raman systems at the TLK

The experimental work presented in this thesis has been mainly performed by making use of two different Raman systems. The employed systems in this thesis are:

1. **LARA system for monitoring of isotopic composition (MonLARA)**
   The first system is basically identical to the one used in the previous studies [Sch09], albeit with slight modifications. The main purpose of systems of this conceptual class is to continuously provide the measured isotopic compositions during KATRIN runs. Recall, that the requirements for this task are (i) the simultaneous measurement of all six hydrogen isotopologues; (ii) short acquisition times (order of 100 s); and (iii) a precision on the 0.1% level or better (see Section 2.4).

   Therefore, all calibration efforts are targeted at this system. A sketch of the MonLARA system is found in Fig. 4.2.

2. **LARA system for high resolution spectroscopy (HighResLARA)**
   In the first calibration approach the system-independent theoretical Raman intensities are required. The verification of the theoretical intensity calculation, for which no trueness statements is provided, was obtained from so-called depolarization measurements (see Chapter 5). This involved measuring the depolarization ratios of each individual $Q_1(J'')$ rotationally-resolved Raman line. Therefore, high resolution is of greater importance than short acquisition times and full coverage of all hydrogen isotopologues. This feature is realized in the HighResLARA system of which a sketch is shown in Fig. 4.3.

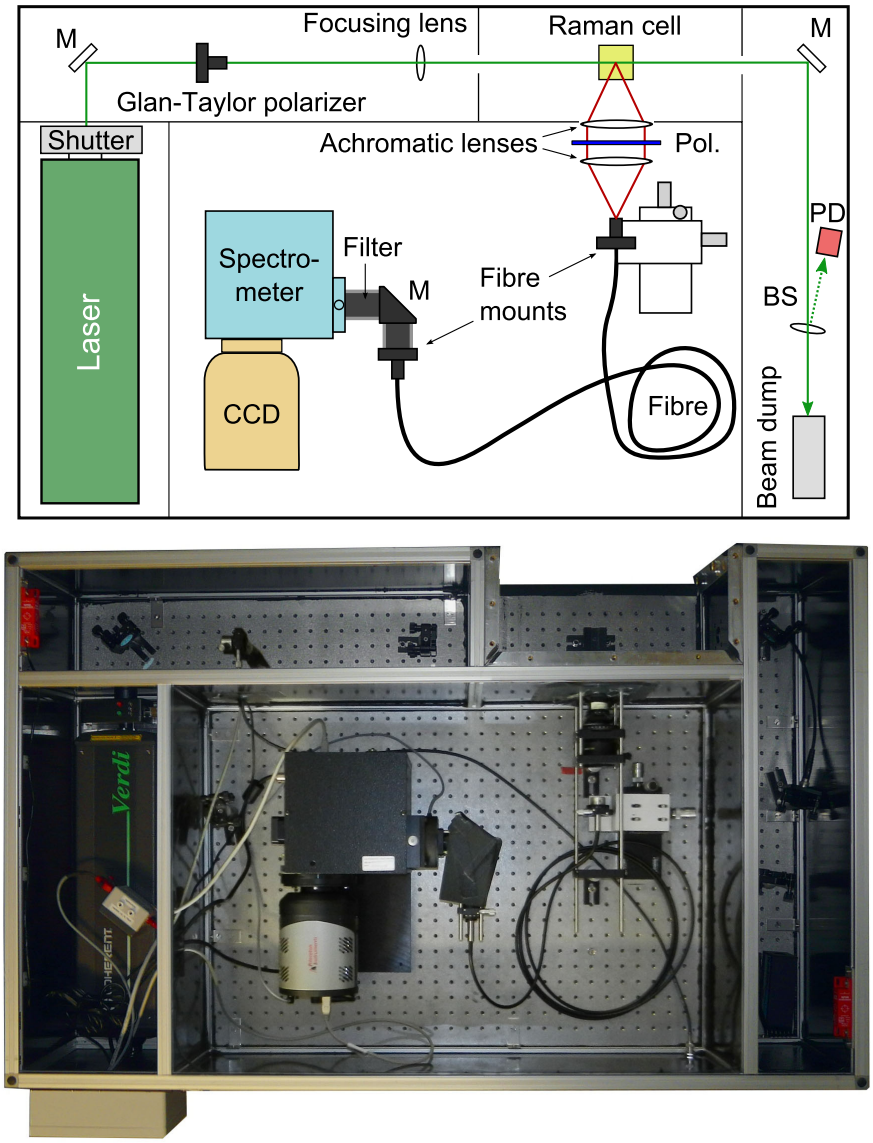

Figure 4.2: Sketch and picture of MonLARA system. This system is designed for the simultaneous monitoring of all hydrogen isotopologues with high sensitivity. *Top panel:* The description of the employed parts is found in Tab. 4.1. M: Mirror; BS: Beam sampler; Pol.: Polarizer; PD: Photo diode. *Bottom panel:* Picture into the MonLARA system without Raman cell. An outside view of a LARA system is given in Fig. 4.3.

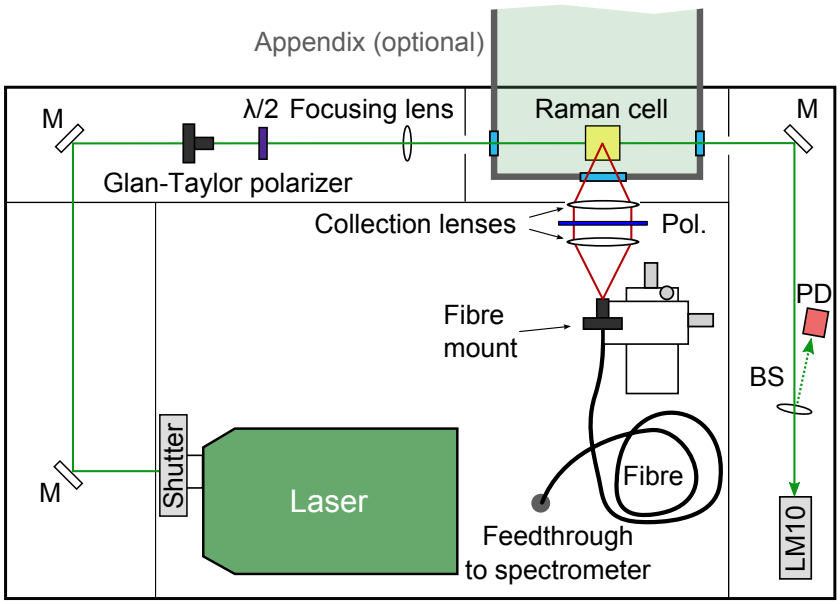

Figure 4.3: Sketch of HighResLARA system. This system is designed for the high resolution spectroscopy of single hydrogen isotopologues with precise control on the polarization of excitation laser. *Top panel:* The description of the employed parts is found in Tab. 4.1. M: Mirror; BS: Beam sampler; Pol.: Polarizer; PD: Photo diode; $\lambda/2$: Half-wave plate. Note that the SP500i spectrometer is too large for the optical table and thus located outside in a separate box. A picture of the glove-box appendix is found in Fig. 4.5. *Bottom panel:* Picture of the HighResLARA system. Note that the system in the picture is operated at a different location (grayed out) and is not connected to the glove-box appendix. The box in the foreground is the water chiller for laser head cooling. The external spectrometer box is not shown on this picture. An view inside a LARA system is given in Fig. 4.2.

4.1.3 Components of the Raman systems

A general overview on the components (model names, parameters and properties) utilized in both Raman systems is given in Tab. 4.1. Changes of individual components or analysis procedures between certain measurements will be indicated at the paragraphs where it is needed.

In the following list, the choice of the components and their implications for the Raman calibration task are discussed.

Laser excitation source Normally, commercial Raman systems are equipped with lasers which have output powers of some hundred milliwatts (see *e.g.* www.lambdaphoto.co.uk). However, the low Raman scattering cross-sections of gases below atmospheric pressures require a compensation by higher laser powers to maintain a decent signal intensity. Therefore, the lasers employed in MonLARA and HighResLARA are both diode pumped solid state (DPSS) lasers with an output power of 5 W. In the bachelor's thesis of Simon Kudella [Kud11] it was shown that pointing and power stability of DPSS lasers can be

Table 4.1: Overview of selected components of the LARA systems used for measurements within this thesis.

Parameter	MonLARA	HighResLARA
	Laser	
Model (Manufacturer)	Verdi V5 (Coherent)[a]	Finesse (Laser Quantum)[b]
Gain medium (Wavelength)	Nd:YVO_4 (532 nm)	Nd:YAG (532 nm)
Power	5 W	5 W
Cooling	N.A.	Water chiller (Laird Tech.)
Output polarization	vertical, linear	horizontal, linear
	CCD-detector	
Model (Manufacturer)	PIXIS:400B (Princeton Instruments)[c]	PIXS:400B (Princeton Instruments)[c]
Sensor dimension	26.8×8.0 mm	26.8×8.0 mm
Pixel dimension	1340×400 array , 20×20 µm pixel	1340×400 array , 20×20 µm pixel
Operating temperature	$-75\,^{\circ}$C	$-75\,^{\circ}$C
Dark noise at $75\,^{\circ}$C	$\sim 0.001\, e^{-}\mathrm{s}^{-1}\mathrm{pixel}^{-1}$	$\sim 0.001\, e^{-}\mathrm{s}^{-1}\mathrm{pixel}^{-1}$
Readout noise[d]	$3-5\, e^{-1}$ RMS	$3-5\, e^{-1}$ RMS
	Spectrometer	
Model (Manufacturer)	SP2150i (Princeton Instruments)[e]	SP500i (Acton Research Corp.)[f]
Focal length	150 mm	500 mm
Aperture ratio	$f/4.0$	$f/6.5$
Installed gratings	600 gr mm^{-1}, 1800 gr mm^{-1}	150 gr mm^{-1}, 600 gr mm^{-1}, 2400 gr mm^{-1}
	Sheet polarizer in collection optics	
Model (Manufacturer)	LPVISE200-A (Thorlabs Inc.)[g]	NT43-787 (Edmund Optics)[h]
Extinction ratio (600-700nm)	$> 5000 : 1$	$> 1500 : 1$
Transmission (600-700nm)	$> 72\%$	30%

[a] From Verdi data sheet [Cor05].
[b] From Finesse data sheet [Las12b].
[c] From PIXIS:400B data sheet [Pri11].
[d] Readout noise at a readout rate of 100 kHz.
[e] From SP2150i data sheet [Pri10b].
[f] From SP500i manual [Act02]. Note that the follow-up models are now produced by Princeton Instruments.
[g] Thorlabs Inc., Newton, New Jersey, USA
[h] Edmund Optics, Barrington, New Jersey, USA

strongly improved by temperature stabilization of the laser plate. Accordingly, the Finesse laser was equipped with a water cooled base plate which can stabilize the temperature down to $\Delta T = 0.1\,\mathrm{K}$ corresponding to a power stability of better than 0.1% [Fis13, Fis10b]. In Section 5.3 the depolarization measurements with the HighResLARA system will be presented and it will be shown there, that the power stability is essential since absolute intensities are used in that analysis. This is in contrast to the measurement with the MonLARA system for which only relative Raman signals matter. These signals are only marginally affected by power instabilities and therefore a temperature stabilization of the employed Verdi Laser is not required.

The Glan-Taylor polarizer (Thorlabs, model GT5-A) installed in the laser path before the LARA cell improves the cleanness of the linear polarization of the beam with a nominal extinction ratio of $10^5 : 1$. The high laser cleanness is required for the depolarization investigations in which minor polarization aberrations could already bias the measurement results (see Section 5.3).

The MonLARA system was equipped with a retro reflection mirror (not shown in Fig. 4.2) which could be used to reflect the laser beam back a second time through the sample cell. The usage of this configuration (double-pass mode) aims at doubling of the Raman signal. For further discussion see [Her11, Mir11].

Raman cell The cell design developed at the TLK [Tay01] is shown and mainly described in Fig. 4.4. According to the regulations of the TLK concerning tritium-bearing components [TLA13], stainless steel in general should be used as primary containment of the tritium gas[1]. However, Raman spectroscopy requires an optically transparent light access. The fused silica windows which take this function are widely tolerated for containing tritium [DOE93] despite their permeability which is about 1-2 orders of magnitude higher as compared to stainless steel. The real difficulty arises at the metal-glass transition at which a sealing is required. Standard rubber O-ring sealings cannot be used since (i) they do not fulfill leak-tightness requirements, (ii) their materials do not withstand the radio-chemical aggressivity of tritium, and (iii) they may contain substances like fluorine which then form secondary chemically aggressive compounds with tritium, like for example tritium fluoric acid, TF. This problem is overcome by diffusion bonding of the glass by a tantalum ring to the ConFlat®-flange [Eng92]. The drawback of this method is, that due to the manufacturing process at elevated temperatures, stress is exerted to the window. This stress induces birefringence in the fused silica which can lead to polarization aberrations in the transmitted light. Details on the effect and its ramifications are discussed in Section 5.3.2.2. The laser light is focused inside the Raman cell by an anti-reflection coated lens with a focal-length of $f = 250\,\mathrm{mm}$.

In the case of a sample containing more tritium than the permitted limit ($10^{10}\,\mathrm{Bq}$), it has to be placed in a secondary enclosure for reason of radiation protection[2]. Putting the whole Raman system into an additional enclosure, *e.g.* into a glove-box, is not practical due to the risk of tritium contamination as well as the constrained access for assembly and alignment. Therefore, an appendix was mounted to the glove-box which contains

[1] Further discussion in Section 6.3.

[2] Note that the general permitted limit in Germany for gaseous tritium is $10^9\,\mathrm{Bq}$. The special limit of $10^{10}\,\mathrm{Bq}$ for handling tritium under a suitable radionuclide hood is only valid at the TLK [Hah07].

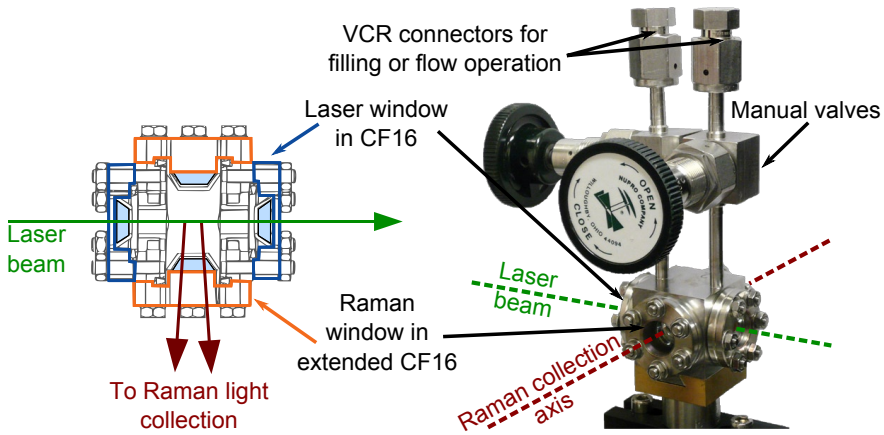

Figure 4.4: Cross-sectional view from top and photo of the Raman cell. All windows are made of fused silica and diffusion bonded into CF16-flanges. The laser windows are coated with an AR-coating optimized for 532 nm. The Raman windows are recessed into the cell to enhance the acceptance angle and to reduce the dead volume. They are coated with a broad-band AR-coating to provide a nearly lossless transmission of the scattered light [Tay01]. *Right:* Shown is a completely assembled Raman cell consisting of cell body, laser windows, Raman windows and manual valves.

the KATRIN Inner Loop [Stu10b, Fis11]. The Raman cell is part of this appendix as it is the only component which comes in contact with tritium. The optical table is attached to the outside of the appendix and the laser is guided to the cell and away from it via two window ports. The Raman light is then collected through another window in the appendix. A photograph of the appendix is shown in Fig. 4.5.

Light collection optics The light collection optics consists of a pair of 2" plano-convex lenses. One of the focal points lies within the scattering region in the cell and the other at the entrance of the optical fiber. In [Mir11] it was found by experimental investigations, that the absolute and relative Raman intensities depend on the position on the focal point. It was shown that already minute movements by a fraction of a millimeter could change the measurement of the relative composition by several percent. The reason for this behavior was found in the chromatic aberration caused by the wavelength dependence in the refractive index of the optical material. This caveat has been mitigated by replacing the standard plano-convex lenses by a pair of achromatic doublets (Thorlabs, model AC508-075-A-ML, $f = 75\,\mathrm{mm}$).

Fiber The light is collected by an optical fiber bundle. It consists of 48 single fibers (100 µm core and 125 µm cladding) aligned side by side and forming a 6 mm wide slit. The other side of the fiber is connected to the input coupling of the filter / spectrometer unit by which the fiber slit is imaged onto the CCD detector. The numerical aperture of the

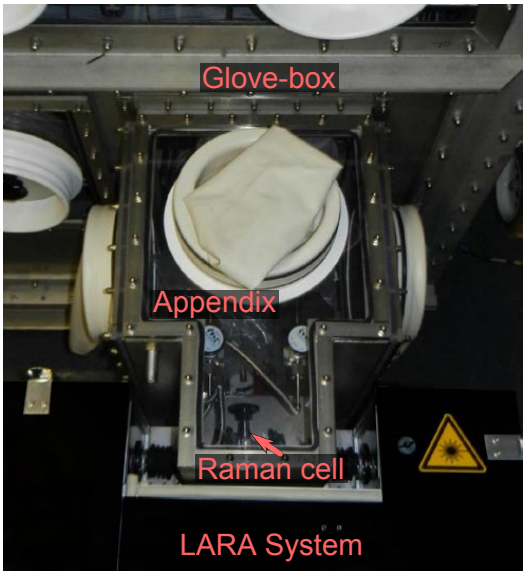

Figure 4.5: The Appendix as interface between glove-box and the LARA system. The Raman system is fixed to the Appendix to prevent misalignment. The laser path to the appendix and inside it is covered by light tight bellows. More details about the construction are available in the PhD thesis of Michael Sturm [Stu10b].

fiber is $\mathrm{NA} = 0.22$ [Lew07] which corresponds to a f-number of

$$f/\# \sim \frac{1}{2\mathrm{NA}} \tag{4.1}$$

$$\sim f/2.3\,. \tag{4.2}$$

Rayleigh line suppression filter The light which is generated inside the Raman cell does not originate from Raman scattering only. Additionally, Rayleigh scattering and inner cell reflections are collected by the fiber bundle [Sch09]. This light has the same wavelength as the excitation laser light. The intensity of the Rayleigh light alone is already at least three orders of magnitude higher than the Raman intensity [Hen70]. In case that light enters the spectrometer, the resulting stray-light would induce a spectral background which would prohibit quantitative Raman measurements. For this reason a long-pass filter is installed in front of the spectrometer entrance in order to suppress the light at the excitation line by more than 6 orders of magnitude. In the Raman systems RazorEdge® filters (LP03-532RU-25) by Semrock are installed [Sem12]. Their generic transmittance curve is shown in Fig. 4.6. It should be noted that the long-pass transmission is neither equal to unity nor uniform with regard to wavelength. Distinct ripples of the order of one percent transmittance change are visible in the relevant wavelength range ($\sim 600-700\,\mathrm{nm}$). The filter is the main cause for the "fine structure" which is found in the system's spectral sensitivity (see Section 5.4).

Spectrometer The specifications of the components described so far are quite similar in both Raman systems, or even the same. The different designations of the two system

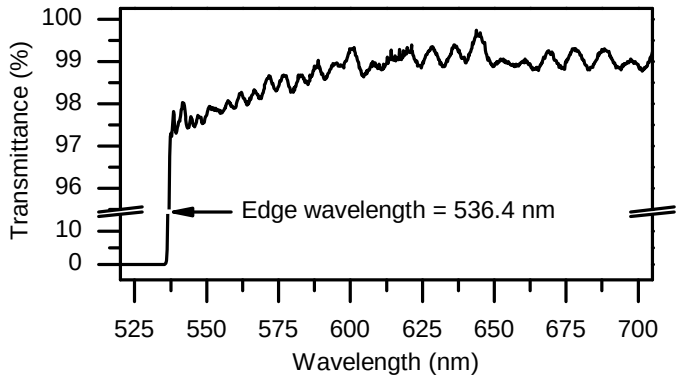

Figure 4.6: Transmittance curve of Semrock Razor RazorEdge® filter (LP03-532RU-25). At the excitation line ($532\,\mathrm{nm}$) the transmission is suppressed by 10^6. Graph generated from data provided by [Sem12].

become mainly apparent at the spectrograph as being the dispersive element.

On the one hand, for monitoring of the Q_1-branches of all six hydrogen isotopologues with a $532\,\mathrm{nm}$ laser a wavelength range from $\mathrm{T_2}$ at $2464\,\mathrm{cm^{-1}} \triangleq 612.3\,\mathrm{nm}$ to $\mathrm{H_2}$ at $4161\,\mathrm{cm^{-1}} \triangleq 683.3\ \mathrm{nm}$ needs to be spanned [Sch09]. This means that a wavelength coverage of at least $75\,\mathrm{nm}$ is required. If additionally the laser excitation line and the S_0-lines should be covered this range extends to about $175\,\mathrm{nm}$.

The wavelength coverage interval is a consequence of the dispersion of the grating, the focal length, and the limited CCD chip width. The spectrometer SP2150i by Princeton Instruments with focal length of $f = 150\,\mathrm{mm}$ is equipped with a $600\,\mathrm{grooves/mm}$ grating which covers about $250\,\mathrm{nm}$ [Pri10b]. Therefore, it is suitable for the measurements intended with the MonLARA system.

On the other hand, the aim of the HighResLARA system is not to cover all isotopologues at the same time, but to resolve the single lines of the individual Q_1-branches. The spacing[3] between the $Q_1(0)$ and $Q_1(1)$, and $Q_1(1)$ and $Q_1(2)$-lines of $\mathrm{H_2}$ is $5.9\,\mathrm{cm^{-1}} \triangleq 0.28\,\mathrm{nm}$ and $11.8\,\mathrm{cm^{-1}} \triangleq 0.55\,\mathrm{nm}$, respectively, for a laser excitation wavelength of $532\,\mathrm{nm}$. For the corresponding $Q_1(J'')$-lines of the $\mathrm{T_2}$ molecule the spacing is only $1.2\,\mathrm{cm^{-1}} \triangleq 0.04\,\mathrm{nm}$ and $2.3\,\mathrm{cm^{-1}} \triangleq 0.08\,\mathrm{nm}$, respectively. Thus high dispersion is needed and a longer focal length and gratings with a higher number of grooves per millimeter are required. The $f = 500\,\mathrm{mm}$ focal length of the SP500i spectrometer by Acton Research Corporation can offer the high dispersion by a grating[4] with $2400\,\mathrm{grooves/mm}$ [Act02]. The wavelength coverage is then only about $17\,\mathrm{nm}$. The spatial dispersion is $0.63\,\mathrm{nm/mm}$ which means that the image of the $0.1\,\mathrm{mm}$ wide fiber bundle will have a spectral width of about $0.06\,\mathrm{nm}$. This can be put in relation to the numbers above, so it should be possible, in principle, to resolve all single Q_1-lines, with the exception of $J'' = 0$ of $\mathrm{T_2}$.

Another aspect is the different light collecting power of both spectrometers, defined by their aperture ratios. Both spectrometers have higher f-numbers (MonLARA: $f/4.0$; HighResLARA: $f/6.5$) than the fiber bundle ($f/2.3$) as calculated in Eq. 4.2. Accordingly,

[3]The spacing was calculated according the spectroscopic data from Veirs and Rosenblatt [Vei87].

[4]Even higher dispersion could be offered by a $3600\,\mathrm{grooves/mm}$ grating, but this is not suitable for the selected wavelength range and therefore was not installed in the spectrograph.

the spectrometers capture only a fraction of light from the fiber. To compare the two spectrometers, the multiplicity m of the light collection is calculated from the square ratio of both f-numbers:

$$m = \left(\frac{f/\#(\mathrm{MonLARA})}{f/\#(\mathrm{HighResLARA})} \right)^2 \tag{4.3}$$

$$= \frac{6.5^2}{4.0^2} = 2.64\,. \tag{4.4}$$

This means that more than 2.5 times of the amount of light is collected by the SP2150i as compared to the SP500i. This is important when considering the acquisition time, which should be rather short to meet the purpose of the MonLARA system. In contrast, the HighResLARA measurements are not time-critical and thus the drawback of lower light-throughput can be compensated for by adopting longer acquisitions times.

Finally, it should also be mentioned that the wavelength-dependent efficiency of the gratings of the two spectrometers differ. Specifically, the $2400\,\mathrm{grooves/mm}$ grating of the SP500i spectrometer is not optimized for the wavelength region of the Q_1-branches of the hydrogen isotopologues, and its efficiency drops significantly towards higher wavelengths (note that the grating's cut-off wavelength is at about $800\,\mathrm{nm}$).

CCD array detector The technical specifications of the PIXIS:400B [Pri11] are given in Tab. 4.1. The back-illumination technique provides a high quantum efficiency of $\sim 95\%$ in the wavelength range of the hydrogen isotopologues. A detailed discussion of the detector resolution and different noise sources (shot noise, dark noise and readout noise) is given in the authors's diploma thesis [Sch09] and will not be repeated here. The dark noise in the spectrum is reduced by operating the detector at a temperature of $-75\,^\circ\mathrm{C}$ and the readout noise can be significantly reduced by the binning technique as will be discussed in the following Section 4.2.

Polarization control of the scattered light Finally, a topic is discussed which affects several components of both Raman systems.

An important modification to the collection optics with regard to the previous design of the MonLARA system [Sch09] is the insertion of a sheet polarizer (for model names and manufacturers see Tab. 4.1). In this way any polarization dependence in the subsequent optical components (fiber, filter, grating and CCD), which might otherwise affect the depolarization ratios, does not have to be known. It should be highlighted that the fiber bundle (only) partly depolarizes the light (and thus partly conserves the polarization), as discussed in [Ste84, Hol94]. The spectrometer grating has a response which is strongly dependent on the polarization orientation [Pal05]. If no polarizer were used in the collection path, then the analytic relation between the emitted Raman intensity and the signal measured by the CCD detector would not necessarily be linear. It should be noted that the polarization preservation depends on the actual position of the fiber. Strong manipulation of the fiber can modify the spectral sensitivity and thus the measured Raman spectrum. It is therefore strongly recommended not to touch the fiber after any alignment and spectral calibration.

4.2 Spectrum acquisition, processing and analysis

In the previous work of the author [Sch09] methods for processing and analysis were already introduced. However, most of these methods have been refined or replaced by more effective ones. It should be noted that parts of the content have been published in *Applied Spectroscopy*. For details, the reader is thus referenced to this paper and the corresponding supporting information [Jam13d]. Additionally, the following routines which have been implemented into LabVIEW® in cooperation with Timothy James are collated in an open-source "Spectral analysis suite" downloadable from Sourceforge[5].

4.2.1 Data acquisition

In this subsection, techniques for the improvement of the signal-to-noise ratio of spectra, which have not been employed in the previous work, are briefly described.

Coupling of light to the spectrometer In the previous dissertations on Raman spectroscopy for KATRIN (*e.g.* by [Lew07, Sch09, Fis10a]) the light from the fiber exit was focused "somehow" onto the input slit of the spectrometer which was shut to about the size of the fiber ($\sim 100 - 125\,\mu\mathrm{m}$). This allowed precise controlling of the peak width (see [Sch09]) but caused the loss of light that did not pass the slit. With a suitable adjustment of the focal spot (by aligning the position of the coupling optics) it was possible to image the $\sim 100\,\mu\mathrm{m}$ wide fiber exit directly onto the CCD plane while the slit was fully opened. This technique allows nearly all light to enter the spectrometer without widening the peak shapes on the CCD. This issue will not be further discussed here, but the reader is referred to the PhD thesis of Timothy James [Jam13a] for more details. There it is shown, that the gain in signal-to-noise ratio corresponds to about a factor of five.

On chip binning In the description of the CCD-detector in the previous section various noise sources have been mentioned (see also [Dem07, Ham12, Pel03]). The thermal or dark current noise can in general be minimized by adequate cooling of the detector chip. The second instrument-related noise component is the readout noise which results from analogue-to-digital conversion during readout of each single detector pixel. The noise can be reduced significantly by collective readout of (vertical) pixel blocks, named "bins" in the following. The corresponding feature provided by modern CCDs is called "on-chip binning". By making use of this option, read-out noise contributes only once per readout operation, and hence its prominent influence is substantially reduced in relation to the signal strength. Finally, the signal-to-noise ratio, SNR, is significantly improved. Another beneficial consequence of the lower number of readout cycles is the reduced total readout time and data size per recorded spectrum. For example, the readout of a spectrum from the PIXIS:400B without on-chip binning lasts about $(1340 \cdot 400)/100\,\mathrm{kHz} = 5.4\,\mathrm{s}$; a spectrum with only five vertical bins is then being readout in $1/80$ of this time which is less than $0.1\,\mathrm{s}$.

The implications of on-chip binning for the SNR were experimentally determined and are visualized in Fig. 4.7. The measurements for this study have been performed with a

[5] http://spectools.sourceforge.net/

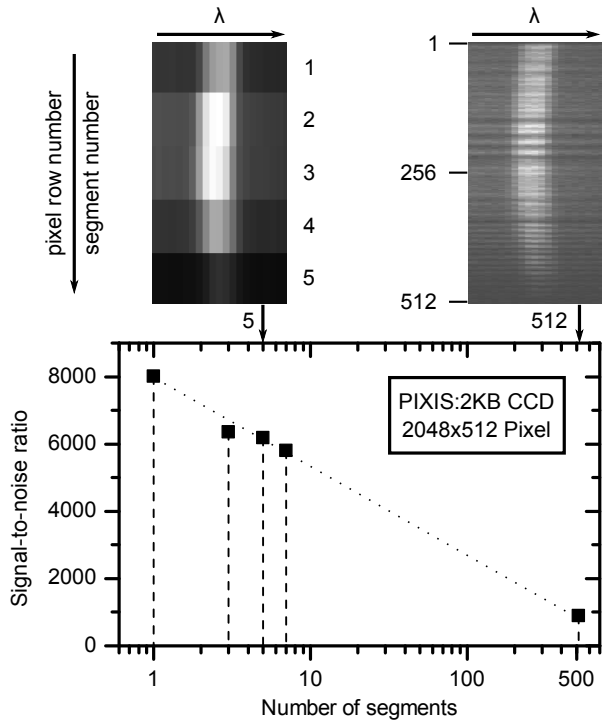

Figure 4.7: Signal-to-noise ratio (SNR) of a H_2 Raman line, as a function of binning segments. *Bottom panel:* The SNR dependence is shown from complete on-chip binning (1 segment) to no on-chip binning (512 segments). *Top-right panel:* a 21×512 pixel area of the raw 2D spectrum. *Top-left panel:* the identical spectral region acquired with on-chip binning; the five (vertically-stretched) segments constitute averages over $512/5 \sim 102$ pixel rows. Note that the slight line curvature is due to the astigmatism of the spectrometer.

PIXIS:2KB CCD detector, which is essentially the same detector as listed in Tab. 4.1, but with resolution of 2048 horizontal times 512 vertical pixels.

The top of Fig. 4.7 shows two-dimensional CCD chip segments representing each the same H_2 Raman line. The right panel shows the full resolution (512 rows) where the individual fiber bundle structure is visible; whereas the left one shows the binned data in five segments. The structure is no longer visible, but the increased grayscale contrast indicates the higher SNR.

The quantitative improvement to the SNR of the particular spectral line maximum is evident in the plot in the lower half of Fig. 4.7. Between the two extremes, full binning and no binning, the SNR varies by nearly one order of magnitude. Generally, a binning of three or five segments has been utilized in most of the Raman measurement performed during this work, yielding an increase in SNR of about a factor of six. This is only marginally worse than the full-chip binning. There are two reasons, however, why full-chip binning has not been used throughout.

First, the two chip-image inserts in Fig. 4.7 clearly reveal a curvature of the spectral line over the detector height, which is caused by the spectrometer's astigmatism [Hec74]. This implies that straight averaging over the full vertical pixel columns would result in distorted, asymmetric spectral line profiles [Sch09]. This deficiency is compensated for

by applying a correction step after readout. It could be shown that about five (or three as minimum) segments are necessary for an efficient correction of the astigmatism aberration.

Second, the 16-bit ADC limits the maximum counts per readout and thus the dynamic range of the detection. Not more than 65,535 counts can be collected for one vertical bin[6]. This implies that the number of bins cannot be reduced arbitrarily without reaching the detector saturation.

Combined improvement of signal-to-noise ratio Both techniques described lead to a total SNR increase by about a factor of 30. This dramatically increases the precision for the same acquisition time, or consequently allows shorter acquisitions at the same precision level. In the final Section 4.3 the actual performance improvement will be discussed.

4.2.2 Data processing

Before any quantitative information can be extracted from a spectrum, several pre-processing steps are necessary. These steps are required for correction of aberrations or artifacts from the acquisition such as astigmatism, dead pixels or cosmic ray induced counts. Another important issue is the flattening of the baseline. If this step is successful, then an accurate extraction of the Raman signal amplitude is finally possible. Previously, procedures for the aforementioned tasks were introduced [Sch09]. However, in the thesis in hand important refinements and novel concepts were necessary to overcome several specific problems. The schematic flow chart for the new concept is given in Fig. 4.8. The individual routines are described briefly in the sections below, following the same sequence as in the overall processing chain.

It is worth noting that all routines described here are programmed as separate LabVIEW® subroutines (subVIs). All subroutines are collected in a framework, called *SpecTools*, which comprises the data flow as shown in Fig. 4.8. The whole framework, as well as the separate routines, are available under `http://spectools.sourceforge.net`. Extensive documentation, help-files, tutorial and sample files are provided within the package. Therefore, for further descriptions and details of the routines, the reader is referred to the *SpecTools* documentation [Jam12].

The routines require manual configuration, but only once; thereafter they can operate in full automatic mode. This enables the processing of thousands of consecutive spectra without user intervention. In a recent diploma thesis [Kas12], it could be demonstrated that the routines can be directly linked to the data acquisition at the system, and a fully incorporated real-time monitoring was successfully demonstrated. This verification has important implications for KATRIN since real-time data processing is also required there.

Cosmic ray removal In long-term spectra recorded by CCDs, cosmic ray events are encountered on a frequent but random basis. They manifest themselves as (mostly) single-pixel spikes with a much higher intensity recorded by the involved pixel in comparison to its neighbors. These cosmic ray events need to be removed prior to data analysis. The following statement from Ehrentreich and Sümmchen [Ehr01] is an adequate introduction

[6] For five bins this level is at 327,679 counts.

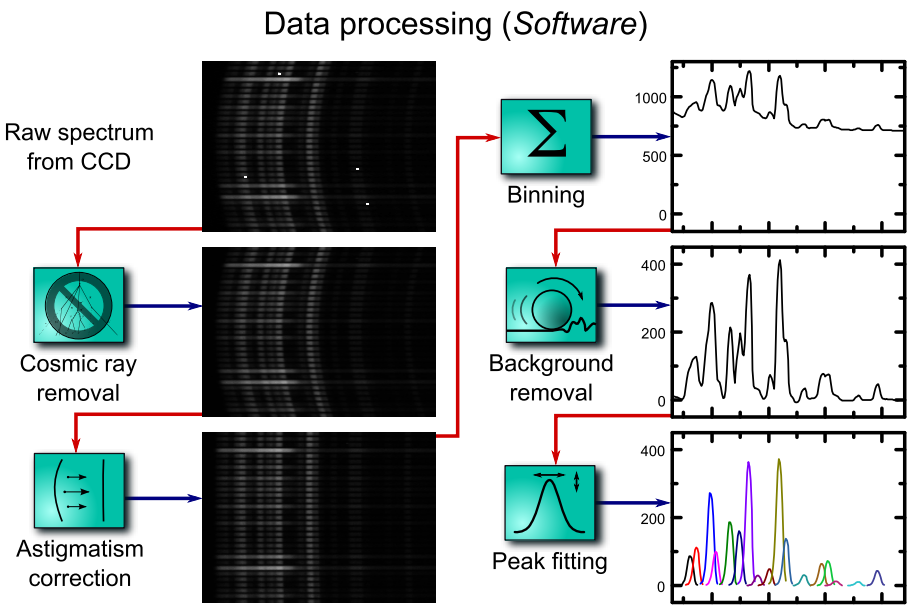

Figure 4.8: Flow-chart for integrated, processing chain, indicating the action of each individual step. Details are found within the text.

to the subject: "Selection of denoising strategies, including parameter selection, is strongly problem-dependent. It depends on the signal-to-noise ratio (S/N), the shape of the signals and its superposition, the resolution of complex overlaid signals, and justification or violation of model assumptions regarding noise distribution."

Generally, two categories of correction techniques exist, which make use either of spatial spectral information (single scan) or temporal spectral information (multiple scans). Single scan techniques which require only one spectrum are highly suitable if repetitive acquisition is not available. But there are also certain problems in cosmic ray detection with false positives or negatives and consequent artifacts. Bussian and Härdle used a robust smoothing technique for removal of single spike outliers (=cosmic ray events) [Bus84]. However, smoothing always affects peak shapes and can over-smooth low-intensity but relevant Raman lines, thus this method is not recommended for the quantitative Raman spectroscopy task of this thesis. In later years, said smoothing technique was refined, *e.g.* by Katsumoto and Ozaki, whose technique overcomes some of the caveats [Kat03]. A wavelet-based technique for spike removal in Raman spectra has been demonstrated by Ehrentreich and Sümmchen [Ehr01], but they also show that it is not a straightforward procedure and exhibits some deficiency in mis-detection of peaks. Furthermore, other principles of single scan approaches exist (*e.g.* by Li and Dai [Li11]). Another single scan technique which was used regularly, *e.g.* in the previous work of the author [Sch09], was the *Differential Cosmic Ray Removal* technique (DCRR) developed by Richard Lewis [Lew08, Lew07]. This procedure requires the input spectral information to be two-dimensional. The tagging of cosmic rays is performed via a double-differentiation over the full vertical "row-axis" and subsequent detection of a characteristic pattern. However, the DCRR technique showed some deficits such as (i) the quite long computation time (order of tens seconds) and (ii) the non-negligible mis-identification of cosmic rays events. In addition, the DCRR method is less useful if significant binning is applied in the acquisition thus reducing the benefit

from the two-dimensionality.

The Raman measurements at KATRIN will be performed in a continuous series on a time sequence of $\sim 100\,\mathrm{s}$. It is not expected that the composition and thus the intensity will change by a large degree during this interval. Therefore, the other category of techniques can be applied which uses the spectral difference of two or more repetitive measurements. The method of choice is similar to the one described in [Tak93]. The method is called *Temporal Cosmic Ray Removal* (TCRR) in the following and it uses the principle of spectral difference comparison. This concept is implemented by comparing (at least) two consecutive spectra recordings and determining the signal difference pixel-by-pixel. If this difference is less than a pre-selected threshold, the two spectral data points are averaged and this average is taken as the "cleaned" output value. Otherwise, the smaller value is taken as the output. The threshold value has to be a compromise of being large enough to cover noise fluctuations and of being small enough to efficiently capture most of the cosmic ray events, which can have a wide range of random amplitudes. The details of the implementation and the limitation of the method have been explored and the findings are discussed in the *SpecTools* documentation [Jam12]. To summarize in a nutshell: TCRR was chosen since it is least-complicated, robust, fast and very efficient for identifying and eliminating cosmic rays for the KATRIN monitoring purpose.

Removal of low-gain or dead pixel Occasionally, CCD detectors may exhibit one or more pixels whose response differs significantly from the average over all pixels, or pixels that do not respond at all (so-called "dead" pixels). The presence of such pixels leads to singular (generally downward) spikes in the spectra. Therefore, before averaging and data analysis such events should be removed. Because dead pixels are stationary, and not random like cosmic rays, the procedure for removal is rather simple. Once the pixels are identified by the user, the (dead) pixel value is replaced by a neighboring pixel at which a similar intensity is expected.

Astigmatism correction Optical systems are generally affected by an optical aberration called astigmatism. In the case of the Raman system this manifests itself as a distortion of straight spectral lines by curved optical components. This distortion is visible in Fig. 4.7 showing the two-dimensional image of a Raman line. Such a distortion can be described by a geometric transformation. The task is now to find the mathematical function to reverse this transformation and to arrive at an undistorted image. This approach consists of two steps, namely (i) the characterization of the astigmatism curvature throughout the two-dimensional chip, and (ii) the interpolation for the (fractional-value) pixel shift necessary for the straightening of the lines. In a first version of this correction method, the algorithm was only able to apply shifts which were valid for every complete row [Lew08, Lew07]. But, it should be noted that the magnitude of distortion by astigmatism is a function of wavelength. Even if this dependence is only small, it has to be accounted for in order to enable a correction of all lines in the spectrum. Therefore, the current version of the algorithm includes the wavelength dependence. Its implementation and details about it are again described in [Jam12].

Background removal The task of the background removal is to discriminate the signal from the background while both are subjected to noise.

One very common way of baseline removal is performed by so-called "manual methods" in which the (experienced) user needs to cope with the just mentioned task. Corresponding routines are provided in most spectroscopy software such as Origin® or GRAMS®. Despite the suspicion that these methods are not very reproducible and rather biased, it could be shown that the results obtained are in general reasonably accurate and precise [Jir04].

However, a problem arises if the number of spectra becomes very large, or if real-time evaluation and long-term operation is required. Therefore, automated procedures are unavoidable which then should perform equally well or better than the manual methods. Schulze *et al* give an extensive summary on the various methods which have the potential for an automated baseline removal [Sch05]. They also developed test-scenarios under which the recovery of the baseline and signal could be investigated quantitatively. Very promising results were obtained by "Artificial Neural Networks" [Hus93] and methods including (*e.g.* polynomial) fits of the baseline [Lie03]. However, these methods explicitly require estimates of the baseline. The suggested neural network technique requires extensive training before it can be applied to data. Furthermore, the training set might not remain valid if unknown features in the background arise. Recently, the number of fully model-free baseline estimation methods suitable for automated operation has been extended further [Sch11e, Sch12b].

It should be evident that certain of above methods may be viewed as being "all-rounders", meaning that they can cope satisfactorily well with various baseline and noise scenarios. On the other hand, under well-defined conditions other methods may be superior for this specific task. Therefore, a method was developed which is able to perform well under the KATRIN operation conditions, but can be applied equally well under the high-resolution measurement conditions for the depolarization studies.

The Rolling-Circle filter (RCF) The concept of the Rolling-Circle filter (RCF), which requires no further user intervention once parameters have been chosen, was adopted as strategy of choice. It is able to cope automatically with nearly any "not-too-sudden" variation in background/noise during long measurement periods. The first concept of the Rolling Circle filter was suggested by Mikhailyuk *et al* [Mik03], which was then further improved by Brandt *et al* [Bra06]. The action of the Rolling-Circle filter is visualized in Fig. 4.9. Its concept is basically equivalent to a rolling circle of radius r underneath the measured spectra which is treated as a rigid surface. The so-called "locus" at the top of the circle is taken as baseline estimate.

The Savitzky-Golay Coupled Advanced Rolling-Circle Filter (SCARF) The RCF procedure has a serious disadvantage since it overestimates the baseline level if a gap (*e.g.* a peak) is encountered which is of width, $w > 2r$. This is due to an effect which can be imagined as "rolling into the gaps". In [Jam13d] it is shown that the deficiency remains despite the fact that larger radii are employed.

The effect of inaccurate baseline overestimation can be minimized by the SCARF algorithm. It works by applying a Savitzky-Golay filtering [Sav64] step to the locus line generated in

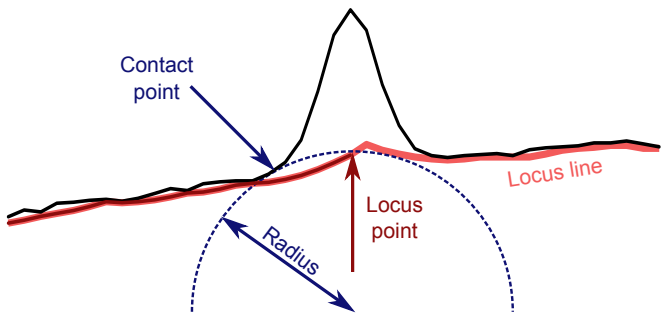

Figure 4.9: Sketch of Rolling Circle Filter (RCF) action The filter tends to "roll" into the peak, overcompensating the background level. In the SCARF filter routine this is overcome by using an additional Savitzky-Golay filtering stage. The full discussion is found in the main text.

the prior RCF pass. The Savitzky-Golay filter is characterized by the number of side-points, s. The parameters r and s need to be tuned once to obtain an optimal removal of the baseline[7]. Even better results can be achieved from multiple passes of the SCARF filter with varying radii r and side-points s.

The performance of the SCARF routine is demonstrated in Fig. 4.10. It shows a real N_2 spectrum superimposed by an additional non-linear background contribution (here *e.g.* light from a $605\,\mathrm{nm}$-LED).

Different configurations of the RCF or SCARF removal routines are shown, demonstrating the improved success of the baseline reduction. The reader is again referred to the corresponding publication for a deeper discussion [Jam13d].

Finally, it should be noted, that the application of RCF/SCARF for background removal as-is exhibits a minor deficiency. The circle always rolls below the points of the spectrum by which the noise slightly offsets the resulting spectrum above zero. This can be compensated for by shifting the baseline back by the median of the noise fluctuations.

Analysis of peak intensities The last step in the data-processing chain is the extraction of peak intensities. Two types of techniques have been considered for their determination. A straight forward technique is based on simple summing of the intensity from all pixels within a peak profile (*e.g.* the total intensity in a certain wavelength or Raman shift interval). This method yields very accurate values for peak areas as long as the line does not overlap with another feature.

Convoluted lines are treated in general by fitting a combination of Voigt profiles to the spectrum (or even more simple line shapes such as Gaussians) [Als04, Kri08]. Often these assumed line shapes represent only a simplification of the true shape generated by the spectroscopic imaging system. In general the measured shape deviates from the "pure" Voigt profile since it is influenced by certain optical components, being the exit of the small-core optical fiber bundle, the spectrometer entrance slit, the dispersion grating and finally the discrete CCD-detector pixel structure. The Voigt profile fitting

[7]Further details and investigation on synthetic line spectra and real Raman spectra are found in [Jam13d].

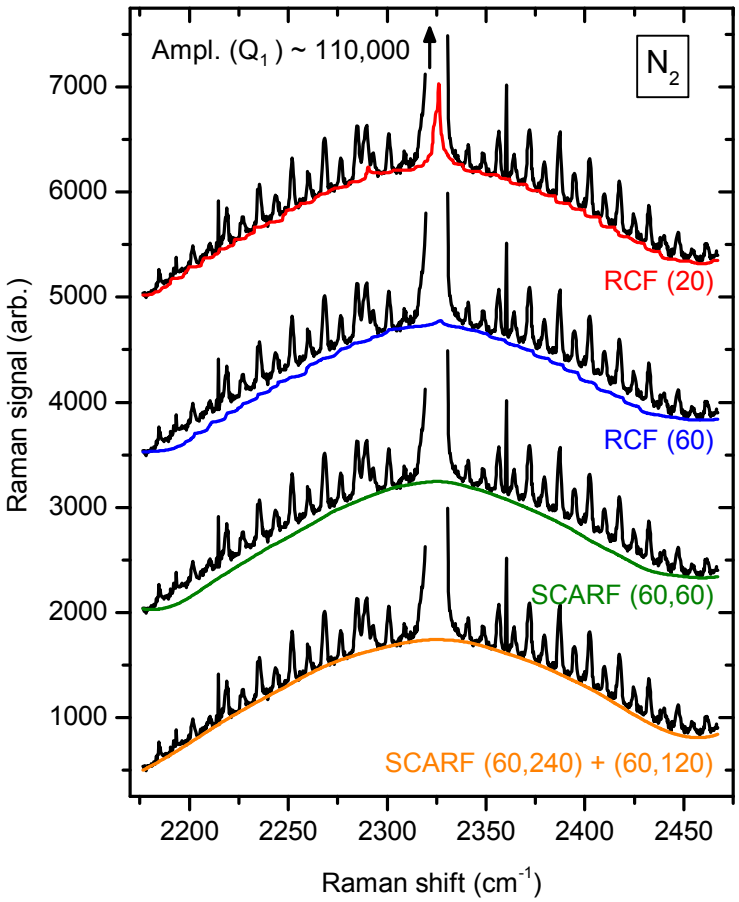

Figure 4.10: Background removal study for a Raman spectrum of N_2, over-laid with shaped background light. Shown are the central Q_1-branch with adjacent O_1 (left) and S_1 (right) branches. The traces are offset by 1500 units, consecutively from top to bottom. The traces are annotated with the respective filter actions used, RCF (r) and SCARF (r, s). Note that the displayed Raman shift range corresponds to the full width of Swansea's detector of 1024 pixel. Figure from [Jam13d], where further details and discussions can be found.

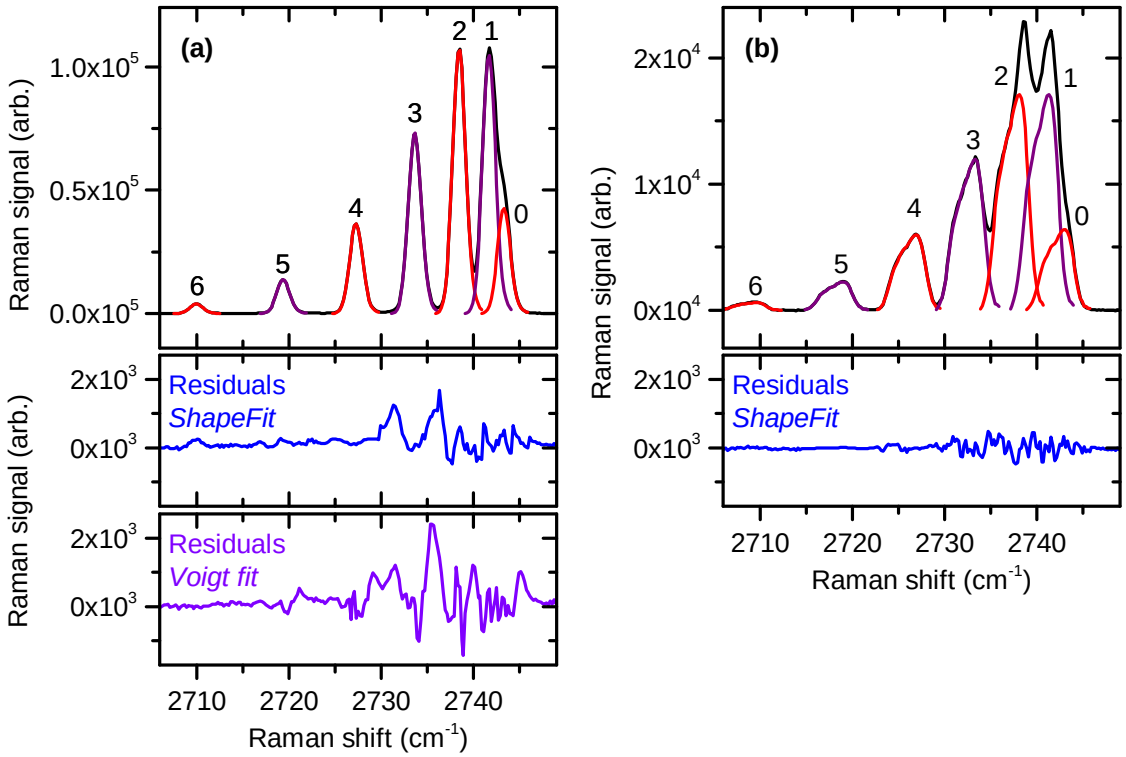

Figure 4.11: Raman spectra of DT with fitted peaks. In the top panels, the recorded spectra (black) and the fitted peaks using *ShapeFit* (colored) are displayed. The spectra are recorded for (a) an ideally aligned fiber bundle and (b) a purposely mis-aligned fiber bundle on the entrance slit. The data in (a) fit well to the experimental data using a numerical line profile (*ShapeFit*) as well as the analytical Voigt-profile; the data in (b) only fit to the numerical line profile of the *ShapeFit* routine.

as implemented in the indirect hard modeling method [Kri08] was already tested in the framework of the previous work [Sch09] which revealed shortcomings in the agreements of the measured and fitted peak shape. Additionally, four parameters are necessary to describe the Voigt profile (position, intensity, FWHM, Gauss-Lorentz ratio). Thus the number of open parameters in the minimization problem is four times the peak number, which increases the computational efforts significantly.

The method which proved to be the most suitable one has been implemented in this thesis. The method was named *ShapeFit*. The basic method is applicable without restriction in the case of equal line shape of all spectra lines of interest. This scenario is present in the high-resolution measurement of single resolved Q_1-lines. In general this condition is valid, if (i) the slit width of the spectrometer and/or optical fiber limits the line width, or if (ii) the natural line width plus broadening of all involved lines is equal.

Before this method can be applied to a spectrum for quantitative analysis, first the line shape has to be determined numerically. It is obtained by selecting an isolated line with sufficient intensity from a measured spectrum. It is important that the line is free from convolution with other lines and if this is not available in the spectrum, then the line has to be extracted from another spectrum, *e.g.* from a spectrum of a calibration lamp. The shape of this peak is then stored pixel-by-pixel in an auxiliary data array.

During the analysis step, this numerical peak shape function is fitted to the peaks in the spectrum using the Levenberg-Marquardt algorithm [Mar63]. The free parameters consist of a multiplicative amplitude factor and the center position per peak. Sub-pixel translation of the peak positions is made possible by interpolation of the numerical peak shape. Finally, a baseline parameter is added as offset which can be either fixed or used as free fitting parameter.

In Fig. 4.11 two examples for the fitting abilities of the *ShapeFit* algorithm are shown. Both show high resolution spectra of DT, one with an ideally aligned fiber bundle, and one with an intentionally "bad" alignment, which results in a deformed peak shape. While the Voigt profile fit only shows a slightly worse performance compared to *ShapeFit* in the first example, it failed completely for the second one. This shows that the fitting performance is generally better than the Voigt-profile fit, and at the same time requires fewer fitting parameters (two instead of four per peak) in the minimization step.

In a more advanced version of the routine, named *ShapeFit deluxe*, the restriction to use equal line shapes is lifted. It furthermore allows to employ specific shapes for each individual line, branch or even combination of lines and branches. This is particularly helpful if main branches such as the Q_1-branch overlap with S_1 or O_1-lines from another isotopologue. A demonstration of using all lines (Q_1, S_1, O_1) of a single isotopologue as one shape is presented in Fig. 4.12. The figure shows that this technique even allows to obtain "virtually" pure spectra from substances which are hardly stable in pure form as the heteronuclear HT, HD or DT.

4.3 Analysis of actual system performance

In this last section an investigation of the actual performance of the MonLARA system is presented and discussed under the following three aspects:

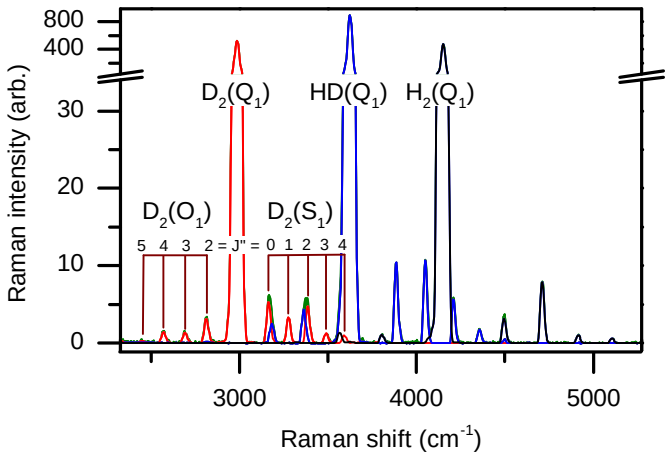

Figure 4.12: Demonstration of *ShapeFit deluxe* for a typical Raman spectrum of $\mathbf{H_2}$, $\mathbf{HD}$, $\mathbf{D_2}$. Total pressure $p \sim 330\,\mathrm{mbar}$; acquisition time $t = 10\,\mathrm{s}$. Note that the vibrational-rotational lines (S_1 and O_1) are labeled only for D_2. The complete spectrum of each individual isotopologues including Q_1-branch as well as S_1/O_1-branches is stored as a single numerical shape. First, the shapes for H_2 and D_2 were obtained from pure substances. Then these shapes were used to obtain the pure HD spectrum as the residual from fitting to a $H_2 : HD : D_2$ mixture in thermodynamical equilibrium. This spectrum has already been visualized in [Sch13a, Rup12].

1. **Signal to noise ratio (SNR).** This ratio defines the noise contrast of a selected spectral feature. A high SNR of a selected peak (line or branch) normally implies that its signal amplitude can be quantized with high precision. A low SNR constrains the possibility of a precise amplitude determination due to the random fluctuation of background and signal.

2. **Level of detection (LOD).** According to Long and Winefordner the minimal detectable spectral feature should be at least three times above the noise, σ_{noise}, which is equivalent to $\mathrm{SNR} = 3$ [Lon83]. The noise is the standard deviation of the intensity at a flat region in the spectrum. The minimal detectable intensity $I_{\mathrm{LOD}} = 3 \cdot \sigma_{\mathrm{noise}}$ is usually related to a minimal amount of the analyte. In the case of gases one is interested in minimal detectable concentrations, c_{LOD}, or partial pressures, p_{LOD}.

3. **Precision.** Simply put, SNR and LOD characterize the quality of single spectra, while precision relates to statistics and thus to a set of measurements. It defines the repeatability (or reproducibility) of a certain value of interest (*e.g.* the Raman signal amplitude of a selected peak) [JCG08]. In this work the precision is determined from the standard deviation σ_{stat} of these values in a time trend.

The study case here is a continuous Raman measurement during the production of accurate gas samples, as employed for the calibration (see Chapter 6). The sample was produced from 50% pure H_2 and 50% pure D_2. In a catalytic process HD was formed until a thermodynamic equilibrium is reached. It should be noted that the gas was dynamically circulated through the mixing system including the Raman cell. Fig. 4.13 shows a selected Raman spectrum after data processing and a time trend segment of about $20\,\mathrm{min}$, after a steady-state was reached.

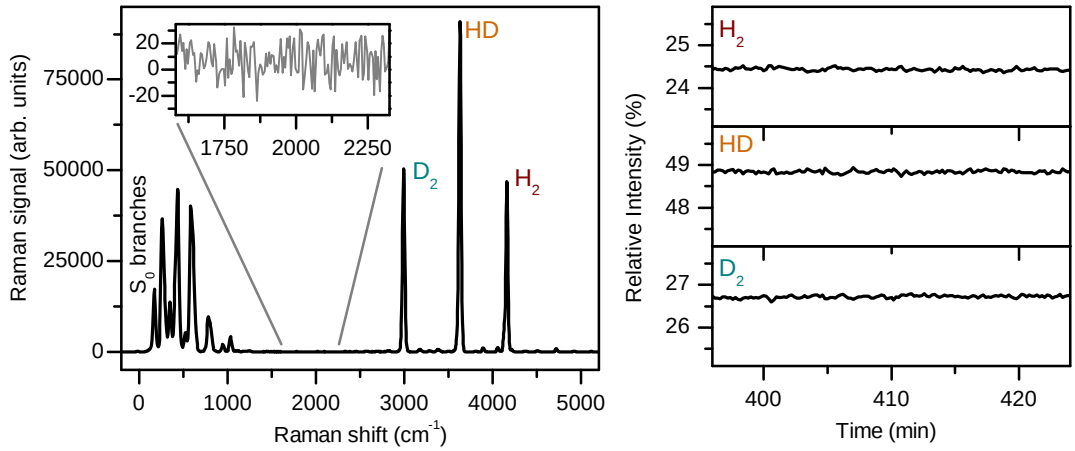

Figure 4.13: Performance tests for a H_2 : HD : D_2 gas mixture. The total gas pressure was about $p \sim 330\,\mathrm{mbar}$. The acquisition time per single measurement was $t = 10\,\mathrm{s}$. *Left panel:* Full Raman spectrum showing S_0 and Q_1-branches. The inset shows the region from which the noise has been determined. In the given case it was determined as $\sigma_{\mathrm{noise}} \sim 13$. *Right panel:* Time trend of the relative intensities of the three isotopologues in a circulating mixture. The selected time period represents a steady state interval during a longer mixing campaign.

Table 4.2: Signal to noise ratios and precision of the selected Raman measurement. The measurement parameters were (i) total pressure $p_{\mathrm{tot}} \sim 330\,\mathrm{mbar}$, (ii) laser power $P = 5\,\mathrm{W}$, (iii) acquisition time $t = 10\,\mathrm{s}$. Note that two consecutive spectra have been averaged in cosmic ray removal (TCRR). The background noise used for obtaining the SNRs from I_{abs} was $\sigma_{\mathrm{noise}} = 13$ (See Fig. 4.13)

	Single spectrum		Time trend	
Isotopologue	I_{abs}	SNR	$I_{\mathrm{rel}} \pm \sigma_{\mathrm{stat}}$ (%)	$\sigma_{\mathrm{stat}}/I_{\mathrm{rel}}$ (%)
H_2	46778	3598	26.72 ± 0.03	0.13
HD	90949	6996	48.84 ± 0.04	0.08
D_2	50368	3874	24.43 ± 0.03	0.14

Measurement of signal to noise ratios The signal to noise ratio (SNR) can be extracted from a Raman spectrum. The left panel of Fig. 4.13 shows a spectrum of the non-radioactive hydrogen isotopologues after all data processing steps. For convenience, the height of the Q_1-branch of each of the three isotopologues is taken as the signal intensity I_x. The noise, σ_{noise}, is extracted from the highlighted spectral region between the S_0-branches and the Q_1-branch of D_2 (see inset of Fig. 4.13 (left)). The standard deviation of the intensities from about 100 data points (pixels) is taken as the background noise intensity, which was determined as $\sigma_{\mathrm{noise}} = 13$. With this the SNR ratio for a certain isotopologue x is simply

$$\mathrm{SNR_x} = \frac{I_x}{\sigma_{\mathrm{noise}}} \,. \tag{4.5}$$

The SNRs for the three isotopologues are tabulated in Tab. 4.2

All SNRs for the three isotopologues are > 3500; their reciprocal values are therefore

$< 3 \cdot 10^{-4}$. This implies that a precision of $< 1 \cdot 10^{-3}$ which is related to the repeatability of a single measurement should be feasible (see below).

Estimation of the level of detection The level of detection (LOD) can be estimated from the following equation [Sch09]

$$p_{\mathrm{LOD}} = \frac{3 \cdot \sigma_{\mathrm{noise}}}{\sum_i I_{i,\mathrm{abs}}} \cdot p_{\mathrm{tot}} \,. \tag{4.6}$$

The total pressure in the cell was about $p_{\mathrm{tot}} = 330\,\mathrm{mbar}$ and the total intensity was $\sum_i I_{i,\mathrm{abs}} = 188095$. This results in a minimal detectable pressure of $p_{\mathrm{LOD}} = 0.068\,\mathrm{mbar}$.

In the diploma thesis by the author [Sch09], which describes the status of the MonLARA system and the data processing at the beginning of the PhD work, the reported minimal detectable pressure was $p_{\mathrm{LOD}} = 0.015\,\mathrm{mbar}$; this is about 4.5 times lower. However, it should be noted that this value was related to an acquisition time of $t = 1000\,\mathrm{s}$ and thus 100 times longer than the measurements reported here. Therefore, the total enhancement is about a factor of $100/4.5 \sim 22$. This is in accordance with the predicted enhancement of about 30, as discussed in Section 4.2.1.

Determination of precision The precision of a measurement is related to statistics and thus can be easily determined from a time trend of a certain measured value. In the right panel of Fig. 4.13 the relative intensities of the three isotopologues are plotted for an interval of about $20\,\mathrm{min}$. The fluctuations of low amplitude in this figure indicate a high stability. The results of a statistical analysis on the relative intensities and the standard deviation from 113 spectra are collated in Tab. 4.2.

The σ_{stat} values are below 0.05%, and the relative $\sigma_{\mathrm{stat}}/I_{\mathrm{rel}}$ values are better than 0.15%.

It should be noted that enhancements in SNR or LOD are mainly related to the hardware characteristics and the way of acquiring the data (see Section 4.2.1). The precision is related to these procedural steps as well, but beyond that it is influenced by the reliability of the data processing routines.

Finally, the implication for the compositional monitoring of the WGTS is discussed. The partial pressure of the constituent HD in the gas mixture shown in Fig. 4.13. It is about $p_{\mathrm{HD}} \sim 0.5 \cdot p_{\mathrm{tot}}$, thus being of the same order as for $\mathrm{T_2}$ in a KATRIN run. Therefore, $\sigma_{\mathrm{stat}}/I_{\mathrm{rel}}$ is already better than the precision requirements of KATRIN (0.1%). This implies that the acquisition time for the LARA system can ultimately be reduced to some 10 seconds while staying within the requirements. This finding is in agreement with the result from the bachelor's thesis in which a possible KATRIN acquisition time has been estimated to be $\leqslant 60\,\mathrm{s}$ [Mir11]. Said estimate for the expected precision in a KATRIN run is assumed to be valid. However, a long-term circulation test of KATRIN-like tritium samples is scheduled for the near future; in this up-coming benchmark measurements all improvements on data acquisition and processing described above will be incorporated [Fis13]. This test will unambiguously demonstrate that LARA can fulfill the precision requirements of KATRIN.

Chapter 5

Calibration based on theoretical intensities and spectral sensitivity (Method I)

5.1 Motivation and overview

In the previous chapter the calibration strategy based on theoretical intensities and spectral sensitivity was introduced. Two main tasks have to be undertaken in order to achieve a reliable calibration.

- **Theoretical intensities**
  The calculation of theoretical intensities is analogous to the determination of the Raman scattering probabilities. Most of the input parameters for this are known with sufficient trueness, so that the calculation is relatively straightforward. Note, however, that two relevant input parameters (average polarizability a and anisotropy γ) depend on quantum theoretical *ab initio* calculations [Sch87]. The underlying theoretical model is in principle able to provide a and γ values for all individual Raman lines; however, the theory does not normally provide any values for systematic uncertainties. Therefore, the use of these quantum theoretical values in this calibration approach is only justified if the validity of the theoretical model can be proven.

  In general, it is a complicated task to verify the quantities of a and γ directly. However, both parameters can be used for a theoretical prediction of so-called depolarization ratios. These ratios are experimentally accessible which allows a comparison with the prediction. A compatibility of predicted and experimental results within the estimated uncertainty would reveal that the quantum theoretical model is consistent and provides accurate values of a and γ.

- **Spectral sensitivity**
  The spectral sensitivity is a unique property of each (Raman) light detection system. It describes the wavelength dependent efficiency with which a photon is transmitted through the system. The determination of the spectral sensitivity is required to link

the system-independent theoretical intensities to the actual experimental Raman setup. The measurement of the spectral sensitivity requires dedicated experimental efforts. First, a suitable calibration light source needs to be identified which provides (i) a high trueness of the calibration spectrum, (ii) an optimal replication of the Raman scattering region, and (iii) a defined calibration procedure to obtain a high reproducibility.

Content of chapter The overview of the rather extensive content of this chapter is visualized in Fig. 5.1. The chapter is mainly divided into two parts according to the two elements required for the calibration method. First, certain aspects of the theoretical intensities are pointed out in Section 5.2. It is shown that the verification of the quantum theoretical values a and γ involves the measurement of the so-called depolarization ratios of each $Q_1(J'')$ Raman line. Section 5.3 deals with this topic.

The accurate measurement of the depolarization ratios is influenced by geometrical effects and polarization aberrations. In order to account for said effects, a correction routine was developed and successfully validated. This evaluation method is subject of a publication by the author and co-workers in the Journal of Raman Spectroscopy (JRS) [Sch13b]. This correction routine allows for the accurate determination of the depolarization ratios of all six hydrogen isotopologues. By this means the depolarization ratios of all six hydrogen isotopologues could be measured for the first time with better accuracy than those achieved in previous measurements by other groups (*e.g.* on H_2). The related results and discussions were also published in the same journal (JRS) [Jam13b]. The setup of the experiment and the measurements at the TLK were performed together with Sebastian Fischer. At Swansea University further depolarization measurements were performed on the non-radioactive isotopologues only, using the same method as mentioned above. This allowed comparison of the individual depolarization ratios from independent systems. The measurements at Swansea were conducted by Timothy James [Jam13a].

In Section 5.4 the measurement of the spectral sensitivity is introduced. Here, a solid luminescence standard was identified as an adequate calibration light source. The systematic and validation studies on the device revealed that the standard is suitable for the calibration purpose. The investigations were performed together with Simone Rupp and are discussed in full detail within her diploma thesis [Rup12].

Finally, the results from the sections about the calculation of the theoretical intensities and the measurement of the spectral sensitivity are combined to obtain the response function R_x for each isotopologue (Section 5.5).

5.2 Calculation of theoretical intensities

In Section 3.3 the basic principle of the calibration of Raman systems was introduced. The correlation of the Raman signal amplitude S_x, the number of molecules N_x, and the related response function R_x is given by Eq. 3.30

$$S_x = R_x \cdot N_x \ . \tag{5.1}$$

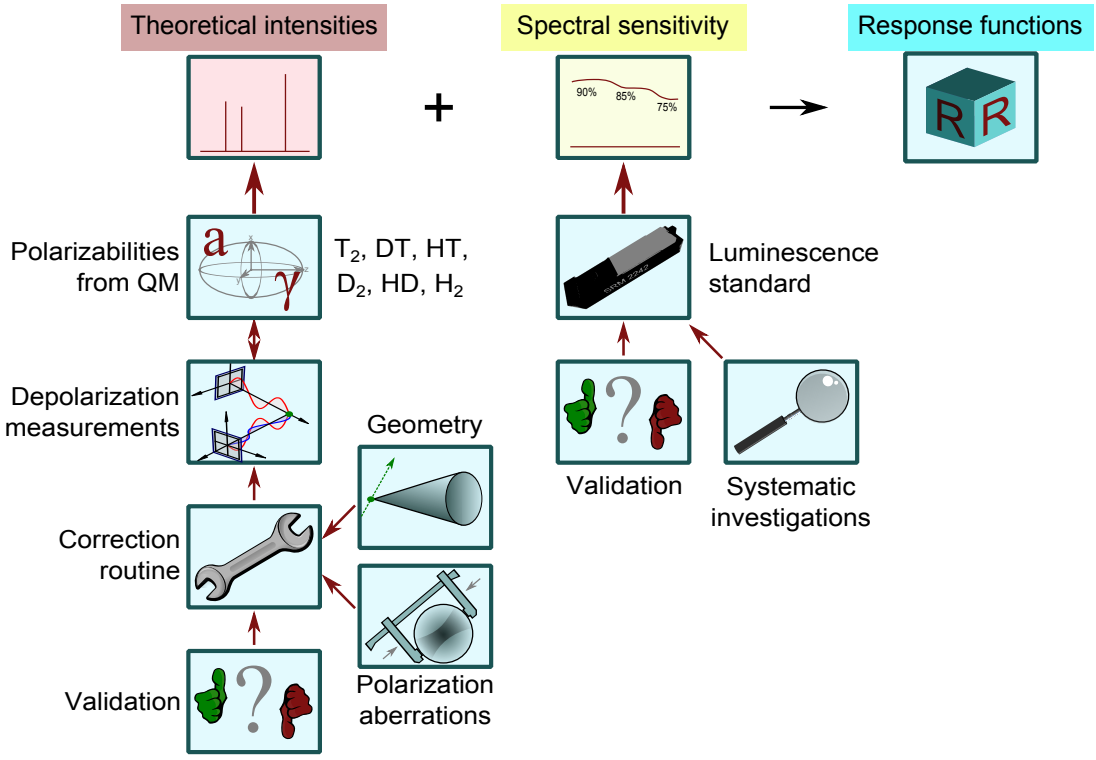

Figure 5.1: Graphical overview of the chapter content. In the approach presented in this chapter the response functions are obtained by combining the theoretical intensities and the spectral sensitivity. For each part methods were developed to provide the desired quantities with high accuracy. In order to verify the polarizabilities from theory, specific depolarization ratio measurements were performed. For the correction of geometrical effects and polarization aberrations in the experimentally measured depolarization ratios a routine was developed and validated. For the determination of the spectral sensitivity a luminescence standard was chosen, studied and validated.

However, in this approach said equation needs to be written in a slightly different form: The Raman signal amplitude is now given as the product of the spectral sensitivity at the according wavelength, $\eta(\lambda_s)$, and the theoretical Raman intensity, $I_{\mathrm{Raman,x}}(\lambda_s, N_x)$ (see Section 3.1.3), and will thus be called "theoretical Raman signal amplitude"

$$S_x = \eta(\lambda_s) \cdot I_{\mathrm{Raman,x}}(\lambda_s, N_x) \tag{5.2}$$

$$= \eta(\lambda_s) \cdot C \cdot \lambda_0^{-1} \cdot \lambda_s^{-3} \cdot N_x \Phi_x \cdot \mathcal{I} \,. \tag{5.3}$$

Constants and terms were defined in Section 3.1.3. Eq. 5.3 makes use of a simplification in which it is assumed that the Raman signal for a certain isotopologue consists of a single monochromatic line. This is not the case in reality, where the employed Q_1-branches consist of a series of unresolved individual lines associated with the different initial rotational states with quantum number J'' (compare "non-Gaussian" line shape in the example spectrum in Fig. 3.9). The population of these initial states can be calculated from the Boltzmann distribution and the nuclear spin degeneracy g_N as discussed in Section 3.1.3. Eqs. 5.2, 5.3 therefore have to take this multi-line scenario into account, and need to be modified to

$$S_x = \underbrace{C \cdot \lambda_0^{-1} \cdot \mathcal{I}}_{\text{const.}} \cdot N_x \cdot \underbrace{\sum_{J''} \left(\eta(\lambda_{s,J''}) \cdot \lambda_{s,J''}^{-3} \Phi_{x,J''} (2J''+1) g_N \exp\left(-\frac{\tilde{F}(J'')hc}{kT} \right) / Q \right)}_{R'_x} \tag{5.4}$$

with the molecular partition function Q [Lon02]

$$Q = \sum_{J''} \left((2J''+1) g_N \exp\left(-\frac{\tilde{F}(J'')hc}{kT} \right) \right) \,. \tag{5.5}$$

This description of the Raman signal in relation to the number of particles is now similar to the initial Eq. 5.1. The first three factors are constant for all isotopologues and will cancel out when calculating the relative response functions (see Eq. 3.32).

The modified response function R'_x in Eq. 5.4 is given as

$$R'_x = \sum_{J''} \left(\eta(\lambda_{s,J''}) \cdot \lambda_{s,J''}^{-3} \Phi_{x,J''} (2J''+1) g_N \exp\left(-\frac{\tilde{F}(J'')hc}{kT} \right) / Q \right) \,. \tag{5.6}$$

The determination of the spectral sensitivity, $\eta(\lambda_{s,J''})$, is the topic of Section 5.4.

Note that R'_x has not the same values as R_x in Eq. 5.1, but will lead to the same relative response function $R_{x,\mathrm{rel}}$ when it is normalized to the mean response function.

The individual parts of Eq. 5.6 are examined with regard to possible sources of uncertainty.

- The temperature in the Boltzmann factor can be assumed as $T = 298\,\mathrm{K}$. A variation of T by a few degrees does not affect the thermal population significantly since the thermal energy kT only changes a few percents.
- The term $\tilde{F}(J'')$ represents the rotational term energies which can be obtained from an accurate measurement of the line positions. These values were provided by Veirs and Rosenblatt and do not require further verification [Vei87]. From their tabulated Raman shifts and the wavenumber of the excitation laser one can also calculate the wavelength of the scattered light, λ_s, with similar accuracy.

- Finally, the only open contribution is related to the line strength function $\Phi_{x,J''}$. It has to be recalled, that this is a function of the polarization configuration (p^s, p^i) and of the scattering angles θ and φ (see Section 3.1.3). The polarization configuration realized in the MonLARA system which yields the highest Q_1-branch intensity is the $(\perp^s, \perp^i)$ scenario from Eq. 3.23:

$$\Phi(\varphi,\theta)_{\perp^s,\perp^i,x,J''} = a^2_{x,J''}\cos(\varphi)^2 + b^{(2)}_{J''}\frac{\gamma^2_{x,J''}}{45}\left(4-\sin(\varphi)^2\right) \tag{5.7}$$

  with the Placzek-Teller factor [Lon02]

$$b^{(2)}_{J''} = \frac{J''(J''+1)}{(2J''-1)(2J''+3)}\,. \tag{5.8}$$

  The tensor invariants $a_{x,J''}$ and $\gamma_{x,J''}$, *i.e.* the isotropic and anisotropic polarizabilities for the different isotopologues x and rotational lines J'', are obtained by theoretical calculations. The suitable values for the laser wavelength employed in MonLARA, $532\,\mathrm{nm}$, was provided by LeRoy [LeR11].

  Finally, the line strength function $\Phi(\varphi,\theta)_{\perp^s,\perp^i,x,J''}$ needs to be integrated over the solid angle of the scattered light. The derivation of such an integration formalism will be discussed below in Section 5.3.2.1.

  Fig. 5.2 shows an overview of the theoretical intensities of all six hydrogen isotopologues. The intensities of the heteronuclear isotopologues HD, HT, and DT show a typical thermal Boltzmann distribution. The homonuclear isotopologues H_2, D_2, and T_2 exhibit their characteristic ortho-para modulation on top of this thermal population.

From this list it becomes clear that all contributions which are not related to the spectral sensitivity in the response function from Eq. 5.6 are available in high accuracy. The exception is the line strength function, Φ, since the uncertainty of the $a_{x,J''}$ and $\gamma_{x,J''}$ contributions therein, which are based on quantum theory, is unknown.

One possible and promising way for the verification of these theoretical predictions are so-called depolarization measurements, which are discussed in the following section.

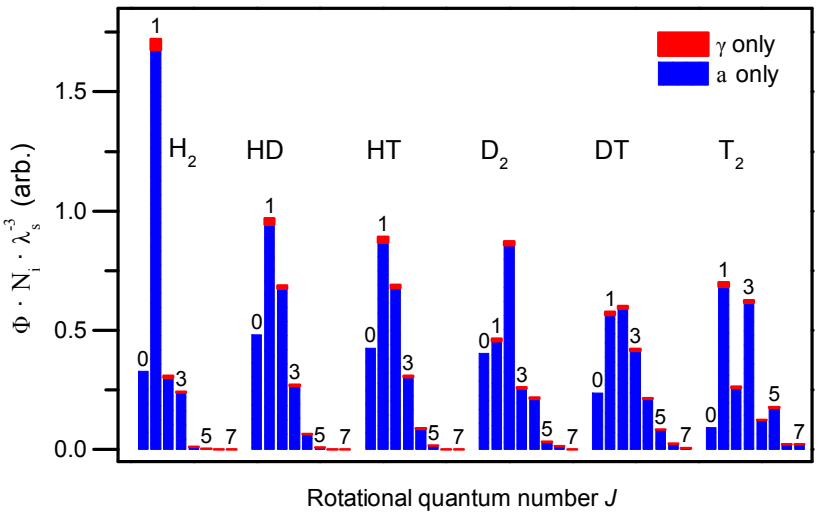

Figure 5.2: Theoretical Raman signal intensity for each $Q_1(J'')$ line of the six hydrogen isotopologues. The intensity is given as the product of line strength function Φ, population factor N_i as well as the wavelength of the scattered light λ_s^{-3}. The products are normalized to a common, but arbitrary value. The figure shows the single contributions from the terms in the line strength function which are related to $a_{x,J''}$ and $\gamma_{x,J''}$. It should be noted, that more than 95% of the total height of each column has its origin in the a part while only a minor contribution is related to the γ part.

5.3 Verification of theoretical intensities via depolarization measurements

Depolarization expresses the change of the amplitude of the parallel and perpendicular E-field components of incident light in a scattering process. This situation is visualized in Fig. 5.3. The ratio between both components after scattering is called the depolarization ratio [All70]. The definition of the ideal depolarization ratio is given in the following sections. However, as will be shown below, the real experimental situation differs from the ideal case. Thus, the theoretical description needs to be transformed from the ideal to a more realistic case.

For this, a brief introduction will be given with respect to the development of the methodology of depolarization measurements and their application to the hydrogen isotopologues in a historical view.

In general, species are identified by their spectral information as wavenumber and peak shapes. The measurement of the degree of depolarization generally extends the capabilities of identifying species. The determination of the depolarization ratio of a molecule can reveal the symmetry of its scattering vibrational modes. Even the quantitative evaluation of tensor invariants of the molecular polarizability is feasible [Bri66, All70, Zie89].

The methodology of depolarization measurements The depolarization ratio is in general related to the ideal case with a vanishing collection solid angle, as sketched in Fig. 5.3. In the early 1970s Dawson discussed the influence of a non-zero collection angle and other effects on the depolarization ratio [Dwa72]. Subsequently, Deb and co-workers derived a method for evaluating the error of finite (small) collection angles on measured

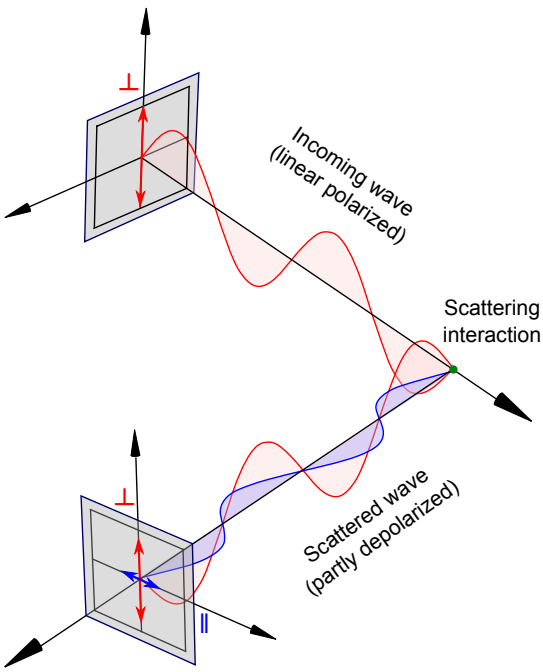

Figure 5.3: Depolarization of initially linearly polarized light in a scattering interaction.

depolarization ratios [Deb84]. Some years later, Teboul *et al* refined this approach and extended it to larger angles ($> 25°$) [Teb92].

Below, it will be shown that Teboul's model has been formulated for single-angle geometry configurations which is not entirely suitable for the application with the Raman systems for KATRIN. Another challenge in the depolarization measurements of this work was related to stress-induced birefringence in the Raman windows which led to polarization aberrations. A strategy on how to counteract this problem was not provided by the previous works cited above. Successful solutions to both problems are provided in the present work.

In the broader context of polarization-dependent Raman micro-spectroscopy, Turrel and co-workers developed a correction model as well as methods for the compensation of said effects in actual measurements [Tur84, Bre87]. However, the experimental situation in Raman micro-spectroscopy is different to the standard $90°$ Raman spectroscopy: the scattered light is observed in backward direction, and the excitation volume is approximately a point-like source of scattered light. Their approach is thus not directly transferable to cases of an extended (elongated) Raman excitation volume and to observation geometries other than back-scattering.

Depolarization measurements of hydrogen isotopologues Experimental depolarization data for the full set of six hydrogen isotopologues are not available from the literature, as only some publications about measurements of H_2 are available. But only two groups have published rotationally-resolved measurements of the Q_1 branch. In 1973, Holzer *et al* reported the data for H_2 and D_2 with remarkable accuracy [Hol73]. Then in 2007, a research group around Yu developed a new technique for the measurement of the depolarization ratio of gases like CH_4 and H_2 [Yu07]. With their photo-acoustic Raman system they could provide depolarization ratios of similar accuracy as those of Holzer.

5.3.1 Definition of the depolarization ratio

In a first step, a simplified geometrical configuration is considered, in which two assumptions are made: (i) The scattered light originates only from a single point, and (ii) the scattered light is observed under a vanishing solid angle. This implies that the scattering is only observed along a single ray line. Measurements assumed under said configuration are indexed as "SP0SA" (standing for "single point, zero solid angle").

The "SP0SA" depolarization ratio which is utilized within the framework of this thesis is defined as the ratio of the line strength functions from Eqs. (3.23) to (3.26):

$$\rho_{\mathrm{SP0SA}} = \frac{\Phi(\varphi = 0, \theta = \pi/2)_{\perp^s,||^i}}{\Phi_{\perp^s,\perp^i}(\varphi = 0, \theta = \pi/2)}. \tag{5.9}$$

$$= \frac{3b^{(2)}\gamma^2}{45a^2 + 4b^{(2)}\gamma^2} \tag{5.10}$$

This corresponds to the depolarization ratio for a scenario with fixed polarizer in $\perp^s$ configuration in the path of light collection [Lon02]. Other experimental scenarios are found in Allemand or Long [All70, Lon02].

5.3.2 Model of depolarization ratios as observed in the experiment

The simple expression introduced for depolarization ratio (Eq. 5.9) does not account for realistic situations in which scattering originates from an extended region, and for which light collection has to be considered over a non-zero solid angle than from a single ray. Additionally, contributions from polarization aberrations need to be taken into account which ultimately lead to the observed depolarization ratio ρ_{obs}.

In the following, specific additional terms which transform the SP0SA to the observed case are considered. First, the influence of the light collection geometry is introduced in Section 5.3.2.1. Second, the aberrations from stress-induced birefringence are accounted for in Section 5.3.2.2. These two parts will make possible the full description of the experimentally observed depolarization ratio, ρ_{obs}. Finally, in Section 5.3.2.3, the model derived here is compared to previous models by other authors.

5.3.2.1 Influence of light collection geometry

In Eq. 5.9 the SP0SA depolarization ratio for a single ray is given. An integration over the spherical angles φ and θ is necessary in order to obtain a realistic expression. Since the scattered light originates from an elongated scattering volume rather than from a single point, an additional integration along the propagation direction z is necessary. A sketch showing the axes, angles and polarizations in relation to each other is found in Fig. 3.7. The integration in spherical polar coordinates then yields the observed Raman intensity,

$$I_{\mathrm{obs}} = c \cdot \iiint\limits_{\varphi,z,\theta} \Phi_{\text{effective}} \, \sin\theta \, \mathrm{d}\theta \, \mathrm{d}z \, \mathrm{d}\varphi \, . \tag{5.11}$$

The bounds of integration are defined by the experimental collection system geometry. In the case of the HighResLARA system, the scattered light first passes through the sample cell window (see Fig. 4.4) with an effective radius r_{w} at a distance x_{w} from the scattering center (aperture 2). The transmitted light is then collected by a focusing lens with aperture radius r_{f} at a distance x_{f} from the scattering center (aperture 1).

A different parameterization is required for light originating at off-axis locations $z \neq 0$. While the bound of integration for the angles are centro-symmetric for light originating at $z = 0$, for all other locii this becomes asymmetric and the mathematical description is more complicated. In particular, as indicated in the sketch in Fig. 5.4, segments of light which are transmitted through the first aperture may be restricted by a second aperture. A suitable parameterization was developed for the case of the present Raman system with two circular apertures (sample cell window and collection aperture); this is described extensively in Appendix B. In general, arbitrary apertures can be used via appropriate parameterization.

The parameterization leads to a nested integration meaning that the bounds of variables in the inner integration depend on the value of the outer integration[1]. This makes it next to impossible to find an analytic solution for the calculation of the observed intensity. A numerical integration procedure was therefore implemented in C++ making use of the mathematical framework of ROOT [Bru97].

[1] As an example: θ_{min} and θ_{max} are functions of the variables z and φ.

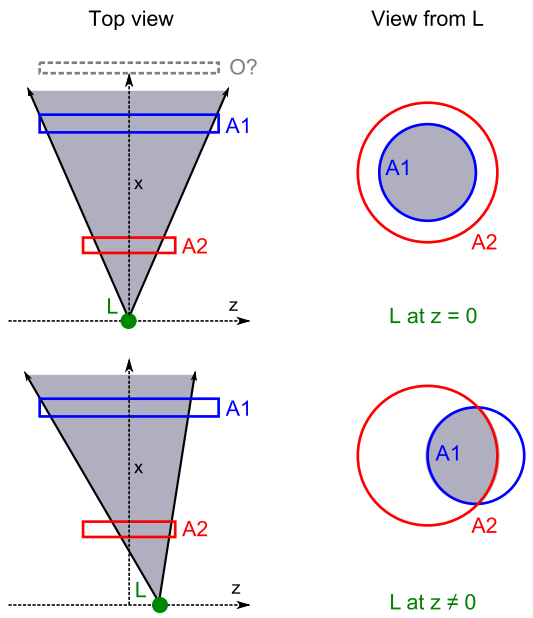

Figure 5.4: Sketch of on-axis ($\mathbf{z = 0}$) and off-axis ($\mathbf{z \neq 0}$) light transmission. The light cone is limited by more than one aperture (*e.g.* window, lens, diaphragm). L - point (origin) of scattering light emission. $A1, 2$ - apertures 1 and 2. $O?$ - possible additional optical element, *e.g.* a polarizer. Note that in the right panel (View from L) the larger aperture A1 appears smaller than the smaller A2. This has perspective reasons since A1 is further away from the frontal viewer.

5.3.2.2 Influence of polarization aberrations

The above model can now be employed for correcting depolarization ratios provided the experimental geometry is accurately known. However, the first attempts to obtain the theoretical ρ_{SP0SA} from the experimental ρ_{obs} failed since the results (*e.g.* for the Q_1-lines of O_2 or N_2) were not in agreement with any theory values. It became clear that optical components within the experimental setup introduce polarization aberrations which were neglected in the initial measurements. Often, mounted optics do suffer polarization aberrations via stress-induced birefringence [Shr02, Log94].

For the Raman cell used in this thesis (see Section 4.1.2), stringent requirements on the leak-tightness had to be met due to the use of radioactive gas species and the rather aggressive radio-chemical properties of tritium. Accordingly, the glass-metal bonding [Eng92] together with metal compression seals will introduce non-negligible stress to the windows. Qualitative and quantitative measurements showed that polarization aberrations indeed do occur in the Raman cell windows, as described in Appendix D. In Fig. 5.5 stress-induced birefringence is made visible in a laser window of the Raman cell which was placed between two cross-polarized sheet polarizers. The effects of polarization aberrations on the incident laser light and the scattered light are discussed in the following paragraphs.

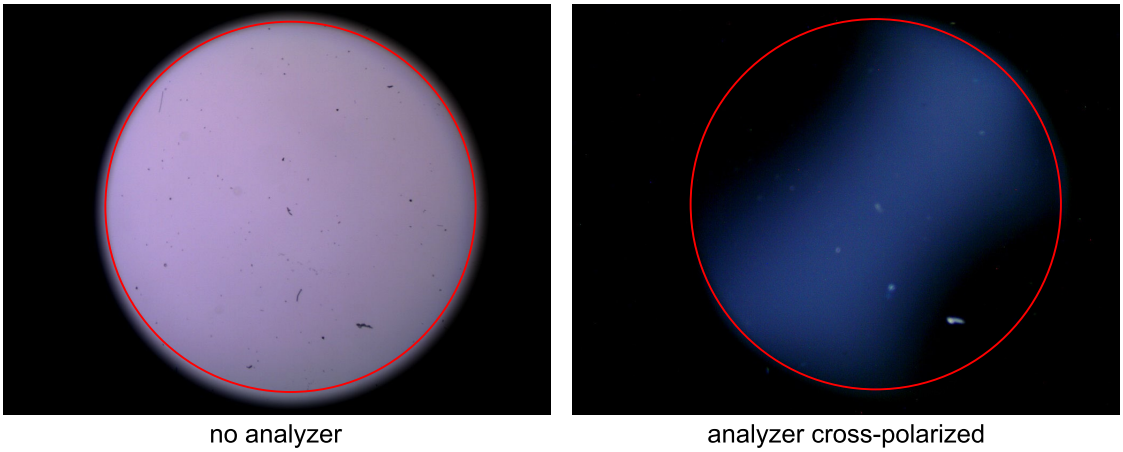

Figure 5.5: Visualization of polarization aberrations from stress-induced birefringence in a laser window. The measurement was acquired with a digital microscope. It was made polarization-sensitive by a polarizer in front of the sample and an analyzer behind it in cross-polarized setting. *Left* - Only the polarizer is in use. The laser window appears to be illuminated homogeneously. *Right* - Polarizer and analyzer are in use (cross-polarized setting). If no polarization aberrations occurred, the whole window area would be black since all light would be blocked by the analyzer. However, it is visible that this is not the case in the picture shown here, which indicates that the initially clean polarization suffers from aberration while it is transmitted through the fused silica window. More details on the measurement procedure are found in Appendix D.

Polarization aberrations affecting the incident monochromatic, nearly parallel collimated beam An initially clean beam may be affected by polarization aberrations associated with (potential) stress-induced birefringence in the window material of the sample cell. In this context, the laser beam diameter is small when passing the window which typically is positioned close to the focal region of the Raman excitation volume. That implies that in general only a small part of the window surface ($\sim \mathrm{mm}^2$) or the bulk volume ($\sim \mathrm{mm}^3$) interacts with the beam. At this point, the surface area of the windows is much larger than the laser beam diameter, thus it may be assumed that the stress-induced birefringence is homogeneous over the small beam cross-section. Therefore, the effect on the associated polarization change will be reasonably approximated by using the cleanness parameter ξ introduced in Eq. 3.28. It should be noted that this approach is similar to the one described by Proffitt and Porto [Pro73].

Polarization aberrations affecting the scattered light In general, this type of aberration is much more difficult to describe than the one affecting the incident laser beam. This difficulty is associated with the experimental situation in the light collection:

(i) The scattered light rays are non-parallel and often exhibit an anisotropic distribution of polarization states.

(ii) They pass through various optical interfaces over a range of inclination angles (*i.e.* they deviate from the ideal perpendicular incidence).

(iii) Due to extended solid angles, they may pass through parts of the optics featuring specific inhomogeneities due to stress-induced birefringence.

In principle, these effects could be taken into account by incorporating them into the model which has been introduced in the previous subsection. To implement this effort, a map of the retardance and di-attenuation properties of the optics would be required. This map would need to include the relevant angles under which light passes through the surfaces and the lateral positions. For practical reasons, this is not recommended due to the corresponding enormous measurement efforts. Therefore, a more simplified approach was selected in which the polarization aberrations in the collection window are calculated using Jones calculus[2]. The formalism employed here is based on the work by Kita [Kit09], and McGuire and Chipman [McG94].

A detailed derivation of formulas within the Jones formalism is written down in Appendix C. However, the following explanations will be necessary to understand the validity of the model and its implications.

The following assumptions have to be made for the model of the polarization aberrations affecting the scattered light:

- the collection system can be simplified as exhibiting a homogeneous net effect on the polarization, which manifests itself mainly in linear di-attenuation and linear retardance;
- the polarization aberrations are (nearly) angular independent; and
- circular di-attenuation and retardance are negligible, as already indicated by Kita [Kit09].

In Jones calculus the single optical components in the light path are expressed as matrices which are multiplied in the order of the transmission. The sketch of the observation path in a depolarization experiment is shown in Fig. 5.4. The sequence of components in this figure is the following: the Raman cell window ($A2$) is the first optical component, second is the light collection lens ($A1$), followed by the (optional) polarizer ($O?$); the Jones matrices below are indexed accordingly. This leads to the relation between the polarization state of the scattered light generated in the Raman interaction volume, $\boldsymbol{E}_{\mathrm{in}}(\theta, \varphi)$, and that after transmission through all optical components

$$\boldsymbol{E}_{\mathrm{out}}(\theta, \varphi) = \mathcal{J}_{O?}\mathcal{J}_{A1}\mathcal{J}_{A2}\boldsymbol{E}_{\mathrm{in}}(\theta, \varphi) \ . \tag{5.12}$$

Jones calculus can be used for all optical components in an experimental system to determine the intensity of scattered Raman light quite accurately by incorporating the light-field strengths for a particular excitation/collection configuration. As an example, the observed Raman signal intensity for an excitation laser beam in p^i-configuration and

[2]Note that the same results can be obtained by using Mueller calculus (see *e.g.* Toro Inesta [Tor03] or Collett [Col05]).

collecting the Raman light in $\perp^s$-configuration (after the polarizer), is given by

$$\begin{aligned} I_{\perp^s,p^i} = & \underbrace{E^2_{\perp^s,p^i}\exp(-2a_{P1})}_{\text{transmitted }\perp^s\text{−component}} + \underbrace{E^2_{||^s,p^i}\exp(2a_{P2})}_{\text{leakage from }||^s\text{−component}} \\ & + \underbrace{2E_{\perp^s,p^i}E_{||^s,p^i}\exp(a_{P2}-a_{P1})\cos(a_{R,\text{tot}})}_{\text{contamination induced by retardance}}, \end{aligned} \tag{5.13}$$

where a_{P2}, $-a_{P1}$ and $a_{R,\text{tot}}$ are related to the (simplified) parameters of di-attenuation and induced retardance, respectively (see [McG94]).

The depolarization ratio defined in Eq. 5.9 is a function of the line strength, Φ. In order to calculate the depolarization ratio from the actually observed quantities, it has to be converted into terms of electric field strength or intensities, as in Eq. 5.13. This can be done by the simple relation $E^2 = k \cdot I = k' \cdot \Phi(\varphi, \theta)$ with k and k' being proportionality constants. Using this relation and Eq. 5.13, one obtains an expression for the observed experimental depolarization ratio:

$$\rho = \frac{I_{\perp^s,||^i}}{I_{\perp^s,\perp^i}} \tag{5.14}$$

$$= \frac{X^2_{\perp^s,||^i} + Y^2_{||^s,||^i} + 2X_{\perp^s,||^i}\cdot Y_{||^s,||^i}\cdot\cos(a_{R_{\text{tot}}})}{X^2_{\perp^s,\perp^i} + Y^2_{||^s,\perp^i} + 2X_{\perp^s,\perp^i}\cdot Y_{||^s,\perp^i}\cdot\cos(a_{R_{\text{tot}}})} \tag{5.15}$$

with

$$\begin{aligned} X_{\perp^s,p^i} &= E_{\perp^s,p^i}\exp(-a_{P1})\ , \\ Y_{||^s,p^i} &= E_{||^s,p^i}\exp(a_{P2})\ . \end{aligned}$$

The X^2- and Y^2-terms are related to the linear di-attenuation, while the cross-terms $2 \cdot X \cdot Y \cdot \cos(a_{R_{\text{tot}}})$ represent the additional, induced retardance. This simplified model approach can now be used to estimate the influence of possible polarization aberrations in the collection path. For reasons of clarification, various polarization aberration scenarios are considered in the following enumeration:

1. Only the geometrical influence is included, while no polarization aberrations are considered (cleanness of the incident laser beam is $\xi = 1$).

2. The geometrical influence is superimposed by a reduced polarization cleanness of the incident beam, *i.e.* $\xi \neq 1$; however, aberrations introduced by the collection optics are not included at this stage.

3. Eq. 5.13 indicates that the cleanness of transmitted beams can be reduced by polarization leakage and/or retardance. Both effects can be investigated individually by the model approach when the collected light intensities (or field strengths) are separated into two mutually perpendicular components. This simplification reduces the complexity of the problem, but also allows for identification of any possible dominating mechanism in the affecting aberration. Two special scenarios are presented here which result from modifications of Eq. 5.15 for the depolarization ratio:

(a) The first sub-scenario neglects the induced retardance, meaning that any polarization shifts are introduced only via different attenuation losses in the polarization components. Thus Eq. 5.15 becomes:

$$\rho_A = \frac{c_{A,\perp^s} E^2_{\perp^s,||^i} + c_{A,||^s} E^2_{||^s,||^i}}{c_{A,\perp^s} E^2_{\perp^s,\perp^i} + c_{A,||^s} E^2_{||^s,\perp^i}} \,. \tag{5.16}$$

(b) The second sub-scenario neglects the leakage term, and only the changes of the polarization introduced by retardance in the optical material are considered (*e.g.* stress-induced birefringence). In this case Eq. 5.15 simplifies to:

$$\rho_B = \frac{c_{B,\perp^s} E^2_{\perp^s,||^i} + c_{B,||^s} E_{||^s,||^i} E_{\perp^s,||^i}}{c_{B,\perp^s} E^2_{\perp^s,\perp^i} + c_{B,||^s} E_{||^s,\perp^i} E_{\perp^s,\perp^i}} \tag{5.17}$$

In these sub-cases a perfect polarization cleanness of the incident beam is assumed ($\xi = 1$). The admixture parameters, c, in Eq. 5.16 and 5.17 are defined as

$$\begin{aligned} c_{A,\perp^s} &= c_{B,\perp^s} = \exp(-2a_{P1}) \,, \\ c_{A,||^s} &= \exp(2a_{P1}) \,, \\ c_{B,||^s} &= 2\exp(a_{P2} - a_{P1}) \cdot \cos\left(a_{R_{\mathrm{tot}}}\right) \,, \end{aligned}$$

with the restriction that $0 \leqslant c \leqslant 1$.

The aforementioned scenarios now provide the possibility to study the influence of the polarization impurities in the incident and scattered light on the effective depolarization ratio. Tab. 5.1 provides an overview of the various scenarios and the corresponding setting of the parameters. The effect on the observed depolarization ratio as a function of the collection (solid) angle, related to the three scenarios (including sub-scenarios) above, is plotted in Fig. 5.6. In the following two paragraphs, the observations are discussed.

Table 5.1: Parameter overview for the investigated polarization scenarios. In all scenarios, the effects from the geometry were included. Note that scenario 2 has been split into two sub-scenarios involving only small impurities (2a: $\xi = 0.999$ and 2b: $\xi = 0.998$) for $\rho_{\mathrm{SP0SA}} = 0$. For scenarios 3a and 3b, the parameter choice $c_{A/B,\perp^s} = 0.9$ and $c_{A/B,||^s} = 0.1$ is rather extreme, and may be viewed as a "worst-case" scenario.

Scenario	ξ	$c_{A,\perp^s}$	$c_{B,\perp^s}$
1	1	-	-
2.a	0.999	-	-
2.b	0.998	-	-
3.a	1	0.9	-
3.b	1	-	0.9

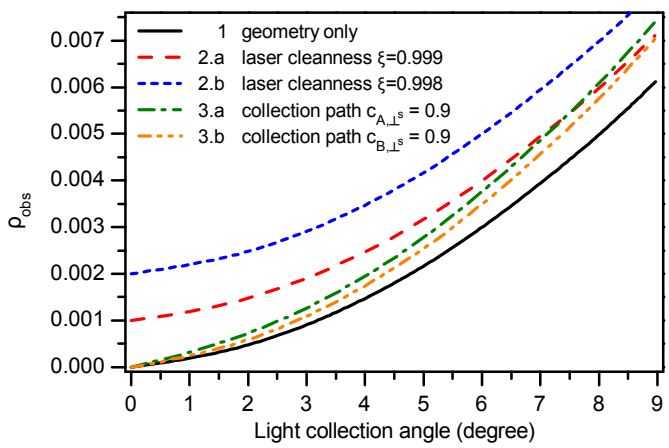

Figure 5.6: Influence of polarization aberrations in the laser excitation and the light observation paths on the effective depolarization ratio. The relevant parameters are polarization cleanness ξ and the admixture parameters $c_{A,\perp^s}$ and $c_{B,\perp^s}$. In this plot $\rho_{\mathrm{SP0SA}} = 0$. The numbering of the scenarios is according to Tab. 5.1. The detailed discussion is found within the main text.

Effects from reduced polarization cleanness in the incident beam

- The most distinguishable contribution to the deviation between theoretical and measured depolarization ratios is related to reduced cleanness of the excitation laser beam. Already tiny admixtures of the unwanted polarization component lead to a considerable offset as discussed below (see Section 5.3.4.3).
- Even for Raman light collection angles which are smaller than what is achievable in many measurement setups, the deviation between expected (from geometry) and measured depolarization ratio is noticeable.

Effects from polarization aberrations in the scattered light

- For small light collection angles of the order $< 5^\circ$, the influence of the induced polarization aberrations on the depolarization ratio, resulting from the collection optics, is in general rather small. This statement remains valid even if the "worst-case" scrambling is assumed. For solid angles larger than $\sim 10^\circ$ the unwanted polarization component reaches 10% and the effect begins to become non-negligible. For lower degrees of polarization scrambling, the effect is likely to drop below the measurement sensitivity (compare with Fig. 5.7).
- The scenarios (3.a) and (3.b) accounting for the polarization aberration in the collection path, indexed A and B, show a similar behavior. Thus, it seems legitimate to assume that neither of them may be regarded as the dominant mechanism in the induced depolarization aberrations on the collection side.

These observations allow the following conclusion: the contributions to the observed depolarization ratio mainly originate from geometrical effects and polarization impurities

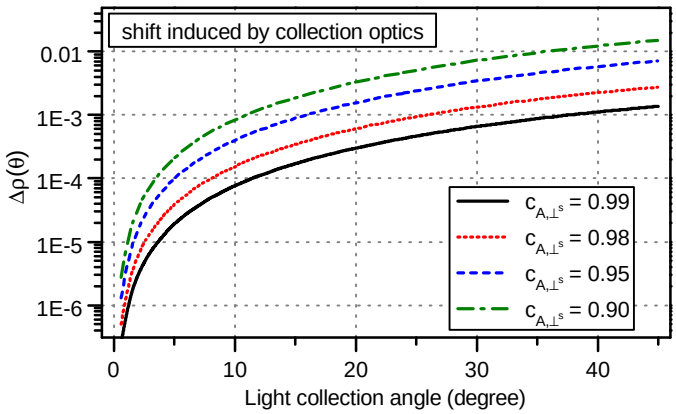

Figure 5.7: Calculated shift $\Delta\rho$ of the observed depolarization ratio from the SP0SA value induced by optical components in the light collection path. This shift is associated with polarization impurities in the scattered light beam (based on the approximation in Eq. 5.16).

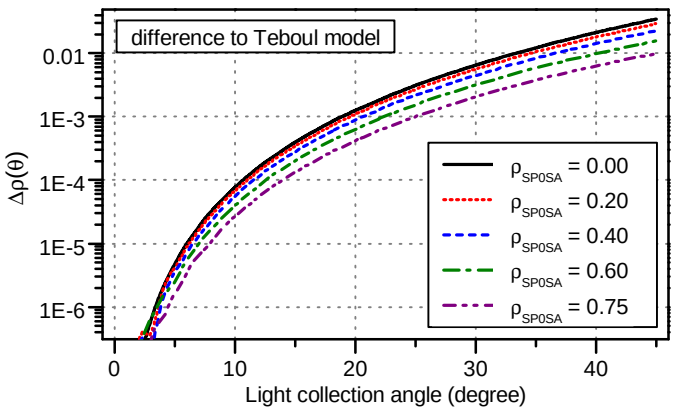

Figure 5.8: Difference between the (numerical) model and the one of Teboul [Teb92]. The parameter $\Delta\rho$ is the difference of the corrected ρ values by both models for selected ρ_{SP0SA} values as a function of the light collection angle.

in the incident laser beam. This is particularly true for small light collection angles. For this reason it can be assumed that the polarization aberrations induced by the optical components in the light collection path can be neglected in the model. The only relevant parameter is ξ which describes the deviations from the ideally clean polarization of the incident laser beam. This approximation will be used in all examples within this thesis.

5.3.2.3 Comparison to a previous correction model

The main methodological difference of the model from the thesis in hand compared to models from previous works is the inclusion of off-center emission of scattered light. In this new model light is emitted from points along the laser excitation axis and thus a further integration step is required. Additionally, this off-center emission requires properly parametrized apertures in the light collection path, accounting for potential shadowing (see Section 5.3.2.1). In the latest corresponding work by Teboul *et al* [Teb92] only scattered

light originating from a point source is considered. Therefore, a z-integration is not required (all light originates from $z = 0$), and an "effective" circular aperture is defined via a single parameter $\theta_{\max}$. Fig. 5.8 shows the difference of the calculated depolarization ratios for both models as a function of $\theta_{\max}$, where a number of depolarization ratios between the two limiting cases $\rho_{\mathrm{SP0SA}} = 0$ and $\rho_{\mathrm{SP0SA}} = 3/4$ has been selected[3]. Both correction methods diverge with increasing light collection angle. For $\theta_{\max} \sim 20°$ and $\rho_{\mathrm{SP0SA}} = 0$, the difference in the two methods surpasses 0.001. This value is close to or even larger than the depolarization measurement uncertainties in this work, as will be reported in Section 5.3.4.4. Thus the use of here developed methodology is clearly required when an accurate correction of polarization aberration errors needs to be implemented.

5.3.3 Routine for correcting observed depolarization ratios

At the beginning of this subsection it should be reconsidered which possibilities are available now after the discussions in the previous subsections, and what is finally required for the measurement.

A numerical model has been introduced which can be used to transform a "single point, zero solid angle" (SP0SA) depolarization ratio to an actually observed one by applying corrections for the effects from a given geometry and polarization aberrations in the excitation beam. However, what is requested is the opposite case. A depolarization ratio ρ_{obs} is observed under a certain geometry with unknown polarization aberration, and finally the ρ_{SP0SA} value should be derived from this. It is obvious that accurate results cannot be obtained without quantification of the amount of polarization aberrations, which manifests itself in the cleanness parameter ξ.

In the following a routine is described which can be used for the quantification of ξ during the depolarization measurement without any auxiliary measurements beforehand[4]. In a second step, this quantity is then used for the correcting the observed depolarization ratio to finally obtain the SP0SA value. The routine comprises two relevant aspects:

1. The light collection geometry needs to be known precisely. Both radii and distances of the limiting apertures are used as input values for the numerical model. Instead of experimentally determining the parameters r_f and x_f for the collection lens, it has been proven to be beneficial to install a circular diaphragm with significantly smaller opening angle in front of it. The introduction of this diaphragm of known opening diameter and distance to the Raman scattering origin simplifies the quantification of geometrical dimensions of the setup. Detailed information and discussion is found in the Section 5.3.4.1 below.

2. The cleanness parameter, ξ, which is in general unknown needs to be quantified. While an external measurement at an auxiliary experimental setup could be considered, this would come with a number of drawbacks. For example, one potential problem that may occur is that the characterization laser beam passes through a

[3]The limiting case $\rho_{\mathrm{SP0SA}} = 0$ is obtained for $b^{(2)}\gamma^2 = 0$ in Eq. 5.10 while $\rho_{\mathrm{SP0SA}} = 3/4$ results from $a^2 = 0$.

[4]The complete analysis is implemented in C++ using ROOT functions. The program is made available under http://depoltools.sourceforge.net.

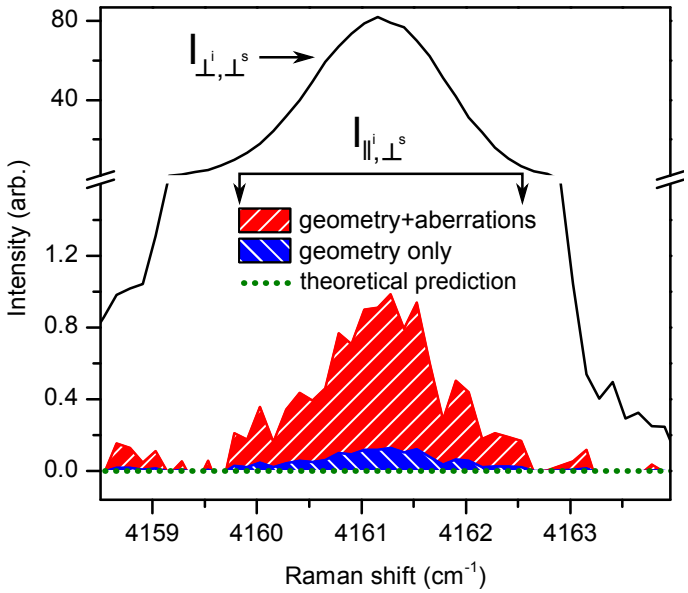

Figure 5.9: Detailed view of $\mathbf{Q_1(J'' = 0)}$ line of H_2. The measured spectrum for $I_{\perp^i,\perp^s}$ is about 100 times more intense than in $I_{||^i,\perp^s}$ configuration. In the latter case, the theoretical prediction is $\rho_{\mathrm{SP0SA}} = 0$, represented by the green dotted line. On top of this a blue peak is shown which includes only contributions from the geometry. It is calculated from the integration over a finite collection angle ($\sim 4°$). Finally, the actually measured peak (red) comprises geometrical influences and polarization aberrations. Note that the polarization aberration is the dominating contribution here. This was valid for most of the measurements performed during the measurement campaign.

slightly different part of the (stressed) laser window than as usual during the depolarization experiment. This would then lead to an incorrect ξ value and thus the correction would fail. Another problem is that the cell windows would have to be de-attached from the cell, which would result in a potentially different mechanical stress acting on the window. Thus again the measured polarization cleanness, ξ, would differ from the one presented during the actual depolarization measurements. These issues call for a method in which no re-positioning of the windows and no change of the experimental setup is necessary.

The solution to circumvent the above problems is to make use of a Raman line which has a well-known depolarization ratio. The trueness of this value then ultimately limits the corrected value. In case of diatomic molecules (like hydrogen isotopologues) such a standard is provided by default. The $J'' = 0$ line of the Q_1-branch has a $\rho_{\mathrm{SP0SA}} = 0$ per definition. This can be made clear from the Placzek-Teller factor, $b^{(2)}$, which vanishes for $J'' = 0$ (see Eq. 3.27). Fig. 5.9 shows the $J'' = 0$ line of H_2 as measured in $I_{\perp^i,\perp^s}$ and $I_{||^i,\perp^s}$ configuration. A vanishing depolarization ratio implies that the measured $I_{||^i,\perp^s}$ component should also be vanishing. The figure shows that this is actually not the case due to contributions from geometry and polarization aberrations, which are always present. The correction procedure for experimental data, based on the above numerical model, is separated into two major steps as visualized in Fig. 5.10:

1. The mathematical model is used to calculate the depolarization ratio with input

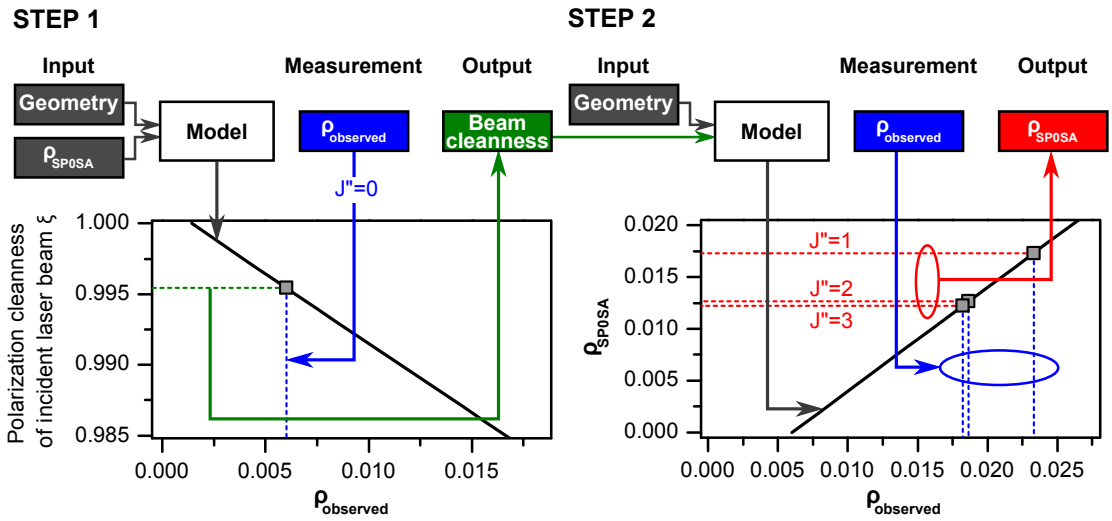

Figure 5.10: Two-step routine for extraction of depolarization values ρ_{SP0SA} from data sets which comprise polarization aberrations. *Step 1* - Determination of the cleanness of the laser polarization. The functional relation of the polarization cleanness ξ and the observed depolarization ratio is calculated for known collection geometry and known SP0SA depolarization ratio $\rho_{\mathrm{SP0SA}} = 0$. From an actually measured depolarization ratio of the $Q_1(J'' = 0)$-line, one derives the related polarization cleanness. *Step 2* - Correction of depolarization ratios of all measured Q_1-branch lines for the given polarization cleanness. The polarization cleanness derived in step 1 is further used in order to transform the ρ_{observed} into the ρ_{SP0SA} values of all Q_1-branch lines with $J'' > 0$.

parameters being given by the actual collection geometry and the defined SP0SA value of a certain line. This generates a functional relation between the (effective) observed depolarization ratio ρ_{obs} and the polarization cleanness ξ of the incident laser beam. In the case of hydrogen isotopologues, the well-known depolarization ratio is the one of the $Q_1(J'' = 0)$-line, for which $\rho_{\mathrm{SP0SA}} = 0$. From this, the polarization cleanness can be determined from the plotted functional dependence, using the experimentally observed value ρ_{observed} of this line. In the data displayed in Fig. 5.10, the depolarization ratio for the $Q_1(J'' = 0)$-line of HT was measured as $\rho_{\mathrm{observed}} = 0.60 \cdot 10^{-2}$, which corresponds to a polarization cleanness of $\xi = 0.9954$.

2. In a second step, the mathematical model is used to extract the SP0SA depolarization ratio for other $Q_1(J'' > 0)$-lines. For this purpose, the polarization cleanness of the incident beam ξ determined in the first step and the same geometrical input values are utilized.

   Note that polarization aberrations in the collection path have not been considered in the procedure as argued in Section 5.3.2.2.

Conclusion The procedure presented above is targeted to derive aberration-corrected depolarization ratios from Raman depolarization measurements. In these measurements, optical elements are employed which introduce a previously not quantified impact on an initially "perfect" light beam polarization (*e.g.* Raman cell windows under stress).

However, before the above method is applied for the correction of measured depolarization

ratios of all hydrogen isotopologues, it is necessary to demonstrate its validity and accuracy. This validation will be performed using experimental data (see Section 5.3.4.3).

5.3.4 Measurement of depolarization ratios of all six hydrogen isotopologues

This section first deals with the description of the experimental setup and the measurement procedure for depolarization ratio measurements (Section 5.3.4.1 and 5.3.4.2). Afterwards, specific investigations are described which were performed to validate the two-step correction procedure (Section 5.3.4.3). Finally, the depolarization ratios of the Q_1-lines of all six hydrogen isotopologues are tabulated and discussed with regard to systematic uncertainties and to the agreement with the theoretical predictions (Section 5.3.4.4).

The depolarization measurements of all hydrogen isotopologues at the TLK were performed with the HighResLARA system. The depolarization ratios of $\mathrm{H_2}$ and $\mathrm{D_2}$ were measured in Swansea University as well [Jam13a]. The lack of a tritium infrastructure at the Swansea site limited the comparative measurements to the non-radioactive isotopologues. However, the opportunity of operating two slightly different experimental setups at two different labs, operated independently by different scientists, could be exploited successfully for the validation of the proposed method.

5.3.4.1 Experimental setup

The description of the HighResLARA system is found in Section 4.1.2. The Raman system in Swansea is quite similar to it in general, meaning that the basic concept is the identical and the same type of cell, spectrometer and polarization optics is employed. However, it is partly composed of different components, and especially the observation geometry deviates from the one realized at the TLK. The differences will be summarized below.

Polarization control of incident light In a depolarization measurement, it is important to obtain an accurate control of the polarization of incident and scattered light. In the collection optics, a sheet polarizer was installed, as already described in Section 4.1.2. The rotational setting of the sheet polarizer was tuned for selecting the $\perp^s$ component only. Thus, the polarization of the scattered light is fixed in the depolarization ratio measurement scenario chosen in this thesis (see Eq. 5.9), so that the polarization direction of the incident light has to be varied between $\perp^i$ and $||^i$. This is achieved by combining a Glan-Taylor polarizer, which first cleans the polarization (intensity ratio of orthogonal components before GT: $\sim 10^2 : 1$; after GT: $\sim 10^5 : 1$), and a precision (multi-order) half-wave plate (see Fig. 4.3). In pre-investigations it had been discovered that a standard half-wave plate causes (laser) beam walk when this birefringent optical medium is rotated. This beam walk influences the collected Raman scattered light since the excitation region moves in and out of focus. In order to counteract this undesired behavior, a $0.95\,\mathrm{mm}$ thin half-wave plate was selected (WPMH05M-532 from Thorlabs). Additionally, the Glan-Taylor / half-wave plate combination was mounted as close as possible to the lens focusing the laser beam ($f = 250\ \mathrm{mm}$). It was shown that beam walk was minimized by these measures down to a negligible limit.

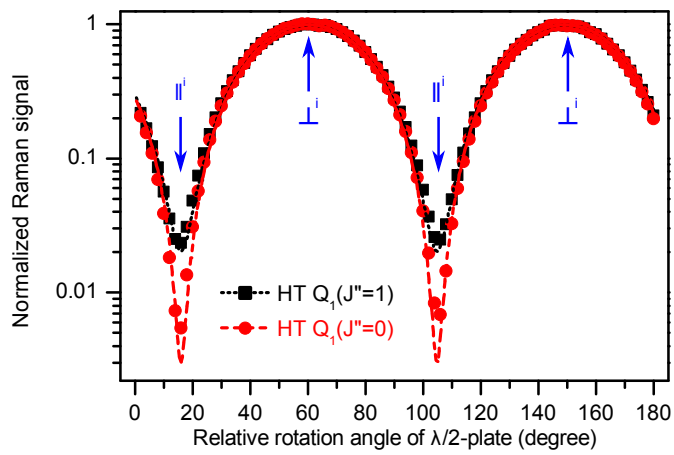

Figure 5.11: Dependence of normalized Raman signal on the half-wave plate angle. Shown are the intensities of two individual Q_1 lines of HT. The data points are fitted by a function $a + b\sin^2(c\alpha - \phi)$ with α being the relative rotation angle of the half-wave plate. The log-scale plot was chosen to show the tiny Raman intensity in the $||^i$ excitation. Note that half-wave plates turn the polarization by twice the relative rotation angle α.

In order to precisely set and reproduce the laser polarization, the half-wave plate was mounted into a motorized rotation mount (PRM1/MZ8 from Thorlabs) which was controlled by custom-written LabVIEW® control software via a computer interface. The precision of the angular setting is quoted to be better than $\pm 0.2°$.

After the half-wave plate is mounted to the rotation mount the exact correlation between its fast axis and the angular setting of the mount is not known. In order to obtain this angular offset, a simple depolarization measurement can be performed. In Fig. 5.11, the normalized Raman signal is plotted as a function of the half-wave plate angle in $2°$-steps. From a $\sin^2$-fit, the phase ϕ can be derived and the angular settings of $\perp^i$ and $||^i$ can be identified.

This measurement procedure would be one possibility of obtaining depolarization ratios. However, it could be shown that a higher accuracy can be achieved with subsequent measurements at the $\perp^i$ and $||^i$ settings only. This is discussed in the following section.

Differences between the TLK and Swansea systems The differences in the employed components in the LARA systems are the following:

- In the HighResLARA system at the TLK, a Finesse Laser from Laser Quantum with a total power of 5 W is installed. In Swansea the lower-power version, Excel, is used. Its maximum laser power is 2 W and the drift of power, beam pointing and laser wavelength is slightly worse (see the data sheets [Las12a, Las12b] or in [Jam13b] for comparison).

- The CCD detector in Swansea is a Synapse CCD from Horiba [Hor12]. The detector chip is subdivided into 1024×256 pixels. This is only $\sim 50\%$ of the pixel number of the PIXIS:400B which is used at the TLK (and only 25% of the pixels of the PIXIS:2KB). The greatest disadvantage of the front-illuminated Synapse CCD is its

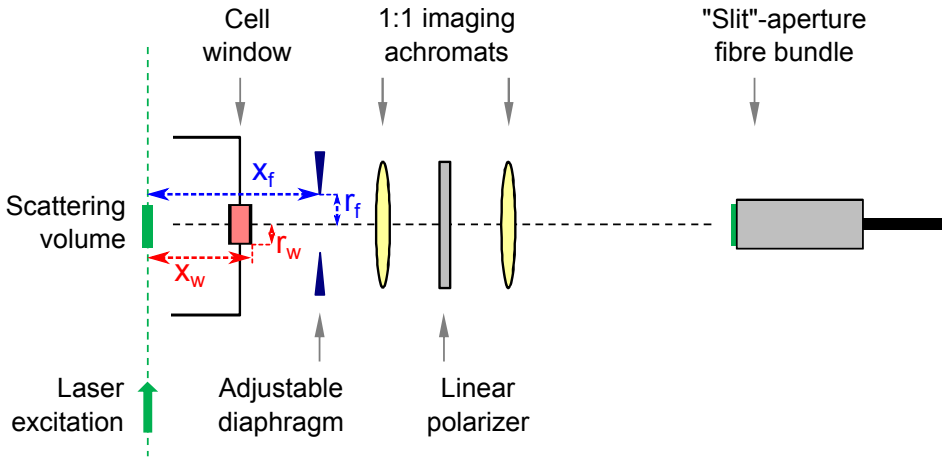

Figure 5.12: Optical components in the light collection path affecting the collection solid angle. x_w and r_w represent the distance from the scattering center to the Raman window and the limiting aperture radius, respectively. x_f denotes the distance from the scattering center to the limiting diaphragm and r_f its opening radius.

reduced quantum efficiency ($< 45\%$) as compared to that of back-illuminated PIXIS CCDs ($\approx 95\%$). The specifications of dark and read-out noise are only marginally different.

The lower laser power and the reduced quantum efficiency of the CCD detector in the Swansea LARA system lead to a sensitivity which should be about a five times smaller than the one of the TLK system. This results in a lower signal-to-noise ratio or in longer acquisition times, respectively.

Geometry of the light collection system Another distinction is found in the geometrical dimensions. An appendix, which is required as second containment for tritium measurements above the permitted limit (10^{10} Bq) at the TLK, is not necessary in Swansea. Thus, the position of the first collection lens is not constrained by this safety installation and can be placed much closer to the cell. In Swansea, two plano-convex lenses with a diameter of $d = 1''$ and a focal length of $f = 50\,\mathrm{mm}$ were installed. The HighResLARA system uses a longer focal length of $f = 75\,\mathrm{mm}$, which requires a diameter of $d = 2''$ to capture the scattered light in the same solid angle.

In Section 5.3.3, it has been emphasized that the observation geometry has to be known precisely. The first aperture is given by the Raman window, which is fixed in size and location. A variable diaphragm is employed as a second aperture limiting the light cone through the collection lens as shown in Fig. 5.12. The use of a diaphragm is essential for the following two reasons:

1. The position and the opening radius of the limiting apertures have to be precisely known in order to achieve a proper correction of the geometrical influence. The use of a diaphragm facilitates the determination of these two parameters. The convex shape of the lens would make it specifically difficult to obtain an accurate knowledge of the distance to the scattering origin.

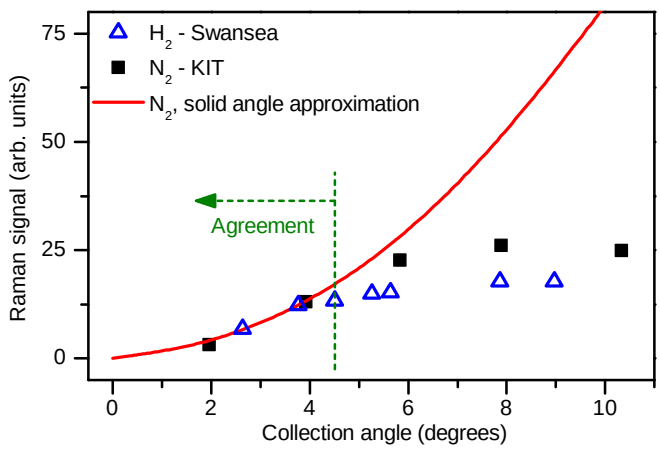

Figure 5.13: Dependence of the Raman signal on the collection angle. The angle was determined by a diaphragm in the collection light cone. It is shown that the signal does not increase beyond an angle of about $4.5°$, and stays approximately the same. From this it can be concluded that the collection limit of the fiber is reached at this angle so that further opening of the diaphragm does not allow more light to enter the fiber. The complete measurement is explained in detail and discussed in [Jam13c]. The measurements were performed at KIT/TLK with nitrogen (black squares). It should be noted that the same behavior was observed in a measurement of H_2 in Swansea (blue triangles) by Timothy James [Jam13a].

2. It is also necessary to make sure, that the aperture radius of the second limiting aperture, r_f is not larger than the effective opening angle of the fiber bundle. Otherwise the correction model for the depolarization ratio will integrate over a solid angle which is larger than the one actually realized. The numerical aperture of the employed fiber, $\mathrm{NA} = 0.22$, corresponds to an angle of $\theta \approx 12°$. This limiting angle was attempted to be verified in a Raman experiment in which the diaphragm radius was variable. Correspondingly, the Raman signal of nitrogen[5] is plotted as a function of the collection angle in Fig. 5.13. The measurements are plotted together with an expected intensity trend proportional to r_f^2. Measurement and expectation agree for angles smaller than $4.5°$ and thus in only a much shorter range than expected. Apparently, the effective fiber collection angle in this setup is limited to smaller values than the claimed one. Therefore, it is required to choose the opening radius of the diaphragm in such a way that it provides slightly smaller collection angles.

In Tab. 5.2, the differences in the geometrical dimensions between the systems at the TLK and in Swansea are summarized.

5.3.4.2 Measurements procedure and analysis

This section introduces the experimental procedure and provides an overview of the performed measurements as well as high resolution spectra.

[5]Note that nitrogen was used in investigations like the described one, since it is easily available as Raman sample from ambient air.

Table 5.2: Apertures and distances of the Raman collection geometry of the LARA systems in Swansea and at the TLK. The distances are always stated as measured from the scattering center to the respective aperture. The dimensions of the Raman windows were derived from a technical drawing, whereas the dimensions of the diaphragm were measured with tools (*e.g.* by a caliper).

Parameter	at the TLK (mm)	in Swansea (mm)
Distance to Raman window, x_w	8.8 ± 0.1	8.8 ± 0.1
Radius of Raman window, r_w	3.5 ± 0.1	3.5 ± 0.1
Distance to diaphragm, x_f	69 ± 1	38 ± 1
Radius of diaphragm opening, r_f	5 ± 0.5	3 ± 0.25

The depolarization measurements were experimentally performed at the TLK in collaboration with Sebastian Fischer and in Swansea by Timothy James [Jam13a]. After a couple of systematic studies and pre-investigations, a common measurement procedure was agreed upon, which is described in the following paragraph.

Experimental procedure The acquisition time with the HighResLARA system per measurement point was chosen to be of the order of $300 - 500\,\mathrm{s}$ (or up to $1000\,\mathrm{s}$ in Swansea) to obtain a sufficiently high signal-to-noise ratio. It should be remembered that the HighResLARA system has a much lower light throughput compared to the MonLARA system.

In Fig. 5.11 a procedure for the measurement of the depolarization ratio was presented: by sequentially turning the half-wave plate and recording the corresponding Raman signal, $I_{\mathrm{obs},\perp^\mathrm{i},\perp^\mathrm{s}}$ and $I_{\mathrm{obs},||^\mathrm{i},\perp^\mathrm{s}}$ can be extracted from a $\sin^2$-fit to the measurement points. A full measurement with a stepsize of $\Delta\alpha = 2^\circ$ and 90 steps to cover at least two minima and two maxima of the $\sin^2$ curve would have a duration of about $450\,\mathrm{min} = 7.5\,\mathrm{h}$ assuming that one measurement takes about $300\,\mathrm{s} = 5\,\mathrm{min}$. During this time, the laser must not be subject to power drifts or unstable beam pointing. However, this ideal case cannot be assumed according to observations described in [Sch09, Fis10a].

This aggravation can be avoided by modifying the measurement procedure. Instead of measuring the complete cycle of angular settings, it was found sufficient to measure at the $\perp^i$ and $||^i$ settings only. In doing so, it is assumed, that the laser should be more stable in this short period compared to the day-long time needed in the first suggested procedure.

The last small amendment to the procedure is that each measurement at the $\perp^i$ or $||^i$ settings is performed twice in order to have the possibility to correct for cosmic ray events. This paired sequence ($2 \times I(\perp^i) \rightarrow 2 \times I(||^i)$) can be repeated any number of times. Subsequently, each pair is analyzed according to the routines described in Section 4.2, and the depolarization ratios are calculated for each J''-line of the Q_1-branch. In the end, the averages and the standard deviations of all pairs are calculated.

Overview of performed measurements The measurements at the TLK and in Swansea were performed by using different sample cells, individually filled with different gas

Table 5.3: Different cells and their gas fillings used in Raman depolarization measurements and for the determination of excitation beam polarization cleanness. The filling of the cells was performed according to the procedures described in Sturm *et al* [Stu10a]. Note that the measurements with tritium at the TLK (D:T-cell, H:T-cell) were performed with the Raman cell in a radiation-safe glove box (*c.f.* the glove appendix as shown in Fig. 4.5) due to the high activity of $\gg 10^{11}$ Bq in the cell..

Data sets	Raman cell	Gas composition	Total pressure mbar	Activity 10^{11} Bq
1,2	D:T-cell (TLK)	$D_2 : 15\%$, $DT : 47\%$, $T_2 : 34\%$, Rest $(HD, HT) : 4\%$	400	1.5
3,4,5	H:T-cell (TLK)	$H_2 : 25\%$, $HT : 46\%$, $T_2 : 26\%$, Rest $(HD, DT) : 3\%$	763.1	2.5
6	H:D-cell (SWA)	$D_2 : 100\%$	900	-
7	H:D-cell (SWA)	$H_2 : 100\%$	870	-
8,9,10	H:D-cell (TLK)	$H_2 : 26.3\%$, $HD : 47.4\%$, $D_2 : 26.3\%$	1500	-

mixtures. The overview of the various measurements is given in Tab. 5.3. Fig. 5.14 shows the spectrum of the "H:T-cell (TLK)", in which T_2, HT, and H_2 appear as major constituents and the other three isotopologues as traces. The spectrum is shown both for the $\perp^i$- and the $||^i$-configuration. It can be noticed that the Q_1-branches drastically drop by a factor of 50 in intensity while the O_1-/S_1-lines drop only by about a factor of $3/4$, as expected from theory [Lon02].

The main attention was on the depolarization measurements of each Q_1-line of the hydrogen isotopologues using high resolution spectroscopy. In Fig. 5.15 the high resolution spectra of the six isotopologues are presented together with the results from *ShapeFit* (see Section 4.2.1). The thermal population and the degeneracy for homonuclear isotopologues (see Section 3.1.3) are noticeable. More details, *e.g.* on the line congestion, are found in the caption of Fig. 5.15.

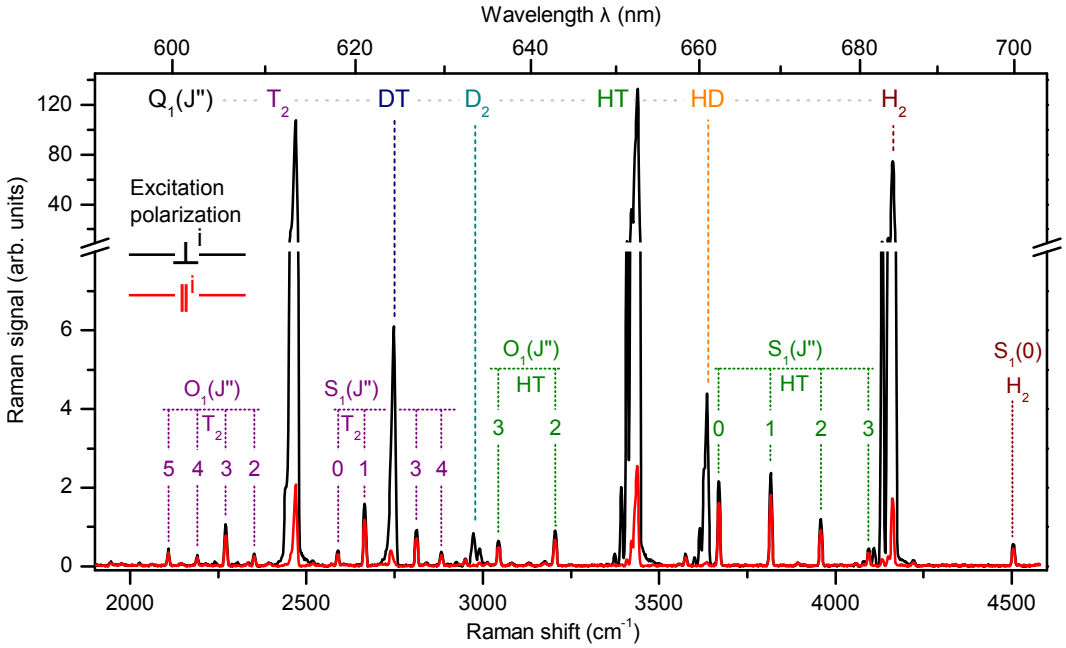

Figure 5.14: Overview Raman spectrum of an equilibrated mixture of T_2, HT, and H_2. Note the break in the scale which allows to make visible the small impurities of DT, D_2 and HD. The spectrum was acquired from the mixture of the "H:T-cell (TLK)" (*c.f.* Tab. 5.3). This measurement was performed with the medium resolution grating (600 gr/mm) and is stitched together from two individual spectra in order to cover all six isotopologues. All relevant O_1-, Q_1- and S_1-branch lines are annotated. The spectrum was acquired for $\perp^i$ and $||^i$ excitation polarization.

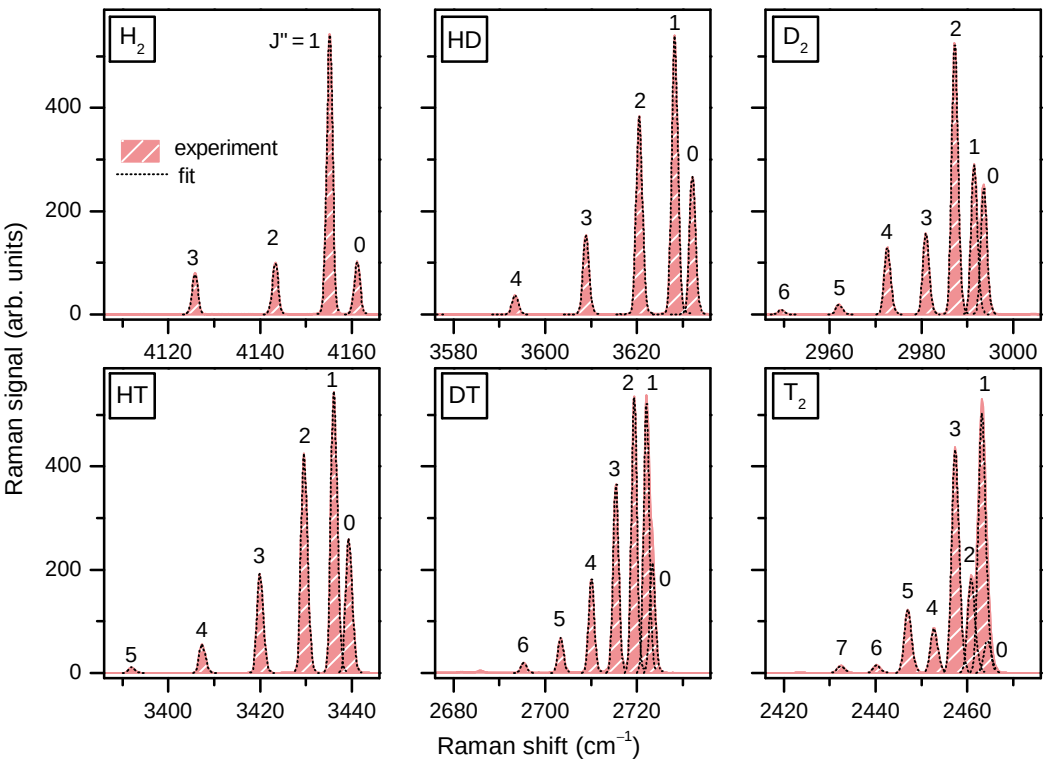

Figure 5.15: High resolution spectra of the Q_1-branch of all six hydrogen isotopologues. All spectra were recorded with the HighResLARA system at the TLK with the $2400\,\mathrm{grooves/mm}$ grating in $\perp^i, \perp^s$ configuration. All spectra were treated by the post-processing steps discussed in Section 4.2.2 and fitted by *ShapeFit*. The number near each peak depicts the rotational quantum number J'' of the transition. The displayed wavenumber range spans $60\,\mathrm{cm}^{-1}$ for each isotopologue for comparative reasons. It can be seen that, the line spacing reduces from the lightest to the heaviest isotopologues. The lines for H_2 and HD are almost uncongested while the lowest J'' line in DT or T_2 strongly overlap. However, the *ShapeFit* routine is able to cope with this congestion successfully.

5.3.4.3 Validation of the correction routine

In Section 5.3.3, a method for the correction of measured depolarization ratios was introduced. Before it is applied to the measurement of all hydrogen isotopologues, its validity is revised with respect to three aspects:

1. It is examined whether the determination of the cleanness of the excitation light beam results in the same value for repeated measurements. This investigation is performed for different sample cells.
2. It is checked whether ρ_{SP0SA} values for the same hydrogen isotopologues agree if derived from a set of different Raman cells.
3. It is investigated whether the application of the corrected depolarization value of a certain molecular species allows one to determine those of a different species, which is present and measured in the same cell.

These validity investigations are estimated to be most relevant for the sound application of the correction model. The discussion of all three aspects in full detail is found in the corresponding publication about the methodology [Sch13b] (see Appendix I). A summarized version, which only discusses the first two aspects, is given below.

The first aspect was the reproducibility of the procedure for determining the polarization cleanness of the incident laser beam (step 1 in the correction procedure). It was demonstrated in a study of a number of cells at the TLK and in Swansea University. These cells were filled with the different gas mixtures of Tab. 5.3. The cells had to be removed from the Raman system in order to be filled and thus an exact repositioning of the cells was not guaranteed. The measured cleanness values for each measurement are graphically summarized in Fig. 5.16. It can be clearly seen that the cleanness values derived for the same cell are on a similar level. For the same cell, the fluctuations are of the order of $\delta\xi < 0.001$. These results support the assumption that the polarization contamination is mainly related to the cell windows.

The second of the three aspects is related to the reproducibility of the procedure with different cells but using the same gas species. In the given example, the depolarization ratios of the Q_1-lines of H_2 were studied. The different cells exhibited differing stress-induced birefringence in the cell windows; two cells were used for measurements at the TLK and one at Swansea University (see set 3, 7 and 10 in Tab. 5.3). Step 1 of the correction procedure leads to polarization cleanness values for the three data sets of $\xi_{\mathrm{set}\#3} = 0.9950$, $\xi_{\mathrm{set}\#7} = 0.9995$ and $\xi_{\mathrm{set}\#10} = 0.9899$, respectively (see Fig. 5.16). The observed Raman depolarization values and the corresponding corrected ρ_{SP0SA} values for $Q_1(J'' = 1, 2, 3)$-lines of H_2 are collated in Tab. 5.4. The statistical fluctuations of the averages of the derived ρ_{SP0SA} values are of the order of $\Delta\rho \leqslant 0.01 \cdot 10^{-2}$. On the other hand, the spread in the uncorrected, observed depolarization values is quite substantial. Thus the data demonstrate that the correction routine is capable to reduce or even compensate for such large variations. In the next section the data will be compared to the theoretical calculations by LeRoy.

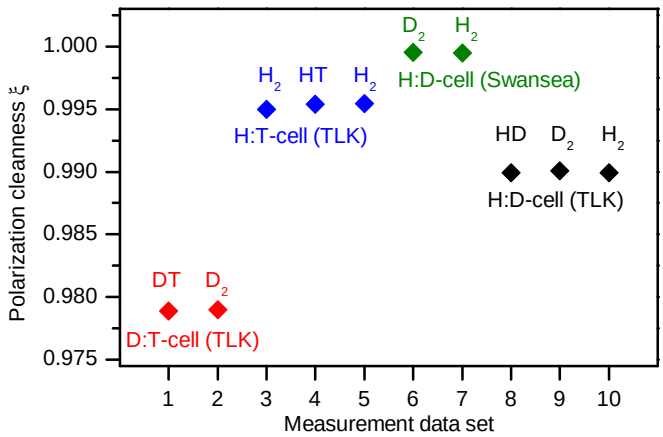

Figure 5.16: Polarization cleanness of various Raman cells, as determined in Step 1 of the correction procedure. The annotation of the data sets (numbering according to Tab. 5.3) indicates the isotopologue which was used for the determination of ξ. The statistical error bars are within the symbol size. For isotopologue measurements within a given mixture, *i.e.* sets (1,2), (3-5) and (8-10), the cell was stationary; in the case of measurement data sets 6 and 7 the cell was removed and reinserted between the measurements.

Table 5.4: Demonstration of the capability of the depolarization ratio correction procedure. The observed and corrected ρ-values are from measurements of the Q_1-branch lines of H_2. The numbers in brackets denote the measurement uncertainty in the last digit. In the case of the averaged SP0SA values, the brackets denote the standard deviation in the last digit. The numbering is according to the data sets summarized in Tab. 5.3.

H_2	ρ_{obs} in 10^{-2}			ρ_{SP0SA} in 10^{-2}			
J''	#3	#7	#10	#3	#7	#10	average
1	2.41(1)	2.12(1)	2.85(1)	1.77(1)	1.89(3)	1.80(1)	1.82(6)
2	1.97(1)	1.62(1)	2.52(1)	1.33(1)	1.40(3)	1.48(1)	1.40(8)
3	1.92(1)	1.54(1)	2.34(1)	1.28(1)	1.32(3)	1.30(1)	1.30(2)

5.3.4.4 Results and discussion

After the successful validation of the two-step correction approach for the observed depolarization ratios, the method can now be applied to the data of all hydrogen isotopologues. Their individual Q_1-spectra are found in Fig. 5.15.

Tab. 5.5 contains the list of the corrected depolarization ratios of the six hydrogen isotopologues measured at the TLK. The table lists only one selected data set per isotopologue and only those $Q_1(J'' > 0)$-lines with sufficient signal-to-noise ratio[6]. To each of these values an uncertainty was assigned, this can be traced back to three main sources:

1. known inadequacies in the used correction model/procedure (mostly due to simplifications or assumptions);
2. uncertainties in the determination of the geometrical dimensions of the light collection region as input parameters for the model; and
3. experimental uncertainties in the measured depolarization ratios.

A detailed discussion of individual noise sources and their quantitative estimation is found in Appendix E. In the following, the total (and propagated) uncertainty will be denoted by the symbol $\Delta\rho_{\mathrm{tot}}$.

Each experimentally determined and corrected depolarization ratio, ρ_{cor}, in Tab. 5.5 is listed together with the theoretical expectation, ρ_{theo}, which was calculated from the matrix elements of the polarizability provided by LeRoy [LeR11].

Most of the values of the individual lines show a good agreement to the theory within the given uncertainty, while greater deviation is found for the lines of T_2. This is possibly due to the fact, that the $Q_1(J'' = 0)$-line of T_2 could not be used for the determination of the polarization cleanness of the cell as it is strongly convoluted with the $Q_1(J'' = 1)$-line (see Fig. 5.15). According to the results in the validation section (5.3.4.3), the determined cleanness, ξ, does not differ much if determined using different species from one sample. Thus, the cleanness for the correction procedure of T_2 was determined from the HT data from the same sample and cell. Although this indirect determination was proven to be valid, a slight shift is assumed that is added to the corrected value.

In order to gauge the general agreement of experimental and theoretical values, the following quantitative method was chosen. The depolarization ratio difference ($\rho_{\mathrm{theo}} - \rho_{\mathrm{cor}}$) was calculated for each measured value and then normalized to the propagated uncertainty, $\Delta\rho_{\mathrm{tot}}$:

$$e = \frac{\rho_{\mathrm{theo}} - \rho_{\mathrm{cor}}}{\Delta\rho_{\mathrm{tot}}(\rho_{\mathrm{cor}})} \,. \tag{5.18}$$

All measurements and their individual uncertainties were independent of each other. Therefore, the functional dependence e for all the measured, corrected depolarization ratios should form a Gaussian distribution if plotted as a statistical histogram (see Fig. 5.17).

[6]The full tabulation of all data sets measured at the TLK and Swansea is found in Appendix G.

Table 5.5: Selected set of results of depolarization ratios for all six hydrogen isotopologues. The uncertainty, $\Delta\rho_{\mathrm{tot}}$, in the last digit of the observed depolarization ratios are given in parentheses. The theoretical depolarization ratios, ρ_{theo}, were derived from LeRoy's *ab initio* calculations for the laser wavelength of the LARA systems, $\lambda = 532\,\mathrm{nm}$ [LeR11]. Note that the ordering is according to Fig. 5.15 in which the labeled spectra of the Q_1 branches of all hydrogen isotopologues can be found.

J″	H_2		HD		D_2	
	ρ_{cor}	ρ_{theo}	ρ_{cor}	ρ_{theo}	ρ_{cor}	ρ_{theo}
	in 10^{-2}		in 10^{-2}		in 10^{-2}	
1	1.77(6)	1.83	1.77(6)	1.80	1.74(6)	1.76
2	1.33(6)	1.33	1.26(6)	1.30	1.18(6)	1.27
3	1.28(6)	1.25	1.21(6)	1.22	1.12(4)	1.19
4					1.13(7)[a]	1.17
5					1.38(10)[a,b]	1.16

J″	HT		DT		T_2	
	ρ_{cor}	ρ_{theo}	ρ_{cor}	ρ_{theo}	ρ_{cor}	ρ_{theo}
	in 10^{-2}		in 10^{-2}		in 10^{-2}	
1	1.73(6)	1.79	1.70(6)	1.75	1.65(6)	1.74
2	1.26(6)	1.29	1.23(6)	1.26	1.19(6)	1.25
3	1.22(6)	1.21	1.27(6)	1.18	1.12(6)	1.17
4	1.25(6)	1.19	1.15(6)	1.16	1.04(6)	1.15
5			1.30(6)[b]	1.15	1.13(6)	1.14
6			1.26(9)[b]	1.15	1.16(7)	1.14

[a] from different data set
[b] approaching noise level

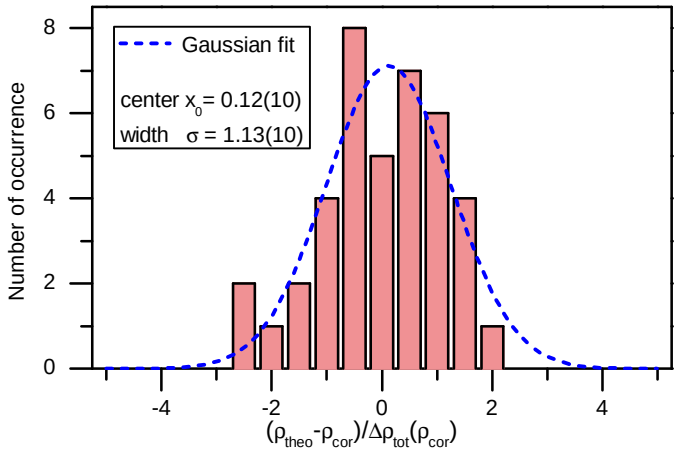

Figure 5.17: Statistical plot of deviations between measured and theoretical depolarization ratios. Note that this histogram contains all 40 measurement results of all individual hydrogen isotopologue runs (*i.e.* TLK and Swansea data as well as repeated data sets for the same isotopologues). Thus, it covers far more entries than listed in Tab. 5.5. The histogram was fitted with a Gaussian function. For further details see text.

The fit of a Gaussian function to the distribution returns a width of $\sigma_{\text{fit}} = 1.13 \pm 0.10$ and mean value of $x_0 = 0.12 \pm 0.10$. This agrees reasonably well with the expectation for a standard normal distribution[7] with $\sigma = 1$ and being centered at zero. It can therefore be concluded that the measured depolarization ratios, which were corrected by the two-step procedure agree with the theoretically derived values of LeRoy within a 1σ confidence level. This will allow using use these values for a calibration of the LARA system covering all six hydrogen isotopologues.

In the introduction to the depolarization measurements, a few other groups have been mentioned who have made efforts to measure the depolarization ratio of hydrogen. However, none of the groups has ever been able to measure the rotationally resolved Q_1-branches of all six isotopologues. Some measurements of H_2 and one of D_2 have been reported in the literature, and only two groups tabulate rotationally resolved Q_1-branches (Holzer[8] *et al* in 1973 [Hol73] and more recently, in 2007, Yu *et al* [Yu07]). In Tab. 5.6 their values are collated together with the values from this work and the theoretical values as obtained via LeRoy's calculations.

The table reveals that nearly all reported experimental values agree with those of LeRoy within their experimental uncertainty. However, it should be stressed that the ρ_{cor} values from this work are generally (i) smaller than the values from the other groups, (ii) closer to the theoretical values, and (iii) have a smaller measurement uncertainty. Presumably, points (i) and (ii) are associated with the fact that Holzer and Yu did not apply any correction for the polarization purity or geometrical effects in the light collection. Their depolarization ratios are consistently larger than the theory values. This shows that the two-step correction procedure is indeed required in order to obtain accurate depolarization values.

[7]Note that in this case the "normal distribution" is not normalized to an area equal to 1.
[8]Holzer *et al* also measured D_2.

Table 5.6: Comparison of corrected depolarization ratios of H_2 with experimental and theoretical data from literature. The data of Yu and Holzer are found in [Yu07] and [Hol73], respectively. Note that the correction methodology developed in the frame of this thesis forces the corrected depolarization ratio of $Q_1(J'' = 0)$ to be zero.

J''	ρ_{cor} in 10^{-2}	$\rho_{\mathrm{lit-Yu}}$ in 10^{-2}	$\rho_{\mathrm{lit-Holzer}}$ in 10^{-2}	$\rho_{\mathrm{theo-LeRoy(532\,nm)}}$ in 10^{-2}
0	0.00(6)	0.2(2)	0.1(1)	0
1	1.77(6)	2.1(2)	1.9(1)	1.83
2	1.33(6)	1.5(2)	1.4(1)	1.32
3	1.28(6)	1.4(2)	1.35(10)	1.25
4		1.3(5)		1.23

5.3.4.5 Summary and conclusion

It has been found that the integration over the solid angle of the light collection cone and stress-induced birefringence in the Raman cell windows lead to an observed depolarization ratio, ρ_{obs}, which is generally higher than the "single point zero solid angle" value, ρ_{SP0SA}. A two-step correction procedure has been developed. Given a known geometry, the approach is the following:

(i) An exactly known SP0SA depolarization ratio (*e.g.* of the $Q_1(J'' = 0)$-lines of hydrogen isotopologues) is needed to determine the cleanness of the incident laser beam in the cell, ξ.

(ii) This ξ is then used to correct the ρ_{obs} value in the given geometry. Said methodology has been successfully validated.

This approach made possible the first successful measurement of the depolarization ratios of the Q_1-lines of all six hydrogen isotopologues. The values are in good agreement with the theoretical prediction by LeRoy. Additionally, one can say with confidence that the data measured and analyzed within the framework of this thesis are the most accurate to date. This was shown in the comparison with other groups which measured the depolarization ratios of H_2 before.

This is not only of interest for the community of experimental spectroscopists, but also for the colleagues from the theoretical side who are interested in validating their calculations of molecular properties like the polarizability.

In the context of KATRIN the implications were profound. Recall specifically, that the aim of this section was the verification of the theoretical Raman intensities which require the polarizabilities from LeRoy [LeR11] as input. The depolarization ratios, which can be calculated from these predictions, have been found to agree with the corrected depolarization ratios of all six hydrogen isotopologues to better than 5% for almost all of the investigated $Q_1(J'')$-lines, within a 1σ confidence level. Using error propagation and certain assumptions[9] one can show that this relative uncertainty of the depolarization ratios is about equal to the relative uncertainty of the line strength function.

[9]The derivation is given in detail in Appendix F.

Together with the determination of the spectral sensitivity, which is the topic of the following section, the theoretical intensities can therefore be employed for a calibration of the LARA system including all six hydrogen species. This will finally allow KATRIN to obtain proper quantitative measurements of gas composition of the tritium source.

Finally, it should be pointed out that the progress of developing the methodology reported in this section has helped to better understand the LARA systems better in general[10].

[10]To give an example, the MonLARA system was then also equipped with a sheet polarizer in the light collection system, which is necessary in order to choose the correct polarization composition of the scattered light in the intensity calculations.

5.4 Measurement of the system's spectral sensitivity

The calibration approach which is discussed in this chapter requires (i) the theoretical Raman intensities which were subject of the previous section, and (ii) the spectral sensitivity of the Raman system employed. The spectral sensitivity, $\eta(\lambda)$, describes how the light which is to be analyzed is influenced on its way through the detection system.

In theory, one could derive the total spectral sensitivity of the system from the individual contributions of each component. However, this cannot be realized, since (i) the spectral sensitivity of the component is not necessarily known, and (ii) $\eta(\lambda)$ often depends on the polarization configuration of the transmitted light and thus would make any given curve unusable if the polarization differed from the certified one. Moreover, it is in general safer to measure a quantity than to rely on calculations or data sheets from the manufacturer. In this calibration approach, the measurement of the system's spectral sensitivity is preferred.

The spectral sensitivity is defined as the ratio of the light spectrum which is measured at the end of the detection system, $I_{\mathrm{meas}}(\lambda)$, and the spectrum which is actually generated at the position of scattering in the Raman cell, $I_{\mathrm{theo}}(\lambda)$:

$$\eta(\lambda) = \frac{I_{\mathrm{meas}}(\lambda)}{I_{\mathrm{theo}}(\lambda)} \,. \tag{5.19}$$

The determination of $I_{\mathrm{meas}}(\lambda)$ is straightforward, while $I_{\mathrm{theo}}(\lambda)$ is harder to obtain since the full characteristics of the light source have to be well understood. The focus in measuring the spectral sensitivity is thus to find a reliable source for obtaining a well-known $I_{\mathrm{theo}}(\lambda)$.

It should be noted at this point, that the proof of concept of the sensitivity measurement and related systematic investigations were conducted within the diploma thesis of Simone Rupp [Rup12] supervised by the author. For this reason, the content presented here represents only a summarized version. The reader is referred to Simone Rupp's thesis for deeper insights and further information.

5.4.1 Requirements for the determination of the spectral sensitivity

For the accurate determination of the spectral sensitivity, a light source with a well-known emission spectrum $I_{\mathrm{theo}}(\lambda)$ is required. In the following, this source will be called "calibration light source". This light source needs to fulfill certain requirements:

- **Coverage of the spectral range of interest**
  The focus of quantitative Raman analysis is on the Q_1-branches of the six hydrogen isotopologues. The valid spectral range of the calibration light source should therefore cover at least all Q_1-branches of the hydrogen isotopologues (see Fig. 5.14). The excitation laser has an emission wavelength of $532\,\mathrm{nm}$, so that the Q_1-branch of the heaviest isotopologue, $\mathrm{T_2}$, is found at around $612\,\mathrm{nm}$, while the corresponding line of the lightest one, $\mathrm{H_2}$, is found around $683\,\mathrm{nm}$.

- **Trueness of the spectrum**
  Specifically in the spectral region, where the most relevant species for the KATRIN experiment ($\mathrm{T_2}$, DT, and $\mathrm{D_2}$) are found, the systematic uncertainty of $I_{\mathrm{theo}}(\lambda)$ should be in the few-percent range, or lower.

- **Replication of the Raman scattered light**
  "Replication" means that the geometry of the calibration light source should resemble the geometry of the Raman scattering region as closely as possible. In particular, position and exit angles of the calibration light should be like the one of the Raman light originating from the excited gas volume. The importance of this requirement can already be estimated from a Raman measurement by Sebastian Mirz [Mir11], who investigated the dependence of the relative Raman intensities on the focal distance of the collection optics. A strong dependence was observed, which was mainly related to chromatic aberrations. The optimum solution would thus be to replicate exactly the position of Raman light generation; less recommended would be to guide the light of the calibration source to this point via additional optics.

- **Known polarization behavior**
  The detection systems of the Raman systems are in general polarization-dependent. For this reason, a linear polarizer was installed in the light collection system, so that the light passing through the system always has the same polarization. The use of the calibration light source is not expected to be impeded by this additional polarization optics.

5.4.2 Possible calibration sources for the measurement of the spectral sensitivity

With regard to the above requirement several possible candidates for the calibration source were considered. The different alternatives were grouped in "external" and "internal" sources. "External" implies, that the light is generated at any place and is then guided to the light collection system of the Raman system. In contrast to this, "internal sources" produce their light exactly at the position at which the Raman light is generated normally.

External sources This type of source always suffers from the disadvantage, that additional optics are required to transport the light to the collection region. These extra optics can be *e.g.* lenses, mirrors or optical fibers. The geometrical shape of the source can be much different from the geometry of the illuminated gas cylinder of some micrometer diameter as present in Raman scattering. Furthermore, emission angles can be different.

The following light sources were taken into account in this category:

- **Commercially available calibration sources**
  These off-the-shelf devices are often based on a tungsten halogen lamp and provide a wide spectral range with a calibration uncertainty of only a few percent. The certified spectrum is generally traceable to NIST[11] standards. This is provided in quite coarse steps ($\Delta\lambda \sim 5 - 10\,\mathrm{nm}$). In [Rup12], the results of a market research are found. The possibly best choice among the candidates, the Newport QTH 63978, provides an uncertainty of $\sim 2.5\%$ in the spectral region of interest [New12]. The unit costs about 4500 € and has only a limited (calibrated) lifetime of $\sim 50\mathrm{h}$, which makes it quite expensive.

[11] NIST = American National Institute of Standards and Technology

- **Custom-built devices**
  Custom-built calibration sources can be assembled from stabilized halogen lamps like in the commercial devices [Sch11a], or from other light sources, like LEDs [Rup12]. LEDs have the big advantage that their emission spectrum is stable if the temperature and current are stabilized to a certain value [Dav12]. The stabilization of the LEDs is in general easier to obtain than in case of the halogen lamps, which operate at some thousand degrees Kelvin. Furthermore, LEDs have a much longer lifetime ($\sim 100,000\,\mathrm{h}$) as compared to halogen lamps ($\sim 1000\,\mathrm{h}$).

  Building a custom calibration light source may be a cheaper alternative on the first view, but it has certain drawbacks. The main disadvantage is, that the calibration light source needs to be calibrated itself before it can be employed. This may not be straightforward, and it is hard to achieve a similar or better performance compared to commercial devices.

Internal sources All previously mentioned calibration sources have the major disadvantage that their intrinsic replication of the scattering region is poor or not possible. Thus, a larger systematic uncertainty compared to the certified value is expected. This drawback is alleviated by internal sources. The possibilities are:

- **In-cell black body radiator**
  One supposable idea is to replace the laser windows of an ordinary Raman cell (see a drawing of a cell in Fig. 4.4.) with electrical feedthroughs and to install a thin tungsten wire in between the connectors [Sch11b]. This wire would be at exactly the same position as the laser beam in the Raman cell. If heated by a current, the wire would emit black body radiation. Its spectrum could be calculated from Planck's law, in principle, if temperature and emissivity were known accurately. Since this is not the case, this approach would again lead back to the problem that a calibration of this device would be required beforehand.

- **Internal standard medium (gas or liquid)**
  One further possibility is to fill the Raman cell with a certain gas or liquid which emits a well-known spectrum if excited by the laser (see *e.g.* [Res05]). The true shape then has to be provided from literature or certain calibration institutions like NIST. The replication of the scattering region would be almost perfect in this case since the experimental setup is quasi-identical to a standard Raman measurement setup. It should be noted that no external power supplies or temperature controlling equipment are needed in this approach.

- **Luminescence intensity standard**
  An approach which is similar to the previous one is to use a solid luminescence intensity standard. Such an approach was suggested by Ray and McCreery in 1997 [Ray97]. It is basically a fluorescent material which emits a broadband spectrum if exposed to laser radiation. Further details are found in [McM06]. As in the previous option, the light is generated by the same laser beam which is normally used for the Raman light generation. Thus, the replication of the Raman scattering region should be equally possible.

5.4.3 NIST-traceable luminescence standard SRM 2242

The calibration method of choice was to make use of an internal standard. Since no liquid or gaseous standard which fulfills the requirement was available, a solid luminescence standard was chosen. This choice was especially motivated by the features of the device named Standard Reference Material (SRM) 2242 developed and distributed by NIST. The standard is designed for a laser excitation of $532\,\mathrm{nm}$ and is well-documented in a publication by Choquette *et al* [Cho07] and in the calibration certificate of NIST [NIS08].

Features of the SRM 2242 A photograph of the SRM 2242 standard is shown in the top panel of Fig. 5.18. The standard is basically a $2\,\mathrm{mm}$ thick borate glass slide doped with $\mathrm{MnO_2}$. One of the surfaces is frosted for optimizing the emission profile of the luminescence light. The relative spectral intensity I_{SRM} of the luminescence spectrum was calibrated according to the calibration protocol of NIST [NIS08]. Its shape is represented by a fifth-order polynomial

$$I_{\mathrm{SRM}}(\lambda) = \frac{10^7}{\lambda^2} \cdot \sum_{i=0}^{5} A_i Y(\lambda)^i \tag{5.20}$$

with

$$Y(\lambda) = 10^7 \cdot \left(\frac{1}{532\,\mathrm{nm}} - \frac{1}{\lambda} \right) . \tag{5.21}$$

The coefficients A_0 to A_5 are provided by NIST and are valid for an operating temperature between $20\,^\circ\mathrm{C}$ and $25\,^\circ\mathrm{C}$. The middle panel of Fig. 5.18 shows the spectrum in the relevant wavelength region of the hydrogen isotopologues. NIST provides $\pm 2\sigma$ confidence curves together with the shape of the luminescence spectrum. This relative uncertainty is shown in the bottom panel of Fig. 5.18.

The figure shows that the isotopologues with the highest relevance for KATRIN ($\mathrm{T_2}$, DT, and $\mathrm{D_2}$) are in the spectral region where the calibration standard provides the smallest uncertainty ($|\sigma(I_{\mathrm{SRM}})| < 0.5\%$). This already promises a small final calibration uncertainty by this method. However, the luminescence standard has one major drawback as indicated in Fig. 5.18. The certified calibration region only spans from $536.4\,\mathrm{nm}$ to $676.1\,\mathrm{nm}$ and thus does not cover the Q_1-branch of $\mathrm{H_2}$ at about $\sim 683\,\mathrm{nm}$. Fig. 5.18 also shows that the certified polynomial diverges outside of the limits of the certification. This failing extrapolation is of course an expected behavior for any high order polynomial. In order to deal with this constraint, an extended set of measured data was requested and obtained from NIST.

This extended set is not provided in form of a polynomial, but as discrete array and without any stated uncertainty. Nevertheless, the quantification of the final calibration uncertainty requires an estimate for the uncertainty of the extended data beyond the certification. The bottom panel of Fig. 5.18 shows that the polynomials describing the uncertainty quickly diverge outside of the certified region, where they lose their validity. If this uncertainty is now transfered to the extended data in this spectral region, it can be assumed that it represents a rather conservative estimate for the uncertainty of the actual measurement curve. It should be noted that the larger uncertainty linked to the $\mathrm{H_2}$ isotopologue will not be a show-stopper for the calibration task of the KATRIN LARA system, since $\mathrm{H_2}$ will only be a minor constituent of the WGTS gas content [KAT05].

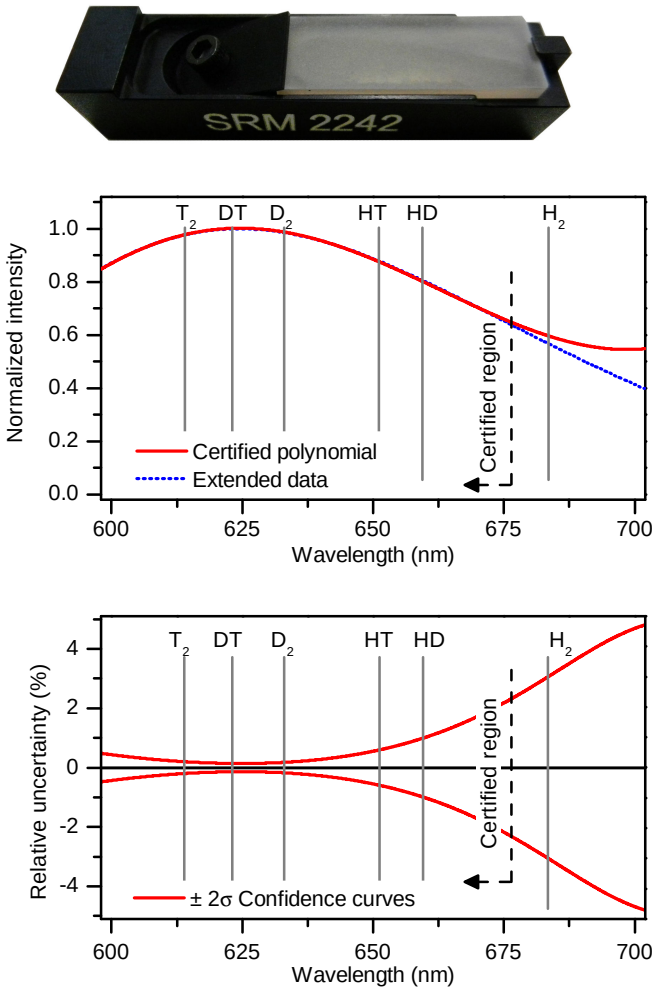

Figure 5.18: The NIST luminescence standard SRM 2242. *Top panel:* A view of the SRM 2242 luminescence standard in its slide mount. The dimensions of the glass slide are $(30.4 \times 10.7 \times 2.0)\,\mathrm{mm}$. *Middle panel:* (Normalized) certified spectrum of the luminescence standard and extended data. The positions of the Q_1-branches of the six hydrogen isotopologues and the limit of certification are indicated. *Bottom panel:* Confidence curves ($\pm 2\sigma$) for the certified spectral range. Note that the shape of the certified data (spectrum and confidence curves) is given by a fifth order polynomial which diverges outside of the certified region.

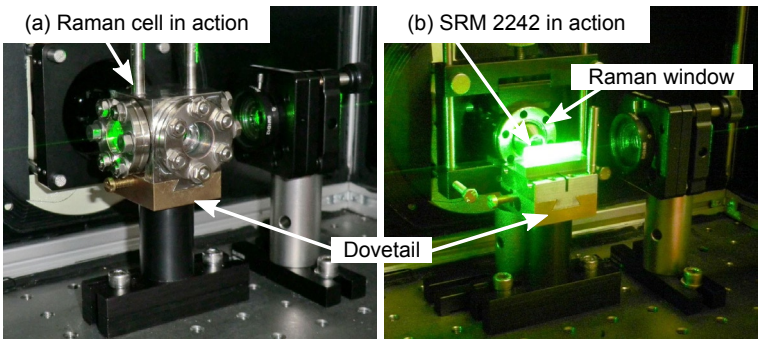

Figure 5.19: Replication of the Raman scattering region by the SRM 2242 luminescence standard. The SRM 2242 was removed from the mount shown in Fig. 5.18 and attached to a dovetail mount. This facilitates the exchange between cell and luminescence standard. A Raman window was aligned between standard and collection optics to replicate the transmission of the scattered light through the window of the cell. The green glow in both pictures is related to laser light which is diffusely reflected or elastically scattered (Rayleigh-scattering). The Raman and luminescence light is several orders of magnitude less intense and thus not visible.

Application of the SRM 2242 The SRM 2242 features very low uncertainties in the wavelength region of interest, with the exception of the Q_1-branch of H_2. Other advantages of the luminescence standard are its simple application and outstanding capability of replicating the scattering region. Fig. 5.19 shows the SRM 2242 in action at the position where normally the cell is placed.

The crucial point for the almost perfect replication of the scattering region is that Raman light and luminescence light are excited by the same laser, so that the position of light generation as well as the light emission angles are as similar as possible. Furthermore, realignment is required after changing between Raman cell and SRM 2242.

Further advantages are

(i) that the standard works passively, meaning that no additional electronic devices are required which would again be prone to instabilities;

(ii) that the lifetime is quasi-infinite and no re-calibration is necessary,

(iii) and that the simple handling facilitates the calibration procedure of the LARA system for non-LARA experts which is an important feature for the long measurement time of the KATRIN experiment.

Differences between the NIST reference system and the MonLARA system In the previous paragraphs, many advantages of the luminescence standard for the determination of the spectral sensitivity were discussed. Also, it was shown how the "flaw" of H_2 being out of the certified region can be compensated.

However, the applicability of the luminescence standard needs to be contemplated carefully when comparing the principal experimental setup of the MonLARA system and the reference system which NIST used for their calibration. Specifically, two major differences need to be mentioned:

- **The scattering geometry**
  The SRM 2242 was designed for experiments in a 180° back-scattering geometry (*e.g.* micro-Raman experiments [Die11]). In contrast, all Raman systems currently used at the TLK use a 90° scattering geometry. It may be expected that the passage of the laser beam through the glass as well as the scattered light will be different in both configurations. NIST does not quote investigations of the standard in this altered geometry and thus does not report on the validity of the certified polynomials for this case.

- **Polarization effects**
  In Section 5.3 focusing on the depolarization measurements, the sensitivity of Raman scattering on the polarization was discussed. Polarization is generally also an issue in fluorescence processes [Feo61]. In order to remove all polarization dependent effects in the light detection system, NIST installed an achromatic depolarizer (polarization scrambler) which randomly polarizes the scattered light. In contrast to this, the Raman systems used in this work have a linear polarizer installed in their collection optics. This unit allows one to accurately select the component of the scattered light which is required for the comparison of experimental results and theoretical predictions (see Section 5.3). Both techniques for handling the polarization may lead to a differing outcome.

In order to study and finally validate the usability of the SRM 2242 luminescence standard under these "unconventional" conditions, dedicated experiments were conducted also to lead to a preferred calibration procedure which offers the smallest possible systematic uncertainty. This study was a major part of the diploma thesis of Simone Rupp and can be found in all details in [Rup12]. In the following section, only the most important results and implications will be summarized to finally give the answer whether the standard can be applied for the determination of the spectral sensitivity.

5.4.3.1 Systematic investigations

Systematic studies were performed in which certain experimental parameters were varied in order to investigate their influence on the spectral shape. It has to be mentioned that the investigations are not able to determine which of the spectra recorded under different conditions was the "right" one. Nevertheless, the investigations can indicate if the certified spectral shape is valid for differing experimental conditions compared to those from NIST.

The experimental parameters with possible influence on the spectral shape under investigation were

- the incident position of the laser beam,
- the polarization of incident and scattered light,
- the presence of a Raman cell window,
- the number of passages of the laser beam (single- or double-pass mode),
- the temperature and laser power.

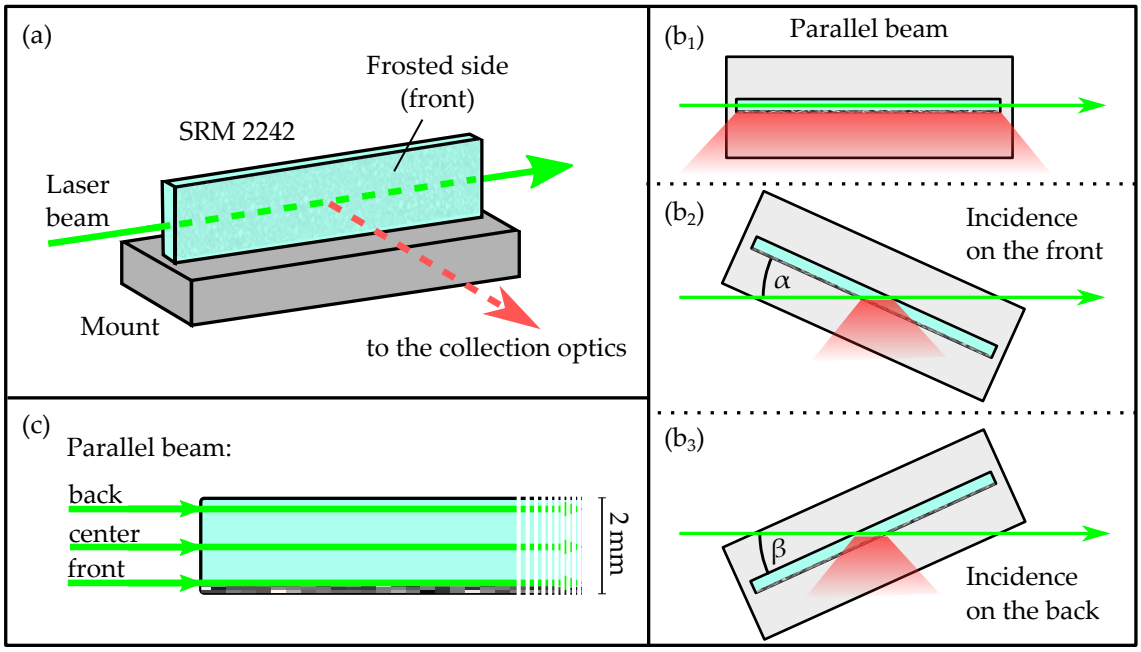

Figure 5.20: Different incident positions of the laser beam on SRM 2242. (a) The SRM 2242 is aligned parallel to the laser beam. The laser beam is incident on the small side of the SRM 2242, hence passing through the full length of the glass slide. This should provide an optimal replication of the scattering region. (b_i) Different incident angles of the laser beam (top view). (c) Different incident positions of the parallel beam (top view). Figure from [Rup12].

The findings of the individual investigations implied certain consequences for a measurement procedure. This procedure has then become obligatory for all later measurements of the spectral sensitivity.

Influence of the incident position of the laser beam on the spectral shape A certain discrepancy is given in the usage of the SRM 2242 luminescence standard for the calibration of the spectral sensitivity. On the one hand, the extended scattering region with light collection at an angle of 90° relative to the laser beam should be replicated as close as possible. But on the other hand, the measurement condition should be as close as possible to the conditions used by NIST (point-like backscattering geometry) in order to obtain a spectrum close to the certified one. This discrepancy can only be resolved by systematic investigations to resolve whether both aforementioned measurement conditions are really in conflict with each other.

In a set of experiments, the position and angle of incidence of the laser beam were varied. Fig. 5.20 gives an overview of the experimental configuration. A grazing incidence should provide a good replication of the scattering region, while a more vertical angle of incidence would be closer to the NIST situation.

The following findings were obtained:

- Measurements with incidence on the front (see Fig. 5.20, case (b_2)) at an angle of up to $\alpha = 60^\circ$ are closest to the NIST configuration. They were in good agreement

(difference $< 1\%$) with spectra measured for grazing incidence (see Fig. 5.20 case (b_1) and (c)). Therefore, it could be inferred that the use of the SRM 2242 in a parallel configuration is valid.

- It can also be assumed that, as already indicated, the parallel configuration provides the best replication of the scattering region since it is closest to the situation in Raman measurements. The position of incidence in this configuration (back, center or front in Fig. 5.20, case (c)) has no significant influence.

Influence of the polarization on the spectral shape The certified luminescence spectrum was calibrated by NIST in a back-scattering geometry with a polarization scrambler installed to fully randomize the scattered light before it is guided into the spectrometer. This configuration differs significantly from what is realized in the LARA setup. Thus, it is of high relevance to understand how to choose the right polarization setting to be compatible to the NIST calibration.

In order to investigate the polarization dependence of the measured luminescence light, two sets of measurements were performed.

1. In the first experiment, an additional half-wave plate was installed in the MonLARA system before the laser light was focused into the SRM 2242. By this measure, the normally $\perp^i$ polarized incident laser light could be rotated stepwise by an automated rotation mount. The sheet polarizer in the collection optics was in $\perp^s$ configuration as usual.

2. In the second experiment, the half-wave plate was turned back to obtain again $\perp^i$ polarized laser light. Then only the sheet polarizer was rotated stepwise.

In both experiments a periodic modulation of the total intensity and the spectral shape could be observed, with the largest deviation found between the vertical and horizontal polarization configurations. The case for the laser polarization is shown in Fig. 5.21. The modulation of the amplitude of about 30% reveals a partly polarized emission[12]. This behavior of fluorescent material illuminated by polarized laser light is to be expected according to the literature [Feo61]. The superposition of an unpolarized part (without angular dependence) and a polarization maintaining part (with angular dependence) allows one to explain the change in total intensity and in spectral shape.

In [Rup12] a detailed derivation for the phenomenon is shown and it is mathematically argued that one should expect the following relation for the measured SRM 2242 intensity:

$$I_{\mathrm{meas}}(\lambda, \chi = 45^\circ) = \frac{1}{2}\left(I_{\mathrm{meas}}(\lambda, \chi = 0^\circ) + I_{\mathrm{meas}}(\lambda, \chi = 90^\circ)\right) \ , \tag{5.22}$$

with χ being the relative rotation angle of the polarization with respect to $\perp^i$. This assumption was indeed verified by the measured data, which indicates that the polarization characteristic of the SRM 2242 in the LARA setup was understood.

[12] In the case of unpolarized emission, no modulation would be expected, while in the case of fully polarized emission, a modulation of 100% of the amplitude would be assumed.

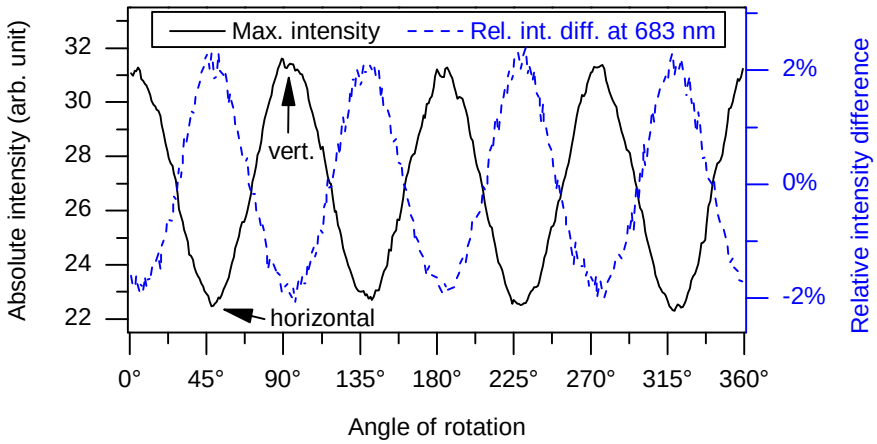

Figure 5.21: Influence of the laser polarization on the measured spectra. The plot shows the dependence of the measured luminescence spectra on the half-wave plate's angle of rotation with respect to (i) the maximum intensity of the non-normalized spectra, and (i) the respective relative intensity difference to the average spectrum at a selected wavelength of 683 nm. The latter serves as an approximate value for the largest deviation in spectral shape in the wavelength range of interest. The positions of vertical and horizontal laser polarization are indicated by the arrows; they recur at intervals of $90°$. At these positions, the extrema of both curves coincide. Figure from [Rup12].

The same theoretical considerations were then applied to the conditions under which NIST calibrated its standards. It can be derived that the polarization of the incident laser beam needs to be turned to $\chi = 45°$ under the conditions present in the LARA system, in order to obtain close to the same (certified) spectrum.

Influence of the presence of a Raman cell window on the spectral shape When the Raman cell is replaced by the SRM 2242 luminescence standard (compare Fig. 5.19), the geometry of the scattering region remains the same. However, there is a (small) difference between the path the emitted light takes in the two cases. The light which originates from the Raman scattering can only be transmitted through the opening of the Raman window, and it also experiences a slight lateral shift due to the refractive index of the window. In contrast, this window is normally not present for the light from the illuminated SRM 2242. In order to investigate the effect of the presence of the window, measurements of the SRM 2242 spectrum with and without an additional Raman window were performed. Here, the window was positioned to exactly the same location as if the cell were present, as already shown in Fig. 5.19. The effect of a Raman window in the setup is shown in Fig. 5.22.

Additionally, measurements were conducted to investigate the required precision in positioning.

Overall it was concluded, that the use of a cell window is necessary during the spectral sensitivity calibration and that its position should be aligned to better than $0.5\,\mathrm{mm}$.

Further influences on the spectral shape Besides these main investigations which were required to decide whether the SRM 2242 luminescence standard can be employed at

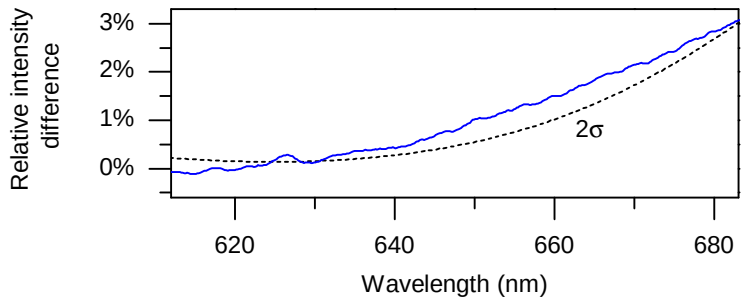

Figure 5.22: Difference in the spectral shape for measurements with and without Raman window. For comparison, the 2σ confidence curve provided by NIST is plotted as well (gray, dashed line). The importance of the Raman window is pointed out by the difference being of the order of the confidence curves. Figure from [Rup12].

all, and besides the investigations of the window influence, several further studies were conducted.

- In one set of experiments, the difference between single-pass and double-pass mode (see Section 4.1.2) was investigated. However, the scattering region could not be replicated as adequately as necessary since the back-reflection of the double-pass has to be implemented under a slight angle. This prevents resending the beam into the laser head. The measurement data allow to assume that the difference in measured spectral sensitivity between both modes is negligible.
- In the last measurement set, the influence of temperature and laser power on the spectral shape was investigated. Such measurements had already been conducted by NIST and were repeated as a cross-check. The temperature behavior of the standard reacting to external heating or to thermal heat from the excitation could be confirmed. Based on the measured data, a laser power of around $100\,\mathrm{mW}$ was suggested for the calibration measurements. The temperature increase from absorption of laser light would induce only an insignificant spectral shift in this case.

Conclusions for the measurement procedure As a summary of the conclusions of the single investigations, a dedicated measurement procedure for the calibration measurement could be defined. The measurement should be performed under the following settings:

- The incident light should enter the SRM 2242 from the side. The parallel laser light then replicates the Raman scattering region as closely as possible (see Fig. 5.20 (c)). The frosted side should face the collection optics.
- The linear polarization of the incident laser light should be rotated by 45° relative to the scattering plane (*e.g.* by a half-wave plate).
- A Raman window should be accurately placed between the SRM 2242 and the collection optics to account for the optical influence of this window on the emitted light.
- The calibration measurements should be performed within the recommended temperature range ($20 - 25\,^\circ\mathrm{C}$) and with a laser power of around $100 - 150\,\mathrm{mW}$.

Validity cross-checks of the measurement procedure for the determination of the spectral sensitivity From the discussions above one expects that the measurement procedure defined above should yield the lowest systematic uncertainty. However, this does not intrinsically proof its validity. For this reason, independent cross-checks are required to gauge if the spectral sensitivity can be measured with the luminescence standard under the described conditions.

For the following tests the investigations were extended to two further LARA systems at the TLK which differ in the experimental setup. They are equipped with different spectrometers so that different spectral sensitivities are expected.

In a first step, the spectral sensitivity of each of the three systems was obtained according to the procedure described within the previous paragraph. Then, the following two tests were performed on these calibrated systems [Rup12].

1. A white light LED was used to illuminate a frosted glass slide in the scattering region via an optical fiber with a small diameter of $100\,\mu\mathrm{m}$. This glass slide was placed at the standard position of the SRM 2242 so that a similar light transmission was expected. The raw spectra (see top panel of Fig. 5.23) were corrected by the spectral sensitivity of the respective LARA system. In the bottom panel of Fig. 5.23, the corrected spectra of the white light LED measured at MonLARA and another LARA system are shown. The corrected curves agree quite well; the relative intensity differences are about 0.8% (-1.8%) in the spectral region of the Q_1-branch of T_2 (H_2).

2. The spectrum of a sample cell filled with a gas mixture consisting of H_2, HD, and D_2 was recorded by all three Raman systems and corrected by their spectral sensitivity. It could be shown in one case that the difference of the relative Raman intensity measured in two independent systems differed by up to 3.2%. This was reduced to less than 0.7% after the correction of the individual spectral sensitivities.

Both cross-checks performed with different LARA systems demonstrate the potential of a spectral sensitivity calibration using the SRM 2242 and prove the validity of the proposed procedure under the conditions different to the ones of NIST.

5.4.4 Resulting spectral sensitivity and discussion

Finally, after the systematic investigations which led to the measurement procedure and the successful validation measurements, the standard was used to determine the spectral sensitivity of the MonLARA system. The plot of the sensitivity curve is shown in Fig. 5.24 together with the $\pm 2\sigma$ confidence band. The certified polynomial was used for the wavelength region below $676\,\mathrm{nm}$, and the extended data was used above it. This transition is indicated by a step in the spectral sensitivity as certified and extended data are not continuous at this point. The confidence band for the extended data was obtained from the diverging uncertainty polynomial as discussed before (see Fig. 5.18).

Fig. 5.24 reveals that the spectral sensitivity is higher for shorter wavelengths. For illustration, the sensitivity at the wavelength region of T_2 is about 10% higher compared to that of H_2. The overall shape can be mainly described by overlaying the effiencies of the

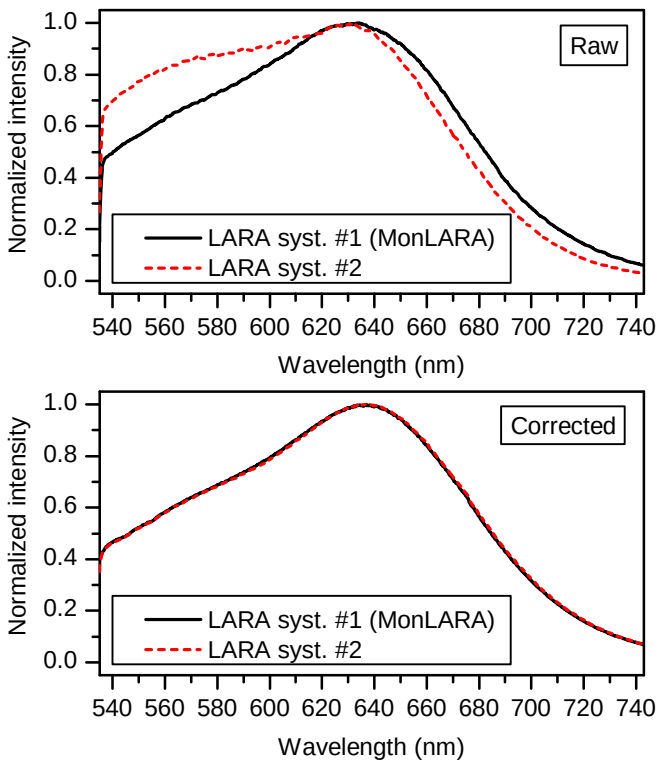

Figure 5.23: Spectra of a white light LED measured with two different LARA systems. *Top panel:* Raw spectra. *Bottom panel:* The spectra after correction of the individually measured spectral sensitivity. Both spectra agree after the application of the spectral sensitivity correction. The main difference of LARA system #2 to the MonLARA system is the employed spectrometer, which is a lens spectrograph (High Throughput Spectrograph (HTS), Acton/Princeton Instruments) with a higher light throughput efficiency.

spectrometer grating and the CCD detector. The ripple in the data traces can be associated with the transmission function of the razor-edge Raman filter (Semrock LP03-532RU-25) as discussed in Section 4.1.2.

5.5 Discussion of the calibration results

At this point it should be recalled that the two ingredients required for the calibration method discussed in this chapter were the theoretical Raman intensities and the spectral sensitivity.

1. **Theoretical Raman intensities** The calculations of LeRoy [LeR11] provide the components of the polarizability, a and γ, for all six hydrogen isotopologues. They are used in the line strength function together with the energy eigenvalues of the Raman lines and with the thermal population of each isotopologue to obtain theoretical Raman intensities. The quantum-theoretical input data of LeRoy could be validated by showing the agreement between experimental and theoretical results of depolarization measurements, which was within 5%. However, it should be made clear at this point that the aforementioned uncertainties do not necessarily express the actual uncertainty of the values, as obtained from the theory. Rather, they define the degree of confidence which can be currently placed in the theoretical data.

2. **Measurement of the spectral sensitivity** The NIST certified SRM 2242 luminescence standard turned out to be suitable for the determination of the spectral sensitivity of the LARA system for KATRIN. Systematic investigations and validation measurements show that the device can be successfully used in the $90°$ configuration. The valid operation is assured if the measurements are performed according to the defined procedure.

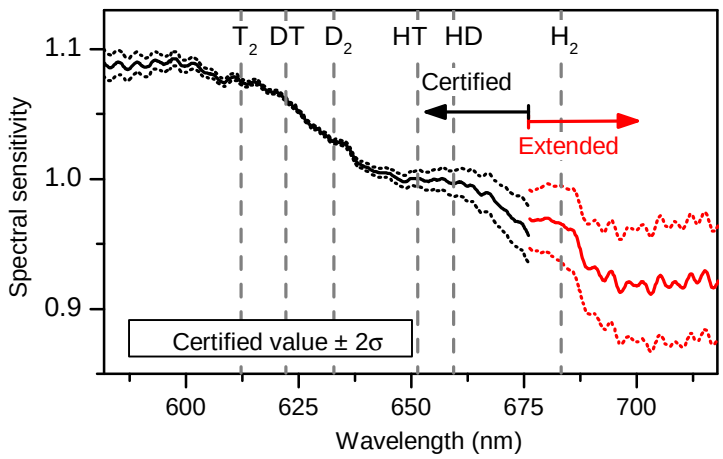

Figure 5.24: Spectral sensitivity of the detection system of the MonLARA system. The calibration was performed with the NIST SRM2242 luminescence standard. The spectral sensitivity curve was normalized to $\eta(651.4\,\mathrm{nm}) = 1$, which is at the wavelength of the Q_1-branch of HT. Note the discontinuity at the transition from the certified to the extended range (extended data also provided by NIST).

Table 5.7: Raman response functions obtained via theoretical Raman signal amplitudes and the related uncertainties. All R'_x were normalized so that $R'_{\mathrm{H_2}} = 1$. For the meaning of $\Delta R'_{\mathrm{theo}}$ and $\Delta R'_{\mathrm{sens}}$ see the main text.

Isotopologue	R'_x	$\Delta R'_{\mathrm{theo}}$ (%)	$\Delta R'_{\mathrm{sens}}$ (%)	$\Delta R'_{\mathrm{tot}}$ (%)
H_2	1.000	2.9	3.0	4.2
HD	0.981	3.0	1.0	3.1
HT	0.960	3.1	0.6	3.2
D_2	0.925	3.4	0.2	3.4
DT	0.914	3.7	0.1	3.7
T_2	0.866	3.9	0.2	3.9

The luminescence standard offers an almost perfect replication of the Raman scattering region and yields an uncertainty of less than 1% in the wavelength region of interest.

Both parts can be combined to obtain the response functions R'_x according to Eq. 5.6. In Tab. 5.7 these values are tabulated, as well as the estimated uncertainties. The uncertainties are split into two terms, namely

1. $\mathbf{\Delta R}'_{\mathrm{theo}}$. This contribution is associated with the confidence placed in the theoretical values. Previously, it was discussed that the relative uncertainty of the depolarization ratios is about equal to the relative uncertainty of the line strength function. A common value of $\Delta\rho = 0.055 \cdot 10^{-2}$ (see Tab. 5.5) for the experimental uncertainty of the depolarization ratios of each Raman line was used. This can be propagated into the uncertainty of the theoretical Raman intensity of this line, which is denoted as $\Delta R'_{\mathrm{theo}}$.

2. $\mathbf{\Delta R}'_{\mathrm{sens}}$. This contribution stems from the calibration of the spectral sensitivity. It is directly obtained from the $\pm 2\sigma$ curves.

The quadratic sum of both uncertainty contributions constitutes the overall uncertainty:

$$\Delta R'_{\mathrm{tot}} = \sqrt{\left(\Delta R'_{\mathrm{theo}}\right)^2 + \left(\Delta R'_{\mathrm{sens}}\right)^2}\,. \tag{5.23}$$

The overall uncertainty in the response function, as summarized in Tab. 5.7, is well below 5%. However, it is obvious that the confidence in the theory (which is deduced from the depolarization measurements undertaken to cross-check the *ab initio* line strengths) currently dominates the total error estimation, with the exception of H_2. Its $\Delta R'_{\mathrm{sens}}$ error is comparatively higher, since the required calibration data are out of the certified range provided by NIST.

5.6 Conclusions

This chapter introduced the idea of a sample-free calibration method by using theoretical Raman intensities and the spectral sensitivity of the Raman system employed. It could

be shown that both required contributions can be provided with a sufficiently small uncertainty. The resulting overall systematic uncertainty of the assembled response functions is at most 4.2%.

However, for the sake of verification it is required to validate the results of this approach with an independent method. In particular, the polarizabilities, a and γ, as input parameters in the theoretical intensity calculation have only been checked for each line individually by the means of the depolarization measurements. However, the intensity ratios between different isopotologues are not accessible by this method. Therefore, an independent method is required which can probe the intensity ratio between the isotopologues. The validation was conducted by accurate production of calibration samples of H_2, HD, and D_2, this will be discussed in the next chapter. The comparison of the resulting response functions R_x of these non-radioactive isotopologues could be used to ultimately decide if the sample-free calibration approach can be applied for the LARA system of KATRIN.

At this point it should be emphasized that the experimental findings reported in the main sections above, 5.3 and 5.4, are of benefit also for a broader scientific community and are not restricted to KATRIN only. The model for including the polarization aberrations and the geometrical effects from solid angle integration over the Raman intensity forms the basis for the two-step correction procedure for observed depolarization ratios. This method can enable other research groups to obtain depolarization ratios, which are closer to the true SP0SA value than before.

For this work, said correction procedure made it possible to measure the depolarization ratios of all hydrogen isotopologues accurately. The agreement with the theoretical expectations leads to a high degree of confidence in the accuracy of this type of theoretical calculations of the polarizabilities.

Finally, the applicability of the SRM 2242 standard was validated for an experimental configuration differing from the one used for the calibration at NIST. The 90° observation of Raman light instead of a 180° backscattering setup and the different polarization configurations are thus no obstacle for the use of the luminescence standard. The standard with its distinct advantages may thus find its way into the many 90° Raman applications where a determination of the spectral sensitivity is required.

Chapter 6

Calibration based on accurate gas samples (Method II)

6.1 Motivation and overview

In the previous chapter, the calibration of the Raman system was performed via theoretical intensities and the spectral sensitivity of the Raman system over a wavelength range covering all six hydrogen isotopologues. However, the unknown confidence in the theoretical intensities calls for a comparison with an independent calibration method via gas samples in the range in which reference samples are expected to be produced with adequate accuracy. In this context it is assumed that the generation of mixtures of the non-radioactive hydrogen isotopologues H_2, D_2, and HD does meet the requirements.

In general, accurate homogeneous calibration gas mixtures can be produced according to ISO standards 6142 and 6145 [ISO01, ISO03]. For example, ISO 6142 describes the generation of accurate gas mixtures by gravimetric means. However, these methods cannot easily be used for hydrogen isotopologues since the involved species are "potentially interactive substances" and "can decompose" [ISO01], as will be discussed in the following paragraph.

The method developed within the framework of this thesis provides an accurate preparation of samples consisting of H_2 and D_2, and their reaction product HD. It should be noted that HD is not commercially available in high purity. Also, as a consequence of thermodynamic exchange reactions, HD gas dissociates when kept in a container for a long time [Oht11, Oht12]. Thus, the heteronuclear isotopologue needs to be produced in a controlled manner within a specific mixing device. The concept of the **HY**drogen **D**euterium **E**quilibration loop (HYDE) at the TLK has been inspired by Kawamura *et al* [Kaw08] who used a similar technique for the characterization of gas chromatographs. The main differences are that in the HYDE system, two instead of one mixing vessel are installed, and the whole device is designed as a loop rather than a "once-through" line. These essential modifications accrue several advantages in the performance and analysis of measurements.

In a publication of Okuno *et al*, a similar mixing device was described [Oku91]. However, no details concerning the experimental setup and the calibration procedure were included. In addition, these authors did not include an uncertainty study or discussion.

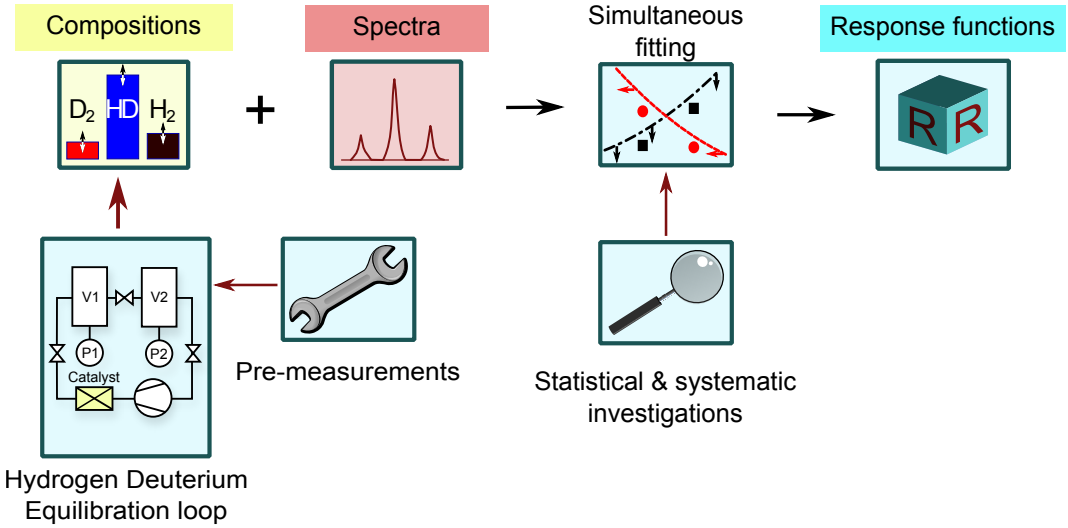

Figure 6.1: Graphical overview of the chapter content. The Hydrogen Deuterium Equilibration Loop (HYDE) provides accurate compositions. In order to ensure and to validate its performance, several pre-measurements have been performed. Then, the compositions of the samples and the corresponding Raman spectra are the input for the simultaneous fitting routine which finally provides the response functions. The fitting routine undergoes certain investigations in order to obtain statistical and systematic uncertainties of the response functions.

Content of chapter The content of this chapter is summarized in the flowchart of Fig. 6.1. First, the actual calibration method and related issues are introduced. Then, the HYDE loop employed for the calibration is described. Subsequently, results of the methods are presented and discussed with emphasis on the related calibration uncertainties. Some remarks on the usability and the prospects of these methods are given (*e.g.* use with tritium and options for integration into in-line process monitoring), before finally the implications of the calibration for the KATRIN sensitivity are summarized.

It should be noted that in this method a platinum catalyst is used for the production of equilibrated H_2, D_2, and HD mixtures. In previous studies within the diploma thesis of Philipp Herwig [Her11], a permeator (a heated Pd-Ag membrane which is only permeable by hydrogen isotopologues) was employed for the equilibration of the mixtures. However, the use of this device led to several systematic effects, like a partial demixing of the H_2, D_2, and HD sample or enhanced wall interactions at elevated operation temperatures ($\sim 400\,^{\circ}\mathrm{C}$), which could not be quantified. Parts of these findings are discussed in Section 6.5.2. As a consequence of these findings, the loop was altered to its current state with the main modification being the addition of a catalyst pebble bed. This was mainly done in the course of the bachelor thesis of Hendrik Seitz [Sei11]. Together with him, the final calibration procedure was developed and successfully applied. After minor modifications to the Raman system, Simone Rupp used this loop to perform the calibration again, which was necessary for the direct comparison of the calibration methods I and II. The measurement results discussed below are also found in her diploma thesis [Rup12]. All three theses have been supervised by the author within the framework of this PhD thesis. Only the parts which are important in the context of the calibration task for KATRIN are reported here. The reader is referenced to the individual theses for further details.

The most important results were also published in *Analytical Chemistry* [Sch13a] (see Appendix I).

6.2 Calibration method

In Section 3.3, the aims of a calibration were introduced: the measured Raman signal[1], S_x, shall be linked to the number of molecules N_x of a certain species x in the gas via the so-called response function R_x. The relation given according to Eq. 3.31 for a normalized Raman signal is

$$S_{x,\mathrm{rel}} = \frac{R_x \cdot N_x}{\sum_j R_j \cdot N_j} \ . \tag{6.1}$$

The determination of R_x for the three isotopologues H_2, HD, and D_2 is deemed to be straightforward, if gas mixtures of known composition are measured by Raman spectroscopy. However, HD gas of high purity is in general not commercially available and can only be produced with great efforts (*e.g.* from cryogenic distillation [Oht12]). Thus, the production of such a well-known mixture including the three gases cannot be simply produced by mixing. HD needs to be catalytically produced from well-known amounts of H_2 and D_2 via the isotopic exchange reaction

$$\mathrm{H_2} + \mathrm{D_2} \rightleftharpoons 2\mathrm{HD} \ . \tag{6.2}$$

The reaction is quantified by N_x^{i}, the known initial quantities of the hydrogen isotopologues ($x = \mathrm{H_2}$, $\mathrm{D_2}$, HD) before equilibration, and the final quantities, N_x^{eq}, at equilibrium conditions, which can be obtained from the reaction equation (Eq. 6.2):

$$N_{\mathrm{H_2}}^{\mathrm{eq}} = N_{\mathrm{H_2}}^{\mathrm{i}} - r \ , \tag{6.3}$$

$$N_{\mathrm{D_2}}^{\mathrm{eq}} = N_{\mathrm{D_2}}^{\mathrm{i}} - r \ , \tag{6.4}$$

$$N_{\mathrm{HD}}^{\mathrm{eq}} = N_{\mathrm{HD}}^{\mathrm{i}} + 2r \ , \tag{6.5}$$

with r being the so-called extent of reaction[2]. The concentrations of educts and products at equilibrium follow the law of mass action with the equilibrium constant

$$K = \frac{[\mathrm{HD}]^2}{[\mathrm{H_2}] \cdot [\mathrm{D_2}]} \ . \tag{6.6}$$

Eqs. 6.3 to 6.5 can be inserted into Eq. 6.6 which leads to

$$K = \frac{(N_{\mathrm{HD}}^{\mathrm{eq}})^2}{N_{\mathrm{H_2}}^{\mathrm{eq}} \cdot N_{\mathrm{D_2}}^{\mathrm{eq}}} \tag{6.7}$$

$$= \frac{(N_{\mathrm{HD}}^{\mathrm{i}} + 2r)^2}{(N_{\mathrm{H_2}}^{\mathrm{i}} - r)(N_{\mathrm{D_2}}^{\mathrm{i}} - r)} \ . \tag{6.8}$$

[1] The Raman signal is given by the integrated area under a certain peak.

[2] Note that the standard symbol for the extent of reaction is ξ. This symbol is also used in this publication: [Sch13a]. However, ξ has previously been utilized for the polarization cleanness in the depolarization ratio measurements. Therefore, the symbol r is used here to avoid ambiguities.

This is solved for the extent of reaction r (for $K \neq 4$)

$$r_{\pm}(K) = \frac{b \pm \sqrt{b^2 - 4(K-4)(K \cdot N^{\mathrm{i}}_{\mathrm{H_2}} \cdot N^{\mathrm{i}}_{\mathrm{D_2}} - \left(N^{\mathrm{i}}_{\mathrm{HD}}\right)^2)}}{2(K-4)} \tag{6.9}$$

with

$$b = K(N^{\mathrm{i}}_{\mathrm{H_2}} + N^{\mathrm{i}}_{\mathrm{D_2}}) + 4N^{\mathrm{i}}_{\mathrm{HD}} \,. \tag{6.10}$$

Only the solution r_- provides meaningful physical results. By inserting r_- into Eqs. 6.3 to 6.5, the quantities of the hydrogen isotopologues in the thermodynamical equilibrium N^{eq}_x can be calculated for a given reaction constant K and initial concentrations in the mixture, N^{i}_x.

In the mixing loop described in Section 6.3, well-known amounts N^{i}_x of hydrogen and deuterium can be mixed, and subsequently equilibrated. In addition, the value of the reaction constant K has to be well-known in order to obtain the gas composition accurately. This reaction constant is a function of temperature. In principle, the functional relation of $K(T)$ can be calculated accurately from statistical mechanics[3] as discussed in relevant literature [McQ76, Atk06].

However, the actual reaction temperature during a measurement run needs to be determined. The measurement of the temperature inside a catalyst pebble-bed reactor, as well as the thermocouple itself, are limited in measurement trueness. Thus, the uncertainty of the temperature measurement will propagate into the functional relation of $K(T)$. For this reason, an analysis method is needed which is less sensitive on the knowledge of the true reaction temperature value. The method presented here makes use of the possibility of reproducing the reaction temperature precisely ($\pm 2\,\mathrm{K}$) in different measurements without knowing its true value[4]. The experimental procedure will be discussed in Section 6.3. By taking several measurements at the same temperature T_0, but with varying gas composition, the same $K(T_0)$ should be found for different gas quantities N^{eq}_x. A term for the quantities N^{eq}_x in equilibrium state is obtained from Eqs. 6.3 to 6.5 with r_- inserted from (6.9). Exemplarily, this is demonstrated for $N^{\mathrm{eq}}_{\mathrm{H_2}}$:

$$N^{\mathrm{eq}}_{\mathrm{H_2}} = N^{\mathrm{i}}_{\mathrm{H_2}} - \frac{b - \sqrt{b^2 - 4(K-4)(K \cdot N^{\mathrm{i}}_{\mathrm{H_2}} \cdot N^{\mathrm{i}}_{\mathrm{D_2}} - \left(N^{\mathrm{i}}_{\mathrm{HD}}\right)^2)}}{2(K-4)} \tag{6.11}$$

with b from Eq. 6.10. Note that $N^{\mathrm{eq}}_{\mathrm{H_2}}$ is a function of $N^{\mathrm{i}}_{\mathrm{H_2}}$, $N^{\mathrm{i}}_{\mathrm{D_2}}$, $N^{\mathrm{i}}_{\mathrm{HD}}$, and K only.

Finally, the quantities N^{eq}_x and the measured relative Raman signals, $S_{x,\mathrm{rel}}$, can be inserted into Eq. 6.1. The parameters of interest, the three response functions R_x as well as $K(T_0)$, are then obtained from a simultaneous fit, which will be described below.

[3] In literature it is found, that theoretical calculations of $K(T)$ (*e.g.* [McQ76]) and experimental measurement [Rit34] agree within less than 2%. The theoretical calculations have been redone within this work by the author using the spectroscopic constants via [Vei87, Sch87]. The results deviated less than 0.3% from those of [McQ76].

[4] Note that in general the precision, *i.e.* reproducibility, of a measurement is not restricted by the limitations in the measurement trueness.

6.3 Experimental setup of the Hydrogen Deuterium Equilibration loop

Fig. 6.2 shows a sketch of the mixing loop setup HYDE. All vessels and pipes are made of stainless steel, which is the recommended material for hydrogen isotopologues processing facilities at the TLK [TLA13]. It features the material characteristics required from the *Pressure Equipment Directive 97/23/EC (PED)* such as chemical resistivity, ductility, toughness, and manufacturing properties [PED97]. Two gas bottles with H_2 and D_2 act as supply of the pure gases. From there, the evacuated volumes V1 and V2 can be filled. Both volumes are of the same size[5], so that a certain H_2-to-D_2 ratio in the gas composition can be achieved according to the ideal gas law by choosing the same ratio of pressures[6] in V1 and V2. The gas can then be circulated in the actual loop by a pump. There are three possible operation modes as indicated in Fig. 6.2:

(I) The gas can be cycled through the bypass. This mode is needed if only mixing of the pure gases is intended.

(II) The gas can be directed through a heated catalyst, in which parts of the H_2 and D_2 react to HD. The catalyst temperature defines the resulting thermal equilibrium state (see Eq. 6.8) and thus determines the amount of produced HD. The catalyst is made of $1/16$" Al_2O_3 pebbles coated with 0.5% Pt (Alfa Aesar). The pebbles are located inside a subsection (length of $130\,\mathrm{mm}$) of a stainless steel tube with a total length of about $180\,\mathrm{mm}$ and an inner diameter of $10\,\mathrm{mm}$. A NiCr-Ni thermocouple is integrated into the assembly to measure the temperature of the gas at the catalyst pebbles. The catalyst tube is surrounded by heating tape which is connected to a heating controller. Further details are given in [Sei11].

(III) The gas can be sent through the permeator, a Leybold-Heraeus palladium diffusion cell PA 150. There, hydrogen isotopologues can be absorbed and diffuse in atomic form through the membrane driven by a gradient of partial pressure (see Shu *et al* [Shu91] and references therein). Behind the membrane, the atoms recombine and form molecules again. The cell needs to be operated at $\sim 400\,^{\circ}\mathrm{C}$ since the membranes become brittle if operated with hydrogen at lower temperatures. Further details are given in [Her11].

The Raman cell is part of the HYDE loop and the mixture of inactive hydrogen isotopologues is pumped through it continuously. This allows one the continuous monitoring of the mixing or equilibration progress, respectively. A flow controller (F) provides a uniform gas flow (type 1179AX24CR1BVSPC1 of MKS).

[5]The volumes are $\mathrm{V1} = (1665 \pm 9)\ \mathrm{cm}^3$ and $\mathrm{V2} = (1655 \pm 8)\ \mathrm{cm}^3$ as determined by the method described in [Köl11].

[6]The pressure is measured by pressure gauges P1 and P2; $\mathrm{range} = 0 \ldots 1000\,\mathrm{mbar}$; $\mathrm{accuracy} = 0.3\,\mathrm{mbar}$ (Baratron type 626AX13MBD, MKS).

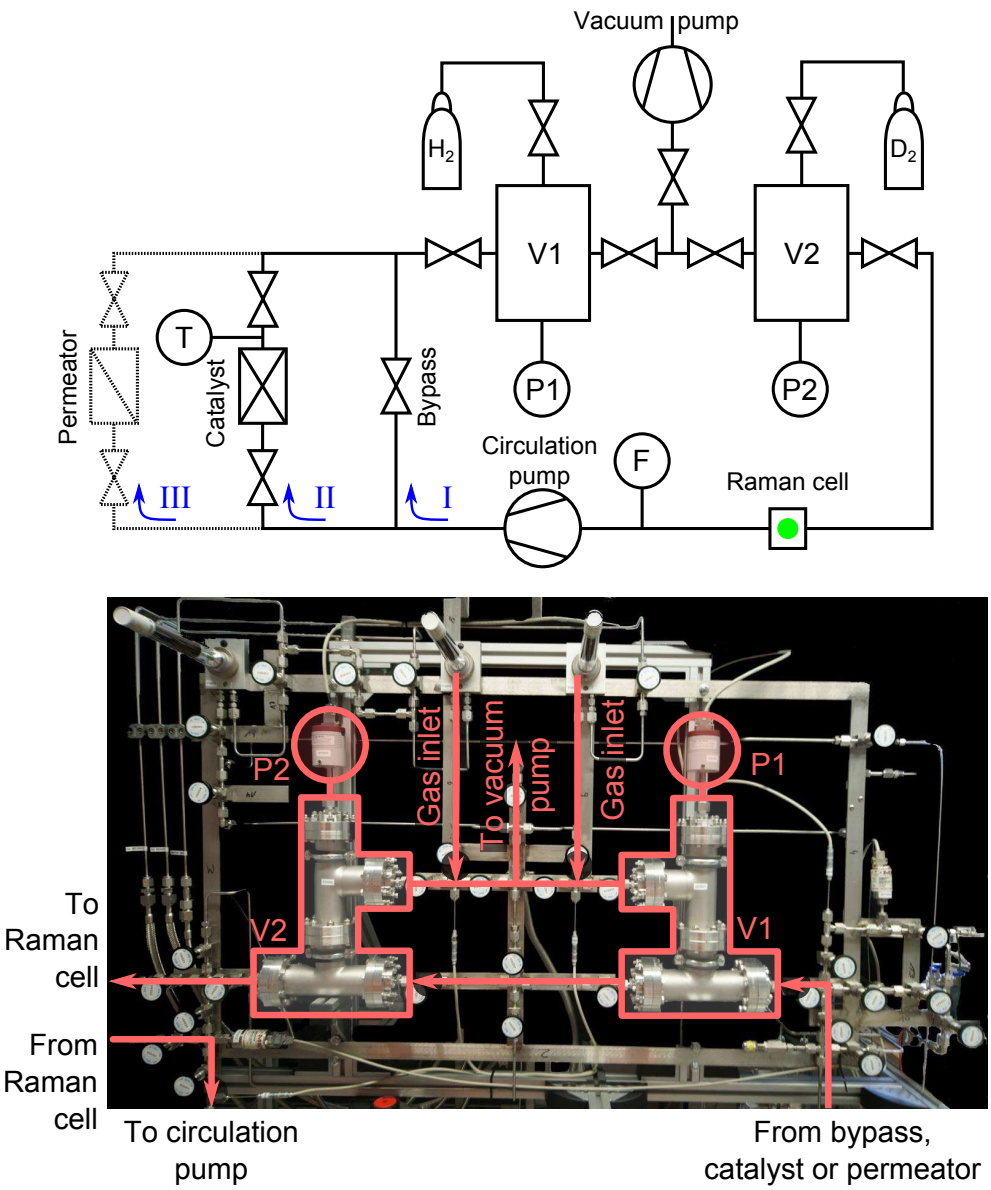

Figure 6.2: Setup of the HYDE loop. *Top:* Simplified sketch of the setup. As indicated on the left side of the flow-diagram, the loop can be operated in three different operational modes (bypass (I), catalyst (II), or permeator (III)). For details see text. *Bottom:* View on the main armature for gas mixing. Not shown are the LARA setup, the circulation pump and the catalyst and permeator.

6.4 Measurements

6.4.1 Preparations and pre-measurements

Before the actual calibration measurements can be performed, several steps are necessary to prepare the gas mixing loop. The detailed measurements are described in [Sei11]; here only an overview of the steps is presented:

1. A leak test of the loop is performed. This test is required for safety reasons due to the explosion hazard of hydrogen. It is also necessary to exclude the possibility that hydrogen leaks out of the system or that impurities leak into the system. The integral leak rate was found to be $< 10^{-9}\,\mathrm{mbar}\,\ell\,\mathrm{s}^{-1}$.

2. The loop is purged for an hour by circulating dry neon. The gas is heated to $300\,^{\circ}\mathrm{C}$ in the catalyst and then sent through a cold trap at LN_2 temperature. By this method residual moisture is removed. This is necessary, since water in the system can influence the gas composition via the exchange reaction $\mathrm{H_2O} + \mathrm{D_2} \rightleftharpoons \mathrm{HD} + \mathrm{HDO}$.

3. In order to reduce changes of the gas composition due to outgassing from the catalyst or the walls, the system is evacuated with a turbomolecular pump for more than $12\,\mathrm{h}$. Then the catalyst is baked out at $300\,^{\circ}\mathrm{C}$ and evacuated simultaneously for at least $3\,\mathrm{h}$.

4. A pre-run is performed to obtain a forced isotope exchange in the catalyst and its reactor walls, in order to avoid an influence by memory effects. This is done by loading the catalyst surfaces with the intended mixture of the main run. This is performed by heating the catalyst to $300\,^{\circ}\mathrm{C}$ and then circulating the mixture through it. At this temperature, exchange reactions are likely to happen (see *e.g.* Mizuno *et al* [Miz94]). By this procedure it should be assured that in case of outgassing in the following main run the gas composition does not change significantly.

Note that the first two steps have to be performed only once, whereas steps three and four are performed prior to each measurement.

6.4.2 Calibration measurements

The main calibration measurements were performed with different initial ratios of $\mathrm{H_2} : \mathrm{D_2}$ ($5:95$, $10:90$, $20:80$, ..., $90:10$, $95:5$). The preparation and measurement of the $20:80$ and $80:20$ mixtures were performed twice to have a handle on the reproducibility of the method. Measurements were performed for each composition at different temperature setpoints of the catalyst: 25, 50, 75, 100, and $125\,^{\circ}\mathrm{C}$. Higher catalyst temperatures were not employed due to enhanced exchange reactions above this level [Miz94].

The full measurement procedure is found in the appendix of the diploma thesis of S. Rupp [Rup12] and the publication of Schlösser *et al* [Sch13a].

The purity of the used gases was $99.9999\,\%$ for $\mathrm{H_2}$ and 99.7% for $\mathrm{D_2}$ (Air Liquide). In Raman measurements, these gas purities were confirmed. The residual 0.3% in the $\mathrm{D_2}$

bottle was identified as HD. This initial $N^{\mathrm{i}}_{\mathrm{HD}}$ was accounted for in the calculations (*c.f.* Eq. 6.11).

During the whole process of mixing and equilibration, Raman measurements were taken in order to monitor whether the composition was still changing or if a steady (equilibrium) state had been established. The standard acquisition time of a single measurement was $10\,\mathrm{s}$.

6.5 Discussion of the measurement results

In this section the main focus is on the results of the calibration and their uncertainties. After this description, supplementary information is given about the use of the permeator, further improvements to the setup, and the extension for potential use with tritium.

6.5.1 Calibration results and uncertainties

The initial ratios of $\mathrm{H_2} : \mathrm{D_2}$ in the mixture will be written in the form of mole fractions y_x rather than in the form of absolute numbers of molecules N_x :

$$y_x = \frac{N_x}{\sum\limits_j N_j} \quad \text{with j} = \mathrm{H_2,\ HD,\ D_2}\ . \tag{6.12}$$

For each measurement, the mole fractions y^{i}_x of the initial quantities were calculated from the inlet pressures, vessel volumes, and gas purities. The Raman spectra were pre-treated by the methods introduced in Section 4.2. In order to obtain the absolute Raman signal S_x for any of the isotopologues, the integrated area under the respective vibrational Q_1-branch was taken. Overlaps of the Q_1-branch of one isotopologue with the S_1 and O_1-lines of another isotopologue (compare Fig. 6.3) were corrected. Then, the relative Raman intensities, $S_{x,\mathrm{rel}}$, were calculated according to Eq. 6.1, and error propagation was performed in order to assign a statistical uncertainty, $\sigma\left(S_{x,\mathrm{rel}}\right)$, to each measurement point. These data were collated in analysis sets. The analysis principle has already been introduced in Section 6.2. Substituting Eqs. 6.3, 6.4, and 6.5 in Eq. 6.1 leads to the following expression (exemplarily given for $\mathrm{H_2}$):

$$S_{\mathrm{H_2,rel}} = \frac{R_{\mathrm{H_2}} N^{\mathrm{eq}}_{\mathrm{H_2}}}{R_{\mathrm{H_2}} N^{\mathrm{eq}}_{\mathrm{H_2}} + R_{\mathrm{D_2}} N^{\mathrm{eq}}_{\mathrm{D_2}} + R_{\mathrm{HD}} N^{\mathrm{eq}}_{\mathrm{HD}}} \tag{6.13}$$

$$= \frac{R_{\mathrm{H_2}}(N^{\mathrm{i}}_{\mathrm{H_2}} - r_-)}{R_{\mathrm{H_2}}(N^{\mathrm{i}}_{\mathrm{H_2}} - r_-) + R_{\mathrm{D_2}}(N^{\mathrm{i}}_{\mathrm{D_2}} - r_-) + R_{\mathrm{HD}}(N^{\mathrm{i}}_{\mathrm{HD}} + 2r_-)}\ . \tag{6.14}$$

Recall that r_- depends on the equilibrium constant K as shown in Eq. 6.9 above. The three $S_{\mathrm{x,rel}}$ terms are all functions of the measured mole fractions, y^{i}_x (which are proportional to N^{i}_x), with the three response functions $R_{\mathrm{H_2}}$, $R_{\mathrm{D_2}}$, R_{HD} and $K(T)$ as parameters. Since $S_{x,\mathrm{rel}}$ and y^{i}_x are known, the aforementioned parameters can be obtained by regression which were performed with a least-square fit using the MINUIT routine of ROOT [Bru97]. The three individual curves ($S_{\mathrm{H_2,rel}}$, $S_{\mathrm{D_2,rel}}$, and $S_{\mathrm{HD,rel}}$ according to Eq. 6.14) were fitted simultaneously to the measured data sets for each of the five catalyst temperatures T. The

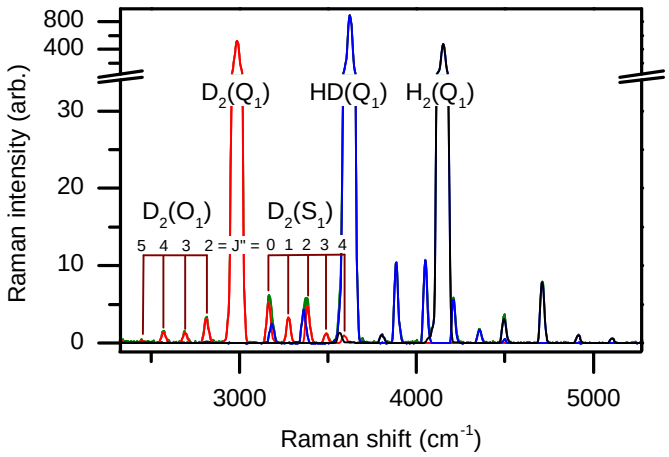

Figure 6.3: Raman spectrum of H_2, HD, D_2 obtained in a calibration measurement. Here, the total cell pressure $p \approx 330\,\mathrm{mbar}$; an acquisition time $t = 10\,\mathrm{s}$. The individual components (red, blue and black) were obtained by fitting to the measured spectrum (green). Note that the vibrational-rotational lines (S_1 and O_1) are labeled only for D_2. Figure already published in [Sch13a].

data and fitting curves before and after the equilibration process are displayed in Fig. 6.4. The standard errors of each coefficient's estimate, which are returned from MINUIT, are of the order of about 70%. This is probably due to the strong correlation in the fitting parameters. Therefore, the estimation of the statistical uncertainty of the fitting results was performed by statistical techniques such as the Jackknife and the Bootstrap method (according to [Efr94, Efr83]). These re-sampling techniques are recommended in general for statistical analysis if the sample size is not too low ($n < 5$) [Dav03]. Details of the application of the Bootstrap method on the HYDE measurement data is found in Appendix H.

Said methods only provide information on the statistical uncertainty. In order to investigate systematic influences of this analysis method, one can fix different fitting parameters in the regression of the ternary mixture and evaluate the resulting effect on the free parameters. Thus, three scenarios were selected for the systematic study:

1. In the basic scenario, all parameters (R_{H_2}, R_{D_2}, R_{HD}, and $K(T)$) are free.

2. From the binary fit of the non-equilibrated mixture, only R_{H_2} and R_{D_2} can be obtained. However, these values should be less influenced by systematic uncertainties than in the ternary fit of the equilibrated mixture, since no catalysis-related effects occur. Thus, in the second scenario for the ternary fit, the ratio of $R_{\mathrm{H}_2}/R_{\mathrm{D}_2}$, as obtained from the binary mixture fit, is fixed. R_{HD} and $K(T)$ are the only free parameters in this case.

3. In the last scenario, the temperature-dependent reaction constants $K(T)$, which are obtained from calculations, can be fixed as external input in the fitting. Therefore, only the response functions are free parameters.

In addition, the measurements at different catalyst temperatures provide a further systematic study since only the parameter $K(T)$ should be influenced by the temperature while

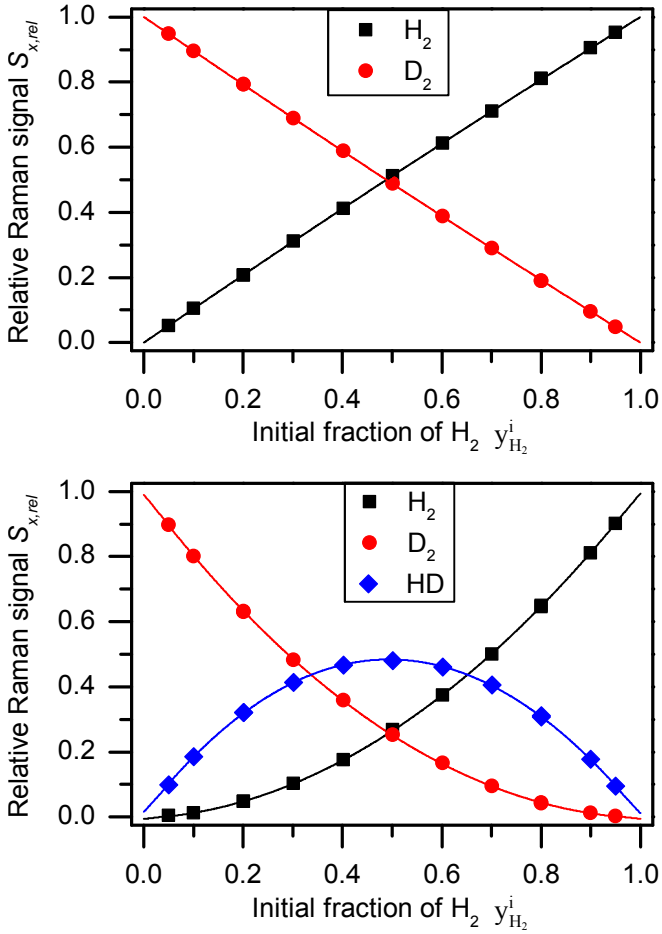

Figure 6.4: Fitting of the HYDE data at a catalyst temperature of 25 °C. The horizontal axis represents the initial mole fraction of H_2, $y^i_{H_2}$, before the equilibration of the mixture. The vertical axis represents the measured relative Raman intensities of the three components. Legend: symbols represent measurement points; lines are fit curves. *Top panel:* before equilibration (binary mixture). *Bottom panel:* after equilibration (ternary mixture). Note, that the error bars of the measurement points, which are calculated via error propagation from Raman intensity and pressure/volume uncertainties, are all < 0.002 and thus smaller than the size of the symbols. Figure already published in [Sch13a].

Table 6.1: Overview of the results of the relative response functions for different catalyst temperatures. The present values are obtained for the fit scenario in which the $R_{\mathrm{H}_2}/R_{\mathrm{D}_2}$ ratio is fixed. σ is the relative statistical uncertainty obtained by bootstrapping. Δ is the relative difference to the values obtained for the fit scenario where all parameters are free. T is the catalyst temperature setpoint. Full tabulations of the results of all fitting scenarios including K are given in the appendix of [Rup12].

T	$R_{\mathrm{H}_2,\mathrm{rel}}$			$R_{\mathrm{D}_2,\mathrm{rel}}$			$R_{\mathrm{HD},\mathrm{rel}}$		
(° C)	Value	σ (%)	Δ (%)	Value	σ (%)	Δ (%)	Value	σ (%)	Δ (%)
25	1.0128	0.15	0.33	0.9692	0.14	-0.33	1.0180	0.29	-0.01
50	1.0116	0.17	0.40	0.9681	0.16	-0.42	1.0202	0.33	0.00
75	1.0103	0.21	0.44	0.9669	0.20	-0.44	1.0228	0.41	-0.02
100	1.0084	0.27	0.39	0.9651	0.25	-0.37	1.0265	0.51	-0.03
125	1.0053	0.37	0.24	0.9620	0.35	-0.20	1.0327	0.70	-0.04

the R_x parameters are expected to be mostly unaffected.

In Tab. 6.1 the relative response functions

$$R_{x,\mathrm{rel}} = R_x/R_{\mathrm{mean}} = n \cdot R_x / \sum_{j=1}^{n} R_j \tag{6.15}$$

are listed, with R_x being the fit results at the different catalyst temperatures. In the employed fit scenario the ratio $R_{\mathrm{H}_2}/R_{\mathrm{D}_2}$ is fixed; as uncertainties, bootstrap errors and the difference to the results of one of the other fit scenarios (all parameters are kept free) are given.

Discussion of uncertainties of the calibration method The evaluation of the calibration method requires discussing statistical uncertainties and systematic effects. The latter can be investigated by modifying the parameter settings of the aforementioned fit routines (*e.g.* by the three fit scenarios), or by establishing different environmental conditions such as different temperature levels. In Fig. 6.5, the results of the three fit scenarios are shown. In addition, the graph shows the influence of the catalyst temperature on the fit results. The following observations can be made:

1. The error bars as obtained from bootstrapping become larger with increasing temperatures. The error bars at the $125\,^{\circ}\mathrm{C}$ temperature setting are about twice as large as the ones from the measurements at around $25\,^{\circ}\mathrm{C}$. On first sight, this increase can be deemed to be purely statistical, but on closer inspection the effect has a systematic reason.

   Probably this is due to a combination of effects, namely (i) a higher exchange rate of atoms or molecules with the heated stainless steel walls [Miz94] and the catalyst material (*e.g.* [Chr76] and references therein) and thus high dependence of the current composition on the previous; and (ii) the strong isotope effect for hydrogen isotopes/isotopologues (compared to other elements). In this context, especially the different permeation constants (*e.g.* [Kat81] and references therein) and thermal

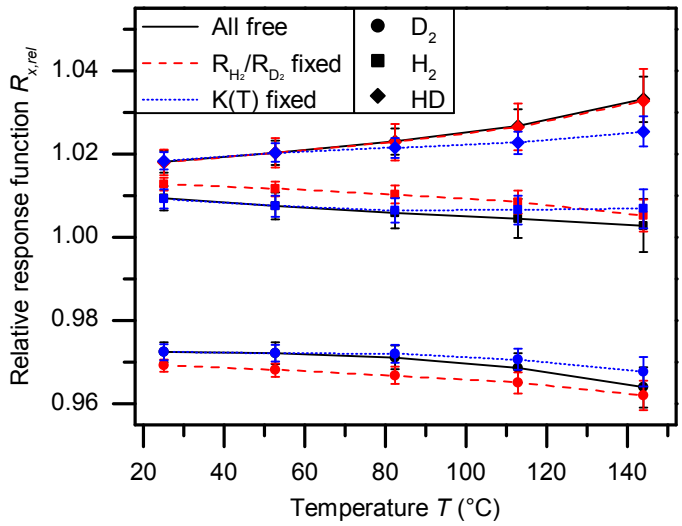

Figure 6.5: Influence of the catalyst temperature on the fit results of the relative response function $\mathbf{R_{x,rel}}$. Color and line style indicate the fit scenario; the symbol style represents the type of isotopologue. Values and errors bars are obtained by bootstrapping. Note that the measured temperature values differ from the temperature setpoints. Further explanations in the main text. Figure already published in [Sch13a].

conductivities are of relevance (*e.g.* [Sax70]). The individual points in the graphs are affected systematically by these temperature-dependent effects and thus slightly shifted in a certain direction. The bootstrapping method randomly resamples the data. In some of the resampled sets, said systematic effects can manifest themselves in a shift of the fitting results in one or the other direction. Thus, the statistical distribution can tend to larger bootstrap errors. For this reason, in the following discussion it will be assumed that the values at $T = 25\,^{\circ}\mathrm{C}$ are most trustworthy.

2. The fitting results for the fit scenario with fixed ratio of $R_{\mathrm{H_2}}/R_{\mathrm{D_2}}$ obtained from the binary fit, *i.e.* from the non-equilibrated mixtures (red dashed lines), is compared to those obtained by other fit methods with free ratio (black straight and blue dotted lines) in Fig. 6.5. In case of R_{HD}, the results are almost identical at $25\,^{\circ}\mathrm{C}$. In the case of $R_{\mathrm{H_2}}$ and $R_{\mathrm{D_2}}$ the fit results exhibit a small offset ($< 0.5\%$). This shows that the use of the catalyst and its pre-conditioning run (see Section 6.4.1) have a slight effect on the H:D ratio in the gas mixture and thus on the $\mathrm{H_2} : \mathrm{D_2}$ ratio. This is probably due to reactions of H and D atoms with walls or catalyst material. It should be noted that the systematic shift in the $R_{x,\mathrm{rel}}$ functions is only of the order of the statistical error.

3. If the reaction constant $K(T)$ is not fixed in the fit (black straight and red dashed line), R_{HD} increases with temperature while $R_{\mathrm{H_2}}$ and $R_{\mathrm{D_2}}$ decrease. Naturally, R_x should not have any temperature dependence. When fixing the reaction constants to the value from calculation (blue dotted line), this temperature dependence is strongly suppressed. K and R_{HD} are correlated due to their similar impact on the trend of the HD curve in Fig. 6.4. Therefore, the tendency to larger values of $R_{\mathrm{HD,rel}}$ at higher temperatures in cases with free K hints to a slight underestimation of K. It is also interesting to note that the $R_{x,\mathrm{rel}}$ values for fixed (blue dotted) and free (black

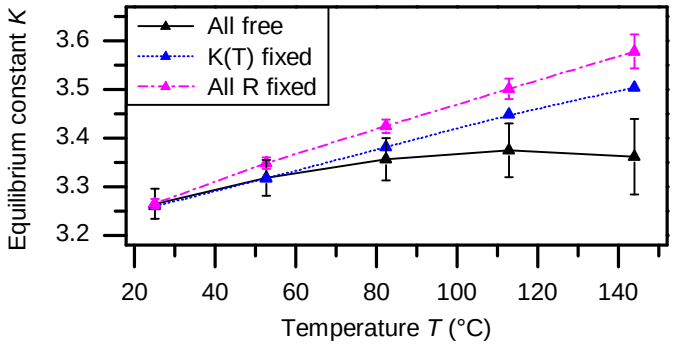

Figure 6.6: Fit results of the equilibrium constant $\mathbf{K(T)}$. No error bars are given for the "K(T) fixed" scenario, since these values are derived from theory. The $K(25\,^{\circ}\mathrm{C})$ values agree for a three scenarios, but the difference of these theory results to the fitted results increases with larger temperature.

straight) $K(T)$ values are nearly identical for temperatures smaller than $T < 85\,^{\circ}\mathrm{C}$, which shows the overall robustness of this approach.

Further investigation of the $K(T)$ dependence of the equilibration reaction is performed by a further fit, in which all three R_x values are fixed, as obtained from the "all free" fit at $T = 25\,^{\circ}\mathrm{C}$. Thus, the only free parameter remaining is K. In Fig. 6.6 the fitted K values are plotted together with the literature values as a function of temperature. Though following the same trend, it can be seen that these fitted K are higher than the expected literature values. However, it cannot be ascertained whether this is due to inaccurate literature values or incorrect temperature measurements. Despite this, it should be noted that all curves agree at $K(25\,^{\circ}\mathrm{C}) = 3.26 \pm 0.01$.

Based on these considerations, the final results for the response functions, $R_{x,\mathrm{rel}}$, were chosen from the scenario with a fixed ratio of $R_{\mathrm{H}_2}/R_{\mathrm{D}_2}$ at a setpoint temperature of $25\,^{\circ}\mathrm{C}$ (see Tab. 6.1). The fit of the binary mixture should exhibit the highest trueness since it takes advantage of the absence of any systematic effects which occur only during the equilibration. In summary of the enumeration above, the $T = 25\,^{\circ}\mathrm{C}$ values were chosen as final results for the following reasons: (i) the statistical errors from the bootstrap method are the smallest for this temperature; (ii) the temperature gradient between the catalyst reactor and the rest of the gas system is minimal since said temperature is approximately room temperature, so that the equilibrium constant K is the same in the whole gas system; (iii) exchange reactions with walls are minimized; and (iv) the confidence in the equilibrium constant is the highest.

Concerning the fitting uncertainty obtained in this manner, the most essential point which should be recalled from the previous paragraphs is that the fit converges to results with statistical errors in the sub-percent range. The systematic shift is of similar size if different parameters are fixed (R and/or $K(T)$), or if the operational temperature is changed. The discussion above shows that it is legitimate to use this spread as systematic error. Therefore, the systematic and statistical uncertainty as listed in 6.1 are added:

$$\Delta R_{x,\mathrm{rel}}^{\mathrm{tot}} = \sqrt{\sigma(R_{x,\mathrm{rel}})^2 + \Delta(R_{x,\mathrm{rel}})^2}\,. \tag{6.16}$$

The following results, valid for the employed Raman system, are obtained:

$$R_{\mathrm{H_2,rel}} = 1.0128 \pm 0.0037 \tag{6.17}$$

$$R_{\mathrm{D_2,rel}} = 0.9692 \pm 0.0036 \tag{6.18}$$

$$R_{\mathrm{HD,rel}} = 1.0180 \pm 0.0029 \tag{6.19}$$

This means that the calibration uncertainty of the Raman system at HYDE is within 0.5%, which proves that this method and device is well capable to provide accurate calibration mixtures. Further conclusions are found in Section 6.6.

6.5.2 Remarks on the use of the permeator

The hydrogen mixtures presented in this work so far were all equilibrated by the means of a catalyst reactor. However, in Section 6.3 it was mentioned that the use of a permeator would be another possibility for the equilibration of gas mixtures. In 2005, Borysow and Fink used a Raman system to monitor exchange reactions in gaseous hydrogen and deuterium samples [Bor05]. For the generation of HD, they employed a unit manufactured by Gas Technologies (model HP-4), which is based on permeation through a palladium membrane. In test measurements performed in the framework of this thesis, it was confirmed that these membranes[7] change the gas composition due to different permeabilities of atomic H and D through the bulk of the membranes, as predicted by Glugla *et al* [Glu06]. This is demonstrated in Fig. 6.7, which shows a measurement of a mixture with initial composition of $50\%\,\mathrm{H_2}$ and $50\%\,\mathrm{D_2}$. According to Eqs. 6.3 and 6.4, the ratio of $N^{\mathrm{eq}}_{\mathrm{H_2}}/N^{\mathrm{eq}}_{\mathrm{D_2}}$ (or $S_{\mathrm{H_2}}/S_{\mathrm{D_2}}$) should not be influenced in this special case, even when the extent of reaction, r, changes due to shifts in $K(T)$. The measurement results as shown in Fig. 6.7 prove that this ratio is constant as long the mixture is cycled through the catalyst, independently of the catalyst temperature. However, when the gas flow is directed from the catalyst to the permeator, this ratio suddenly changes by about 3% and stays at this value if the flow is switched back through the catalyst again. Deuterium has a lower permeability coefficient than hydrogen [Glu06], which is why its atoms are partly retained by the membranes; this in turn manifests itself in the reduced Raman signal. Accordingly, it can be concluded that permeators cannot be recommended for the production of highly accurate hydrogen mixtures. For further discussions see [Her11, Sei11].

6.5.3 Possible improvements for further reduction of systematic uncertainties

Even though the calibration results reveal that a high accuracy can be reached with the demonstrated method, some modifications to the actual gas mixing setup (see Fig. 6.2) are suggested to further reduce systematic effects:

(i) The length of the piping between pump, Raman cell, vessels, and catalyst is of the order of $5\,\mathrm{m}$. This permits convenient handling of the valves, but at the same time it offers a large inner surface ($\sim 0.07\,\mathrm{m}^2$), where exchange reactions can happen. In principle, the piping could be reduced by a factor of 2 to 3. In general, it is recommended to minimize the piping as much as possible in similar setups.

[7] In this case the Leybold-Heraeus palladium diffusion cell PA 150.

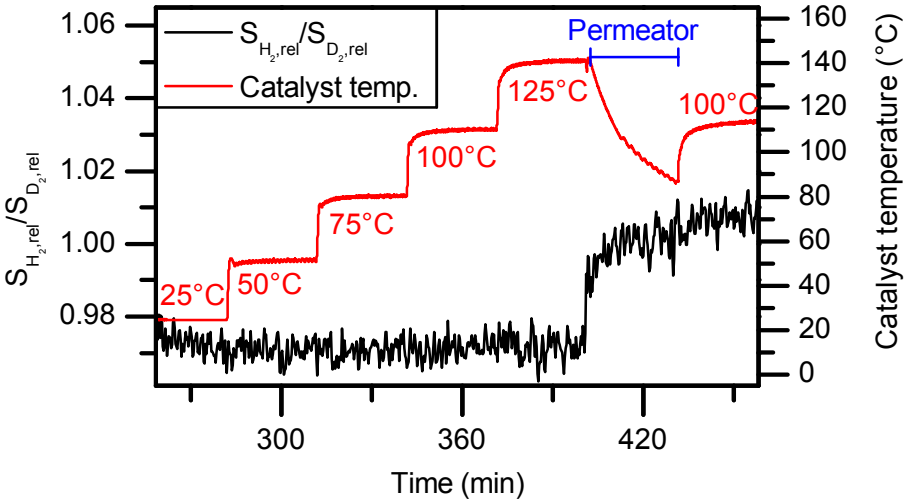

Figure 6.7: Time trend of catalyst temperature and relative intensity ratio of H_2/D_2 influenced by permeator operation. The initial concentration $[H_2] : [D_2]$ was 1:1. The HD concentration is not shown here. Note that this measurement was performed with a different grating spectrometer than the one used in the other calibration measurements, so that the ratio of $S_{H_2,rel}/S_{D_2,rel}$ differs from what would be expected from the reported $R_{H_2,rel}/R_{D_2,rel}$ ratio. The temperature labels refer to the temperature setpoints of the heating tape outside of the catalyst tube; the actual temperatures were measured directly within the catalyst pebbles. Figure already published in [Sch13a]; based on [Sei11].

(ii) Currently, the gas mixing vessels consist of two off-the-shelf ConFlat®-T-pieces. Using these standard components offers a high similarity of both vessel volumes and thus small systematic uncertainties in the initial mole fractions y_x^i. However, due to inadequate pipe routing in the setup, a 'dead volume' was created where the mixing of the gas is suppressed. This difficulty has been overcome by long mixing periods ($\sim 25\,\mathrm{min}$) with intermittent blocking of the gas stream in order to pump all gas in one of the vessels while the other was emptied [Her11, Sei11]. Instead, a more sophisticated gas flow design through the vessels would ease the efforts of forcing the species to mix.

(iii) Finally, the design of the catalyst reactor could be optimized to gain a better control over the reaction temperature and its homogeneity within the reactor tube, so that the equilibrium condition can be obtained more accurately.

6.5.4 Upgrade for the use with tritium

Thus far the application of the method has only been demonstrated for the three non-radioactive isotopologues. The extension of the described calibration method to tritiated molecules is a demanding task. The arguments were already mentioned in Section 3.3.1 and will now be re-discussed, in particular with regard to the current results and experiences.

(i) The β-activity of tritium will induce radio-chemical reactions [Sou86]. This means that gas mixtures will equilibrate even in the absence of a catalyst. The time constant

of this self-equilibration was reported by Uda *et al* [Uda92] to be of the order of 12 hours. This implies additional systematic uncertainties for the binary mixture of T_2 with H_2 or D_2, since the formation of HT or DT, respectively, will commence as soon as the pure gases merge.

Another radio-chemical effect is related to exchange reactions with the stainless steel walls [Gil80] or the formation of methane [Mor77], as already observed in past experiments at LOOPINO [Fis11].

(ii) The purity of the available T_2 is limited. At the TLK, a purity of up to 98% can be obtained from the isotope separation system [Dör05]. In addition, the effects mentioned in the previous point degrade the purity of stored T_2 with time. A high purity of the initial gases is important for the calculation of the mole fractions which find their way into the regression analysis. Unaccounted impurities of only several percents can deteriorate the trueness of the calibration results. A possible solution may be the measurement of the tritium purity before the calibration to have a first rough idea.

(iii) When tritium is stored over longer periods of time, the amount of $^3\mathrm{He}$ from radioactive decay increases (about 0.5% of an amount of tritium decays every month). This noble gas is Raman inactive, so that it can not any longer be assumed that the sum of the branch intensities in the Raman spectra is equivalent to 100% of hydrogen isotopologues in the gas. Therefore, the $^3\mathrm{He}$ impurities need to be removed efficiently before the gas is mixed.

(iv) All tritium handling facilities need additional technical efforts. The system needs to be integrated into a secondary containment (*e.g.* a glove-box), and a tritium retention system needs to be connected to this containment. Furthermore, all parts in the system need to fulfill requirements for tritium compatible systems [TLA13].

The aforementioned caveats may prohibit that the calibration accuracy obtained with the HYDE loop ($< 0.5\%$) can be reached by a potential hydrogen-deuterium-tritium mixing loop. Furthermore, safety considerations such as the maximum allowed tritium inventory may constrain the employed amount of tritium gas in the mixtures.

Despite these issues, a hydrogen-deuterium-tritium mixing loop is currently being designed, and based on the experiences of the calibration performance of HYDE [Röl13]. It should allow investigating the quantitative influence of said limitations involved with the handling of tritium.

6.6 Conclusions

In this chapter, a method for the accurate production of gas samples with non-radioactive hydrogen isotopologues was presented, and results of a calibration of the KATRIN Raman system were presented and discussed. The total uncertainty of the calibration is less than 0.5%. This is far better than the requirements of the KATRIN experiment. However, it should be kept in mind that the calibration is not possible for the tritiated molecules. The coverage of all six hydrogen isotopologues is obtained by the method using theoretical

intensities and the measurement of the spectral intensities as discussed in the previous chapter.

The following chapter will bring both calibration approaches together in order to compare the resulting response functions.

Chapter 7

Comparison of calibration methods

In the previous chapters two independent calibration approaches were introduced.

The first approach was based on a sample-free method using theoretical Raman intensities and experimental data on the spectral sensitivity of the Raman system. The input parameters for the theoretical intensity calculations, a and γ, were verified by depolarization ratio measurements. The predicted and experimental results agree within the estimated uncertainty. The compatibility thus reveals that the quantum theoretical model by Schwartz and LeRoy [Sch87] is well-able to provide consistent values for the polarizabilities. It should be recalled that this method of measuring depolarization ratios can only provide a comparison of the a and γ pair for each individual Q_1 Raman line, but not for theoretically predicted a (or γ) values of different Raman lines.

In order to handle this caveat, a fully independent calibration approach was required, despite the verified power of prediction of the theoretical data for the depolarization ratio. This second calibration approach is based on the production of accurate gas samples by using the HYDE loop. Due to several reasons connected to the intrinsic β-activity of tritium, this procedure was limited, for the time being, to the three non-radioactive isotopologues, H_2, HD, and D_2 only.

Both approaches independently were successful and yielded accurate values. In this chapter, the results of both approaches are compared in order to ascertain whether they agree within the estimated uncertainties. The second issue of this chapter is then related to the implication for the KATRIN experiment.

7.1 Discussion of calibration results

The response functions obtained from both approaches, R_x and R'_x, were normalized to different reference values. Therefore, it is necessary to find a common base for the comparison. The recommended normalization is to use relative response functions as introduced in Eq. 6.15:

$$R_{x,\mathrm{rel}} = R_x/R_{\mathrm{mean}} = n \cdot R_x/\sum_{i=1}^{n} R_i \,. \tag{7.1}$$

Another possibility to compare the calibration results is to take the ratios of two response functions R_i/R_j, where the indices relate to the different isotopologues. The related data of both approaches are summarized in Tab. 7.1. The systematic uncertainties, Δ_x, are derived from error propagation of the relative response functions. Recall that the uncertainties from the response functions generated from the theoretical intensity and spectral sensitivity approach were in general dominated by the error related to the theory (*c.f.* Tab. 5.7). In Tab. 7.1 it can now be seen that the uncertainty related to the spectral sensitivity, Δ_{sens}, has become an essential part of the total uncertainty, Δ_{tot}, in the formation of relative response functions ($R_x \rightarrow R_{x,\mathrm{rel}}$). The reason for this is the large uncertainty of the response function for H_2 (associated with the larger errors in the uncertified spectral sensitivity), which dominates the uncertainties of all $R_{x,\mathrm{rel}}$ functions by error propagation.

On the other hand, the uncertainties of the relative response function values obtained by using the gas sample method with HYDE are well below 0.5%. As expected, this technique offers a significantly better accuracy, but at present has the tritium-related limitation explained in Chapter 6.

The table entries show that the relative response function values $R_{x,\mathrm{rel}}$ and the response function ratios R_i/R_j obtained from the two approaches overall agree to better than 2%. The only exception is the $R_{\mathrm{H_2}}/R_{\mathrm{D_2}}$ ratio, which differs by 3.4%. As was pointed out above, the higher uncertainty in the calibration of the spectral sensitivity in the wavelength range of H_2 is the most likely the cause for this deviation. Nevertheless, the overall agreement of both approaches is well within the bounds given by the total uncertainties in the theoretical Raman signal amplitudes of about 3.1% for the relative R-values and 5.2% for the ratios.

The power of prediction of the quantum-theoretical model from Schwartz and LeRoy [Sch87], which provides the a and γ values for each individual Raman line, has been demonstrated in Chapter 5 by the depolarization measurements. Now, the deficit of not being able to compare theoretical intensities between different Raman lines was compensated by the gas sampling method in the HYDE investigations. The agreement of the two calibration approaches increases the confidence in the use of the theoretical

Table 7.1: Comparison of response functions obtained from both calibration approaches. Note that the $R_{x,\mathrm{rel}}$-representation is more suitable for comparing the two approaches than the R'_x-representation, for which the data are normalized to $R'_{\mathrm{H_2}} = 1$ (*c.f.* Tab. 5.7). Δ_{theo} describes the uncertainty related to the theoretical intensities, Δ_{sens} relates to the uncertainty of the determination of the spectral sensitivity. The total uncertainty is given as $\Delta R'_{\mathrm{tot}} = \sqrt{(\Delta R'_{\mathrm{theo}})^2 + (\Delta R'_{\mathrm{sens}})^2}$.

	(A) Theoretical Raman signals				(B) HYDE measurements		Difference $((\mathrm{A}) - (\mathrm{B}))/(\mathrm{B})$
	Value	Δ_{theo} (%)	Δ_{sens} (%)	Δ_{tot} (%)	Value	Δ_{tot} (%)	(%)
$R_{\mathrm{H_2,rel}}$	1.032	2.4	2.0	3.1	1.013	0.4	1.9
$R_{\mathrm{D_2,rel}}$	0.955	2.7	1.1	2.9	0.969	0.4	−1.5
$R_{\mathrm{HD,rel}}$	1.013	2.4	1.2	2.8	1.018	0.3	−0.5
$R_{\mathrm{H_2}}/R_{\mathrm{D_2}}$	1.081	4.5	3.0	5.4	1.045	0.7	3.4
$R_{\mathrm{HD}}/R_{\mathrm{D_2}}$	1.061	4.5	1.0	4.6	1.050	0.3	1.0

intensities and spectral sensitivity for the sample-free determination of the response functions for all hydrogen isotopologues.

Regardless of this fact, future comparisons including then also the tritiated species HT, DT and $\mathrm{T_2}$ are of high interest to finally support this versatile calibration approach. These studies require a similar gas mixing device as the one used here (HYDE), but which fulfills the tritium-compatibility requirements recommended in Section 6.5.4.

7.2 Implications for the KATRIN experiment

The agreement of the two independent calibration approaches within the estimated uncertainties is a very important result for the future long-term, high-accuracy monitoring of the gas composition of the Windowless Gaseous Tritium Source (WGTS) of KATRIN. It puts the use of a sample-free calibration procedure for all available and future Raman systems on solid experimental footing. In particular, the KATRIN requirement of a trueness of the response function of about 10% or better is met (see Section 2.4). The difference of the determination of the response function determination of the two approaches is less than 2%, with an uncertainty of the relative response function being better than 3.1%. This is an indication that the requirement can easily be met with the suggested methods.

In the following, the impact of the calibration uncertainties in R_x on the systematic error in the mole fractions y_x (relative concentrations) for a KATRIN-like tritium mixture will be outlined. The illustration will be shown for the case of the LOOPINO long-term test reported in [Fis11, Stu10b]. The runs at the test circulation loop, LOOPINO, were intended to verify the reliability of LARA measurements under the same conditions as for KATRIN. Thus, the gas mixture, which was circulated, exhibited a high tritium purity of $\sim 97\%$ at the beginning. Its Raman spectrum is shown in Fig. 7.1.

The relative intensities of the Q_1-branches of all hydrogen isotopologues, $S_{x,\mathrm{rel}}$, were extracted from the spectrum. Overlaps between the S_1-branch of $\mathrm{T_2}$ and the Q_1-branches of DT and $\mathrm{D_2}$ were corrected. The signal intensity of the Q_1-branch of $\mathrm{H_2}$ was below the noise level. Statistical uncertainties and temporal fluctuations in the Raman intensity are not considered in the scope of this illustration, so that the $S_{x,\mathrm{rel}}$ is reported in Tab. 7.2 without error.

At the time when the LOOPINO measurement was performed, no method for the spectral sensitivity determination of the system was available. However, the aim of this example case is rather to provide an impression of the resulting systematic uncertainty than to show the exact sample concentration. Therefore, the R_x values from the calibration of the MonLARA system were used. This procedure can be legitimized using the following arguments:

1. The spectral sensitivity profiles of both systems exhibit a similar trend. This statement is supported by investigations of the spectral sensitivity of both systems with different spectrometers in the thesis of Simone Rupp [Rup12].

2. The part of the uncertainty related to ΔR_{theo} is completely system-independent. Furthermore, the other part, ΔR_{sens}, depends almost exclusively on the certification of the luminescence standard by NIST (see Section 5.4.4).

Due to these reasons, the R_x values and uncertainties employed here are taken from Tab. 5.7.

Finally, the mole fractions, y_x, should be calculated from the response functions, R_x and relative intensities, $S_{x,\mathrm{rel}}$. Using Eq. 3.30 and solving it by N_x leads to

$$S_x = R_x \cdot N_x \ , \tag{7.2}$$

$$N_x = \frac{S_x}{R_x} \ . \tag{7.3}$$

Note that S_x will be substituted in the following by $S_{x,\mathrm{rel}} = \frac{S_x}{\sum_j S_j} = \frac{R_x \cdot N_x}{\sum_j R_j \cdot N_j}$ (Eq. 3.31).

From Eq. 6.12, the mole fraction y_x is obtained:

$$y_x = \frac{N_x}{\sum_j N_j} = \frac{\frac{S_x}{R_x}}{\sum_j \frac{S_j}{R_j}} \tag{7.4}$$

with $j = \mathrm{T}_2, \ldots, \mathrm{H}_2$. The uncertainty is then propagated to obtain Δy_x:

$$\Delta y_x = \sqrt{\sum_j \left(\frac{\mathrm{dy_x}}{\mathrm{dR_j}}\right)^2 (\Delta R_j)^2} \ . \tag{7.5}$$

The analytical calculation is performed with the help of a computer algebra system. The numeric results for $y_x \pm \Delta y_x$ are also tabulated in Tab. 7.2.

The table presents these values with absolute systematic errors (Δy_x) and relative errors ($\Delta y_x / y_x$). The absolute systematic errors all lie below the 0.1% limit. For the most relevant

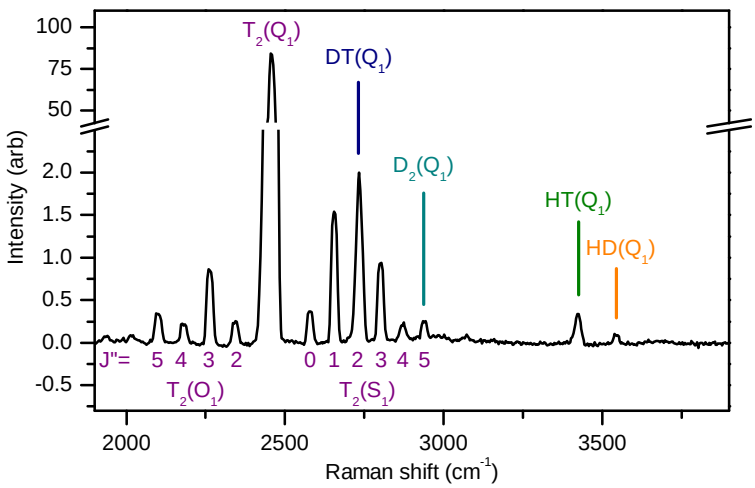

Figure 7.1: Spectrum of a circulating tritium sample with high purity. The Q_1-branches of all isotopologues present in this mixture are indicated as well as the S_1/O_1-branches from T_2 with rotational quantum number J''. The overlap of the T_2 ($\mathrm{S}_1(\mathrm{J}'' = 2)$)-line and the DT ($\mathrm{Q}_1$)-branch was corrected for in the determination of the Raman intensities. The same was done for the overlap of the T_2 ($\mathrm{S}_1(\mathrm{J}'' = 5)$) line and the D_2 (Q_1)-branch. The spectrum was acquired at the beginning of the long-term run of the LOOPINO test experiment [Fis11].

Table 7.2: Systematic uncertainty in a KATRIN-like measurement. All R_x values and their uncertainties are obtained from Tab. 5.7. The values for $S_{x,\mathrm{rel}}$ are extracted from the spectrum in Fig. 7.1. The parameters $y_x \pm \Delta y_x$ is obtained from the evaluation of Eqs. 7.4 and 7.5. For further details see text.

Isotopologue	$R_x \pm \Delta R_x$	$S_{x,\mathrm{rel}}$ (%)	$y_x \pm \Delta y_x$ (%)	$\Delta y_x / y_x$ (%)
T_2	0.866 ± 0.034	97.72	97.86 ± 0.10	0.10
DT	0.914 ± 0.034	1.57	1.49 ± 0.08	5.28
D_2	0.925 ± 0.031	0.35	0.33 ± 0.02	5.10
HT	0.960 ± 0.031	0.32	0.29 ± 0.01	4.97
HD	0.981 ± 0.030	0.04	0.04 ± 0.00	4.92
H_2	1.000 ± 0.042	-	-	-

component, T_2, also the relative systematic error is at this level. For a KATRIN-like composition, this implies that the systematic uncertainty (trueness) and statistical uncertainty (precision) are on the same 10^{-3}-level regarding the tritium content measurement. KATRIN will therefore have access to a highly accurate measurement of the content of its WGTS.

The trace components naturally have a higher relative uncertainty. However, this error is only around 5% and thus remarkably small for such tiny traces.

It should be noted that said conclusion is only applicable for this KATRIN-like mixture with a high content of a certain species. However, an equilibrated mixture of about 25% T_2, 50% DT, 25% D_2 correspondingly would lead to absolute uncertainties of $< 1.1\%$ (DT) and relative uncertainties of $< 3.5\%$ (D_2). Even this scenario would still fully cover the KATRIN requirements.

Chapter 8

Summary and outlook

Summary The observation of neutrino oscillations has proved that neutrinos have non-zero mass, in contrast to the Standard Model of particle physics where neutrinos were assumed to be massless. The exploration of the absolute mass scale is thus an important experimental path to discriminate between underlying theoretical mechanisms which have been proposed to give mass to neutrinos. Furthermore, relic neutrinos act as hot dark matter and are thought to have influenced the evolution of the Universe, *e.g.* in the formation of large-scale structures. The direct measurement of the neutrino mass thus remains an experimental challenge of fundamental importance.

The KATRIN experiment aims at measuring the neutrino mass by high-precision electron-spectroscopy of the tritium β-decay with an unprecedented sensitivity of $200\,\mathrm{meV/c^2}$. This is a factor of 10 better (and a factor of 100 in the observable m_ν^2) as compared to the predecessor experiments at Mainz and Troitsk. In order to reach this challenging goal, statistical and systematic uncertainties need to be reduced significantly. The major part of the systematic uncertainties is related to the Windowless Gaseous Tritium Source (WGTS). One crucial aspect therein is the accurate determination of the gas composition of the tritium gas employed as β-source. Fluctuations of the composition result in a change of the count rate and modify the shape of the spectrum in the narrow region-of-interest (some eV around the kinematic energy endpoint of $18.6\,\mathrm{keV}$).

At the TLK, Raman spectroscopy is employed for in-line and near-time monitoring of this composition. In earlier works (including works by the author) it had already been shown that the Raman system developed within the framework of KATRIN fulfills the precision requirements of 0.1% for monitoring the tritium purity. However, the question of trueness had not been addressed so far. To ascertain this latter issue, KATRIN-sensitivity simulations were performed, which explored the influence of actual gas compositions within the WGTS on the neutrino-mass results. These showed that the calibration trueness of the Raman system should be better than 10% in order not to add significantly to the error budget of the systematic uncertainty of the source.

Therefore, one of the main goals of the research underlying this thesis was to develop a calibration principle for the Raman system, which would reach said trueness requirements. Indeed, as the results presented in the thesis show, the trueness requirement has well been surpassed. Note that in the wake of these efforts to provide high trueness for the tritium monitoring, the Raman system's precision capabilities were improved as well,

down from some hundreds of seconds to some tens of seconds of sampling time to reach the benchmark of 0.1%.

Two complementary calibration approaches were pursued (see sketch of the principle in Fig. 3.10), and the main findings from these are highlighted below.

1. **Approach based on theoretical intensities and spectral sensitivity determination.** The generation of accurate gas samples which contain tritium is not straightforward and raises several complications. For this reason, the first calibration approach is a sample-free method, which however requires (i) theoretical predictions of the Raman intensity for all six hydrogen isotopologues (T_2, DT, D_2, HT, HD, and H_2), as well as (ii) the spectral sensitivity of the Raman detection system. The theoretical values were obtained from *ab initio* calculations by Schwartz and LeRoy [LeR11]. However, the values provided were stated without systematic uncertainty, which implies that the model behind needs to be tested experimentally.

   The theory provides a set of input parameters, a and γ, for each individual Raman line for the calculation of intensities. These parameters can also be utilized to predict so-called depolarization ratios. Such ratios were determined in an experimental campaign for each relevant Raman line (Q_1-lines) of all six isotopologues. In order to obtain accurate results, a correction model was developed, which - amongst other things - could accurately account for polarization aberrations from the employed optics. This model approach was validated successfully. The overall uncertainty was better than 5% for each line. It could be shown that the theoretically predicted and experimental depolarization ratios agreed within 1σ confidence level. This is substantially better than other depolarization measurements reported in the literature; in particular, thus far none had been available for non-radioactive hydrogen isotopologues.

   The spectral sensitivity of the Raman detection system was measured by using a NIST-certified SRM2422 luminescence standard. If mounted and illuminated appropriately, it provides an almost perfect replication of the Raman scattering region and a very low calibration uncertainty. Since the standard was designed for back-scattering applications like micro-Raman spectroscopy, its usability as a luminescence standard in 90°-configuration had to be proved first. Several systematic investigations and theoretical considerations showed that indeed it was possible to use it for the spectral sensitivity measurements of the KATRIN LARA system.

2. **Approach based on accurate gas samples of non-radioactive hydrogen isotopologues**. The experimental measurement of the depolarization ratio showed that the theoretical model is able to provide verifiable predictions. However, the depolarization ratio can only probe the a and γ values (from theory) of each line individually. It cannot judge if the intensity between different lines of different isotopologues is predicted truly. Therefore, a second approach was employed as a cross-check. Gas samples of H_2, HD, and D_2 were produced in a custom-built gas mixing and equilibration loop. For the reason that no tritium was involved in this process, the achievable accuracy of the gas sample was high. After systematic investigations of the performance of the mixing loop and after upgrades of components, calibration measurements were performed. An uncertainty in the sub-percent range was achieved.

The comparison of both calibration approaches for the three non-radioactive isotopologues showed a relative difference of the order of 2%, which is within the total uncertainty of each of them. In the relevant cross-check two aspects were targeted: (i) to test - based on the depolarization ratio measurements - whether the theoretical model is intrinsically consistent for all hydrogen isotopologues; and (ii) to check with the non-radioactive isotopologues that accurate gas sample compositions could be confirmed in Raman measurements. The successful cross-calibration procedure hints at the possibility of a sample-free calibration of the KATRIN Raman system, which includes all six hydrogen isotopologues. Of course, a final check with accurate mixtures of tritiated hydrogen isotopologues would be desirable but looks out of reach for the foreseeable future.

Every future calibration effort is thus reduced to the measurement of the Raman system's spectral sensitivity, which revealed itself as a rather fast and uncomplicated procedure.

The achieved calibration uncertainty $2-3\%$ is well within the aforementioned uncertainty budget. This is an important finding for KATRIN's aim to measure the neutrino mass at design sensitivity. The Raman system will not only safely stay within the precision requirement (0.1%), but also within the trueness requirement ($< 10\%$) of KATRIN. This implies that an accurate monitoring of the WGTS source composition is possible, and the designed systematic uncertainty of the source will therefore be met or even exceeded.

Finally, it should be noted, that methods were developed and experiments were performed in this thesis which are of relevance for the scientific community beyond the achievements in the context of KATRIN (*e.g.* [Sch12a, Bab12, Sch13d]).

- The developed evaluation method for the analysis of depolarization ratio measurements allows for accurate results in the case that spurious polarization aberrations and extended Raman scattering regions are present [Sch13b].
- The depolarization ratios, which were measured and corrected, using the novel approach developed for this thesis, showed excellent agreement with the theoretical prediction [Jam13b], which is a clear confirmation of the validity of the theoretical quantum calculations.
- Accurate gas samples of H_2, HD, and D_2 are required in other areas of science as well, *e.g.* in frozen-spin polarized HD targets in photonuclear experiments [Oht11, Oht12]. The methods for producing and the discussion of the involved uncertainties can thus be of further benefit [Sch13a].
- Finally, the methods developed for the processing of Raman spectra (*e.g. SCARF* or *ShapeFit*) can be used in numerous other spectroscopic applications [Jam13d].

Outlook related to KATRIN There are three possible avenues which could be followed, in order to improve or enhance the information gathered in this thesis.

- The systematic investigation of the two complementary calibration techniques has led to a high confidence in the validity of the extrapolation of the sample-free calibration calibration approach from the non-radioactive to the radioactive isotopologues. Unfortunately, the latter could not be cross-checked by the gas mixing method.

Thus it is desirable to extend the cross-check to these three species. Therefore, a special mixing loop including tritium is currently at the design stage [Röl13, Rup16]. It will be set-up in the TLK and studies are intended to find out whether the same uncertainty can be reached as with the non-radioactive isotopologues. In this context the Raman system performance can be compared to that of other analytical systems which will be included in the new mixing loop.

- The use of the NIST-certified SRM2242 luminescence standard for the spectral calibration of the Raman system turned out be the perfect option. Specifically, the investigations for its applicability in the originally not intended 90°-configuration were successful.

  However, it is thought that, prior to the intended publication, some last open issues need to be studied and further cross-checks need to be conducted, to obtain a comprehensive overview (see summary in [Rup12]). The investigations will be performed within the framework of an on-going Bachelor's project [Bru13].

- Raman spectroscopy may also be suitable to other fundamental physics questions relevant for KATRIN. Molecular tritium T_2 (as well as D_2 and H_2) has two possible spin-configuration states of the two identical nuclei. These states are known as para (singlet) and ortho (triplet) states. At room temperature their population ratio is given by 1:3 (para:ortho); however, at very low temperatures the para-states become more populated [Sou86]. The conversion to the cold state, starting from room temperature equilibrium, is generally slow without any additional catalysts.

  The KATRIN tritium gas is at near to room temperature as long as it is circulating in the Inner Loop, but it is rapidly cooled down to $30\,\mathrm{K}$ while it is pumped into the WGTS via the $5\,\mathrm{m}$ long injection capillary. It is an open question which ortho-para ratio is finally reached after this quick cool-down process (of the order of seconds). The accurate calculation of the final states of the daughter molecule of the tritium decay requires the appropriate ortho-para ratio as input (see [Dos07]). Raman spectroscopy can measure the ortho-para ratio quite precisely from the intensity ratio of the individual odd and even J'' lines of the S_0, S_1 or Q_1 branch.

  Thus, transient measurements of the ortho-para ratio down to $30\,\mathrm{K}$, in an ancillary experiment, may be of great benefit to further reduce the uncertainties of the calculations of the final state distribution.

Outlook beyond KATRIN From the discussions throughout this thesis it should be evident that the methodology developed in this work has not only significant impact on the physics potential of KATRIN, as intended, but it might have implications and applications well beyond direct neutrino mass measurements. It is straightforward to envisage the following applications.

- At the point where the Raman measurement cell is located at KATRIN, only hydrogen isotopologues are expected in the gas composition because the gas is cleaned by a permeation filter.

  However, other applications can be imagined in which impurities play a role. Therefore, any calibration, sample-free or sample-based, would have to be extended to these species as well.

- In future large-scale thermonuclear fusion power plants, like ITER or DEMO, tritium and deuterium will be used as fuel. Accurate accountancy and fast process control are of utmost importance for a safe and reliable operation of the fueling systems of such a system. In this task, Raman spectroscopy has many advantages over other analytical techniques (see [Sch11c, Dem12]). Therefore, it is considered now as key part of the analytical system of ITER [Shu12].

  The required accuracy there is almost achieved by the current KATRIN Raman system so that only minor improvements may have to be investigated. In principle, however, for a real-time process control, special measures such as dedicated sensitivity- or speed-enhancement steps should be planned.

  One future strategy here is to develop a well calibrated reference system, against which other Raman systems or methods can be cross-calibrated (much in the same way as in other branches of metrology).

- In this thesis it was demonstrated that Raman spectroscopy can be considered as a fast, precise and accurate technique for quantitative analysis of gases. Its field of application goes far beyond tritium accountancy and is already employed for process monitoring and control.

  In particular, the sample-free calibration, as applied within this thesis, is a recommended method, if the production of calibration samples is completely impossible or involves similar constraints as related to tritium. On the other hand, to provide the required, reliable quantum calculations for transition moment functions for molecules other than the relatively simple hydrogen isotopologues may be quite a challenge for theorists.

Finally, to come back to the main focus of this thesis which is related to the precision β-spectroscopy of tritium to determine the absolute mass scale, future steps targeted at searching for light (eV-scale) and heavy (keV-scale) sterile neutrinos are already in the conceptual design phase. In all these exciting future research activities based on tritium as ideal β-emitter, Raman systems with even better performance are required. This opens up avenues to further develop this technique to meet even more stringent experimental demands to better understand the Universe and its constituents.

Appendix A

Statistical terms

The terms "precision" and "accuracy" are often used as synonyms by mistake or they are mixed up. The term "trueness" is not necessarily part of vocabulary of every scientific community. The terminology is defined, *e.g.* , in the ISO 5725 norm [ISO94] or other international norms and guides such as the [JCG08]. However, the trueness definition is ambiguous to a certain degree when comparing various norms.

Therefore, a specific norm has been selected for the definitions used in the framework of this thesis. The following listing is a direct quote from the *JCGM 200:2008 International vocabulary of metrology - Basic and general concepts and associated terms (VIM)* section 2.13-2.15 [JCG08].

(Measurement) accuracy Closeness of agreement between a measured quantity value and a true quantity value of a measurand

(Measurement) trueness Closeness of agreement between the average of an infinite number of replicate measured quantity values and a reference quantity value

(Measurement) precision Closeness of agreement between indications or measured quantity values obtained by replicate measurements on the same or similar objects under specified conditions

In order to clarify these terms, the bow-and-arrow analogy is shown in Fig. A.1, demonstrating how an archer performs in shooting at a target.

In a nutshell: trueness is related to the systematical uncertainty, whereas precision is related to the statistical uncertainty.

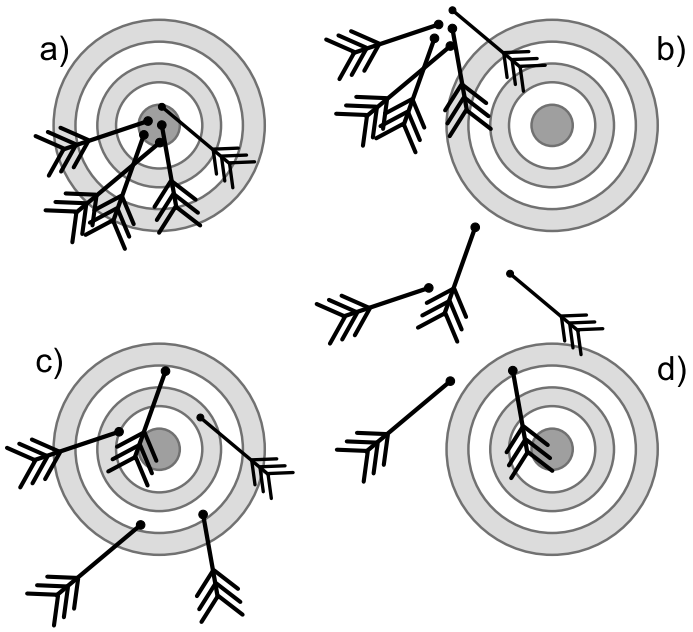

Figure A.1: Bow-and-arrow analogy for accuracy, precision and trueness. *a)* Trueness and precision high (accuracy high). *b)* Trueness low, but precision high (low accuracy). *c)* Trueness high, but precision low (low accuracy). *d)* Trueness and precision low (low accuracy).

Appendix B

Complete derivation of integration formula for depolarization measurements

The following appendix is published "as-is" by the author in the Supporting Information [Sch13c]. The layout and references have been adapted; the text has been slightly modified. The integration and the depolarization ratio correction routines are implemented in C++ using ROOT functions. The program is made available under http://depoltools.sourceforge.net.

Raman light is generally collected by making use of non-zero solid angle configurations through an aperture; the rays can be defined by the angles φ and θ according to Fig. B.1 (and to Fig. 3.7). The four combinations for $\perp$- and $||$-polarized light are recalled below from Chapter 3 as functions of the angles φ and θ [Lon02]

$$\Phi(\varphi,\theta,a,\gamma)_{\perp^s,\perp^i} = a^2\cos(\varphi)^2 + b^{(2)}\frac{\gamma^2}{45}\left(4-\sin(\varphi)^2\right) \ , \tag{B.1}$$

$$\Phi(\varphi,\theta,a,\gamma)_{\perp^s,||^i} = a^2\sin(\varphi)^2 + b^{(2)}\frac{\gamma^2}{45}\left(3+\sin(\varphi)^2\right) \ , \tag{B.2}$$

$$\Phi(\varphi,\theta,a,\gamma)_{||^s,||^i} = a^2\cos(\theta)^2\cos(\varphi)^2 + b^{(2)}\frac{\gamma^2}{45}\left(3+\cos(\theta)^2\cos(\varphi)^2\right) \ , \tag{B.3}$$

$$\Phi(\varphi,\theta,a,\gamma)_{||^s,\perp^i} = a^2\cos(\theta)^2\sin(\varphi)^2 + b^{(2)}\frac{\gamma^2}{45}\left(3+\cos(\theta)^2\sin(\varphi)^2\right) \ . \tag{B.4}$$

Here, $b^{(2)}$ is the Placzek-Teller factor; for rotational states, J'', in a Q_v-branch it is given as [Lon02]

$$b^{(2)}_{J''} = \frac{J''(J''+1)}{(2J''-1)(2J''+3)} \ . \tag{B.5}$$

If the polarization aberrations from transmission optics are taken into account, then an associated parameter, $\xi = \cos^2\beta$, can be used in the mathematical representation; where β is the angular deviation from the vertical polarization direction. In this context, a value ξ=1 would correspond to perfect vertical (linear) polarization, a value $\xi = 0.5$ would

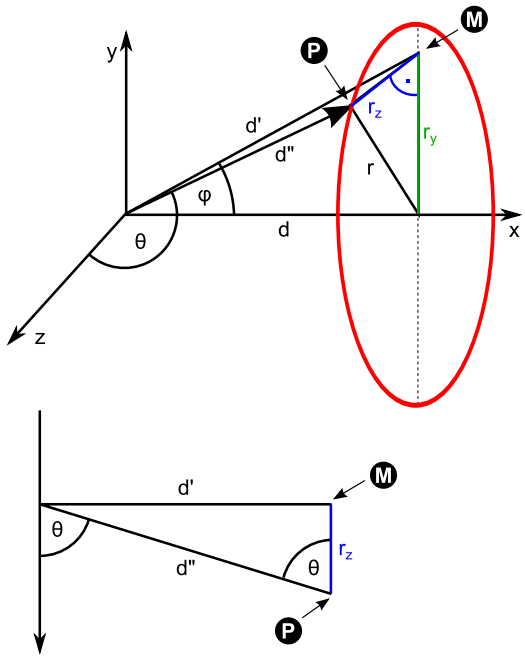

Figure B.1: Sketch for angles and distances to a circular aperture.

represent a beam whose $\perp^i$- and $||^i$-polarization components are of equal magnitude, and a value $\xi = 0$ would correspond to perfect horizontal (linear) polarization.

This parameterized approach makes it rather straightforward to accommodate different polarization components in the incident beam contributing to the Raman signal, provided a linear polarizer is suitably inserted in the observation light path. For example, inserting an analyzer that only transmits the $\perp^s$-polarized light component, the resulting line strength function becomes

$$\Phi_{\text{depol}}(\varphi, \theta, a, \gamma) = \xi \cdot \Phi(\varphi, \theta, a, \gamma)_{\perp^s, \perp^i} + (1 - \xi) \cdot \Phi(\varphi, \theta, a, \gamma)_{\perp^s, ||^i} \,. \tag{B.6}$$

The aim is now to obtain the observed Raman light intensity from an extended scattering volume the overall integration has also to include integration in z-direction. The integration is performed in spherical polar coordinates, yielding for the observed Raman light intensity

$$I_{\text{observed}} = c \cdot \iiint\limits_{\varphi, z, \theta} \Phi_{\text{depol}} \, \sin\theta \, \mathrm{d}\theta \, \mathrm{d}z \, \mathrm{d}\varphi \,. \tag{B.7}$$

The main chapter stops the derivation at this position. Therefore, this is now done in this appendix.

The difficulty in solving the integral in Eq. B.7 lies in the correct parameterization of the bounds of φ, θ, and z in the given collection geometry.

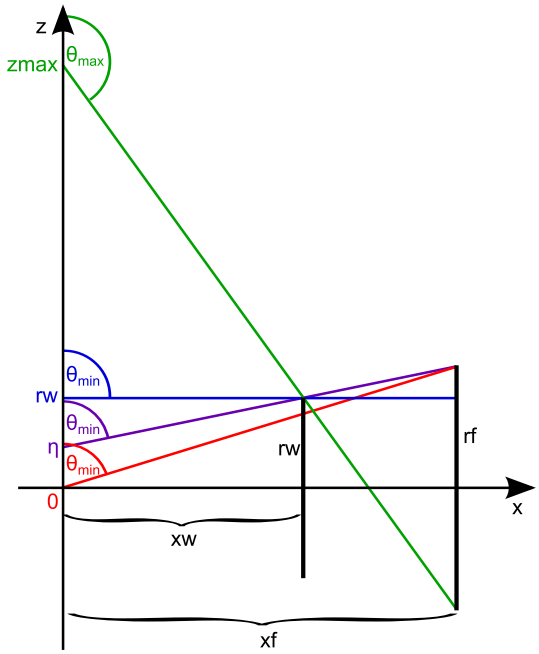

Figure B.2: Sketch of collection geometry. The z-axis is the line from which the scattered light originates. The line associated with radius r_w is the LARA-cell window. The line associated with radius r_f is the collection lens.

B.1 Bounds of integration

In Eq. B.7 the order of integration is evident. The outer integration is in the φ dimension. The next inner integration is then in the $z(\varphi)$ dimension and the innermost integration is finally in the $\theta(\varphi, z)$ dimension. Since θ depends on z and φ, and z depends on φ, the order of integration cannot be changed.

The bounds and the corresponding dependence of φ, z and θ are described in the following subsections. It should be noted, that in general two limiting cases for the parameterization have to be considered. In the most common case, the aperture configuration is one in which a small Raman cell window is followed by a larger collection lens aperture ($r_\mathrm{f} > r_\mathrm{w}$). This "normal" case will be described in the following subsections. The other "inverse" case will be briefly shown at the subsection towards the end of this appendix.

Parameterization of z

Introducing the bound of integration for the variable z is straightforward. The ranges of the integral for z are sketched in Fig. 3.7. In this subsection the bounds of integration are derived first for $\varphi = 0$. Below, $\varphi > 0$ will be applied via a substitution of r_w and r_f. The maximum viewable z (z_max) is calculated by making use of the intercept theorem (also known as Thales's theorem); one finds

$$z_\mathrm{max}\left(r_\mathrm{w}, x_\mathrm{w}, r_\mathrm{f}, x_\mathrm{f}\right) = r_\mathrm{w} + \frac{x_\mathrm{w}}{x_\mathrm{f} - x_\mathrm{w}}\left(r_\mathrm{f} + r_\mathrm{w}\right) . \tag{B.8}$$

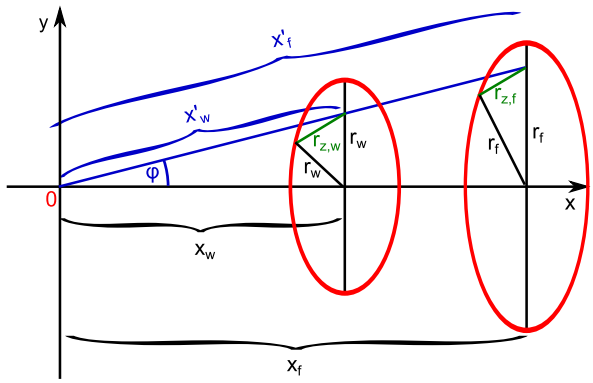

Figure B.3: Sketch for clarification of the φ-dependence. The blue line represents the plane which is inclined at an angle ϕ from the $x - z$ plane. This plane intersects with both apertures and leads to effective radii $r_{z,w}$ and $r_{z,f}$. In addition the distances from the origin to the intersection are stretched ($x_\mathrm{w} \mapsto x'_\mathrm{w}(\varphi)$, $x_\mathrm{f} \mapsto x'_\mathrm{f}(\varphi)$).

The characteristic distance η is given as

$$\eta\left(r_\mathrm{w}, x_\mathrm{w}, r_\mathrm{f}, x_\mathrm{f}\right) = r_\mathrm{w} - x_\mathrm{w}\frac{r_\mathrm{f} - r_\mathrm{w}}{x_\mathrm{f} - x_\mathrm{w}} \,. \tag{B.9}$$

Parameterization of θ

With these characteristic distances one can define the ranges of θ. First, the minimum θ angles are defined piecewise as follows

$$\theta_\mathrm{min}\left(r_\mathrm{w}, x_\mathrm{w}, r_\mathrm{f}, x_\mathrm{f}, z\right) = \begin{cases} \sin^{-1}\left(\frac{x_\mathrm{f}}{\left(x_\mathrm{f}^2+(r_\mathrm{f}-z)^2\right)^{1/2}}\right) & 0 \leqslant z \leqslant \eta \\ \sin^{-1}\left(\frac{x_\mathrm{w}}{\left(x_\mathrm{w}^2+(r_\mathrm{w}-z)^2\right)^{1/2}}\right) & \eta < z \leqslant r_\mathrm{w} \\ \pi - \sin^{-1}\left(\frac{x_\mathrm{w}}{\left(x_\mathrm{w}^2+(r_\mathrm{w}-z)^2\right)^{1/2}}\right) & r_\mathrm{w} < z \leqslant z_\mathrm{max} \end{cases} \,. \tag{B.10}$$

The maximum θ in the range $0 \leqslant z \leqslant z_\mathrm{max}$ is

$$\theta_\mathrm{max}\left(r_\mathrm{w}, x_\mathrm{w}, r_\mathrm{f}, x_\mathrm{f}, z\right) = \frac{\pi}{2} + \tan^{-1}\left(\frac{r_\mathrm{f} + z}{x_\mathrm{f}}\right) \,. \tag{B.11}$$

Parameterization of φ

The current derivation of $\theta_\mathrm{min}/\theta_\mathrm{max}$ is a simplification for the case $\varphi = 0$. If $\varphi \neq 0$ then the geometry has to be modified to some extent. In Fig. B.3 a sketch is given for clarification. The new reference plane is defined by the angle φ as it can be seen in the aforementioned sketch. This plane intersects with the apertures and leads to effective radii in z-direction

$r_{z,w}$ and $r_{z,f}$:[1]

$$r_{\mathrm{w}} \mapsto r_{z,w}(\varphi) = \left(r_{\mathrm{w}}^2 - \tan^2\varphi \cdot x_{\mathrm{w}}^2\right)^{1/2} \ , \tag{B.12}$$

$$r_{\mathrm{f}} \mapsto r_{z,f}(\varphi) = \left(r_{\mathrm{f}}^2 - \tan^2\varphi \cdot x_{\mathrm{f}}^2\right)^{1/2} \ . \tag{B.13}$$

At the same time the inclination of the φ-defined plane 'stretches' the distances from the origin to the aperture cross-sections

$$x_{\mathrm{w}} \mapsto x'_{\mathrm{w}}(\varphi) = \frac{x_{\mathrm{w}}}{\cos\varphi} \ , \tag{B.14}$$

$$x_{\mathrm{f}} \mapsto x'_{\mathrm{f}}(\varphi) = \frac{x_{\mathrm{f}}}{\cos\varphi} \ . \tag{B.15}$$

These expressions need to be replaced in Eqs. B.8 to B.11. The corrected formulas which are obtained after this replacement are:

$$\begin{aligned} z_{\mathrm{max}}\left(r_{\mathrm{w}}, x_{\mathrm{w}}, r_{\mathrm{f}}, x_{\mathrm{f}}, \varphi\right) = &\left(r_{\mathrm{w}}^2 - \tan^2\varphi \cdot x_{\mathrm{w}}^2\right)^{1/2} \\ &+ \frac{x_{\mathrm{w}}}{x_{\mathrm{f}} - x_{\mathrm{w}}}\left(\left(r_{\mathrm{f}}^2 - \tan^2\varphi \cdot x_{\mathrm{f}}^2\right)^{1/2} + \left(r_{\mathrm{w}}^2 - \tan^2\varphi \cdot x_{\mathrm{w}}^2\right)^{1/2}\right) \ , \end{aligned} \tag{B.16}$$

$$\begin{aligned} \eta\left(r_{\mathrm{w}}, x_{\mathrm{w}}, r_{\mathrm{f}}, x_{\mathrm{f}}, \varphi\right) = &\left(r_{\mathrm{w}}^2 - \tan^2\varphi \cdot x_{\mathrm{w}}^2\right)^{1/2} \\ &- \frac{x_{\mathrm{w}}}{x_{\mathrm{f}} - x_{\mathrm{w}}}\left(\left(r_{\mathrm{f}}^2 - \tan^2\varphi \cdot x_{\mathrm{f}}^2\right)^{1/2} - \left(r_{\mathrm{w}}^2 - \tan^2\varphi \cdot x_{\mathrm{w}}^2\right)^{1/2}\right) \ , \end{aligned} \tag{B.17}$$

$$\theta_{\mathrm{min}}\left(r_{\mathrm{w}}, x_{\mathrm{w}}, r_{\mathrm{f}}, x_{\mathrm{f}}, z, \varphi\right) = \begin{cases} \sin^{-1}\left(\frac{x_{\mathrm{f}}/\cos\varphi}{\left((x_{\mathrm{f}}/\cos\varphi)^2 + \left(\left(r_{\mathrm{f}}^2 - \tan^2\varphi \cdot x_{\mathrm{f}}^2\right)^{1/2} - z\right)^2\right)^{1/2}}\right) & 0 \leqslant z \leqslant \eta \\ \sin^{-1}\left(\frac{x_{\mathrm{w}}/\cos\varphi}{\left((x_{\mathrm{w}}/\cos\varphi)^2 + \left((r_{\mathrm{w}}^2 - \tan^2\varphi \cdot x_{\mathrm{w}}^2)^{1/2} - z\right)^2\right)^{1/2}}\right) & \eta < z \leqslant r_{\mathrm{w}} \\ \pi - \sin^{-1}\left(\frac{x_{\mathrm{w}}/\cos\varphi}{\left((x_{\mathrm{w}}/\cos\varphi)^2 + \left((r_{\mathrm{w}}^2 - \tan^2\varphi \cdot x_{\mathrm{w}}^2)^{1/2} - z\right)^2\right)^{1/2}}\right) & r_{\mathrm{w}} < z \leqslant z_{\mathrm{max}} \end{cases} \ , \tag{B.18}$$

$$\theta_{\mathrm{max}}\left(r_{\mathrm{w}}, x_{\mathrm{w}}, r_{\mathrm{f}}, x_{\mathrm{f}}, z, \varphi\right) = \frac{\pi}{2} + \tan^{-1}\frac{\left(r_{\mathrm{f}}^2 - \tan^2\varphi \cdot x_{\mathrm{f}}^2\right)^{1/2} + z}{x_{\mathrm{f}}/\cos\varphi} \ . \tag{B.19}$$

Note, that the $\cos\varphi$ in the $\frac{x_{\mathrm{w}}}{x_{\mathrm{f}} - x_{\mathrm{w}}}$ terms of Eqs. B.16 and B.17 have canceled out.

[1] Derivation from $r_{\mathrm{w}}^2 = r_{z,w}^2 + r_{y,w}^2$ and $r_{y,w} = \tan\varphi \cdot x_{\mathrm{w}}$. Use respectively r_{f} and x_{f} for $r_{z,f}$.

B.2 Final integration formula

Parameterization of z and θ in the normal case

The way the dependences between z, θ and φ were introduced defines the order of integration. As depicted in the previous subsections, z is a function of φ and θ is a function of z and φ. In addition, the z integration is defined piecewise.

$$\begin{aligned} I_{\text{observed}} = c \cdot 2 \cdot \int_0^{\varphi_{\text{max}}} \Bigg(& \int_0^{\eta(\varphi)} \int_{\theta_{\text{min}}(z,\varphi)}^{\theta_{\text{max}}(z,\varphi)} \Phi(\varphi,\theta) \sin\theta \, \mathrm{d}\theta \, \mathrm{d}z \, \mathrm{d}\varphi \\ & + \int_{\eta(\varphi)}^{r_{\text{w}}} \int_{\theta_{\text{min}}(z,\varphi)}^{\theta_{\text{max}}(z,\varphi)} \Phi(\varphi,\theta) \sin\theta \, \mathrm{d}\theta \, \mathrm{d}z \, \mathrm{d}\varphi \\ & + \int_{r_{\text{w}}}^{z_{\text{max}}(\varphi)} \int_{\theta_{\text{min}}(z,\varphi)}^{\theta_{\text{max}}(z,\varphi)} \Phi(\varphi,\theta) \sin\theta \, \mathrm{d}\theta \, \mathrm{d}z \, \mathrm{d}\varphi \Bigg) \end{aligned} \tag{B.20}$$

with $\varphi_{\text{max}} = \tan^{-1}(r_{\text{f}}/x_{\text{f}})$. $\Phi(\varphi,\theta)$ can be any combination of the expressions in Eqs. B.1 to B.4. In the case of depolarization measurements in the schemes described in the main chapter, the expression for $\Phi_{\text{depol}}(\varphi,\theta)$ in Eq. B.6 can be used. The observed depolarization ratio is then given by (bound of integration according to Eq. B.20)

$$\rho_{\text{observed}} = \frac{\iiint\limits_{\varphi,z,\theta} \xi \cdot \Phi(\varphi,\theta,a,\gamma)_{\perp^s,||^i} + (1-\xi) \cdot \Phi(\varphi,\theta,a,\gamma)_{\perp^s,\perp^i} \, \sin\theta \, \mathrm{d}\theta \, \mathrm{d}z \, \mathrm{d}\varphi}{\iiint\limits_{\varphi,z,\theta} \xi \cdot \Phi(\varphi,\theta,a,\gamma)_{\perp^s,\perp^i} + (1-\xi) \cdot \Phi(\varphi,\theta,a,\gamma)_{\perp^s,||^i} \, \sin\theta \, \mathrm{d}\theta \, \mathrm{d}z \, \mathrm{d}\varphi} \, . \tag{B.21}$$

This can be re-written in simplified form as

$$\rho_{\text{observed}} = \frac{\xi \cdot A + (1-\xi) \cdot B}{\xi \cdot B + (1-\xi) \cdot A} \tag{B.22}$$

with

$$\begin{aligned} A &= \iiint\limits_{\varphi,z,\theta} \Phi(\varphi,\theta,a,\gamma)_{\perp^s,||^i} \, \sin\theta \, \mathrm{d}\theta \, \mathrm{d}z \, \mathrm{d}\varphi \\ B &= \iiint\limits_{\varphi,z,\theta} \Phi(\varphi,\theta,a,\gamma)_{\perp^s,\perp^i} \, \sin\theta \, \mathrm{d}\theta \, \mathrm{d}z \, \mathrm{d}\varphi \end{aligned}$$

Overview of the terms

- $\mathbf{z}_{\text{max}}(\varphi)$ is the maximal viewable z as a function of φ, see Eq. B.16.
- $\eta(\varphi)$ is the characteristic distance as a function of φ, see Eq. B.17.

- $\theta_{\mathbf{min}}(\mathbf{z}, \varphi)$ is the minimal θ as a function of z and φ, see Eq. B.18 for the three ranges $0 \leqslant z \leqslant \eta$, $\eta < z \leqslant r_{\mathrm{w}}$ and $r_{\mathrm{w}} < z \leqslant z_{\mathrm{max}}$.
- $\theta_{\mathbf{max}}(\mathbf{z}, \varphi)$ is the maximal θ as a function of z and φ, see Eq. B.19.
- $\mathbf{\Phi}_{\text{depol-LARA}}(\varphi, \chi)$ is The line-strength function as a function of φ and polarization rotation χ, see Eq. B.6.

Overview of the parameters

- ξ is the cleanness of the incident polarization of the laser light.
- $\mathbf{r}_{\mathrm{w}}$ is the radius of the cell window.
- $\mathbf{x}_{\mathrm{w}}$ is the distance between the cell window and the scattering origin.
- $\mathbf{r}_{\mathrm{f}}$ is the radius of the focus lens aperture.
- $\mathbf{x}_{\mathrm{f}}$ is the distance between the focus lens and the scattering origin.

Parameterization of z and θ in the inverse case

In this subsection the so-called "inverse" case with the configuration $r_{\mathrm{w}} > r_{\mathrm{f}}$ is described and the difference in the parameterization of z and θ is shown. A visualization is found in Fig. B.4. The maximum viewable z (z_{max}) is the same as in Eq. B.8:

$$z_{\mathrm{max}}\left(r_{\mathrm{w}}, x_{\mathrm{w}}, r_{\mathrm{f}}, x_{\mathrm{f}}\right) = r_{\mathrm{w}} + \frac{x_{\mathrm{w}}}{x_{\mathrm{f}} - x_{\mathrm{w}}}\left(r_{\mathrm{f}} + r_{\mathrm{w}}\right) . \tag{B.23}$$

Then a new characteristic distance $\bar{\eta}$ is introduced as

$$\bar{\eta}\left(r_{\mathrm{w}}, x_{\mathrm{w}}, r_{\mathrm{f}}, x_{\mathrm{f}}\right) = r_{\mathrm{f}} + x_{\mathrm{f}}\frac{r_{\mathrm{w}} - r_{\mathrm{f}}}{x_{\mathrm{f}} - x_{\mathrm{w}}} . \tag{B.24}$$

With these characteristic distances one can define the ranges of θ. First, the minimum θ angles are defined piecewise as follows

$$\theta_{\mathrm{min}}\left(r_{\mathrm{w}}, x_{\mathrm{w}}, r_{\mathrm{f}}, x_{\mathrm{f}}, z\right) = \begin{cases} \sin^{-1}\left(\frac{x_{\mathrm{f}}}{\left(x_{\mathrm{f}}^2 + (r_{\mathrm{f}} - z)^2\right)^{1/2}}\right) & 0 \leqslant z \leqslant r_{\mathrm{f}} \\ \pi - \sin^{-1}\left(\frac{x_{\mathrm{f}}}{\left(x_{\mathrm{f}}^2 + (r_{\mathrm{f}} - z)^2\right)^{1/2}}\right) & r_{\mathrm{f}} < z \leqslant \bar{\eta} \\ \pi - \sin^{-1}\left(\frac{x_{\mathrm{w}}}{\left(x_{\mathrm{w}}^2 + (r_{\mathrm{w}} - z)^2\right)^{1/2}}\right) & \bar{\eta} < z \leqslant z_{\mathrm{max}} \end{cases} . \tag{B.25}$$

The maximum θ in the range $0 \leqslant z \leqslant z_{\mathrm{max}}$ is again the same as in Eq. B.11

$$\theta_{\mathrm{max}}\left(r_{\mathrm{w}}, x_{\mathrm{w}}, r_{\mathrm{f}}, x_{\mathrm{f}}, z\right) = \frac{\pi}{2} + \tan^{-1}\left(\frac{r_{\mathrm{f}} + z}{x_{\mathrm{f}}}\right) . \tag{B.26}$$

As above the substitution (*e.g.* $r_{\mathrm{w}} \mapsto r_{z,w}(\varphi) = \left(r_{\mathrm{w}}^2 - \tan^2\varphi \cdot x_{\mathrm{w}}^2\right)^{1/2}$) needs to be implemented to take the z- and φ-dependences into account.

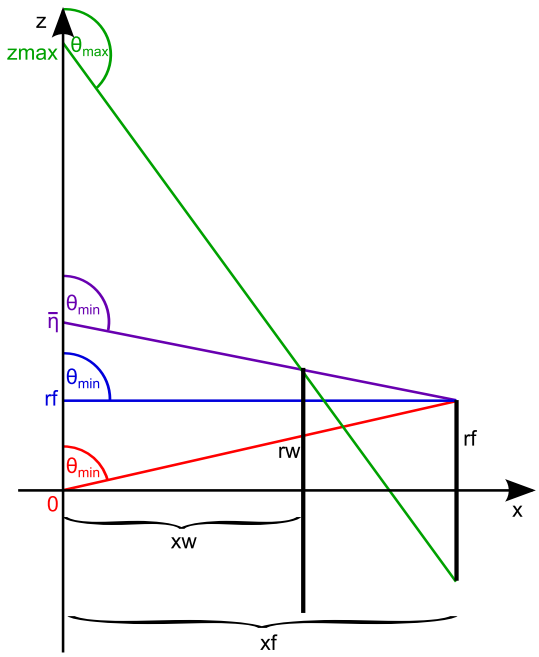

Figure B.4: Sketch of inverse collection geometry. The z-axis is the line from which the scattered light originates. The line with radius r_{w} is the LARA-window. The line with radius r_{f} is the collection lens. Note that in this "inverse" case $r_{\mathrm{w}} > r_{\mathrm{f}}$.

Appendix C

Jones calculations for polarization aberrations in the Raman collection system

The following appendix is published "as-is" by the author in the Supporting Information [Sch13c]. The layout and references have been adapted; the text has been slightly modified.

Fig. B.3 shows the general light collection configuration for Raman depolarization measurements, comprising in general a sample cell window (aperture $A2$), a collection lens (aperture $A1$) and a polarizer ($O? = P$). The relation between the polarization state of the incoming and transmitted light beams follows from Jones-calculus, using 2×2 Jones matrices $\mathcal{J}$ (for further details see Hecht [Hec74] or Kita [Kit09])

$$\boldsymbol{E}_{\text{out}}(\theta, \varphi) = \mathcal{J}_P \mathcal{J}_{A1} \mathcal{J}_{A2} \cdot \boldsymbol{E}_{\text{in}}(\theta, \varphi) \ . \tag{C.1}$$

The following assumptions need to be valid (they are restated from Section 5.3):

- the system as a whole can be described as one sustaining a (homogeneous) net change in its polarization content (mainly linear di-attenuation and linear retardance);
- the polarization aberrations have (nearly) no angular dependence; and
- circular di-attenuation and retardance are negligible, as indicated *e.g.* by Kita. [Kit09].

With the aforementioned assumptions that we are only concerned about an angular-independent net effect from the collection system, Eq. C.1 can be simplified by using a new Jones matrix $\mathcal{J}_C$ describing the net effect of the collection system

$$\boldsymbol{E}_{\text{out}}(\theta, \varphi) = \mathcal{J}_P \mathcal{J}_C \cdot \boldsymbol{E}_{\text{in}}(\theta, \varphi) \ . \tag{C.2}$$

The vector $\boldsymbol{E}_{\text{in}}$ defines the effective polarization state of integrated Raman light generated in the scattering region. For an incident polarization state p^i the scattered horizontal and

Table C.1: Physical significance of the Pauli coefficients $\mathbf{a_k}$. Table adapted from [McG94].

Coeff.	Physical significance of $\Re(a_k) = a_{Pk}$	Physical significance of $\Im(a_k) = a_{Rk}$
a_0	Pol.-indep. amplitude	Pol.-indep. phase
a_1	Lin. diattenuation along coord. axes	Lin. retardance along coord. axes
a_2	Lin. diattenuation at $45°$ to the coord. axes	Lin. retardance $45°$ to the coord. axes
a_3	Circ. diattenuation	Circ. retardance

vertical light components can be calculated, using the model derived in Appendix B:

$$\boldsymbol{E}_{\text{in}} = \begin{pmatrix} E_{||^s,p^i} e^{i\phi_{||}} \\ E_{\perp^s,p^i} e^{i\phi_{\perp}} \end{pmatrix} \tag{C.3}$$

with $\phi_{||}$ and $\phi_{\perp}$ being initial phase shifts. The Jones matrix of the polarizer for vertical transmission is given as [Hec74]

$$\mathcal{J}_P = \begin{pmatrix} 0 & 0 \\ 0 & 1 \end{pmatrix} . \tag{C.4}$$

Overall, the unknown part is the Jones matrix of the collection system. It is convenient to write the Jones matrix in exponential form $\mathcal{J} = \exp \mathcal{V}$; $\mathcal{V}$ is a matrix exponential expression that substitutes the Jones matrix [Kit09]. This matrix can be expressed by Pauli expansion (σ_i are the Pauli matrices)

$$\mathcal{V} = \sum_{k=0}^{3} a_k \sigma_k . \tag{C.5}$$

With this, the Jones matrix of the light collection system can be written as

$$\mathcal{J}_C = \exp\left(a_0\sigma_0 + a_1\sigma_1 + a_2\sigma_2 + a_3\sigma_3\right) . \tag{C.6}$$

The Pauli coefficients a_k are given as $a_k = a_{Pk} + ia_{Rk}$ (see Tab. C.1). As mentioned above it is assumed, that no circular polarization effects occurs and thus $a_3 \approx 0 + i0$. Therefore, the matrix $\mathcal{J}_C$ becomes

$$\mathcal{J}_C = \exp\begin{pmatrix} (a_{P0} + a_{P1}) + i\,(a_{R0} + a_{R1}) & a_{P2} + ia_{R2} \\ a_{P2} + ia_{R2} & (a_{P0} - a_{P1}) + i\,(a_{R0} - a_{R1}) \end{pmatrix} . \tag{C.7}$$

According to the entries in Tab. C.1 the parameter $a_{P0}(\neq 0)$ is associated with a polarization-independent, *i.e.* isotropic change in amplitude. This means that the amplitudes of vertical and horizontal light components are affected likewise, and the factor $\exp(2a_{P0})$ appears in both the $I_{\perp^s,p^i}$ and $I_{||^s,p^i}$ terms. As a consequence, this constant factor cancels out when calculating the depolarization ratio (see Eq. B.22). Thus it seems justifiable to set this constant to a convenient, arbitrary value; for reasons of simplicity one may chose $a_{P0} = 0$.

Because of the above, Eq. C.2 becomes

$$\boldsymbol{E}_{\text{out}}(\theta,\phi) = \begin{pmatrix} 0 \\ E_{||^s,p^i} e^{a_{P2}} e^{i\left(a_{R2}+\phi_{||^s}\right)} + E_{\perp^s,p^i} e^{-a_{P1}} e^{i(a_{R0}-a_{R2}+\phi_{\perp^s})} \end{pmatrix} . \tag{C.8}$$

This equation now allows one to calculate the observed intensity $I = |\boldsymbol{E}_{\text{out}}|^2$. In the following, the parameters $a_{R0},\ a_{R1}$ and a_{R2} have been collated into a total parameter $a_{R,\text{tot}}$ and it is assumed that no initial phase difference is encountered for the two polarization components ($\phi_{||^s} - \phi_{\perp^i} = 0$) of the incoming light beam. Thus, the resulting term for the intensity with incident polarization p^i becomes

$$\begin{aligned} I_{\perp^s,p^i} = & \underbrace{E^2_{\perp^s,p^i} \exp(-2a_{P1})}_{\text{transmitted } \perp^{\text{s}}-\text{component}} + \underbrace{E^2_{||^s,p^i} \exp(2a_{P2})}_{\text{leakage from } ||^{\text{s}}-\text{component}} \\ & + \underbrace{2E_{\perp^s,p^i} E_{||^s,p^i} \exp(a_{P2} - a_{P1}) \cos\left(a_{R,\text{tot}}\right)}_{\text{contamination induced by retardance}} . \end{aligned} \tag{C.9}$$

This implies that the scattered light expression has been reduced to a three-parameter problem, associated with linear diattenuation ($a_{P1},\ a_{P2}$) and the retardance from stress birefringence ($a_{R,\text{tot}}$).

Appendix D

Measurements of polarization aberrations in Raman cell windows

The following appendix is published "as-is" by the author and co-authors in the Supporting Information [Jam13c]. The layout and references have been adapted.

The polarization cleanness of the laser light, when it scatters in the gas, has an influence on the measured depolarization ratio. All optics in front of the observed region of Raman scattering could influence the polarization state and thus pose a problem for the laser beam cleanness. The optical elements in the beam are mirrors, lenses, a half-wave plate and the cell window for the incident laser beam. Prior to entering the Raman cell, the laser polarization is "cleaned" by a Glan laser polarizer, and therefore the only possible polarization aberrations are expected to originate from the latter two components; thus, both are investigated in detail. In Section D.1, the influence of the half-wave plate is investigated. Then, in Sections D.2 and D.2.1, the polarization aberrations due to stress-induced birefringence in the cell windows are measured qualitatively and quantitatively.

D.1 Polarization aberrations induced by the half wave plate

A Glan laser polarizer is placed in the beam path to ensure the laser light is linearly polarized. The laser beam then passes through a half-wave plate, which in the depolarization measurements is used to turn the polarization direction. Note that the theory of a half-wave plate requires that the wave plate crystal is perfectly perpendicular to the incident laser beam for best performance. Small tilts of the crystal may lead to a decrease in the cleanness of the polarization of the light exiting the wave plate. This cleanness for the half-wave plates used in the depolarization measurements has been measured. To measure the cleanness, ξ, a second, rotatable Glan polarizer serves as a polarization analyzer; the transmitted power is recorded using a photodiode detector. The setup is shown schematically in Fig. D.1.

The transmitted power will vary with $\sin^2\theta$. The cleanness ξ is then defined as

$$\xi = 1 - P_{\min}/P_{\max} \,. \tag{D.1}$$

This parameter is related to the angular deviation of the polarization direction. A value of $\xi = 1$ corresponds to perfect linear polarization (at $\theta = 0°$), while a value of $\xi = 0$ corresponds to perfect suppression of the $90°$-rotated polarization. For the measurements the second Glan laser polarizer was rotated in $4°$-steps. Dark measurement readings were subtracted from the measured signal. The half-wave plate was then tilted to 20, 12, 8, 4, 0 and $4°$ (with respect to the laser beam). The cleanness was calculated for each tilt, and compared to the value when the half-wave plate was removed; the resulting graph is shown in Fig. D.2.

The figure shows that for a tilt of $-4°$ the cleanness is highest (approximately equal to 1). The reason the minimum is not at the precisely perpendicular ($0°$) position may be associated with mounting and manufacturing imprecisions. The results also show that it is important to keep the wave plate tilt fixed throughout a measurement, otherwise the cleanness will change. Overall, the measured polarization aberrations in the half-wave plate have a very small effect ($\sim 1 \times 10^{-5}$) on the cleanness of the laser beam and should not contribute to the errors in the depolarization measurements.

D.2 Measurement of stress-induced birefringence in Raman cell windows

Polarization aberrations in the windows of the Raman cell can significantly alter the linear polarization of the incident laser beam. This has an effect on the observed depolarization ratio. The origin of these aberrations is stress-induced birefringence in the fused silica windows.

Logan *et al* [Log94] investigated spatially distributed birefringence induced by isotropically distributed stress. In their introduction to the experiment they write: *"It [fused silica] is a material which is neither naturally birefringent nor optically active. However, birefringence may be induced by the application of a mechanical or thermal stress. The resulting effective optic axis would be in the direction of the applied stress, and the birefringence proportional to the magnitude of the stress."* [Log94]. They have performed

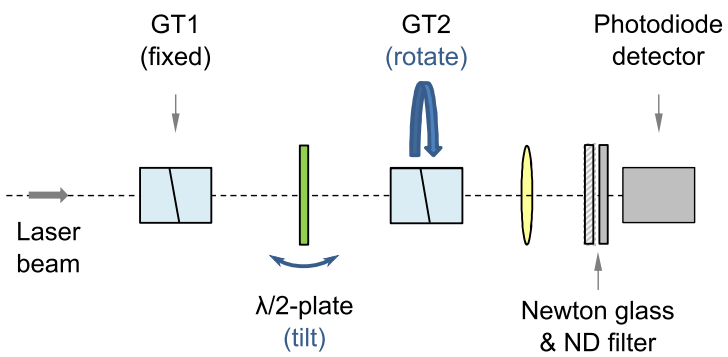

Figure D.1: Setup to measure the laser beam cleanness quantitatively. GT = Glan-Taylor polarizer.

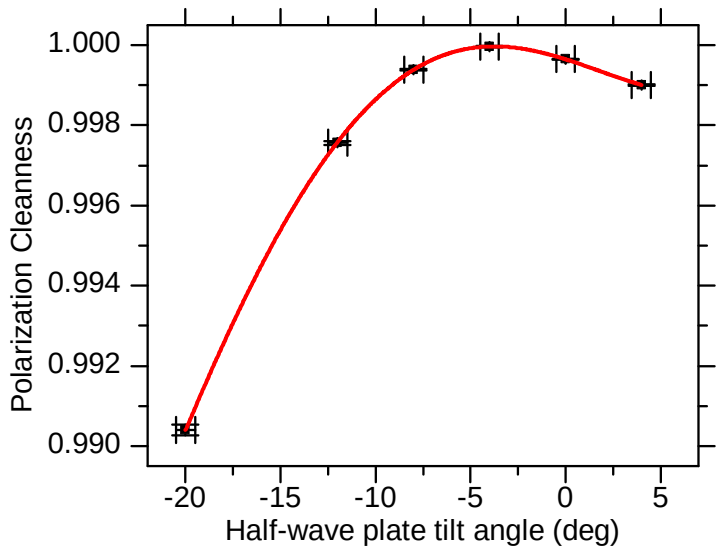

Figure D.2: Measurement curve of the polarization cleanness vs. the half-wave plate tilt angle. The uncertainties are obtained from the standard deviation of the repeat measurements.

measurements of birefringence on a suspended sample, mounted in stainless steel, and measured the polarization change in a linearly polarized laser beam.

The windows of the Raman cell have to fulfill certain safety requirements, due to the radioactivity of the tritium gas employed in the measurements. This includes a metal body construction and UHV leak-tightness (maximum leak rate $< 10^{-9}\,\mathrm{mbar} \cdot \ell \cdot \mathrm{s}^{-1}$); see *e.g.* Schlösser *et al* [Sch11c]. Standard rubber or plastic O-ring seals cannot be used due to the radio-chemical reactions with the organic material. Thus, the fused-silica windows are diffusion-bonded to stainless steel by the use of a tantalum ring; see Taylor *et al* [Tay01]. The bonding procedure is performed at several hundred degrees Celsius; internal stress may occur after cooling down to room temperature. Therefore, it is important to ascertain whether the individual window has suffered a reduction in polarization cleanness.

In the following two methods are presented, which are used for the investigation of polarization aberrations in the cell windows of the Raman system. The first method constitutes a qualitative measurement of the spatial distribution of polarization aberrations throughout the window, while the second method is used to measure the aberration quantitatively at a single point of the window.

D.2.1 Qualitative measurement of polarization aberration with a polarization sensitive microscope

The polarization aberrations from stress-induced birefringence in the optical cell windows have been qualitatively investigated with a polarization-sensitive microscope.

In Fig. D.3 the experimental arrangement is shown. One linear sheet polarizer is placed directly onto the illuminated ground surface of the microscope. The sample object (*e.g.* a cell window) is then placed on top. A second linear sheet polarizer is used as an analyzer, between the object and the microscope's objective. The sample is observed through the

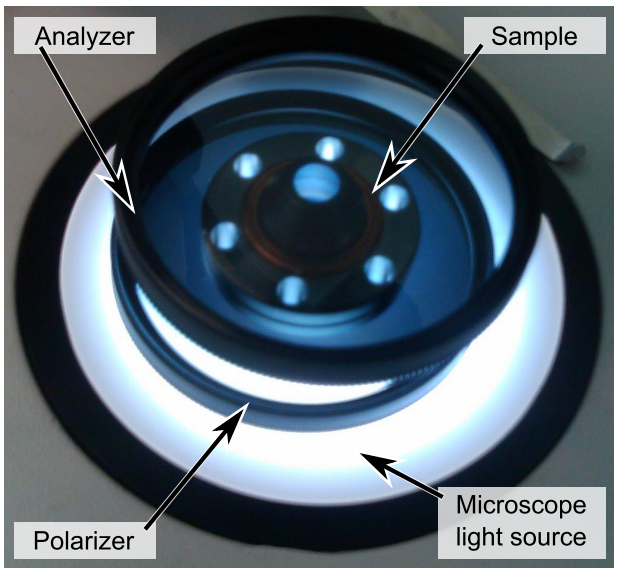

Figure D.3: Setup of the polarization-sensitive measurements by using a microscope and two Polaroid sheet polarizers. For further details see text.

microscope while the analyzer is rotated stepwise until the transmitted light intensity is minimal when polarizer and analyzer are crossed. Images are acquired via the internal camera of the microscope.

In pre-measurements the polarizer and analyzer were set to cross-polarization without anything in between them, serving as a reference. The resulting image was almost completely black proving that the extinction of the cross-polarizer was high enough for the sensitivity of the internal camera. A small selection of the overall measurement campaign of the various windows is shown in here. In Fig. D.4 measurement results for two windows for transmission of the laser beam (top four panels) and two windows for the collection of the Raman light (bottom four panels) are shown. Note that all images obtained with crossed polarizer - analyzer setting have been post-processed using an imaging-editing software ("Color Tool - Curves" of GNU Image Manipulation Program / GIMP 2.8.0), to enhance the contrast. The settings for this enhancement step have been the same in all recorded images. The following observations can be made when inspecting the images in Fig. D.4.

Firstly, lighter areas indicate that the initial linear polarization becomes less clean due to stress-induced birefringence in the window: light leaks through the analyzer when it is in the cross-polarization setting. Secondly, most of the cell windows exhibit a certain amount of stress-induced birefringence (in this selection three out of the four windows.) However, the spatial distribution of the polarization aberration is not always the same. For example, laser window II exhibits a strong polarization aberration zone with a broad distribution diagonally throughout the window, while Raman windows I and II reveal aberration hot spots, which are limited to a certain zone. These differences might be due to variations in the pressure, stress, position or temperature during the individual bonding process. Note that, despite these valuable qualitative results no quantitative measurements could be performed with the current microscope setup. The results are broadly in line with the

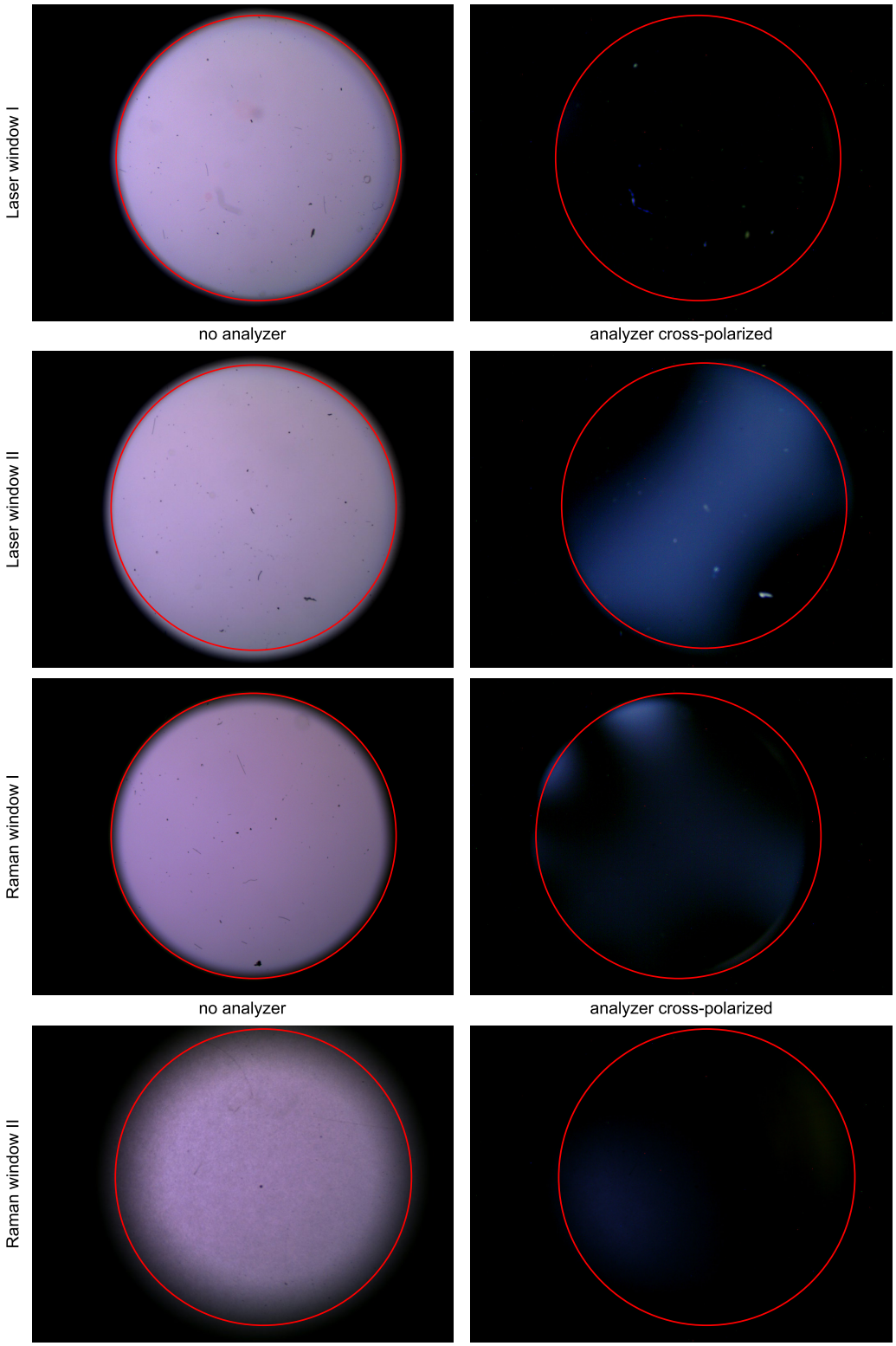

Figure D.4: Visualization of polarization aberrations in windows of the Raman cell. Shown are photographs of two laser windows (top four panels) and two Raman collection windows (bottom four panels) in the polarization sensitive microscope. *Left:* No analyzer was employed. *Right:* Polarizer and analyzer are set to cross-polarization. The red circle is plotted for orientation. Sketch and picture of a Raman cell are found in Fig. 4.4.

findings in the theoretical and experimental study of aberrations in windows by Shribak and co-workers [Shr02]. For further discussions on polarization aberrations the reader is referred to publications and reviews by McGuire and Chipman [McG94] or Kita [Kit09].

D.2.2 Quantitative measurement of polarization aberration at a single point

In order to quantitatively verify the amount of stress in the laser windows the same methodology for determining the cleanness as in Section D.1 has been employed. Instead of the half-wave plate, now the laser windows have been inserted between the two Glan laser polarizers. Note that the actual cell windows in use could not be used individually as they are fixed in location at the cell(s).

The half-wave plate (at the tilt which maximizes the cleanness, as found in Section D.1) was placed in front of the windows to make the situation as similar as possible to the actual Raman depolarization measurement as described in the main text. The polarization determination measurement procedure was performed twice: (1) with the half-wave plate only and (2) with the half-wave plate plus window. A difference between those two measurements indicates a reduced polarization cleanness of the window. For reasons of reproducibility each measurement was repeated a few times, with the window being slightly repositioned for each. The measured cleanness when the laser window was inserted into the beam bath was found to be

$$\xi = 1 - P_{\mathrm{min}}/P_{\mathrm{max}} = 0.9923 \pm 0.0024 \tag{D.2}$$

and when the laser window was removed it was found to be

$$\xi = 1 - P_{\mathrm{min}}/P_{\mathrm{max}} = 0.9993 \pm 0.0005\,. \tag{D.3}$$

This shows that the window does indeed reduce the cleanness. However, these numbers cannot be directly used for the correction of the depolarization ratios as they are different windows compared to the ones of the cell(s). When the windows are mounted to the cell there is a good chance that the stress acting on the optic could change because of the tightening of the CF16 flange in which they are mounted.

The measurements with this method show that the obtained cleanness values are of the same order as determined by the procedures described in Section 5.3. Thus, this finding suggests that the procedure to obtain corrected depolarization ratios, which agree with the ρ_{SP0SA} from theory, is reliable.

Appendix E

Error estimation in depolarization ratio measurements

The following appendix is published "as-is" by the author in the Supporting Information [Jam13c]. The layout and references have been adapted; the text has been slightly modified.

The main sources of uncertainty are associated with the inadequacies in the correction model, uncertainties in the determination of geometrical input parameters for the model, and the propagated experimental uncertainties in the measured depolarization ratios.

Uncertainty from inadequacies in the correction model

In the model used in this work only the polarization aberrations in the incident laser beam generated from stress-induced birefringence in the laser window are considered (see Section 5.3.2.2). However, qualitative and quantitative measurements of the second type of windows, the Raman collection windows, show that the aberrations are in the same order of magnitude (see Section 5.3.2.2). In Appendix C the aberrations in the Raman collection window are estimated using Jones matrices. The finding was that the Raman collection windows do hardly affect the measured depolarization ratio, being one to two orders of magnitude lower than the effect from the laser entrance window, at the chosen apertures.

The cleanness, ξ, of the laser windows obtained in the Raman measurements in this work was generally around $\xi > 0.99$ ($\xi = 1$ denotes a perfectly aberration-clean window). In one exceptional case a cleanness of around $\xi \sim 0.98$ was measured. Note that, even if a worst case is assumed, such as a cleanness of only about $\xi = 0.95$ for the collection Raman windows, the effect would just become noticeable. The relevant data are plotted, as a function of solid angle parameter, in Fig. 5.6. According to the figure the resulting contribution to the depolarization ratio at a light collection angle of about 4° would roughly equals 0.00025. Thus, neglecting these aberrations from the Raman collection window in the correction model, the maximum deviation is expected to be of the order $\Delta\rho_{\mathrm{model}} = 0.00025$.

Table E.1: Geometrical input parameters and their effect on the depolarization ratios.

Parameter	Units	at Swansea	at KIT
Distance of scattering volume to diaphragm, x	mm	38 ± 1	69 ± 1
Diaphragm opening radius, r	mm	3 ± 0.25	5 ± 0.5
$\Delta\rho_x$		0.0002	0.0001
$\Delta\rho_r$		0.0005	0.0005

Uncertainty in determination of geometrical input parameter

The accuracy of the applied correction is dependent on the input parameters to the mathematical model described in Appendix B. The relevant parameters are the radius of the limiting diaphragm, r, and its distance to the scattering center, x. In principle, the effect can be directly read from Fig. E.1, since x and r determine the collection angle via $\tan^{-1}(r/x)$. In Tab. E.1 the experimental values and uncertainties for r and x are restated from Section 5.3.2.2, together with the propagated errors into the corrected depolarization ratios (as extracted from Fig. E.1 further below).

Uncertainty in measured depolarization ratios

In addition to the geometry-related uncertainties above, error sources are also found in the procedural approach used to derive the SP0SA depolarization ratios from the measured spectra. Said errors are associated with the propagated statistical uncertainties of the measured intensities.

The routine for correcting the measured values is a two-step procedure, as visualized in Fig. E.1.

In the first step, the observed ρ-value (ρ_{obs}) of the $Q_1(J'' = 0)$ line is used to derive the cell window cleanness. This derived cleanness is used as input parameter for the model in the second step, to transform the ρ_{obs}-values for $J" > 0$ into the ρ_{SP0SA}-values. Naturally, the errors (in cleanness) from the first step propagate into the next phase. This is indicated by the series of 'correlation' lines (gray, parallel lines in Fig. E.1), corresponding to the 1σ - and 2σ-boundaries associated with the statistical uncertainty in the first step. This correlation distribution is folded into the statistical distribution of the ρ_{obs}-value for $J" > 0$, which leads to a two-dimensional uncertainty distribution. Its 1σ-contour area (with 68.3% of the product probability) is used to determine the final ρ_{SP0SA}-error, using the minimum and maximum values of $\Delta\rho_{\mathrm{SP0SA}}$ from this probability contour.

Note, that no overall uncertainty is given at this point since it is calculated individually for each experimental line.

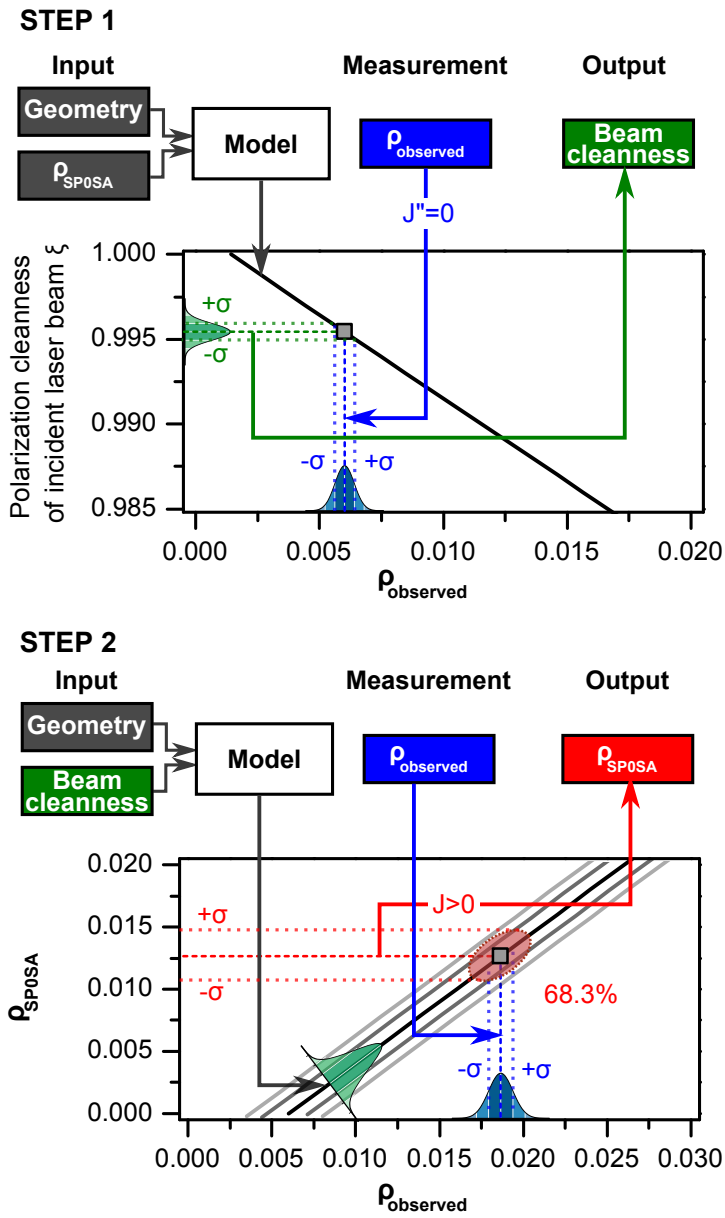

Figure E.1: Two-step procedure to extract depolarization values ρ_{SP0SA} from data sets with unclean beam polarization. Step 1 - Determination of cleanness of the laser polarization. The theoretical data (full line) are calculated for known collection geometry and known SP0SA depolarization ratio $\rho_{\mathrm{SP0SA}} = 0$. From the observed depolarization ratio of the $Q_1(J'' = 0)$ line one derives the related polarization cleanness ξ. Step 2 - Correction of depolarization ratios of all measured Q_1-branch lines, for a given polarization cleanness. The polarization cleanness derived in step 1 is used to correlate the ρ_{observed} to the ρ_{SP0SA} values of all Q_1-branch lines with $J'' > 0$. The Gaussian in the graphs denote the statistical uncertainties of the measured and propagated values.

Total uncertainty

The aforementioned errors are independent of each other and their squares can be added to obtain the total uncertainty of the determined SP0SA depolarization ratios

$$\Delta\rho_{\mathrm{tot}} = \sqrt{\Delta\rho^2_{\mathrm{model}} + \Delta\rho^2_x + \Delta\rho^2_r + \Delta\rho^2_{\mathrm{analysis}}}\,. \tag{E.1}$$

Appendix F

Relation between experimental error of Raman intensities and depolarization ratios

The following appendix is published "as-is" by the author in the Supporting Information [Sch13e]. The layout and references have been adapted; the text has been slightly modified.

Using error propagation and certain assumptions one can show that this relative uncertainty of the depolarization ratios is about equal to the relative uncertainty of the line strength function.

In Section 5.3.2.2 it was shown that values derived from theory [LeR11] agree with those from the depolarization measurement within the experimental uncertainty of about 5%. In the following it will be shown, how to link the experimental uncertainty of the depolarization measurements to the uncertainty of the line strength function. By and large it follows the derivation and notation as given in Long [Lon02].

The line strength function, Φ, is a function of the parameters for isotropic polarizability, a, and for anisotropic polarizability, γ:

$$\Phi = \frac{45a^2 + 4b_{J''}\gamma^2}{45} = a^2 + \frac{4}{45}b_{J''}\gamma^2 \,. \tag{F.1}$$

Here, $b_{J''}$ stands for the Placzek-Teller factor.

$$b_{J''} = \frac{J''(J''+1)}{(2J''-1)(2J''+3)} \,. \tag{F.2}$$

Note, that $b_{J''} = 0$ for lines with $J'' = 0$. Any error in the parameters a and γ propagates into the uncertainty of the line strength function Φ as

$$\begin{aligned}\Delta\Phi &= \sqrt{\left(\frac{\mathrm{d}\Phi}{\mathrm{da}}\right)^2 (\Delta a)^2 + \left(\frac{\mathrm{d}\Phi}{\mathrm{d}\gamma}\right)^2 (\Delta\gamma)^2} \\ &= \sqrt{(2a\Delta a)^2 + \left(\frac{8}{45}b_{J''}\gamma\Delta\gamma\right)^2} \,.\end{aligned} \tag{F.3}$$

Since the values for Δa and $\Delta\gamma$ are not known, they may be obtained via the experimental uncertainty of the depolarization ratios

$$\rho = \frac{3b_{J''}\gamma^2}{45a^2 + 4b_{J''}\gamma^2} \ , \tag{F.4}$$

with the propagated error

$$\begin{aligned}\Delta\rho &= \sqrt{\left(\frac{d\rho}{da}\right)^2 (\Delta a)^2 + \left(\frac{d\rho}{d\gamma}\right)^2 (\Delta\gamma)^2} \\ &= \frac{270b_{J''}a\gamma}{\left(45a^2 + 4b_{J''}\gamma^2\right)^2}\sqrt{\gamma^2 (\Delta a)^2 + a^2 (\Delta\gamma)^2} \ .\end{aligned} \tag{F.5}$$

In order to simplify the equation above one may strive to eliminate one of the contributions. The contribution by the second term in Eq. F.1, $4/45b_{J''}\gamma^2$, is very small compared to the a^2 term in the same equation. This becomes clear from the data displayed in Fig. 5.2 in Chapter 5.2; they show that the major part of the line strength has its origin in the isotropic part a and only a minor contribution is coming from the anisotropic part γ. The contribution of the latter is zero for all lines with $J'' = 0$, less than 3% for all lines with $J'' = 1$ and less than 2% for all other lines with $J'' > 1$.

Consequently, it is a reasonable simplification to neglect γ, which means that one can set $\Delta\gamma = 0$.

By eliminating $\Delta\gamma$ from the error Eq. F.5, one forces the full uncertainty onto Δa. Note that this way one can simply link the experimental uncertainty of the depolarization ratios, $\Delta\rho$, to Δa. With this equation (F.5) becomes

$$\Delta\rho = \frac{270b_{J''}a\gamma^2}{\left(45a^2 + 4b_{J''}\gamma^2\right)^2} (\Delta a) \tag{F.6}$$

which can be rewritten in terms of Δa as

$$\Delta a = \frac{\left(45a^2 + 4b_{J''}\gamma^2\right)^2}{270b_{J''}a\gamma^2} (\Delta\rho) \ . \tag{F.7}$$

The (systematic) error in $\Delta\rho$ in Eq. F.7 is determined experimentally via the depolarization ratio measurements (see Section 5.3.2.2).

With the $\Delta\gamma = 0$ simplification applied to Eq. F.3 and replacing Δa by Eql F.7 one obtains

$$\Delta\Phi = 2a\Delta a = \frac{\left(45a^2 + 4b_{J''}\gamma^2\right)^2}{135b_{J''}\gamma^2} (\Delta\rho) \ . \tag{F.8}$$

The relative error becomes

$$\frac{\Delta\Phi}{\Phi} = \frac{45a^2 + 4b_{J''}\gamma^2}{3b_{J''}\gamma^2} (\Delta\rho) = \frac{\Delta\rho}{\rho} \ . \tag{F.9}$$

This means that a good approximation of the relative uncertainty of the line strength function can be obtained by setting it equal to the relative uncertainty of the (measured) depolarization ratio.

Appendix G

Full tabulation of measured depolarization ratios

The following appendix is published "as-is" by the author and co-authors in the Supporting Information [Jam13c]. The layout and references have been adapted; the text has been slightly modified.

The analysis methods described in Section 5.3 have been applied to sets of depolarization measurements taken from four separate cells (3 at TLK and 1 at Swansea). The cell fillings are shown in Tab. G.1. The numbers are only rough indications for the actual mixture which are provided by the mixing facility (see [Stu10a]).

The corrected depolarization ratios obtained for the four cells are collated in Tab. G.2. Note that the data set numbers correspond to the gases within each cell filling. All the values summarized in Tab. G.2 are used in the functional dependence calculation (see Eq. 5.18 and Fig. 5.17) and in the discussion in Section 5.3.4.4.

Table G.1: Overview on the fillings of the various laser Raman cells. The Raman cell at Swansea was refilled and thus its fillings are denoted by 1a and 1b. The * in a cell of certain isotopologues indicates that this isotopologue was part of the minor rest which, if available, is quantized in the last column.

Location	Number	Total pressure (mbar)	Isotopologue fraction (%)						
			H_2	HD	HT	D_2	DT	T_2	Rest
TLK	1	763.1	25	*	46	*	-	26	3
TLK	2	400	-	*	*	15	47	34	4
TLK	3	1500	26.3	47.4	-	26.3	-	-	-
Swansea	1a	900	100	-	-	-	-	-	-
Swansea	1b	870	-	-	-	100	-	-	-

Table G.2: Overview on obtained depolarization ratios. The corresponding filling number is found in Tab. G.1. †: these values have been corrected by the $\rho_{\mathrm{obs}}(J'' = 0)$ value from TLK-1, HT. ‡: these values have been corrected by the $\rho_{\mathrm{obs}}(J'' = 0)$ value from TLK-1, H_2.

Filling	Isotopologue	J″	$\rho_{\mathrm{SP0SA-cor}}$	Error 1σ	$\rho_{\mathrm{lit-LeRoy-532nm}}$
TLK-1†	T_2				
		1	0.01650	0.00056	0.01735
		2	0.01193	0.00055	0.01250
		3	0.01115	0.00055	0.01171
		4	0.01041	0.00056	0.01146
		5	0.01133	0.00057	0.01138
		6	0.01155	0.00071	0.01136
		7	0.01563	0.00083	0.01139
TLK-1‡	T_2				
		1	0.01612	0.00056	0.01735
		2	0.01155	0.00056	0.01250
		3	0.01077	0.00055	0.01171
		4	0.01003	0.00056	0.01146
		5	0.01094	0.00057	0.01138
		6	0.01117	0.00071	0.01136
		7	0.01524	0.00083	0.01139
TLK-2	DT				
		1	0.01699	0.00055	0.01750
		2	0.01227	0.00056	0.01262
		3	0.01274	0.00056	0.01183
		4	0.01151	0.00056	0.01159
		5	0.01302	0.00061	0.01151
		6	0.01263	0.00085	0.01152
TLK-2	D_2				
		1	0.01798	0.00056	0.01764
		2	0.01330	0.00055	0.01272
		3	0.10698	0.00058	0.01194
		4	0.01089	0.00057	0.01171
		5	0.01380	0.00098	0.01164
		6	0.04561	0.00170	0.01166
TLK-3	D_2				
		1	0.01743	0.00055	0.01764
		2	0.01176	0.00055	0.01272
		3	0.01115	0.00055	0.01194
		4	0.01100	0.00055	0.01171
Swansea-1b	D_2				
		1	0.01824	0.00101	0.01764
		2	0.01306	0.00091	0.01272
		3	0.01277	0.00155	0.01194
		4	0.01209	0.00166	0.01171

to be continued on next page

Filling	Isotopologue	J″	$\rho_{\mathrm{SP0SA-cor}}$	Error 1σ	$\rho_{\mathrm{lit-LeRoy-532nm}}$
TLK-1	HT				
		1	0.01730	0.00055	0.01788
		2	0.01263	0.00055	0.01291
		3	0.01221	0.00055	0.01214
		4	0.01254	0.00056	0.01192
		5	0.01501	0.00077	0.01188
TLK-3	HD				
		1	0.01765	0.00055	0.01800
		2	0.01263	0.00055	0.01300
		3	0.01205	0.00055	0.01223
TLK-1	H_2				
		1	0.01769	0.00055	0.01830
		2	0.01332	0.00055	0.01324
		3	0.01284	0.00056	0.01248
TLK-3	H_2				
		1	0.01798	0.00055	0.01830
		2	0.01478	0.00055	0.01324
		3	0.01293	0.00056	0.01248
Swansea-1a	H_2				
		1	0.01899	0.00089	0.01830
		2	0.01414	0.00086	0.01324
		3	0.01329	0.00152	0.01248

Appendix H

Demonstration of bootstrapping on HYDE data

In Section 6.5.1 about the analysis of the HYDE data it was discussed, that the estimation of the statistical uncertainty of the fitting results was performed by statistical techniques such as the Jackknife and the Bootstrap method (according to [Efr94, Efr83]). These re-sampling techniques are recommended in general for statistical analysis if the sample size is not too low ($n < 5$) [Dav03].

In this Appendix details of the application of the Bootstrap method on the HYDE measurement data are presented.

General principle

Bootstrapping is a re-sampling technique in which the limited statistics of the sample data set is increased by generation of new sample sets.

Assume, that the sample set consists of the n elements

$$F : X_1,\, X_2,\, \cdots\, ,\, X_n\, . \tag{H.1}$$

A fit on this data set returns m fit parameters

$$a_1,\, a_2,\, \cdots,\, a_m\, . \tag{H.2}$$

Now, a new data set is created by re-sampling. This is realized by drawing n elements from F *with replacement* (independent random sampling [Efr83]).

$$F' : X'_1,\, X'_2,\, \cdots\, ,\, X'_n\, . \tag{H.3}$$

Note that due to the random sampling, in F' some elements from F appear multiple times and some are left out. A fit on this re-sampled data set will return m new fit parameters

$$a'_1,\, a'_2,\, \cdots,\, a'_m\, . \tag{H.4}$$

The process of re-sampling and fitting can be repeated for a large number N of iterations. Finally, the set of fit parameters, $a_i^{(j)}$, are then used to calculate and estimators for mean $\bar{a}_i$ and standard deviation $\sigma(a_i)$.

Application to HYDE data

The general principle of bootstrapping is now applied to the example of the HYDE data, which is also used to further illustrate the technique.

In the case of the HYDE measurements at a certain catalyst temperature T each elements X_k consist of the relative Raman signals (including propagated error) and the initial mole fractions for each isotopologue at a certain mixing ratio (element number k of a total n initial mixtures).

$$X_k = \left\{ S_{\mathrm{H_2,rel,k}},\, S_{\mathrm{D_2,rel,k}},\, S_{\mathrm{HD,rel,k}},\, \sigma(S_{\mathrm{H_2,rel,k}}),\, \sigma(S_{\mathrm{D_2,rel,k}}),\, \sigma(S_{\mathrm{HD,rel,k}}),\, y^i_{\mathrm{H_2,k}},\, y^i_{\mathrm{D_2,k}},\, y^i_{\mathrm{HD,k}} \right\} . \tag{H.5}$$

The fit parameters are

$$R_{\mathrm{H_2}},\, R_{\mathrm{D_2}},\, R_{\mathrm{HD}},\, K(T) . \tag{H.6}$$

Fig. H.1 shows histograms for each of the four parameters after $N = 1000$ times resampling and subsequently fitting. The following results are given for a catalyst temperature of $T = 25\,^{\circ}\mathrm{C}$ and the scenario where all fit parameters were left free (*c.f.* Section 6.5.1). The results are presented in the form $\bar{a}_i \pm \sigma(a_i)$:

$$R_{\mathrm{H_2}} = 0.9981 \pm 0.0037 , \tag{H.7}$$

$$R_{\mathrm{D_2}} = 0.9475 \pm 0.0037 , \tag{H.8}$$

$$R_{\mathrm{HD}} = 1.0242 \pm 0.0033 , \tag{H.9}$$

$$K(T) = 3.051 \pm 0.030 . \tag{H.10}$$

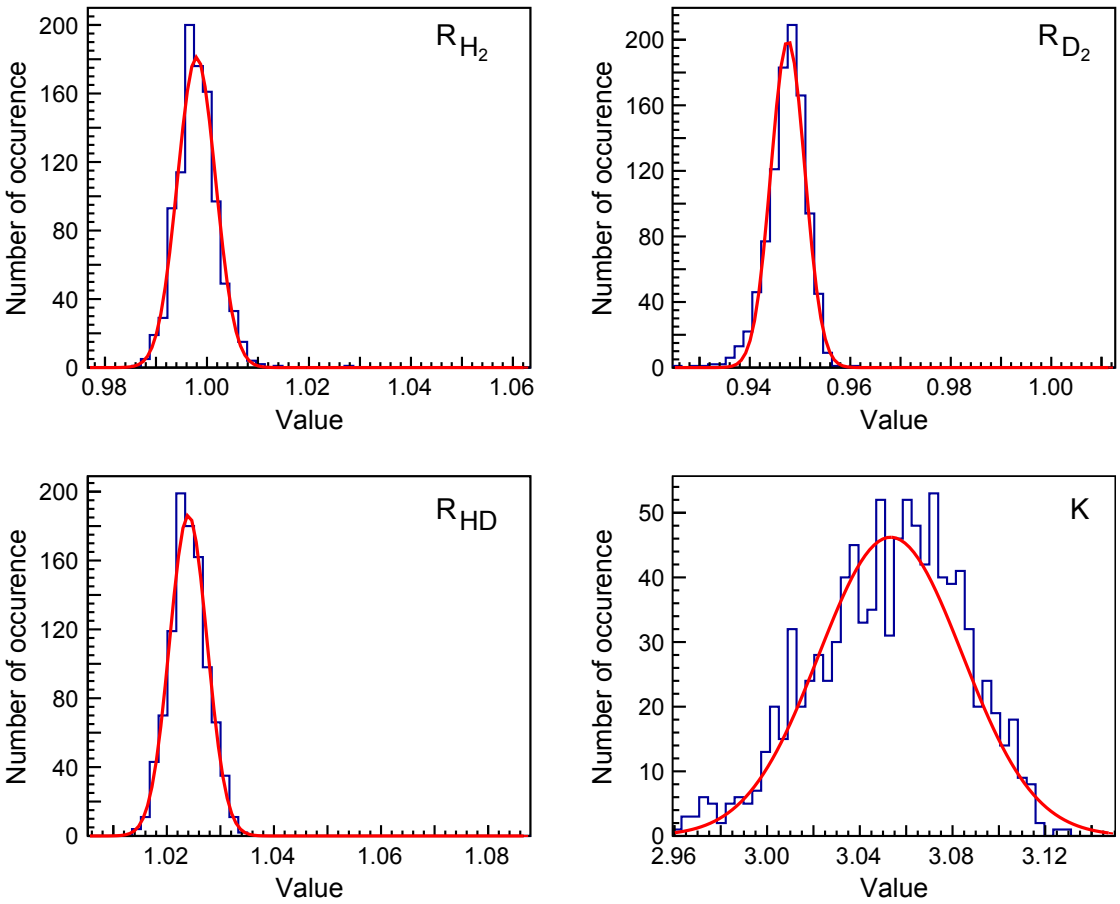

Figure H.1: Bootstrapping example with HYDE data. For each of the four fit parameters a histogram is shown fitted by a Gaussian to visualize the statistical distribution. Mean and standard deviation are obtained as estimator from the histrogram. The histograms contain $N = 1000$ entries corresponding to the number of re-sampled data sets. The data were obtained with a catalyst temperature of $T = 25\,^{\circ}\mathrm{C}$.

Appendix I

Publications

In course of this work several articles were published in scientific journals. A list of them is found below.

Peer-reviewed publications

1. M. Sturm, **M. Schlösser**, R. J. Lewis, B. Bornschein, G. Drexlin, H. H. Telle, *Monitoring of all hydrogen isotopologues at Tritium Laboratory Karlsruhe using Raman spectroscopy*, Laser Phys., **20** (2) (2010) 493-507

2. S. Fischer, M. Sturm, **M. Schlösser**, B. Bornschein, G. Drexlin, F. Priester, R.J. Lewis, H.H. Telle, *Monitoring of Tritium Purity During Long-Term Circulation in the KATRIN Test Experiment LOOPINO Using Laser Raman Spectroscopy*, Fus. Sci. Tech., **60** (2011) 925-930

3. **M. Schlösser**, S. Fischer, M. Sturm, B. Bornschein, R.J. Lewis, H.H. Telle, *Design Implications For Laser Raman Measurement Systems for Tritium Sample-Analysis, Accountancy or Process-Control Applications* , Fus. Sci. Tech., **60** (2011) 976-981

4. M. Babutzka, M. Bahr, J. Bonn, B. Bornschein, A. Dieter, G. Drexlin, K. Eitel, S. Fischer, F. Glück, S. Grohmann, M. Hötzel, T. M. James, W. Käfer, M. Leber, B. Monreal, F. Priester M. Röllig, **M. Schlösser**, U. Schmitt, F. Sharipov, M. Steidl, M. Sturm, H. H. Telle, N. Titov, *Monitoring of the operating parameters of the KATRIN Windowless Gaseous Tritium Source*, New J. Phys., **14** (2012) 103046

5. D. Demange, C.G. Alecu, N. Bekris, O. Borisevich, B. Bornschein, S. Fischer, N. Gramlich, Z. Köllö, T. L. Le, R. Michling, F. Priester, M. Röllig, **M. Schlösser**, S. Stämmler, M. Sturm, R. Wagner, S. Welte, *Overview of R&D at TLK for process and analytical issues on tritium management in breeder blankets of ITER and DEMO*, Fus. Eng. Des., **87** (7-8) (2012) 1206-1213

6. **M. Schlösser**, H. Seitz, S. Rupp, P. Herwig, C. G. Alecu, M. Sturm, B. Bornschein, *In-Line Calibration of Raman Systems for Analysis of Gas Mixtures of Hydrogen Isotopologues with Sub-Percent Accuracy*, Anal. Chem., **85** (5), (2013) 2739-2745

7. **M. Schlösser**, T. M. James, S. Fischer, R. J. Lewis, B. Bornschein, H. H. Telle, *Evaluation Method for Raman Depolarization Measurements including Geometrical Effects and Polarization Aberrations*, J. Raman Spectrosc., **44** (3) (2013) 453-462

Accepted / in press

8. **M. Schlösser**, S. Rupp, H. Seitz, S. Fischer, B. Bornschein, T. M. James, H. H. Telle, *Accurate calibration of the laser Raman system for the Karlsruhe Tritium Neutrino Experiment*, J. Mol. Struct. (2013), available online (in press), doi:10.1016/j.molstruc.2012.11.022

9. T. M. James, **M. Schlösser**, S. Fischer, M. Sturm, B. Bornschein, R. J. Lewis, H. H. Telle *Accurate depolarization ratio measurements for all diatomic hydrogen isotopologues*, J. Raman Spectrosc. (2013), (in press), doi:10.1002/jrs.4283

10. T. M. James, **M. Schlösser**, R. J. Lewis, S. Fischer, B. Bornschein, H. H. Telle, *Automated Quantitative Spectroscopic Analysis Combining Cosmic-Ray Removal, Background Subtraction and Peak Fitting*, Appl. Spectrosc. (2013), (in press), no DOI yet

Peer-reviewed publications (Proceedings)

1. S. Fischer, M. Sturm, **M. Schlösser**, R. J. Lewis, B. Bornschein, G. Drexlin, H.H. Telle, *Laser Raman Spectroscopy for KATRIN*, Nucl. Phys. B - Proc. Supp. 229-232 (2012) 492.

2. **M. Schlösser**, S. Fischer, M. Hötzel and W. Käfer, *Accuracy of the Laser Raman system for KATRIN*, in Proc. of the Int. School of Phys. "Enrico Fermi", Course CLXXXII "Neutrino Physics and Astrophysics", ed. G. Bellini (IOS, Amsterdam; SIF, Bologna) 2012, 333-336 or arXiv:1203.4099.

The publications with the highest relevance for the topic of this thesis have been attached in the following order:

(i) Pub. 6: M. Schlösser *et al* , "In-Line Calibration of Raman Systems for Analysis of Gas Mixtures of Hydrogen Isotopologues with Sub-Percent Accuracy".
Reprinted with permission from [Sch13a]. Copyright 2013 American Chemical Society.

(ii) Pub. 7: M. Schlösser *et al* , "Evaluation Method for Raman Depolarization Measurements including Geometrical Effects and Polarization Aberrations".
Copyright © 2013 John Wiley & Sons, Ltd.

(iii) Pub. 8: M. Schlösser *et al* , "Accurate calibration of the laser Raman system for the Karlsruhe Tritium Neutrino Experiment".
Reprinted from Publication [Jam13b]. Copyright 2013, with permission from Elsevier.

(iv) Pub. 9: T. M. James, M. Schlösser *et al* , "Accurate depolarization ratio measurements for all diatomic hydrogen isotopologues".
Copyright © 2013 John Wiley & Sons, Ltd.

Pub. 10 was not available online at the time of writing.

analytical chemistry

Article

pubs.acs.org/ac

In-Line Calibration of Raman Systems for Analysis of Gas Mixtures of Hydrogen Isotopologues with Sub-Percent Accuracy

Magnus Schlösser,* Hendrik Seitz, Simone Rupp, Philipp Herwig,† Catalin Gabriel Alecu, Michael Sturm, and Beate Bornschein

Institute for Technical Physics (ITEP), Tritium Laboratory Karlsruhe (TLK), Karlsruhe Institute of Technology (KIT), P.O. Box 3640, 76021 Karlsruhe, Germany

Supporting Information

ABSTRACT: Highly accurate, in-line, and real-time composition measurements of gases are mandatory in many processing applications. The quantitative analysis of mixtures of hydrogen isotopologues (H_2, D_2, T_2, HD, HT, and DT) is of high importance in such fields as DT fusion, neutrino mass measurements using tritium β-decay or photonuclear experiments where HD targets are used. Raman spectroscopy is a favorable method for these tasks. In this publication we present a method for the in-line calibration of Raman systems for the nonradioactive hydrogen isotopologues. It is based on precise volumetric gas mixing of the homonuclear species H_2/D_2 and a controlled catalytic production of the heteronuclear species HD. Systematic effects like spurious exchange reactions with wall materials and others are considered with care during the procedure. A detailed discussion of statistical and systematic uncertainties is presented which finally yields a calibration accuracy of better than 0.4%.

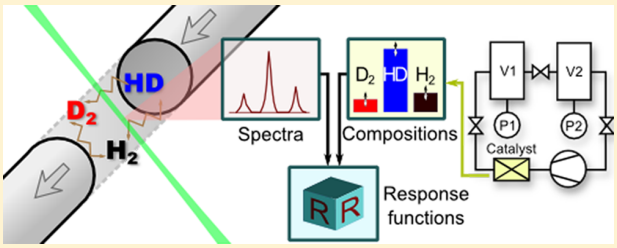

The quantitative analysis of the composition of gaseous samples of hydrogen isotopologues (H_2, D_2, T_2, HD, HT, and DT) with high accuracy is important in various fields of research; three of them are shortly mentioned in the following.

First, T_2 is used as gaseous β-source in the Karlsruhe Tritium Neutrino Experiment (KATRIN).[1] The other isotopologues appear as impurities and have to be measured accurately[2] in order to minimize systematic effects on the measurement of the neutrino mass. Second, tritium and deuterium will be used as fuel for future fusion reactors (such as ITER). The accurate analysis of the isotopic composition within the closed fuel cycle is of utmost importance for operational and safety reasons.[3] In fuel cycle R&D activities, often H_2, D_2, and HD runs are performed first for feasibility studies before radioactive tritium is employed. A reliable analysis of the gas composition at multiple stages of chemical processing facilities is therefore required for testing of functionality.[4] Third, frozen-spin polarized HD targets are employed in photonuclear experiments. The targets are made of high purity HD gas in which the residual H_2 and D_2 concentrations need to be known.[5,6]

For these applications, Raman spectroscopy is recommended as the method of choice, being a noncontact, in-line, multispecies analysis technique with high sensitivity.[7] KATRIN already employs Raman spectroscopy successfully for the compositional in-line analysis of the source gas.[8] For the accountancy of tritium in the fusion fuel cycle of ITER, Raman spectroscopy has become the preferred method.[9] In the HD target production for photonuclear research, currently, gas chromatography is the standard method. However, Raman spectroscopy would be an alternative there as well benefiting from the above-mentioned advantages. Besides these special applications on gaseous hydrogen isotopologues, it should be noted that Raman spectroscopy is used as a multipurpose tool in a large number of research fields.[10]

From a Raman spectrum, as shown in Figure 1, Raman signals can be obtained. Relative temporal changes in the

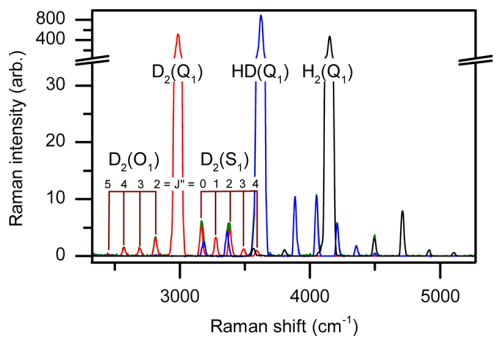

Figure 1. Typical Raman spectrum of H_2, HD, D_2. Total pressure $p \sim 330$ mbar; acquisition time $t = 10$ s. The individual components (red, blue, and black) are obtained by fitting to the measured spectrum (green); see color web version. Note that the vibrational−rotational lines (S_1 and O_1) are labeled only for D_2.

Received: November 7, 2012
Accepted: January 15, 2013
Published: January 15, 2013

composition can thus be monitored precisely. In many cases one is interested in the composition itself and thus in performing quantitative Raman spectroscopy.[11] Thus, the measurement technique employed requires a certain trueness. (The terminology of "precision", "trueness", and "accuracy" can be found in a publication by the Joint Committee for Guides in Metrology.[12] In short: precision is the reproducibility of a measurement (spread of single values around the mean value); trueness is the deviation of the mean value to the true value; and the deviation of a single measurement value to the true value is the accuracy. Thus, if a measurement is both "precise" and "true", it is called "accurate".) A high degree of trueness can be achieved by an adequate calibration. In general, accurate homogeneous calibration gas mixtures can be produced according to ISO standards 6142 and 6145.[13,14] However, these methods cannot be used for hydrogen isotopologues since the involved species are "potentially interactive substances" and "can decompose"[13] as it will be discussed in the following paragraph.

In this paper, a method is demonstrated for the accurate preparation of samples consisting of H_2 and D_2 and their reaction product HD. HD is not commercially available in high purity, and HD gas dissociates when kept in a container for a long time.[6] Thus, the heteronuclear isotopologue needs to be produced in a controlled manner within the mixing device. Our device, the HYdrogen Deuterium Equilibration loop (HYDE), is inspired by a technique used for the characterization of a gas chromatograph by Kawamura et al.[15] In our gas mixing device, two instead of one mixing vessel are installed and the whole system is designed as a loop rather than a "once-through" line. These modifications accrue several advantages in the performance and analysis of measurements. A similar mixing device was employed in a work by Okuno et al.[16] They, however, did not include details about the experimental setup and the calibration procedure. Additionally, no uncertainty study or discussion was included.

We start with a closer look on the actual calibration method and related issues. Then, the gas mixing loop and the Raman system employed for the calibration are introduced. Subsequently, results of the methods are presented and discussed with emphasis on the related calibration uncertainties. Finally, we conclude with some remarks on usability and prospects of this methods (e.g., use with tritium and options for in-line process monitoring).

■ CALIBRATION METHOD

Figure 1 shows a typical Raman spectrum of a gas mixture of the nonradioactive hydrogen isotopologues $x = H_2, D_2, HD$. Our aim is to derive the composition of such gas mixtures from their Raman spectra. From these spectra the Raman signals, S_x, can be obtained for each species x. They are given by the integrated areas under the respective Q_1-branches corrected for crosstalk from sidebands of other components. A calibration is required in order to link S_x to the number of molecules, N_x, in the gas via the so-called response function, R_x:

$$S_x = R_x N_x \tag{1}$$

This can be rearranged to obtain an equation for the normalized Raman signal:

$$S_{x,\mathrm{rel}} = \frac{S_x}{\sum_j S_j} = \frac{R_x N_x}{\sum_j R_j N_j} \tag{2}$$

with j representing the different components. By taking the Raman spectrum of a gas mixture of known composition, the determination of R_x for the three isotopologues would be no problem. However, such a well-known mixture of the three gases is not easy to produce by mixing, since, as stated above, high purity HD gas is in general not commercially available and can only be produced with great efforts.[6] Therefore, the method discussed here is based on the catalytic production of HD from well-known amounts of H_2 and D_2 via the isotopic exchange reaction

$$H_2 + D_2 \rightleftharpoons 2HD \tag{3}$$

In the following, a method will be presented to determine the response functions R_x for the three isotopologues $x = H_2, D_2, HD$ by using such equilibrated H_2−D_2-mixtures.

N_x^{i} are the known initial quantities of the hydrogen isotopologues ($x = H_2, D_2, HD$) before equilibration. The final quantities at equilibrium conditions, N_x^{eq}, can be calculated from the reaction equation:[17]

$$N_{H_2}^{\mathrm{eq}} = N_{H_2}^{\mathrm{i}} - \xi \tag{4}$$

$$N_{D_2}^{\mathrm{eq}} = N_{D_2}^{\mathrm{i}} - \xi \tag{5}$$

$$N_{HD}^{\mathrm{eq}} = N_{HD}^{\mathrm{i}} + 2\xi \tag{6}$$

Here, ξ is the extent of reaction.

The concentrations of educts and products at equilibrium obey the law of mass action with the equilibrium constant

$$K = \frac{[HD]^2}{[H_2][D_2]} \tag{7}$$

Inserting eqs 4−6 into eq 7 leads to

$$K = \frac{(N_{HD}^{\mathrm{eq}})^2}{N_{H_2}^{\mathrm{eq}} N_{D_2}^{\mathrm{eq}}} \tag{8}$$

$$K = \frac{(N_{HD}^{\mathrm{i}} + 2\xi)^2}{(N_{H_2}^{\mathrm{i}} - \xi)(N_{D_2}^{\mathrm{i}} - \xi)} \tag{9}$$

This is solved for ξ (for $K \neq 4$)

$$\xi_{\pm}(K) = \frac{b \pm \sqrt{b^2 - 4(K-4)\left(K N_{H_2}^{\mathrm{i}} N_{D_2}^{\mathrm{i}} - (N_{HD}^{\mathrm{i}})^2\right)}}{2(K-4)} \tag{10}$$

with

$$b = K(N_{H_2}^{\mathrm{i}} + N_{D_2}^{\mathrm{i}}) + 4N_{HD}^{\mathrm{i}} \tag{11}$$

Only the solution ξ_- is physical. By inserting ξ_- into eqs 4−6, the quantities of the hydrogen isotopologues in the thermodynamical equilibrium N_x^{eq} can be calculated for a certain K, if the initial concentrations in the mixture, N_x^{i}, are known.

In the mixing loop described in the next section, mixtures consisting of hydrogen and deuterium of well-known amounts N_x^{i} can be mixed and equilibrated. However, in addition a thorough knowledge of the reaction constant K is necessary in order to obtain accurate information about the gas composition. This reaction constant, which determines the ratio of the reaction partners in thermodynamical equilibrium (see eq 7), is a function of temperature. In principle, its values $K(T)$ can be calculated accurately from statistical mechanics as

discussed in relevant literature.[18,19] However, the determination of the actual reaction temperature is not a straightforward task. The measurement of the temperature inside a reactor which contains catalyst pebbles and the thermocouple itself are limited in measurement trueness. Therefore the uncertainty in the temperature will propagate into any functional relation of $K(T)$. For these reasons, an analysis method which is less sensitive to the knowledge of the true reaction temperature value is strongly favored.

The method presented in this publication makes use of the possibility to reproduce the reaction temperature precisely (±2 K) in different measurements as will be discussed in the Experimental Section below. Note, that in general, the precision, i.e., reproducibility, of a measurement is not restricted by the limitations in the measurement trueness. By taking several measurements at the same temperature T_0, but with varying gas composition, the same $K(T_0)$ should be found for different gas quantities N_x^{eq}.

A term for the quantities N_x^{eq} is obtained from eqs 4−6 with ξ_- inserted from eq 10. Finally, the parameters of interest, the three response functions R_x as well as $K(T_0)$, are then obtained from a fit of the right side of eq 2 to the actually measured relative Raman signals.

■ EXPERIMENTAL SECTION

Gas Mixing Device. In Figure 2, a sketch of the mixing loop setup HYDE is shown. All vessels and pipes are made of stainless steel. From the H_2 and D_2 gas bottles, the evacuated volumes ($\ll 10^{-2}$ mbar) V1 and V2 can be filled with the corresponding gas. Since both volumes are of the same size (the volumes are V1 = 1665 ± 9 cm^3 and V2 = 1655 ± 8 cm^3 as determined by the method described in ref 20), according to the ideal gas law a certain H_2-to-D_2 ratio in the gas mixture can be achieved by choosing the same ratio of pressures in V1 and V2 (measured by pressure gauges P1 and P2; range = 0...1000 mbar; accuracy = 0.3 mbar; type 626AX13MBD, MKS, www.mksinst.com). The gas can then be sent around the actual loop by the circulation pump, passing a heated catalyst in which parts of the H_2 and D_2 react to HD. The amount of HD produced depends on the catalyst temperature which defines the resulting thermal equilibrium state (see eq 9). The catalyst is located inside an about 130 mm long part of a stainless steel tube with an inner diameter of 10 mm and a total length of about 180 mm. The catalyst pebbles are made of 0.5% Pt on 1/16 in. Al_2O_3 (Alfa Aesar, www.alfa.com). A NiCr-Ni thermocouple is integrated into the tube to measure the temperature of the gas within the catalyst pebbles. The catalyst tube is surrounded by heating tape which is connected to a heating controller.

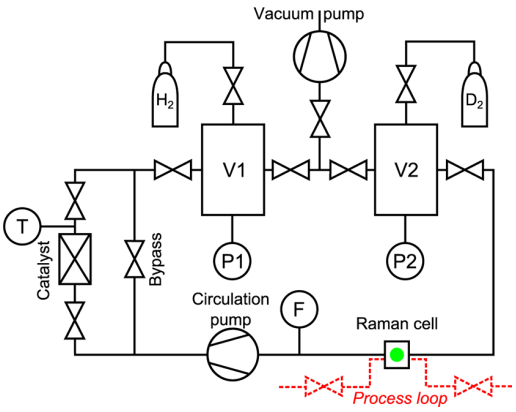

Figure 2. Sketch of the HYDE loop setup. The optional process loop is discussed in the Discussion section.

The Raman measurement cell is part of the loop, so that the resulting mixture of inactive hydrogen isotopologues is pumped through the measurement region continuously. A flow controller (F) provides a uniform gas flow (type 1179AX24CR1BVSPC1, www.mksinst.com).

Raman System. The Raman system employed in this work is by and large the same system as described in Sturm et al.[21] It contains a light collection and detection system, comprising optics for imaging the Raman excitation volume onto an optical fiber bundle, optics to transfer the fiber bundle output through a razor-edge Rayleigh filter onto the spectrometer slit, a Czerny-Turner spectrometer, and a CCD 2D array detector (PIXIS:400B, Princeton Instruments, www.princetoninstruments.com).

Some modifications were made, namely, (i) a retro-reflecting mirror for nearly doubled laser intensity in the Raman cell was inserted; (ii) the plano-convex lenses in the light collection path were replaced by two 2 in.-diameter achromatic lenses with f = 75 mm, to reduce chromatic aberrations; and (iii) the PI-Acton HTS spectrometer was replaced by a PI-Acton SP2150 unit (Princeton Instruments, www.princetoninstruments.com; f = 150 mm, 600 gr/mm). In addition, a linear polarizer was introduced between the two collection achromats. A typical spectrum acquired with this Raman system is shown in Figure 1.

■ MEASUREMENTS

Before the start of the actual measurements, several steps to prepare the gas mixing loop were necessary. First, a leak test of the loop was performed. The integral leak rate was found to be $<10^{-9}$ mbar L s^{-1}. Then the loop was purged for an hour with dry Ne which was heated to 300 °C in the catalyst and then sent through a cold trap at liquid nitrogen (LN_2) temperature. By this method, residual moisture was removed, since water in the system could influence the gas composition via the reaction $H_2O + D_2 \rightleftharpoons HD + HDO$. Third, in order to reduce changes of the gas composition due to outgassing from the walls or the catalyst, the system was evacuated with a turbomolecular pump for more than 12 h and then the catalyst was baked out at 300 °C for at least 3 h. Finally, in order to avoid the influence by memory effects in the catalyst and its reactor walls as being the active component, a prerun was performed to obtain a forced isotope exchange. An additional goal of this prerun was to load the catalyst surfaces with the mixture of the intended measurement, so that in case of outgassing in the main run the gas composition is not changed significantly. The prerun was performed by heating the catalyst up to 300 °C and then circulating the same mixture through it as in the main run. At this temperature, exchange reactions are likely to happen (see Mizuno et al.[22]). Note that the first two steps had to be performed only once, whereas steps three and four were performed prior to each measurement.

The main calibration measurements were performed at different temperature set points of the catalyst: 25, 50, 75, 100, and 125 °C. Higher temperatures were not employed due to enhanced exchange reactions above this level.[22] Measurements were performed with different initial ratios of H_2−D_2 (5:95,

10:90, 20:80, ..., 90:10, 95:5). The full measurement protocol is found in the Supporting Information.

The purity of the employed gases was 99.9999% for H_2 and 99.7% for D_2 (Air Liquide, www.airliquide.com). In a Raman premeasurement, the purity for D_2 was confirmed, with the rest being HD. This has been accounted for in the calculations.

During the whole process of mixing and equilibration, Raman measurements were taken continuously in order to monitor whether the composition was still changing or if a steady (equilibrium) state had been established.

RESULTS

For each measurement, the mole fractions y_x^i of the initial quantities have been calculated from the inlet pressures, vessel volumes, and gas purities. The Raman spectra have been pretreated by the open-source Spectral Analysis software (download from spectools.sourceforge.net) as discussed in ref 23. In order to obtain the absolute Raman signal S_x for any of the isotopologues, the area under the respective vibrational Q_1 branch has been taken. Overlaps of S_1 and O_1 lines of one isotopologue with the Q_1 branch of another isotopologue (compare Figure 1) have been corrected. From these, the relative Raman intensities $S_{x,\mathrm{rel}}$ have been calculated according to eq 2 and error propagation has been performed in order to obtain the statistical uncertainty $\sigma(S_{x,\mathrm{rel}})$. These data have been collated in analysis sets.

The analysis principle has already been introduced in the Calibration Method section. If eqs 4, 5, and 6 are substituted in eq 2, one obtains the expression (exemplarily given for H_2)

$$S_{H_2,\mathrm{rel}} = \frac{R_{H_2}N_{H_2}^{eq}}{R_{H_2}N_{H_2}^{eq} + R_{D_2}N_{D_2}^{eq} + R_{HD}N_{HD}^{eq}} \tag{12}$$

$$= \frac{R_{H_2}(N_{H_2}^{i} - \xi_-)}{R_{H_2}(N_{H_2}^{i} - \xi_-) + R_{D_2}(N_{D_2}^{i} - \xi_-) + R_{HD}(N_{HD}^{i} + 2\xi_-)} \tag{13}$$

Note that ξ_- is dependent on K as shown in eq 10. Thus, four fit parameters are required: the three response functions R_x and the equilibrium constant K. The fits have been performed with a least-squares fit using the Minuit routine of ROOT.[24] For each of the five catalyst temperatures T, the three individual curves ($S_{H_2,\mathrm{rel}}$, $S_{D_2,\mathrm{rel}}$, and $S_{HD,\mathrm{rel}}$ according to eq 13) are fitted simultaneously to the measured data sets. Each of the curves is a function of the measured mole fractions y_x^i (which are proportional to N_x^i) and is dependent on the same parameters R_{H_2}, R_{D_2}, R_{HD}, and $K(T)$. The fitting curves for the data before and after the equilibration are displayed in Figure 3. Note that the gas mixtures with initial H_2−D_2 ratios of 20:80 and 80:20 have been prepared twice. However, this cannot be noticed from Figure 3 because of the high reproducibility of the preparation and measurement. The estimation of the statistical uncertainty of the fitting results has been performed by recommended statistical techniques such as the Jackknife and the Bootstrap methods.[25,26] In order to investigate systematic influences of this analysis method, different fitting scenarios were considered in which some parameters were fixed in the fit of the ternary mixture. In one scenario, all parameters were kept free. In another, the ratio R_{H_2}/R_{D_2} as obtained from the binary mixture fit was fixed. Finally, the values of $K(T)$ as calculated from statistical mechanics were fixed in a third scenario. In Table 1 the resulting relative response functions

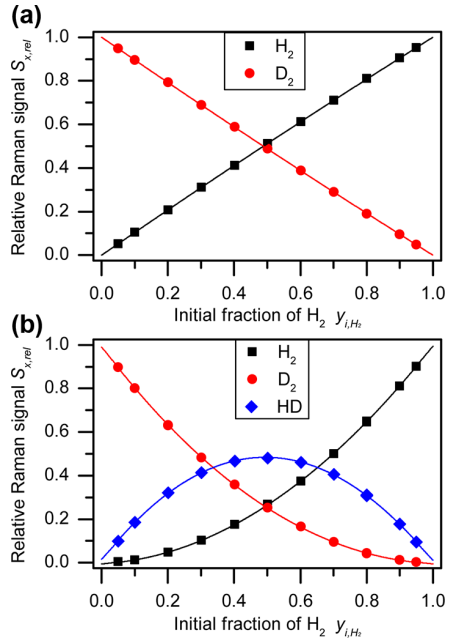

Figure 3. Fitting of the HYDE data at a catalyst temperature of 25 °C. The horizontal axis represents the mole fraction $y_{H_2}^i$ of H_2 before the equilibration of the mixture. The vertical axis represents the measured relative Raman intensities of the three components. Legend: symbols, measurement points; lines, fit curves. Top panel: before equilibration (binary mixture); bottom panel: after equilibration (ternary mixture). Note, that the error bars of the measurement points which are calculated via error propagation from Raman intensity and pressure/volume uncertainties are all <0.002 and thus smaller than the size of the symbols.

$$R_{x,\mathrm{rel}} = R_x \Big/ R_{\mathrm{mean}} = nR_x \Big/ \sum_{j=1}^{n} R_j \tag{14}$$

are listed.

In Figure 4 the results of the various fit scenarios are shown. In addition this graph shows the influence of the temperature on the results. The following observations can be made: First, the error bars as obtained from bootstrapping become larger with higher temperatures. The size of the error bar at the 125 °C temperature setting is in general twice as large compared to the measurement at about 25 °C. Possibly this is due to a combination of effects, namely, (i) a higher exchange rate with the heated stainless steel walls[22] and the catalyst material and thus high dependence of the current composition on the previous and (ii) the strong isotope effect for hydrogen isotopes/isotopologues (compared to other elements). In this context especially, different permeation constants (see, e.g., Katsuta and Furukawa[27] and references therein) and thermal conductivities (see, e.g., Saxena and Saxena[28]) are of relevance. For this reason, in the following discussion it will be assumed that the values at T = 25 °C are most trustworthy.

Second, for the fit with a fixed ratio of R_{H_2}/R_{D_2} as obtained from the binary fit, i.e., from the nonequilibrated mixtures, the fitting results (red dashed lines) are almost identical to those obtained by other fit methods with free ratio (black straight and blue dotted lines) in the case of R_{HD}. In the case of R_{H_2} and R_{D_2}, the fitting results have a certain offset (<0.5%). This shows that the use of the catalyst has an effect on the H−D ratio in the gas

Table 1. Results Overview of the Relative Response Functions for Different Catalyst Temperatures[a]

T	$R_{H_2,rel}$			$R_{D_2,rel}$			$R_{HD,rel}$		
(°C)	value	σ_{rel} (%)	Δ_{rel} (%)	value	σ_{rel} (%)	Δ_{rel} (%)	value	σ_{rel} (%)	Δ_{rel} (%)
25	1.0128	0.15	0.33	0.9692	0.15	−0.33	1.0180	0.29	−0.01
50	1.0116	0.17	0.40	0.9681	0.17	−0.42	1.0202	0.33	0.00
75	1.0103	0.21	0.44	0.9669	0.21	−0.44	1.0228	0.41	−0.02
100	1.0084	0.26	0.39	0.9651	0.26	−0.37	1.0265	0.51	−0.03
125	1.0053	0.37	0.24	0.9620	0.37	−0.20	1.0327	0.70	−0.04

[a]The present values are obtained for the fit scenario in which the ratio R_{H_2}/R_{D_2} from the binary fit was fixed. σ_{rel} is the relative statistical uncertainty as obtained by bootstrapping. Δ_{rel} is the relative difference to the values obtained for the fit scenario where all parameters were kept free. T: catalyst temperature set point. Full tabulations of the results of all fitting scenarios including K are given in the Supporting Information in Table S-1.

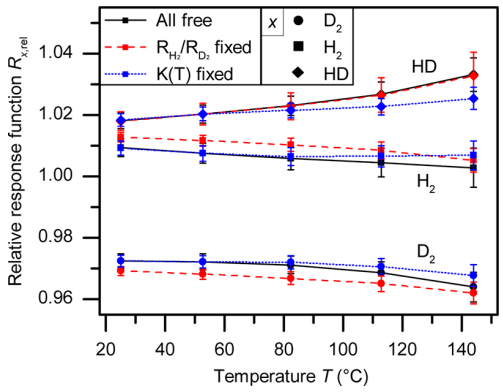

Figure 4. Influence of the catalyst temperature on the fit results of the relative response function. Color and line style indicate the fitting scenario, while the symbol style represents the type of isotopologue. Values and error bars have been obtained by bootstrapping. Note that the obtained temperature values differ from the temperature set points.

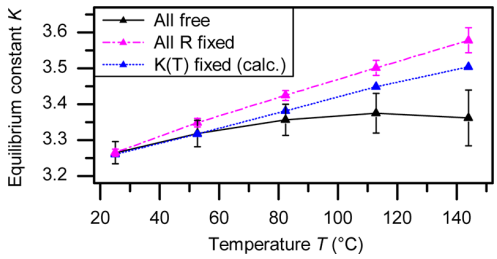

Figure 5. Fit results of the equilibrium constant K. No error bars are given for the "$K(T)$ fixed" scenario, since these values are derived from accurate statistical mechanics calculations.

mixture and thus on the H_2−D_2 ratio, possibly due to reactions of H and D atoms with the walls or catalyst material. It should be noted, that the systematic shift in the $R_{x,rel}$ functions is of the order of the statistical error.

Third, if the reaction constant $K(T)$ is not fixed in the fit (black straight and red dashed line), then R_{HD} increases while R_{H_2} and R_{D_2} decrease. Naturally, R_x should not have any temperature dependence. When fixing the reaction constants to those as expected from the calculations (blue dotted line), this seeming temperature dependence is suppressed. K and R_{HD} are correlated due to their similar effect on the trend of the HD curve in Figure 3. Therefore, the trend of high R_{HD} values in cases with free K and with higher temperatures hints to a slight underestimation of K. It is also interesting that the R_x values for fixed (blue dotted) and free (black straight) $K(T)$ values are nearly identical for T < 85 °C, which shows the robustness of this approach. In order to investigate the $K(T)$ dependence of the equilibration reaction, we performed a further fit in which we fixed all three R_x values as obtained from the "all free" fit at T = 25 °C. Thus, the only remaining free parameter was K. In Figure 5 the fitted K values are plotted together with the calculated values as a function of temperature. Though following the same trend, it can be seen that these fitted K are higher than the expected values. However, despite this it should be noted that all curves agree at K(25 °C) = 3.26 ± 0.01.

On the basis of these considerations, the results from the scenario with a fixed ratio of R_{H_2}/R_{D_2} at a set-point temperature of 25 °C were chosen as the final results for the response function $R_{x,rel}$ (see Table 1). The fit of the binary mixture takes advantage of the absence of any systematic effects which occur only during the equilibration and thus should exhibit the highest trueness.

The T = 25 °C values were chosen for several reasons: (i) The statistical errors from the bootstrap methods are the smallest for this temperature; (ii) the temperature gradient between catalyst reactor and the rest of the gas system is minimal since said temperature is approximately room temperature, so that the equilibrium constant K is the same in the whole gas system; (iii) exchange reactions with walls are minimized; and (iv) the confidence in the equilibrium constant is the highest.

Concerning the uncertainty of the values obtained in this manner, the most important point, which should be recalled from the previous sections, is that the fit converges to results with statistical errors in the subpercent range. The systematical spread is in a similar range if different parameters are fixed (R_x and/or $K(T)$) or left free or if the operational temperature is changed. The discussion above shows that it is legitimate to use this spread as a systematic error. We therefore add the squared systematic and statistical uncertainty (from Table 1) and finally obtain the following results valid for our Raman system:

$$R_{H_2,rel} = 1.0128 \pm 0.0037 \quad (15)$$

$$R_{D_2,rel} = 0.9692 \pm 0.0036 \quad (16)$$

$$R_{HD,rel} = 1.0180 \pm 0.0029 \quad (17)$$

This means that the calibration uncertainty is within 0.4%, proving that this method and device is well capable to provide accurate calibration mixtures.

■ DISCUSSION

Remarks on the Use of a Permeator. The hydrogen mixtures in this work have been equilibrated by the means of a

catalyst reactor. Another possibility would be the use of a permeator mainly consisting of a palladium membrane which is heated to about 400 °C (see Shu et al.[29] and references therein). In 2005, Borysow and Fink used a Raman system to monitor exchange reactions in gaseous hydrogen and deuterium.[30] For the generation of HD, they used a Gas Technologies model HP-4 which is based on permeation through a palladium membrane. We could show in test measurements that these membranes (in our case, a Leybold-Heraeus palladium diffusion cell PA 150) change the relative concentration due to different permeabilities of atomic H and D through the membranes (as predicted by Glugla et al.[31]). This is demonstrated in Figure 6 which shows a measurement

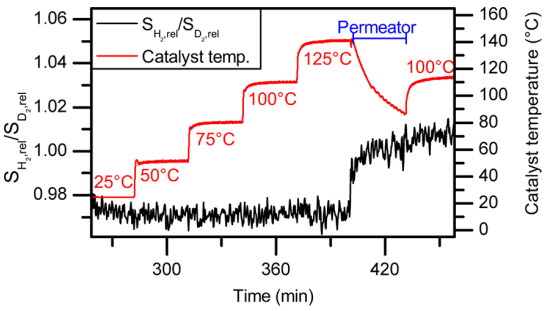

Figure 6. Time trend of catalyst temperature and relative intensity ratio of H_2−D_2 influenced by permeator operation. The initial concentration $[H_2]$−$[D_2]$ was 1:1. The HD concentration is not shown here. Note that this measurement was performed with a different grating spectrometer, so that the ratio of $S_{H_2,rel}/S_{D_2,rel}$ differs from what would be expected from the calibrated $R_{H_2,rel}/R_{D_2,rel}$ from eqs 15−17. The temperature labels refer to the temperature set points of the heating tape; the actual temperatures (second vertical axis) were measured directly within the catalyst tube.

of a mixture with initially 50% H_2 and 50% D_2. According to eqs 4 and 5, the ratio of $N^{eq}_{H_2}/N^{eq}_{D_2}$ (or S_{H_2}/S_{D_2}) should not change in this special case, even when the extent of reaction ξ changes due to shifts in $K(T)$. The measurement shows that this ratio is constant as long as the mixture is cycled through the catalyst, independent of its temperature. However, when the gas flow is switched from the catalyst to the permeator, this ratio suddenly changes by about 3% and stays at the new value if the flow is redirected through the catalyst again. This can be explained by the fact that deuterium atoms have a lower permeability coefficient than hydrogen atoms,[31] so that they are partly retained by membranes and thus do not appear in the Raman signal. Therefore, we cannot recommend permeators for the production of highly accurate hydrogen mixtures.

Suggested Improvements. Even though the calibration results reveal a high accuracy, some modifications to the actual gas mixing setup (see Figure 2) are suggested to further reduce systematic effects: (i) The piping between vessels, Raman cell, catalyst, and pump is rather long (∼5 m) in our setup, which permits convenient handling, but at the same time implies a large inner surface, where exchange reactions could happen. In principle, in our setup the piping could be reduced by half. In general, the authors recommend to reduce the piping as much as possible in similar setups. (ii) Currently, the gas mixing vessels are made of two off-the-shelf ConFlat-T-pieces. The use of these standard components offers a high similarity of volume of both vessels and thus low systematic uncertainties in the initial mole fractions y^i_x. However, because of inadequate pipe routing in our setup, a "dead volume" was created in which the mixing of the gas is suppressed. We have overcome this difficulty by long mixing periods (∼25 min) with intermittent blocking of the gas stream in order to pump all gas into one of the vessels while the other was emptied. These extra efforts of forcing the species to mix could also be obtained by a more sophisticated gas flow design through the vessels. (iii) Finally, the catalyst reactor design could be optimized to achieve a better control on reactor temperature and its homogeneity within the reactor tube to obtain the equilibrium condition more accurately.

Use with Tritium. The extension of the described calibration method to tritiated molecules is a demanding task, mainly because of (i) radio-chemical reactions (such as self-equilibration) due to tritium β-activity,[17] (ii) limited T_2 purity (a purity of up to 98% can be obtained at the Tritium Laboratory Karlsruhe)[32], (iii) the necessity to efficiently remove the Raman inactive decay product ^3He from stored tritium before mixing (about 0.5% of an amount of tritium decays every month), and (iv) the technical efforts for the installation of a tritium-compatible system.

These caveats may inhibit that the same calibration accuracy is reached. Also, safety considerations such as the maximum allowed tritium inventory may constrain the technical realization of a potential hydrogen−deuterium−tritium mixing loop.

Thus, an alternative calibration approach has been pursued by the authors.[33] In the said alternative approach, the full coverage of the response functions of all six hydrogen isotopologues has been obtained by the use of *ab initio* theoretical Raman intensities calculated from quantum mechanics in combination with an accurate measurement of the system's spectral sensitivity. The calibration results obtained in this way for the nontritiated isotopologues agree to better than 2% with the results of the HYDE method described in this paper.

Application of the Calibration Technique for in-Line Monitoring Systems. The results above show that the achievable calibration accuracy is below 1%. This accuracy would exceed monitoring requirements for in-line accountancy systems in future fusion applications.[3,34]

After realigning of the optical system or even repositioning the Raman cell, the calibration may become invalid. In order to avoid any changes to the Raman system and its alignment to maintain the accurate calibration, one could implement a simplified HYDE-like calibration loop directly into the process loop in which the accountancy should take place. This is sketched in Figure 2. The black (solid) loop is active during calibration but is disconnected by closing the connection valves in standard operation, i.e., when the process loop (red, dashed) is active. By employing automatic valves and a software process control, the calibration process could be employed completely automatically, which may be quite useful for application in large process facilities like fusion power plants.

■ CONCLUSIONS

We have demonstrated a method which uses accurately produced gas samples of H_2, D_2, HD for a successful calibration of an in-line Raman system. Because of the nonavailability of pure HD, a mixing loop was built which mixes H_2−D_2 volumetrically and then uses the thermodynamic equilibrium exchange reaction accelerated by catalysis to produce HD. It

has been shown, that this condition can be established in the most reliable way at low (room) temperature. Statistical and systematical uncertainties at this temperature lead to total uncertainties in the relative Raman response functions, $R_{x,\mathrm{rel}}$, of less than 0.4%.

These results are beyond the trueness requirements of the current applications at KATRIN[2,33] and nuclear fusion[3,9] and thus are able to confirm the choice of Raman spectroscopy for in-line gas analysis. Currently, a loop including the ability to produce accurate mixture of all six hydrogen isotopologues is installed at the Tritium Laboratory Karlsruhe to investigate the performance of this method when tritiated species are employed.

It should be noted that even if the focus was on the calibration of a Raman system, in principle the described technique is equally suitable for the calibration of various analytic techniques (e.g., IR/UV−Vis spectroscopy, mass spectroscopy, gas chromatography, ...). The same applies for mixtures of gases other than the hydrogen isotopologues which are also only stable in thermodynamic equilibrium. In general, Raman spectroscopy with a highly accurate calibration is a superior technique for quantitative compositional analysis, especially when only known species like hydrogen isotopologues are present in the sample.[7,8] Moreover, recalibration does not need to be performed as frequently as compared to other techniques like gas chromatography since the analyte is not in contact with the detection system.

■ ASSOCIATED CONTENT

Supporting Information

Detailed measurement protocol and full tabulation of all fit scenarios. This material is available free of charge via the Internet at http://pubs.acs.org.

■ AUTHOR INFORMATION

Corresponding Author

*E-mail: magnus.schloesser@googlemail.com.

Present Address

†MPIK, Heidelberg, Germany.

Notes

The authors declare no competing financial interest.

■ ACKNOWLEDGMENTS

This research was supported by the Helmholtz Association (HGF) and the Federal Ministry of Education and Research (BMBF) through Grants 05A08VK2 and 05A11VK3. The authors wish to thank D. Adami for the mechanical construction works. Furthermore we appreciate the vital discussions about chemical properties of hydrogen with D. Demange, R. Michling, R. Wagner, and J. Wendel (all TLK) and about Raman spectroscopy with S. Fischer (TLK) and H. H. Telle (Swansea University). We gratefully thank A. Poon (Berkeley Lab) for discussions about the statistical analysis. Finally, we thank the administrative and technical staff of TLK for their support.

■ REFERENCES

(1) The KATRIN collaboration. KATRIN Design Report 2004; FZKA Scientific Report 7090, 2005.

(2) Babutzka, M.; et al. *New J. Phys* **2012**, *14*, 103046.

(3) Nishi, M.; Yamanishi, T.; Hayashi, T. *Fusion Eng. Des.* **2006**, *81*, 745−751.

(4) O'Hira, S.; et al. *Nucl. Fusion* **2000**, *40*, 519.

(5) Whisnant, C. S.; Hansen, P. A.; Kelley, T. D. *Rev. Sci. Instrum.* **2011**, *82*, 024101.

(6) Ohta, T.; et al. *Nucl. Instrum. Meth. A* **2012**, *664*, 347−352.

(7) Schlösser, M.; Fischer, S.; Sturm, M.; Bornschein, B.; Lewis, R. J.; Telle, H. H. *Fusion Sci. Technol.* **2011**, *60*, 976−981.

(8) Fischer, S.; Sturm, M.; Schlösser, M.; Bornschein, B.; Drexlin, G.; Priester, F.; Lewis, R.; Telle, H. *Fusion Sci. Technol.* **2011**, *60*, 925−930.

(9) Shu, W. *Raman Spectroscopy for the ITER Tritium Plant Analytical System (ITER organisation)*; Private communication, 2012.

(10) Lyon, L. A.; Keating, C. D.; Fox, A. P.; Baker, B. E.; He, L.; Nicewarner, S. R.; Mulvaney, S. P.; Natan, M. J. *Anal. Chem.* **1998**, *70*, 341−362.

(11) Pelletier, M. J. *Appl. Spectrosc.* **2003**, *57*, 20A−42A.

(12) Working Group 2 of the Joint Committee for Guides in Metrology. *International vocabulary of metrology - Basic and general concepts and associated terms (VIM)*, 3rd ed.; JCGM 200:2008; Bureau International des Poids et Mesures (BIPM): Sèvres, France, 2008.

(13) International Organization for Standardization. ISO 6142, *Gas analysis - Preparation of calibration gas mixtures - Gravimetric method*; 2001.

(14) International Organization for Standardization. ISO 6145, *Gas analysis - Preparation of calibration gas mixtures using dynamic volumetric methods*; 2003.

(15) Kawamura, Y.; Onishi, Y.; Okuno, K.; Yamanishi, T. *Fusion Eng. Des.* **2008**, *83*, 1384−1387.

(16) Okuno, K.; Uda, T.; O'Hira, S.; Naruse, Y. *J. Nucl. Sci. Technol.* **1991**, *28*, 509−516.

(17) Souers, P. C. *Hydrogen Properties for Fusion Energy*; University of California Press, Berkeley, CA, 1986.

(18) McQuarrie, D. A. *Statistical Mechanics (Harper's Chemistry Series)*; HarperCollins College Division: New York, 1976.

(19) Atkins, P. W.; de Paula, J. *Physical Chemistry*, 8th ed.; W.H. Freeman: New York, 2006.

(20) Köllö, Z.; Alecu, C. G.; Moosmann, H. *Fusion Sci. Technol.* **2011**, *60*, 972−975.

(21) Sturm, M.; Schlösser, M.; Lewis, R. J.; Bornschein, B.; Drexlin, G.; Telle, H. H. *Laser Phys.* **2009**, *20*, 493−507.

(22) Mizuno, M.; Anzai, H.; Aoyama, T.; Suzuki, T. *Mater. Trans., JIM* **1994**, *35*, 703−707.

(23) James, T. M.; Schlösser, M.; Lewis, R. J.; Fischer, S.; Bornschein, B.; Telle, H. H. *Appl. Spectrosc.* **2012**, submitted for publication.

(24) Brun, R.; Rademakers, F. *Nucl. Instrum. Meth. A* **1997**, *389*, 81−86.

(25) Efron, B.; Tibshirani, R. *An Introduction to the Bootstrap*; Chapman and Hall/CRC: New York, 1994.

(26) Efron, B.; Gong, G. *Am. Stat.* **1983**, *37*, 36−48.

(27) Katsuta, H.; Furukawa, K. *J. Nucl. Sci. Technol.* **1981**, *18*, 143−151.

(28) Saxena, S. C.; Saxena, V. K. *J. Phys. A: Math. Gen.* **1970**, *3*, 309.

(29) Shu, J.; Grandjean, B. P. A.; Neste, A. V.; Kaliaguine1, S. *Can. J. Chem. Eng.* **1991**, *69*, 1036−1060.

(30) Borysow, J.; Fink, M. *J. Nucl. Mater.* **2005**, *341*, 224−230.

(31) Glugla, M.; Cristescu, I. R.; Cristescu, I.; Demange, D. *J. Nucl. Mater.* **2006**, *355*, 47−53.

(32) Dörr, L.; Besserer, U.; Glugla, M.; Hellriegel, G.; Hellriegel, W.; Schäfer, P.; Wendel, J. *Fusion Sci. Technol.* **2005**, *48*, 262−267.

(33) Schlösser, M.; Rupp, S.; Seitz, H.; Fischer, S.; Bornschein, B.; James, T. M.; Telle, H. H. *J. Mol. Struct.* **2012**, DOI: 10.1016/j.molstruc.2012.11.022.

(34) Demange, D.; et al. *Fusion Eng. Des.* **2012**, *87*, 1206−1213.

Research article

Journal of RAMAN SPECTROSCOPY

Received: 2 August 2012 Revised: 10 September 2012 Accepted: 14 September 2012 Published online in Wiley Online Library: 24 January 2013

(wileyonlinelibrary.com) DOI 10.1002/jrs.4201

Evaluation method for Raman depolarization measurements including geometrical effects and polarization aberrations

M. Schlösser,[a]* T. M. James,[b] S. Fischer,[a] R. J. Lewis,[b,c] B. Bornschein[a] and H. H. Telle[b]

In this article, we address the notoriously difficult problem to quantitatively link measured Raman depolarization values to theoretical polarizability tensor quantities, since quantum calculations do not incorporate experimental parameters. For this, we introduce a numerical model to calculate, for realistic experimental configurations, effective Raman line strength functions, ϕ, which find their way into depolarization ratios, ρ. The model is based on interlinked integrations over the angles in the light collection path and a finite Raman source volume along the excitation laser beam. The model deals also with the conditional aperture parameters, associated with more than one optical component in the light collection path. Finally, we also can take into account polarization aberrations introduced by the sample cell windows. The procedure was fully tested for Raman depolarization spectra of selected hydrogen isotopologues. Distinct aspects affecting Raman depolarization data were validated, namely: (1) excitation polarization impurities; (2) extended Raman excitation volumes; (3) Raman light collection over finite solid angles; and (4) polarization aberrations introduced by optics in the light collection path. The correction of the experimental measurement data for the aforementioned effects resulted in depolarization ratios for the $Q_1(J'')$ Raman lines of H_2 and T_2, which mostly differed by less than 5% from those obtained by quantum-calculations. Copyright © 2013 John Wiley & Sons, Ltd.

Supporting information may be found in the online version of this article.

Keywords: Raman depolarization; depolarization ratio; polarization aberrations; stress-induced birefringence

Introduction

Depolarization is associated with the change of the intensity of parallel and perpendicular components of the electric field of incident light after scattering (e.g. Raman scattering from optical anisotropic molecules). The ratio between the two components is normally called the depolarization ratio.[1]

Measuring this depolarization ratio helps one to interpret the symmetry of the scattering molecules' vibrational modes, and even the quantitative evaluation of tensor invariants of the molecular polarizability are feasible.[1–3] Furthermore, the measurement of the degree of depolarization also expands on the capabilities of identifying species beyond the standard spectral information.

In general, to measure depolarization ratios may be deemed a straightforward task. However, two major effects have a severe influence on the derived values and require careful consideration and treatment; this is particularly important for depolarization ratios that have values very close to zero.

The first effect is that the collection angle of the Raman scattered light in experiments is finite. This non-zero solid angle in the light collection path means that rays with different angular-dependent polarization may be collected. As a consequence, the measured depolarization ratio is bound to differ from the theoretical values, which are invariably calculated for zero solid angle. This problem was addressed for the first time by Dawson in the early 1970s who discussed the influence of non-zero collection angle and other effects on depolarization.[4] In 1984, Deb and co-workers calculated the error contribution of finite (small) collection angles to depolarization ratios.[5] This approach was later refined for larger angles by Teboul *et al.*[6] However, it has to be noted that Teboul's model is formulated for single-angle geometry configurations, which are only suitable for point-like emission and circular collection apertures. Furthermore, the model calculations are based on a fourth-order series expansion; clearly, for larger angles this approximation will become increasingly inaccurate.

The second effect is related to depolarization which is introduced by the measurement equipment itself.[7] For example, polarization changes can be caused by stress-induced birefringence in lenses, cell windows, and other optical components, as discussed by Logan *et al.*[8] As a consequence, all measured depolarization values will exhibit an unknown bias if these effects are neglected.

* *Correspondence to: M. Schlösser, Tritium Laboratory Karlsruhe, Institute for Technical Physics, Karlsruhe Institute of Technology, P. O. Box 3640, 76021 Karlsruhe, Germany. E-mail: magnus.schloesser@googlemail.com*

a *Tritium Laboratory Karlsruhe, Institute for Technical Physics, Karlsruhe Institute of Technology, P. O. Box 3640, 76021, Karlsruhe, Germany*

b *Department of Physics, College of Science, Swansea University, Singleton Park, Swansea, SA2 8PP, United Kingdom*

c *Optoelectronics Research Centre, University of Southampton, Highfield, Southampton, SO17 1BJ, United Kingdom*

It is worth noting that Turrell and co-workers discussed the two aforementioned effects jointly, and developed correction integrals for depolarization measurements, in the context of polarization-dependent Raman micro-spectroscopy.[9,10] Their mathematical model is quite comprehensive in taking into account all possible effects influencing the depolarization ratios in their measurements. However, in Raman micro-spectroscopy, the scattered light is observed in the backward direction, and the excitation volume may in general be approximated as a circular, nearly point-like source. Thus, their approach is not directly applicable to cases of an extended (elongated) Raman excitation volume and observation geometries other than back-scattering.

In this paper, we seek to offer a generalized, complete methodology for the quantitative implementation and analysis of standard depolarization ratio experiments of gaseous samples. The numerical calculations employed here expand the simple collection geometry treatment used by Teboul, to now include a detailed treatment of configurations in commonly used measurement setups. Particular attention is paid to cases where the transmitting optical components introduce a (sometimes) non-quantifiable amount of polarization aberrations.

Of particular relevance and novelty to the formalism described in this paper is the fact that emission from extended Raman excitation volumes can be treated, i.e. light rays that are substantially off-center. This is in stark contrast to the work of Teboul and Turrell addressed further above, in which basically centro-symmetric emission from a 'point-like' source is considered. In addition, multiple-aperture scenarios (associated with optical components in the light-detection path) can be evaluated. This is particularly relevant for off-center beams from extended sources, but even for point-like sources, this may become an issue if the alignment is not perfect.

The overall approach described here has been applied successfully to evaluate depolarization ratios of the Raman Q_1-branches of the hydrogen isotopologues, of which examples for H_2 and T_2 are included here.[1]

Note that besides depolarization measurements, the methodology described here can also be used to calculate any geometry and aberration dependence of Raman line strength functions, and thus spectral line intensities.

The tools for the calculation of the 'effective' depolarization ratios, including geometry and polarization aberrations, presented in this work are available for use (see the online 'Supporting Information').

Theoretical aspects

Before the depolarization ratio is introduced, it is beneficial to sketch the relevant issues on Raman intensities. The reader is referred to the textbook by Long[11] for further details.

Raman intensities

The intensity of light which is scattered by diatomic molecules via the Raman effect is given as[11]

$$I(\varphi,\theta)_{p^s,p^i} = k_{\tilde{\nu}} \cdot \tilde{\nu}_s^4 \cdot N_i \cdot \phi_{p^s,p^i}(\varphi,\theta) \cdot \mathcal{I} \tag{1}$$

Here, p^s and p^i are the polarization states of the scattered and incident light beams, $\tilde{\nu}_s$ is the wavenumber of the scattered radiation, $k_{\tilde{\nu}}$ is a constant for adjustment of dimensions and units, N_i is the Boltzmann population state, and $\mathcal{I}$ is the irradiance of the exciting light source. Note that throughout this paper, we restrict the treatment to linear polarized light components, although in principle, similar expressions could be derived for other polarization scenarios. The quantity of relevance for depolarization measurements is the line strength function, ϕ, for given scattering angles φ and θ, which depends on the polarization states p^i and p^s of the incident and scattered light, respectively. The definitions of the angles φ and θ, relative to the laser beam direction and the scattering plane, become clear from the sketch in Fig. 1.

The four line strength functions for $\perp$- and $||$-polarized light are given below, as functions of the angles φ and θ[11]

$$\phi_{\perp^s,\perp^i}(\varphi,\theta) = a^2 cos(\varphi)^2 + b^{(2)}\frac{\gamma^2}{45}\left(4 - sin(\varphi)^2\right) \tag{2}$$

$$\phi_{\perp^s,||^i}(\varphi,\theta) = a^2 sin(\varphi)^2 + b^{(2)}\frac{\gamma^2}{45}\left(3 + sin(\varphi)^2\right) \tag{3}$$

$$\phi_{||^s,||^i}(\varphi,\theta) = a^2 cos(\theta)^2 cos(\varphi)^2 + b^{(2)}\frac{\gamma^2}{45}\left(3 + cos(\theta)^2 cos(\varphi)^2\right) \tag{4}$$

$$\phi_{||^s,\perp^i}(\varphi,\theta) = a^2 cos(\theta)^2 sin(\varphi)^2 + b^{(2)}\frac{\gamma^2}{45}\left(3 + cos(\theta)^2 sin(\varphi)^2\right) \tag{5}$$

When the incident light is composed of both polarizations ($\perp^i, ||^i$) and/or both scattered polarization states ($\perp^s, ||^s$) are collected, then the total observed line strength becomes a superposition of contributions from Eqns (2)–(5). The factor $b^{(2)}$ in the above equations is the Placzek–Teller factor; for rotational states, J, in a Q_v-branch (v is the quantum number of the vibrational state), it is given as[11]

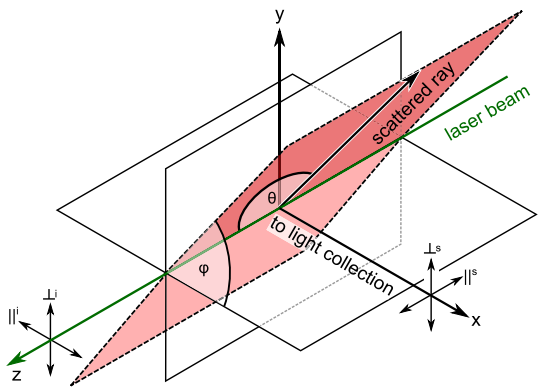

Figure 1. Definition of Raman scattering angles. The scattering plane is determined by the light excitation z-axis and its azimuth angle φ with respect to the light collection x-axis. The zenith angle θ is defined as the angle between the z-axis and the scattered ray in the scattering plane. In the direction of the light collection, imaging lenses and polarization optics are found. The notation of the variables is according to Long.[11]

[1]The full description of our Raman depolarization experiments and their evaluation, for all hydrogen isotopologues – H_2, D_2, T_2, HD, HT, and DT – has been submitted for publication.

$$b_J^{(2)} = \frac{J(J+1)}{(2J-1)(2J+3)}. \quad (6)$$

The (angular) transmission function for any optical component depends on the actual polarization content in the beam. Thus, invariably, the polarization purity of a light beam is affected on passage through optical elements. Specifically, the polarization content after passage normally depends on the angle of incidence on the optic's surface. For larger solid angles of light collection, this may adversely affect any polarization-sensitive measurement; as a consequence, its evaluation becomes increasingly difficult. For this reason, depolarization measurements are mostly performed with a polarizer in the collection light path. Confining the polarization of the scattered light to only one component by and large eradicates much of the severe uncertainties which otherwise would be encountered for any optical components beyond the analyzing polarizer. Regardless, one still may have to deal with polarization 'impurities' in the incident light beam, meaning that the stimulating (laser) light is not perfectly polarized. In the mathematical description, such an admixture can be catered for by using an associated parameter $\xi = cos^2\alpha$, where α is the angular deviation from the vertical polarization direction. In this context, a value $\xi = 1$ would correspond to perfect vertical (linear) polarization, a value $\xi = 0.5$ would represent a beam whose $\perp^i$- and $\|^i$-polarization components are of equal magnitude, and a value $\xi = 0$ would correspond to perfect horizontal (linear) polarization.

This parameterized approach then makes it rather straightforward to accommodate different polarization components in the incident beam contributing to the Raman signal, provided a linear polarizer is suitably inserted in the collection light path. For example, inserting an analyzer that only passes the $\perp^s$-polarized light component, the resulting line strength function becomes

$$\phi_{\text{effective}}(\varphi,\theta) = \xi \cdot \phi_{\perp^s,\perp^i}(\varphi,\theta) + (1-\xi)\cdot\phi_{\perp^s,\|^i}(\varphi,\theta) \quad (7)$$

Of course, other scenarios can equally be implemented, resulting in similar (simple) superposition expressions. However, for all example measurements discussed below the situation described by Eqn (7) was prevalent.

Definition of the depolarization ratio

The depolarization ratio is conceptually defined in a simplified geometrical configuration, in which it is assumed that (1) the scattered light only originates from a single point, and that (2) scattering is observed for vanishing solid angle, i.e. ultimately along a single ray line. The depolarization ratio for any specific molecule thus defined is not influenced by the measurement apparatus, and may be indexed by 'single point, zero solid angle' (SP0SA)). The SP0SA depolarization ratio for a scenario with fixed polarizer in the collection light path is given by[11]

$$\rho_{\text{SP0SA}} = \frac{\phi_{\perp^s,\|^i}(\varphi=0,\theta=\pi/2)}{\phi_{\perp^s,\perp^i}(\varphi=0,\theta=\pi/2)}. \quad (8)$$

For other scenarios, the reader is referred to see Allemand or Long.[1,11]

Experimentally, more realistic is a situation in which scattering originates from an extended region, and for which light collection over a non-zero solid angle needs to be taken into account. Together with contributions from polarization aberrations, this leads to the observed depolarization ratio ρ_{obs}.

Influence of geometry on observed Raman light intensities

Equation (7) only describes the light intensity scattered into one specified direction. Experimentally, Raman light is always collected over a finite collection angle. Thus, the relevant line strength function needs to be integrated over φ and θ. While largely improved, the resulting integral still is of limited value, since it only describes the light collected from a point-like scattering center. Experimentally, only in rare cases can the origin of the Raman scattering be approximated by a point source. More realistically, scattering regions extend along the laser beam direction. Thus, referring to the notation convention in Fig. 1, the overall integration has also to include integration in the z-direction. The integration is performed in spherical polar coordinates, yielding for the observed Raman light intensity

$$I_{\text{obs}} = c \cdot \iiint_{\varphi,z,\theta} \phi_{\text{effective}} \, sin\,\theta \, d\theta \, dz \, d\varphi \quad (9)$$

However, before the integration can be performed, it is necessary to specify the integration limits which are defined by the actual geometry of the experimental collection system. In our case, which may be viewed as sort of a standard scenario, the scattered light passes first through a sample cell window, with radius r_w at a distance x_w from the scattering center (aperture 1). Then, the light is collected by a focussing lens with aperture radius r_f at a distance x_f from the scattering center (aperture 2). In general, arbitrary apertures have to be described via appropriate parametrization. It has to be noted, that the transmission of light emitted from $z \neq 0$ through a system with more than one aperture has the complication that segments of the emitted light cone through the first aperture may be restricted by a second aperture. A sketch clarifying this argument can be found in Fig. 2.

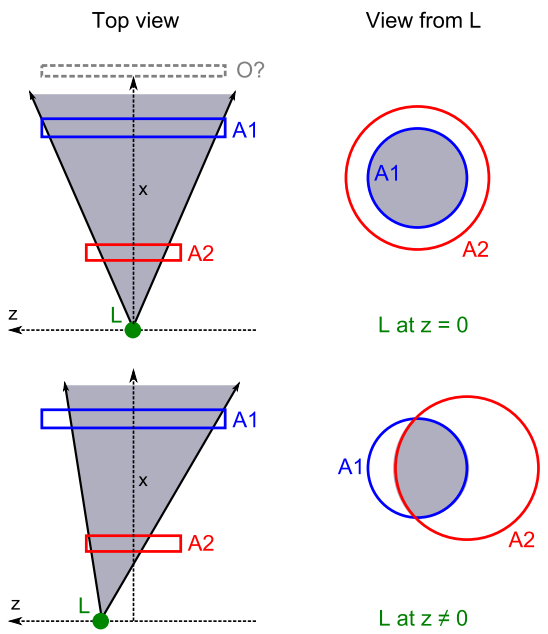

Figure 2. Sketch of off-axis ($z \neq 0$) light transmission through more than one aperture (e.g. window, lens, diaphragm). *L* - point (origin) of scattered light emission. *A*1, 2 - apertures 1 and 2. *O*? - possible other optical element, for example a polarizer.

A suitable parameterization has been developed for the case of two circular apertures (sample cell window and collection aperture); this is described in more detail in the Supporting Information.

The parameterization leads to a nested integration where the limits of the variable in the inner integration depend on the value of the outer integration (e.g. θ_{min}, θ_{max} are functions of z and φ). For this reason, it will be next to impossible to arrive at analytic solutions for the given problem. Thus, numerical integration procedures have to be implemented; in our case, they have been programmed in ROOT/C++[12] and NI LabVIEW.[2]

Polarization aberration

The model derived up to this point can be easily put into use, provided that none of the optical components within the experimental setup introduces polarization aberrations. However, quite often mounted optics exhibit polarization aberrations, induced in general via stress-induced birefringence.[7,8]

This latter effect is normally unavoidable if experiments with harmful specimen – like radioactive, poisonous, or reactive gases – are performed: stringent requirements on the leak tightness have to be met. In general, this means that O-ring sealing cannot be used but that glass–metal-bonded components (windows) are required; these, together with metal compression seals, introduce stress to the window which often is non-negligible. Qualitative and quantitative measurements have shown that polarization aberrations occur in the Raman cell windows used in experiments referred to in this work. In the following, the polarization aberration effects on the incident laser light and the scattered light are discussed.

First, a monochromatic, nearly parallel laser beam, incident on a sample cell entrance window, suffers a certain degree of polarization aberration associated with (potential) stress-induced birefringence in the window. However, in general, only a small fraction of the window surface and bulk volume of the order of mm^2 or mm^3, respectively, contribute to the polarization aberration. This is because the windows of a sample cell are often positioned close to the focal region of the Raman excitation volume; accordingly, the beam diameter is normally small. For window areas much larger than the laser beam diameter, one may well assume that the stress-induced birefringence is homogeneous over a small beam cross section, and thus the effect on the associated polarization change will be as well. Therefore, the effect can be reasonably approximated by using the cleanness parameter ξ introduced in Eqn (7). Note that this approach is similar to the one described by Proffitt and Porto.[13]

Second, any polarization aberration affecting the scattered light is much more difficult to describe. This difficulty is associated with the fact that in experiment setups, one usually collects light beams (1) which are non-parallel and which often exhibit an un-isotropic distribution of polarization states; (2) which pass through optical interfaces over a range of inclination angles (i.e. deviating from perpendicular incidence); and (3) which – because of extended solid angles – may pass through parts of the optics, suffering from inhomogeneities in their stress-induced birefringence.

In principle, all these effects could be taken into account in the model which has been introduced above. However, this requires that the retardance and di-attenuation properties of the optics would have to be mapped (1) with regard to the relevant angles under which light passes through the surfaces; and (2) with respect to lateral position. Since this would constitute an enormous measurement effort, it will become impractical in all but the simplest cases. Therefore, in a more simplified approach, the polarization aberrations in the collection window (and possibly other optical components) are calculated using Jones calculus; here, we utilized the formalism based on the work by Kita[14] and McGuire and Chipman.[15] Note that, in principle, the same results can be obtained by using Mueller calculus (see e.g. Toro Inesta[16] or Collett[17]). For the model, the following assumptions need to be valid:

- the whole collection system can be described as exhibiting a (homogeneous) net effect on the polarization (mainly linear di-attenuation and linear retardance);
- the polarization aberrations have (nearly) no angular dependence; and
- circular di-attenuation and retardance are negligible, as indicated, e.g. by Kita.[14]

The conceptual setup for the right-angle observation path in a depolarization experiment is shown in Fig. 2. Following the figure's notation, the sequence of components is that the Raman cell window (*A2*) is the first, then the light collection lens (*A1*), followed by the (optional) polarizer (*O*?); the Jones matrices below are indexed accordingly. The relation between the polarization state of the scattered light generated in the Raman interaction volume and that after transmission through all optical components is, according to the Jones calculus,

$$\vec{E}_{out}(\theta,\varphi) = \mathcal{J}_{O?}\mathcal{J}_{A1}\mathcal{J}_{A2}\cdot\vec{E}_{in}(\theta,\varphi). \tag{10}$$

The detailed calculation can be found in the Supporting Information section, derived both via Jones or Mueller calculus.

Using Jones calculus for all optical components in an experimental system, the intensity of scattered Raman light can now be determined quite accurately by incorporating the 'exact' light-field strengths for a particular excitation/collection configuration. For example, for an excitation laser beam in p^i-configuration, and collecting the Raman light in $\perp^s$-configuration (after the polarizer), the observed Raman signal intensity is given by

$$\begin{aligned} I_{\perp^s,p^i} = {} & \underbrace{E^2_{\perp^s,p^i}exp(-2a_{P1})}_{\text{transmitted}\perp^s-\text{component}} + \underbrace{E^2_{||^s,p^i}exp(2a_{P2})}_{\text{leakage from}||^s-\text{component}} \\ & + \underbrace{2E_{\perp^s,p^i}E_{||^s,p^i}exp(a_{P2}-a_{P1})cos(a_{R,\text{tot}})}_{\text{contamination induced by retardance}}, \end{aligned} \tag{11}$$

where a_{P2}, $-a_{P1}$, and $a_{R,\text{tot}}$ are the (simplified) di-attenuation and induced retardance parameters, respectively.[15] Equation (11) can be formulated for $p^i = \perp^i$ or $||^i$.

In Eqn (8), the depolarization ratio was written in terms of the (theoretical) line strengths, ϕ. More appropriate for the evaluation of experimental measurements – in which the aforementioned polarization aberration effects might be encountered – would be a formulation in terms of light-field strengths, or intensities. This approach is relatively easy to realize because of the relation $E^2 = k\cdot I = k'\cdot\phi(\varphi,\theta)$ where k and k' are proportionality constants (see Eqn (1)). With this equivalence, and exploiting the scattered light intensity expressions in the form of Eqn (11), one finds for the observed, experimental depolarization ratio

[2]The integration programs are available from the authors, with download information provided in the Supporting Information.

$$\rho = \frac{I_{\perp^s,||^i}}{I_{\perp^s,\perp^i}} \tag{12}$$

$$= \frac{X^2_{\perp^s,||^i} + Y^2_{||^s,||^i} + 2X_{\perp^s,||^i} \cdot Y_{||^s,||^i} \cdot cos(a_{R_{tot}})}{X^2_{\perp^s,\perp^i} + Y^2_{||^s,\perp^i} + 2X_{\perp^s,\perp^i} \cdot Y_{||^s,\perp^i} \cdot cos(a_{R_{tot}})} \tag{13}$$

with

$$\begin{aligned} X_{\perp^s,p^i} &= E_{\perp^s,p^i} exp(-a_{P1}) \\ Y_{||^s,p^i} &= E_{||^s,p^i} exp(a_{P2}) \\ X_{\perp^s,p^i} \cdot Y_{||^s,p^i} &= E_{\perp^s,p^i} \cdot E_{||^s,p^i} \cdot exp(a_{P2} - a_{P1}) \end{aligned}$$

Note that the X^2- and Y^2-terms are related to the linear di-attenuation, while the cross-terms $X \cdot Y \cdot cos(a_{R_{tot}})$ correspond to the additional, induced retardance. Using this simplified model approach, the influence of possible polarization aberrations in the collection path can now be estimated. Here, a set of four polarization aberrations scenarios are considered:

1. Only the geometrical influence is included, i.e. no polarization aberrations are included (cleanness of the incident laser beam is $\xi = 1$).
2. The geometrical influence is superimposed by a reduced polarization cleanness of the incident beam, i.e. $\xi \neq 1$; however, aberrations introduced by the collection optics are not included.
3. It is clear from Eqn (11) that the cleanness of transmitted beams can be reduced by leakage and/or retardance. In order to investigate both effects individually, in our model approach, the collected light intensities (or field strengths) are broken down into two mutually perpendicular components. This parameterization into (simplified) fractions reduces the complexity of the problem, but also allows one to identify any possible dominating mechanism. Two special, simplified scenarios are contemplated here (note that the parameterization results in a modification of Eqn (13) for the depolarization ratio):

3a) In the first sub-scenario, the induced retardance is neglected; any polarization shifts are introduced via different attenuation losses in the polarization components alone (e.g. the related reflection losses strongly depend on the angle of incidence). Then, one may rewrite Eqn (13) as:

$$\rho_A = \frac{c_{A,\perp^s} E^2_{\perp^s,||^i} + c_{A,||^s} E^2_{||^s,||^i}}{c_{A,\perp^s} E^2_{\perp^s,\perp^i} + c_{A,||^s} E^2_{||^s,\perp^i}}. \tag{14}$$

3b) In the second sub-scenario, the leakage term is neglected, and only polarization changes introduced by retardance in an optical material are considered (e.g. stress-induced birefringence). For this case, Eqn (13) approximates to

$$\rho_B = \frac{c_{B,\perp^s} E^2_{\perp^s,||^i} + c_{B,||^s} E_{||^s,||^i} E_{\perp^s,||^i}}{c_{B,\perp^s} E^2_{\perp^s,\perp^i} + c_{B,||^s} E_{||^s,\perp^i} E_{\perp^s,\perp^i}} \tag{15}$$

In both sub-cases, the polarization cleanness of the incident beam is assumed to be perfect, i.e. $\xi = 1$. The c-parameters in Eqns (14) and (15) are defined as

$$\begin{aligned} &c_{A,\perp^s} = c_{B,\perp^s} = exp(-2a_{P1}), \\ &c_{A,||^s} = exp(2a_{P1}), \text{and} \\ &c_{B,||^s} = 2exp(a_{P2} - a_{P1}) \cdot cos(a_{R_{tot}}), \end{aligned}$$

with the restriction $0 \leq c \leq 1$.

In order to study the influence of polarization impurity in the excitation channel or any shift in the exit channel on the effective depolarization ratio, for each, only a single parameter has to be changed. In the former case, it is the cleanness parameter ξ, and in the latter case, it is the ratio between $c_\perp$ and $c_{||}$. The dependence of the effective depolarization ratios on the collection (solid) angle, related to the four scenarios above, is plotted in Fig. 3. Note that for the data relating to scenario 2, only small impurities have been considered ($\xi = 0.999$ and $\xi = 0.998$) for $\rho_{SPOSA} = 0$, but that for scenarios 3a and 3b, the parameter choice $c_{A,\perp^s} = 0.9$ and $c_{A,||^s} = 0.1$ is rather extreme, and may be viewed as a 'worst-case' scenario. The following observations can be made:

First, the immediately evident contribution to deviations between the theoretical and measured depolarization ratios stems from polarization impurities in the excitation laser beam. Even minute admixtures of the unwanted polarization result in offsets substantially larger than the uncertainty in many measurement setups (in our latest depolarization experiments, a measurement uncertainty of $\Delta\rho \approx \pm 5 \times 10^{-4}$ could routinely be achieved).

Second, even for small Raman light collection angles, smaller than practicable in many measurement setups, the deviation between theoretical and measured depolarization ratios becomes quite noticeable, quickly surpassing our measurement uncertainty with increasing solid angle.

Third, for small light collection angles (of the order $<5°$), the influence of the induced polarization impurities on the depolarization ratio, stemming from the collection optics, is in general rather small. Even when assuming a 'worst-case' scrambling, namely that the unwanted polarization component reaches 10%, the effect begins to become non-negligible for solid angles larger than ~10°. For lesser degrees of polarization scrambling, the effect may already have dropped below the measurement sensitivity (see the top panel in Fig. 4).

Fourth, the scenarios which account for the polarization aberration in the collection path, indexed A and B, exhibit very similar behavior. Thus, neither of them may be regarded as the dominant mechanism in observation-side-induced depolarization

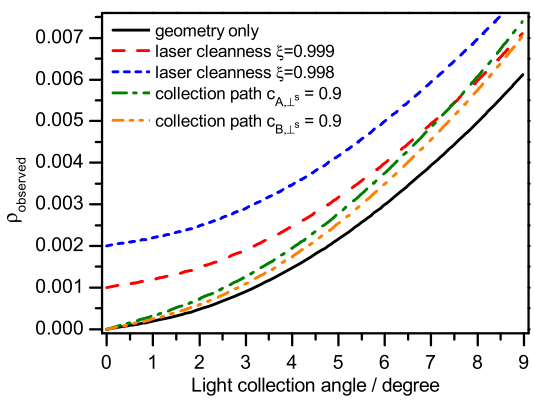

Figure 3. Influence of polarization aberrations in the laser excitation (polarization cleanness ξ) and the light observation paths (admixture parameters $c_{A,\perp^s}$ and $c_{B,\perp^s}$) on the effective depolarization ratio. In this plot, $\rho_{SPOSA} = 0$. For details, see the main text.

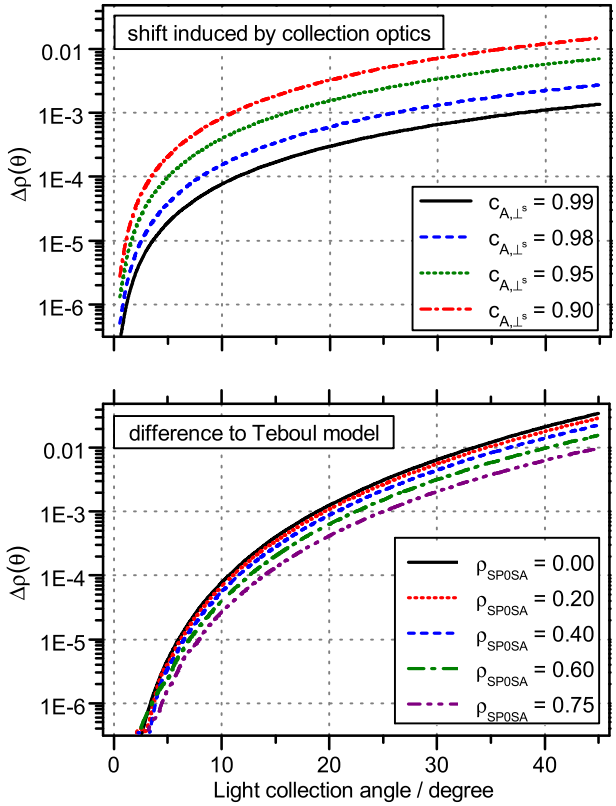

Figure 4. Calculated deviation $\Delta\rho$ from the theoretical ρ_{SP0SA} depolarization values, when taking the light collection angle θ_{max} into account. Top panel - deviations of the depolarization ratio induced by optical components in the light collection path, associated with polarization impurities in the scattered light beam (based on the approximation in Eqn (12)). Bottom panel - difference between our (numerical) model and that of Teboul[6] (based on analytical expansion) for selected ρ_{SP0SA} values as a function of the light collection angle θ_{max}.

aberrations, i.e. di-attenuation and retardation effects seem to be of the same order of magnitude for standard optical components.

One can conclude from this discussion that contributions to the effective depolarization ratio will mainly originate from geometrical effects and polarization impurities in the incident laser beam, in particular for small light collection angles. Therefore, it may seem quite legitimate to neglect in the model the polarization aberrations induced by the optical components in the light collection path, and only to include deviations from ideally clean polarization of the incident laser beam via the parameter ξ. This approximation has been adopted in all examples discussed further below.

Comparison to previous models

In our model, the main difference to previous work is the inclusion of off-center emission of scattered light, from points along the laser excitation axis, which requires an additional integration step. Note that integration limits have to be carefully considered, in order to properly account for (sequential) finite apertures along the light collection path. It therefore is of interest to compare the results of this model with that of Teboul *et al.*[6]

In Teboul's work, only scattered light originating from a point source is considered, passing through on-axis aligned apertures. This constitutes the sub-case in our model in which no z-integration is required (all light originates at $z = 0$), and an 'effective' circular aperture is defined via a single parameter θ_{max}. In the lower panel of Fig. 4, the difference of the calculated depolarization ratios for both models are plotted as a function of θ_{max}, for a range of ratios between the two limiting cases $\rho_{SP0SA} = 0$ and $\rho_{SP0SA} = 3/4$. The two correction methods diverge rapidly with increasing light collection angle. For example, for the (theoretical) depolarization ratio $\rho_{SP0SA} = 0$, the difference in the two methods surpasses 0.001 for a light collection angle of about 20°; this value is close to or even larger than our depolarization measurement uncertainties (see Tables 2 and 3 below). Thus, the use of our methodology is clearly required when accurate correction of polarization aberration errors needs to be implemented.

Comment on possible extensions to the model. Finally, we would like to comment that, in principle, our model can also account for the non-uniform intensity distribution of a focused Gaussian laser beam, using the formulas derived by Alda.[18] For this, the scattering centers along the z-axis are weighted by the related intensity distribution function. However, the resulting effect for standard focusing lenses with $f > 100$ mm is found to be negligible; therefore, here we do not describe further details.

Results

The described model can be used to extract SP0SA depolarization values from imperfect, experimentally observed data. This also allows a direct comparison to *ab-initio* calculations. We first describe the principles and routine for the related correction procedure; then, the performance and reliability of this approach are validated for selected experimental data sets.

Methodology for correcting observed depolarization ratios

As stated, observed depolarization ratios are influenced by the finite collection geometry, and (in our case) by stress-induced birefringence in the cell windows. The birefringence leads to reduced polarization cleanness in the Raman excitation laser beam. Thus, the observed Raman depolarization values are expected to differ from the SP0SA values. However, if the contributions from geometry and aberrations can be quantified, then it should be possible to back-trace the (theoretical) SP0SA depolarization ratio from the observed one.

Including the light collection geometry will constitute a simple step, provided the position of any component, which limits the collection (solid) angle, is precisely known. Should this not be the case, one may introduce a diaphragm of known diameter and distance to the scattering Raman center as the 'effective' limiting aperture.

On the other hand, the determination of polarization cleanness of the incident laser beam, reaching the scattering center, is not a trivial task. Normally, it has to be determined from auxiliary measurements, characterizing the effect of each individual optical component in the laser beam path. However, these characterization data have to be treated with care, since the characterization measurement setup may be quite different to the setup of the actual depolarization experiments. For example, one possible problem that may occur is that the characterization laser beam passes through a different part of the (stressed) laser window than during the later depolarization experiment; normally, some beam realignment is required between the two types of measurement.

To circumvent this problem (although for cross-comparison, we measured the polarization-changing effects for all optical

components in our setup), the method which has been employed here allows the correction of the observed depolarization ratios without any additional measurements. For this to succeed, access to a line with a well-known depolarization ratio is required. Fortuitously, any diatomic molecule provides such a line by default, namely the $J''=0$ line of the Q_1-branch. Its associated SP0SA Raman depolarization ratio is $\rho=0$, meaning that the numerator in Eqn (8) is zero, and associated with this, the observed Raman line intensity $I_{\perp^s,||^i}$ should be zero as well.[11] The reason for this is the vanishing Placzek–Teller $b^{(2)}$-factor for $J''=0$ (see Eqn (6)). When inspecting the Q_1-branch spectra for H_2, HT, and T_2 in Fig. 5, which displays the $I_{\perp^s,\perp^i}$ Raman signal, evidently the $J''=0$ line exhibits finite amplitude in the $I_{\perp^s,||^i}$ configuration (see the insert in the H_2 panel of the figure) and is not zero, as theory predicts. This is a clear indication that experimentally, one cannot normally measure the SP0SA-value for ρ because angular collection geometry and polarization-impurity contributions are always present; Eqn (13) affords to take these into account. The insert in Fig. 5 clearly shows that the minor contribution to the non-vanishing intensity has its origin in the finite collection angle and that the major contribution is due to polarization aberrations.

The background noise fluctuation, S_{noise}, is of the order ± 0.1 units and thus is not visible on the scale of the spectra in Fig. 5 (recorded for $\perp^i$-polarization configuration); only in the scale-enlarged insert for the $H_2(J''=0)$ line (recorded for $||^i$-polarization configuration with much lower peak intensities) are the noise fluctuations evident. Thus, all lines in Fig. 5 exhibit a signal-to-noise ratio as high as 5000, with even the weakest lines having a SNR >50. Of course, for the $||^i$-polarization signals, which are a factor of 30–50 weaker than the $\perp^i$-polarization signals, the SNR is substantially lower, and for the weakest lines can reach the noise level. This then will be reflected in much larger errors for the depolarization ratios of those very weak lines.

In the context of Raman lines with known, vanishing polarization components, it is worth noting that also some larger, polyatomic molecules exhibit such behavior. An example is the vibrational ν_1-mode of CH_4.[19]

The actual correction procedure for experimental data, based on the above mathematical model, is separated into two stages.

In the first step, for the given collection geometry, the mathematical model is used to model the depolarization ratio for a Raman line whose SP0SA value is known, and ρ_{model} is plotted as a function of the polarization cleanness ξ of the incident laser beam (see top panel in Fig. 6). Conveniently, for diatomic molecules, a line with known depolarization value is the $Q_1(J''=0)$ line for which $\rho_{SP0SA}=0$. Thus, one can determine the polarization cleanness from the plotted functional dependence, using the experimentally observed value $\rho_{observed}$ of this line. For example, in one of our test experiments, the depolarization ratio for the $Q_1(J''=0)$ line of HT was measured as $\rho_{observed}=0.0060$, which corresponds to a cleanness of the polarization of $\xi=0.9954$ (this data is displayed in Fig. 6).

In the second step (bottom panel in Fig. 6), the mathematical model is used to back-track the SP0SA depolarization ratio for other $Q_1(J''>0)$ lines, and any further Raman branch lines, utilizing polarization cleanness of the incident beam ξ determined in the first step.

Note, that polarization aberrations in the collection path have not been included here, based on the findings associated with Eqns (14) and (15). The implementation of the overall procedure is shown graphically for the measurement of the depolarization ratio of the hydrogen isotopologue HT (see data in Fig. 6, step 2).

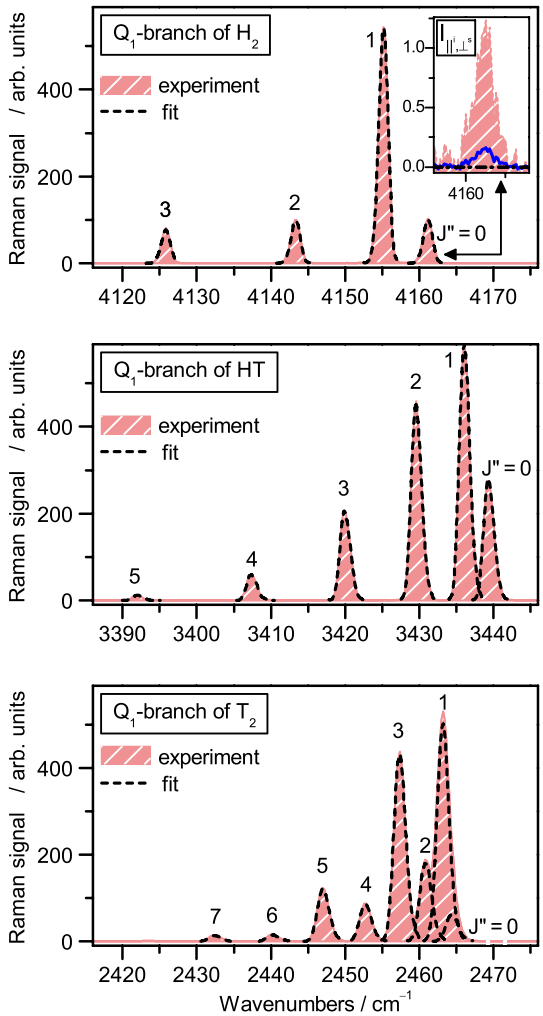

Figure 5. High-resolution Raman spectra of Q_1-branches of the diatomic isotopologues H_2, HT, and T_2, measured in $\perp^s, \perp^i$ polarization configuration. The spectral lines are annotated with their rotational state quantum number, J''. Note that with increasing molecular weight of the isotopologues, Q_1-branch lines with low rotational quantum number progressively overlap. Insert in the H_2 panel: $H_2(J''=0)$ line, measured in $\perp^s, ||^i$ polarization configuration. The (black) dashed/dotted lines represent the theoretical prediction (SP0SA); the solid (blue) line denotes the calculated effect by a finite collection angle (~4°) only; and the (red) filled-in area represents the measured signal, including contributions from solid angle and polarization aberrations.

Therefore, applying the above methodology to Raman depolarization measurements, in which optical elements with unknown impact onto an initially 'perfect' light beam polarization had to be used (e.g. Raman cell windows under stress), one should be able to derive aberration-corrected depolarization ratios from observed ones.

Validation of the correction routine

The validity and the accuracy of our approach have been demonstrated under three aspects, namely (1) the determination of the cleanness of the excitation light beam during repeat measurements for different sample cells; (2) the agreement of ρ_{SP0SA} values for the same hydrogen isotopologues derived from a set of different Raman cells; and (3) application of the corrected depolarization value of one molecular species to determine those of a different species, measured in the same cell. This has been

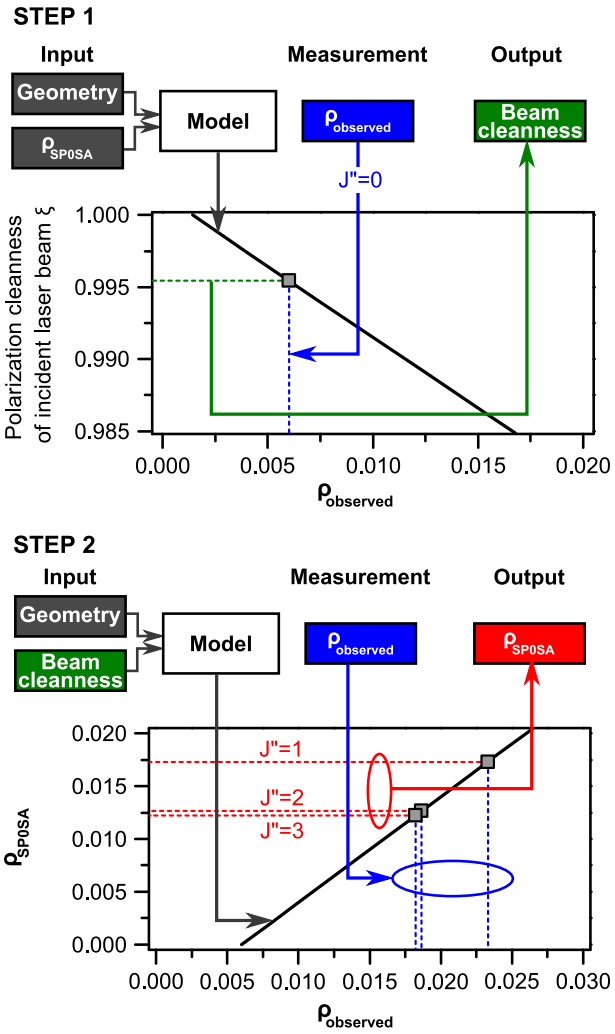

Figure 6. Two-step procedure to extract depolarization values ρ_{SP0SA} from data sets with unclean beam polarization. Step 1 - Determination of cleanness of the laser polarization. The theoretical data (full line) are calculated for known collection geometry and known SP0SA depolarization ratio $\rho_{SP0SA} = 0$. From the observed depolarization ratio of the $Q_1(J''=0)$ line one derives the related polarization cleanness ξ. Step 2 - Correction of depolarization ratios of all measured Q_1-branch lines, for a given polarization cleanness. The polarization cleanness derived in step 1 is used to correlate the $\rho_{observed}$ to the ρ_{SP0SA} values of all Q_1-branch lines with $J > 0$.

exemplified for depolarization experiments for the hydrogen isotopologues H_2 and T_2.

In the demonstration of the first aspect, i.e. the determination of the excitation beam polarization cleanness (step 1 in the procedure), a number of cells at Tritium Laboratory Karlsruhe (TLK) and Swansea University (SWA) were checked. These cells

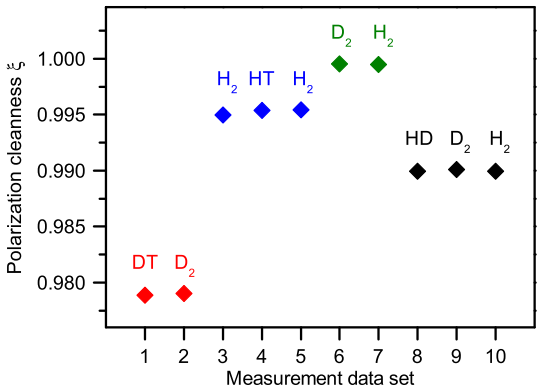

Figure 7. Polarization cleanness of measurement cells, as determined in Step 1 of the evaluation procedure. The annotation of the data sets (numbering according to Table 1) indicates the isotopologue which is used in the determination of ξ. The statistical measurement errors are within the symbol size. For further details, see text.

were filled with different gas mixtures, at different pressures (see Table 1). It should be noted that for a change in filling gas, the cell had to be removed from the measurement setup and then be reintroduced; this meant that exact local repositioning was not necessarily guaranteed. For isotopologue measurements within a given mixture, i.e. sets (1,2), (3–5), and (8–10), the cell was stationary; in the case of measurement data sets 6 and 7, the cell was removed and reintroduced between measurements. The results for the measured cleanness values are summarized in Fig. 7. Clearly, the values derived for the same cell are very close together. The variation for the same cell is overall of the order $\delta\xi < 0.001$, with relative uncertainties for individual measurements of less than 0.1% (the error bars for the data points in Fig. 7 are smaller than the symbols). These results demonstrate that, by and large, the cell windows are responsible for the induced polarization contamination; different cells normally exhibit different stress-induced birefringence in the cell windows. Furthermore, repositioning of the cell may introduce in general only minor deviations associated with spatial inhomogeneity of the stress-induced birefringence. Overall, we find that the beam polarization cleanness is largely independent of the gas filling.

The second aspect in validating the procedure is the reproducibility in the determination of the depolarization ratios of the Q_1-lines of H_2 from repeat measurements (for example, at different times, with different cell pressures and filling composition, or other small changes). Typical spectra exploited in the procedure are shown in Fig. 5. Measurements were performed with different cells, which exhibited varied stress-induced birefringence in the cell windows, and thus different transmitted laser beam cleanness. Two of the measurements were undertaken at the TLK and one at SWA; the data set numbering is related to that in Table 1. Note also that different aperture sizes were prevalent in the measurement setups

Table 1. Different cells and their gas fillings used in Raman depolarization measurements, and for the determination of excitation beam polarization cleanness. The filling of the cells was performed according to the procedures described in Sturm *et al.*[21]

Data sets	Raman cell	Gas composition	Total pressure mbar
1,2	D:T-cell (TLK)	D_2: 15%, DT: 47%, T_2: 34%, Rest (HD, HT): 4%	400
3,4,5	H:T-cell (TLK)	H_2: 25%, HT: 46%, T_2: 26%, Rest (HD, DT): 3%	763.1
6	H:D-cell (SWA)	D_2: 100%	900
7	H:D-cell (SWA)	H_2: 100%	870
8,9,10	H:D-cell (TLK)	H_2: 26.3%, HD: 47.4%, D_2: 26.3%	1500

Table 2. Performance demonstration of the depolarization ratio correction routine for different cells (the numbering is according to the data sets collected in Table 1). The presented ρ-values (observed and corrected) are from measurements of the Q_1-branch lines of H_2 (in brackets: measurement uncertainty). The averaged SP0SA values (in brackets: standard deviation in the last digit) are compared to the theoretical values from LeRoy.[20]

	ρ_{obs}			ρ_{SP0SA}				ρ_{SP0SA}
H_2 J''	#3	#7	#10	#3	#7	#10	average	theory
1	.0241(1)	.0212(1)	.0285(1)	.0177(1)	.0189(3)	.0180(1)	.0182(6)	.0183
2	.0197(1)	.0162(1)	.0252(1)	.0133(1)	.0140(3)	.0148(1)	.0140(8)	.0132
3	.0192(1)	.0154(1)	.0234(1)	.0128(1)	.0132(3)	.0130(1)	.0130(2)	.0125

at the two sites; this was easy to account for by setting the appropriate 'geometry' input parameter in the analysis model. The derived polarization cleanness values for the three data sets were $\xi_{set\#3} = 0.9950$, $\xi_{set\#7} = 0.9995$, and $\xi_{set\#10} = 0.9899$, respectively (see Fig. 7).

The results from these measurements, i.e. the observed Raman depolarization values and the corrected ρ_{SP0SA} values, for H_2 Q_1 ($J'' = 1, 2, 3$) are collated in Table 2.

The averages of the derived ρ_{SP0SA} values exhibit a statistical variance of $\Delta\rho \leq 0.001$; considering the substantial spread in the uncorrected, observed depolarization values demonstrates that our correction routine is capable to compensate for such large variations. It is also noteworthy that these corrected values by and large agree, within the statistical reproducibility, with the theoretical values calculated by LeRoy.[20]

The last aspect in the verification process is to ascertain the validity of the overall procedure if the polarization cleanness of the cell is not determined by the $Q_1(J'' = 0)$ line from the same molecule, but that from a different molecule which, however, was measured in the same cell. This has been demonstrated for the isotopologue T_2. As shown in the spectrum in Fig. 5 (bottom panel), its $J'' = 0$ line is strongly convoluted with the $J'' = 1$ line, and thus it is unsuitable to be used for the polarization cleanness determination.

The ρ_{SP0SA} values for T_2 $Q_1(J'' > 1)$ are summarized in Table 3. The observed depolarization ratios were corrected using cell cleanness values derived from the $J'' = 0$ lines of HT and H_2, respectively, for the three cell data sets given in Table 1. The standard deviations for the differently corrected depolarization ratios confirm that the assumption made earlier is valid: the determined cleanness can be treated as a wavelength- and isotopologue-independent property of the cell.

Table 3. Performance demonstration of depolarization ratio correction routine, for Q_1-branch lines of T_2, based on indirect polarization cleanness determination (in brackets: measurement uncertainty). The ρ_{SP0SA}-values have been corrected using the polarization cleanness determined from the $J'' = 0$ depolarization of other constituents, $H_2(0)$ or HT(0), in the cell (the numbering is according to the data sets collected in Table 1). The averaged ρ_{SP0SA} values (in brackets: standard deviation in the last digit) are compared to the theoretical values from LeRoy[20]

		ρ_{SP0SA}				ρ_{SP0SA}
T_2 J''	ρ_{obs}	HT(0), set#4	$H_2(0)$, set#3	$H_2(0)$, set#5	average	theory
1	.0225(1)	.0165(1)	.0161(1)	.0166(1)	.0164(3)	.0174
2	.0179(1)	.0119(1)	.0115(1)	.0120(1)	.0118(3)	.0125
3	.0171(1)	.0111(1)	.0108(1)	.0112(1)	.0111(3)	.0117
4	.0164(1)	.0104(1)	.0100(1)	.0105(1)	.0103(3)	.0115

We like to conclude with two remarks. First, measurements for the individual data sets addressed in Table 1 were repeated at least 50–100 times. All spectra within a particular measurement configuration were reproducible (after normalization to laser power) to better than 0.15% of the peaks, which is of the order of the shot-noise limit. This is much smaller than other errors in the evaluation of the depolarization ratios, at least for the strong Q_1-branch lines tabulated here. Second, we like to comment on the T_2 data in Table 3. While the agreement between the experimentally derived and theoretical[20] depolarization ratio values is quite reasonable, it is not as close as for H_2 discussed further above: the experimental results seem to be systematically higher. A full discussion of this apparent discrepancy is beyond the scope of this work but will be subject of a pending publication.

Conclusion

In this paper, we presented an extended model for the quantitative analysis of Raman spectral intensities and line depolarization ratios, specifically taking into account three, normally difficult-to-gauge experimental complications, namely (1) excitation polarization impurities; (2) extended Raman excitation volumes; and (3) Raman light accumulation over finite solid angles. The main goal has been to quantitatively link (imperfect) measured depolarization ratios to values obtained via quantum-theoretical calculations.

The most straight-forward task proved to be accounting for polarization aberrations (e.g. induced by birefringence from stress/strain in the Raman cell windows) in the incident laser beam. This has been done by introducing a single cleanness factor ξ and incorporating two perpendicular, ξ-weighted linear polarization components into the model.

The second and third tasks are interlinked. The numerical evaluation of the integrals in the light collection path is over, in principle, the full (φ,θ) angular range, and over the accessible z-range (the laser excitation path constitutes the z-direction). This allows for treating arbitrary geometrical scenarios of excitation lengths (not only point sources as in other models) and aperture-limited solid angles in the light observation path. In addition, the model allows for Raman light collection through more than one optical component. Note that for the analysis of depolarization ratios, aberrations in the collection window could be neglected in the test examples presented in the results section, although a simplified model for calculating and including these aberrations is provided. However, as discussed further above, in most experimental Raman setups, their contribution is about one or two orders of magnitude lower than the aberrations induced by a laser entrance window.

The overall correction procedure for experimental Raman depolarization ratios was implemented in two steps. In the first stage, the cleanness parameter ξ of the polarization of an incident laser

beam in a Raman cell is determined. In the second stage, this polarization cleanness is used to correct the observed depolarization ratio to deduce the (theoretical) SP0SA depolarization ratios.

The overall performance of this correction procedure was demonstrated successfully, with regard to the three aforementioned experimental aspects, for some $Q_1(J'')$ Raman lines of the diatomic isotopologues H_2 and T_2. Regardless of the experimental distortion encountered in the signals, by and large the extracted depolarization values, ρ_{SP0SA} were nearly always reproducible to the order 1–2%. Hence, we are a rather confident to recommend that our analysis strategy should be used for the evaluation of all depolarization measurements for which aberrations and geometrical effects play a significant role. This recommendation comes in the light that the analytical geometry model of Teboul looks easier on first glance, but that its expansion approach leads to severe deviations when larger Raman light collection angles are involved, and if the excitation volume is not a point source (which is rarely true for common Raman measurement configurations). Actual applications of the described techniques to the determination of the depolarization ratios for all six hydrogen isotopologues, including a full comparison to quantum-theoretical values, and for a range of atmospheric gases are subject to forthcoming publications that are in preparation.

Acknowledgements

This research was supported by the Helmholtz Association (HGF), the Federal Ministry of Education and Research (BMBF), through grants 05A08VK2 and 05A11VK3, and the German Research Foundation (DFG) within the framework of the TransRegio project 'Neutrinos and Beyond', grant SFB/TR 27. T.M.J. acknowledges the financial support for his PhD studentship by the UK Engineering and Physical Sciences Research Council. T.M.J. and M.S. thank the Karlsruhe House of Young Scientists for supporting part of this study via a visiting-scientist stipend. Also, the authors wish to thank T.L. Le, K.H. Simon, and E. Fanghänel of the TLK-CAPER team for the preparation of tritium containing gas samples. Finally, we like to thank Robert LeRoy for recalculating the Raman transition matrix elements of the hydrogen isotopologues for 532 nm laser excitation.

Supporting information

Supporting information may be found in the online version of this article. The programs related to the evaluation procedures described in this paper may be downloaded from http://sourceforge.net/projects/depoltools/.

References

[1] C. D. Allemand, *Appl. Spectrosc.* **1970**, *24*, 348–353.
[2] N. J. Bridge, A. D. Buckingham, *Proc. Royal. Soc. A* **1966**, *295*, 334–349.
[3] L. D. Ziegler, Y. C. Chung, P. Wang, Y. P. Zhang, *J. Chem. Phys.* **1989**, *90*, 4125–4143.
[4] P. Dawson, *Spectrochim. Acta A* **1972**, *28*, 715–723.
[5] S. K. Deb, M. L. Bansal, A. P. Roy, *Appl. Spectrosc.* **1984**, *38*, 500–504.
[6] V. Teboul, J. L. Godet, Y. L. Duff, *Appl. Spectrosc.* **1992**, *46*, 476–478.
[7] M. Shribak, S. Inoue´, R. Oldenbourg, *Opt. Eng.* **2002**, *41*, 943–954.
[8] J. Logan, N. Robertson, J. Hough, *Opt. Commun.* **1994**, *107*, 342–346.
[9] G. Turrell, *J. Raman Spectrosc.* **1984**, *15*, 103–108.
[10] C. Brémard, J. Laureyns, J.-C. Merlin, G. Turrell, *J. Raman Spectrosc.* **1987**, *18*, 305–313.
[11] D. Long, *The Raman Effect: A Unified Treatment of the Theory of Raman Scattering by Molecules*, Wiley, Chichester, **2002**.
[12] R. Brun, F. Rademakers, *Nucl. Instrum. Meth. A* **1997**, *389*, 81–86.
[13] W. Proffitt, S. P. S. Porto, *J. Opt. Soc. Am.* **1973**, *63*, 77–80.
[14] N. Kita, *Opt. Rev.* **2009**, *16*, 305–312.
[15] J. P. McGuire, R. A. Chipman, *Appl. Opt.* **1994**, *33*, 5080–5100.
[16] J. C. del Toro Iniesta, *Introduction to Spectropolarimetry*, Cambridge University Press, Cambridge, UK, **2003**.
[17] E. Collett, *Field Guide to Polarization (SPIE Vol. FG05)*, SPIE, Bellingham, WA, USA, **2005**.
[18] J. Alda, in *Encyclopedia of Optical Engineering*, (Eds: R. G. Driggers, C. Hoffman, R. Driggers), Taylor & Francis, Abingdon, UK, **2003**.
[19] P. G. Wang, L. D. Ziegler, *J. Phys. Chem.* **1993**, *97*, 3139–3145.
[20] R. J. LeRoy, Recalculation of Raman transition matrix elements of all hydrogen isotopologues for 532 nm laser excitation, Private communication, **2011**.
[21] M. Sturm, M. Schlösser, R. J. Lewis, B. Bornschein, G. Drexlin, H. H. Telle, *Laser Phys.* **2009**, *20*, 493–507.

ARTICLE IN PRESS

Journal of Molecular Structure xxx (2012) xxx–xxx

Contents lists available at SciVerse ScienceDirect

Journal of Molecular Structure

journal homepage: www.elsevier.com/locate/molstruc

Accurate calibration of the laser Raman system for the Karlsruhe Tritium Neutrino Experiment

Magnus Schlösser [a,*], Simone Rupp [a], Hendrik Seitz [a], Sebastian Fischer [a], Beate Bornschein [a], Tim M. James [b], Helmut H. Telle [b]

[a] Institute for Technical Physics (ITEP), Tritium Laboratory Karlsruhe (TLK), Karlsruhe Instiute of Technology (KIT), P.O. Box 3640, Karlsruhe 76021, Germany
[b] Department of Physics, College of Science, Swansea University, Singleton Park, Swansea SA2 8PP, United Kingdom

HIGHLIGHTS

- ▶ Mixing technique using catalytic-reactor to obtain calibrated H_2:HD:D_2 ratios.
- ▶ Raman sensitivity calibration using NIST-traceable SRM2242 luminescence standard.
- ▶ Combined spectral sensitivity and theoretical intensities for absolute Raman signals.
- ▶ Cross-calibration of H_2, HD and D_2 Raman response functions to better than 2%.

ARTICLE INFO

Article history:
Available online xxxx

Keywords:
Quantitative Raman spectroscopy
Absolute calibration
Hydrogen isotopologues
Tritium

ABSTRACT

The Karlsruhe Tritium Neutrino (KATRIN) experiment aims to measure the neutrino mass via high-precision electron spectroscopy of the tritium β-decay with a sensitivity of $m_\nu = 200$ meV/c^2 (90% C.L.). This can only be achieved if systematic uncertainties are minimized. An important parameter is the isotopic composition of the tritium gas used as the gaseous β-electron source, which is measured inline by Raman spectroscopy. The KATRIN experiment requires a measurement trueness of better than 10% of said composition; to achieve this, accurate calibration of the Raman system for all hydrogen isotopologues (H_2, HD, D_2, HT, DT, T_2) is required. Here we present two independent calibration methods, namely (i) a gas sampling technique, which promises high accuracy, but which is difficult to apply to tritiated species; and (ii) an approach via theoretical Raman signals (theoretical intensities plus spectral sensitivity), which in principle includes all six isotopologues. For the latter method we incorporated *ab initio* off-diagonal matrix elements of the polarizability from the literature; these have been verified by depolarization measurements. The system's spectral sensitivity was determined by a NIST-traceable SRM2242 luminescence standard. Both methods exhibited their individual merits and difficulties, but in cross calibration proved to be successful: a comparison for the non-radioactive isotopologues (H_2, HD, D_2) yielded agreement to better than 2% for the relative Raman response function. This is within the estimated (dominant) uncertainty of the theoretical Raman signal approach of about 3%. Therefore, one can be confident that, when using this approach, the trueness requirement of 10% for the KATRIN-relevant species (T_2, DT, D_2 and HT) will in all likelihood be exceeded.

1. Introduction

The **KA**rlsruhe **TRI**tium **N**eutrino experiment (KATRIN) will measure the neutrino mass with a sensitivity of $m_\nu = 200$ meV/c^2 (90% C.L.). The methodology is based on high-precision electron spectroscopy of the tritium β-decay near its kinematic endpoint at about 18.6 keV [1]. The systematic uncertainty of this measurement is influenced by several parameters; of particular importance is the precise knowledge of the purity of the tritium gas which is used as the gaseous β-electron source [2].

While one strives for the highest possible tritium purity, due to the way it is produced the gas is always composed of a mixture of T_2 (>90%), DT (<10%), and traces of HT, D_2, HD and H_2. In a first instance, the gas composition of the gaseous β-electron source influences the activity and thus the count-rate in the β-spectrum. For this, only relative changes are of interest. However, the composition has to be monitored continuously in time intervals of less than 250 s and with a measurement precision of at least 0.1% [1]. The operating pressure is in the range 150–200 mbar [2]. The feasibility

* Corresponding author.
E-mail address: magnus.schloesser@googlemail.com (M. Schlösser).

0022-2860/$ - see front matter © 2012 Elsevier B.V. All rights reserved.
http://dx.doi.org/10.1016/j.molstruc.2012.11.022

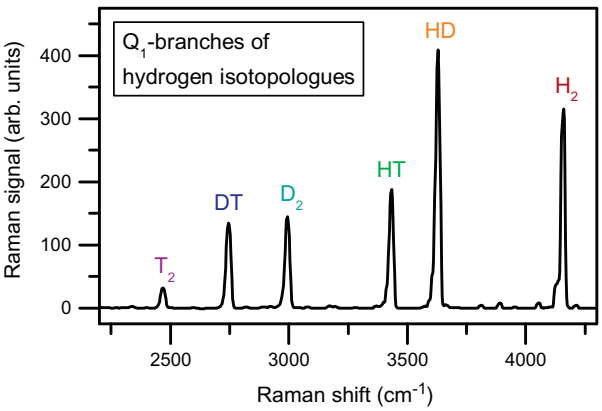

Fig. 1. Typical Raman spectrum of a gas mixture containing all six hydrogen isotopologues. All minor, unassigned lines between the Q_1 branches are S_1 and O_1 lines of the six hydrogen isotopologues.

of these requirements has been demonstrated using laser Raman spectroscopy (LARA) [3].

It has to be noted that the tritium-containing isotopologues (T_2, DT, HT) exhibit different final-state distributions of ro-vibrational excitations of the corresponding daughter nuclei (^{3}HeT, ^{3}HeD, ^{3}HeH), which in turn influence the energy of the β-electrons in the region of interest [4]. To account for this in the KATRIN experiment, tracing the relative changes in the tritium gas composition is not any longer sufficient, but now the trueness[1] of the LARA measurements is of crucial importance. According to simulations, the trueness should be at least better than 10% [6] for a period of at least 60 days, which is equivalent to one single KATRIN neutrino measurement run. To gauge the actual trueness of the LARA measurement an accurate intensity calibration of the LARA system is necessary. In this context calibration means that the relative Raman intensities (as shown in a typical Raman spectrum in Fig. 1) can be converted into absolute component concentrations.

In this paper we present a calibration strategy for the LARA system of the KATRIN experiment which consists of two approaches, and we demonstrate their successful application to calibrating our system, together with a detailed analysis of the systematic uncertainties associated with the two methods. Finally, both methods are compared to each other. It should be pointed out, that the methods and results presented within this publication are not limited to the application in the KATRIN experiment. A similar accountancy task is found within the fuel cycle of future fusion reactors [7]. Here, the requirements for the trueness are of the order of 1% [8]. In general, the calibration methods presented are applicable to most gas analysis systems, but in particular to those which include species which cannot be obtained by simple gas mixing.

2. Experimental system and procedures

The Raman system employed in this work is essentially the system described in Sturm et al. [9] with the light collection and detection system comprising optics for imaging the Raman excitation volume onto an optical fiber bundle, optics to transfer the fiber bundle output through a razor-edge Rayleigh filter onto the spectrometer slit, a Czerny–Turner spectrograph and a CCD 2D-array detector. Some modifications were made to that early system version, namely (i) a retro-reflecting mirror for nearly doubled laser intensity was inserted; (ii) the plano-convex lenses in the light collection path were replaced by two 2"-diameter achromatic lenses with $f = 75$ mm, to reduce chromatic aberrations; and (iii) the PI-Acton HTS spectrometer was replaced by a PI-Acton SP2150 unit ($f = 150$ mm, 600 grooves/mm). In addition, a linear polarizer was introduced between the two collection achromats, which ensures that polarization effects in the light collection and detection system (associated with the fiber bundle, edge filter, grating, CCD-detector) do not have to be considered. A typical spectrum acquired with this Raman system is shown in Fig. 1; all six hydrogen isotopologues present in the particular gas mixture can be identified.

From such a spectrum the Raman signal amplitude, S_x, of a certain isotopologue x can be obtained. It is related to the number of molecules in the sample, N_x. A system-dependent response function, R_x, provides the proportionality between the Raman signal and the particle number,

$$S_x = R_x \cdot N_x. \tag{1}$$

Note that in general the area under a certain Q_1-branch peak is taken as the total Raman signal. Relative Raman signal amplitudes, $S_{x,\mathrm{rel}}$, are obtained by normalizing the individual signal amplitudes to the sum of the signal amplitudes of all isotopologues in the sample. Accordingly, Eq. (1) is modified to

$$S_{x,\mathrm{rel}} = R_x \cdot N_x \Big/ \left(\sum_i R_i \cdot N_i \right). \tag{2}$$

The objective of a calibration is to determine values for R_x for any of the constituents in the sampled gas, in our case all hydrogen isotopologues. For easier comparison of the individual components it is useful to normalize the absolute response functions by the mean of all response functions, arriving at the relative response functions, $R_{x,\mathrm{rel}}$,

$$R_{x,\mathrm{rel}} = R_x / R_{\mathrm{mean}} = n \cdot R_x \Big/ \sum_{i=1}^{n} R_i. \tag{3}$$

In this paper we have contemplated three possible approaches to achieve an accurate calibration of our Raman system, namely (i) to use reference method(s) for cross-calibration; (ii) to measure spectra of known calibration samples; and (iii) to employ literature or theoretical values for the Raman cross-sections in combination with the measurement of the system's spectral sensitivity.

With the respect to the first, there is hardly any reference method available for the compositional measurement of tritium mixtures, which provides sufficient trueness [10,7]. Certainly, at the Tritium Laboratory Karlsruhe (TLK), a laboratory with renowned expertise in tritium analytics, no system is currently available to provide the required trueness.

As for the second approach, the generation and use of accurate samples is a widely used technique; specifically, such samples are very accurate in solid or liquid form, especially if they are produced by gravimetric preparation. However, in general, to provide accurate, homogeneous gas mixtures is substantially more complicated, as described in the ISO standard 6142 [11]. When dealing with tritium gas mixtures additional difficulties are encountered: (a) restricted handling of tritium due to safety regulations; (b) limited purity of the desired T_2 constituent; and (c) radio-chemical and exchange reactions with other species and the walls (Souers [12] and references therein).

With regard to the third approach, experimentally verified literature values for the cross-sections of the radioactive hydrogen isotopologues T_2, DT and HT are not available.

[1] The terminology of "precision", "trueness" and "accuracy" can be found in a publication by the Joint Committee for Guides in Metrology [5]. In short: **Precision** is the reproducibility of a measurement (spread of single values around the mean value); **trueness** is the deviation of the mean value to the true value; and the deviation of a single measurement value to the true value is the **accuracy**. Thus, if a measurement is both "precise" and "true", it is called "accurate".

It should be noted that a theoretical concept allows one to predict so-called "theoretical intensities" for all six hydrogen isotopologues [13]. However, since no trueness of these values is discussed within said publication, the question arises as to which level of confidence one can rely on these theoretical values.

Therefore, the solution for a successful calibration can only be a combination of the two latter approaches (ii) and (iii), i.e. to use theory values and the system's (measured) spectral sensitivity to arrive at the aforementioned relative response functions, $R_{x,\mathrm{rel}}$. These are verified by preparing calibration samples of the non-radioactive isotopologues H_2, HD and D_2. The restriction to non-tritiated species was necessary since a tritium-certified mixing system with sufficient accuracy was not available at the time of these calibration measurements. A successful verification of the relative response functions for the three non-radioactive isotopologues should then provide sufficient confidence to deduce the relative response functions of the tritiated isotopologues without direct experimental verification.

Of course, in a future step, the sampling method may be extended to cover all isotopologues to allow for a complete comparison. While seemingly straightforward in its concept, this calibration procedure has to fulfill certain requirements. Firstly, the approach needs a method and an apparatus to obtain highly accurate H_2, D_2 and HD samples. Secondly, it is necessary to generate appropriate theoretical intensity values and compare them with accurately measured ones, so that a high level of confidence can be placed in the theoretical values. Finally, an accurate method for measuring the system's spectral sensitivity is needed. Below the realization of both approaches (ii) and (iii) is discussed, together with the estimated systematic uncertainties of each.

3. Results

3.1. Approach I: calibration based on accurate gas samples

As stated above, the calibration with gas samples only includes the three non-radioactive isotopologues H_2, HD and D_2. The method and the experimental device are briefly introduced here; a full description and discussion can be found in a separate publication.[2] One should recall that Eq. (2) represents the relation between the relative Raman signal amplitudes, $S_{x,\mathrm{rel}}$, from the Raman measurements and the isotopologue compositions, N_x. Thus, if the latter is known from the sample mixing, then R_x can be obtained. The basic principle behind our accurate gas mixing is that two gas vessels of the same volume are filled with pure H_2 and D_2 gas at precisely determined pressures. The ratio of the pressures is then automatically equal to the ratio of the number densities in the mixtures once both vessels are connected to each other. The direct extension of this calibration method to HD is not possible, since in general HD is not commercially available in a high purity [14]. However, by cycling the mixed H_2/D_2 gas through a catalyst reactor (0.5% Pt on 1/16" Al_2O_3 from Alfa Aesar), HD is produced in the equilibrium exchange reaction $H_2 + D_2 \rightleftharpoons 2HD$ (with the equilibrium constant $K = [HD]^2/([H_2][D_2])$) during the calibration procedure itself. Said gas mixing system, including the catalyst reactor, has been set up at TLK; its schematic layout is shown in Fig. 2. The construction and functionality of the system as well as the measurement results are described elsewhere (see Footnote 2). Using this system, sets of measurements with different initial concentrations of H_2 and D_2 were performed. The simultaneous fit to the relative Raman signal amplitudes $S_{H_2,\mathrm{rel}}$, $S_{D_2,\mathrm{rel}}$ and $S_{\mathrm{HD,rel}}$ generates the related calibration functions R_{H_2}, R_{D_2} and R_{HD}, without the necessity for accurate control of the reaction temperature, which defines the equilibrium constant $K(T)$. The measurement points and resulting fit curves from such a calibration set are shown in Fig. 3. Note, that (i) the error bars are smaller than the symbols in the plot; and that (ii) measurements at initial hydrogen mole fractions of $y_{i,H_2} = 0.2$ and $y_{i,H_2} = 0.8$ have been performed twice to test the reproducibility of the procedure. The related repeat data points overlap to such an extent that no data scatter is noticeable on the scale of the symbols. The full fitting results are tabulated in the comparison section further below.

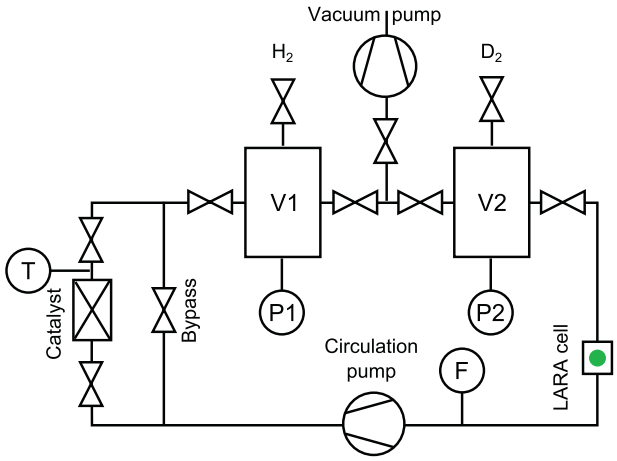

Fig. 2. Simplified flow diagram of the HYdrogen Deuterium Equilibration loop (HYDE). V_i = calibrated pressure vessels; P_i = pressure gauges; F = flow controller; T = thermocouple.

3.2. Approach II: calibration based on theoretical intensities and spectral sensitivity

Other than in the sampling approach described in Section 3.1, in the second approach all six hydrogen isotopologues are in principle covered. Eq. (1) needs to be written in a slightly different form: The Raman signal amplitude is now given as the product of the spectral sensitivity, $\eta(\lambda_s)$, and theoretical Raman intensity, $I_{\mathrm{Raman},x}(\lambda_s, N_x)$, and will thus be called "theoretical Raman signal amplitude" for the remainder of this publication:

$$S_x = \eta(\lambda_s) \cdot I_{\mathrm{Raman},x}(\lambda_s, N_x) \tag{4}$$

$$= \eta(\lambda_s) \cdot C \cdot \lambda_0^{-1} \cdot \lambda_s^{-3} \cdot \Phi_x \cdot \Im \cdot N_x. \tag{5}$$

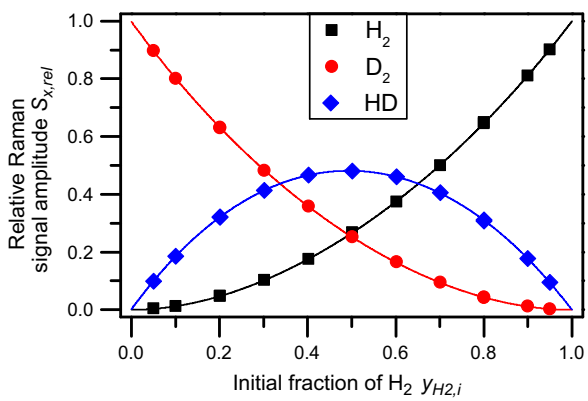

Fig. 3. Fitting of the HYDE data at a catalyst temperature of 25 °C. Horizontal axis: mole fraction y_{i,H_2} of H_2 before the equilibration of the mixture. Vertical axis: measured relative Raman intensities of the three components. Legend: symbols – measurement points; lines – fit curves. For further details see main text.

[2] Description and data are part of a manuscript submitted to *Anal. Chem.* but as yet unpublished, therefore a preview on the results in given in the "Supplementary material".

Here, C is a proportionality constant, λ_0 is the wavelength of excitation laser, λ_s is the wavelength of the Raman scattered light[3], Φ_x is the molecule dependent line strength function, and $\Im$ is the irradiance. It should be noted that Eq. (5) is a simplification; it is assumed that the signal only consists of a single monochromatic line. In reality, the Q_1-branches used in the calibration consist of a series of unresolved individual lines associated with the different initial rotational states with quantum number J (this feature is evident from the "non-Gaussian" shape in the example spectrum in Fig. 1). The population of these initial states can be calculated from the Boltzmann distribution and the nuclear spin degeneracy g_N[4]. Thus, for the actual case encountered in our calibration measurements Eq. (5) has to take this multi-line scenario into account, and needs to be modified to

$$S_x = \underbrace{C \cdot \lambda_0^{-1} \cdot \Im}_{\text{const.}} \cdot N_x \cdot \underbrace{\sum_J \left(\eta(\lambda_{sJ}) \cdot \lambda_{sJ}^{-3} \Phi_{xJ} (2J+1) g_N \exp\left(-\frac{\widetilde{F}(J)hc}{kT} \right) / Q \right)}_{R'_x} \tag{6}$$

with the molecular partition function Q [16]

$$Q = \sum_J \left((2J+1) g_N \exp\left(-\frac{\widetilde{F}(J)hc}{kT} \right) \right). \tag{7}$$

This description of the Raman signal in relation to particle numbers is now similar to Eq. (1) again. Note that, since the first three factors are constant, they will cancel out when calculating the relative response functions (see Eq. (3)). Therefore, only the functions R'_x are of interest, which will be discussed in detail below.

3.2.1. Raman intensities

The contribution of R'_x in Eq. (6) is related to theoretical Raman intensities,

$$R'_x = \sum_J \left(\eta(\lambda_{sJ}) \cdot \lambda_{sJ}^{-3} \Phi_{xJ} (2J+1) g_N \exp\left(-\frac{\widetilde{F}(J)hc}{kT} \right) / Q \right) \tag{8}$$

where $\widetilde{F}(J)$ represents the rotational term energies. The $\widetilde{F}(J)$-values can be obtained from the accurate measurement of the line positions.[17] The term Φ_{xJ} is the line strength function, which is a function of the tensor invariants a and γ, i.e. the isotropic and anisotropic polarizabilities, respectively. [16] As indicated by the symbol, these tensor invariants are individually different for each rotational J-level of the different isotopologues x. These values can be obtained from *ab initio* quantum calculations. In the 1980s Schwartz and LeRoy calculated the potentials and tensor invariants for all six hydrogen isotopologues, for the laser excitation wavelength $\lambda_0 = 488$ nm. [13] For our particular case here, i.e. Raman excitation based on 532 nm lasers (Nd:YAG/Nd:VO_4), the tensor invariants a and γ were recalculated for this specific wavelength [18]. However, since no trueness of these values is discussed in LeRoy's publications, the question arises as to which level of confidence one can rely on these theoretical values. This is associated with the fact that no uncertainties are published for said calculations. Therefore, we conducted an experiment for their verification. In that context, direct access to the individual tensor invariants is normally difficult; however, verification is feasible via depolarization ratio measurements [19]. Our methodology for accurately measuring and analyzing the depolarization ratios is discussed elsewhere [20]. There we describe the development of methods to correct for the non-zero collection angle and depolarization effects occurring in the Raman cell windows. Recently, we measured the depolarization ratios of the Q_1-lines ($J'' = 0$ to $J'' > 3$) of all six hydrogen isotopologues.[5] Our experimental values agree with the theoretically derived values, based on the calculations of LeRoy, [18] to within 5%. Using error propagation[6] it can be shown that the relative uncertainty of the depolarization ratio is about equal to the relative uncertainty of the line strength function. However, it should be made clear at this point that the aforementioned errors do not necessarily express the true uncertainty of the values, as obtained from the theory. Rather, they define the degree of confidence we currently place in the theoretical data.

3.2.2. Spectral sensitivity

Broadly speaking, the spectral sensitivity is the relative efficiency for the detection of photons in a light acquisition system, as a function of wavelength. Foremost, it is determined by the wavelength-dependent responses of the diffraction grating of the spectrograph and the CCD-detector. However, in general the spectral sensitivity becomes even more complex because of further components in the complete acquisition system (like e.g. optical fiber bundle, AR-coated lenses, edge filters, etc.); all of them exhibit their own polarization dependence. Therefore, as already mentioned in Section 2 above, a linear polarizer is introduced at the front end of the light collection system to minimize the influence of the latter components on the depolarization ratio measurements. An external light source is needed for the calibration of the system's spectral sensitivity. A common approach for calibrating the spectral sensitivity is the use of a certified blackbody radiator. However, commercial blackbody radiators with small uncertainties (e.g. <2%) are not only relatively expensive but also have a rather short certified lifetime, with often only about 50 h (note that in general already ~30 min are needed each time of use before the output is stabilized). A major disadvantage of such sources is that the volume/area of light generation normally differs considerably from the scattering region, which produces the Raman light. In our case, the Raman excitation volume can be approximated by a cylinder of diameter $d \approx 150$ μm, with a length of some millimeters. Blackbody radiators are by and large based on tungsten filaments of much larger size and often non-uniform shape. Measurements performed within the framework of our current research program showed that the exact position of the light, be it the Raman light or the calibration light, is crucial for the accuracy of the measured data, due to chromatic aberrations throughout the chain of optics. The solution employed in this work overcomes all above-mentioned difficulties, i.e. the calibration device (i) has a longer lifetime; (ii) provides and acts as a nearly perfect imitation of the Raman scattered light region; and (iii) is substantially cheaper. The device in question is a SRM2242 Raman standard, manufactured, certified and distributed by NIST (for more details see the corresponding NIST certificate for Standard Reference Material 2242 and Choquette et al. [21]). Note that this SRM2242 luminescence standard is designated for the use in backscattering Raman experiments (e.g. micro-Raman measurement devices). Therefore, the use of this device in a 90°-configuration constitutes a non-standard operation condition; however, in extensive checks we confirmed that the spectral distribution function remained valid (see below). The Raman shift range covered by the NIST-certified polynomial is 150–4000 cm^{-1}; the $\pm 2\sigma$ calibration uncertainties are tabulated over the full range. According to the certification protocol, the relative uncertainty is

[3] The wavelength dependence is often given as λ_s^{-4} in the literature. McCreery discusses in reference [15] that this term is valid for intensity measurements in W/s, whereas the λ_s^{-3} term is valid for measurements in photons/s (e.g. as in a CCD detector).

[4] For even J: ($g_N = 1$ for H_2, T_2; $g_N = 2$ for D_2); For odd J: ($g_N = 3$ for H_2, T_2; $g_N = 1$ for D_2). The heteronuclear molecules (HD, HT, DT) have no nuclear spin degeneracy and thus $g_N = 1$.

[5] Results are part of a publication to be published in *J. Raman Spectrosc.* Also see the "Supplementary material".

[6] Given in detail within the "Supplementary material" of this publication.

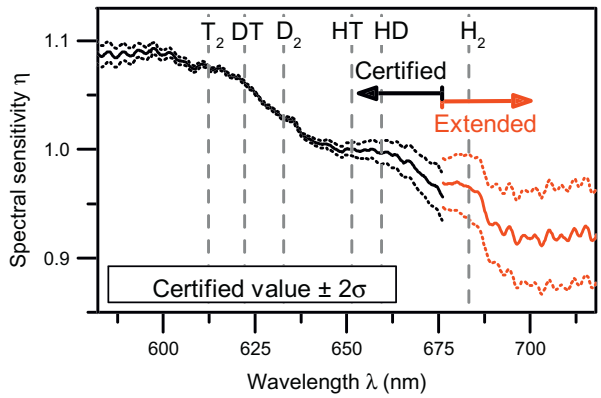

Fig. 4. Spectral sensitivity of the detection system, measured using the SRM2242 NIST standard. Note the discontinuity at the transition from the certified to the extended range (extended data also provided by NIST).

less than 1% for the Q_1-branch lines of the isotopologues of relevancy to the KATRIN measurements, i.e. T_2, DT, D_2 and HT. The Q_1-branch of H_2 (at ~4200 cm^{-1}), which is included in our analysis for completeness, lies just outside the certified region. NIST provided an extended dataset up to 7000 cm^{-1}, yet without certification of that extended range. The calibrated spectral sensitivity of our system is shown in Fig. 4. The ripple in the data traces can be associated with the transmission function of the razor-edge Raman filter for rejection of the Rayleigh scattered light (see the *Semrock* LP03–532RU-25 datasheet). Perfect mimicking of the Raman light excitation region can be established using a simple setup as shown in Fig. 5. The mount for the SRM2242 standard is attached to the same type of dovetail, which is used for mounting the Raman cell. Thus, the Raman cell can be removed and replaced by the calibration standard, with very high spatial reproducibility. The following systematic investigation have been performed in order to verify whether operating the SRM2242 standard in non-backscatter geometry is influenced systematically by the following effects: (i) changes in the incident excitation laser polarization; (ii) temperature variation; (iii) variation in laser power; and (iv) influence of the cell windows in the direction of the light collection. It could be shown that the variations associated with these effects are within the range of the certified $\pm 2\sigma$ standard deviation. The detailed results of this investigation will be subject of a future publication.

3.2.3. Resulting theoretical Raman signal amplitudes and uncertainties

In Table 1 the system response values, R'_x, derived from the theoretical Raman signal amplitudes are tabulated, together with the estimated uncertainties. The uncertainties are split into two terms, namely (i) the contribution $\Delta R'_{theo}$, which is associated with the confidence we place in the theoretical values, as obtained from the depolarization measurements; and (ii) the contribution $\Delta R'_{sens}$, which stems from the calibration of the spectral sensitivity. The quadratic sum of both uncertainty contributions, constitutes the overall uncertainty, $\Delta R'_{tot}$.

As can be seen, the overall uncertainty in the response function, as summarized in Table 1, is well below 5%. However, it is obvious that the confidence in the "theory" (which includes the depolarization measurements undertaken to cross-check the *ab initio* line strengths) currently dominates the total error estimation, with the exception of H_2. Its $\Delta R'_{sens}$ error is comparatively higher, since the required spectral calibration data are out of the certified range provided by NIST.

3.3. Comparison

The two calibration approaches have been performed for H_2, D_2 and HD. The results from both techniques are now compared to ascertain whether they agree within the estimated uncertainties. The related data are collated in Table 2. Here we compare the relative response functions, as defined in Eq. (3), and ratios of two response functions R_i/R_j, where the indices relate to different isotopologues. The uncertainties, Δ, are obtained from error propagation through the relative response functions. Note, that in the formation of relative response functions, the response function for H_2 with its large uncertainty (associated with the larger errors in the uncertified spectral sensitivity) dominates the uncertainties of the $R_{x,rel}$ functions.

The uncertainties of the response function values, obtained using the gas sample method, are well below 1%. A detailed discussion of the error estimation for this method can be found elsewhere (see Footnote 2).

The table entries show that the relative response function values, $R_{x,rel}$, and the response function ratios, R_i/R_j, obtained from the two approaches agree to better than 2%. The only exception is encountered for the R_{H_2}/R_{D_2} ratio, which has a difference of 3.4%. As pointed out above, this is most likely caused by the higher uncertainty in the calibration of the spectral sensitivity in the wavelength range of H_2. Nevertheless, the overall agreement for both approaches is well within the bounds given by the total uncertainties in the theoretical Raman signal amplitudes of about 3% for the relative R-values and 5.2% for the ratios. However, further comparisons are needed, including the tritiated species HT, DT and T_2 in a similar gas mixing device (HYDE) as used here. Unfortunately, a unit able to handle these radioactive gases in this way is not yet available.

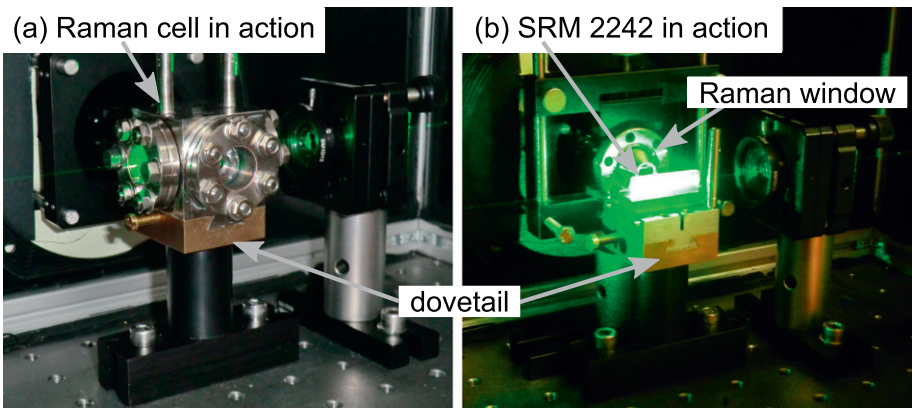

Fig. 5. Operation of the LARA system with (a) Raman cell, or (b) SRM 2242 luminescence reference standard.

Table 1
Raman response functions based on theoretical Raman signal amplitudes, and the related uncertainties. All R'_x have been normalized so that $R'_{H_2} = 1$. For the meaning of $\Delta R'_{theo}$ and $\Delta R'_{sens}$ see the main text.

Isotopologue	R'_x	$\Delta R'_{theo}$ (%)	$\Delta R'_{sens}$ (%)	$\Delta R'_{tot}$ (%)
H_2	1.000	2.9	2.7	3.9
HD	0.981	3.0	0.9	3.1
HT	0.960	3.1	0.5	3.2
D_2	0.925	3.4	0.2	3.4
DT	0.914	3.7	0.1	3.7
T_2	0.866	3.9	0.2	3.9

Table 2
Comparison of response functions as obtained by the two approaches discussed in this publication. Note that the $R_{x,rel}$-representation offers better means for comparing the two than the R'_x-representation, for which the data are normalized to $R'_{H_2} = 1$ (cf. Table 1).

	Theoretical Raman signals			HYDE measurements		Difference
	Value	Δ_{sens} (%)	Δ_{tot} (%)	Value	Δ_{tot} (%)	Theoretical Raman signals–HYDE (%)
$R_{H_2,rel}$	1.032	1.9	3.0	1.013	<0.5	1.9
$R_{D_2,rel}$	0.955	2.1	2.9	0.969	<0.5	−1.5
$R_{HD,rel}$	1.013	2.0	2.7	1.018	<0.5	−0.5
R_{H_2}/R_{D_2}	1.081	2.8	5.2	1.045	<0.6	3.4
R_{HD}/R_{D_2}	1.061	0.9	4.9	1.050	<0.6	1.0

4. Conclusion

The KATRIN experiment aims to measure the neutrino mass with a sensitivity of $m_\nu = 200\ \mathrm{meV/c^2}$ (90% C.L.). This can only be achieved if systematic uncertainties are minimized. Of utmost importance is the isotopic composition of the tritium gas injected into the source cryostat which is measured inline by Raman spectroscopy. KATRIN requires a trueness of better than 10%, which can be obtained by proper calibration. In this work we have discussed two independent calibration methods, which on their own have individual difficulties. The sampling technique promises high accuracy, but cannot be easily applied to tritiated species. The approach via theoretical Raman signals (theoretical intensities and spectral sensitivity) could cover all isotopologues, but the confidence in the theory is unknown since no experimental literature values exist. In the context of the spectral sensitivity calibration it is worth noting that the use of a solid fluorescence standard, such as the SRM2242 sample used in our measurements, may be judged as being generally advantageous exhibiting low calibration uncertainties, longevity and almost perfect imitation of the Raman scattering region. A comparison in the range of the non-radioactive isotopologues (H_2, HD, D_2) shows agreement of better than 2% for the relative response function obtained by both methods. This is within the estimated uncertainty of the theoretical Raman signal approach of about 3%. Thus, this approach applied for the KATRIN relevant species (T_2, DT, D_2 and HT) will exceed the trueness requirements. Finally, together with a HYDE-type gas mixing facility it should be also possible to extend our methodology to accurately measure relative cross-sections to other gases (especially those which are only stable in mixtures).

Acknowledgments

This research was supported by the Helmholtz Association (HGF), the Federal Ministry of Education and Research (BMBF), through grants 05A08VK2 and 05A11VK3, and the German Research Foundation (DFG) within the framework of the TransRegio Project "Neutrinos and Beyond", Grant SFB/TR 27. T.M.J. acknowledges the financial support for his PhD studentship by the UK Engineering and Physical Sciences Research Council (EPSRC). The authors thank D. Adami, C.G. Alecu, and M. Sturm for the design and mechanical construction of the HYDE loop. Furthermore, we appreciate the vital discussions about process engineering and chemical properties of hydrogen with D. Demange, R. Michling, R. Wagner, and J. Wendel. We gratefully thank A. Poon for discussions about the statistical analysis of the HYDE data. Finally, we like to thank R. LeRoy for recalculating the Raman transition matrix elements of the hydrogen isotopologues for 532 nm laser excitation.

Appendix A. Supplementary material

Supplementary data associated with this article can be found, in the online version, at http://dx.doi.org/10.1016/j.molstruc.2012.11.022.

References

[1] The KATRIN collaboration, J. Angrik et al., KATRIN Design Report 2004, FZKA Scientific Report 7090, 2005.
[2] M. Babutzka, M. Bahr, J. Bonn, B. Bornschein, A. Dieter, G. Drexlin, K. Eitel, S. Fischer, F. Glück, S. Grohmann, M. Hötzel, T.M. James, W. Käfer, M. Leber, B. Monreal, F. Priester, M. Röllig, M. Schlösser, U. Schmitt, F. Sharipov, M. Steidl, M. Sturm, H.H. Telle, N. Titov, New J. Phys. 14 (2012) 103046.
[3] S. Fischer, M. Sturm, M. Schlösser, B. Bornschein, G. Drexlin, F. Priester, R.J. Lewis, H.H. Telle, Fusion Sci. Technol. 60 (2011) 925–930.
[4] N. Doss, J. Tennyson, A. Saenz, S. Jonsell, Phys. Rev. C 73 (2006) 025502.
[5] Working Group 2 of the Joint Committee for Guides in Metrology, International vocabulary of metrology – Basic and general concepts and associated terms (VIM), third ed., JCGM 200:2008, Bureau International des Poids et Mesures (BIPM), 2008.
[6] M. Schlösser, S. Fischer, M. Hötzel, W. Käfer, in: G. Bellini (Ed.), Proc. Int. School of Physics 'E. Fermi', Course CLXXXII 'Neutrino Physics and Astrophysics', IOS, Amsterdam; SIF, Bologna, 2012, pp. 333–336. arXiv/1203.4099.
[7] M. Nishi, T. Yamanishi, T. Hayashi, Fusion Eng. Des. 81 (2006) 745–751.
[8] R. Lässer, ITER Design Description Document, Tritium Plant and Detritiation Systems, WBS32H, Analytical system, Technical Report, 2001.
[9] M. Sturm, M. Schlösser, R.J. Lewis, B. Bornschein, G. Drexlin, H.H. Telle, Laser Phys. 20 (2009) 493–507.
[10] D. Demange, C. Alecu, N. Bekris, O. Borisevich, B. Bornschein, S. Fischer, N. Gramlich, Z. Köllö, T. Le, R. Michling, F. Priester, M. Röllig, M. Schlösser, S. Stämmler, M. Sturm, R. Wagner, S. Welte, Fusion Eng. Des. 87 (2012) 1206–1213.
[11] ISO 6142:2001, Gas Analysis – Preparation of Calibration Gas Mixtures – Gravimetric Methods, The International Standard Organisation, Geneva, Switzerland, 2001.
[12] P.C. Souers, Hydrogen Properties for Fusion Energy, University of California Press, Berkeley, CA, USA, 1986.
[13] C. Schwartz, R.J. LeRoy, J. Mol. Spectrosc. 121 (1987) 420–439.
[14] T. Ohta, S. Bouchigny, J.-P. Didelez, M. Fujiwara, K. Fukuda, H. Kohri, T. Kunimatsu, C. Morisaki, S. Ono, G. Rouillé, M. Tanaka, K. Ueda, M. Uraki, M. Utsuro, S.Y. Wang, M. Yosoi, Nucl. Instrum. Methods A 664 (2012) 347–352.
[15] R.L. McCreery, Photometric standards for raman spectroscopy, in: J.M. Chalmers, P.R. Griffith (Eds.), Handbook of Vibrational Spectroscopy, John Wiley & Sons Ltd, Chichester, UK, 2006.
[16] D. Long, The Raman Effect: A Unified Treatment of the Theory of Raman Scattering by Molecules, John Wiley & Sons Ltd, Chichester, UK, 2002.
[17] D.K. Veirs, G.M. Rosenblatt, J. Mol. Spectrosc. 121 (1987) 401–419.
[18] R.J. LeRoy, Calculation of the Raman transition matrix elements of all hydrogen isotopologues for 532 nm laser excitation, Private communication, 2011.
[19] C.D. Allemand, Appl. Spectrosc. 24 (1970) 348–353.
[20] M. Schlösser, T.M. James, S. Fischer, R.J. Lewis, B. Bornschein, H.H. Telle, J. Raman Spectrosc, in press. doi:http://dx.doi.org/10.1002/jrs.4201.
[21] S.J. Choquette, E.S. Etz, W.S. Hurst, D.H. Blackburn, S.D. Leigh, Appl. Spectrosc. 61 (2007) 117–129.

Research article

Journal of RAMAN SPECTROSCOPY

Received: 17 December 2012 Revised: 29 January 2013 Accepted: 4 February 2013 Published online in Wiley Online Library

(wileyonlinelibrary.com) DOI 10.1002/jrs.4283

Accurate depolarization ratio measurements for all diatomic hydrogen isotopologues

T. M. James,[a] M. Schlösser,[b] S. Fischer,[b] M. Sturm,[b] B. Bornschein,[b] R. J. Lewis[a,c] and H. H. Telle[a]*

The Raman depolarization ratios for individual $Q_1(J'')$ branch lines of all diatomic hydrogen isotopologues – H_2, HD, D_2, HT, DT, and T_2 – were measured, for all rotational levels with population larger than 1/100 relative to the Boltzmann maximum at room temperature. For these measurements, the experimental setup normally used for the monitoring of the tritiated hydrogen molecules at KArlsruhe TRItium Neutrino experiment was adapted to optimally control the excitation laser power and polarization, and to precisely define the Raman light collection geometry. The measured Raman depolarization values were compared to theoretical values, which are linked to polarizability tensor quantities. For this, the 'raw data' were corrected taking into account distinct aspects affecting Raman depolarization data, including (1) excitation polarization impurities; (2) extended Raman excitation volumes; and (3) Raman light collection over finite solid angles. Our corrected depolarization ratios of the hydrogen isotopologues agree with the theoretical values (based on *ab initio* quantum calculations by R.J. LeRoy, University of Waterloo, Canada) to better than 5% for nearly all of the measured $Q_1(J'')$ lines, with 1σ confidence level. The results demonstrate that reliable, accurate Raman depolarization ratios can be extracted from experimental measurements, which may be substantially distorted by excitation polarization impurities and by geometrical effects.

Supporting Information may be found in the online version of this article.

Keywords: hydrogen isotopologues; tritium; Raman depolarization ratio

Introduction

The molecular system of (diatomic) hydrogen is often seen as a model case for comparative studies of theory and experiments. For example, the calculation of the polarizabilities, and associated with this Raman line/band intensities, may be presumed to be a simple task because of the perceived simplicity of the quantum mechanical system consisting of two electrons and two nuclei only. However, the enormous efforts necessary to arrive at quantitative agreement between experiment and theory is evident from the long history of the theoretical calculations and re-calculations for H_2.

Theoretical calculations for the hydrogen molecule go back to the 1930s.[1] Since those first, basic attempts, many research groups worked on the hydrogen problem. A comprehensive overview on all relevant contributions up to the late 1980s was given by Schwartz and LeRoy,[2] who also calculated the off-diagonal matrix elements related to the average polarizability and polarizability anisotropy encountered in Raman spectroscopy, for all vibration-rotation states of diatomic hydrogen isotopologues, for laser excitation at 488 nm. However, the overall results may have to be viewed with some caution since Schwarz and LeRoy stated that the values for the tritium containing molecules were obtained via a scaling method beyond the non-adiabatic corrections calculated for H_2, HD, and D_2.

A comprehensive experimental study of hydrogen has been carried out by Veirs and Rosenblatt[3] who measured a large range of Raman lines for all six diatomic hydrogen isotopologues, using an argon ion laser operating at 488 nm as the excitation source. The publication of their experimental results coincides with the release of Schwartz and LeRoy's aforementioned theoretical data.[2]

While Raman line position measurements and extraction of energy levels prove to be relatively straightforward, the measurement of the off-diagonal transition matrix elements of the polarizability turns out to be a much more challenging task, if high accuracy is desired. In particular, if these matrix elements are intended to be used in quantitative spectroscopy, it is necessary to validate their absolute values. However, direct access to average polarizability and polarizability anisotropy is experimentally difficult. For this it was suggested – and has become one major method of choice for the task – to measure depolarization ratios, which then can be used in the validation of theoretical line intensities.

Experimental depolarization data for the Raman lines of the hydrogen molecule are sparse. Only two research groups have measured depolarization ratios for individual Q_1-branch lines of H_2.[4,5] To our knowledge, no depolarization ratio measurements

* Correspondence to: H. H. Telle, Department of Physics, College of Science, Swansea University, Singleton Park, Swansea, SA2 8PP, United Kingdom. E-mail: h.h.telle@swansea.ac.uk

a Department of Physics, College of Science, Swansea University, Singleton Park, Swansea, SA2 8PP, United Kingdom

b Institute for Technical Physics (ITEP), Tritium Laboratory Karlsruhe (TLK), Karlsruhe Institute of Technology (KIT), P.O. Box 3640, 76021, Karlsruhe, Germany

c New affiliation: Optoelectronics Research Centre, University of Southampton, Highfield, Southampton, SO17 1BJ, United Kingdom

have been reported for any of the other hydrogen isotopologues. However, in a number of experiments data for some or all of the other isotopologues are required. This includes the **I**nternational **T**hermonuclear **E**xperimental **R**eactor (ITER) project and the **KA**rlsruhe **TRI**tium **N**eutrino (KATRIN) experiment, in which specifically the tritiated isotopologues T_2, DT, and HT need to be accounted and monitored with high accuracy. For example, in KATRIN, the tritiated isotopologues need to be determined with relative concentration precision of less than 0.1%.[6,7] In this latter context, the main thrust of the work reported here has been to obtain some of the vital data necessary for accurate calibration of the in-line, near real-time Raman analysis system, which is to be used for continuous long-term monitoring of the injected and circulating gas in the windowless gaseous tritium source of the KATRIN apparatus.

The challenging issue has been to quantitatively link the measured Raman depolarization values to theoretical polarizability tensor quantities, since quantum-theoretical calculations do not incorporate experimental parameters. To achieve this, we recently developed a numerical model to correct, for realistic experimental configurations, experimentally measured depolarization ratios. In brief, our methodology allows one to take into account aspects normally affecting Raman depolarization measurements, namely (1) excitation polarization impurities; (2) extended Raman excitation volumes; and (3) Raman light collection over finite solid angles. These corrected depolarization ratios can then be directly compared with expressions that are based on theoretical polarizability tensor elements.[8]

In this paper, we describe the apparatus and the measurement philosophy which were successfully used to acquire Raman depolarization ratios, corrected for the aforementioned effects, for the $Q_1(J'')$ branch lines of all diatomic hydrogen isotopologues – H_2, HD, D_2, HT, DT, and T_2 – up to J″-levels with ~1% population relative to the Boltzmann maximum at room temperature. To our knowledge, this is the first time that Raman depolarization ratios have been reported for individual rotational transitions of all isotopologues of hydrogen, beyond those for H_2.[4,5] Moreover, by and large, our measurement data differ by less than 5% from those based on recent quantum-theoretical calculations by LeRoy.[9]

Methodology and theoretical aspects

A glance into Raman intensity theory is required before the depolarization ratio is introduced. For a rigorous treatment of the theory of the Raman effect, the reader is referred to, for example, the textbook by Long.[10]

Raman intensities

The intensity of light which is scattered by diatomic molecules via the Raman effect is given as[10,11]

$$I_{p^s,p^i}(\varphi,\theta) = k_{\tilde{\nu}}\tilde{\nu}_L\cdot\left(\tilde{\nu}_L - \tilde{\nu}_{v,J}\right)^3\cdot N_i\cdot\Phi_{p^i,p^s}(\varphi,\theta)\cdot\Im, \qquad (1)$$

where p^i and p^s are the polarization states of the incident and scattered light beams, respectively; $\tilde{\nu}_L$ and $\tilde{\nu}_L - \tilde{\nu}_{v,J}$ are the wavenumbers of the laser excitation and Raman scattered radiation (with ro-vibrational level shift $\tilde{\nu}_{v,J}$); $k_{\tilde{\nu}}$ is a constant to adjust the dimensions and units; N_i is the Boltzmann population of the initial state (v″; J″); and $\Im$ is the irradiance of the exciting radiation.

In this paper, the exciting radiation is always linearly polarized; therefore, we restrict the treatment to linear polarized scenarios. The angular-dependent component which is analyzed in depolarization measurements is the line strength function Φ, at given scattering angles φ and θ. This function depends on the polarization states of the scattered p^s and incident p^i light, respectively.

The definitions of the angles φ and θ relative to the laser beam direction and the scattering plane are visualized in a sketch in Fig. 1. The scattering plane is determined by the light excitation *z*-axis and its azimuth angle φ (with respect to the light collection *x*-axis). The zenith angle θ is defined as the angle between the *z*-axis and the scattered ray in the scattering plane. Note that in the direction of the light collection, imaging lenses, and polarization optics are normally found. The notation of the variables is according to Long.[10] There, also the line strength function, Φ, is given as a function of the polarizability tensor invariants, a and γ, which are the isotropic and anisotropic tensor invariants, respectively. These tensor invariants can be calculated *ab initio*. The tensor elements required for our study of the hydrogen isotopologues were calculated using the methodology described in Schwartz and LeRoy.[2]

Depolarization ratios

The depolarization ratio is defined as the ratio between the intensity of the scattered light with polarization direction parallel and perpendicular to the scattering plane. Allemand *et al.*[12] describe two different methods for determining these ratios. Either the ratio can be derived for fixed incident laser polarization and measuring the ratio of the scattered polarization states ($\|^s$ and $\perp^s$); or the signal ratio of the incident polarization states ($\|^i$ and $\perp^i$) is used, and the scattered polarization state is fixed to one component using a polarizer. For the experiments in our investigation of the hydrogen isotopologues, the latter approach is followed.

In general, theoretical formulation of depolarization ratios is only made for (experimental) situations where the scattered light originates from a single point and scattering is observed for a vanishingly narrow solid angle. We will label the index of this depolarization ratio by **s**ingle **p**oint, '**zero**' **s**olid **a**ngle (SP0SA). For a fixed scattering angle of $\theta = \pi/2$ and $\varphi = 0$, this depolarization ratio for the Q_1-branches ($\Delta J = 0$) of the hydrogen isotopologues is given as[10]

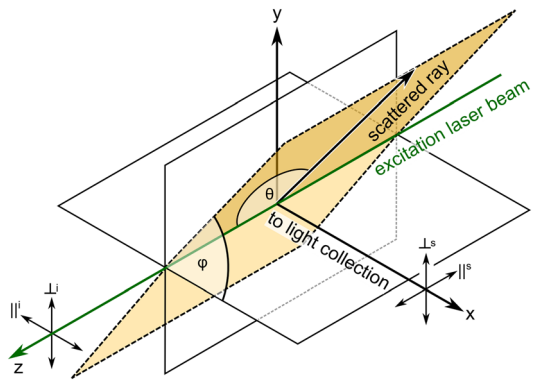

Figure 1. Definition of Raman scattering directions and angles; for details, see text.

$$\rho_{SP0SA} = \frac{I_{\perp^s,||^i}(\varphi=0,\theta=\pi/2)}{I_{\perp^s,\perp^i}(\varphi=0,\theta=\pi/2)} = \frac{\Phi_{\perp^s,||^i}(\varphi=0,\theta=\pi/2)}{\Phi_{\perp^s,\perp^i}(\varphi=0,\theta=\pi/2)} = \frac{3b_J^{(2)}\gamma^2}{45a^2+4b_J^{(2)}\gamma^2}. \quad (2)$$

Here, $b_J^{(2)}$ is the Placzek-Teller factor for the Raman transitions with $\Delta J = 0$:

$$b_J^{(2)} = \frac{J(J+1)}{(2J-1)(2J+3)}. \quad (3)$$

For the meaning of the parameters a and γ in Equation (2), the following should be recalled. In order to determine the intensity and polarization components of the scattered radiation, two appropriately chosen isotropic averages of the transition polarizability tensor are required, for example the diagonal and off-diagonal components $\langle(\alpha_{xx})^2\rangle$ and $\langle(\alpha_{xy})^2\rangle$, respectively, (see Long[10] for a full derivation). These incorporate the Raman transition matrix elements between an initial (v^i) and a final (v^f) state, $\left|\left\langle v^f\left|\alpha_{\Delta K}^{(j)}\right|v^i\right\rangle\right|^2$, with $\Delta K = 0$ for diatomic molecules. These matrix elements find their way into Equation (2) in the form of the "average polarizability" and the "anisotropy" contributions:

$$a^2 = (1/3)\cdot\left|\alpha_0^{(0)}\right|^2 \text{ and } \gamma^2 = (3/2)\cdot\left|\alpha_0^{(2)}\right|^2 .$$

For the molecules of interest to this work – i.e. all hydrogen isotopologues – the respective a- and γ-values were calculated by Leroy for 532 nm laser excitation.[9]

Experimentally, this situation is not realistic, as the scattered light originates along the extended region of the laser beam and is usually collected over fairly large solid angles; thus non-zero solid angles need to be taken into account. This has an effect on the measured depolarization ratio; it can be taken into account by integrating over the scattering geometry. This results in an effective depolarization ratio which can significantly differ from Equation (2). Deb *et al.*[13] calculated the error in the measured depolarization ratio due to this finite collection angle and later Teboul *et al.*[14] refined the model for larger solid angles. However, Teboul's models only consider a single angle θ, which is only suitable for point like emission and circular apertures. In addition, the calculation is based on a fourth-order series expansion, which will be inaccurate for larger angles. As described above, point-like emission is not realistic when the scattering occurs in an extended region. Experimentally, this is normally the case if a beam is focused with long focal length lenses, which lead to a focal depth of a few millimeters.

We have generated a mathematical model, by which we can calculate the difference between a SP0SA depolarization ratio and the one which is actually observed concerning the realistic scattering/collection geometry. This is obtained via a numerical integration over the angles θ, φ, and the position along the laser beam axis, z. In Schlösser *et al.*[8], this model is described in detail. The solid angle is defined explicitly to obtain correct definitions of integration bounding curves that intrinsically account for the correct transmission of off-centre scattered light through multiple apertures such as sample cell windows, collection lenses, etc. Polarization aberrations by stress-induced birefringence in the cell windows can reduce the polarization cleanness.[8] In our case, that means the incident laser light is no longer perfectly polarized after passage through a laser window. In the said model, the polarization cleanness of the incident laser beam is catered for mathematically by using an associated parameter $\xi = \cos^2\beta$, where β is the angular deviation from the initial polarization direction.

In Equation (2), the theoretical depolarization ratio, ρ_{SP0SA}, is defined as a ratio of two line strength functions obtained under different polarization configurations. In order to retrieve the experimentally observed depolarization ratio, ρ_{obs}, this ratio is now modified by taking into account the integration over the solid angle and position along the laser beam axis, z, and the reduced polarization purity:

$$\rho_{obs} = (\xi A + (1-\xi)B)/(\xi B + (1-\xi)A) \quad (4)$$

$$A = \iiint_{\varphi,z,\theta} \Phi_{\perp^s,||^i}(\varphi,\theta)\sin\theta \; d\theta \; dz \; d\varphi \quad (5)$$

$$B = \iiint_{\varphi,z,\theta} \Phi_{\perp^s,\perp^i}(\varphi,\theta)\sin\theta \; d\theta \; dz \; d\varphi. \quad (6)$$

The procedure works in two stages. As a first step, the cleanness of the laser beam ξ is determined from the measurement of the depolarization ratio of a line whose value is precisely known. For example, for the hydrogen isotopologues, this would be $\rho(Q_1(0)) = 0$ because the Placzek-Teller factor vanishes; see Equation (3). In the second step, this cleanness is taken into account, which then allows one to correct the observed depolarization ratios for the polarization aberrations and collection solid angle to finally obtain the desired ρ_{SP0SA}-values.

In the following, we discuss the application of these recipes to correcting observed (experimental) depolarization ratios ρ_{obs} to yield ρ_{SP0SA}-values; these are then compared with the literature values.

Experimental

In this section, we describe the generation and analysis of 'raw' data for the measurement of the depolarization ratios, discussing in sequence (1) the *experimental setup* used in the measurements at KIT and Swansea; (2) the underlying *measurement strategy* to achieve best signal strength with good signal-to-noise ratios, for excitation at vertical and horizontal laser beam polarization; (3) the analysis strategy including cosmic ray removal, baseline flattening, line fitting, and calculating the depolarization ratios; (4) the interpretation of raw data spectra, and the determination of the correction parameters to the experimental depolarization ratios ρ_{obs}; and (5) the estimation of statistical and systematic errors.

Description of the measurement setup

The measurement setups used for the depolarization measurements of the hydrogen isotopologues were, by and large, identical to the setups used in our analytical Raman measurements at Swansea and the LOOPINO facility at KIT (for a description see Fischer *et al.*[15]). Only a few minor modifications have been introduced to allow for (1) controlled changes in the polarization orientation of the excitation laser, and pre-selection of the polarization in the light collection path; and for (2) higher spectral resolution to resolve all $Q_1(J'')$-branch lines. A schematic summary of our measurement setups is shown in Fig. 2.

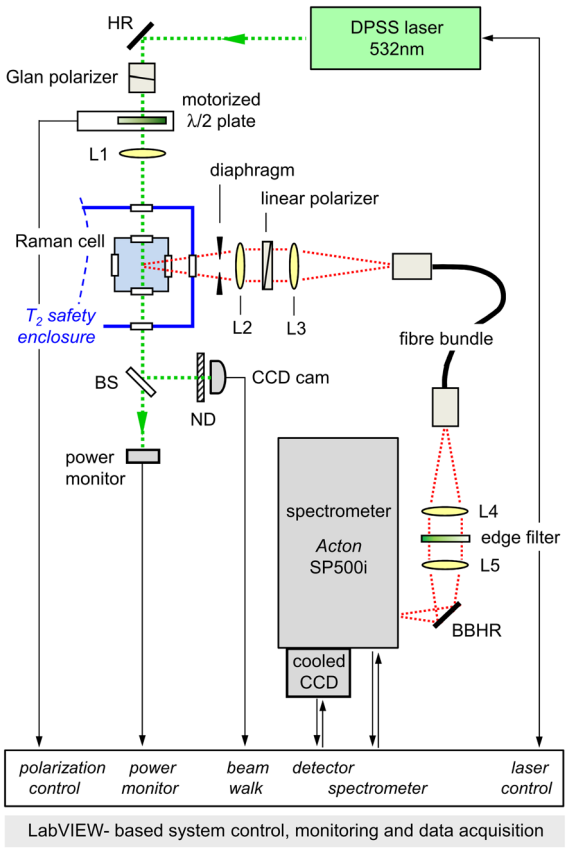

Figure 2. Conceptual setup for Raman depolarization measurements of hydrogen isotopologues. HR = high reflector; L1 – L5 = plano-convex lenses; BS = beam sampler; ND = neutral density filter; BBHR – broad-band high reflector. For further details, see text.

As in all our measurements of hydrogen isotopologues, laser excitation of the Raman transitions is at 532 nm; we used (multi-mode) DPSS Nd:YAG lasers manufactured by *Laser Quantum* ('Excel' and 'Finesse' models with 2 W and 5 W output power, respectively). These lasers are temperature stabilized to keep their emission wavelength constant to better than the resolution of the spectrometer used in the measurements; at the same time, drift and fluctuation of the laser output power are minimized.

A combination of a Glan-Taylor polarizer and a precision (multi-order) half-wave plate is used to set the polarization direction of the Raman excitation laser. The polarization direction is adjusted to any desired angular orientation, using a motorized rotational assembly (*Thorlabs* PRM1/MZ8 plus TDC001), with a quoted overall precision and repeatability of better than $\pm 0.2°$. Note that the (thin) half-wave plate was placed after the Glan-Taylor polarizer; while this is a less common sequence, the combined, initial polarization cleanness is still of the order 1.5×10^{-4}. However, more importantly, it minimizes any beam walk which may occur during polarization rotation. The polarized laser beam is focused into the Raman cell by an AR-coated plano-convex lens with f = 250 mm.

The Raman gas cell is the same cell we have used in all our previous measurements,[16,17] which is tritium compatible and is based on the design by Taylor *et al.*[18] For measurements using tritium-containing isotopologues, the cell has to be placed into a secondary safety enclosure, which requires that the laser beam (and the Raman scattered light) has to pass through additional windows. We also would like to note that our specific cell has an additional drawback, inasmuch as the compatibility with tritium gas requires particular sealing, which by its nature results in stress-induced birefringence in the cell windows; this introduces deterioration in the cleanness of the excitation polarization. While annoying, this problem cannot be avoided when dealing with tritium-containing gases; however, we can live with it since the effect can be accounted for in the corrected polarization ratios (see '"Raw" depolarization data and their correction' below). It should be noted, too, that any optical components introduce some deterioration in polarization cleanness, which in turn will impact on precision Raman depolarization measurements. Therefore, care has been taken to minimize the number of optical components in the laser path. Note that we have characterized all relevant optical components for their influence on polarized light, to enable post-measurement correction procedures (for more details see 'Raw depolarization data and their correction' below and the 'Supporting Information' associated with this publication).

The scattered light is imaged by an achromatic-lens pair onto a position-ordered fiber bundle (48 fibers of 100 μm core diameter, arranged in slit-slit configuration; NA = 0.22 for individual fibers). The output from the fiber bundle is imaged onto the entrance slit of the spectrometer, after passage through a 532 nm Raman edge filter (*Semrock* razor edge filter 'LP03-532RU', edge transition 186 cm^{-1}).

Note that an analyzing polarizer (linear glass polarizer, *Edmund Optics*, with polarization cleanness better than 1.5×10^{-4} over the wavelength range of the measured Raman spectra) was inserted between the two imaging lenses. In this way, the polarization dependence in any of the following optical components, which might otherwise affect the depolarization ratios, does not have to be known; in particular, the fiber bundle and the spectrometer grating would be difficult to characterize.

Note further that a diaphragm was introduced at the entrance to the Raman light collection system to allow for controlled changes in the solid angle of collection (for further details on this aspect see '"Raw" depolarization data and their correction' below).

Because high spectral resolution is required to measure individual Q_1-branch lines, here we employed spectrometers with f/# = 1/6.5 (*Acton*, SP500i), with interchangeable gratings. For all high-resolution Q_1-branch measurements the gratings with 2400 gr/mm were selected, providing spectral resolutions of the order ~2 cm^{-1}. Two different CCD array detectors are used in our setups, namely a 1024 × 256 front-illuminated open-electrode device (*Horiba*, 'Synapse', held at −70 °C) at Swansea and a 1340 × 400 pixel back-illuminated device (*Princeton Instruments*, 'Pixis 400B', held at −75 °C) at KIT. Both detectors are read out via user-written LabVIEW VIs.

Measurement strategy

The main considerations when acquiring the spectra to calculate the depolarization ratios are (1) exposure times; (2) binning; (3) stepping of polarization direction over 180° range to determine the minimum and maximum angles – once only; and (4) the actual measurements for vertical (⊥) and horizontal (∥) polarization excitation. The settings and parameters for measurement of the depolarization ratios are shown in Table 1.

Exposure times

The detector exposure times were chosen for each individual isotopologue measurement to maximize the intensity of the

Table 1. Settings and parameters for depolarization measurements

Parameter	Units	at Swansea	at KIT
Laser (532 nm) power [a]	W	2.1 (±0.15% drift)	5.0 (±0.10% drift)
Laser wavelength drift [a]	cm^{-1}	0.5 – 1.5	0.3 – 0.8
Laser focussing lens, f =	mm	250	250
Light collection lenses, f =	mm	50	75
Distance scattering volume to diaphragm	mm	38 (±1)	69 (±1)
Diaphragm opening, r =	mm	3 (±0.25)	5 (±0.5)
Spectral resolution (FWHM), with 2400 gr/mm grating	cm^{-1}	2.3 (±0.2)	1.8 (±0.2)
Binning areas on CCD chip		3	5
Acquisition order		repetitive 2× max/2× min	repetitive 2× max/2× min

[a]measured over a period of 8h.

⊥-polarization (maximum) Raman signal. Care was taken that the maximum count intensity was kept close to but below the saturation intensity of the CCD detector. The detector exposure times to acquire individual spectra were in the range 200–1000 s; by and large, the actual duration was influenced by the partial pressure of the molecule under investigation (relative particle concentrations for the individual hydrogen isotopologues can be deduced from the cell filling protocol provided in Table S2 in Section 5 of the 'Supporting Information').

Binning

As stated in the table, the detectors were set to acquire spectra using the on-chip binning technique, namely to average over sub-regions of the two-dimensional CCD array. Tests showed that selecting three or five binning areas maximized the signal-to-noise ratio whilst maintaining a sufficient number of regions so that astigmatism of the spectral lines can be corrected (for a description of the astigmatism correction procedure see Lewis *et al.*[15]).

Determining the exact vertical and horizontal polarization directions

To determine the depolarization ratio, spectra of the Q_1-branch need to be taken for ⊥- and ∥-polarization of the exciting laser beam. These exhibit maximum and minimum intensity, respectively. As has been mentioned in 'Description of the measurement setup' above, a half-wave plate mounted in an automated rotation stage was used to adjust the polarization of the laser beam. In each setup, this mount was rotated between 0 and 180° in 2° steps, and multiple spectra were taken for each angle. Plotting the Raman signal *versus* the rotation angle enables one to determine the angles required for the maximum and minimum intensities. The exact ⊥- and ∥-orientations could be determined from the λ/2-plate scans to ±0.15°.

Analysis strategy

A procedure was developed, which on the one hand reduced the main disturbing quantities, such as cosmic ray events and background distortions, while one the other hand retaining the intensities and line shapes nearly unperturbed. The principles behind the individual-step sequence in the preparation of spectra for depolarization analysis are briefly outlined below; for a detailed description, including relevant algorithms, see our open-access software package '*SpecTools*'.[19]

In the **cosmic ray removal** step, our sequential-spectrum removal method TCRR ('temporal' cosmic ray removal) is employed. This involves comparing consecutive spectra from the recording sequence (a minimum of two spectra is required), and setting an appropriate threshold. As a reasonable default value, one may set this threshold to 5× the noise level.

In the **baseline flattening** step, our SCARF routine (Savitzky-Golay Coupled Advanced Rolling Circle Filter) is applied, which is optimized to remove any background but to maintain the peak shape and amplitude as accurately as possible. Note that our SCARF routine produces only positive corrected-spectrum values. Thus, the baseline needs to be pulled down again to obtain a symmetric noise distribution around the zero line; this latter step can be automated.

Intensity determination is performed by our *ShapeFit* routine, which uses numerical peak shape functions. This is applied for each of the peaks of the Q_1-branch spectra (also done for selected lines of the S_0-, S_1-, and O_1-branches). Note that in general, all spectra from a particular run are averaged prior to fitting the peaks, in order to reduce the spectral noise.

The last step is the **calculation of the measured depolarization ratio** from the intensities of the sets of ⊥ – and ∥-polarization spectra. The calculation includes the error propagation of the statistical uncertainties (see further below).

'Raw' depolarization data and their correction

Depolarization measurements have been performed for all hydrogen isotopologues, i.e. including the tritiated species HT, DT, and T_2. The overview raw spectrum in Fig. 3 (top panel) shows the Q_1-branches of all hydrogen isotopologues and additional O_1- and S_1-branches for both states of excitation polarization. For the high-resolution grating of the SP500i spectrometer, the individual Q_1-branch lines are resolved (two examples shown in the bottom panels of Fig. 3).

As described in 'Description of the measurement setup', the rotation angle of the wave plate for ⊥- and ∥-orientation were once determined by acquiring high-resolution spectra for subsequent wave plate angles (stepping through in 2° steps) and fitting a $\sin^2$-function to the acquired Q_1-branch line intensities (see Fig. 4 for first two Q_1-branch lines of HT).

Subsequent to the determination of the angular positions for the exact minima and maxima positions, high-resolution spectra were acquired for each isotopologue for the associated ⊥- and ∥-polarization Raman excitation. The spectra-acquisition times for the individual isotopologues were set to maximize the line intensities without reaching saturation.

Here, we would like to make two comments.

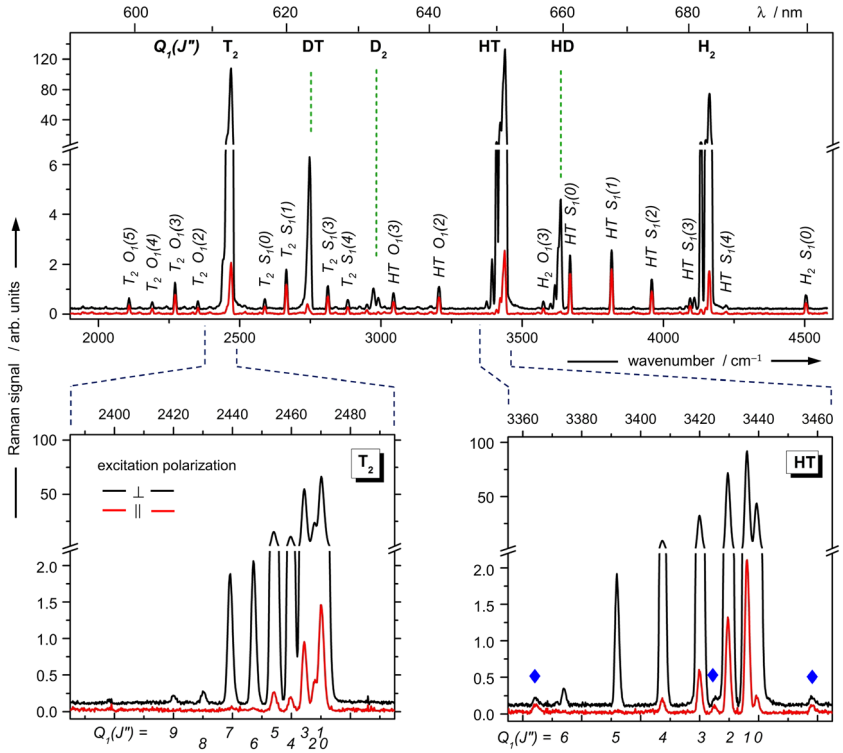

Figure 3. Raman spectra (for both ⊥ and || excitation polarization) of an equilibrated mixture of T_2 and H_2, utilized in the depolarization measurements of HT; a small impurity of D_2 means that all hydrogen isotopologues are observed in the mixture. Upper panel – 'low' resolution (600gr/mm) with relevant O_1-, Q_1- and S_1-branch lines annotated; lower panels – 'high' resolution (2400gr/mm) spectra for the *J*-resolved Q_1-branches of T_2 (left) and HT (right). The (blue) diamond symbols ● indicate polarization-independent lines from stray ambient light. For further details, see text.

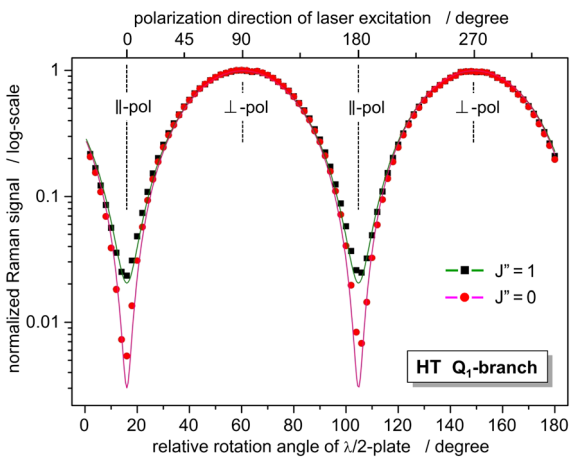

Figure 4. Dependence of the Raman signal of the $Q_1(0)$ (black ■ symbols) and $Q_1(1)$ (red ● symbols) lines of HT, as a function of excitation polarization; ⊥ = excitation laser polarization vertical to the excitation-observation plane (maximum Raman signal); || = excitation laser polarization horizontal to the excitation-observation plane (minimum Raman signal). For clarity of the minima, the (normalized) data are shown on a logarithmic intensity scale. The solid lines are $\sin^2$-function fits to the data points. For further details, see text.

First, the spectra in Fig. 3 reveal quite clearly the different depolarization behavior in the O_1- and S_1-branches with respect to the Q_1-branches, reflecting the well-known difference in the polarization tensors for the two cases. Recall that O_1- and S_1-branch lines the theoretical depolarization ratio is always $\rho_{theo} = 0.75$.[10]

Second, visual inspection of the Q_1-branch peaks in Fig. 3 and the depolarization ratios in Fig. 4 reveals that the $Q_1(0)$-line does not decrease to zero for ||-polarization, in contrast to theoretical expectations. This latter finding implies that corrections in the evaluation of these raw-data need to be applied to extract the 'true' depolarization ratios.

According to the mathematical model underlying said correction procedure two parameters need to be known, or measured with high precision.

The first one is the polarization-cleanness parameter, ξ, which describes the fractional admixture of an unwanted polarization component to the initially 'pure' polarized laser beam, induced by birefringence in the cell window. Of course, the polarization purity of the incident laser beam needs to be known for this. The polarization cleanness of the laser beam after the Glan-polarizer – $\lambda/2$-plate combination (see Fig. 2) was measured using a precision Glan-analyzer. The measured polarization impurity was about 0.00015(3). This is substantially lower than the observed cross-polarization ratio $\rho_{obs}(Q_1(0)) \sim 0.003$ for the particular HT-measurement documented in Fig. 4.

The second parameter finding its way into the correction model is the solid angle over which the Raman scattered light is collected. For its determination, a precision diaphragm is positioned between the Raman excitation volume and the first scattered-light collection lens, at a distance *x* from the Raman scattering centre, and with aperture opening radius *r*. The positioning and aperture opening parameters are included in Table 1 above.

Error estimation

The main sources of uncertainty can be traced back (1) to some inadequacies in the used correction model; (2) to uncertainties

in the determination of geometrical input parameters for the model; and (3) to the experimental uncertainties in the measured Raman signals. A detailed discussion of these can be found in the Supplemental Material associated with this publication.

Uncertainties from inadequacies in the correction model

In the simplification of the correction model, only the polarization aberration effect in the incident laser beam is considered.[8] While the polarization aberrations introduced by the Raman collection optics are estimated to be nearly negligible, and are therefore omitted in our treatment, this notion is not entirely correct. The systematic uncertainty introduced by this simplification is estimated to be about $\Delta\rho_{model} = 2.5 \times 10^{-4}$. Note, however, that this value varies slightly for the five individual cells used in our measurements, and because of small positioning errors associated with the re-insertion of the cells in repeated measurements.

Uncertainties in the determination of the geometrical input parameter

The correction procedure model depends on the accuracy of the input parameters.[8] These are the distance between the limiting diaphragm to the scattering centre, and its aperture opening radius. The propagated errors for the distance uncertainty are $\Delta\rho_x = 1 \times 10^{-4}$, and for the radius uncertainty are $\Delta\rho_r = 5 \times 10^{-4}$. These two values are minutely affected by positioning errors associated with the re-insertion of the cells in repeat measurements.

Uncertainties in the measured depolarization ratios

The measurement uncertainty can be propagated through the two-step correction approach. The value for ρ_{obs} for $J'' = 0$, which is used for the analysis correction, is measured repeatedly; this therefore leads to a statistical uncertainty in the cleanness ξ. This cleanness uncertainty and the error in the ρ_{obs} for $J'' > 0$ (these are the lines of interest) can be further propagated to finally obtain individual $\Delta\rho$-values. The measured uncertainties are of the order of 4×10^{-5}, whereas the propagated statistical measurement uncertainties are of the order of $\Delta\rho_{analysis} = 1 \times 10^{-4}$. The increase is caused by the propagation through the model.

The aforementioned errors are independent of each other and thus yield a total error estimate of

$$\Delta\rho_{tot} = \sqrt{\Delta\rho_{model}^2 + \Delta\rho_x^2 + \Delta\rho_r^2 + \Delta\rho_{analysis}^2}.$$

Note that this total uncertainty comprises a combination of statistical and systematic uncertainties. Some terms (e.g. the $\Delta\rho_{model}$) are deemed to be purely systematic. On the other hand, each time when a new cell was inserted and had to be re-aligned between the measurements, the actual (unknown) systematic error takes always a new (random, statistical) value. Note also that the aforementioned estimates of model-dependent errors constitute a worst-case scenario; the actual errors in individual measurements are thought to be smaller than this.

Results

Based on the procedures outlined above, we have analysed and evaluated a substantial number of depolarization measurements for all hydrogen isotopologues, including data obtained using different Raman cells and gas mixings, both at our laboratories at Swansea and Karlsruhe. For brevity, here we present only one single set of corrected depolarization data for each isotopologue.

The observed and corrected depolarization ratios of the $J'' = 0$ line of the Q_1-branches are collated in Table 2. These data demonstrate that the observed (raw) depolarization ratios for the $J'' = 0$ line vary by nearly an order of magnitude (between 0.00339 and 0.02291) and are clearly non-zero.

Our correction procedure is laid out to force the $Q_1(J'' = 0)$ depolarization values to be zero; the errors noted in the table reflect the upper limit of deviation from the theoretically expected zero-value. As pointed out in 'Raw' depolarization data and their correction' this error is dominated by inaccuracies in the geometrical measurements rather than the spectral intensity data. The non-zero result for T_2 is a consequence of the fact that its $J'' = 0$ and $J'' = 1$ Q_1-branch lines cannot be fully deconvolved; this is particularly detrimental for the very weak ||-polarization component (see Fig. 3, lower right panel). Therefore, the parameters for the correction procedure were not extracted for T_2 itself but from the Q_1-branch of H_2, present in the mixture of the same cell run.

The corrected depolarization ratios of the six hydrogen isotopologues, for all $Q_1(J'' > 0)$ lines with sufficient signal-to-noise ratio, are collated in Table 3. To gauge how well these corrected depolarization values replicate theoretical expectations, we have constructed theoretical ratios, ρ_{theo}, based on the polarizability tensor elements calculated by LeRoy[9]; these are inserted in Table 3 to the right of the experimental values. From these, we then calculated the depolarization ratio difference (theoretical values minus measured values) for each measurement and normalized to the propagated deviation, $\Delta\rho_{tot}$, for each. Since all our measurements and their individual errors were independent of each other, plotting the functional dependence

$$F_d = \frac{(\rho_{theo} - \rho_{SP0SA-cor})}{\Delta\rho_{tot}(\rho_{SP0SA-cor})}$$

for all the measured, corrected depolarization ratios in the form of a statistical histogram (see Fig. 5), should result in a Gaussian distribution.

The histogram in the figure has been fitted with a Gaussian function. The fit returns a width of $\sigma_{fit} = 1.13 \pm 0.10$, and is centred at $\rho_{theo} - \rho_{SP0SA-cor} = 0.12 \pm 0.10$. This is in reasonably good agreement with the expectation for a standard Gaussian distribution with $\sigma = 1$ and being centred at zero. Therefore, we can conclude that indeed the corrected depolarization ratios of the hydrogen isotopologues agree with the theoretical values of LeRoy to a 1σ confidence level. This also means that we can be rather confident that in future calibration measurements of

Table 2. Measured (observed raw data) ρ_{obs} and corrected $\rho_{SP0SA-cor}$ depolarization ratios for $Q_1(J'' = 0)$ of all hydrogen isotopologues, for $\lambda = 532$ nm laser excitation. The errors in the last digits are given in brackets

	H_2	HD	HT	D_2	DT	T_2
ρ_{obs}	0.01048 (4)	0.01153 (1)	0.00601 (5)	0.01137 (2)	0.02291 (5)	0.00339 (24)
$\rho_{SP0SA-cor}$	0.00000 (60)	0.00000 (50)	0.00000 (60)	0.00000 (50)	0.00000 (60)	−0.00300 (1000)

Table 3. Experimentally derived (corrected) depolarization ratios $\rho_{SP0SA\text{-}cor}$ for $Q_1(J''=1\ldots9)$ of all hydrogen isotopologues, for $\lambda=532$ nm laser excitation. The errors in the last digits are given in brackets. The theoretical depolarization ratios ρ_{theo} are derived from LeRoy's *ab initio* calculations, for $\lambda=532$ nm laser excitation[9]

J″	H_2		HD		HT	
	$\rho_{SP0SA\text{-}cor}$	ρ_{theo}	$\rho_{SP0SA\text{-}cor}$	ρ_{theo}	$\rho_{SP0SA\text{-}cor}$	ρ_{theo}
1	0.0177 (6)	0.0183	0.0177 (6)	0.0180	0.0173 (6)	0.0179
2	0.0133 (6)	0.0132	0.0126 (6)	0.0130	0.0126 (6)	0.0129
3	0.0128 (6)	0.0125	0.0121 (6)	0.0122	0.0122 (6)	0.0121
4		0.0123		0.0120	0.0125 (6)	0.0119
5		0.0124		0.0120		0.0119
6		0.0126		0.0121		0.0119
7		0.0128		0.0122		0.0120
J″	D_2		DT		T_2	
	$\rho_{SP0SA\text{-}cor}$	ρ_{theo}	$\rho_{SP0SA\text{-}cor}$	ρ_{theo}	$\rho_{SP0SA\text{-}cor}$	ρ_{theo}
1	0.0174 (6)	0.0176	0.0170 (6)	0.0175	0.0165 (6)	0.0174
2	0.0118 (6)	0.0127	0.0123 (6)	0.0126	0.0119 (6)	0.0125
3	0.0112 (4)	0.0119	0.0127 (6)	0.0118	0.0112 (6)	0.0117
4	0.0113 (7) [a]	0.0117	0.0115 (6)	0.0116	0.0104 (6)	0.0115
5	0.0138 (10) [ab]	0.0116	0.0130 (6) [b]	0.0115	0.0113 (6)	0.0114
6		0.0117	0.0126 (9) [b]	0.0115	0.0116 (7)	0.0114
7		0.0117		0.0116		0.0114

[a]from different data set
[b]approaching noise level

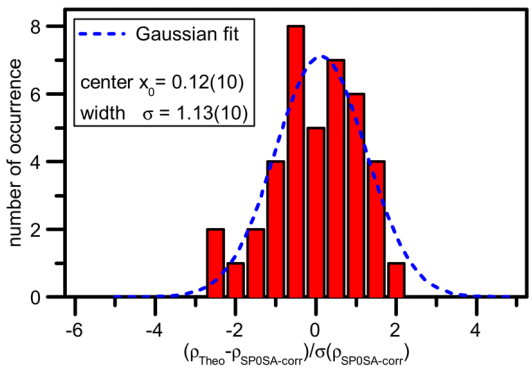

Figure 5. Statistical plot of deviations between measured and theoretical depolarization ratios for all individual hydrogen isotopologue runs. The histogram has been fitted with a Gaussian function. For further details, see text.

Table 4. Comparison of experimental and theoretical depolarization ratios for $Q_1(J'')$ of hydrogen, H_2, for $\lambda=532$ nm laser excitation. Note: the data entries for Holzer *et al.*[4] and Yu *et al.*[5] exhibit three significant digits only, compared with four significant digits of this work and LeRoy's theoretical calculations[9]

J″	$\rho_{SP0SA\text{-}cor}$	$\rho_{lit\text{-}Yu}$	$\rho_{lit\text{-}Holzer}$	$\rho_{theo\text{-}LeRoy\text{-}532nm}$
0	0.0000 (6)	0.002 (2)	0.001 (1)	0
1	0.0177 (6)	0.021 (2)	0.019 (1)	0.0183
2	0.0133 (6)	0.015 (2)	0.014 (1)	0.0132
3	0.0128 (6)	0.014 (2)	0.0135 (10)	0.0125
4		0.013 (5)		0.0123
5				0.0123

the KATRIN LARA system[20], the theoretical values derived from LeRoy's *ab initio* calculations can be used as input parameters in the line strength functions, with the 1σ uncertainties of the depolarization ratio measurements propagated through to the polarizability tensors.

To re-enforce the improvement in the measurement technique for depolarization ratios described here, we have compared our values with available literature values. Several groups have reported depolarization ratios for hydrogen, H_2; but only two groups tabulate rotationally resolved data (Holzer *et al.*[4] and more recently Yu *et al.*[5]). These are collated in Table 4 along with the values measured in this work, and the theoretical values derived from LeRoy's calculations.

The table reveals that nearly all available experimental values agree with those of LeRoy, within their experimental error. However, our $\rho_{SP0SA\text{-}cor}$ values are consistently lower than the previously measured values, closer to the theoretical values, and carry a smaller total uncertainty. It is also quite evident from Holzer's and Yu's entries for the depolarization ratio of the Q_1 ($J''=0$) line that their data are uncorrected for the effects of polarization purity and geometrical polarization distortion in the detection channel; these effects consistently return depolarization values which are too high. Therefore, we conclude with some confidence that the measurements performed here are the most accurate to date, not only for the widely used model molecule H_2 but also for all other hydrogen isotopologues.

Finally, we like to note that we found no evidence in the open literature that depolarization ratio measurements have been performed on the radioactive hydrogen isotopologues HT, DT, and T_2. Therefore, our experimental measurements and verification of the depolarization ratios of the radioactive hydrogen isotopologues constitute the first successful data set for all six hydrogen isotopologues, with rotational line resolution.

Conclusions

The successful measurement of depolarization ratios of all six hydrogen isotopologues has been reported for the first time. The measured values were corrected for geometrical polarization distortion and the effects of polarization purity. This enabled us to quantitatively compare these corrected depolarization ratios with the theoretical values derived from *ab initio* calculations by LeRoy.[9]

The corrected depolarization ratios of the hydrogen isotopologues have been found to agree with the theoretical values of LeRoy to better than 5% for nearly all of the measured $Q_1(J'')$ lines, with 1σ confidence level. This enables one to use the theoretical polarizability tensor elements derived by LeRoy as input parameters in the line strength functions for future calibration measurements of the KATRIN LARA system.[20] Equally, such data should be invaluable for the accurate analysis of the hydrogen isotopologue-composition in other contexts: it has been suggested that Raman spectroscopy could become a key methodology for the accountancy of tritium in the fusion fuel cycle of ITER.[21]

We also compared our measured and corrected depolarization values with other experimental values from the literature. Our values are found to be consistently closer to the theoretical values than all others reported in the literature. This implies that the measurements performed here are the most accurate to date.

Finally, we would like to point out that the experimental and data evaluation approach discussed here is not limited to the hydrogen isotopologues. Equally, it can be applied to other molecules found, e.g. in combustion processes or atmospheric studies, including trace gases like CO_2, CH_4, and so on.

Acknowledgements

We would like to thank the CAPER team at TLK for the preparation of the tritium-containing samples (specifically D. Demange, E. Fanghänel, T.L. Le, and K.H. Simon). We also are indebted to R.J. LeRoy (Department of Chemistry, University of Waterloo, Canada) for kindly calculating the relevant Raman transition matrix elements of all hydrogen isotopologues, for laser excitation at 532 nm. T.M. James acknowledges the financial support for his PhD studentship by the UK Engineering and Physical Sciences Research Council (EPSRC). T.M. James and M. Schlösser thank the Karlsruhe House of Young Scientists (KHYS) for supporting part of this study through a visiting-scientist stipend. This research was supported by the Helmholtz Association (HGF), the German Federal Ministry for Education and Research (BMBF), through grants 05A08VK2 and 05A11VK3, and the German Research Foundation (DFG) within the framework of the TransRegio project 'Neutrinos and Beyond', grant SFB/TR 27.

Supporting information

Supporting Information may be found in the online version of this article.

References

[1] B. Mrowka, *Z. Physik* **1932**, *76*, 300.
[2] C. Schwartz, R. J. LeRoy, *J. Mol. Spectrosc.* **1987**, *121*, 420.
[3] D. K. Veirs, G. M. Rosenblatt, *J. Mol. Spectrosc.* **1987**, *121*, 401.
[4] W. Holzer, Y. Le Duff, K. Altmann, *J. Phys. Chem.* **1973**, *58*, 642.
[5] Y. Yu, K. Lin, X. G. Zhou, H. Wang, S. L. Liu, X. X. Ma, *J. Raman Spectrosc.* **2007**, *38*, 1206.
[6] J. Angrik, the KATRIN Collaboration, The KATRIN design report 2004, *FZK Scientific Report 7090*, **2005**, http://bibliothek.fzk.de/zb/berichte/FZKA7090.pdf.
[7] M. Babutzka, M. Bahr, J. Bonn, B. Bornschein, A. Dieter, G. Drexlin, K. Eitel, S. Fischer, F. Glück, S. Grohmann, M. Hötzel, T. M. James, W. Käfer, M. Leber, B. Monreal, F. Priester, M. Röllig, M. Schlösser, U. Schmitt, F. Sharipov, M. Steidl, M. Sturm, H. H. Telle, N. Titov, *New J. Phys.* **2012**, *14*, 103046.
[8] M. Schlösser, T. M. James, S. Fischer, R. J. Lewis, B. Bornschein, H. H. Telle, *J. Raman Spectrosc.* **2013**, *44*, 453.
[9] R. J. LeRoy, Recalculation of Raman transition matrix elements of all hydrogen isotopologues for 532nm laser excitation, Private communication, **2011**.
[10] D. Long, The Raman Effect: A Unified Treatment of the Theory of Raman Scattering by Molecules, Wiley, Chichester, **2002**.
[11] R. L. McCreery, Photometric Standards for Raman Spectroscopy, in Handbook of Vibrational Spectroscopy – Volume 1, (Eds: J. M. Chalmers, P. R. Griffiths), John Wiley & Sons Ltd, Chichester, UK, **2002**, pp 920–932.
[12] C. D. Allemand, *Appl. Spectrosc.* **1970**, *24*, 348.
[13] S. K. Deb, M. L. Bansal, A. P. Roy, *Appl. Spectrosc.* **1984**, *38*, 500.
[14] V. Teboul, J. L. Godet, Y. L. Duff, *Appl. Spectrosc.* **1992**, *46*, 476.
[15] S. Fischer, M. Sturm, M. Schlösser, B. Bornschein, G. Drexlin, F. Priester, R. J. Lewis, H. H. Telle, *Fusion Sci. Technol.* **2011**, *60*, 925.
[16] R. J. Lewis, H. H. Telle, B. Bornschein, O. Kazachenko, N. Kernert, M. Sturm, *Laser Phys. Lett.* **2008**, *5*, 522.
[17] M. Sturm, M. Schlösser, R. J. Lewis, B. Bornschein, G. Drexlin, H. H. Telle, *Laser Phys.* **2010**, *20*, 493.
[18] D. J. Taylor, M. Glugla, R. D. Penzhorn, *Rev. Sci. Instrum.* **2001**, *72*, 1970.
[19] SpecTools - an OpenSource software package, Automated Quantitative Spectroscopic Analysis Combining Background Subtraction, Cosmic-Ray Removal and Peak Fitting programmed in LabVIEW, **2012**, http://spectools.sourceforge.net.
[20] M. Schlösser, S. Rupp, H. Seitz, S. Fischer, B. Bornschein, T. M. James, H. H. Telle, Accurate Calibration of the Laser Raman System for the Karlsruhe Tritium Neutrino Experiment, *J. Mol. Struct.* **2013**, http://dx.doi.org/10.1016/j.molstruc.2012.11.022
[21] W. Shu, Raman Spectroscopy for the ITER Tritium Plant Analytical System, *ITER Organization*, private communication, **2012**.

Bibliography

[Aba06] K. Abazajian and S. M. Koushiappas. *Constraints on sterile neutrino dark matter*. Phys. Rev. D, 74:023527, 2006.

[Act02] *SpectraPro-500i, V1097.1*. Acton Research Corporation, 530 Main Street, Acton, MA 01720 USA, 2002.

[Aga11] S. Agarwal and H. A. Feldman. *The effect of massive neutrinos on the matter power spectrum*. Mon. Not. R. Astron. Soc., 410(3):1647–1654, 2011.

[Aih11] H. Aihara, C. Allende Prieto, D. An, et al. *The Eighth Data Release of the Sloan Digital Sky Survey: First Data from SDSS-III*. Astrophys. J. Suppl. S., 193(2):29, 2011.

[ALE06] ALEPH Collaboration, DELPHI Collaboration, L3 Collaboration, OPAL Collaboration, SLD Collaboration, LEP Electroweak Working Group, SLD Electroweak, and Heavy Flavour Groups. *Precision electroweak measurements on the Z resonance*. Phys. Rep., 427(5-6):257 – 454, 2006.

[Ale87] E. N. Alekseev, L. N. Alekseeva, V. I. Volchenko, and I.V. Krivosheina. *Possible Detection of a Neutrino Signal on 23 February 1987 at the Baksan Underground Scintillation Telescope of the Institute of Nuclear Research*. JETP Lett., 45:589–592, 1987.

[All70] C. D. Allemand. *Depolarization Ratio Measurements in Raman Spectrometry*. Appl. Spectrosc., 24(3):348–353, 1970.

[Als04] F. Alsmeyer and W. Marquardt. *Automatic Generation of Peak-Shaped Models*. Appl. Spectrosc., 58(8):986–994, 2004.

[Ark01] N. Arkani-Hamed, S. Dimopoulos, G. Dvali, and J. March-Russell. *Neutrino masses from large extra dimensions*. Phys. Rev. D, 65:024032, 2001.

[Arn03] C. Arnaboldi, C. Brofferio, O. Cremonesi, E. Fiorini, C. Lo Bianco, L. Martensson, A. Nucciotti, M. Pavan, G. Pessina, S. Pirro, E. Previtali, M. Sisti, A. Giuliani, B. Margesin, and M. Zen. *Bolometric Bounds on the Antineutrino Mass*. Phys. Rev. Lett., 91:161802, 2003.

[Ase00] V.N. Aseev, A.I. Belesev, A.I. Berlev, E.V. Geraskin, O.V. Kazachenko, Yu.E. Kuznetsov, V.M. Lobashev, R.P. Ostroumov, N.A. Titov, S.V. Zadorozhny, Yu.I. Zakharov, J. Bonn, B. Bornschein, L. Bornschein, E.W. Otten, M. Przyrembel,

Ch. Weinheimer, and A. Saenz. *Energy loss of 18 keV electrons in gaseous* T_2 *and quench condensed* D_2 *films*. Eur. Phys. J. D., 10:39–52, 2000.

[Ase11] V. N. Aseev, A. I. Belesev, A. I. Berlev, E. V. Geraskin, A. A. Golubev, N. A. Likhovid, V. M. Lobashev, A. A. Nozik, V. S. Pantuev, V. I. Parfenov, A. K. Skasyrskaya, F. V. Tkachov, and S. V. Zadorozhny. *Upper limit on the electron antineutrino mass from the Troitsk experiment*. Phys. Rev. D, 84:112003, 2011.

[Atk06] P. W. Atkins and J. de Paula. *Physikalische Chemie (v. 4) (German Edition)*. Wiley, 2006.

[ATL12] ALTAS Collaboration. *Observation of a new particle in the search for the Standard Model Higgs boson with the ATLAS detector at the LHC*. Phys. Lett. B, 716(1):1 – 29, 2012.

[Bab11] M. Babutzka et al. *The comprehensive guide to KASSIOPEIA, KATRIN internal document*. Technical report, 2011.

[Bab12] M. Babutzka, M. Bahr, J. Bonn, B. Bornschein, A. Dieter, G. Drexlin, K. Eitel, S. Fischer, F. Glück, S. Grohmann, M. Hötzel, T. M. James, W. Käfer, M. Leber, B. Monreal, F. Priester, M. Röllig, M. Schlösser, U. Schmitt, F. Sharipov, M. Steidl, M. Sturm, H. H. Telle, and N. Titov. *Monitoring of the operating parameters of the KATRIN Windowless Gaseous Tritium Source*. New J. Phys., 14(10):103046, 2012.

[Bah05] J. N. Bahcall, A. M. Serenelli, and S. Basu. *New Solar Opacities, Abundances, Helioseismology, and Neutrino Fluxes*. Astrophys. J. Lett., 621(1):L85, 2005.

[Bah64] J. N. Bahcall. *Solar Neutrinos. I. Theoretical*. Phys. Rev. Lett., 12:300–302, 1964.

[Bea80] G. Beamson, H. Q. Porter, and D. W. Turner. *The collimating and magnifying properties of a superconducting field photoelectron spectrometer*. J. Phys. E Sci. Instrum., 13(1):64–66, 1980.

[Bel95] A. I. Belesev, A. I. Bleule, E. V. Geraskin, A. A. Golubev, N. A. Golubev, O. V. Kazachenko, E. P. Kiev, Yu. E. Kuznetsov, V. M. Lobashev, B. M. Ovchinnikov, V. I. Parfenov, I. V. Sekachev, A. P. Solodukhin, N. A. Titov, I. E. Yarykin, Yu. I. Zakharov, S. N. Balashov, and P. E. Spivak. *Results of the troitsk experiment on the search for the electron antineutrino rest mass in tritium beta-decay*. Phys. Lett. B, 350(2):263 – 272, 1995.

[Ber06] L. Bergström and A. Goobar. *Cosmology and Particle Astrophysics*. Springer, 2006.

[Bon99] J. Bonn, L. Bornschein, B. Degen, E. W. Otten, and C. Weinheimer. *A high resolution electrostatic time-of-flight spectrometer with adiabatic magnetic collimation*. Nucl. Instrum. Meth. A, 421(1-2):256 – 265, 1999.

[Boo96] N. E. Booth, B. Cabrera, and E. Fiorini. *Low-Temperature Particle Detectors*. Annu. Rev. Nucl. Part. S., 46(1):471–532, 1996.

[Bor00] B. Bornschein. *Untersuchung systematischer Effekte und erste Tritiummessungen mit dem verbesserten Mainzer Neutrinomassenexperiment*. Phd thesis, University of Mainz, 2000.

[Bor03] B. Bornschein, J. Bonn, L. Bornschein, E.W. Otten, and Ch. Weinheimer. *Self-Charging of Quench Condensed Tritium Films*. J. Low Temp. Phys., 131:69–88, 2003.

[Bor05] J. Borysow and M. Fink. *NIR Raman spectrometer for monitoring protonation reactions in gaseous hydrogen*. J. Nucl. Mat., 341:224–230, 2005.

[Bra06] N. N. Brandt, O. O. Brovko, A. Y. Chikishev, and O. D. Paraschuk. *Optimization of the Rolling-Circle Filter for Raman Background Subtraction*. Appl. Spectrosc., 60(3):288–293, 2006.

[Bre87] C. Brémard, J. Laureyns, J.-C. Merlin, and G. Turrell. *Polarization measurements in Raman microspectroscopy. I. Isotropic samples*. J. Raman Spectrosc., 18(5):305–313, 1987.

[Bri66] N. J. Bridge and A. D. Buckingham. *The Polarization of Laser Light Scattered by Gases*. Proc. Royal. Soc. A, 295(1442):334–349, 1966.

[Bru13] T. Brunst. *Durchführung von Messungen mit einem Lumineszenzstandard zur Kalibrierung des Laser-Raman-Systems für KATRIN*. Bachelor thesis in preparation, Karlsruhe Institute of Technology, 2013.

[Bru97] R. Brun and F. Rademakers. *ROOT - An object oriented data analysis framework*. Nucl. Instrum. Meth. A, 389(1-2):81–86, 1997.

[Bur08] A. Burck, S. Kempf, S. Schäfer, H. Rotzinger, M. Rodrigues, T. Wolf, L. Gastaldo, A. Fleischmann, and C. Enss. *Microstructured Magnetic Calorimeter with Meander-Shaped Pickup Coil*. J. Low Temp. Phys., 151:337–344, 2008.

[Bur13] R. A. Burenin. *Possible indication for non-zero neutrino mass and additional neutrino species from cosmological observations*. arXiv:1301.4791, 2013.

[Bus84] B.-M. Bussian and W. Härdle. *Robust Smoothing Applied to White Noise and Single Outlier Contaminated Raman Spectra*. Appl. Spectrosc., 38(3):309–313, 1984.

[Cho07] S. J. Choquette, E. S. Etz, W. S. Hurst, D. H. Blackburn, and S. D. Leigh. *Relative Intensity Correction of Raman Spectrometers: NIST SRMs 2241 Through 2243 for 785 nm, 532 nm, and 488 nm/514.5 nm Excitation*. Appl. Spectrosc., 61(2):117–129, 2007.

[Chr76] K. Christmann, G. Ertel, and Pignet T. *Adsorption of hydrogen on a Pt(111) surface*. Surf. Sci., 54:365–392, 1976.

[Cle98] B. T. Cleveland, T. Daily, R. Davis, J. R. Distel, K. Lande, C. K. Lee, P. S. Wildenhain, and J. Ullman. *Measurement of the Solar Electron Neutrino Flux with the Homestake Chlorine Detector*. Astrophys. J., 496(1):505, 1998.

[CMS12] CMS Collaboration. *Observation of a new boson at a mass of 125 GeV with the CMS experiment at the LHC*. Phys. Lett. B, 716(1):30 – 61, 2012.

[Col05] E. Collett. *Field Guide to Polarization (SPIE Vol. FG05)*. SPIE, Bellingham, WA, USA, 2005.

[Cor05] *VERDI V2, V5 & V6 - Data sheet*. Coherent Inc., Santa Clara, CA 95054 USA, 2005.

[Cow56] C. L. Cowan, F. Reines, F. B. Harrison, H. W. Kruse, and A. D. McGuire. *Detection of the Free Neutrino: a Confirmation*. Science, 124(3212):103–104, 1956.

[CUO05] CUORE Collaboration. *CUORE: A Cryogenic Underground Observatory for Rare Events*. arXiv:hep-ex/0501010, 2005.

[Cur49] S.C. Curran, J. Angus, and A.L. Cockroft. *The beta-spectrum of tritium [10]*. Phys. Rev., 76(6):853–854, 1949.

[Dan62] G. Danby, J-M. Gaillard, K. Goulianos, L. M. Lederman, N. Mistry, M. Schwartz, and J. Steinberger. *Observation of High-Energy Neutrino Reactions and the Existence of Two Kinds of Neutrinos*. Phys. Rev. Lett., 9:36–44, 1962.

[Dav03] A. C. Davison, D. V. Hinkley, and G. A. Young. *Recent Developments in Bootstrap Methodology*. Statist. Sci., 18(2):141–157, 2003.

[Dav12] M. W. Davidson. *Fundamentals of Light-Emitting Diodes (LEDs)*. Carl Zeiss Microscopy Online Campus, 2012.

[Dav64] R. Davis. *Solar Neutrinos. II. Experimental*. Phys. Rev. Lett., 12:303–305, 1964.

[Dav68] R. Davis, D. S. Harmer, and K. C. Hoffman. *Search for Neutrinos from the Sun*. Phys. Rev. Lett., 20:1205–1209, 1968.

[Day12] Daya Bay Collaboration. *Observation of Electron-Antineutrino Disappearance at Daya Bay*. Phys. Rev. Lett., 108:171803, 2012.

[Deb84] S. K. Deb, M. L. Bansal, and A. P. Roy. *Calculation of Error in Depolarization Ratio Measurement Due to Finite Collection Angle in Laser Raman Spectroscopy*. Appl. Spectrosc., 38(4):500–504, 1984.

[Dem07] W. Demtröder. *Laserspektroskopie - Grundlagen Und Techniken*. Springer-Verlag GmbH, Heidelberg, 5. erw. u. neubearb. aufl. edition, 2007.

[Dem12] D. Demange et al. *Overview of R&D at TLK for process and analytical issues on tritium management in breeder blankets of ITER and DEMO*. Fusion Eng. Des., 87(7-8):1206–1213, 2012.

[Die11] T. Dieing, O. Hollricher, and J. Toporski. *Confocal Raman Microscopy (Springer Series in Optical Sciences)*. Springer, 2011.

[Doe08] L. Dörr, U. Besserer, N. Bekris, B. Bornschein, C. Caldwell-Nichols, D. Demange, I. Cristescu, I.R. Cristescu, M. Glugla, G. Hellriegel, P. Schäfer, S. Weite, and J. Wendel. *A decade of tritium technology development and operation at the Tritium Laboratory Karlsruhe*. Fusion Sci. Technol., 54(1):143–148, 2008.

[DOE93] *DOE Fundamentals Handbook, Material Sciences, Vol 1 of 2 (DOE-HDBK-1017/1-93)*. U.S. Department of Energy, Washington, D.C. 20585, 1993.

[Doi85] M. Doi, T. Kotani, and E. Takasugi. *Double Beta Decay and Majorana Neutrino*. Prog. Theor. Phys. Supp., 83:1–175, 1985.

[Dol02] A.D. Dolgov. *Neutrinos in cosmology*. Physics Reports, 370(4-5):333 – 535, 2002.

[DON01] DONUT Collaboration. *Observation of tau neutrino interactions*. Phys. Lett. B, 504(3):218 – 224, 2001.

[Dos06] N. Doss, J. Tennyson, A. Saenz, and S. Jonsell. *Molecular effects in investigations of tritium molecule β decay endpoint experiments*. Phys. Rev. C, 73:025502, 2006.

[Dos07] N. Doss. *Calculated final state probability distributions for* T_2 *β-decay measurements*. Phd thesis, University of London, 2007.

[Dou12] Double Chooz Collaboration. *Reactor $\overline{\nu}_e$ disappearance in the Double Chooz experiment*. Phys. Rev. D, 86:052008, 2012.

[Dre13] G. Drexlin, V. Hannen, S. Mertens, and C. Weinheimer. *Current Direct Neutrino Mass Experiments*. Adv. High En. Phys., 2013(293986), 2013.

[Dwa72] P. Dawson. *Polarisation measurements in Raman spectroscopy*. Spectrochim. Acta A, 28(4):715–723, 1972.

[Dör05] L. Dörr, U Besserer, M. Glugla, G. Hellriegel, W. Hellriegel, P. Schäfer, and J. Wendel. *The Closed Tritium Cycle of the Tritium Laboratory Karlsruhe*. Fusion Sci. Technol., 48(1):262–267, 2005.

[EDE12] EDELWEISS Collaboration. *Search for low-mass WIMPs with EDELWEISS-II heat-and-ionization detectors*. Phys. Rev. D, 86:051701, 2012.

[Edw78] H. G. M. Edwards, D. A. Long, and H. R. Mansour. *Pure rotational and vibration-rotational Raman spectra of tritium, 3H2*. J. Chem. Soc., Faraday Trans. 2, 74:1203–1207, 1978.

[Efr83] B. Efron and G. Gong. *A Leisurely Look at the Bootstrap, the Jackknife, and Cross-Validation*. Am. Stat., 37(1):36–48, 1983.

[Efr94] B. Efron and R.J. Tibshirani. *An Introduction to the Bootstrap*. Chapman and Hall/CRC, 1994.

[Ehr01] F. Ehrentreich and L. Sümmchen. *Spike Removal and Denoising of Raman Spectra by Wavelet Transform Methods*. Anal. Chem., 73(17):4364–4373, 2001.

[Ell02] S. R. Elliott and P. Vogel. *Double Beta Decay*. Annu. Rev. Nucl. Part. S., 52(1):115–151, 2002.

[Eng92] U. Engelmann. *Ramanspektroskopische und massenspektroskopische Untersuchungen der Wasserstoffisotope und isotop substituierter Methane*. Phd thesis, Kernforschungszentrum Karlsruhe, 1992.

[Erh12] M. Erhard. *Untersuchung der Langzeitstabilität des nuklearen Standards für die Energieskala des KATRIN-Experiments*. Diploma thesis, Karlsruhe Institute of Technology, 2012.

[EXO12a] EXO Collaboratio. *The EXO-200 detector, part I: detector design and construction*. J. Instrum., 7(05):P05010, 2012.

[EXO12b] EXO Collaboration. *Search for Neutrinoless Double-Beta Decay in* ^{136}Xe *with EXO-200*. Phys. Rev. Lett., 109:032505, 2012.

[Fel98] G. J. Feldman and R. D. Cousins. *Unified approach to the classical statistical analysis of small signals*. Phys. Rev. D, 57:3873–3889, 1998.

[Feo61] P. P. Feofilov. *The physical basis of polarized emission*. Consultants Bureau, New York, USA, 1961.

[Ferm34] E. Fermi. *Versuch einer Theorie der β-Strahlen*. Z. Phys., 88:161–177, 1934.

[Fir99] R. B. Firestone, S. Y. F. Chu, and C. M. Baglin. *Table of Isotopes, 8th Edition*. Wiley-VCH, 1999.

[Fis10a] S. Fischer. *Investigations of laser stability in the KATRIN Raman setup and first depolarisation measurements with tritium at TLK*. Diploma thesis, Karlsruhe Institute of Technology, 2010.

[Fis10b] S. Fischer, P. Herwig, and M. Schlösser. *First tests of Finesse laser at TLK*. Internal report, Karlsruhe Institute of Technology, 2010.

[Fis10c] Fischer, T., Whitehouse, S. C., Mezzacappa, A., Thielemann, F.-K., and Liebendörfer, M. *Protoneutron star evolution and the neutrino-driven wind in general relativistic neutrino radiation hydrodynamics simulations*. Astron. Astrophys., 517:A80, 2010.

[Fis11] S. Fischer, M. Sturm, M. Schlösser, B. Bornschein, G. Drexlin, F. Priester, R. J. Lewis, and H. H. Telle. *Monitoring of tritium purity during long-term circulation in the KATRIN test experiment LOOPINO using laser Raman spectroscopy*. Fusion Sci. Technol., 60(3):925–930, 2011.

[Fis13] S. Fischer. *In preparation*. Phd thesis, Karlsruhe Institute of Technology, 2013.

[For11] J.A. Formaggio and J. Barrett. *Resolving the reactor neutrino anomaly with the KATRIN neutrino experiment*. Physics Letters B, 706(1):68–71, 2011.

[Fra10] F. Fränkle. *Background Investigations of the KATRIN Pre-Spectrometer*. Phd thesis, Karlsruhe Institute of Technology, 2010.

[Fur39] W. H. Furry. *On Transition Probabilities in Double Beta-Disintegration*. Phys. Rev., 56:1184–1193, 1939.

[Gal12] M. Galeazzi, F. Gatti, M. Lusignoli, A. Nucciotti, S. Ragazzi, and M. Ribeiro Gomes. *The Electron Capture Decay of 163-Ho to Measure the Electron Neutrino Mass with sub-eV Accuracy (and Beyond)*. arXiv:1202.4763, 2012.

[GAL99] GALLEX Collaboration. *GALLEX solar neutrino observations: results for GALLEX IV*. Phys. Lett. B, 447(1-2):127 – 133, 1999.

[Gat01] F. Gatti. *Microcalorimeter measurements*. Nucl. Phys. B - Proc. Sup., 91(1-3):293 – 296, 2001.

[Gat99] F. Gatti, F. Fontanelli, M. Galeazzi, A. M. Swift, and S. Vitale. *Detection of environmental fine structure in the low-energy β-decay spectrum of* ^{187}Re. Nature, 397(6715):137 – 139, 1999.

[Gei03] A. Geiser. *Experimental Results on Neutrino Oscillations*. In K. Winter and G. Altarelli, editors, *Neutrino Mass*, volume 190 of *Springer Tracts in Modern Physics*, pages 75–134. Springer Berlin Heidelberg, 2003.

[GER04] GERDA Collaboration. *A New* ^{76}Ge *Double Beta Decay Experiment at LNGS*. arXiv:hep-ex/0404039, 2004.

[Gil10] W. Gil, J. Bonn, B. Bornschein, R. Gehring, O. Kazachenko, J. Kleinfeller, and S. Putselyk. *The Cryogenic Pumping Section of the KATRIN Experiment*. IEEE T. Appl. Supercon., 20(3):316 –319, 2010.

[Gil80] J. T. Gill. *Effect of container preparation on the growth of protium and methane impurities into tritium gas*. J. Vacuum Sci. Technol., 17(2):645 –654, 1980.

[Glu06] M. Glugla, I. R. Cristescu, I. Cristescu, and D. Demange. *Hydrogen isotope separation by permeation through palladium membranes*. J. Nucl. Mat., 355(1-3):47–53, 2006.

[GNO05] GNO Collaboration. *Complete results for five years of GNO solar neutrino observations*. Phys. Lett. B, 616(3-4):174 – 190, 2005.

[Goe35] M. Goeppert-Mayer. *Double Beta-Disintegration*. Phys. Rev., 48:512–516, 1935.

[Gri69] V. Gribov and B. Pontecorvo. *Neutrino astronomy and lepton charge*. Phys. Lett. B, 28(7):493 – 496, 1969.

[Gro09] S. Grohmann. *Stability analyses of the beam tube cooling system in the KATRIN source cryostat*. Cryogenics, 49(8):413 – 420, 2009.

[Gro13] S. Grohmann, T. Bode, M. Hötzel, H. Schön, M. Süßer, and T. Wahl. *The thermal behaviour of the tritium source in KATRIN*. Cryogenics, (0):–, 2013.

[Hah07] B. Hahn and Umweltministerium Baden-Württemberg. *Genehmigung zum Umgang mit radioaktiven Stoffe gemäß § 7 StrlSchV für das Institut für Technische Physik - Tritiumlabor Karlsruhe (ITP-TLK)*. Genehmigung T6/07, 2007.

[Hak06] H. Haken and H. C. Wolf. *Molekülphysik und Quantenchemie: Einführung in die experimentellen und theoretischen Grundlagen (Springer-Lehrbuch) (German Edition)*. Springer, 2006.

[Ham12] T. J. Fellers and M. W. Davidson. *CCD Noise Sources and Signal-to-Noise Ratio*. Website, 2012. Available online at http://learn.hamamatsu.com/articles/ccdsnr.html; visited on December 19th 2012.

[Han10] Steen Hannestad. *Neutrino physics from precision cosmology*. Prog. Part. Nucl. Phys., 65(2):185 – 208, 2010.

[Har12] F. Harms. *Assembly and First Results of the KATRIN Focal-Plane Detector System at KIT*. Diploma thesis, Karlsruhe Institute of Technology, 2012.

[Hec74] E. Hecht and A. Zajak. *Optics*. Addison-Wesley, 1974.

[Hen70] P. J. Hendra and C. J. Vear. *Laser Raman spectroscopy. A review*. Analyst, 95:321–342, 1970.

[Her11] P. Herwig. *Kalibrierung des KATRIN Laser-Raman-Systems mit nicht-tritiierten Wasserstoffisotopologen*. Diploma thesis, Karlsruhe Institute of Technology, 2011.

[Her63] G. Herzberg. *Molecular Spectra and Molecular Structure: I. Spectra of Diatomic Molecules*. D. Van Nostrand Company, Inc., Princeton, New Jeresy, 1963.

[Hes12] V. F. Hess. *Über Beobachtungen der durchdringenden Strahlung bei sieben Freiballonfahrten*. Z. Phys., 13:1084, 1912.

[Hig64] P. W. Higgs. *Broken Symmetries and the Masses of Gauge Bosons*. Phys. Rev. Lett., 13:508–509, 1964.

[Hoe12] M. Hötzel. *Simulation and analysis of source-related effects for KATRIN*. Phd thesis, Karlsruhe Institute of Technology, 2012.

[Hol73] W. Holzer, Y. Le Duff, and K. Altmann. *J Dependence of the depolarization ratio of the rotational components of the Q branch of the* H_2 *and* D_2 *Raman band*. J. Chem. Phys., 58(2):642–643, 1973.

[Hol92] E. Holzschuh. *Measurement of the neutrino mass from tritium beta-decay*. Rep. Prog. Phys., 55(7):1035, 1992.

[Hol94] L. Holder, T. Okamoto, and T. Asakura. *Depolarization measurements of light propagating through an image fiber*. J. Optics, 25(4):139, 1994.

[Hor12] *Synapse CCD 1024 x 256 FIOP (09/2012) - Data sheet*. HORIBA Scientific, HORIBA, Kyoto, Japan, 2012.

[Hun84] J. L. Hunt, J. D. Poll, and L. Wolniewicz. *Ab initio calculation of properties of the neutral diatomic hydrogen molecules* H_2, HD, D_2, HT, DT, *and* T2. Can. J. Phys., 62(12):1719–1723, 1984.

[Hus93] D. R. Hush and B. G. Horne. *Progress in supervised neural networks*. IEEE Signal. Proc. Mag., 10(1):8 –39, 1993.

[IMB87] IMB Collaboration. *Observation of a neutrino burst in coincidence with supernova 1987A in the Large Magellanic Cloud*. Phys. Rev. Lett., 58:1494–1496, 1987.

[Ish52] E. Ishiguro, T. Arai, M. Mizushima, and M. Kotani. *On the polarizability of the hydrogen molecule*. Proc. Phys. Soc. A, 65(3):178–187, 1952.

[ISO01] International Organization for Standardization. *ISO 6142, Gas analysis - Preparation of calibration gas mixtures - Gravimetric method*. 2001.

[ISO03] International Organization for Standardization. *ISO 6145, Gas analysis - Preparation of calibration gas mixtures using dynamic volumetric methods*. 2003.

[ISO94] International Organization for Standardization. *ISO 5725, Accuracy (trueness and precision) of measurement methods and results*. 1994.

[Jac98] J. D. Jackson. *Classical Electrodynamics Third Edition*. Wiley, 1998.

[Jam12] T. M. James, M. Schlösser, R. J. Lewis, S. Fischer, B. Bornschein, and H. H. Telle. *Documentation of SpecTools: Automated Procedure for Quantitative Spectroscopic Analysis Combining Improved Background Subtraction, Cosmic Ray Removal and Peak Analysis*. spectools.sourceforge.net, 2012.

[Jam13a] T. M. James. *Quantitative Raman spectroscopy of gases related to KATRIN*. Phd thesis, Swansea University, 2013.

[Jam13b] T. M. James, M. Schlösser, S. Fischer, M. Sturm, B. Bornschein, R. J. Lewis, and H. H. Telle. *Accurate depolarization ratio measurements for all diatomic hydrogen isotopologues*. J. Raman Spectrosc. (in press) doi:10.1002/jrs.4283, 2013.

[Jam13c] T. M. James, M. Schlösser, S. Fischer, M. Sturm, B. Bornschein, R. J. Lewis, and H. H. Telle. *Supporting Information: Accurate depolarization ratio measurements for all diatomic hydrogen isotopologues*. J. Raman Spectrosc. (in press) doi:10.1002/jrs.4283, 2013.

[Jam13d] T. M. James, M. Schlösser, R. J. Lewis, S. Fischer, B. Bornschein, and H. H. Telle. *Automated Quantitative Spectroscopic Analysis Combining Cosmic-RayRemoval, Background Subtraction and Peak Fitting*. Appl. Spectrosc. (in press), 2013.

[Jan07] H.-Th. Janka, K. Langanke, A. Marek, G. Martínez-Pinedo, and B. Müller. *Theory of core-collapse supernovae*. Phys. Rep., 442(1-6):38 – 74, 2007.

[JCG08] Joint Committee for Guides in Metrology. *VIM, 3rd edition, JCGM 200:2008*. 2008.

[Jir04] A. Jirasek, G. Schulze, M. M. L. Yu, M. W. Blades, and R. F. B. Turner. *Accuracy and Precision of Manual Baseline Determination*. Appl. Spectrosc., 58(12):1488–1499, 2004.

[K2K06] K2K Collaboration. *Measurement of neutrino oscillation by the K2K experiment*. Phys. Rev. D, 74:072003, 2006.

[Kae12] W. Käfer. *Sensitivity studies of the KATRIN experiment*. Phd thesis, Karlsruhe Institute of Technology, 2012.

[Kam13] KamLAND-Zen Collaboration. *Limit on Neutrinoless $\beta\beta$ Decay of ^{136}Xe from the First Phase of KamLAND-Zen and Comparison with the Positive Claim in ^{76}Ge*. Phys. Rev. Lett., 110:062502, 2013.

[Kam87] Kamiokande Collaboration. *Observation of a neutrino burst from the supernova SN1987A*. Phys. Rev. Lett., 58:1490–1493, 1987.

[Kam96] Kamiokande Collaboration. *Solar Neutrino Data Covering Solar Cycle 22*. Phys. Rev. Lett., 77:1683–1686, 1996.

[Kas12] F. Kassel. *Weiterentwicklung der Laser-Ramanspektroskopie an gasförmigen Wasserstoffisopologen zur Prozessüberwachung von Tritiumexperimenten*. Diploma thesis, Karlsruhe Institute of Technology, 2012.

[Kat03] Y. Katsumoto and Y. Ozaki. *Practical Algorithm for Reducing Convex Spike Noises on a Spectrum*. Appl. Spectrosc., 57:317–322, 2003.

[KAT05] KATRIN Collaboration. *KATRIN design report 2004*. FZK - FZKA 7090, 2005.

[Kat81] H. Katsuta and K. Furukawa. *Hydrogen and Deuterium Transport through Type 304 Stainless Steel at Elevated Temperatures*. J. Nucl. Sci. Technol., 18(2):143–151, 1981.

[Kaw08] Y. Kawamura, Y. Onishi, K. Okuno, and T. Yamanishi. *Hydrogen isotope separation capability of low temperature mordenite column for gas chromatograph*. Fusion Eng. Des., 83(10-12):1384 – 1387, 2008.

[Kay12] B. Kayser. *Neutrino oscillation physics*. Proceedings of the International School of Physics "Enrico Fermi", Course CLXXXII “Neutrino Physics and Astrophysics”, edited by G. Bellini, pages 1–14, 2012.

[Kib67] T. W. B. Kibble. *Symmetry Breaking in Non-Abelian Gauge Theories*. Phys. Rev., 155:1554–1561, 1967.

[Kit09] N. Kita. *Technique to manage polarization aberrations*. Opt. Rev., 16:305–312, 2009.

[Kla06] H. V. Klapdor-Kleingrothaus and I. V. Krivosheina. *The evidence for the observation of $0\nu\beta\beta$ decay: The identification of $0\nu\beta\beta$ events from the full spectra*. Mod. Phys. Lett. A, 21(20):1547–1566, 2006.

[Kob73] M. Kobayashi and T. Maskawa. *CP-Violation in the Renormalizable Theory of Weak Interaction*. Prog. Theor. Phys., 49(2):652–657, 1973.

[Kol63] W. Kolos and L. Wolniewicz. *Nonadiabatic theory for diatomic molecules and its application to the hydrogen molecule*. Rev. Mod. Phys., 35(3):473–483, 1963.

[Kol64] W. Kolos and L. Wolniewicz. *Accurate Adiabatic Treatment of the Ground State of the Hydrogen Molecule*. J. Chem. Phys., 41(12):3663–3673, 1964.

[Kol68] W. Kolos and L. Wolniewicz. *Improved theoretical ground-state energy of the hydrogen molecule*. J. Chem. Phys., 49(1):465–466, 1968.

[Kol86] W. Kolos, K. Szalewicz, and H. J. Monkhorst. *New Born–Oppenheimer potential energy curve and vibrational energies for the electronic ground state of the hydrogen molecule*. J. Chem. Phys., 84(6):3278–3283, 1986.

[Kol88] W. Kolos, B. Jeziorski, J. Rychlewski, K. Szalewicz, H. J. Monkhorst, and O. Fackler. *Molecular effects in tritium β decay. IV. Effect of crystal excitations on neutrino mass determination*. Phys. Rev. A, 37:2297–2303, 1988.

[Kom11] E. Komatsu, K. M. Smith, J. Dunkley, et al. *Seven-year Wilkinson Microwave Anisotropy Probe (WMAP) Observations: Cosmological Interpretation*. Astrophys. J. Suppl., 192(2):18, 2011.

[Kos12] A. Kosmider. *Tritium Retention Techniques in the KATRIN Transport Section and Commissioning of its DPS2-F Cryostat*. Phd thesis, Karlsruhe Institute of Technology, 2012.

[Kra05] C. Kraus, B. Bornschein, L. Bornschein, J. Bonn, B. Flatt, A. Kovalik, B. Ostrick, E. W. Otten, J. P. Schall, T. Thümmler, and C. Weinheimer. *Final results from phase II of the Mainz neutrino mass searchin tritium decay*. Eur. Phys. J. C., 40(4):447–468, 2005.

[Kri08] E. Kriesten, D. Mayer, F. Alsmeyer, C. B. Minnich, L. Greiner, and W. Marquardt. *Identification of unknown pure component spectra by indirect hard modeling*. Chemom. Intel. Lab. Syst., 93(2):108 – 119, 2008.

[Kru83] P. Kruit and F. H. Read. *Magnetic field paralleliser for 2p electron-spectrometer and electron-image magnifier*. J. Phys. E, 16(4):313, 1983.

[Kud11] S. Kudella. *Suche nach Gravitationswellen mittels Laserinterferometrie und Untersuchungen zur Laserstabilität im Rahmen des KATRIN-Raman-Systems*. Bachelor thesis, Karlsruhe Institute of Technology, 2011.

[Köl11] Z. Köllö, C. G. Alecu, and H. Moosmann. *A New Method to Measure Small Volumes in Tritium Handling Facilities, Using p-V Measurements*. Fusion Sci. Technol., 60(3):972–975, 2011.

[Las12a] *Excel - 532nm compact laser: Technical data sheet. v2.2*. Laser Quantum Ltd., Cheshire, SK4 3GL, England, 2012.

[Las12b] *Finesse - The ultra quiet CW 532nm laser: Technical data sheet v5.8*. Laser Quantum Ltd., Cheshire, SK4 3GL, England, 2012.

[Laz81] G. Lazarides, Q. Shafi, and C. Wetterich. *Proton lifetime and fermion masses in an SO(10) model*. Nucl. Phys. B, 181(2):287 – 300, 1981.

[Lee79] S.-Y. Lee and E. J. Heller. *Time-dependent theory of Raman scattering*. J. Chem. Phys., 71(12):4777–4788, 1979.

[LeR11] R. J. LeRoy. *Recalculation of Raman transition matrix elements of all hydrogen isotopologues for 532nm laser excitation*. Private communication, 2011.

[Les12] J. Lesgourgues and S. Pastor. *Neutrino Mass from Cosmology*. Adv. High En. Phys, 2012(2):608515, 2012.

[Lew07] R. J. Lewis. *Development of a Raman System for In-Line Monitoring of Tritium at the Karlsruhe Tritium Neutrino (KATRIN) Experiment*. Phd thesis, Swansea University, 2007.

[Lew08] R. J. Lewis, H. H. Telle, B. Bornschein, O. Kazachenko, N. Kernert, and M. Sturm. *Dynamic Raman spectroscopy of hydrogen isotopomer mixtures in-line at TILO*. Laser Phys. Lett., 5(7):522–531, 2008.

[Li11] S. Li and L. Dai. *An Improved Algorithm to Remove Cosmic Spikes in Raman Spectra for Online Monitoring*. Appl. Spectrosc., 65(11):1300–1306, 2011.

[Lie03] C. A. Lieber and A. Mahadevan-Jansen. *Automated Method for Subtraction of Fluorescence from Biological Raman Spectra*. Appl. Spectrosc., 57(11):1363–1367, 2003.

[Liu85] J. W. Liu. *Elastic scattering of fast electrons by* $H_2(^1\Sigma_g^+)$ *and* $N_2(X^1\Sigma_g^+)$. Phys. Rev. A, 32:1384–1394, 1985.

[Liu87] J. W. Liu. *Total cross sections for high-energy electron scattering by* H_2 $(^1\Sigma_g^+)$, N_2 $(^1\Sigma_g^+)$, *and* O_2 $(^3\Sigma_g^-)$. Phys. Rev. A, 35:591–597, 1987.

[Lob85] V. M. Lobashev and P. E. Spivak. *A method for measuring the electron antineutrino rest mass*. Nucl. Instrum. Meth. A, 240(2):305 – 310, 1985.

[Lob99] V. M. Lobashev, V. N. Aseev, A. I. Belesev, A. I. Berlev, E. V. Geraskin, A. A. Golubev, O. V. Kazachenko, Y. E. Kuznetsov, R. P. Ostroumov, L. A. Rivkis, B. E. Stern, N. A. Titov, S. V. Zadorozhny, and Y. I. Zakharov. *Direct search for mass of neutrino and anomaly in the tritium beta-spectrum*. Phys. Lett. B, 460(1-2):227 – 235, 1999.

[Log94] J. E. Logan, N. A. Robertson, and J. Hough. *Measurements of birefringence in a suspended sample of fused silica*. Opt. Commun., 107(5-6):342–346, 1994.

[Lon02] D. A. Long. *The Raman Effect: A Unified Treatment of the Theory of Raman Scattering by Molecules*. Wiley, Chichester, 2002.

[Lon83] G. L. Long and J. D. Winefordner. *Limit of detection. A closer look at the IUPAC definition*. Anal. Chem., 55(7):712A–724A, 1983.

[Lor02] T. J. Loredo and D. Q. Lamb. *Bayesian analysis of neutrinos observed from supernova SN 1987A*. Phys. Rev. D, 65:063002, 2002.

[Luc00] L. L. Lucas and M. P. Unterweger. *Comprehensive Review and Critical Evaluation of the Half-Life of Tritium*. J. Res. Natl. Inst. Stan., 105(4):541–549, 2000.

[Luk12] S. Lukic, B. Bornschein, L. Bornschein, G. Drexlin, A. Kosmider, K. Schlösser, and A. Windberger. *Measurement of the gas-flow reduction factor of the KATRIN DPS2-F differential pumping section*. Vacuum, 86(8):1126 – 1133, 2012.

[Lyo98] L. A. Lyon, C. D. Keating, A. P. Fox, B. E. Baker, L. He, S. R. Nicewarner, S. P. Mulvaney, and M. J. Natan. *Raman Spectroscopy*. Anal. Chem., 70(12):341–362, 1998.

[MAC01] MACRO Collaboration. *Matter effects in upward-going muons and sterile neutrino oscillations*. Phys. Lett. B, 517(1-2):59 – 66, 2001.

[MAJ12] MAJORANA Collaboration. *The MAJORANA experiment: an ultra-low background search for neutrinoless double-beta decay*. J. Phys. Conf. Ser., 381(1):012044, 2012.

[Mak62] Z. Maki, M. Nakagawa, and S. Sakata. *Remarks on the Unified Model of Elementary Particles*. Prog. Theor. Phys., 28(5):870–880, 1962.

[MAR12] MARE Collaboration. *MARE-1 in Milan: Status and Perspectives*. J. Low Temp. Phys., 167:1035–1040, 2012.

[Mar63] D. W. Marquardt. *An algorithm for least-squares estimation of nonlinear parameters*. J. Soc. Industr. Appl. Math., 11(2):431–441, 1963.

[Mas07] S. S. Masood, S. Nasri, J. Schechter, M. A. Tórtola, J. W. F. Valle, and C. Weinheimer. *Exact relativistic β decay endpoint spectrum*. Phys. Rev. C, 76:045501, 2007.

[McG94] J. P. McGuire and R. A. Chipman. *Polarization aberrations. 1. Rotationally symmetric optical systems*. Appl. Opt., 33(22):5080–5100, 1994.

[McM06] R. L. McCreery. *Photometric Standards for Raman Spectroscopy*. John Wiley & Sons, Ltd, 2006.

[McQ76] D. A. McQuarrie. *Statistical Mechanics (Harper's Chemistry Series)*. Harpercollins College Div, 1976.

[Mer12] S. Mertens. *Study of Background Processes in the Electrostatic Spectrometers of the KATRIN experiment*. Phd thesis, Karlsruhe Institute of Technology, 2012.

[Mer13] S. Mertens, G. Drexlin, F.M. Fränkle, D. Furse, F. Glück, S. Görhardt, M. Hötzel, W. Käfer, B. Leiber, T. Thümmler, N. Wandkowsky, and J. Wolf. *Background due to stored electrons following nuclear decays in the KATRIN spectrometers and its impact on the neutrino mass sensitivity*. Astropart. Phys., 41(0):52 – 62, 2013.

[Mik03] I. K. Mikhailyuk and A. P. Razzhivin. *Background Subtraction in Experimental Data Arrays Illustrated by the Example of Raman Spectra and Fluorescent Gel Electrophoresis Patterns*. Instrum. Exp. Techn., 46(6):765–769, 2003.

[MIN11] MINOS Collaboration. *Measurement of the Neutrino Mass Splitting and Flavor Mixing by MINOS*. Phys. Rev. Lett., 106:181801, 2011.

[Mir11] S. Mirz. *Aufbau und Charakterisierung eines verbesserten Laser-Raman-Systems für das KATRIN-Experiment*. Bachelor thesis, Karlsruhe Institute of Technology, 2011.

[Miz94] M. Mizuno, H. Anzai, T. Aoyama, and T. Suzuki. *Determination of hydrogen concentration in austenitic stainless steels by thermal desorption spectroscopy*. Mater. T. JIM, 35(10):703–707, 1994.

[Moh06] R. N. Mohapatra, S. Nasri, and H.-B. Yu. *Grand unification of symmetry*. Phys. Lett. B, 636(2):114 – 118, 2006.

[Moh07] R. N. Mohapatra et al. *Theory of neutrinos: a white paper*. Rep. Prog. Phys., 70(11):1757, 2007.

[Moh80] R. N. Mohapatra and G. Senjanović. *Neutrino Mass and Spontaneous Parity Nonconservation*. Phys. Rev. Lett., 44:912–915, 1980.

[Mor77] G. A. Morris. *Methane formation in tritium gas exposed to stainless steel*. Lawrence Livermore Laboratory Report, UCRL-52262, 1977.

[Mro32] B. Mrowka. *Wellenmechanische Berechnung der Polarisierbarkeit des Wasserstoffmoleküls*. Z. Phys., 76(5-6):300–308, 1932.

[Nag06] Sz. Nagy, T. Fritioff, M. Björkhage, I. Bergström, and R. Schuch. *On the Q -value of the tritium ß-decay*. Europhys. Lett., 74(3):404, 2006.

[New12] Newport Corporation. *Calibrated Sources and Services*. Newport Resource e-Catalog, pages 233–234, 2012.

[Nis06] M. Nishi, T. Yamanishi, and T. Hayashi. *Study on tritium accountancy in fusion DEMO plant at JAERI*. Fusion Eng. Des., 81(1-7):745–751, 2006.

[NIS08] *Certificate of Analysis (Standard Ref. Mat. 2242)*. NIST, Gaithersburg, MD, USA, 2008.

[Nuc08] A. Nucciotti. *The MARE Project*. J. Low Temp. Phys., 151:597–602, 2008.

[Ohi00] S. O'hira, T. Hayashi, H. Nakamura, K. Kobayashi, T. Tadokoro, H. Nakamura, T. Itoh, T. Yamanishi, Y. Kawamura, Y. Iwai, T. Arita, T. Maruyama, T. Kakuta, S. Konishi, M. Enoeda, M. Yamada, T. Suzuki, M. Nishi, T. Nagashima, and M. Ohta. *Improvement of tritium accountancy technology for ITER fuel cycle safety enhancement*. Nucl. Fusion, 40(3Y):519, 2000.

[Ohi92] S. O'hira, H. Nakamura, S. Konishi, K. Okuno, T. Hayashi, Y. Naruse, R.H. Sherman, M.A. King, J.R. Bartilt, D.J. Taylor, and J.L. Anderson. *On-line tritium process gas analysis by laser Raman spectroscopy at TSTA*. Fusion Technol., 21(2):465–470, 1992.

[Ohi96] S. O'hira and K. Okuno. *Development of real-time and remote fuel process gas analysis system using laser Raman spectroscopy*. Fusion Technol., 30(3):869–873, 1996.

[Oht11] T. Ohta, S. Bouchigny, J.-P. Didelez, M. Fujiwara, K. Fukuda, H. Kohri, T. Kunimatsu, C. Morisaki, S. Ono, G. Rouillé, M. Tanaka, K. Ueda, M. Uraki, M. Utsuro, S.Y. Wang, and M. Yosoi. *HD gas analysis with gas chromatography and quadrupole mass spectrometer*. Nucl. Instrum. Meth. A, 640(1):241 – 246, 2011.

[Oht12] T. Ohta, S. Bouchigny, J.-P. Didelez, M. Fujiwara, K. Fukuda, H. Kohri, T. Kunimatsu, C. Morisaki, S. Ono, G. Rouillé, M. Tanaka, K. Ueda, M. Uraki, M. Utsuro, S.Y. Wang, and M. Yosoi. *Distillation of hydrogen isotopes for polarized HD targets*. Nucl. Instrum. Meth. A, 664(1):347 – 352, 2012.

[Oku91] K. Okuno, T. Uda, S. O'Hira, and Y. Naruse. *Development of In-Situ Gas Analyzer for Hydrogen Isotopes in Fusion Fuel Gas Processing*. J. Nucl. Sci. Technol., 28(6):509–516, 1991.

[Ott08] E. W. Otten and C. Weinheimer. *Neutrino mass limit from tritium ß decay*. Rep. Prog. Phys., 71(8):086201, 2008.

[Pal05] C. Palmer. *Diffraction Grating Handbook*. Newport Corporation, Rochester, NY 14605 USA, 2005.

[Pau85] W. Pauli, A. Hermann, K. v. Meyenn, and V. F. Weisskopf. *1930-1939, Wolfgang Pauli - Wissenschaftlicher Briefwechsel mit Bohr, Einstein, Heisenberg, u.a.* Springer, 1985.

[PDG12] Particle Data Group. *2012 Review of Particle Physics*. Phys. Rev. D, 86:010001, 2012.

[PED97] European Parliament and Council. *Pressure Equipment Directive 97/23/EC (PED)*. Technical report, 1997.

[Pel03] M. J. Pelletier. *Quantitative Analysis Using Raman Spectrometry*. Appl. Spectrosc., 57(1):20A–42A, 2003.

[Pen00] R.-D Penzhorn, N Bekris, P Coad, L Dörr, M Friedrich, M Glugla, A Haigh, R Lässer, and A Peacock. *Status and research progress at the Tritium Laboratory Karlsruhe*. Fusion Eng. Des., 49-50(0):753 – 767, 2000.

[Pen65] A. A. Penzias and R. W. Wilson. *A Measurement of Excess Antenna Temperature at 4080 Mc/s.* Astrophys. J., 142:419–421, 1965.

[Pet03] R. Petry, M. Schmitt, and J. Popp. *Raman Spectroscopy - A Prospective Tool in the Life Sciences*. ChemPhysChem, 4(1):14–30, 2003.

[Pic92] A. Picard, H. Backe, H. Barth, J. Bonn, B. Degen, Th. Edling, R. Haid, A. Hermanni, P. Leiderer, Th. Loeken, A. Molz, R.B. Moore, A. Osipowicz, E.W. Otten, M. Przyrembel, M. Schrader, M. Steininger, and Ch. Weinheimer. *A solenoid retarding spectrometer with high resolution and transmission for keV electrons*. Nucl. Instrum. Meth. B, 63(3):345 – 358, 1992.

[Pla10] Planck Collaboration. *Planck pre-launch status: The Planck mission*. Astron. Astrophys., 520(A1):1–22, 2010.

[Pla13] Planck Collaboration. *Planck 2013 results. XVI. Cosmological parameters*. submitted to Astron. Astrophys., 2013.

[Poh04] B. Povh, K. Rith, C. Scholz, and F. Zetsche. *Teilchen und Kerne: Eine Einführung in die physikalischen Konzepte (Springer-Lehrbuch) (German Edition)*. Springer, 2004.

[Pon68] B. Pontecorvo. *Neutrino Experiments and the Problem of Conservation of Leptonic Charge*. Sov. J. Exp. Theo. Phy., 26:984, 1968.

[Pra11] M. Prall. *Background Reduction of the KATRIN Spectrometers: Transmission Function of the Pre-Spectrometer and Systematic Test of the Main-Spectrometer Wire Electrode*. Phd thesis, University of Münster, 2011.

[Pri10a] F. Priester. *Systematische Untersuchungen zum Stabilitätsverhalten des KATRIN Tritiumloop*. Diploma thesis, Karlsruhe Institute of Technology, 2010.

[Pri10b] *Acton Standard Series of Monochromators and Spectrographs, Rev. N1*. Princeton Instruments, 3660 Quakerbridge Road Trenton, NJ 08619 USA, 2010.

[Pri11] *PIXIS:400 eXeclon, Rev. N3*. Princeton Instruments, 3660 Quakerbridge Road Trenton, NJ 08619 USA, 2011.

[Pri13] F. Priester. *Tritiumtechnologie für die fensterlose Quelle WGTS von KATRIN*. Phd thesis, Karlsruhe Institute of Technology, 2013.

[Pro12] Project 8 Collaboration. *Measuring Neutrino Masses Using Radio-Frequency Techniques*. J. Phys. Conf. Ser., 375(4):042005, 2012.

[Pro73] W. Proffitt and S. P. S. Porto. *Depolarization ratio in Raman spectroscopy as a function of frequency*. J. Opt. Soc. Am., 63(1):77–80, 1973.

[Raf12] G. G. Raffelt. *Neutrinos and the stars*. Proceedings of the International School of Physics "Enrico Fermi", Course CLXXXII "Neutrino Physics and Astrophysics", edited by G. Bellini, pages 61–144, 2012.

[Ram28] C. V. Raman and K. S. Krishnan. *A new type of secondary radiation*. Nature, 121:501–502, 1928.

[Ran12] P.C.-O. Ranitzsch, J.-P. Porst, S. Kempf, C. Pies, S. Schäfer, D. Hengstler, A. Fleischmann, C. Enss, and L. Gastaldo. *Development of Metallic Magnetic Calorimeters for High Precision Measurements of Calorimetric* ^{187}Re *and* ^{163}Ho *Spectra*. J. Low Temp. Phys., 167:1004–1014, 2012.

[Ray97] K. G. Ray and R. L. McCreery. *Simplified calibration of instrument response function for Raman spectrometers based on luminescent intensity standards*. Appl. Spectrosc., 51(1), 1997.

[Rei09] J. Reich. *Magnetfeldmessungen und Designarbeiten für das EMCS Luftspulensystem am KATRIN Hauptspektrometer*. Diploma thesis, Karlsruhe Institute of Technology, 2009.

[REN12] RENO Collaboration. *Observation of Reactor Electron Antineutrinos Disappearance in the RENO Experiment*. Phys. Rev. Lett., 108:191802, 2012.

[Res05] U. Resch-Genger, D. Pfeifer, C. Monte, W. Pilz, A. Hoffmann, M. Spieles, K. Rurack, J. Hollandt, D. Taubert, B. Schönenberger, and P. Nording. *Traceability in Fluorometry: Part II. Spectral Fluorescence Standards*. J. Fluorescence, 15:315–336, 2005.

[Rii11] A. S. Riis and S. Hannestad. *Detecting sterile neutrinos with KATRIN like experiments*. Journal of Cosmology and Astroparticle Physics, 2011(02):011, 2011.

[Rit34] D. Rittenberg, W. Bleakney, and H. C. Urey. *The Equilibrium Between the Three Hydrogens*. J. Chem. Phys., 2(1):4–49, 1934.

[Rob91] R. G. H. Robertson, T. J. Bowles, G. J. Stephenson, D. L. Wark, J. F. Wilkerson, and D. A. Knapp. *Limit on $\bar{\nu}_e$ mass from observation of the β decay of molecular tritium*. Phys. Rev. Lett., 67:957–960, 1991.

[Rod11] W. Rodejohann. *Neutrino-less Double Beta Decay and Particle Physics*. Int. J. Mod. Phys. E, 20(09):1833–1930, 2011.

[Roe12] M. Röllig, F. Priester, M. Babutzka, J. Bonn, B. Bornschein, G. Drexlin, S. Ebenhöch, Ernst W. Otten, M. Steidl, and M. Sturm. *Activity monitoring of a gaseous tritium source by beta induced X-ray spectrometry*. Fusion Eng. Des. (in press) doi:10.1016/j.fusengdes.2012.11.001, 2012.

[Rup12] S. Rupp. *Proof of concept of a calibration method for the laser Raman system for KATRIN based on the determination of the system's spectral sensitivity*. Diploma thesis, Karlsruhe Institute of Technology, 2012.

[Rup16] S. Rupp. *In preparation*. Phd thesis, Karlsruhe Institute of Technology, 2016.

[Ryc82] J. Rychlewski. *Frequency dependent polarizabilities for the ground state of* H_2, HD, *and* D_2. J. Chem. Phys., 78(12):7252–7259, 1982.

[Röl13] M. Röllig. *In preparation*. Phd thesis, Karlsruhe Institute of Technology, 2013.

[Sae00] A. Saenz, S. Jonsell, and P. Froelich. *Improved Molecular Final-State Distribution of* HeT^+ *for the* β*-Decay Process of* T_2. Phys. Rev. Lett., 84:242–245, 2000.

[SAG02] SAGE Collaboration. *Solar neutrino flux measurements by the Soviet-American gallium experiment (SAGE) for half the 22-year solar cycle*. J. Exp. Theo. Phys., 95:181–193, 2002.

[San12] A. G. Sánchez, C. G. Scóccola, A. J. Ross, et al. *The clustering of galaxies in the SDSS-III Baryon Oscillation Spectroscopic Survey: cosmological implications of the large-scale two-point correlation function*. Mon. Not. R. Astron. Soc., 425(1):415–437, 2012.

[Sav64] A. Savitzky and M. J. E. Golay. *Smoothing and Differentiation of Data by Simplified Least Squares Procedures.* Anal. Chem., 36(8):1627–1639, 1964.

[Sax70] S. C. Saxena and V. K. Saxena. *Thermal conductivity data for hydrogen and deuterium in the range 100-1100 degrees C.* J. Phys. A: General Phys., 3(3):309, 1970.

[Sch03] H. W. Schrötter. *Update of reviews on Raman spectra of gases I. Linear Raman spectroscopy*. J. Mol. Struct., 661 - 662(0):465 – 468, 2003.

[Sch05] G. Schulze, A. Jirasek, M. M. L. Yu, A. Lim, R. F. B. Turner, and M. W. Blades. *Investigation of Selected Baseline Removal Techniques as Candidates for Automated Implementation*. Appl. Spectrosc., 59(5):545–574, 2005.

[Sch09] M. Schlösser. *First Laser Raman measurements with tritium for KATRIN and studies of systematic effects of the LARA-setup*. Diploma thesis, Karlsruhe Institute of Technology, 2009.

[Sch11a] M. Schlösser and S. Fischer. *Investigation of halogen lamps as suitable black body radiators.* Internal report, Karlsruhe Institute of Technology, 2011.

[Sch11b] M. Schlösser. *The cLARAbrator – a tool for a true in-situ calibration source of the quantum efficiency of a LARA system*. Internal report, Karlsruhe Institute of Technology, 2011.

[Sch11c] M. Schlösser, S. Fischer, M. Sturm, B. Bornschein, R. J. Lewis, and H. H. Telle. *Design Implications for Laser Raman Measurement Systems for Tritium Sample-Analysis, Accountancy or Process-Control Applications*. Fusion Sci. Technol., 60(3):976–981, 2011.

[Sch11d] K. Schönung. *Test von Anti-Reflexionsbeschichtungen unter Tritiumatmosphäre für KATRIN*. Diploma thesis, Karlsruhe Institute of Technology, 2011.

[Sch11e] H. G. Schulze, R. B. Foist, K. Okuda, A. Ivanov, and R. F.B. Turner. *A Model-Free, Fully Automated Baseline-Removal Method for Raman Spectra*. Appl. Spectrosc., 65(1):75–84, 2011.

[Sch12a] M. Schlösser, S. Fischer, M. Hötzel, and W. Käfer. *Accuracy of the Laser Raman system for KATRIN*. Proceedings of the International School of Physics "Enrico Fermi", Course CLXXXII "Neutrino Physics and Astrophysics", edited by G. Bellini, pages 333–336, 2012.

[Sch12b] H. G. Schulze, R. B. Foist, K. Okuda, A. Ivanov, and R. F. B. Turner. *A Small-Window Moving Average-Based Fully Automated Baseline Estimation Method for Raman Spectra*. Appl. Spectrosc., 66(7):757–764, 2012.

[Sch13a] M. Schlösser, H. Seitz, S. Rupp, P. Herwig, C. G. Alecu, M. Sturm, and B. Bornschein. *In-Line Calibration of Raman Systems for Analysis of Gas Mixtures of Hydrogen Isotopologues with Sub-Percent Accuracy*. Anal. Chem., 85(5):2739–2745, 2013.

[Sch13b] M. Schlösser, T. M. James, S. Fischer, R. J. Lewis, B. Bornschein, and H. H. Telle. *Evaluation method for Raman depolarization measurements including geometrical effects and polarization aberrations*. J. Raman Spectrosc., 44(3):453–462, 2013.

[Sch13c] M. Schlösser, T. M. James, S. Fischer, R. J. Lewis, B. Bornschein, and H. H. Telle. *Supporting Information: Evaluation method for Raman depolarization measurements including geometrical effects and polarization aberrations*. J. Raman Spectrosc., 44(3):453–462, 2013.

[Sch13d] M. Schlösser, S. Rupp, H. Seitz, S. Fischer, B. Bornschein, T. M. James, and H. H. Telle. *Accurate calibration of the laser Raman system for the Karlsruhe Tritium Neutrino Experiment*. J. Mol. Structr. (in press) doi:10.1016/j.molstruc.2012.11.022, 2013.

[Sch13e] M. Schlösser, S. Rupp, H. Seitz, S. Fischer, B. Bornschein, T. M. James, and H. H. Telle. *Supplementary material: Accurate calibration of the laser Raman system for the Karlsruhe Tritium Neutrino Experiment*. J. Mol. Structr. (in press) doi:10.1016/j.molstruc.2012.11.022, 2013.

[Sch13f] V. Schäfer. *Charakterisierung des Coating Test Experiments zur Verbesserung der Langzeitstabilität und der Reproduzierbarkeit*. Diploma thesis, Karlsruhe Institute of Technology, 2013.

[Sch80] J. Schechter and J. W. F. Valle. *Neutrino masses in SU(2) $\otimes$ U(1) theories*. Phys. Rev. D, 22:2227–2235, 1980.

[Sch87] C. Schwartz and R. J. Le Roy. *Nonadiabatic eigenvalues and adiabatic matrix elements for all isotopes of diatomic hydrogen*. J. Mol. Spectrosc., 121:420–439, 1987.

[Sch95] P. Schmüser. *Feynman - Graphen und Eichtheorien Für Experimentalphysiker*. Springer-Verlag GmbH, 1995.

[Sch97] N. Schmitz. *Neutrinophysik*. Teubner Studienbücher. Teubner B.G. GmbH, 1997.

[Sei11] H. Seitz. *Kalibrierung des KATRIN Laser-Raman-Systems mit katalytisch hergestellten, inaktiven Wasserstoffisotopologmischungen*. Bachelor thesis, Karlsruhe Institute of Technology, 2011.

[Sem12] *532 nm RazorEdge® ultrasteep long-pass edge filter (LP03-532RU-25)*. Semrock Inc., 3625 Buffalo Road, Suite 6 Rochester, New York 14624 USA, 2012.

[Sha04] F. Sharipov. *Calculations of tritium flow between the buffer vessel up to the first vacuum system*. KATRIN internal report, 2004.

[Shr02] M. Shribak, S. Inoue, and R. Oldenbourg. *Polarization aberrations caused by differential transmission and phase shift in high-numerical-aperture lenses: theory, measurement, and rectification*. Opt. Eng., 41(5):943–954, 2002.

[Shu12] W. Shu (ITER org.). *Raman Spectroscopy for the ITER Tritium Plant Analytical System*. Private communication, 2012.

[Shu91] J. Shu, B. P. A. Grandjean, A. Van Neste, and S. Kaliaguine1. *Catalytic palladium-based membrane reactors: A review*. Can. J. Chem. Eng., 69(5):1036–1060, 1991.

[Sig12] B. Kayser. *High energy neutrinos and cosmic rays*. Proceedings of the International School of Physics "Enrico Fermi", Course CLXXXII "Neutrino Physics and Astrophysics", edited by G. Bellini, pages 145–184, 2012.

[Sis04] M. Sisti, C. Arnaboldi, C. Brofferio, et al. *New limits from the Milano neutrino mass experiment with thermal microcalorimeters*. Nucl. Instrum. Meth. A, 520(1-3):125 – 131, 2004.

[Sme23] A. Smekal. *Zur Quantentheorie der Dispersion*. Naturwissenschaften, 11:873–875, 1923.

[Smi06] A. Y. Smirnov. *Neutrino mass and New physics*. J. Phys. Conf. Ser., 53(1):44, 2006.

[Sne05] M. Sneep and W. Ubachs. *Direct measurement of the Rayleigh scattering cross section in various gases*. J. Quant. Spectrosc. Rad. Transfer, 92(3):293 – 310, 2005.

[SNO01] SNO Collaboration. *Measurement of the Rate of $\nu_e + d \rightarrow p + p + e^-$ Interactions Produced by ^8B Solar Neutrinos at the Sudbury Neutrino Observatory*. Phys. Rev. Lett., 87:071301, 2001.

[SNO08] SNO Collaboration. *Independent Measurement of the Total Active* ^{8}B *Solar Neutrino Flux Using an Array of* ^{3}He *Proportional Counters at the Sudbury Neutrino Observatory*. Phys. Rev. Lett., 101:111301, 2008.

[SNO12] SNO+ Collaboration. *Neutrinoless Double Beta Decay with SNO+*. J. Phys. Conf. Ser., 375(4):042015, 2012.

[Sou03] Soudan 2 Collaboration. *Measurement of the L/E distributions of atmospheric ν in Soudan 2 and their interpretation as neutrino oscillations*. Phys. Rev. D, 68:113004, 2003.

[Sou86] P. C. Souers. *Hydrogen Properties for Fusion Energy*. Univ of California Pr, 1986.

[Ste84] P. Steeger, T. Asakura, and A. Fercher. *Polarization preservation in circular multimode optical fibers and its measurement by a speckle method*. J. Lightwave Technol., 2(4):435 – 441, 1984.

[Stu10a] M. Sturm, M. Schlösser, R. J. Lewis, B. Bornschein, G. Drexlin, and H. H. Telle. *Monitoring of all hydrogen isotopologues at tritium laboratory Karlsruhe using Raman spectroscopy*. Laser Phys., 20(2):493–507, 2010.

[Stu10b] M. Sturm. *Aufbau und Test des Inner-Loop-Systems der Tritiumquelle von KATRIN*. Phd thesis, Karlsruhe Institute of Technology, 2010.

[Sup05] Super-Kamiokande Collaboration. *Measurement of atmospheric neutrino oscillation parameters by Super-Kamiokande I*. Phys. Rev. D, 71:112005, 2005.

[Sup98a] Super-Kamiokande Collaboration. *Measurements of the Solar Neutrino Flux from Super-Kamiokande's First 300 Days*. Phys. Rev. Lett., 81:1158–1162, 1998.

[Sup98b] Super-Kamiokande Collaboration. *Evidence for Oscillation of Atmospheric Neutrinos*. Phys. Rev. Lett., 81:1562–1567, 1998.

[T2K11] T2K Collaboration. *Indication of Electron Neutrino Appearance from an Accelerator-Produced Off-Axis Muon Neutrino Beam*. Phys. Rev. Lett., 107:041801, 2011.

[Tak93] H. Takeuchi, S. Hashimoto, and I. Harada. *Simple and Efficient Method to Eliminate Spike Noise from Spectra Recorded on Charge-Coupled Device Detectors*. Appl. Spectrosc., 47(1):129–131, 1993.

[Tay01] D. J. Taylor, M. Glugla, and R.-D. Penzhorn. *Enhanced Raman sensitivity using an actively stabilized external resonator*. Rev. Sci. Instrum., 72(4):1970–1976, 2001.

[Teb92] V. Teboul, J. L. Godet, and Y. Le Duff. *Collection Angle Dependence of the Depolarization Ratio in Light-Scattering Experiments*. Appl. Spectrosc., 46(3):476–478, 1992.

[Tel07] H. H. Telle, A. G. Ureña, and R. J. Donovan. *Laser Chemistry: Spectroscopy, Dynamics and Applications*. Wiley, 2007.

[Thu09] T. Thümmler, R. Marx, and C. Weinheimer. *Precision high voltage divider for the KATRIN experiment*. New J. Phys., 11(10):103007, 2009.

[TLA13] TLK Betriebsbüro. *Technische Liefer- und Abnahmebedingungen des Tritiumlabor Karlsruhe (TLA)*. TLK, 2013.

[Tor03] J. C. del Toro Iniesta. *Introduction to Spectropolarimetry*. Cambridge University Press, Cambridge, UK, 2003.

[Tur84] G. Turrell. *Analysis of polarization measurements in Raman microspectroscopy*. J. Raman Spectrosc., 15(2):103–108, 1984.

[Uda92] T. Uda, K. Okuno, and Y. Naruse. *Hydrogen isotope exchange reaction rate in tritium and methane mixed gas*. J. Radioanal. Nucl. Ch., 159:145–154, 1992.

[Val10] K. Valerius. *The wire electrode system for the KATRIN main spectrometer*. Prog. Part. Nucl. Phys., 64(2):291 – 293, 2010.

[Val11] K. Valerius, H. Hein, H. Baumeister, M. Beck, K. Bokeloh, J. Bonn, F. Glück, H.-W. Ortjohann, B. Ostrick, M. Zboril, and C. Weinheimer. *Prototype of an angular-selective photoelectron calibration source for the KATRIN experiment*. J. Instrum., 6(01):P01002, 2011.

[Van12] B. A. VanDevender, L. I. Bodine, A. W. Myers, J. F. Amsbaugh, M. A. Howe, M. L. Leber, R. G. H. Robertson, K. Tolich, T. D. Van Wechel, and B. L. Wall. *Performance of a TiN-coated monolithic silicon pin-diode array under mechanical stress*. Nucl. Instrum. Meth. A, 673(0):46 – 50, 2012.

[Veg13] H.J. de Vega, O. Moreno, E. Moya de Guerra, M. Ramón Medrano, and N.G. Sánchez. *Role of sterile neutrino warm dark matter in rhenium and tritium beta decays*. Nucl. Phys. B, 866(2):177 – 195, 2013.

[Vei87] D. K. Veirs and G. M. Rosenblatt. *Raman line positions in molecular hydrogen: H_2, HD, HT, D_2, DT, and T_2*. J. Mol. Spectrosc., 121:401–419, 1987.

[Wal82] G. E. Walrafen and P. N. Krishnan. *Model analysis of the Raman spectrum from fused silica optical fibers*. Appl. Opt., 21(3):359 – 360, 1982.

[Wan09] N. Wandkowsky. *Design and Background Simulations for the KATRIN Main Spectrometer and Air Coil System*. Diploma thesis, Karlsruhe Institute of Technology, 2009.

[Web00] R. (Eds.) Weber, W. H.; Merlin. *Raman Scattering in Materials Science (Springer Series in Materials Science)*. Springer, 2000.

[Wei03] C. Weinheimer. *Laboratory Limits on Neutrino Masses*. In Klaus Winter and Guido Altarelli, editors, *Neutrino Mass*, volume 190 of *Springer Tracts in Modern Physics*, pages 25–52. Springer Berlin Heidelberg, 2003.

[Wei13] C. Weinheimer. *Direct neutrino mass measurements*. Hyperfine Interact., pages 1–9, 2013.

[Woo05] S. Woosley and T. Janka. *The physics of core-collapse supernovae*. Nat. Phys., 1:47 – 154, 2005.

[Yu07] Yuanqin Yu, Ke Lin, Xiaoguo Zhou, Hua Wang, Shilin Liu, and Xingxiao Ma. *Precise measurement of the depolarization ratio from photoacoustic Raman spectroscopy*. J. Raman Spectrosc., 38(9):1206–1211, 2007.

[Zie89] L. D. Ziegler, Y. C. Chung, P. Wang, and Y. P. Zhang. *Depolarization ratios of resonance Raman scattering in the gas phase*. J. Chem. Phys., 90(8):4125–4143, 1989.

[Zub11] K. Zuber. *Neutrino Physics, Second Edition (Series in High Energy Physics, Cosmology and Gravitation)*. Taylor & Francis, 2011.

Danksagung

Beim Gelingen dieser Arbeit haben mich viele Personen in verschiedenster Weise unterstützt. Hiermit möchte ich allen danken, die ihren Anteil an dem Erfolg meiner Promotion haben.

Zunächst möchte ich meinem Betreuerdreigestirn danken, auf deren exzellente Betreuung und Förderung ich mich stets verlassen konnte. Ich habe somit in meiner Promotionszeit weit mehr lernen dürfen, als das was im direkten Bezug zu dieser Arbeit steht. Zunächst möchte ich hierbei meiner Vorortbetreuerin Dr. Beate Bornschein danken, die neben der wissenschaftlichen Diskussion und Motivation sehr viel Wert auf die Förderung meiner Persönlichkeit als Wissenschaftler gelegt hat. Das offene und vertrauensvolle Verhältnis (auch zu ihrem Mann Lutz Bornschein) habe ich sehr zu schätzen gelernt. Ebenso großen Dank möchte ich meinen beiden Referenten der Arbeit zukommen lassen. Prof. Dr. Guido Drexlin danke ich, da er mir nicht nur die Durchführung dieser spannenden Arbeit ermöglicht hatte, sondern mich ebenfalls in jeglicher Hinsicht gefördert und gefordert hatte, wo durch mir einige Türen geöffnet wurden. Schließlich danke ich Prof. Helmut Telle für die herausragende Zusammenarbeit auf jeglichster Ebene mit ihm. Ich konnte nicht nur von seiner Fachkompetenz profitieren, sondern ebenfalls beeindruckte mich seine Arbeitsweise und Einstellung nachhaltig.

Ich danke ebenfalls herzlich der Laser-Raman Gruppe von KATRIN, in der über Ländergrenzen hinweg eine vorbildliche und hocheffiziente Zusammenarbeit möglich ist. Den aktuellen und ehemaligen Mitglieder (inkl. Studenten) (Dr. Ahmed Alshahrie, Alex Bainbridge, Dr. Beate Bornschein, Tim Brunst, Sebastian Fischer, Philipp Herwig, Dr. Tim James, Steven Jones, Florian Kassel, Bennet Krasch, Simon Kudella, Dr. Richard Lewis, Sebastian Mirz, Silvia Napoli, Simone Rupp, Vera Schäfer, Kerstin Schönung, Hendrik Seitz, Dr. Michael Sturm und Prof. Dr. Helmut Telle) danke ich für das hervorragende Teamwork, das maßgeblich zum Gelingen dieser Arbeit beitrug. Hierbei möchte mich zunächst bei meinem langjährigen Doktorandenkollegen Sebastian Fischer für eine wunderbare Zusammenarbeit bedanken. In dem vertrauensvollen Verhältnis war nicht nur stets für die wissenschaftliche Diskussionen Platz, sondern ebenfalls für strategische und persönliche Ratschläge. Ich hoffe in der Zukunft ebenfalls mit einem Kollegen wie ihm zusammen arbeiten zu können. Furthermore, I want to thank Dr. Tim James who worked with me on the research field of depolarization measurements in a very intense and fruitful collaboration. Our quite complementary approaches to certain problems helped to profit strongly from each other. Thanks for the very nice time at Karlsruhe, Swansea, Madrid and Cluj.

Natürlich möchte ich noch jedem meiner sehr talentierten Diplomanden (Philipp Herwig, Simone Rupp) und Bachelorstudenten (Hendrik Seitz, Bennet Krasch) danken, in deren Betreuung ich zwar viel investiert habe, doch anderseits noch viel mehr zurückbekommen habe. Die Betreuung war stets von einem freundschaftlichen Verhältnis und erstklassiger Zusammenarbeit geprägt. Es freut mich sehr jetzt eure Entwicklung zu sehen. Ich danke ich auch Dr. Michael Sturm, der mir damals bei der Diplomarbeit einen einfachen Einstieg ermöglichte, für die gewissenhafte Leitung des übergeordneten Tasks "Tritiumloops" und die Organisation der Finanzen.

Ich danke dem Team des CAPER Experiments (Dr. David Demange, Eleonore Fanghänel, Thanh-Long Le und Karl-Heinz Simon) für die Füllung der Laser-Raman-Zellen mit Tritiumproben und für die damit verbundenen Vorbereitungen und aufwendigen Analysen.

Für Umbauarbeiten oder technische Anfertigungen aller Art danke ich Hans-Dieter Adami und Frank Kramer. Auf ihre die stete Hilfsbereitschaft sowie unkomplizierte Unterstützung konnte ich mich immer verlassen.

Ebenfalls bedanke ich mich für jegliche Hilfe bei elektronischen Problemen und deren Fehlersuche bei Helmut Dittrich, Frank Rehlinghaus, Florian Priester und Marco Röllig, sowie Steffen Jokisch und Georg Prokott vom IKP.

Bei der Inbetriebnahme und des Umbaus des HYDE Loops danke ich für tatkräftige Unterstützung Hans-Dieter Adami, Dr. Catalin-Gabriel Alecu und Stefan Welte.

Für eine gute und interessante Zusammenarbeit bei der Studie zur Bestimmung der Richtigkeitsanforderung an LARA mittels Kassiopeia-Simulationen danke ich Dr. Markus Hötzel sowie Dr. Wolfgang Käfer.

Ich danke weiterhin Prof. Dr. Robert J. LeRoy von der University of Waterloo in Kanada für die quantenmechanische Berechnung der Polarisierbarkeiten für alle sechs Wasserstoffisotopologe bei einer Wellenlänge von $532\,\mathrm{nm}$.

Für die hilfreiche Diskussion über die Bootstrapping-Methode danke ich Dr. Alan Poon vom Berkeley Lab in Kalifornien. Außerdem danke ich ihm für die konstruktiven Kritiken zu unseren Veröffentlichungen in seiner Funktion im KATRIN Publication-Committee.

Für die große Unterstützung bei der Lösung von technischen und wissenschaftlichen Problemen, danke ich Martin Babutzka, Dr. Uwe Besserer, Erhan Cilbir, Dr. David Demange, Bernhard Heinle, Robert Michling, Manfred Göckel, Dirk Osenberg, Florian Priester, Marco Röllig, Peter Schäfer, Robert Wagner, Stefan Welte sowie Dr. Jürgen Wendel.

Ebenfalls konnte ich mich bei der Unterstützung und Erledigung von administrativen (und informellen) Aufgaben stets auf die Sekretärinnen Eva Porter, Sylvia Krieger und Sonja Pawlowski verlassen.

Für das gewissenhafte und sorgfältige Korrekturlesen, danke ich meinen drei Betreuern, sowie Sebastian Fischer, Dr. Markus Hötzel, Dr. Klaus Schlösser, Hendrik Seitz, Dr. Michael Sturm und ganz besonders Simone Rupp.

Nicht unerwähnt bleiben sollen die "Back- und Kochevents im TLK" von Kerstin Schönung und Robin Größle, die stets ein besonders kulinarisches Erlebnis darstellten.

Ich danke außerdem dem Karlsruhe House of Young Scientists (KHYS) für die Unterstützung der Sommerschule 2011 in Varenna, des Gaststipendiums (zusammen mit Tim James beantragt), sowie für Veranstaltungsunterstützungen von Workshops in Österreich und Bad Herrenalb.

Weiterhin danke ich dem Graduiertenkolleg "Elementarteilchenphysik bei höchster Energie und höchster Präzision" für die Ermöglichung der Teilnahme an verschiedenen Workshops als Kollegiat.

Ich danke allen wechselnden 'Container'-Zimmerkollegen über die gesamte Diplom- und Doktorarbeitszeit: Tim Brunst, Sebastian Fischer, Philipp Herwig, Norbert Kernert, Bennet Krasch, Kerstin Schönung, Hendrik Seitz, Monika Sirch, Simone Rupp, Johannes Weis, Werner Wurster und (als Quasikollegin auch) Thouraya Chabbi. Es war von einer überaus freundlichen Stimmung geprägt, sodass ich mich Tag für Tag freute das Büro zu betreten.

Natürlich danke ich auch allen bisher nicht genannten Kollegen des Tritiumlabors für eine äußerste angenehme Arbeitsatmosphäre, sowie für die zahlreichen Aktionen außerhalb der Arbeit: Alaadin Aktas, Alexander Beck, Dr. Nicolas Bekris, Olga Borisevich, Adalbert Braun, Dr. Andras Bükki-Deme, Dr. Ion Cristescu, Julia Dusold, Sylvia Ebenhöch, Dr. Woo Sik Gil, Nando Gramlich, Moritz Hackenjos, Manuel Klein, Beate Kloppe, Zoltan Köllö, Alexander Krauß, Lusia La Cascio, Nancy Lohr, Christin Melzer, Harald Moosmann, Simon Niemes, Ioan-Catalin Petrutiu, Christoph Plusczyk, Fabian Schneck, Peter Schuster, Michael Schwarz und Sascha Singer.

Ich bedanke mich außerdem bei allen Mitarbeitern von KATRIN, die täglich mit vollem Einsatz zum erfolgreichen Gelingen des Experiments beitragen. Besonderer Dank gilt den Bachelor- und Masterstudenten, Diplomanden und Doktoranden (einschließlich denen von EDELWEISS) für eine interessante, gemeinsame Zeit auch außerhalb des KITs (Tagungen, Stammtische, Sportaktionen, ...). Stefan Groh und Nancy Wandkowsky danke ich für eine erlebnis- und lehrreiche Woche bei der Sommerschule in Varenna.

Ebenso danke ich Prof. Dr. Mathias Noe für die anerkennende Förderung, sowie der ITEP Administration für die reibungslose Zusammenarbeit. Allen ITEP "Young-Scientists" gilt mein Dank für vier hochinteressante und unvergessliche Workshops in Österreich.

Zuletzt möchte ich noch meinen Eltern und Geschwistern danken, die mir stets den Rücken freigehalten haben und viel Verständnis für Zeiten aufgebracht haben, in denen ich mich vorwiegend der Arbeit widmen musste. Dies gilt ebenso für Freunde und Judokollegen mit denen ich ein wunderbare Zeit neben der Arbeit verbracht habe, wodurch ich einen guten Ausgleich hatte. Zuallerletzt danke ich Theresa für das langjährige Verständnis für die zeitliche Einschränkung, die eine solche Arbeit manchmal mit sich bringt.